Attachment 2: Westinghouse Responses to NRC RAIs Related to WCAP-17788, Volumes 1 and 4 Supporting the Closure of GSI-191 (PA-SEE-1090) and Mark-ups to WCAP-17788 NON-PROPRIETARY Attachment

The RAIs addressed herein were provided to the Pressurized Water Reactor Owners Group (PWROG) via the following document:

NRC Correspondence, "Request for Additional Information Related to Volume 1 of Pressurized Water Reactor Owners Group Topical Report WCAP-17788 'Comprehensive Analysis and Test Program for GSI-191 Closure,'" April 2016, ADAMS Accession No. ML16078A166.

NRC Correspondence, "Request for Additional Information Regarding Pressurized Water Reactor Owner's Group Topical Report WCAP-17788, 'Comprehensive Analysis and Test Program for GSI-191 Closure,' (TAC No. MF6536)," August 2016, ADAMS Accession No. ML16228A527.

RAI-1.1

The method to define debris limits provided in the submittal is said to apply to all fuel designs in production by Westinghouse and Areva as of January 2015, except for Areva fuel with the TRAPPER fine mesh filter. This design was not tested as part of the program even though it is still used in some plants. The submittal states:

> "The use of the TRAPPER fine mesh filter fuel design in limited quantities would not alter the limits defined by the methodology."

a. Provide justification that the limits in this methodology would not be altered if the TRAPPER fine mesh filter fuel design is in use. Provide any pertinent limitations regarding the presence of fuel assemblies with this filter in the reactor core.

Response

The response to this question is provided in OG-17-70 (Reference RAI-1.1-1).

b. Provide a list of fuel types and designs that were tested as part of the program.

Response

The response to this question is provided in OG-17-70 (Reference RAI-1.1-1).

c. Provide a list of fuel designs that the method in this submittal applies to. Include identification and description of the fuel types, bottom nozzle designs, and spacer grid designs.

Response

The NRC reviewer is requesting additional information that justifies how the tested fuel designs bound the untested designs. Additionally, information is provided to explain how a fuel assembly with a pitch not equal to the tested value of [ ]^{a,c} is scaled to determine an equivalent fibrous debris loading in units of grams per fuel assembly (g/FA).

In the original response to this question (Reference RAI-1.1-1), a list of Westinghouse and AREVA fuel designs that the WCAP-17788 in-vessel debris methodology applies to was provided. Table RAI-1.1-1 repeats the list of Westinghouse fuel for convenience. Table RAI-1.1-2 repeats the list of AREVA fuel for convenience (note that Table RAI-1.1-2 is updated to include the fuel assembly pitch in lieu of the rod pitch).

Table RAI-1.1-1 Applicable Westinghouse Fuel Designs

Fuel Array	Fuel Assembly Pitch (in)	Fuel Assembly Flow Area (in^2)	Fuel Rod OD (in)	Bottom Nozzle Hole Dia. (in)	Debris Grid Filter Design
14x14 422V+	[			] a,c	NA
15x15 UFA					P-Grid
16x16 STD					Guardian
16x16 CE					Guardian
16x16 NGF					Guardian
17x17 OFA					P-Grid
17x17 RFA					P-Grid
17x17 XL RFA					P-Grid
17x17 NGF					P-Grid

Table RAI-1.1-2 Applicable AREVA Fuel Designs

Fuel Assembly Type	Plant Type	Lattice	FA Pitch (in)	Rod Diameter (in)	Intermediate Grid Type	Bottom Grid Type	Lower End Fitting
Mark-B-HTP-1	B&W	15x15	[				] a,c
Advanced W17 HTP	Westinghouse	17x17					
W17HTP	Westinghouse	17x17					
W17HTP	Westinghouse	17x17					
W15HTP	Westinghouse	15x15					
CE16HTP	CE	16x16					
CE15HTP	CE	15x15					
CE14HTP	CE	14x14	]				[

Not all fuel designs listed in Tables RAI-1.1-1 and RAI-1.1-2 were explicitly tested in the WCAP-17788 subscale head loss test program. The subscale head loss program tested the Westinghouse 17x17 RFA bottom nozzle with a Protective Grid (P-grid) and the AREVA **FUELGUARD™** lower end fitting to define the WCAP-17788 core inlet debris limits.

The testing determined that formation of a single debris bed on the bottom nozzle surface resulted in the limiting head loss, compared to a situation in which the fibrous debris is distributed across multiple debris beds at different locations within the fuel assembly. With regard to head loss across a debris bed formed on the bottom nozzle, it was determined that bottom nozzle hole diameter was the critical geometric parameter. Smaller hole sizes resulted in increased fiber capture and head loss. Therefore, the RFA bottom nozzle was selected to define the subscale final limits for Westinghouse supplied fuel since it had the smallest bottom nozzle hole diameter.

As shown in Table RAI-1.1-1, the tested bottom nozzle hole size of [ ]^{a,c} is equal to or smaller than the bottom nozzle hole sizes of all fuel types except the 14x14 422V+ design. This fuel design is only used in Westinghouse 2-loop upper plenum injection (UPI) plants. As described in Section 8 of WCAP-17788, Volume 1, the in-vessel debris methodology for Westinghouse UPI plants does not rely on testing results from the subscale head loss test program. Rather, UPI plants use the approved 15 g/FA core inlet fibrous debris limit defined in WCAP-16793-NP-A, Rev. 2 (Reference RAI-1.1-2). As such, justification of this fuel type is not required since the subscale testing results are not used to define the core inlet debris limit.

The entrance gap for the AREVA FUELGUARD is identical for all fuel designs described in Table RAI-1.1-2. Therefore, the tested design is applicable to all of the AREVA supplied fuel.

The fuel assembly pitch is another factor that needs to be considered when justifying the applicability of the WCAP-17788 debris limits to fuel designs not tested. The tested fibrous debris loads, and associated limits defined in WCAP-17788 are presented in units of g/FA. The tested debris loads were scaled to a full-area fuel assembly assuming an assembly pitch of [ ]^{a,c} If the assembly pitch is different, the fibrous debris load must be adjusted to account for this difference. Table 3-7 of WCAP-17788, Volume 6 reports the scaling factor for the tested bottom nozzles (fuel assembly pitch [ ]^{a,c}) to be [ ]^{a,c}

If the fuel design has a different fuel assembly pitch, the first step is to determine the appropriate scaling factor, R_m:

$$R_m = \frac{R}{A_s}(P_{FA})^2 = \left[\quad\right]^{a,c} \qquad \text{Eq. RAI-1.1-1}$$

FUELGUARD is a trademark or registered trademark of its respective owner. Other names may be trademarks of their respective owners.

Where,

R = the scaling factor applied in WCAP-17788, Volume 6.

A_s = the subscale test column flow area.

P_{FA} = the pitch of the fuel assembly being scaled.

Using Eq. RAI-1.1-1, the fibrous debris limits reported in WCAP-17788 can be scaled to a fuel assembly pitch that is different than the tested pitch of [ ]^{a,c}

$$M_{sd} = M_d \times R_m \left[\frac{g}{FA}\right] \quad \text{Eq. RAI-1.1-2}$$

Where,

M_{sd} = the scaled debris load in units of g/FA for a fuel assembly with pitch, P_{FA}.

M_d = the debris load in units of g/FA reported in WCAP-17788.

R_m = the scaling factor determined from Eq. RAI-1.1-1.

Review of Tables RAI-1.1-1 and RAI-1.1-2 indicates that the Babcock and Wilcox (B&W) and Combustion Engineering (CE) fuel products have a different fuel assembly pitch than what was used to determine the WCAP-17788 fibrous debris limits presented in units of g/FA. As such, the fibrous debris limits for these fuel products need to be determined from the scaling approach defined above.

For example, the scaling factor R_m for 16x16 STD and 16x16 NGF fuel products is calculated as:

$$R_m = \left[\quad\right]^{a,c}$$

This value is then applied to the fibrous debris loads reported in WCAP-17788. For example, per Table 6-3 in WCAP-17788, Volume 1, a CE plant with Westinghouse fuel has a reported core inlet fibrous debris limit of [ ]^{a,c} If the plant has 16x16 STD or 16x16 NGF fuel, this value must be scaled using the calculated R_m value of [ ]^{a,c} which results in a scaled core inlet fibrous debris limit of [ ]^{a,c} for these fuel types.

In conclusion, the WCAP-17788 in-vessel debris methodology is applicable to all Westinghouse fuel products listed in Table RAI-1.1-1 and the AREVA fuel products listed in Table RAI-1.1-2 provided that the appropriate scaling is made to the debris limits presented in WCAP-17788 to account for any difference in fuel assembly pitch. If the fuel assembly pitch is different than [ ]^{a,c}

Eq. RAI-1.1-1 is used to calculate a scaling factor which is applied to the debris limits defined in WCAP-17788 to adjust the debris limit to a specific fuel assembly pitch.

Updates will be made to WCAP-17788, Volume 1, Sections 6.3 and 6.5 to identify and explain this additional step.

d. What are the evaluation criteria for applicability of this method to fuel designs developed after January 2015?

Response

As described in WCAP-17788, Volume 1, Section 4, the debris limits defined can be applied directly to fuel assembly designs that are in production by Westinghouse and AREVA as of January 2015. A list of applicable fuel assembly designs is provided in the response to RAI-1.1.c. However, fuel assembly designs are continuously evolving and changing in order to improve fuel reliability and increase performance during both normal operation and postulated accidents. The majority of design changes are small, incremental changes to existing fuel assembly components. Occasionally, the changes are significant enough such that they result in a "new" fuel assembly design.

As the fuel assembly designs evolve and change, the following question must be answered regardless of the extent of the design change(s), "*Will the proposed change affect the in-vessel debris limits calculated using the method described in WCAP-17788?*" This question will have to be answered by the licensee and/or fuel vendor in accordance with applicable regulatory guidance and regulations, including 10CFR50.59. An overview of the evaluation process, including specific criteria that should be considered when evaluating fuel assembly design changes or new fuel assembly designs when applying the WCAP-17788 methodology (i.e., answering the above question), is provided below. The evaluation can include: (1) an analytical assessment, (2) additional testing, or (3) some combination of both. The details of the evaluation process will be defined by each utility and/or fuel vendor.

As described in WCAP-17788, Volume 1, the primary concern related to in-vessel debris is the accumulation of debris on fuel assembly components (e.g., bottom nozzle/lower end fitting or spacer grids). Changes to fuel assembly components that have the potential to affect the debris accumulation characteristics are of primary importance. Changes that affect the fuel assembly loss coefficient can be an indicator of such changes. While a change in the fuel assembly loss coefficient is normally not a significant concern for post-LOCA conditions (the post-LOCA flow rates are too low to register a meaningful pressure drop across these components without debris), a change in the fuel assembly loss coefficient (or steady-state pressure drop) may be indicative of a change that should be investigated relative to the ability to capture debris.

Bottom Nozzle/Lower End Fitting Changes

The bottom nozzle/lower end fitting is an important fuel assembly component relative to GSI-191. The subscale testing documented in WCAP-17788, Volume 6 determined that for a given fibrous

debris mass, the limiting fuel assembly pressure drop occurred when a single debris bed formed on the bottom nozzle/lower end fitting (as opposed to a condition in which debris is distributed in multiple beds at several locations within the bundle). The subscale testing considered two distinct bottom nozzle/lower end fitting designs. The results of this testing may be used to evaluate bottom nozzle/lower end fitting changes relative to their ability to capture debris. If the changes are too extensive to provide an analytical assessment (i.e., too unlike the designs tested), testing may be required to justify the WCAP-17788 limits or to define new debris limits for the bottom nozzle/lower end fitting design change.

Spacer Grid Changes

The spacer grids are also important fuel components relative to the GSI-191 issue as they can result in the capture of debris due to their complex geometry and small flow areas. While typically not limiting for GSI-191, if the changes to the spacer grid designs are extensive, the fuel assembly testing conclusions reached in WCAP-17788, Volume 6 could be affected. The results of previous testing may be used to evaluate new spacer grid designs relative to their ability to capture debris. If an analytical assessment cannot be made, testing may be required to provide new data for the spacer grid changes.

Top Nozzle/Upper End Fitting Changes

The top nozzle/upper end fitting is not a limiting fuel component relative to the GSI-191 issue and specifically with respect to the capture of debris in the fuel assembly. Unless there is a significant change, such as increasing the component loss coefficient such that the fuel assembly pressure drop is significantly increased, most changes to this fuel component could be evaluated as having no adverse impact on the GSI-191 issue. The results and conclusions of WCAP-17788 would remain valid and bounding in this case.

Fuel Rod, Guide Tube and Instrument Tube Changes

The fuel rod, guide tube, and instrument tube designs are typically not limiting fuel components relative to the GSI-191 issue and specifically with respect to the capture of debris in the fuel assembly. Unless there is a significant design change, such as increasing the fuel rod and/or tube diameter or adding more guide tubes to the fuel assembly, most changes to these fuel components could be evaluated as having no adverse impact on the GSI-191 issue. The results and conclusions of WCAP-17788 would remain valid and bounding in this case.

Summary and Conclusion

In general, most changes to fuel assembly designs tend to fall into the category of minor manufacturability/design changes which are small improvements to existing designs. These types of changes can generally be evaluated to be bounded by the testing and analyses presented within WCAP-17788. However, certain changes may have an uncertain or potentially significant effect on the GSI-191 in-vessel debris limits, and they must be more extensively evaluated to ensure that the WCAP-17788 limits continue to be applicable.

It is important that cumulative effects also be considered. That is, any new evaluation of a fuel assembly component change needs to consider any prior evaluations of other component changes related to the GSI-191 issue. While a single design change may not have a significant impact on the GSI-191 issue, a combination of changes of relatively small magnitude may have a larger cumulative effect.

Plants that use the WCAP-17788 methodology to determine in-vessel debris limits must evaluate fuel assembly design changes in accordance with applicable regulatory guidance and regulations. The evaluation of a fuel assembly design change can include: (1) an analytical assessment, (2) additional testing, or (3) some combination of both. The details of this evaluation process will be defined by each utility and/or fuel vendor.

References

RAI-1.1-1 PWR Owners Group Correspondence, ADAMS Accession No. ML17069A174, "Submittal of Responses to NRC Requests for Additional Information (RAIs) and Revisions to Topical Report WCAP-17788-P/WCAP-17788-NP, Revision 0, "Comprehensive Analysis and Test Program for GSI-191 Closure" related to Volume 1 and Volume 6 in Support of the Closure of GSI-191 (PA-SEE-1090)," March 8, 2017.

RAI-1.1-2 WCAP-16793-NP-A, Revision 2, "Evaluation of Long-Term Cooling Considering Particulate, Fibrous and Chemical Debris in the Recirculation Fluid," July 2013.

RAI-1.2 Item a

The trends in Figures 6-4, 6-6, and 6-8 show that as the resistance at the core inlet ($K\text{-}K_{split}$) increases, the flow through the alternate flow paths increases for various emergency core cooling system (ECCS) recirculation flow rates.

a. As seen in Figure 6-4, there is a nearly vertical ramp in the fraction of ECCS flow through the upper head spray nozzles (UHSN) at $K\text{-}K_{split}$ of about 10,000 for a flow rate of 40 gallons per minute (gpm) per fuel assembly (FA). What is the reason for this sudden increase in the UHSN flow fraction amounting to about 15 percent of the maximum observed value?

Response

WCOBRA/TRAC uses flow regime maps to describe two-phase flow patterns and subsequent calculations for interfacial heat and mass transfer, interfacial drag, and wall drag. These calculations are dependent on the flow regime identified by the flow regime maps. Before selecting a flow regime for a given mesh cell, WCOBRA/TRAC performs a check to assure that the local flow regime is consistent with the global flow pattern. This is done by checking the void fraction difference between two axial mesh cells. These checks are described in WCAP-16009-P-A, Section 3-2-1 (Reference RAI-1.2-1). If a large void gradient is calculated, certain ramps are applied and the void fractions used in the calculations of the interfacial quantities to determine flow regime transitions for the mesh cell are redefined using averaging schemes that depend on the specific condition. When a large void gradient between two cells is not present, the void fractions at the momentum cell center are assumed to be [ ]^{a,c}

When resistance due to the accumulation of debris is simulated in the downflow plant model, liquid provided by the ECCS fills the downcomer and cold leg piping. Eventually, the downcomer liquid level reaches the UHSN nozzles and liquid begins to fill the upper head region. When the upper head liquid level reaches the upper guide tube elevation liquid begins to drain into the upper plenum. As the upper guide tubes are initially highly voided, the resulting flow pattern is an inverted pool with a large void gradient between the upper head region and the upper guide tubes. The sudden increase in the UHSN flow fraction is related to the WCOBRA/TRAC logic used to determine the void fraction at the upper head and guide tube interface and the subsequent calculations for the interfacial drag and wall drag. The void fraction logic to determine the local flow regime at this interface transitions between averaging schemes at this point, and the global two-phase flow pattern changes as a result.

This behavior was only observed in the 40 gpm/FA case because this was the only case that had an UHSN flow large enough to fill the upper head region to nearly liquid solid. In the other cases the UHSN flow was lower and the switch in void fraction logic did not occur. It is also noted that the revised 40 gpm/FA downflow plant K_{split}/m_{split} calculations presented in the response to RAI-4.20 do not experience this effect because the UHSN resistance was increased as described in the response to RAI-4.2. The increase in UHSN resistance limited the flow into the upper head such that the volume did not fill with liquid to the same level observed in the original 40 gpm/FA flow case.

Reference

RAI-1.2-1 WCAP-16009-P-A, "Realistic Large-Break LOCA Evaluation Methodology Using the Automated Statistical Treatment Of Uncertainty Method (ASTRUM)," January 2005.

RAI-1.9

How is the flow area used in the thermal hydraulics analysis to simulate resistance due to a debris bed (A_{TH}) calculated in Equation 6-3?

Response

In the original response to this question (Reference RAI-1.9-1), the Combustion Engineering (CE) and Babcock & Wilcox (B&W) flow areas calculated were slightly different than the values reported in WCAP-17788. The response stated that the differences were negligible and did not require revisions to WCAP-17788 to reflect the recalculated flow areas.

The NRC reviewer has requested that WCAP-17788 be updated to reflect the new flow areas. As such, the original response to this question is being revised to state that the CE and B&W flow areas used in the thermal hydraulics analysis to simulate resistance due to a debris bed will be updated to be consistent with the flow areas calculated in the original response to this question. The updated CE fuel assembly flow area is [ ]^{a,c} Since each of the 217 assemblies in the core have these dimensions, the full core area is calculated to be [ ]^{a,c} The updated B&W fuel assembly flow area is [ ]^{a,c} Since each of the 177 assemblies in the core have these dimensions, the full core flow area is calculated to be [ ]^{a,c}

WCAP-17788, Volumes 1 and 4 will be updated to reflect these areas.

Reference

RAI-1.9-1 PWR Owners Group Correspondence, ADAMS Accession No. ML17069A174, "Submittal of Responses to NRC Requests for Additional Information (RAIs) and Revisions to Topical Report WCAP-17788-P/WCAP-17788-NP, Revision 0, "Comprehensive Analysis and Test Program for GSI-191 Closure" related to Volume 1 and Volume 6 in Support of the Closure of GSI-191 (PA-SEE-1090)," March 8, 2017.

RAI-4.1, Vol. 4

General Design Criterion (GDC) 35, "Emergency Core Cooling," in Appendix A, "General Design Criteria for Nuclear Power Plants," to Title 10 of the Code of Federal Regulations (10 CFR) Part 50, requires that a single failure be assumed when analyzing safety system performance. Sections 8.2, 9.2, 10.2, and 11.2 present safety system performance analysis results for four different plant categories.

a. Describe the single failure assumptions implemented in the analyses of the safety system performance for the four analyzed plant categories. Identify the single failure assumption(s) applied in the modeling of the reactor coolant system (RCS) response including the performance of the emergency core cooling system (ECCS). Justify the assumptions by describing pertinent conditions, supporting considerations, and applicable analyses.

Response

The analyses consider the effect of the limiting single failure on ECCS performance. During the injection phase of the accident transient, failure of one train of ECCS is assumed. The minimum safety injection (SI) flowrate for a single train of ECCS and maximum SI delay times are used based on plant technical specification limits from the base plant models selected for each plant category. The base plant models are identified and described in the response to RAI-4.29. The limiting single failure also takes into account the effect on containment pressure. Failure of an entire safety train would result in the loss of one or several containment spray and fan cooling units, reducing containment cooling, and increasing containment pressure, which will reduce cladding temperatures during a debris-induced secondary heatup by increasing the liquid inventory in the reactor vessel. The inputs to the containment pressure are skewed in order to obtain a conservative (low) pressure transient such that cladding temperatures during any calculated debris-induced secondary heatup are maximized.

The ECCS performance assumptions applied during the recirculation phase of the accident are disconnected from those applied during the injection phase of the accident transient. In the simulations, an early sump switchover time is applied that is representative of two trains of safety injection during the injection phase. An early sump switchover time is more limiting for Generic Safety Issue (GSI) -191 scenarios since the decay heat is higher and RCS liquid inventory is lower. Sensitivity studies presented in the response to RAI-4.19 Item b. demonstrate that an earlier arrival of debris results in a higher calculated cladding temperature during the debris-induced heatup. The ECCS recirculation flow rates used in the analyses considered both single and two-train operation. As described in the response to RAI-4.1 Item c., utilities implementing the WCAP-17788 in-vessel debris methodology will need to verify that they fall within the range of conditions considered by the analyses. More details regarding how this check is performed are provided in the response to RAI-4.5 Item a.

b. The analyses for the Combustion Engineering (CE) plant category were performed with the containment backpressure computed by a coupled containment code. Demonstrate how the single failure assumptions implemented in the RCS response analysis for this plant category, as well as any additional and related assumptions, were considered for the purposes of calculating the containment backpressure response. Verify that treatment is consistent with Assumption No. 6 in Section 4.1, "Major Assumptions," and Input No. 6 in Section 4.2, "Critical Inputs."

The response to this question is provided in the CE submittal

c. Provide information that demonstrates whether plant-specific considerations are necessary to address GDC 35 when considering safety system performance on a plant-specific basis. Explain how the single failure assumptions implemented in the T-H analyses in Sections 8.2, 9.2, 10.2, and 11.2, as considered in the response to Items a and b above, remain valid for each plant category. Describe how it was determined whether additional single failure assumptions and applicable supporting considerations were required for plant specific T-H analyses. If necessary, identify the types of plant specific information related to systems, conditions, parameters, and other relevant items that will need to be considered for adequate implementation of the topical report (TR) with respect to GDC 35 on a plant specific basis.

Response

Plant-specific considerations are necessary to address GDC 35 and should be addressed by each utility when implementing the WCAP-17788 methodology as part of their GL 2004-02 supplemental responses. Each plant-specific submittal will have to justify applicability of the methodology. Each plant will need to determine their limiting GSI-191 scenario relative to debris accumulation in the reactor vessel, considering appropriate single-failure assumptions. Once the limiting GSI-191 in-vessel debris accumulation scenario is defined, a plant will need to demonstrate that it falls within the bounds of the WCAP-17788 methodology. The response to RAI 4.5 provides details regarding the confirmation checks that each utility must complete to justify applicability of the WCAP-17788 methodology.

RAI-4.2, Vol. 4

Section 6.1 states that "a method was developed to calculate appropriate BB [Barrel/Baffle] flow resistances for use in this analysis" so that all Westinghouse upflow plants in operation in the U.S. are represented. The section further clarifies that "the method and supporting calculations are contained in Reference 6-2, which confirms that the BB flow resistances shown in Table 6-1 bound all Westinghouse upflow plants." With regard to the Westinghouse downflow plant design category, Section 6.2 explains that "a method was developed to calculate appropriate UHSN [Upper Head Spray Nozzle] flow resistances for use in this analysis" and that "the method and supporting calculations are contained in Reference 6-2, which confirms that the UHSN flow resistances shown in Table 6-2 bound all Westinghouse downflow plants." Reference 6-2 is identified in Section 6.5, as follows.

Reference 6-2: [

].

a. Provide a copy of Reference 6-2.

Response

Responding to this RAI resulted in changes to WCAP-17788, Volume 4, Reference 6-2. As such, Reference 6-2 is superseded by this RAI response. WCAP-17788, Volume 4, Section 6.1, Section 6.2, and Section 6.5 will be updated to reflect removal of Reference 6-2, and the following discussion will be added as an appendix to WCAP-17788, Volume 4.

Barrel/baffle (BB) and upper head spray nozzle (UHSN) loss coefficients are needed for modeling core inlet blockage scenarios for the GSI-191 thermal-hydraulic (TH) analyses. The BB channel and UHSNs are considered alternate flow paths (AFPs) for which coolant can bypass the core inlet during core blockage scenarios. Since the AFPs are being credited to remove decay heat following core inlet blockage, loss coefficients need to be determined that bound all plants being evaluated. The objective is to determine maximum BB and UHSN resistances that bound all Westinghouse pressurized water reactors (PWRs) operating in the U.S. Three exceptions exist:

1. The GSI-191 TH analyses do not include upper plenum injection (UPI) plants. As discussed in WCAP-17788, Volume 1, Chapter 8, the UPI plant in-vessel debris methodology does not rely on the GSI-191 TH analyses. Therefore, UPI plants are not considered when determining maximum AFP resistances

2. The South Texas Project (STP) plant is unique in that it has a 14 ft active core. All other U.S. PWRs have a 12 ft active core. As such, STP could not be bounded by the base plant models used for the GSI-191 AFP analyses. A description of the STP BB channel is provided in the response to this RAI; however, the STP BB channel is not considered when determining the maximum BB channel resistance for the Westinghouse upflow base plant model (See Step 2 below).

3. The Westinghouse downflow plant category uses two different UHSN resistances. The resistance used in the analyses that determine the parameters K_{max}, K_{split}, and m_{split} bound all downflow plants considered.

The analysis used to determine the parameter t_{block} does not bound all downflow plants. (See Step 3 below). For plants with UHSN resistances that are not bounded by the t_{block} analysis, the hot leg switchover time can be justified as an appropriate surrogate for the parameter t_{block} when implementing the WCAP-17788 in-vessel debris methodology.

The Westinghouse U.S. PWR fleet is broken into two plant categories. Westinghouse upflow BB plants credit the BB channel and Westinghouse downflow plants credit the UHSNs. It is noted that WCAP-17788, Volume 4 also provides a minimum BB channel loss coefficient. The analyses that used the minimum BB channel resistance have since been revised to use a maximum BB resistance (See RAI-4.20). As such, discussion regarding determination of the minimum BB and UHSN resistance is omitted herein.

The following general approach is applied for determining the AFP resistances used in the GSI-191 TH analyses:

Step 1 – Determine the total resistance (K/A^2) for the AFP (BB channel or UHSNs) from physical plant geometry.

Step 2 – Determine an equivalent maximum AFP resistance for the base plant models (upflow and downflow plant categories) for use in the GSI-191 analyses that bound all plant AFP resistances.

Step 3 – Convert the equivalent maximum AFP resistances to equivalent loss coefficients for entry into the WCOBRA/TRAC base plant models.

Each step is discussed in the following sections.

Step 1

The name, plant type, and rated power for each Westinghouse unit considered in determining the AFP resistances are provided in Table RAI-4.2-1. The rated power in the table is the licensed power for each unit taken from Reference RAI-4.2-1. In general, the AFP geometry is similar among plant types; however, there are exceptions. Determination of the AFP resistances is broken into the plant types shown in Table RAI-4.2-1. Any plant-specific exceptions are discussed separately.

When determining total BB channel resistance, losses through the BB channel inlet, former plates, and outlet are considered. Tables RAI-4.2-2 through RAI-4.2-4 list the plant drawing numbers used to determine the BB channel inlet, former plates, and outlet geometry, respectively. The total UHSN resistance considers losses through the upper core barrel flange (inlet), nozzle body, upper support plate, and nozzle exit. Table RAI-4.2-5 lists the plant drawing numbers used to determine the UHSN geometry.

In WCAP-17788, Volume 4, Reference 6-2 AFP geometry (reference area) and loss coefficients were taken directly from THRIVE, which is a methodology used to calculate core bypass flows under normal operating conditions. In response to this RAI, the THRIVE calculations were reviewed and repeated using the plant drawings identified in Tables RAI-4.2-2 through RAI-4.2-5. In most cases, the recalculated areas and loss coefficients agreed very well with the THRIVE values. In a few instances adjustments were made to the values used for the GSI-191 TH analyses.

Barrel/Baffle Inlet Reference Area

The BB inlet geometry is similar for Westinghouse 3 and 4 loop standard (design) upflow and 3 loop converted upflow plants. The BB inlet for these plants consists of a gap between the bottom of the baffle plates and the top of the lower core plate that extends around the entire core periphery. Figure RAI-4.2-1 shows the BB inlet geometry for these plant types. The dimension of the gap varies across plant types. The BB inlet geometry is different for Westinghouse 4 loop converted upflow plants. The BB inlet for these plants consists of a series of holes in the periphery of the lower core plate. Figure RAI-4.2-2 shows the BB inlet geometry for these plant types. The red highlighted holes connect the lower plenum to the BB channel.

Table RAI-4.2-6 provides the dimensions and the inlet reference area for the BB inlets. The BB inlet reference area for Westinghouse 3 and 4 loop standard upflow and 3 loop converted upflow plants is calculated by multiplying the gap dimension by the inside perimeter of the baffle plates:

$$A_{inlet} = GAP \times P_{Baffle\ Plate}. \qquad \text{Eq. RAI-4.2-1}$$

The BB inlet reference area for Westinghouse 4 loop converted upflow plants is calculated by summing the areas of the three hole sizes together:

$$A_{inlet} = N_1 \frac{\pi}{4} {D_1}^2 + N_2 \frac{\pi}{4} {D_2}^2 + N_3 \frac{\pi}{4} {D_3}^2 \qquad \text{Eq. RAI-4.2-2}$$

The BB inlet reference areas, calculated using the dimensions provided in Table RAI-4.2-6, agree well with the historical THRIVE values.

Barrel/Baffle Inlet Loss Coefficient

The loss coefficients originally used as input to the Westinghouse thermal hydraulic analyses were taken from THRIVE. Many of the loss coefficients calculated for THRIVE are historical and finding source documentation for description of the calculations is difficult. For this reason Idelchik (Reference RAI-4.2-2) has been used to recalculate the loss coefficients for instances where reliable source documentation could not be located. Each loss coefficient is discussed separately below.

The THRIVE BB inlet loss coefficient for Westinghouse 3 and 4 loop standard upflow and 3 loop converted upflow plants is 1.5. A value of 1.5 is a typical limiting value for a fluid stream turning 90 degrees. To investigate the 1.5 value, Idelchik (Reference RAI-4.2-2) is used to calculate a loss coefficient for flow through an elbow with sharp corners, smooth walls, and a 90 degree bend. Idelchik Diagram 6-6 represents this configuration and the calculations are summarized in Table RAI-4.2-7. As the table shows, the calculation assumes that l_o/D_h is approximately 0 since the BB inlet is directly downstream of the inlet collector. Based on the BB inlet geometry, a_o/b_o is large since the value for a_o is the baffle plate perimeter and the value for b_o is the annular gap between the baffle plates and the lower core plate. In the BB channel, the value of b_1 is variable, but regardless of the value chosen, the ratio of b_1/b_o can never be less than unity. Based on Diagram 6-6, for large a_o/b_o values and values of b_1/b_o greater than unity, the loss coefficient, K, (ζ) is always less than unity. As such, the historic THRIVE value is higher than that predicted by Idelchik and

will be maintained for the Westinghouse thermal hydraulic analysis of Westinghouse 3 and 4 loop standard upflow and 3 loop converted upflow plants.

The THRIVE BB inlet loss coefficient for Westinghouse 4 loop converted upflow plants varies between [ ]^{a,c} depending on the time the calculation was performed. More recently, the BB inlet loss coefficient was recalculated for an upflow conversion. The revised calculation determined a value of [ ]^{a,c} Since this value is higher than the historical THRIVE inlet loss coefficients for 4 loop converted downflow plants, it will be used for the Westinghouse TH analysis. The calculation is shown in Table RAI-4.2-8.

Table RAI-4.2-6 summarizes the BB inlet loss coefficients for the Westinghouse upflow plants.

Barrel/Baffle Former Plate Reference Area

The BB channel for Westinghouse 3 loop plants is shown in Figure RAI-4.2-3. The BB channel is the same for all 3 loop plants, except that the former plate design is different. The former plates for Westinghouse 3 loop standard upflow plants are shown in Figure RAI-4.2-4, which shows that the bottom former plate has a different number of holes compared to the other seven former plates. The former plates for Westinghouse 3 loop converted upflow plants are shown in Figure RAI-4.2-5, which shows that the top former plate is different compared to the other seven former plates. The former plates in Westinghouse 3 loop downflow plants are the same as those shown in Figure RAI-4.2-5 except that the top former plate does not have holes.

The BB channel for Westinghouse 4 loop plants is shown in Figure RAI-4.2-6. The BB channel is the same for all 4 loop plants, except that the former plate design is different between standard upflow, converted upflow, and standard downflow plants. It is also noted that STP, being a 4 loop XL plant, has nine former plates. The former plates for Westinghouse 4 loop standard upflow plants are shown in Figure RAI-4.2-7, which shows that all former plants in a specific plant are identical. One unique feature of Vogtle Unit 2 is that the former plates have core barrel bolt cooling holes. The former plate design for Vogtle Unit 2 is also shown in Figure RAI-4.2-7. The former plates for Westinghouse 4 loop converted upflow plants is shown in Figure RAI-4.2-8, which shows that the top former plate is different compared to the other seven former plates. The McGuire Units 1 and 2 former plates are slightly different than the ones illustrated in Figure RAI-4.2-8 because the upflow conversion was done differently. The number of holes in the bottom and top former plates is different in McGuire Units 1 and 2. The former plates in Westinghouse 4 loop downflow plants are the same as those shown in Figure RAI-4.2-8 except that the top former plate does not have holes.

The former plate reference areas consider holes, chamfers, stress relief holes, and gaps between the former plate segments. Two types of holes exist in standard upflow plants. The first type are standard through holes and the second type are baffle bolt cooling holes, in which a baffle bolt runs perpendicular through the former plate hole. Converted upflow plants do not have baffle bolt cooling holes. Tables RAI-4.2-9 through RAI-4.2-15 summarizes the geometry, dimensions, and areas for each type of Westinghouse plant that credits the BB channel in the GSI-191 analyses.

Barrel/Baffle Former Plate Loss Coefficients

The THRIVE loss coefficients for the former plate holes have values of [ ]^{a,c} The area associated with the chamfers, stress relief holes, and gaps are lumped with [ ]^{a,c} In order to verify the THRIVE loss coefficient values, Idelchik (Reference RAI-4.2-2) is used to calculate loss coefficients for the two types of former plate holes.

For Type 1 holes, which are typical through holes with no obstructions, two calculations were performed. The first calculation considers flow through an orifice plate. The second calculation considers flow through an abrupt contraction and an abrupt expansion. Both calculations yielded a loss coefficient of [ ]^{a,c} The calculations are summarized in Table RAI-4.2-16. For Type 2 holes, which are baffle bolt cooling holes, the loss coefficient is expected be higher due to the additional contraction and expansion past the baffle bolt. Two calculations were performed for the Type 2 hole as well. The first calculation considered flow through an abrupt contraction, then the flow around the baffle bolt was modeled as a diverging and converging wye, then finally flow out of the hole was modeled as an abrupt expansion. In the second calculation, flow through an abrupt contraction was considered, then flow around the baffle bolt was modeled as an abrupt expansion with flow across an obstruction and another abrupt contraction, then finally flow out of the hole was modeled as an abrupt expansion. The first calculation resulted in a total loss coefficient of [ ]^{a,c}

Since the calculations performed herein produce loss coefficients greater than the historical THRIVE values, the newly calculated values will be used for the GSI-191 TH analyses; namely, [ ]^{a,c}

The average loss coefficient for the upflow plant category, K_{AVG}, from Type 1 and Type 2 former plate holes was computed from the individual loss coefficients, K_i. The average former plate loss coefficient for the upflow plant category considering Type 1 and Type 2 holes has been recalculated using a different averaging scheme. The revised scheme is consistent with the THRIVE methodology for determining average loss coefficients for parallel flow paths. The following section describes the method and performs an example calculation for the 3 loop standard upflow plant.

THRIVE can only designate former plate flow area as 2 hole types per former elevation. The first step in calculating the average loss coefficient is to determine an equivalent number of Type 1 holes for the additional flow area due to the presence of the chamfers, stress relief holes, and gaps based on an equivalent K/A^2.

The additional area is converted to equivalent Type 1 holes with the same equivalent loss coefficient:

[ ]^{a,c}

Eq. RAI-4.2-3

Where, N_1 is the number of holes, K_1 the loss coefficient of the hole, A_1 the hole area, and A_0 the total area of the chamfers, stress relief holes, and the gaps.

The number of equivalent Type 1 holes, accounting for the additional area is then:

[ ]^{a,c}

Eq. RAI-4.2-4

Using Eq. RAI-4.2-3, the equivalent resistance for the 3 loop standard upflow plant is:

[ ]^{a,c}

Using Eq. RAI-4.2-4, the equivalent number of Type 1 holes in Former Plate 1 is calculated as:

[ ]^{a,c} Type 1 equivalent holes (Former Plate 1)

Performing the same calculations for the remaining former plates results in:

[ ]^{a,c} Type 1 equivalent holes (Former Plates 2-8)

These values agree with the historical THRIVE values of [ ]^{a,c} respectively.

Now that the additional flow area due to the chamfers, stress relief holes, and gaps has been accounted for, the total resistance through each former plate can be determined.

The first former plate has only Type 1 holes. The reference area is [ ]^{a,c} times the hole area:

$A_{ref} = N \times A_h =$ [ ]^{a,c}

The loss coefficient is [ ]^{a,c}

For the remaining former plates with Type 1 and Type 2 holes, the resistance for the two flow paths is summed together:

[ ]a,c

Eq. RAI-4.2-5

Where N is the number of holes, A the hole area, and K the hole resistance. The subscripts 1 and 2 represent the hole types.

Using Eq. RAI-4.2-5 the summed resistance for Former Plates 2-8:

[ ]a,c

and the total area is:

[ ]a,c

The resulting equivalent loss coefficient is calculated as:

[ ]a,c

Eq. RAI-4.2-6

Using Eq. RAI-4.2-6, the resulting equivalent loss coefficient for Former Plates 2-8 is [ ]a,c

Table RAI-4.2-17 summarizes the average former plate loss coefficients for each Westinghouse upflow plant considered in the GSI-191 TH analyses.

Barrel/Baffle Outlet Reference Area

The BB outlet geometry is similar for all Westinghouse 3 and 4 loop standard and converted upflow plants. The BB outlet for these plants consists of a gap between the top of the baffle plates and the bottom of the upper core plate that extends around the entire core periphery. Figure RAI-4.2-9 shows the BB outlet geometry for these plant types. The dimension of the gap varies across plant types.

Table RAI-4.2-18 provides the dimensions and the reference area for the BB outlets. The BB outlet reference area for Westinghouse 3 and 4 loop standard upflow and 3 loop converted upflow plants is calculated by multiplying the gap dimension by the inside perimeter of the baffle plates using Eq. RAI-4.2-1.

The BB outlet reference areas, calculated using the dimensions provided in Table RAI-4.2-18, agree well with the historical THRIVE values.

Barrel/Baffle Outlet Loss Coefficient

The THRIVE BB outlet loss coefficient for all Westinghouse upflow plants is 1.5. A value of 1.5 is a typical value for a fluid stream turning 90 degrees. Since the BB outlet geometry is similar to the inlet geometry, the loss coefficient described above for the BB inlet is applicable to the outlet as well and is not repeated here.

Since the historic THRIVE value would be higher than that predicted by Idelchik, it will be maintained for the Westinghouse thermal hydraulic analysis of Westinghouse upflow plants. Table RAI-4.2-18 lists the BB outlet loss coefficients.

Total Barrel/Baffle Channel Resistance

A geometric dimensional form loss (K/A^2) for the BB channel was determined by taking the summation of the K/A^2 for the BB inlet, all former plates, and the BB outlet. The total K/A^2 for the BB region is defined as:

$$\left(\frac{K}{A^2}\right)_{BB} = \left(\frac{K}{A^2}\right)_{LCP} + \left(\frac{K}{A^2}\right)_{F1-8} + \left(\frac{K}{A^2}\right)_{GAP} \qquad \text{Eq. RAI-4.2-7}$$

The three terms on the right hand side of the equation were determined using the reference areas and loss coefficients determined above. Table RAI-4.2-23 provides the total BB channel resistance for each upflow plant type.

Upper Head Spray Nozzle Reference Area

The upper head spray nozzle (UHSN) geometry is similar for Westinghouse 3 and 4 loop plants with T-Hot upper heads. The UHSN flow path is created by a series of holes around the periphery of the upper core barrel flange and upper support plate. Westinghouse 3 loop T-Hot plants have two types of UHSNs, as shown in Figure RAI-4.2-10. The first type has a three-way nozzle design at the exit of each hole. The second type has a single nozzle design at the exit. Figure RAI-4.2-11 shows the UHSN design for Westinghouse 4 loop T-Hot upper head plants. As the figure shows, all UHSNs in the 4 loop T-Hot design have the three-way nozzle machined into the upper support plate.

Another type of UHSN geometry is shown in Figure RAI-4.2-12. This figure shows the UHSN design for Westinghouse 4 loop plants with T-Cold upper heads. As shown in the figure, the holes in the core barrel flange and the upper support plate are considerably larger in the T-Cold UHSN design. Since the UHSN area is considerably larger than the T-Hot design, the UHSN maximum resistance is easily bounded by the T-Hot resistance.

The number and diameter of UHSN holes is used to calculate the total UHSN reference area:

$$A = N\frac{\pi}{4}D^2 = \left[\quad\right]^{a,c} \qquad \text{Eq. RAI-4.2-8}$$

The UHSN reference area is shown in Tables RAI-4.2-20 through RAI-4.2-22 for 3 loop T-Hot, 4 loop T-Hot, and 4 loop T-cold plant categories, respectively.

Upper Head Spray Nozzle Loss Coefficients for Westinghouse 3 Loop T-Hot Plants

All Westinghouse 3 loop standard downflow plants have T-Hot UHSN designs. The THRIVE UHSN loss coefficients for these plants vary between [ ]^{a,c} Review of the UHSN drawings, identified in Table RAI-4.2-5, indicates that the UHSN design is identical for all Westinghouse 3 loop T-Hot plants. As such, it is determined that the variations in the THRIVE data is due to the calculational method used to determine the loss coefficient. The following calculations are performed to determine the UHSN loss coefficient for Westinghouse 3 loop T-Hot plants.

a) Contraction to Upper Core Barrel Flange

The inlet diameter of an UHSN is:

[ ]^{a,c}

For an abrupt contraction from Idelchik Diagram 4-9 (Reference RAI-4.2-2)

$$K = 0.5(1 - A_0 / A_1)^{0.75}$$

where A_0 is the entrance area of a single UHSN hole and A_1 is the area upstream of the UHSN hole (upper downcomer area).

Assume A_1 is much larger than A_0 such that:

$$A_0 / A_1 \sim 0$$

This results in the highest possible loss coefficient for an abrupt contraction, based on Diagram 4-9:

$$K = 0.5(1 - 0)^{0.75} = 0.5$$

The reference area is that of a single UHSN entrance:

$A_{ref} = A_0 =$ [ ]^{a,c}

$K/A^2 =$ [ ]^{a,c}

b) Expansion and Contraction loss into flow nozzle body

A chamfer exists at the inlet to the flow nozzle body, resulting in an expansion of flow from the upper core barrel to the flow nozzle chamfered inlet. The nozzle body has a diameter of [ ]^{a,c} consistent with the UHSN hole diameter through the core barrel flange.

[

]a,c

c) Expansion and Contraction loss to the upper support plate flange

Single Branch Nozzles

Similar to the inlet to the flow nozzle body, the inlet to the hole in the upper support plate has a chamfered inlet. [

]^{a,c}

Three-Way Branch Nozzles

The nozzle locations with three branch exits do not have chamfers at the entrance to the upper support plate. Therefore, the loss is only an expansion loss from the nozzle body to the upper support plate.

[

]^{a,c}

d) Expansion and Contraction for the nozzle design

Three-Way Branch Nozzles

The three-way branch nozzle mates with the upper support plate and there is a chamfer at the interface.
[

]^{a,c}

Thus,

[

]^{a,c}

To account for losses through the three-way branch:

[

]^{a,c}

Note that this equation takes into account the two side branches and the one center branch of the three-way nozzle.

[

]^{a,c} Eq. RAI-4.2-9

The form loss coefficients for the branch and center nozzles in the three-way nozzle design can be determined from Diagram 7-34 (Reference RAI-4.2-2). For division of flow (intake four-way wye), the individual form loss coefficients are determined tentatively as for diverging wyes from Diagrams 7-18 and 7-20 (Reference RAI-4.2-2).

Therefore,

For Path "c" to "b" – Diagram 7-18 (Reference RAI-4.2-2)

$\delta_{cb} = A'\{1.0 + (W_b / W_c)^2 - 2(W_b / W_c)\cos \alpha\}$ based on A_c

[

]^{a,c} Eq. RAI-4.2-10

For Path "c" to "s" – Figure 7-20 (Reference RAI-4.2-2)

[

]^{a,c} Eq. RAI-4.2-11

Setting Eq. RAI-4.2-10 equal to Eq. RAI-4.2-11 and substituting in Eq. RAI-4.2-9 and solving for (W_b / W_c) gives:

[Eq. RAI-4.2-12

]^{a,c}

[

]^{a,c}

e) Expansion loss from the nozzle

Three-Way Nozzles

[

]^{a,c}

Single Nozzles

[

]^{a,c}

Therefore, the total hydraulic resistance for this path is:

Three-Way Nozzles

[

]^{a,c}

Single Nozzles

[

]^{a,c}

This value is less than the historical THRIVE values of [ ]^{a,c} Since the historical THRIVE value of [ ]^{a,c} is larger than the value calculated here, it will be used for the GSI-191 TH analysis. Table RAI-4.2-23 summarizes the loss coefficient and reference area for this plant type.

Upper Head Spray Nozzle Loss Coefficients for Westinghouse 4 Loop T-Hot Plants

The THRIVE UHSN loss coefficient for all Westinghouse 4 loop T-Hot plants is [ ]^{a,c} Review of the UHSN drawings, identified in Table RAI-4.2-5, indicates that the UHSN design is identical for all Westinghouse 4 loop T-Hot plants. The following calculations are performed to determine the UHSN loss coefficient for Westinghouse 4 loop T-Hot plants.

a) Contraction to Upper Core Barrel Flange

The diameter of each UHSN hole in the upper core barrel flange is:

[ ]^{a,c}

There is a chamfer at the inlet to each hole. The diameter at the inlet is:

[

]^{a,c}

b) Expansion and Contraction loss into flow nozzle body

[

]^{a,c}

Therefore, the diameter in the flow nozzle body in the chamfer area can be represented as:

[

]a,c

c) Expansion and Contraction loss to the upper support flange

[

]a,c

Therefore,

[

]a,c

d) Expansion and Contraction for the three-way nozzle design

[

]a,c

Note that this equation takes into account the two side branches and the one center branch of the three-way nozzle.

[

]a,c

[

]a,c Eq. RAI-4.2-13

The form loss coefficients for the branch and center nozzles in the three-way nozzle design can be determined from Diagram 7-34 (Reference RAI-4.2-2). For division of flow (intake four-way wye), the individual form loss coefficients are determined tentatively as for diverging wyes from Diagrams 7-18 and 7-20 (Reference RAI-4.2-2). Therefore,

For Path "c" to "b" – Figure 7-18 (Reference RAI-4.2-2)

$\delta_{cb} = A'\{1.0 + (W_b / W_c)^2 - 2(W_b / W_c)\cos \alpha\}$ based on A_c

[

]^{a,c} Eq. RAI-4.2-14

For Path "c" to "s" – Figure 7-20 (Reference RAI-4.2-2)

[

Eq. RAI-4.2-15

]^{a,c} Eq. RAI-4.2-16

[

]^{a,c}

e) Expansion loss from the three-way nozzle

[

]^{a,c}

Therefore, the total hydraulic resistance for this path is:

[

]^{a,c}

This value is higher compared to the historical THRIVE value of [ ]^{a,c} and will be used for the GSI-191 TH analysis. Table RAI-4.2-23 summarizes the loss coefficient and reference area for this plant type.

Upper Head Spray Nozzle Loss Coefficients for Westinghouse 4 Loop T-Cold Plants

The THRIVE UHSN loss coefficient for all Westinghouse 4 loop T-Cold plants is [ ]^{a,c} Since the flow area associated with T-Cold upper head plants is an order of magnitude higher than T-Hot plants, the loss coefficient is less important. Since the GSI-191 TH analyses lump all downflow plants into a single analysis category, T-Hot plants are used to determine the limiting maximum UHSN resistance. As such, a detailed calculation of the loss coefficient for T-Cold plants is not warranted and the historical THRIVE value is used. Table RAI-4.2-23 summarizes the loss coefficient and reference area for this plant type.

Total Upper Head Spray Nozzle Resistance

The reference areas and loss coefficients provided in Table RAI-4.2-23 can be used to determine the geometric dimensional form loss (K/A^2) for the UHSNs. The dimensional form loss is also provided in Table RAI-4.2-23. As the table indicates, 3 and 4 loop T-Hot upper head plants have similar UHSN resistance, while the T-Cold plant type has a much lower resistance.

Step 2

In order to determine an equivalent maximum AFP resistance for the base plant models (upflow and downflow plant categories), it is necessary to scale the base plant AFP resistance. All plants except UPI plants and STP are considered in the scaling assessment. UPI plants are not included since the GSI-191 AFP analyses are not used for this plant type's GSI-191 in-vessel debris methodology (See WCAP-17788, Volume 1, Chapter 8). STP is unique in that it has a 14 ft active core. All other U.S. PWRs have 12 ft active cores. Given STP's unique design feature, it is not included in the GSI-191 TH analyses.

The parameter chosen for preservation is the total pressure drop across the AFP:

$$\Delta P = \frac{\dot{m}_{boil}^2 \cdot \left(\frac{K}{A^2}\right)_{AFP}}{2 \cdot \rho_f} \qquad \text{Eq. RAI-4.2-17}$$

Where,

$\left(\frac{K}{A^2}\right)_{AFP}$ is the total dimensional resistance through the AFP (BB channel or UHSNs),

ρ_f the fluid density, and

$\dot{m}_{boil}$ the mass flow rate through the AFP.

The mass flow rate through the AFP is set equal to the steaming rate within the core:

$$\dot{m}_{boil} = \frac{P_0 \cdot f_D}{h_{fg}} \qquad \text{Eq. RAI-4.2-18}$$

Where P_0 is the nominal core power, f_D the decay heat fraction, and h_{fg} the latent heat of vaporization.

Using the steaming rate in the scaling formulation accounts for differences in the core power between plants considered in each GSI-191 plant category. Since the primary objective of the GSI-191 TH analyses is to demonstrate adequate decay heat removal following complete core inlet blockage, the amount of flow required to bypass the core inlet through the AFP is important. A plant with a higher power will require more flow through the AFP to adequately remove decay heat compared to a plant with lower power. Since the base plant models a single core power, it is necessary to account for plant-to-plant variations in core power. This is accomplished by including core power in the scaling of the AFP resistance.

The following scaling group is defined:

$$\Pi_{\Delta P} = \frac{\Delta P_{base}}{\Delta P_{limit}} \qquad \text{Eq. RAI-4.2-19}$$

Where ΔP_{base} is the base plant AFP pressure drop, and ΔP_{limit} the AFP pressure drop from the plant with the highest pressure drop.

Using Eqs. RAI-4.2-17 and RAI-4.2-18, the scaling group becomes:

$$\Pi_{\Delta P} = \frac{\left[\frac{\left(\frac{P_0 \cdot f_D}{h_{fg}}\right)^2 \cdot \left(\frac{K}{A^2}\right)_{AFP}}{2 \cdot \rho_f}\right]_{base}}{\left[\frac{\left(\frac{P_0 \cdot f_D}{h_{fg}}\right)^2 \cdot \left(\frac{K}{A^2}\right)_{AFP}}{2 \cdot \rho_f}\right]_{limit}} \qquad \text{Eq. RAI-4.2-20}$$

Assuming fluid property similitude, and equal decay heat fractions between the base plant and the limiting plant, Eq. RAI-4.2-20 reduces to:

$$\Pi_{\Delta P} = \frac{(P_{base})^2 \cdot \left(\frac{K}{A^2}\right)_{base}}{(P_{limit})^2 \cdot \left(\frac{K}{A^2}\right)_{limit}} \qquad \text{Eq. RAI-4.2-21}$$

Where the numerator is the base plant model nominal power squared times the base plant AFP resistance, and the denominator is the limiting plant nominal power squared times the limiting plant AFP resistance.

Setting the scaling group, $\Pi_{\Delta P}$, equal to unity and solving for $\left(\frac{K}{A^2}\right)_{base}$ will ensure that the AFP resistance used in the base plant model will result in a pressure drop across the AFP when the flow rate is equal to boil-off in the base plant that is equivalent to the pressure drop across the AFP in the limiting plant when the flow rate is equal to the boil-off in the limiting plant.

Setting $\Pi_{\Delta P}$ equal to unity and solving Eq. RAI-4.2-21 for $\left(\frac{K}{A^2}\right)_{base}$ yields:

$$\left(\frac{K}{A^2}\right)_{base} = \left(\frac{K}{A^2}\right)_{limit} \cdot \frac{(P_{limit})^2}{(P_{base})^2} \qquad \text{Eq. RAI-4.2-22}$$

Upflow Plant Category Maximum Barrel/Baffle Channel Resistance

In this section, the base plant model BB channel resistance is determined that bounds all upflow plants. The first step is to calculate the pressure drop for each plant in the category to determine which plant has the highest pressure drop. The pressure drop is determined using Eqs. RAI-4.2-17 and RAI-4.2-18. In the calculations, the decay heat fraction is set to 0.02412, which is the Appendix K decay heat fraction at 20 minutes after trip. The fluid properties are set to saturated conditions at atmospheric pressure; ρ_f = 59.8 lbm/ft^3 and h_{fg} = 970.3 Btu/lbm. The licensed powers, listed in Table RAI-4.2-1, are used in the calculation, and the total AFP resistance is taken from Table RAI-4.2-19.

Table RAI-4.2-24 provides the calculated pressure drops and shows that the highest value is [
]^{a,c} With the maximum pressure drop determined, the base plant model BB channel

resistance can be calculated using Eq. RAI-4.2-22. The upflow base plant power is taken from WCAP-17788, Volume 4, Table 6-1; 3658 MW. The resulting upflow base plant BB channel resistance is:

$$\left(\frac{K}{A^2}\right)_{base} = \left(\frac{K}{A^2}\right)_{limit} \cdot \frac{(P_{limit})^2}{(P_{base})^2} = \left[\quad \right]^{a,c}$$

Table RAI-4.2-24 also provides the adjusted (scaled) AFP resistances based on Eq. RAI-4.2-22. As expected, all adjusted AFP resistances are less than the value used in the base plant model.

Downflow Plant Category Maximum Upper Head Spray Nozzle Resistance

In this section, the base plant model UHSN resistance is determined that bounds all downflow plants. Consistent with the process for the upflow plant category, the first step is to calculate the pressure drop for each plant in the category to determine which plant has the highest pressure drop. The pressure drop is determined using Eqs. RAI-4.2-17 and RAI-4.2-18. In the calculations, the decay heat fraction is set to 0.02412, which is the Appendix K decay heat fraction at 20 minutes after trip. The fluid properties are set to saturated conditions at atmospheric pressure; ρ_f = 59.8 lbm/ft^3 and h_{fg} = 970.3 Btu/lbm. The licensed powers, listed in Table RAI-4.2-1, are used in the calculation, and the total AFP resistance is taken from Table RAI-4.2-23.

Table RAI-4.2-24 provides the calculated pressure drops and shows that the highest value is [ ]^{a,c} With the maximum pressure drop determined, the base plant model UHSN resistance can be calculated using Eq. RAI-4.2-22. The downflow base plant power is taken from WCAP-17788, Volume 4, Table 6-2; 2951 MW. The resulting downflow base plant UHSN resistance is:

$$\left(\frac{K}{A^2}\right)_{base} = \left(\frac{K}{A^2}\right)_{limit} \cdot \frac{(P_{limit})^2}{(P_{base})^2} = \left[\quad \right]^{a,c}$$

Table RAI-4.2-24 also provides the adjusted (scaled) AFP resistances based on Eq. RAI-4.2-22. As expected, all adjusted AFP resistances are less than the value used in the base plant model.

Step 3

In this step, an equivalent dimensionless form loss coefficient for the WCOBRA/TRAC models is determined.

WCOBRA/TRAC Upflow Plant Model

The WCOBRA/TRAC upflow plant model BB channel dimensionless form loss coefficient, K_{WCT}, is calculated as:

$$K_{WCT} = \left(\frac{K}{A^2}\right)_{Base} \cdot {A_{WCT}}^2 \qquad \text{Eq. RAI-4.2-23}$$

Where $\left(\frac{K}{A^2}\right)_{Base}$ is the equivalent maximum BB channel resistance determined in Step 2, and A_{WCT} is the WCOBRA/TRAC model BB channel flow area; [ ]^{a,c}

Using Eq. RAI-4.2-24, the WCOBRA/TRAC upflow plant model BB channel form loss coefficient is calculated:

[ ] a,c

The total BB channel equivalent form loss is evenly distributed across the 8 former plate elevations:

[ ] a,c

As such, a former loss coefficient of [ ]^{a,c} applied at each former plate elevation in the WCOBRA/TRAC model would bound the BB channel resistance for all Westinghouse upflow plants considered in the GSI-191 AFP analysis.

Additional Margin in the Barrel/Baffle Channel Resistance

Additional margin was added to the BB channel resistance in the WCOBRA/TRAC upflow plant model. A loss coefficient of [ ]^{a,c} per former plate was used in the analysis. That relates to a total form loss of:

[ ]^{a,c}

This corresponds to an equivalent resistance of:

$$\left(\frac{K}{A^2}\right)_{Base} = \left(\frac{K_{WCT}}{A_{WCT}^{\ 2}}\right) = \left[\ \right]^{a,c}$$

This value is approximately 4% larger than the maximum AFP resistance determined in Step 2.

WCOBRA/TRAC Downflow Plant Model

The WCOBRA/TRAC downflow plant model UHSN dimensionless form loss coefficient, K_{WCT}, is calculated using Eq. RAI-4.2-23. The UHSN area in the WCOBRA/TRAC model is set to the upper downcomer area; [ ]^{a,c} The WCOBRA/TRAC downflow plant model UHSN form loss coefficient is calculated as:

[ ] a,c

As such, a loss coefficient of [ ]^{a,c} applied at the top of each downcomer channel in the WCOBRA/TRAC model would bound the UHSN resistance for all Westinghouse downflow plants considered in the GSI-191 AFP analysis.

Additional Margin in the Upper Head Spray Nozzle Resistance

Additional margin was added to the UHSN resistance in the WCOBRA/TRAC downflow plant model. A loss coefficient of [ ]^{a,c} per downcomer channel was used in the analysis.

This corresponds to an equivalent resistance of:

$$\left(\frac{K}{A^2}\right)_{Base} = \left(\frac{K_{WCT}}{A_{WCT}{}^2}\right) = \left[\quad\right]^{a,c}$$

This value is approximately 10% larger than the maximum AFP resistance determined in Step 2, and is applied to the downflow plant analyses used to define the parameters K_{max}, K_{split}, and m_{split}.

Upper Head Spray Nozzle Resistance used to Determine the Parameter t_{block}

The WCOBRA/TRAC analysis used to determine the parameter t_{block} for the downflow plant category applies an UHSN resistance that does not bound all downflow plants. As UHSN resistance is increased, flow through the UHSN decreases and the time that earliest complete core inlet blockage can be tolerated (t_{block}) extends further into the post-LOCA transient. All Westinghouse downflow plants perform hot leg switchover to mitigate the potential for boric acid precipitation several hours after the LOCA begins. The WCOBRA/TRAC GSI-191 analyses only consider cold leg recirculation. As a result, simulating the transient further to define an acceptable time for t_{block} becomes less realistic since the transfer to hot leg recirculation is not considered in the analysis. Further, following transfer to hot leg recirculation there is sufficient ECCS coolant entering the top of the core such that coolant flow through the UHSN flow path is not necessary to adequately remove decay heat. For these reasons, the UHSN resistance used in the downflow plant analysis used to determine the parameter t_{block} was reduced to [ ]^{a,c} per downcomer channel.

This corresponds to an equivalent resistance of:

$$\left(\frac{K}{A^2}\right)_{Base} = \left(\frac{K_{WCT}}{A_{WCT}{}^2}\right) = \left[\quad\right]^{a,c}$$

Downflow plants that are not bounded by the generic t_{block} time can justify the use of their plant-specific hot leg switchover time as a surrogate for the parameter t_{block} when implementing the WCAP-17788 in-vessel debris methodology. Westinghouse downflow plants should use the adjusted USHN resistances provided in Table RAI-4.2-24 to determine if their UHSN resistance is bounded.

Table RAI-4.2-1 Name, Licensed Power, and Type of Westinghouse Plants		
Plant	**Licensed Power (MW)**	**Plant Type**
Shearon Harris Nuclear Power Plant, Unit 1	2900	3 Loop Standard Upflow
Beaver Valley Power Station, Unit 2	2900	
Byron Station, Units 1 & 2	3645	4 Loop Standard Upflow
Braidwood Station, Units 1 & 2	3645	
Catawba Nuclear Station, Units 1 & 2	3411	
Comanche Peak Nuclear Power Plant, Units 1 & 2	3612	
Vogtle Electric Generating Plant, Units 1 & 2	3625.6	
Seabrook Station, Unit 1	3648	
Millstone Power Station, Unit 3	3650	
Wolf Creek Generating Station, Unit 1	3565	
Callaway Plant	3565	
South Texas Project, Units 1 & 2[1]	3853	4 Loop XL Standard Upflow
Joseph M. Farley Nuclear Plant, Units 1 & 2	2775	3 Loop Converted upflow
Virgil C. Summer Nuclear Station, Unit 1	2900	
North Anna Power Station, Unit 1	2940	
McGuire Nuclear Station, Units 1 & 2	3411	4 Loop Converted Upflow
Watts Bar Nuclear Plant, Unit 1	3459	
Watts Bar Nuclear Plant, Unit 2	3411	
Diablo Canyon Nuclear Power Plant, Unit 2	3411	
Surry Power Station, Units 1 & 2	2587	3 Loop Standard Downflow with T-Hot Upper Head
Turkey Point Nuclear Generating Units 3 & 4	2644	
H. B. Robinson Steam Electric Plant, Unit 2	2339	
North Anna Power Station, Unit 2[2]	2940	
Donald C. Cook Nuclear Plant, Unit 1	3304	4 Loop Standard Downflow with T-Hot Upper Head
Donald C. Cook Nuclear Plant, Unit 2	3468	
Indian Point Nuclear Generating, Units 2 & 3	3216	
Salem Nuclear Generating Station, Units 1 & 2	3459	
Diablo Canyon Nuclear Power Plant, Unit 1	3411	
Sequoyah Nuclear Plant, Units 1 & 2	3455	4 Loop Standard Downflow with T-Cold Upper Head

Notes [1] South Texas Project is not considered in the GSI-191 thermal hydraulic analyses. However, the plant was included in this RAI response to provide a description of the plant's AFP geometry.

[2] North Anna Power Station, Unit 2 is now a converted upflow plant with AFP geometry identical to Unit 1

Table RAI-4.2-2 Barrel/Baffle Inlet Drawing Identification for Westinghouse Upflow Plants

Plant	Barrel/Baffle Inlet		
	Drawing Numbers	**Revision**	**Title**
Shearon Harris Nuclear Power Plant, Unit 1	6116E55	5	(3) Loop Core Barrel Assembly
	6121E75	5	3 Loop Core Barrel Assy.
Beaver Valley Power Station, Unit 2	6116E55	3	(3) Loop Core Barrel Assembly
	6121E75	5	3 Loop Core Barrel Assy.
Byron Station, Units 1 & 2	6116E99	2 (Unit 1) 3 (Unit 2)	4 Loop Core Barrel Assembly
Braidwood Station, Units 1 & 2	6116E99	7	4 Loop Core Barrel Assembly
Catawba Nuclear Station, Units 1 & 2	6116E99	5 (Unit 1) 7 (Unit 2)	4 Loop Core Barrel Assembly
Comanche Peak Nuclear Power Plant, Units 1 & 2	6116E99	4 (Unit 1) 7 (Unit 2)	4 Loop Core Barrel Assembly
Vogtle Electric Generating Plant, Units 1 & 2	6116E99	7	4 Loop Core Barrel Assembly
Seabrook Station, Unit 1	6116E99	7	4 Loop Core Barrel Assembly
Millstone Power Station, Unit 3	6116E99	3	4 Loop Core Barrel Assembly
Wolf Creek Generating Station, Unit 1	6116E99	7	4 Loop Core Barrel Assembly

Table RAI-4.2-2 Barrel/Baffle Inlet Drawing Identification for Westinghouse Upflow Plants (cont'd)			
Plant	**Barrel/Baffle Inlet**		
	Drawing Numbers	**Revision**	**Title**
Callaway Plant	6116E99	5	4 Loop Core Barrel Assembly
South Texas Project, Units 1 & 2	6120E03	5 (Unit 1) 7 (Unit 2)	4 Loop XL Core Barrel Assembly
Joseph M. Farley Nuclear Plant, Units 1 & 2	1096E26	6 (Unit 1) 3 (Unit 2)	3 Loop Core Barrel Assembly
	6121E75	5	3 Loop Core Barrel Assy.
Virgil C. Summer Nuclear Station, Unit 1	6114E02	11	3 Loop Core Barrel Assembly
	6121E75	5	3 Loop Core Barrel Assy.
North Anna Power Station, Unit 1	686J461	3	Core Barrel Assembly
	6121E75	5	3 Loop Core Barrel Assy.
McGuire Nuclear Station, Unit 1	114E018	3	4 Loop Core Plate - Lower
McGuire Nuclear Station, Unit 2	1097E09	4	4 Loop Core Plate - Lower
Watts Bar Nuclear Plant, Unit 1	1097E09	4	4 Loop Core Plate - Lower
Watts Bar Nuclear Plant, Unit 2	1097E09	4	4 Loop Core Plate – Lower
Diablo Canyon Nuclear Power Plant, Unit 2	114E018	4	4 Loop Core Plate - Lower

Table RAI-4.2-3 Barrel/Baffle Former Plate Drawing Identification for Westinghouse Upflow Plants

Plant	Barrel/Baffle Former Plate		
	Drawing Numbers	Revision	Title
Shearon Harris Nuclear Power Plant, Unit 1	6116E38	4	(3) Loop Formers
Beaver Valley Power Station, Unit 2	6116E38	4	(3) Loop Formers
Byron Station, Units 1 & 2	6118E09	1	(4) Loop Formers
Braidwood Station, Units 1 & 2	6118E09	1 & 2	(4) Loop Formers
Catawba Nuclear Station, Units 1 & 2	6118E09	1 & 2	(4) Loop Formers
Comanche Peak Nuclear Power Plant, Units 1 & 2	6118E09	1 & 2 (Unit 1) 3 & 4 (Unit 2)	(4) Loop Formers
Vogtle Electric Generating Plant, Unit 1	6118E09	4	(4) Loop Formers
Vogtle Electric Generating Plant, Unit 2	6118E09	5	(4) Loop Formers
	6117E01	7	(4) Loop Barrel & Baffle Assy.
Seabrook Station, Unit 1	6118E09	1	(4) Loop Formers
Millstone Power Station, Unit 3	6118E09	1	(4) Loop Formers
Wolf Creek Generating Station, Unit 1	6118E09	1	(4) Loop Formers
Callaway Plant	6118E09	1 & 2	(4) Loop Formers
South Texas Project, Units 1 & 2	6118E09	2	(4) Loop Formers
Joseph M. Farley Nuclear Plant, Unit 1	686J093	3	157-15-157-000 PWR Formers
	6130E70	1	ALA. Reactor Internals Upflow Conversion

Table RAI-4.2-3 Barrel/Baffle Former Plate Drawing Identification for Westinghouse Upflow Plants (cont'd)			
Plant	**Barrel/Baffle Former Plate**		
	Drawing Numbers	**Revision**	**Title**
Joseph M. Farley Nuclear Plant, Unit 2	1086J58	2	(3) Loop Formers
	CN-MSI-02-6[1]	0	Farley Unit #2 Upflow Conversion Top Former Plate Hole Sizing
Virgil C. Summer Nuclear Station, Unit 1	1086J58	4	(3) Loop Formers
North Anna Power Station, Unit 1	686J093	2	Formers
	5D64157	2	North Anna Unit 1 Reactor Internals Upflow Conversion
McGuire Nuclear Station, Unit 1	113E943	3	4 Loop Formers
	RPVSA-92-2116[2]	0	McGuire THRIVE – 18% SGTP
McGuire Nuclear Station, Unit 2	6113E44	2	4 Loop Formers
	RPVSA-92-2116[2]	0	McGuire THRIVE – 18% SGTP
Watts Bar Nuclear Plant, Units 1 & 2	6113E44	4 (Unit 1) 3 (Unit 2)	4 Loop Formers
	FCN-WATM-10773[3]	0	WAT Upflow Conversion

Table RAI-4.2-3 Barrel/Baffle Former Plate Drawing Identification for Westinghouse Upflow Plants (cont'd)			
Plant	**Barrel/Baffle Former Plate**		
	Drawing Numbers	**Revision**	**Title**
Diablo Canyon Nuclear Power Plant, Unit 2	113E943	3	4 Loop Formers
	CN-RCUWF-03-1[4]	1	Diablo Canyon Unit 2 Upflow Conversion and Upper Head Temperature Reduction Hydraulic Design
Notes [1] CN-MSI-02-6 describes the top former plate modifications made during the Farley Unit 2 upflow conversion. [2] RPVSA-92-2116 describes the top former plate modifications made during the McGuire Unit 1 & 2 upflow conversion. [3] FCN-WATM-10773 describes the top former plate modifications made during the Watts Bar Unit 1 & 2 upflow conversion. [4] CN-RCUWF-03-1 describes the top former plate modifications made during the Diablo Canyon Unit 2 upflow conversion.			

Table RAI-4.2-4 Barrel/Baffle Outlet Drawing Identification for Westinghouse Upflow Plants			
Plant	**Barrel/Baffle Outlet**		
	Drawing Numbers	**Revision**	**Title**
Shearon Harris Nuclear Power Plant, Unit 1	686J500	6	Reactor General Assy.
	6116E55	5	(3) Loop Core Barrel Assembly
	6121E75	5	3 Loop Core Barrel Assy.
	6116E42	3	3 Loop Baffle Plate
Beaver Valley Power Station, Unit 2	701J564	2	Reactor General Assy.
	6116E55	3	(3) Loop Core Barrel Assembly
	6121E75	5	3 Loop Core Barrel Assy.
	6116E42	3	3 Loop Baffle Plate
Byron Station, Unit 1	701J707	6	Exelon Nuclear - Byron 1 Reactor General Assembly
	6116E99	2	4 Loop Core Barrel Assembly
Byron Station, Unit 2	701J781	4	Byron Static, No. 2 (CBE) Reactor General Assembly
	6116E99	3	4 Loop Core Barrel Assembly

Table RAI-4.2-4 Barrel/Baffle Outlet Drawing Identification for Westinghouse Upflow Plants (cont'd)

Plant	Barrel/Baffle Outlet		
	Drawing Numbers	Drawing Numbers	Drawing Numbers
Braidwood Station, Unit 1	701J784	2	Exelon Nuclear - Braidwood Unit 1 - Reactor General Assembly
	6116E99	7	4 Loop Core Barrel Assembly
Braidwood Station, Unit 2	701J785	3	Braidwood Station 2 (CDE) Reactor General Assembly
	6116E99	7	4 Loop Core Barrel Assembly
Catawba Nuclear Station, Unit 1	6116E99	5	4 Loop Core Barrel Assembly
Catawba Nuclear Station, Unit 2	6116E99	7	4 Loop Core Barrel Assembly
Comanche Peak Nuclear Power Plant, Unit 1	701J751	4	Comanche Peak Station 1 (TBX) Reactor General Assembly
	6116E99	4	4 Loop Core Barrel Assembly
Comanche Peak Nuclear Power Plant, Unit 2	701J835	2	Comanche Peak Station 2 (TCX) Reactor General Assembly
	6116E99	7	4 Loop Core Barrel Assembly

Table RAI-4.2-4 Barrel/Baffle Outlet Drawing Identification for Westinghouse Upflow Plants (cont'd)			
Plant	**Barrel/Baffle Outlet**		
	Drawing Numbers	**Drawing Numbers**	**Drawing Numbers**
Vogtle Electric Generating Plant, Unit 1	1613E12	1	(GAE) Alvin W. Vogtle No. 1 Reactor General Assembly
	6116E99	7	4 Loop Core Barrel Assembly
Vogtle Electric Generating Plant, Unit 2	1679E61	1	Southern Nuclear Vogtle No. 2 - Reactor General Assembly
	6116E99	7	4 Loop Core Barrel Assembly
Seabrook Station, Unit 1	1448E82	2	Seabrook No. 1 (NAH) Reactor General Assembly
	6116E99	7	4 Loop Core Barrel Assembly
Millstone Power Station, Unit 3	701J748	8	Millstone #3 (NEU) Reactor General Assembly
	6116E99	3	4 Loop Core Barrel Assembly
Wolf Creek Generating Station, Unit 1	1455E84	2	Wolf Creek No. 1 SAP Reactor General Assembly
	6116E99	7	4 Loop Core Barrel Assembly

Table RAI-4.2-4 Barrel/Baffle Outlet Drawing Identification for Westinghouse Upflow Plants (cont'd)

Plant	Barrel/Baffle Outlet		
	Drawing Numbers	Drawing Numbers	Drawing Numbers
Callaway Plant	1447E54	2	Callaway Unit 1 (SCP) - Reactor General Assembly
	6116E99	5	4 Loop Core Barrel Assembly
South Texas Project, Unit 1	1455E38	2	STP Nuclear Oper. Co. - Unit 1 - Reactor General Assembly
	6120E03	5	4 Loop XL Core Barrel Assembly
South Texas Project, Unit 2	1598E82	2	(THX) South Texas Project Unit No. 2 Reactor General Assembly
	6120E03	7	4 Loop XL Core Barrel Assembly
Joseph M. Farley Nuclear Plant, Unit 1	686J497	8	J. M. Farley Unit 1 (ALA) Reactor General Assembly
	1096E26	6	3 Loop Core Barrel Assembly
Joseph M. Farley Nuclear Plant, Unit 2	686J498	7	J. M. Farley Unit 2 (APR) Reactor General Assembly
	1096E26	3	3 Loop Core Barrel Assembly

Table RAI-4.2-4 Barrel/Baffle Outlet Drawing Identification for Westinghouse Upflow Plants (cont'd)			
Plant	**Barrel/Baffle Outlet**		
	Drawing Numbers	**Drawing Numbers**	**Drawing Numbers**
Virgil C. Summer Nuclear Station, Unit 1	686J499	6	Virgil C. Summers (CGE) Reactor General Assembly
	6114E02	11	3 Loop Core Barrel Assembly
North Anna Power Station, Unit 1	686J070	5	Virginia Electric & Power Company North Anna No. 1 Reactor General Assy.
	686J461	3	Core Barrel Assembly
McGuire Nuclear Station, Unit 1	686J269	8	DAP Reactor General Assembly
	113E982	7	4 Loop Barrel & Baffle Assembly
McGuire Nuclear Station, Unit 2	686J368	7	McGuire Station No 2 DBP Reactor General Assembly
	6113E84	11	(4) Loop Core Barrel Assembly
Watts Bar Nuclear Plant, Unit 1	686J492	12	Tennessee Valley Authority - Unit 1 - Reactor General Assembly
	1096E65	15	4 Loop Core Barrel Assembly

Table RAI-4.2-4 Barrel/Baffle Outlet Drawing Identification for Westinghouse Upflow Plants (cont'd)			
Plant	**Barrel/Baffle Outlet**		
	Drawing Numbers	**Drawing Numbers**	**Drawing Numbers**
Watts Bar Nuclear Plant, Unit 2	686J493	9	Tennessee Valley Authority – Watts Bar Unit 2 - Reactor General Assembly
	1096E65	15	4 Loop Core Barrel Assembly
Diablo Canyon Nuclear Power Plant, Unit 2	686J371	6	Diablo Canyon No. 2 PEG Reactor General Assembly
	113E851	9	4 Loop Core Barrel Assembly

Table RAI-4.2-5 Upper Head Spray Nozzle Drawing Identification for Westinghouse Downflow Plants

Plant	Drawing Numbers	Revision	Title
Surry Power Station, Units 1 & 2	685J568	3	Core Barrel - Upper
	675C859	1	Flow Nozzle
	685J151	4	Upper Support Assembly
Turkey Point Nuclear Generating Units 3 & 4	684J951	3	Core Barrel - Upper
	675C859	1	Flow Nozzle
	685J150	7	Upper Support Assembly
H. B. Robinson Steam Electric Plant, Unit 2	684J951	3	Core Barrel - Upper
	675C859	1	Flow Nozzle
	685J150	7	Upper Support Assembly
North Anna Power Station, Unit 2[1]	685J568	5	Core Barrel - Upper
	675C859	1	Flow Nozzle
	685J843	8	Upper Support Assembly
Donald C. Cook Nuclear Plant, Unit 1	647J080	15	Core Barrel - Upper
	500B477	2	Flow Nozzle
	685J883	4	Upper Support Assembly
Donald C. Cook Nuclear Plant, Unit 2	647J080	15	Core Barrel - Upper
	500B477	2	Flow Nozzle
	685J884	5	Upper Support Assembly

Table RAI-4.2-5 Upper Head Spray Nozzle Drawing Identification for Westinghouse Downflow Plants (cont'd)

Plant	Drawing Numbers	Revision	Title
Indian Point Nuclear Generating, Unit 2	647J080	8	Core Barrel - Upper
	500B477	2	Flow Nozzle
	647J077	10	Upper Support Assembly
Indian Point Nuclear Generating, Unit 3	647J080	10	Core Barrel - Upper
	500B477	2	Flow Nozzle
	685J459	3	Upper Support Assembly
Salem Nuclear Generating Station, Units 1 & 2	647J080	10	Core Barrel - Upper
	500B477 (E-233-045)	2 (4)	Flow Nozzle
	685J459	3	Upper Support Assembly
Diablo Canyon Nuclear Power Plant, Unit 1	647J080	13	Core Barrel - Upper
	500B477	2	Flow Nozzle
	685J459	5	Upper Support Assembly
Sequoyah Nuclear Plant, Units 1 & 2	1086J67	2	Core Barrel - Upper
	6117D30	2	Flow Nozzle Body
	6124E03	3	4 Loop (TVA & TEN) Upr. & Lwr. Int. Modification for Flow Nozzles

Note [1] North Anna Power Station, Unit 2 is now a converted upflow plant with AFP geometry identical to Unit 1

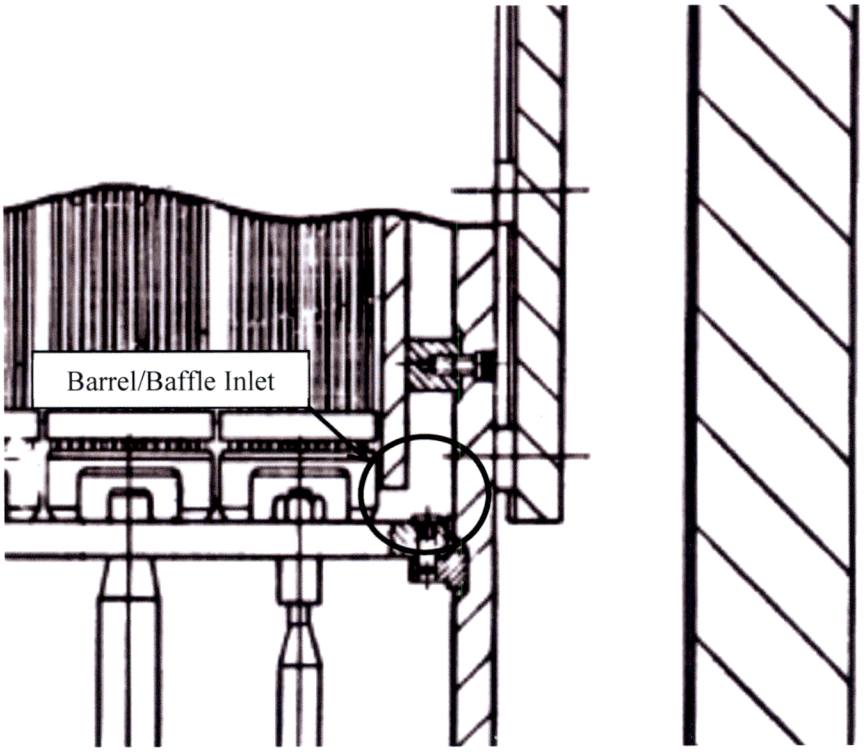

Figure RAI-4.2-1 Westinghouse 3 and 4 Loop Standard Upflow and 3 Loop Converted Upflow Barrel/Baffle Inlet Geometry

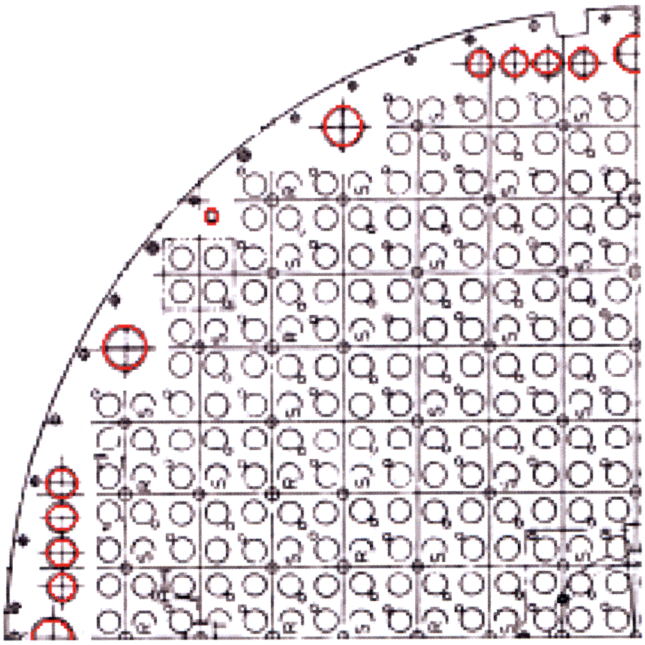

Figure RAI-4.2-2 Westinghouse 4 Loop Converted Upflow Barrel/Baffle Inlet Geometry

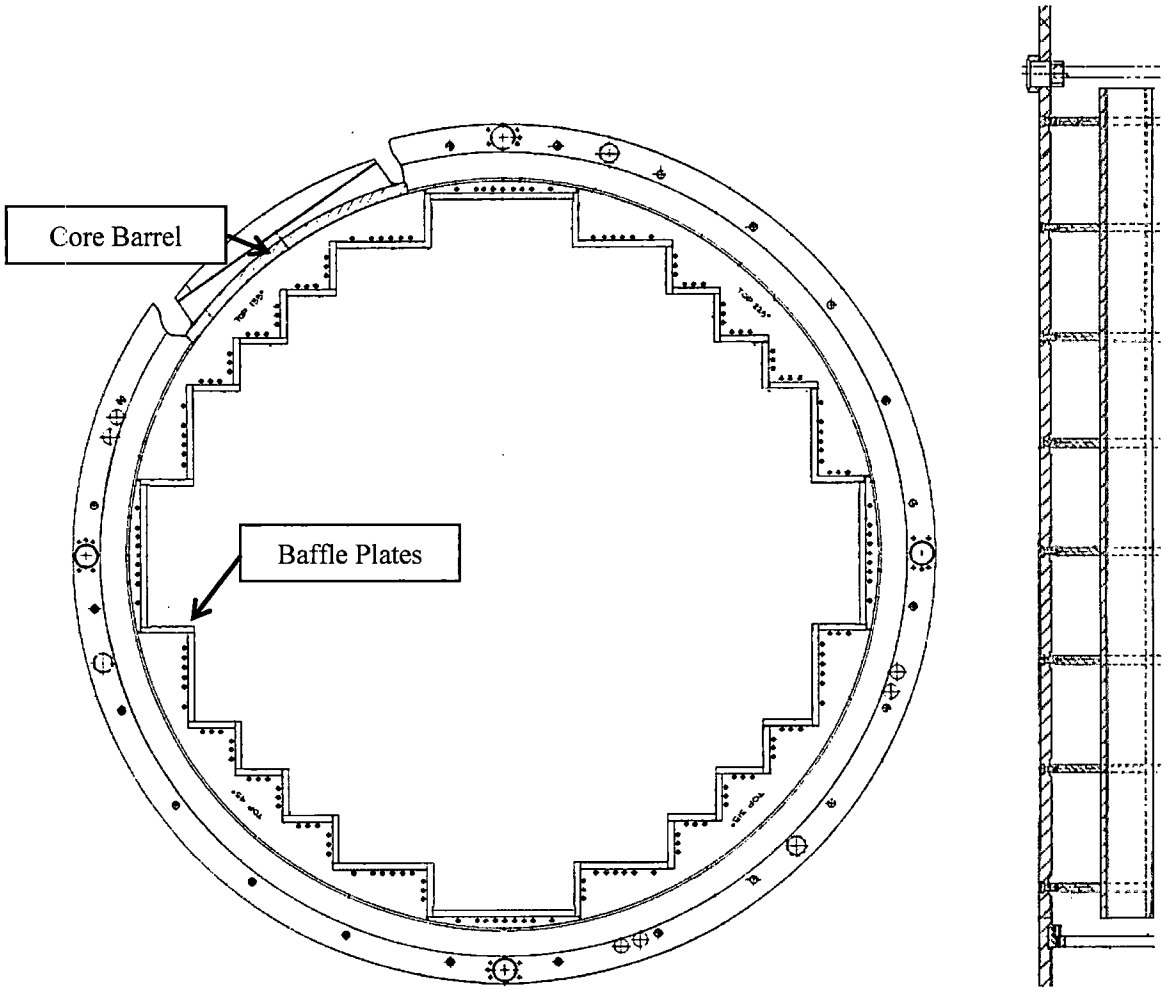

Figure RAI-4.2-3 Westinghouse 3 Loop Barrel/Baffle Channel

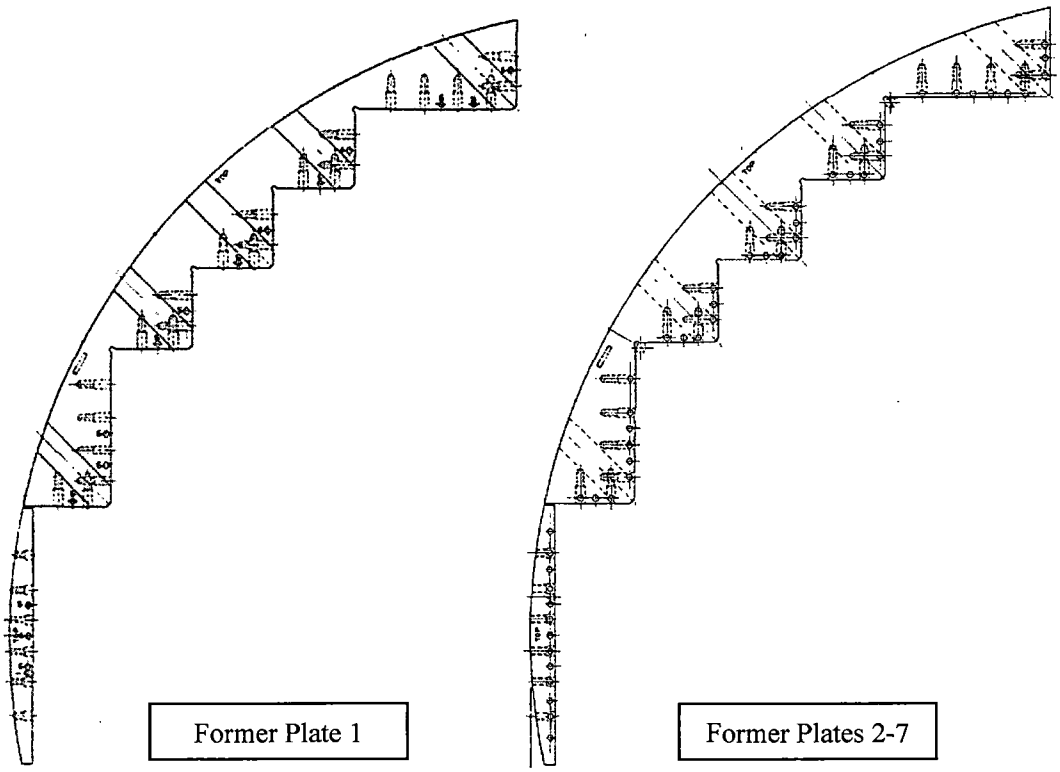

Figure RAI-4.2-4 Westinghouse 3 Loop Standard Upflow Plant Former Plates

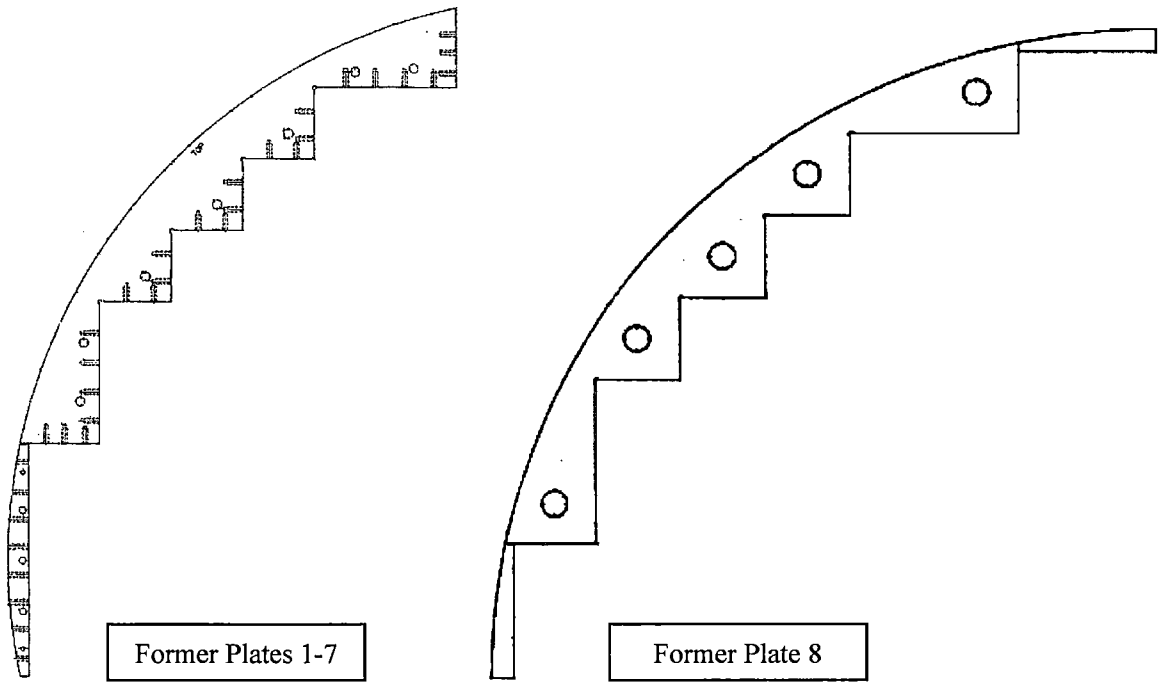

Figure RAI-4.2-5 Westinghouse 3 Loop Converted Upflow Plant Former Plates

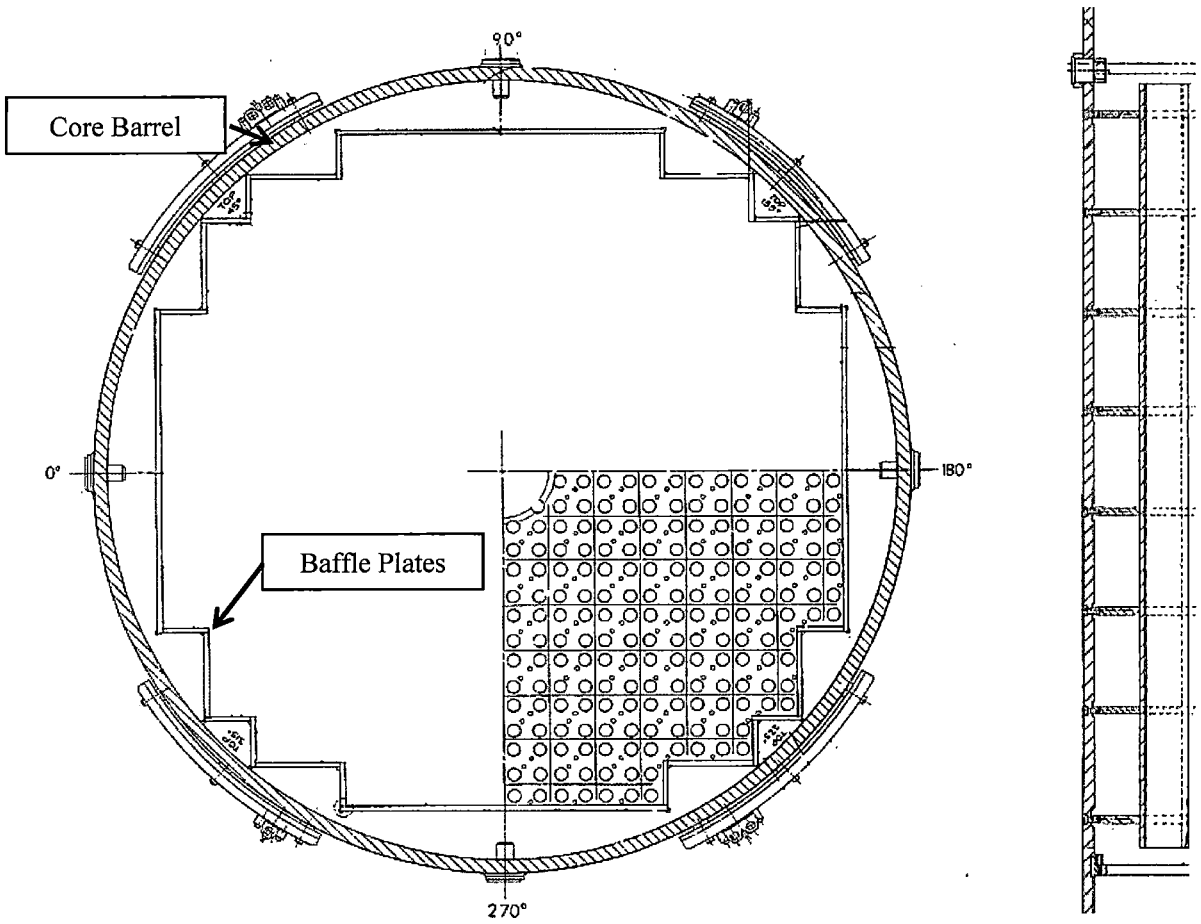

Figure RAI-4.2-6 Westinghouse 4 Loop Barrel/Baffle Channel

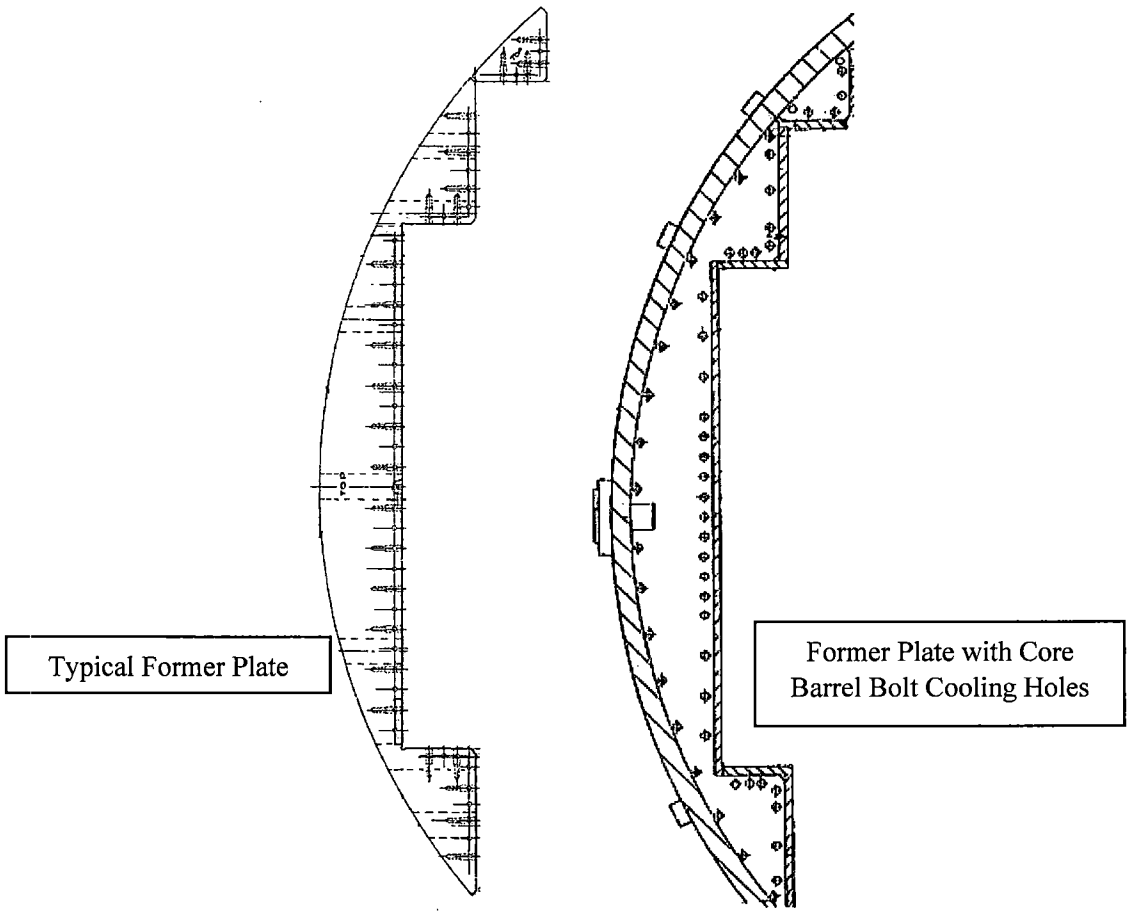

Figure RAI-4.2-7 Westinghouse 4 Loop Standard Upflow Plant Former Plates

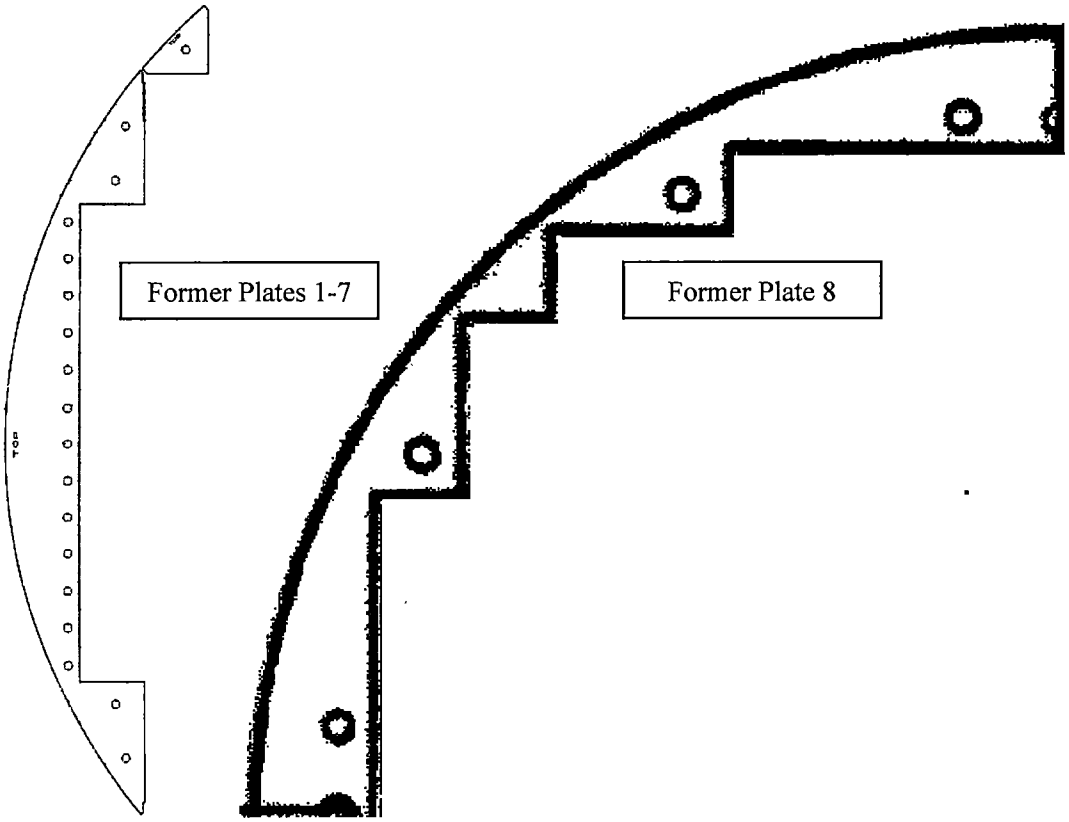

Figure RAI-4.2-8 Westinghouse 4 Loop Converted Upflow Plant Former Plates

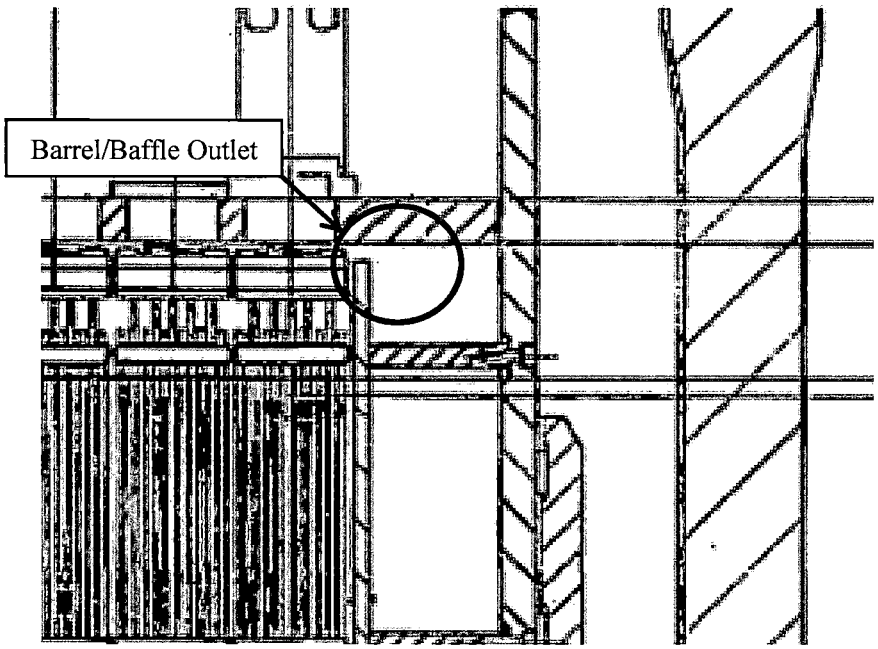

Figure RAI-4.2-9 Westinghouse 3 and 4 Loop Standard and Converted Upflow Barrel/Baffle Outlet Geometry

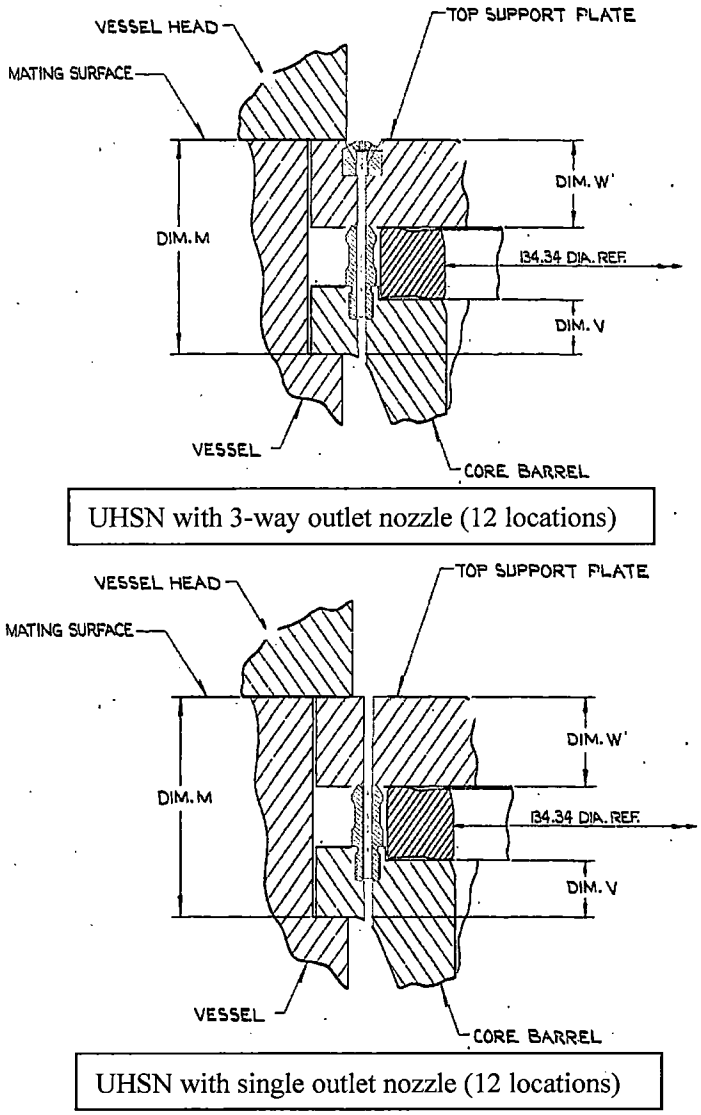

Figure RAI-4.2-10 Westinghouse 3 Loop Plants with T-Hot Upper Head Spray Nozzle Designs

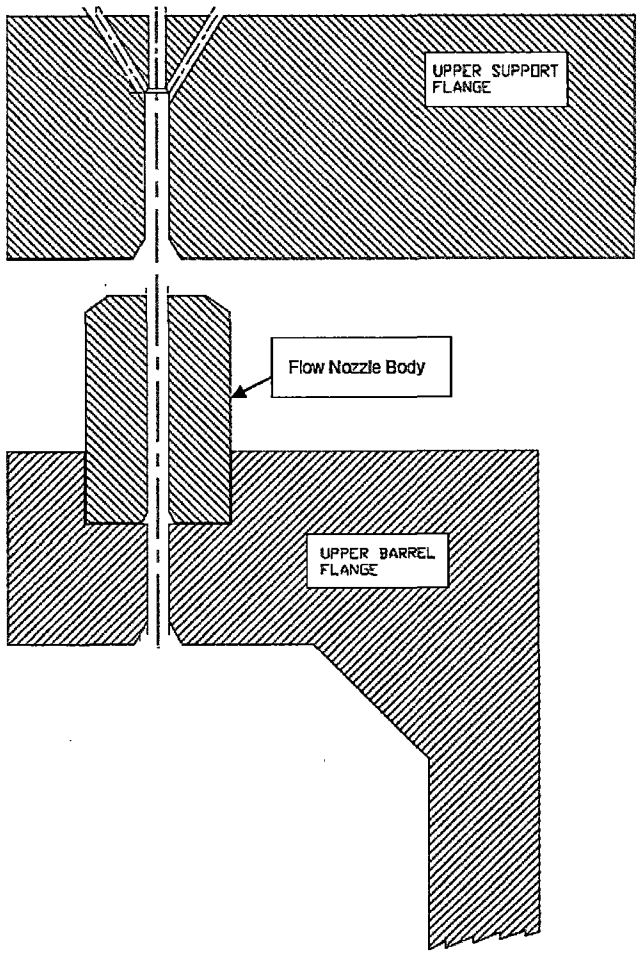

Figure RAI-4.2-11 Westinghouse 4 Loop Plants with T-Hot Upper Head Spray Nozzle Design

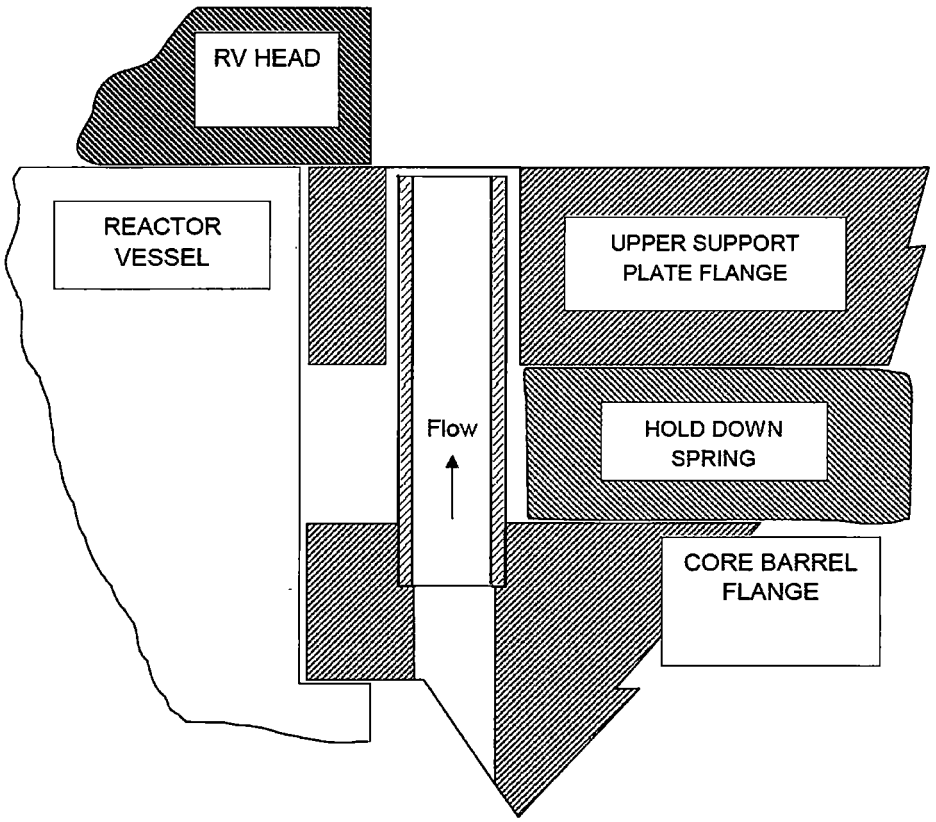

Figure RAI-4.2-12 Westinghouse 4 Loop Plants with T-Cold Upper Head Spray Nozzle Design

[ ] a,c

Figure RAI-4.2-13 The Effect of a Rounded or Chamfered Entrance on the Contraction Coefficient (Reference RAI-4.2-3)

Table RAI-4.2-6 Barrel/Baffle Inlet Geometry, Reference Area, and Loss Coefficient for Westinghouse Plants

[

] a,c

Table RAI-4.2-7 Calculation of Barrel/Baffle Inlet Loss Coefficient for Westinghouse 3 and 4 Loop Standard Upflow and 3 Loop Converted Upflow Design Plants

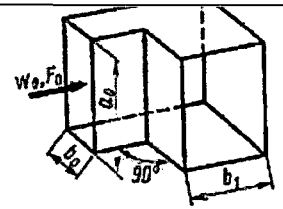

$$D_h = \frac{2a_0 b_0}{a_0 + b_0}$$

1. Smooth walls ($\Delta = 0$), $Re = \frac{w_0 D_h}{\nu} \geq 2 \times 10^5$;

$$\zeta = \frac{\Delta p}{\rho w_0^2/2}$$

at $l_0/D_h = 0$–2; $\zeta = \zeta_{loc} = f\left(\frac{b_1}{b_0}, \frac{a_0}{b_0}\right)$, see graph a;

at $l_0/D_h \geq 10$, $\zeta \approx 1.05\zeta_{loc}$

a,c

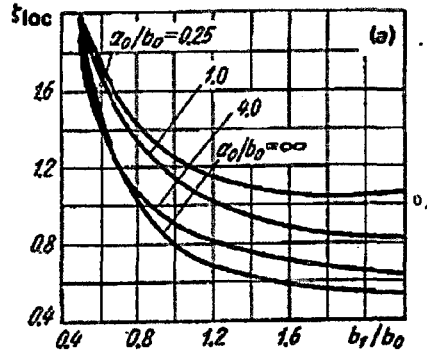

Values of ζ_{loc}

a_0/b_0	b_1/b_0 0.6	0.8	1.0	1.2	1.4	1.6	2.0
0.25	1.76	1.43	1.24	1.14	1.09	1.06	1.06
1.0	1.70	1.36	1.15	1.02	0.95	0.90	0.84
4.0	1.46	1.10	0.90	0.81	0.76	0.72	0.66
∞	1.50	1.04	0.79	0.69	0.63	0.60	0.55

Table RAI-4.2-8 Calculation of Barrel/Baffle Inlet Loss Coefficient for Westinghouse 4 Loop Converted Upflow Design Plants

a,c

Table RAI-4.2-9 Barrel/Baffle Former Plate Geometry and Flow Area for Westinghouse 3 Loop Standard Upflow Plants

[

] a,c

Table RAI-4.2-10 Barrel/Baffle Former Plate Geometry and Flow Area for Westinghouse 4 Loop Standard Upflow Plants[1]

[

] a,c

Table RAI-4.2-11 Barrel/Baffle Former Plate Geometry and Flow Area for Vogtle Unit 2

a,c

Table RAI-4.2-12 Barrel/Baffle Former Plate Geometry and Flow Area for Westinghouse 4 Loop XL Standard Upflow Plants

a,c

Table RAI-4.2-13 Barrel/Baffle Former Plate Geometry and Flow Area for Westinghouse 3 Loop Converted Upflow Plants

a,c

*** This record was final approved on 12/18/2017 11:42:20 AM. (This statement was added by the PRIME system upon its validation)

Table RAI-4.2-14 Barrel/Baffle Former Plate Geometry and Flow Area for Westinghouse 4 Loop Converted Upflow Plants[1]

a,c

Table RAI-4.2-15 Barrel/Baffle Former Plate Geometry and Flow Area for McGuire Units 1 and 2

a,c

Table RAI-4.2-16 Calculation of Former Plate Hole Loss Coefficients

[ ]a,c

Table RAI-4.2-16 Calculation of Former Plate Hole Loss Coefficients (cont'd)

Sudden expansion of a flow having a uniform velocity distribution[12,15,17]	Diagram 4-1

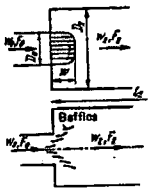

1. At $Re = \frac{w_2 D_2}{\nu} \geq 3.3 \times 10^5$:

a) Without baffles

$$\zeta = \frac{\Delta p}{\rho w_2^2/2} = \left(1 - \frac{F_0}{F_2}\right)^2 + \frac{\zeta_{fr}}{n_w^2} = \zeta_{sw} + \frac{\zeta_{fr}}{n_w^2}$$

where $\zeta_{sw} = f(F_0/F_2)$, see graph a; $\zeta_{fr} = \lambda(l_2/D_{2h})$; for λ see Chapter 2.

b) With baffles

$$\zeta = \frac{\Delta p}{\rho w_0^2/2} = 0.6\left(1 - \frac{F_0}{F_2}\right)^2 + \frac{\zeta_{fr}}{n_w^2}$$

$D_h = \frac{4F_0}{\Pi_0}$ $D_{2h} = \frac{4F_2}{\Pi_2}$

$n_w = \frac{F_2}{F_0}$ Π is the perimeter

Relative losses with a sudden expansion at supersonic velocities are considered in paragraphs 20 and 21 of Section 4-1

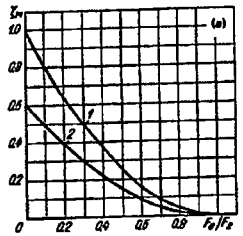

Values of ζ

$$F_0/F_2 = \frac{1}{n_w}$$

	0	0.1	0.2	0.3	0.4	0.5	0.6	0.7	0.8	1.0
Without baffles (curve 1)	1.00	0.81	0.64	0.50	0.36	0.25	0.16	0.09	0.04	0
With baffles (curve 2)	0.60	0.49	0.39	0.30	0.21	0.15	0.10	0.05	0.02	0

	Diagram 4-9
m	Resistance coefficient
	$\zeta = \frac{\Delta p}{\rho w_0^2/2}$

$$\zeta = 0.5\left(1 - \frac{F_0}{F_1}\right)^{3/4} + \zeta_{sh} = 0.5\sigma + \zeta_{sh},$$

where for σ see curve $\sigma = f(F_0/F_1)$; $\zeta_{sh} = \lambda \frac{l_0}{D_h}$; for λ see Chapter 2

1 Sharp

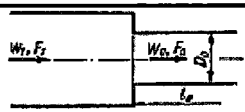

$D_h = \frac{4F_0}{\Pi_0}$

$\frac{F_0}{F_1}$	0	0.2	0.4	0.6	0.8	0.9	1.0
σ	1.0	0.850	0.680	0.503	0.300	0.178	0

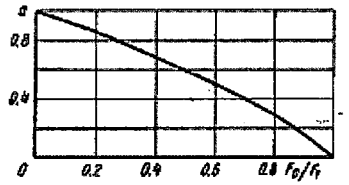

Table RAI-4.2-16 Calculation of Former Plate Hole Loss Coefficients (cont'd)

Thick-edged orifice ($l/D_h > 0.015$) in a straight tube (channel); **Diagram 4-15**
$Re = w_0 D_h/\nu > 10^{3.13.14}$

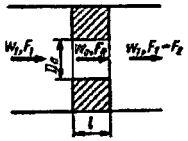

$$\zeta_1 = \frac{\Delta p}{\rho w_1^2/2} = \left[0.5\left(1-\frac{F_0}{F_1}\right)^{0.75} + \tau\left(1-\frac{F_0}{F_1}\right)^{1.375} + \left(1-\frac{F_0}{F_1}\right)^2 + \lambda\frac{l}{D_h}\right]\left(\frac{F_1}{F_0}\right)^2,$$

where τ see the table below or graph a of Diagram 4-12 or

$\tau = (2.4 - l) \times 10^{-\varphi(l)}$;

$\varphi(\bar{l}) = 0.25 + 0.535\bar{l}^{-9}/(0.05 + \bar{l}^{-9})$, see Chapter 2.

$D_h = \frac{4F_0}{\Pi_0}$

$\bar{l} = l/D_h$

$\zeta_0 = 0.5\left(1-\frac{F_0}{F_1}\right) + \left(1-\frac{F_0}{F_2}\right)^2 + \tau\sqrt{1-\frac{F_0}{F_1}}\left(1-\frac{F_0}{F_2}\right)$; for λ

At $\lambda = 0.02$ for the values of $\zeta_1 = f(l/D_h, F_0/F_1)$ see the graph

Values of ζ_1 at $\lambda = 0.02$

$\bar{l} = l/D_h$	τ	F_0/F_1 0.02	0.04	0.06	0.08	0.10	0.15	0.20	0.25	0.30	0.40	0.50	0.60	0.70	0.80	0.90	1.00
0	1.35	6915	1676	716	394	244	99.5	51.4	30.0	18.8	8.56	4.27	2.19	1.11	0.53	0.19	0
0.2	1.22	6613	1602	684	376	233	95.0	49.0	28.6	18.0	8.17	4.08	2.09	1.07	0.51	0.19	0
0.4	1.10	6227	1533	655	360	223	91.0	47.0	27.4	17.2	7.83	3.92	2.01	1.03	0.50	0.19	0.01
0.6	0.84	5708	1382	591	324	201	81.9	42.3	24.6	15.5	7.04	3.53	1.82	0.94	0.46	0.18	0.01
0.8	0.42	4695	1137	485	266	165	67.2	34.6	20.2	12.7	5.77	2.90	1.50	0.78	0.39	0.16	0.02
1.0	0.24	4268	1033	441	242	150	61.0	31.4	18.3	11.5	5.24	2.64	1.37	0.72	0.37	0.16	0.02
1.4	0.10	3948	956	408	224	139	56.4	29.1	17.0	10.7	4.86	2.45	1.29	0.68	0.36	0.16	0.03
2.0	0.02	3783	916	391	215	133	54.1	27.9	16.3	10.2	4.68	2.38	1.26	0.68	0.36	0.17	0.04
3.0	0	3783	916	391	215	133	54.3	28.0	16.4	10.3	4.75	2.43	1.30	0.71	0.39	0.20	0.06
4.0	0	3833	929	397	218	135	55.2	28.6	16.7	10.6	4.82	2.51	1.35	0.75	0.42	0.22	0.08
5.0	0	3883	941	402	221	137	56.0	29.0	17.0	10.8	5.00	2.59	1.41	0.79	0.45	0.24	0.10
6.0	0	3933	954	408	224	139	56.9	29.6	17.4	11.0	5.12	2.67	1.46	0.83	0.48	0.27	0.12
7.0	0	3983	966	413	227	141	57.8	30.0	17.7	11.2	5.25	2.75	1.52	0.87	0.51	0.29	0.14
8.0	0	4033	979	419	231	143	58.7	30.6	18.0	11.4	5.38	2.83	1.57	0.91	0.54	0.32	0.16
9.0	0	4083	991	424	234	145	59.6	31.0	18.3	11.6	6.50	2.91	1.63	0.95	0.58	0.34	0.18
10.0	0	4133	1004	430	237	147	60.5	31.6	18.6	11.9	5.62	3.00	1.68	0.99	0.61	0.37	0.20

Side branch

$\zeta_{s1} = \frac{\Delta p_s}{\rho w_1^2/2} = A\left[1 + \left(\frac{Q_1 F_2}{Q_s F}\right)^2 - 2\left(1-\frac{Q_1}{Q_s}\right)^2 - \frac{F_2}{F_s}\left(\frac{Q_1}{Q_s}\right)^2\right] + AC_s$,

$A = f(F/F_s, Q_1/Q_s)$, see Table 7-1;
for $\zeta_{s\infty}$ see the table and curves $\zeta_{s\infty} = f(Q_1/Q_s)$ at different F/F_s (graph a):

$\zeta_s = \frac{\Delta p_s}{\rho w_1^2/2} = \frac{\zeta_{s\infty}}{(Q_1 F/Q_s F_s)^2}$

Straight passage

$\zeta_{s\infty} = \frac{\Delta p_s}{\rho w_1^2/2} = 1 - \left(1-\frac{Q_1}{Q_s}\right)^2 - \frac{F_2}{F_s}\left(\frac{Q_1}{Q_s}\right)^2$

see the table and curves $\zeta_{s\infty} = f(Q_1/Q_s)$ at different F/F_s (graph b):

$\zeta_s = \frac{\Delta p_s}{\rho w_1^2/2} = \frac{\zeta_{s\infty}}{(1 - Q_1/Q_s)^2}$

Q_s/Q_1	F/F_s 0.1	0.2	0.3	0.4	0.6	0.8	1.0
0	−1.00	−1.00	−1.00	−1.00	−1.00	−1.00	−1.00
0.1	0.26	−0.42	−0.54	−0.58	−0.61	−0.62	−0.62
0.2	3.35	0.55	0.03	−0.13	−0.23	−0.26	−0.26
0.3	8.20	1.85	0.75	0.40	0.10	0	−0.01
0.4	14.7	3.50	1.55	0.92	0.45	0.35	0.28
0.5	23.0	5.50	2.40	1.44	0.78	0.58	0.50
0.6	33.1	7.90	3.50	2.05	1.08	0.80	0.68
0.7	44.9	10.0	4.60	2.70	1.40	0.98	0.84
0.8	58.5	13.7	5.80	3.32	1.64	1.12	0.92
0.9	73.9	17.2	7.65	4.05	1.92	1.20	0.99
1.0	91.0	21.0	9.70	4.70	2.11	1.35	1.00

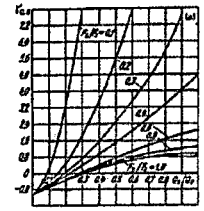

Values of $\zeta_{s\infty}$

Q_s/Q_1	F/F_s 0.1	0.2	0.3	0.4	0.6	0.8	1.0
0	0	0	0	0	0	0	0
0.1	0.09	0.14	0.16	0.17	0.17	0.18	0.18
0.2	0	0.16	0.23	0.26	0.29	0.31	0.32
0.3	−0.40	0.06	0.22	0.30	0.32	0.41	0.42
0.4	−1.00	−0.16	0.11	0.24	0.37	0.44	0.48
0.5	−1.75	−0.50	−0.08	0.13	0.33	0.44	0.50
0.6	−2.80	−0.95	−0.35	−0.10	0.25	0.40	0.48
0.7	−4.00	−1.55	−0.70	−0.30	0.05	0.28	0.42
0.8	−5.44	−2.24	−1.17	−0.64	−0.11	0.16	0.32
0.9	−7.20	−3.08	−1.70	−1.02	−0.38	−0.08	0.18
1.0	−9.00	−4.00	−2.30	−1.50	−0.68	−0.28	0

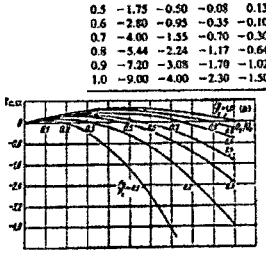

Table RAI-4.2-16 Calculation of Former Plate Hole Loss Coefficients (cont'd)

$$\zeta_s = \frac{\Delta p_s}{\rho w_s^2/2} = A'\left[1 + \left(\frac{w_t}{w_s}\right)^2 - 2\frac{w_t}{w_s}\cos\alpha\right] - A'\zeta_t,$$

where for A' see para. 16 of sec Figure 7-1. At $\alpha = 90°$, A' is taken to be 1.0

2. $\alpha = 90°$ and $h_t/h_s = 1.0$ (up to $w_t/w_s = 2.0$):

$$\zeta_s = \frac{\Delta p_s}{\rho w_s^2/2} = \zeta_{s\alpha}\left[1 + 0.3\left(\frac{w_t}{w_s}\right)^2\right]$$

where for $\zeta_{s\alpha}$ see the table and curves $\zeta_{s\alpha} = f(w_t/w_s)$ as different α.

h_s is the height of the cross section of the side branch;
h_t is the height of the cross section of the common straight channel

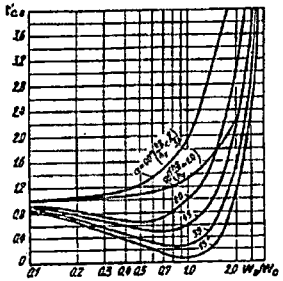

$$\zeta = \frac{\Delta p_t}{\rho w_t^2/2} = \frac{\zeta_{t\alpha}}{(w_t/w_s)^2}$$

$$\frac{w_t}{w_s} = \frac{Q_t F_s}{Q_s F_t}$$

Values of $\zeta_{s\alpha}$

$\frac{w_t}{w_s}$	α, °				$\alpha' = 90°$	
	15	30	45	60	$h_t/h_s \le 2/3$	$h_t/h_s = 1.0$
0	1.0	1.0	1.0	1.0	1.0	1.0
0.1	0.82	0.84	0.87	0.91	1.01	1.0
0.2	0.65	0.70	0.75	0.84	1.04	1.01
0.4	0.38	0.46	0.60	0.76	1.16	1.05
0.6	0.20	0.31	0.50	0.65	1.35	1.11
0.8	0.09	0.25	0.51	0.80	1.64	1.19
1.0	0.07	0.27	0.58	1.00	2.00	1.30
1.2	0.12	0.36	0.74	1.23	2.44	1.43
1.4	0.24	0.70	0.98	1.54	2.96	1.59
1.6	0.46	0.80	1.30	1.98	3.54	1.77
2.0	1.10	1.52	2.16	3.00	4.60	2.20
2.6	2.75	3.23	4.10	5.15	7.76	–
3.0	7.20	7.40	7.90	8.10	9.00	–
4.0	14.1	14.2	14.8	15.0	16.0	–
5.0	23.2	23.5	23.8	24.0	25.0	–
6.0	34.2	34.5	35.0	35.0	36.0	–
8.0	62.0	62.7	63.0	63.0	64.0	–
10	98.0	98.3	98.6	99.0	100	–

Diagram 10-2

Circular rough cylinder in a tube; plane-parallel flow (initial turbulence is slightly increased); $S_s/F_0 < 0.3$[20]

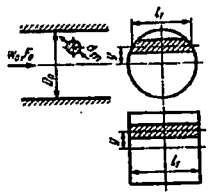

$$\zeta = \frac{\Delta p}{\rho w_0^2/2} = c_s \frac{S_s/F_0}{(1 - 0.5\,S_s/F_0)^2}\left(1 - \frac{2r}{D_t}\right)^{1.5}$$

where $c_s = f(\mathrm{Re}', \bar{\Delta})$, see the graph.

$$S_s = d_s l_s; \quad \mathrm{Re}' = \frac{w_0 d_s}{\nu}$$

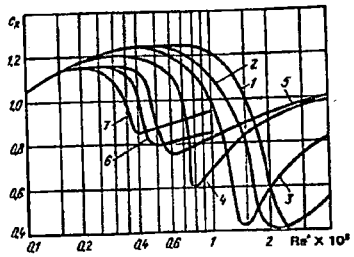

Values of c_s

$\bar{\Delta} \times 10^3$	Re × 10^{-3}																	
	1.0	2.0	2.5	3.0	3.5	4.0	4.5	5.0	5.5	6.0	6.5	7.0	8.0	9.0	10	15	20	40
0 (curve 1)	1.05	1.18	1.21	1.23	1.24	1.25	1.25	1.25	1.25	1.25	1.25	1.25	1.25	1.23	1.20	1.00	0.60	–
5 (curve 2)	1.05	1.18	1.20	1.22	1.24	1.25	1.25	1.25	1.25	1.25	1.25	1.21	1.18	1.15	1.10	0.80	0.40	0.55
20 (curve 3)	1.05	1.18	1.21	1.23	1.24	1.25	1.24	1.23	1.22	1.20	1.18	1.15	1.10	1.06	1.00	0.42	0.60	0.82
40 (curve 4)	1.05	1.18	1.20	1.20	1.20	1.20	1.18	1.17	1.15	1.12	1.07	1.00	0.60	0.65	0.70	0.83	0.90	0.98
70 (curve 5)	1.05	1.15	1.15	1.15	1.15	1.13	1.10	0.90	0.80	0.76	0.75	0.77	0.78	0.80	0.82	0.90	0.98	1.00
90 (curve 6)	1.05	1.15	1.15	1.15	1.10	1.06	0.83	0.79	0.80	0.81	0.82	0.83	0.84	0.85	0.85	–	–	–
200 (curve 7)	1.05	1.15	1.15	1.12	1.00	0.85	0.86	0.87	0.88	0.90	0.91	0.92	0.93	0.94	0.95	–	–	–

Table RAI-4.2-17 Former Plate Loss Coefficients and Reference Areas for Westinghouse Plants

[

] a,c

Table RAI-4.2-18 Barrel/Baffle Outlet Geometry and Flow Area for Westinghouse Plants

a,c

Table RAI-4.2-19 Total Barrel/Baffle Channel Resistance for Westinghouse Upflow Plants

a,c

Table RAI-4.2-20 Upper Head Spray Nozzle Geometry and Flow Area for Westinghouse 3 Loop Standard Downflow Plants with T-Hot Upper Heads

[

] a,c

Table RAI-4.2-21 Upper Head Spray Nozzle Geometry and Flow Area for Westinghouse 4 Loop Standard Downflow Plants with T-Hot Upper Heads

[

] a,c

Table RAI-4.2-22 Upper Head Spray Nozzle Geometry and Flow Area for Westinghouse 4 Loop Standard Downflow Plants with T-Cold Upper Heads

[

] a,c

Table RAI-4.2-23 Upper Head Spray Nozzle Loss Coefficients, Reference Flow Areas, and Total Resistance for Downflow Westinghouse Plants

[

] a,c

Table RAI-4.2-24 Plant Alternate Flow Path Pressure Drop used to Determine Base Plant Alternate Flow Path Resistances used in the GSI-191 Analyses

Plant	Licensed Power (MW)	Total Unadjusted $\frac{K}{A^2}$ (ft^{-4})	Pressure Drop (psi)	Total Adjusted $\frac{K}{A^2}$ (ft^{-4})
Upflow Plants				
Shearon Harris Nuclear Power Plant, Unit 1	2900	[		] a,c
Beaver Valley Power Station, Unit 2	2900			
Byron Station, Units 1 & 2	3645			
Braidwood Station, Units 1 & 2	3645			
Catawba Nuclear Station, Units 1 & 2	3411			
Comanche Peak Nuclear Power Plant, Units 1 & 2	3612			
Vogtle Electric Generating Plant, Unit 1	3625.6			
Vogtle Electric Generating Plant, Unit 2	3625.6			
Seabrook Station, Unit 1	3648			
Millstone Power Station, Unit 3	3650			
Wolf Creek Generating Station, Unit 1	3565			
Callaway Plant	3565			
Joseph M. Farley Nuclear Plant, Units 1 & 2	2775			
Virgil C. Summer Nuclear Station, Unit 1	2900			
North Anna Power Station, Unit 1	2940			
McGuire Nuclear Station, Units 1 & 2	3411			
Watts Bar Nuclear Plant, Unit 1	3459			
Watts Bar Nuclear Plant, Unit 2	3411			
Diablo Canyon Nuclear Power Plant, Unit 2	3411			
WCOBRA/TRAC Upflow Model	3658			]

RAI-4.2-24	**Plant Alternate Flow Path Pressure Drop used to Determine Base Plant Alternate Flow Path Resistances used in the GSI-191 Analyses (cont'd)**			
Plant	**Licensed Power (MW)**	**Total Unadjusted $\frac{K}{A^2}$ (ft^{-4})**	**Pressure Drop (psi)**	**Total Adjusted $\frac{K}{A^2}$ (ft^{-4})**
Downflow Plants				
Surry Power Station, Units 1 & 2	2587	[		] a,c
Turkey Point Nuclear Generating Units 3 & 4	2644			
H. B. Robinson Steam Electric Plant, Unit 2	2339			
North Anna Power Station, Unit 2[1]	2940			
Donald C. Cook Nuclear Plant, Unit 1	3304			
Donald C. Cook Nuclear Plant, Unit 2	3468			
Indian Point Nuclear Generating, Units 2 & 3	3216			
Salem Nuclear Generating Station, Units 1 & 2	3459			
Diablo Canyon Nuclear Power Plant, Unit 1	3411			
Sequoyah Nuclear Plant, Units 1 & 2	3455			
WCOBRA/TRAC Downflow Model (K_{max}, K_{split}, and m_{split} analyses)	2951			
WCOBRA/TRAC Downflow Model (t_{block} analysis)	2951			]
Note [1] North Anna Power Station, Unit 2 is now a converted upflow plant with AFP geometry identical to Unit 1				

b. Include a description of the assumptions used in the maximum and minimum BB flow resistance calculations given in Table 6-1.

Response

The following assumptions were used in the maximum BB flow resistance calculations given in Table 6-1:

- When determining dimensions from plant drawings, nominal values are used unless noted otherwise.
- Standard (design) upflow plants have pressure relief holes in the baffle plates. These flow paths are not credited in the GSI-191 TH analyses and the maximum BB resistance is based on the BB channel from the inlet to the outlet. See the Pressure Relief Hole Subsection at the end of this response for additional details regarding pressure relief holes.
- When determining the former plate reference area, flow holes, chamfers, stress relief holes, and gaps between former plate segments are considered. Gaps between the former plates and baffle plates are neglected, along with any other flow paths. When determining the total former plate reference area, the flow area due to chamfers, stress relief holes, and gaps is converted into equivalent flow holes with an equivalent loss coefficient using Eqs. RAI-4.2-3 and RAI-4.2-4.
- When determining the total former plate loss coefficient, an equivalent loss coefficient is determined used Eqs. RAI-4.2-5 and RAI-4.2-6. These equations ensure that the pressure drop across the former plate is preserved for a given flow rate.
- As the BB inlet, former plates, and BB outlet are in series, the total BB channel resistance can be calculated by summing all the individual resistances using Eq. RAI-4.2-7.
- Since the WCOBRA/TRAC BB channel is modeled with a different reference area, the total BB channel resistance is converted to an equivalent resistance using Eq. RAI-4.2-23, which ensures that the BB channel pressure drop will be preserved for a given flow rate.

The minimum BB flow resistance is no longer used in the GSI-191 thermal-hydraulic analyses, and the value will be removed from Table 6-1.

<u>Pressure Relief Holes in Westinghouse Standard Upflow Plant Designs</u>

RAI Question 6.4 requested additional information regarding the AFP testing completed in WCAP-17788, Volume 6. In the testing two hole sizes were tested over a range of flow conditions, and the tested hole sizes did not bound the smallest clearance present in baffle bolt cooling holes. As described in the response to RAI-4.2 Item a., baffle bolt cooling holes are credited when determining the maximum AFP resistance used in the Westinghouse upflow plant category thermal-hydraulic analysis. Since testing did not demonstrate that baffle bolt cooling holes will not block with debris,

the NRC reviewer has requested additional information regarding the impact of baffle bolt cooling holes in the calculation of the AFP resistance. This discussion provides the requested information.

Westinghouse 3 and 4 loop standard upflow plants have pressure relief holes in the baffle plates that connect the core region to the barrel/baffle channel. These plant types are the only plants that have baffle bolt cooling holes in the former plates. As described in the response to RAI-4.2 Item a., the pressure relief holes are not credited in the calculation of the barrel/baffle form loss coefficient used in the Westinghouse upflow plant category thermal-hydraulic analysis. It is of interest to calculate the total flow resistance from the barrel/baffle inlet to the core via the first row of pressure relief holes considering only through holes (Type 1 holes) in the former plates for Westinghouse standard upflow plants. This effectively assumes that baffle bolt cooling holes will block with debris. If it can be shown that the total flow resistance of this path is bounded by the maximum resistance considered in the thermal-hydraulic analysis, then not demonstrating through testing that baffle bolt cooling holes will not block with debris can be justified.

3 Loop Standard Upflow Plants

The drawing numbers, the number of pressure relief holes in each plate, and the elevations of the holes referenced from the bottom of the plate are provided in Table RAI-4.2-25 for 3 loop standard upflow plants. Each drawing consists of an individual baffle plate, and the 6 plates put together create an eight segment of the total baffle plate circumference.

Table RAI-4.2-25 Pressure Relief Hole Information for Westinghouse 3 Loop Standard Upflow Design Plants

Drawing Number	Drawing Revision	Number of Holes per Elevation	Elevations (in.)
6116E42	3	[	] a,c
6116E43	4		
6116E44	4		
6116E45	3		
6116E46 (Baffle Key Plate)	4		
6116E47	4	[	]

Based on the information provided in Table RAI-4.2-25, there are [ ]^{a,c} at each of the four pressure relief hole elevations. Each of the pressure relief holes has a [ ]^{a,c} diameter. The first pressure relief hole elevation is just below the third former plate. The second elevation is just below the fourth former plate, and so on.

The flow area through each of the four pressure relief hole elevations is calculated as follows:

[ ]^{a,c}

The loss coefficient through the holes is based on a [

]^{a,c}

As shown in Table RAI-4.2-6, 3 loop standard upflow plants have a barrel/baffle inlet area of [ ]^{a,c} and an inlet loss coefficient of 1.5. From Table RAI-4.2-9, the first former plate has [ ]^{a,c} The second former plate has [ ]^{a,c} The loss coefficient for the holes is [ ]^{a,c}

Using this information, the geometric dimensional form loss (K/A^2) for this path is determined by taking the summation of the K/A^2 for the BB inlet, the former plates, and the first elevation of pressure relief holes, similar to Eq. RAI-4.2-7. The total K/A^2 is defined as:

$$\left(\frac{K}{A^2}\right)_{BB\_PR} = \left(\frac{K}{A^2}\right)_{LCP} + \left(\frac{K}{A^2}\right)_{F1-2} + \left(\frac{K}{A^2}\right)_{RP\_1} \qquad \text{Eq. RAI-4.2-24}$$

The three terms on the right hand side of the equation were determined using the reference areas and loss coefficients determined above, and the resulting total loss is:

$$\left(\frac{K}{A^2}\right)_{BB\_PR} = \left[\quad \right]^{a,c}$$

As shown in Table RAI-4.2-24, the two Westinghouse 3 loop standard upflow plants (Shearon Harris Nuclear Power Plant, Unit 1 and Beaver Valley Power Station, Unit 2) use a total unadjusted barrel/baffle channel form loss of [ ]^{a,c} in the calculation of the total adjusted form loss that is compared to the form loss applied in the WCOBRA/TRAC model. Since the total unadjusted form loss calculated for the flow path that credits the first elevation of pressure relief holes is less than the unadjusted form loss shown in Table RAI-4.2-24 for these plants, the resistance of this flow path is bounded by the resistance used in the WCOBRA/TRAC model and demonstrates that baffle bolt cooling holes (Type 2 holes) in the Westinghouse 3 loop standard upflow plant design do not need to be credited in the form loss calculation.

4 Loop Standard Upflow Plants

The drawing numbers, the number of pressure relief holes in each plate, and the elevations of the holes referenced from the bottom of the plate are provided in Table RAI-4.2-26. A quarter segment of the baffle circumference is created when the 7 plates shown in the table are combined.

Table RAI-4.2-26 Pressure Relief Hole Information for Westinghouse 4 Loop Standard Upflow Design Plants			
Drawing Number	**Drawing Revision**	**Number of Holes per Elevation**	**Elevations (in.)**
6116E89 (Baffle Key Plate)	1	[	] a,c
6116E90 (Baffle Key Plate)	1		
6116E91 (2 plates)	2		
6116E92	3		
6116E93 (2 plates)	1		]

Based on the information provided in Table RAI-4.2-26, there are [ ]^{a,c} per each of the four pressure relief hole elevations. Each of the pressure relief holes has a [ ]^{a,c} diameter. The first pressure relief hole elevation is just below the third former plate. The second elevation is just below the fourth former plate, and so on.

The flow area through each of the four pressure relief hole elevations is calculated as follows:

[ ]^{a,c}

The loss coefficient through the holes is the same as that used for the 3 loop plant design; [ ]^{a,c}

From Table RAI-4.2-6, a value of [ ]^{a,c} will be used for the barrel/baffle inlet reference area, and a value of 1.5 will be used for the inlet loss coefficient.

Per Table RAI-4.2-10, 4 loop standard upflow plants have [ ]^{a,c} The loss coefficient for the holes is [ ]^{a,c}

Per Table RAI-4.2-11, Vogtle Unit 2 is different since it has core barrel bolt cooling holes, and has [ ]^{a,c} The loss coefficient for the holes is [ ]^{a,c}

Using this information, the geometric dimensional form loss (K/A^2) for this path is determined by taking the summation of the K/A^2 for the BB inlet, the former plates, and the first elevation of pressure relief holes, as shown in Eq. RAI-4.2-24.

The three terms on the right hand side of the equation were determined using the reference areas and loss coefficients determined above for all 4 loop standard upflow plants except Vogtle Unit 2, and the resulting total loss is:

$$\left(\frac{K}{A^2}\right)_{BB\_PR} = \left[\quad \right]^{a,c}$$

For Vogtle Unit 2, the calculation yields:

$$\left(\frac{K}{A^2}\right)_{BB\_PR} = \left[\quad \right]^{a,c}$$

As shown in Table RAI-4.2-24, the Westinghouse 4 loop standard upflow plants:

- Byron/Braidwood Units 1 & 2,
- Comanche Peak Units 1 & 2,
- Vogtle Unit 1,
- Seabrook Unit 1,
- Millstone Unit 3,
- Wolf Creek Unit, and
- Callaway Plant

use a total unadjusted barrel/baffle channel form loss of [ ]^{a,c} for Catawba Units 1 & 2 in the calculation of the total adjusted form loss that is compared to the form loss applied in the WCOBRA/TRAC model. Since the total unadjusted form loss calculated for the flow path that credits the first elevation of pressure relief holes is less than the unadjusted form loss shown in Table RAI-4.2-24, the resistance of this flow path is bounded by the resistance used in the WCOBRA/TRAC model and demonstrates that baffle bolt cooling holes (Type 2 holes) in the Westinghouse 4 loop standard upflow plant design do not need to be credited in the form loss calculation.

Due to the limited number of Type 1 holes in the Vogtle Unit 2 plant due to the presence of core barrel bolt cooling holes, the form loss for the flow path to the first row of pressure relief holes is not bounded by the value shown in Table RAI-4.2-24 when bolt cooling holes are not credited. As such, additional plant-specific justification is required for this plant to use the GSI-191 thermal-hydraulic analysis results from the Westinghouse upflow plant category. Alternatively, Vogtle Unit 2 could use the GSI-191 thermal-hydraulic analysis results from the Westinghouse downflow plant category since the Vogtle Unit 2 upper head spray nozzle resistance is bounded by the resistance applied to the Westinghouse downflow plant category. The upper head spray nozzle resistance applied in the downflow plant model is based on a T-hot upper head spray nozzle design. Vogtle Unit 2 has a T-cold upper head spray nozzle design that is significantly less resistive because the upper head spray nozzles have a larger flow area.

c. Include a description of the assumptions used in the maximum and minimum UHSN calculations provided in Table 6-2.

Response

The following assumptions were used in the maximum UHSN flow resistance calculations given in Table 6-1:

- When determining dimensions from plant drawings, nominal values are used unless noted otherwise.
- No other flow paths between the upper downcomer and the upper head are credited besides the UHSN flow holes.
- The UHSN reference area is based on the inlet area of the UHSN holes through the upper core barrel flange.
- Since the WCOBRA/TRAC UHSNs are modeled with a different reference area, the UHSN resistance is converted to an equivalent resistance using Eq. RAI-4.2-23, which ensures that the UHSN pressure drop will be preserved for a given flow rate.

The minimum UHSN flow resistance is no longer used in the GSI-191 thermal-hydraulic analyses, and the value will be removed from Table 6-1.

d. For Items a and b, describe whether the flow passages between the downcomer and upper plenum regions via the hot leg nozzle gaps were modeled and provide a justification for the modeling approach.

Response

The mentioned flow passages were not modeled. Neglecting these flow passages maximizes the quantity of debris reaching the core inlet by limiting the quantity that bypasses the core inlet. Neglecting these passages also creates a scenario in which the highest quantity of coolant is required to reach the core through the credited AFP to effectively remove decay heat.

e. For each Westinghouse unit considered in determining the BB and UHSN resistances in Tables 6-1 and 6-2, provide the following information in a table format, separately for both Westinghouse upflow and downflow plant category. In individual columns, include a description for each of the following items:

i. Name and rated power

ii. Identification numbers of design drawings, including the name of the unit for which they were produced, containing the geometric data to calculate the resistance associated with the

1. lower core plate to baffle region gap
2. former holes including the number of former plates with holes
3. upper core plate to baffle region gap
4. UHSNs

iii. For each category of flow passage, identify all types and sizes of openings that are credited in the resistance calculation. As a minimum, include

1. the number of holes or gaps
2. hole diameter or gap width and perimeter length
3. individual hole or gap flow area for each type of holes/gaps
4. total resulting flow area

iv. Loss coefficients associated with each category of passage along with the reference flow area

v. Total unadjusted and adjusted BB/UHSN resistances along with the units

vi. Assumptions related to the way geometric data in the drawings was treated for the purpose of calculating resistances and assumptions related to the consideration of any other existing flow passages such as pressure relief holes in the baffle plates.

Response

i. The name and rated power for each Westinghouse unit considered in determining the BB and UHSN resistances is shown in Table RAI-4.2-1.

ii. The identification numbers of design drawings containing the geometric data to calculate the AFP resistances for each Westinghouse plant considered in the GSI-191 TH analyses are shown in the following tables:

1. lower core plate to baffle region gap - Table RAI-4.2-2
2. former holes including the number of former plates with holes - Table RAI-4.2-3
3. upper core plate to baffle region gap - Table RAI-4.2-4
4. UHSNs - Table RAI-4.2-5

iii. Table RAI-4.2-6 provides the geometry and total resulting flow area for the BB inlet.

Tables RAI-4.2-9 through RAI-4.2-15 provides the geometry of all types and sizes of openings that are credited in the former plate resistance calculation for the various Westinghouse upflow plant designs. The individual hole or gap area and total resulting flow area is also included in the tables.

Table RAI-4.2-18 provides the geometry and total resulting flow area for the BB outlet.

Tables RAI-4.2-20 through RAI-4.2-22 provides the geometry of all types and sizes of holes that are credited in the UHSN resistance calculation for the various Westinghouse downflow plant designs. The individual hole area and total resulting flow area is also included in the tables.

iv. Table RAI-4.2-6 provides the loss coefficients and reference areas associated with the BB inlet.

Table RAI-4.2-17 provides the average loss coefficients and reference areas associated with the former plates. Calculation of the average former plate loss coefficients is provided in the response to RAI-4.2 Item a., Step 1. The individual former plate hole loss coefficients are provided in this section as well.

Table RAI-4.2-18 provides the loss coefficients and reference areas associated with the BB outlet.

Table RAI-4.2-23 provides the loss coefficients and reference areas associated with the UHSNs.

v. The total unadjusted BB/UHSN resistances, K/A^2, in units ft^{-4} for all plants are provided in Table RAI-4.2-24. The table also shows the adjusted BB/UHSN resistances and the values used in the WCOBRA/TRAC models.

vi. Assumptions related to the way geometric data was treated for calculating resistances and assumptions related to the consideration of any other flow passages are provided in the responses to RAI 4.2b. and RAI 4.2c.

f. For each table in Item e, include a figure that illustrates the BB region and UHSN region geometries for each Westinghouse plant category and a separate figure showing an example of a BB former region top view for one-quarter of the core region. (Appropriate examples of such figures appear as Figures 1 and 2 in a March 26, 2001, letter by Exelon Generation Company, LLC, ADAMS Accession No. ML010890050.)

Response

The following figures provide the requested information:

- Figure RAI-4.2-1 Westinghouse 3 and 4 Loop Standard Upflow and 3 Loop Converted Upflow Barrel/Baffle Inlet Geometry
- Figure RAI-4.2-2 Westinghouse 4 Loop Converted Upflow Barrel/Baffle Inlet Geometry
- Figure RAI-4.2-3 Westinghouse 3 Loop Barrel/Baffle Channel
- Figure RAI-4.2-4 Westinghouse 3 Loop Standard Upflow Plant Former Plates
- Figure RAI-4.2-5 Westinghouse 3 Loop Converted Upflow Plant Former Plates

- Figure RAI-4.2-6 Westinghouse 4 Loop Barrel/Baffle Channel
- Figure RAI-4.2-7 Westinghouse 4 Loop Standard Upflow Plant Former Plates
- Figure RAI-4.2-8 Westinghouse 4 Loop Converted Upflow Plant Former Plates
- Figure RAI-4.2-9 Westinghouse 3 and 4 Loop Standard and Converted Upflow Barrel/Baffle Outlet Geometry
- Figure RAI-4.2-10 Westinghouse 3 Loop Plants with T-Hot Upper Head Spray Nozzle Designs
- Figure RAI-4.2-11 Westinghouse 4 Loop Plants with T-Hot Upper Head Spray Nozzle Design
- Figure RAI-4.2-12 Westinghouse 4 Loop Plants with T-Cold Upper Head Spray Nozzle Design

g. During the NRC staff audit of supporting Westinghouse documents and drawings on February 2-4, 2016, it was observed, for the upflow BB plant category, former plate holes of Type 1 were assigned a loss coefficient of [ ] and those of Type 2 were assigned a loss coefficient of [ ]. The staff could not determine the basis for those values. Provide the calculations and supporting documentation for each of these loss coefficients, as well as for other loss coefficients identified in the response to Item e.iv above.

Response

The response to RAI-4.2 Item a., Step 1 provides the calculations for each of the former plate hole types, as well as the other loss coefficients used to determine the total AFP resistance.

h. During the NRC staff audit of supporting Westinghouse documents and drawings on February 2-4, 2016, the average loss coefficient for the upflow plant category, KAVG, from former plate holes of Type 1 and Type 2 was computed from the individual loss coefficients, Ki, [ ]. Explain the rationale for using an averaging equation to obtain an equivalent loss coefficient value and demonstrate whether physical parameters are preserved by using this method (e.g., flow or pressure loss). Examine the effects of the averaging method on the resulting resistances for both maximum and minimum resistance cases. If the averaging method is found inconsistent, implement an appropriate approach and update the BB resistance results for the Westinghouse upflow and downflow plant categories.

Response

In responding to this RAI, a new averaging scheme was developed to compute the average former plate loss coefficient. The new averaging scheme is described in the response to RAI-4.2 Item a., Step 1. Specifically, Eq. RAI-4.2-5 provides the averaging scheme. The use of this scheme ensures that the pressure loss for a given flow rate is preserved. The new averaging scheme reduced the average former plate loss coefficient slightly. For example, the Westinghouse 4 loop standard upflow former plate design, the new averaging scheme produces an average loss coefficient of [ ]^{a,c} as shown in Table RAI-4.2-17. The original averaging scheme produced an average loss coefficient of [ ]^{a,c}

References

RAI-4.2-1 NRC Information Digest (NUREG-1350, Volume 26), "Appendix A: U.S. Commercial Nuclear Power Reactors – Operating Reactors."

RAI-4.2-2 Idelchik, I. E., "Handbook of Hydraulic Resistance," 3rd Edition, CRC Press, 1994.

RAI-4.2-3 WCAP-3269-62, "Hydraulic Design of a Rod Cluster Control Fuel Assembly," September 1965.

RAI-4.3, Vol. 4

Section 6.3, "Combustion Engineering Plant Model," states that a method and supporting calculations for calculating appropriate BB flow resistances that represent all CE plants in operation in the U.S. are contained in Reference 6-3 and Reference 6-4. These two references are identified in Section 6.5 and updated in Letter OG-16-42 dated February 12, 2016, as follows.

Reference 6-3: [

].

Reference 6-4: [

].

a. Provide copies of References 6-3 and 6-4 listed above.

Response

Responding to this RAI resulted in changes to WCAP-17788, Volume 4, Reference 6-3 and Reference 6-4. As such, Reference 6-3 and Reference 6-4 are superseded by this RAI response. WCAP-17788, Volume 4, Section 6.3 and Section 6.5 will be updated to reflect removal of these references, and the following discussion will be added as an appendix to WCAP-17788, Volume 4.

Combustion Engineering (CE) plants have channels that run parallel to the core region that are similar to the barrel/baffle (BB) channel in Westinghouse upflow plants. In CE plants, these channels are commonly referred to as the core shroud annulus; however, for consistency, this RAI response will follow the Westinghouse terminology and refer to this as the BB channel. All CE plants have upflow BB channel designs and the BB channel is the only alternate flow path (AFP) considered in the CE plant GSI-191 thermal-hydraulic (TH) analyses. Since the AFP is being credited to remove decay heat following core inlet blockage, loss coefficients need to be determined that bound all plants being evaluated. The objective is to determine a maximum BB resistance that bounds all CE PWRs operating in the U.S. It is noted that WCAP-17788, Volume 4 also provides a minimum BB channel loss coefficient. The analyses that used the minimum BB channel resistance have since been revised to use a mid-point and maximum BB resistance (See RAI-4.20). As such, discussion regarding determination of the minimum BB resistance is omitted herein.

The following general approach, which is consistent with the Westinghouse approach described in the response to RAI 4.2, is applied for determining the BB channel resistance used in the CE GSI-191 TH analyses:

Step 1 – Determine the total resistance (K/A^2) for the BB channel from physical plant geometry.

Step 2 – Determine an equivalent maximum BB channel resistance for the base plant model for use in the GSI-191 analyses that bound all plant BB channel resistances.

Each step is discussed in the following sections. The response to RAI-4.2 Item a. included a third step that involved converting the maximum resistance determined form plant geometry to an equivalent value based on the WCOBRA/TRAC BB channel area. This same step was applied when determining the equivalent resistance value used in the CE plant S-RELAP5, but it is not discussed as part of this RAI response. The process is similar to that described in Step 3 in the response to RAI-4.2 Item a. A dimensionless loss coefficient is calculated using Eq. RAI-4.2-23 for entry into the CE plant S-RELAP5 model.

Step 1

The name and rated power for each CE unit considered in determining the BB channel resistances is provided in Table RAI-4.3-1. The rated power in the table is the licensed power for each unit taken from Reference RAI-4.3-1. In general, the BB channel geometry is similar among plant sites that have multiple units (e.g., Palo Verde Units 1, 2, and 3). Determination of the BB channel resistances is broken into the eight plants shown in Table RAI-4.3-1.

When determining total BB channel resistance, losses through the BB channel inlet, BB channel girth ribs (girth ribs are equivalent to former plates in Westinghouse plants), and BB channel outlet are considered. Table RAI-4.3-2 lists the plant drawing numbers used to determine the BB channel inlet, former plate, and outlet geometry.

In WCAP-17788, Volume 4, Reference 6-3 and Reference 6-4 BB channel geometry (reference area) and loss coefficients were derived directly from plant drawings or existing sources that calculated core bypass flows under normal operating conditions. The calculations were further divided between vendors. Reference 6-3 provided AFP information calculated by AREVA, and Reference 6-4 provided calculations completed by Westinghouse. In response to this RAI, the previous calculational methods were reviewed and repeated using the plant drawings identified in Table RAI-4.3-2. In most cases, the recalculated areas and loss coefficients agreed very well with the historical values. In a few instances adjustments were made to the values used for the GSI-191 TH analyses. It is noted that THRIVE data, as described in the response to RAI-4.2, does not exist for most CE plants as is does for Westinghouse plants. As such, the THRIVE methodology is not discussed in this RAI response. In general, the previous methodology used by Westinghouse to calculate the BB channel resistance for CE plants is consistent with the THRIVE methodology.

Barrel/Baffle Inlet

CE plants have two basic inlet designs. The earliest design, which is present in Palisades Nuclear Plant and Fort Calhoun, is similar to the Westinghouse design. There are flow holes in the lower core plate that allow coolant to enter the BB channel. This design is shown in Figure RAI-4.3-1. The BB channel inlet for the newer vintage and CE System 80 designs is shown in Figure RAI-4.3-2. As shown in the figure, flow from the core support region enters an annulus between the core support cylinder and the core barrel that leads to the BB channel.

Regardless of inlet design, the BB inlet area is taken as the total area of these flow holes:

$$A_{inlet} = N \times \frac{\pi}{4}(D)^2 \qquad \text{Eq. RAI-4.3-1}$$

Where N is the number of flow holes and D the diameter of the holes.

Table RAI-4.3-3 provides the BB inlet geometry and reference area for the CE fleet.

For the first inlet design (Figure RAI-4.3-1), the resistance is calculated as an abrupt contraction and expansion:

$$K_{inlet} = 0.095\left(1 - \frac{A_1}{A_0}\right) + \left(\frac{1}{C_c} - 1\right)^2 + \left(1 - \frac{A_1}{A_2}\right)^2 \qquad \text{Eq. RAI-4.3-2}$$

Where A_0 is the upstream flow area, A_1 the area through the holes, and A_2 the downstream flow area. The first term on the right hand side of Eq. RAI-4.3-2 is the contraction loss, the third term is the expansion loss, and the second term accounts for the reattachment of the vena-contracta. If the passage length-to-diameter ratio (L/D) is less than 1.0, then the vena-contracta will not reattach and the contraction coefficient, $C_c = 1$. If L/D is greater than 1.0, the contraction coefficient is calculated as follows (See Figure RAI-4.3-3, Reference RAI-4.3-2):

[ ]^{a,c} Eq. RAI-4.3-3

The BB channel inlet loss coefficient for the other shroud inlet design (Figure RAI-4.3-2) has additional losses to account for increased expansion into the support cylinder annulus and a 90 degree turn:

$$K_{inlet} = K_{0-2} + K_{2-3} + K_{90°}, \qquad \text{Eq. RAI-4.3-4}$$

Where the term K_{0-2} is the loss calculated using Eq. RAI-4.3-2, K_{2-3} is calculated as follows:

$$K_{2-3} = \left(1 - \frac{A_2}{A_3}\right)^2 \left(\frac{A_1}{A_2}\right)^2. \qquad \text{Eq. RAI-4.3-5}$$

A_2 corresponds to the expansion area adjacent to the holes in the core support cylinder, A_3 corresponds to the entire area between the core support barrel and the support cylinder (See Figure RAI-4.3-4), and $K_{90°}$ is set equal to:

[ ]^{a,c} which assumes a miter bend. Eq. RAI-4.3-6

For all CE plants, the calculation assumes that the vena-contracta reattaches, and C_c is calculated with Eq. RAI-4.3-3. This assumption is conservative since the reattaching vena-contracta results in a higher resistance. The calculation also assumes that the upstream area (A_0) is equal to the area of the entire core barrel, or core support cylinder for the new CE designs, and neglects any structures below the lower core support plate. This assumption makes the upstream area larger, which is conservative.

Table RAI-4.3-3 provides the BB inlet loss coefficients for the CE fleet.

Barrel/Baffle Former Plates

All CE plants, except the System 80 design (Palo Verde), have some kind of former plate in the BB channel. Figure RAI-4.3-5 shows the BB channel and former plate design for Palisades. As the figure shows, there are 8 former plate elevations, and the BB channel is free of any other structures. Each former plate elevation has 20 slots and there is a gap between each former plate and the core barrel. The reference area is calculated considering the slots and the gap at the core barrel.

The BB channel in Fort Calhoun is similar in design, as shown in Figure RAI-4.3-6. The primary difference between Fort Calhoun and Palisades is the design of the slots in the former plates. As shown in Figure RAI-4.3-6, the slots are thinner and have holes drilled at each end. The gap between the former plates and the core barrel is also larger in Fort Calhoun. When calculating the reference area for the Fort Calhoun former plates, the area created by the [ ]^{a,c} slots is neglected. This reduces the area and increases the resistance through the former plates.

The newer CE BB channel design is shown in Figure RAI-4.3-7, which applies to St. Lucie Unit 1, Calvert Cliffs Units 1 and 2, Millstone Unit 2, and Waterford 3. In this shroud design, the former plates are an integral part of the core baffle plate assemblies, and there are 7 former plate elevations. The first former plate sits directly on the bottom core plate. This region is referred to as the "shroud foot", as shown in Figure RAI-4.3-8. The mid-plane former plate is also twice as thick, since the baffles are constructed as two assemblies stacked on top of each other. There are also vertical ribs welded to the baffle plates that protrude into the BB channel. Each former plate elevation has 8 holes and 16 slots. There is also a gap between the former plates and the core barrel. The mid-plane former plate also has 44 additional holes (not shown in Figure RAI-4.3-7). When calculating the reference area for this former plate design, all slots and holes are neglected, and only the area created by the gap at the core barrel is considered.

Figure RAI-4.3-9 shows a similar BB channel design, which is applicable to St. Lucie Unit 2, and Arkansas Nuclear One Unit 2. As shown in the figure, there are 12 slots per former elevation and no holes, except for the 44 holes drilled in the mid-plane former plate (not shown in Figure RAI-4.3-8). There is also a shroud foot at the first former elevation (Figure RAI-4.3-8), and the mid-plane former is twice as thick. Similarly, the slots and holes in the former plates are not considered in the area calculation for this former plate design.

The BB channel for the CE System 80 design (Palo Verde Units) is shown in Figure RAI-4.3-10 and Figure RAI-4.3-11. As the figures indicate, the System 80 design does not have typical former plates that span the BB channel annulus. Instead, the shroud channel has plates at the top and bottom of the channel and 5 support rings that band the baffle plates. There are also more vertical ribs, and u-channel between each set of support rings. The support rings are less restrictive to flow compared to typical former plate designs.

Based on the above discussion, there are 5 unique BB channel designs that need to be considered when determining reference areas and loss coefficients for the GSI-191 thermal-hydraulic analyses. Tables RAI-4.3-4 summarizes the geometry, dimensions, and areas for each CE plant that credits the BB channel in the GSI-191 analyses.

The former plate loss coefficient is determined using Eq. RAI-4.3-2, which considers an abrupt contraction and expansion through the former plate. The vena-contracta is assumed to reattach in all calculations and the coefficient of contraction is calculated using Eq. RAI-4.3-3. Table RAI-4.3-5 provides the former plate loss coefficients and total reference areas for the CE fleet.

Barrel/Baffle Outlet

Palisades and Fort Calhoun have BB channel outlets that are very similar to Westinghouse upflow plants, as shown in Figure RAI-4.3-12. The BB channel outlet reference area is taken as the gap area between the top of the baffle plates and the bottom of the fuel alignment plate. Using Eq. RAI-4.2-1, the reference area can be calculated for the BB channel outlet. As described in RAI-4.2, an appropriate loss coefficient for this outlet geometry is 1.5.

The shroud outlet for St. Lucie Units 1 and 2, Arkansas Nuclear One Unit 2, Calvert Cliffs Units 1 and 2, Millstone Unit 2, and Waterford are similar, except that the gap between the top of the shroud and the fuel alignment plate is larger, as shown in Figure RAI-4.3-13. In this case the top former plate is considered in the outlet calculation, and the reference area is based on the gap between the former plate and the core barrel, provided in Table RAI-4.3-4. The loss coefficient considers a contraction at the former plate, followed by an expansion into the core barrel region below the fuel alignment plate, and a 90 degree turn.

CE System 80 design plants (Palo Verde Units 1, 2, and 3) have a BB channel outlet as shown in Figure RAI-4.3-14. As the figure illustrates, the core shroud top plate represents the top of the core shroud channel. The total shroud channel outlet area is the sum of the core shroud top plate holes and the annulus between the top plate and the core barrel:

$$A_{outlet} = N \times \frac{\pi}{4}(D_H)^2 + \frac{\pi}{4}\left({D_{CB}}^2 - {D_S}^2\right) = \left[\quad\right]^{a,c} \qquad \text{Eq. RAI-4.3-7}$$

Where N is the number of holes in the top plate, D_H is the hole diameter, D_{CB} the core barrel diameter and D_S the diameter of the shroud channel top plate.

Table RAI-4.3-6 provides the BB outlet reference area and loss coefficients for the CE fleet.

Total Barrel/Baffle Channel Resistance

A geometric dimensional form loss (K/A^2) for the BB channel was determined by taking the summation of the K/A^2 for the BB inlet, all former plates (or support rings for the CE System 80 design), and the BB outlet. The total K/A^2 for the BB region is defined as:

$$\left(\frac{K}{A^2}\right)_{BB} = \left(\frac{K}{A^2}\right)_{Inlet} + \left(\frac{K}{A^2}\right)_{Formers} + \left(\frac{K}{A^2}\right)_{Outlet} \qquad \text{Eq. RAI-4.3-8}$$

The three terms on the right hand side of the equation were determined using the reference areas and loss coefficients determined above. Table RAI-4.3-7 provides the total BB channel resistance for each CE plant.

Step 2

In order to determine an equivalent maximum AFP resistance for the CE thermal-hydraulic plant model, it is necessary to scale the base plant AFP resistance using the method described in Step 2 of the response to RAI-4.2.

The first step is to calculate the pressure drop for each CE plant to determine which plant has the highest pressure drop. The pressure drop is determined using Eqs. RAI-4.2-17 and RAI-4.2-18. In the calculations, the decay heat fraction is set to 0.02412, which is the Appendix K decay heat fraction at 20 minutes after trip. The fluid properties are set to saturated conditions at atmospheric pressure; ρ_f = 59.8 lbm/ft^3 and h_{fg} = 970.3 Btu/lbm. The licensed powers, listed in Table RAI-4.3-1, are used in the calculation, and the total AFP resistance is taken from Table RAI-4.3-7.

Table RAI-4.3-8 provides the calculated pressure drops and shows that the highest value is [ ]^{a,c} With the maximum pressure drop determined, the base plant model BB channel resistance can be calculated using Eq. RAI-4.2-22. The base plant power is taken from WCAP-17788, Volume 4, Table 6-3; 3458 MW. The resulting CE base plant BB channel resistance is:

$$\left(\frac{K}{A^2}\right)_{base} = \left(\frac{K}{A^2}\right)_{limit} \cdot \frac{(P_{limit})^2}{(P_{base})^2} = \left[\quad \right]^{a,c}$$

Table RAI-4.3-8 also provides the adjusted (scaled) AFP resistances based on Eq. RAI-4.2-22. As expected, all adjusted AFP resistances are less than the value used in the base plant model. Table RAI-4.3-8 also provides the base model BB channel resistance, which is shown to be [ ]^{a,c} The base plant model is approximately 6% higher than the scaled value of [ ]^{a,c}

Table RAI-4.3-1 Name and Licensed Power for Combustion Engineering Plants	
Plant	**Licensed Power (MW)**
Palisades Nuclear Plant	2565.4
Fort Calhoun Station, Unit 1	1500
St. Lucie Plant, Units 1 and 2	2700
Arkansas Nuclear One, Unit 2	3026
Calvert Cliffs Nuclear Power Plant, Units 1 and 2	2737
Millstone Power Station, Unit 2	2700
Waterford Steam Electrical Station, Unit 3	3716
Palo Verde Nuclear Generating Station, Units 1, 2, and 3	3990

Table RAI-4.3-2 Drawing Identification for Combustion Engineering Plants			
Plant	**Drawing Number**	**Revision**	**Title**
Palisades Nuclear Plant	2966-J-2312	M	Core Support Plate
	2966-E-2749	K	Core Shroud Assemblies
	2966-J-2402	W	Core Support Barrel
	2966-J-2310	Z	Core Support Assy
	2966-SJ-1752	1	Reactor Internals Layout
Fort Calhoun Station, Unit 1	J-23866-164-018	4	Core Support Plate Assy
	J-23866-164-025	5	Core Shroud Assemblies
	J-23866-164-013	5	Core Support Barrel
	J-23866-164-011	11	Core Support Assy
	J-23866-164-003	8	Reactor Internals Assembly
St. Lucie Plant, Unit 1	E-STD-164-012	3	Core Plate and Lower Support Assy
	E-STD-164-025	5	Core Shroud Assembly
	J-19367-162-001	3	Reactor Assembly

Table RAI-4.3-2	**Drawing Identification for Combustion Engineering Plants (cont'd)**		
Plant	**Drawing Number**	**Revision**	**Title**
St. Lucie Plant, Unit 2	E-STD-164-312	8	Core Plate and Lower Support Assy
	E-STD-164-325	6	Core Shroud Assembly
	E-STD-164-316	6	Core Support Barrel Lower Section
Arkansas Nuclear One, Unit 2	E-STD-164-412	4	Core Plate and Lower Support Assy
	E-STD-164-425	3	Core Shroud Assembly
	E-6370-164-413	2	Core Support Barrel As Builts
Calvert Cliffs Nuclear Power Plant, Units 1 and 2	E-STD-164-012	3	Core Plate and Lower Support Assy
	E-STD-164-025	5	Core Shroud Assembly
	J-8067-164-001	0	Reactor Assy
Millstone Power Station, Unit 2	E-STD-164-012	3	Core Plate and Lower Support Assy
	E-STD-164-025	5	Core Shroud Assembly
	J-18767-164-001	3	Reactor Assy
Waterford Steam Electrical Station, Unit 3	E-9270-164-312	1	Core Plate and Lower Support Assy As Built
	E-9270-164-325	1	Core Shroud Assy As-Built
	J-STD-164-002	2	Reactor internals Dimensional and Interface Assy (3410)
Palo Verde Nuclear Generating Station, Units 1, 2, and 3	E-14273-164-812	3	Lower Support Structure Assembly
	E-STD-164-825	13	Core Shroud Assembly
	E-14273-164-800	1	Reactor Internals Dimensional Assembly

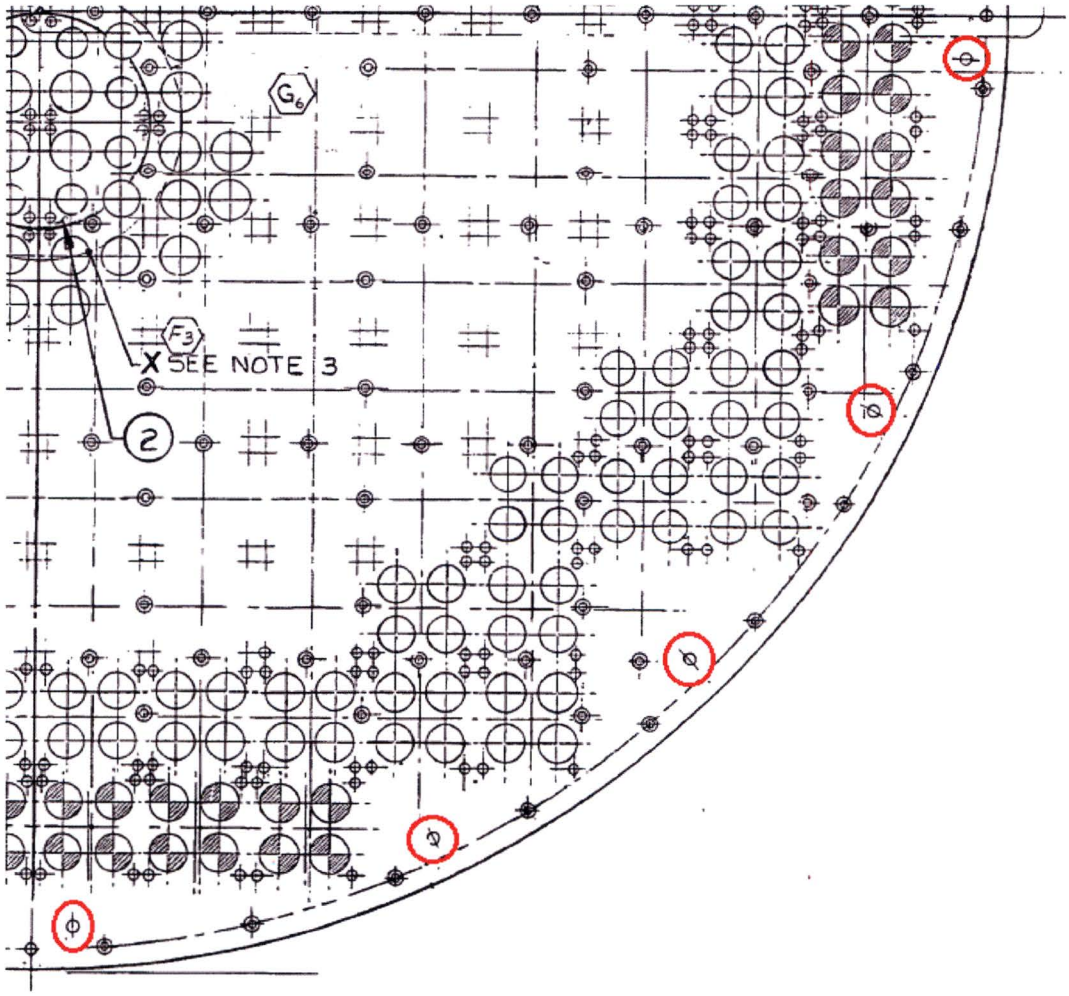

Figure RAI-4.3-1 Combustion Engineering Core Shroud Inlet with Holes in the Lower Core Support Plate

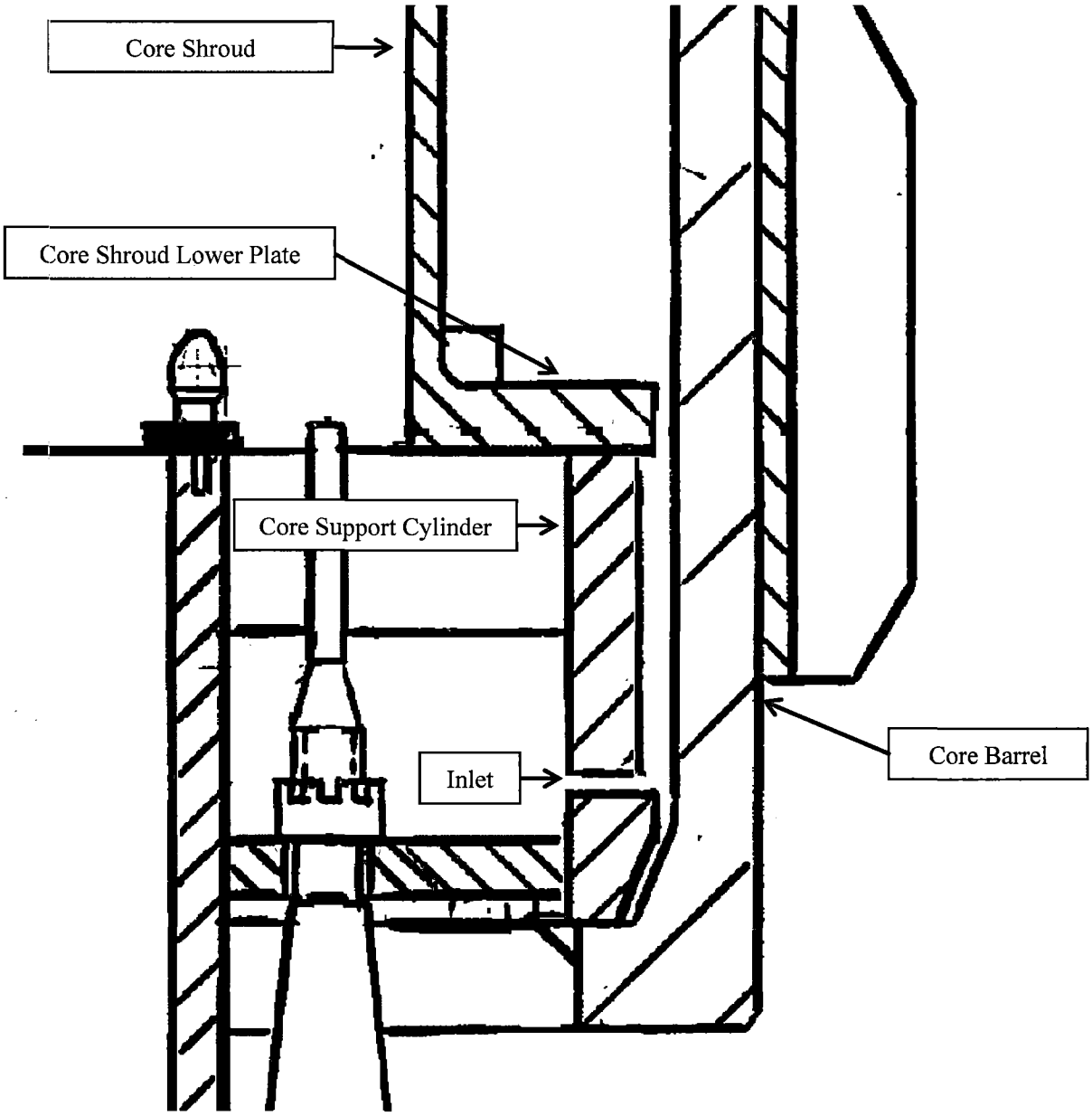

Figure RAI-4.3-2 Combustion Engineering Core Shroud Inlet with Holes in the Core Support Cylinder

[ ] a,c

Figure RAI-4.3-3 Contraction Coefficient used in Combustion Engineering Core Shroud Channel Resistance Calculations (Reference RAI-4.3-1)

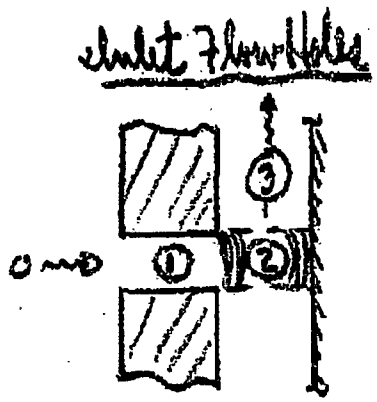

Figure RAI-4.3-4 Area Designation used in Equation RAI-4.3-4 for CE Plants with a BB Inlet Consisting of Holes in the Core Support Cylinder

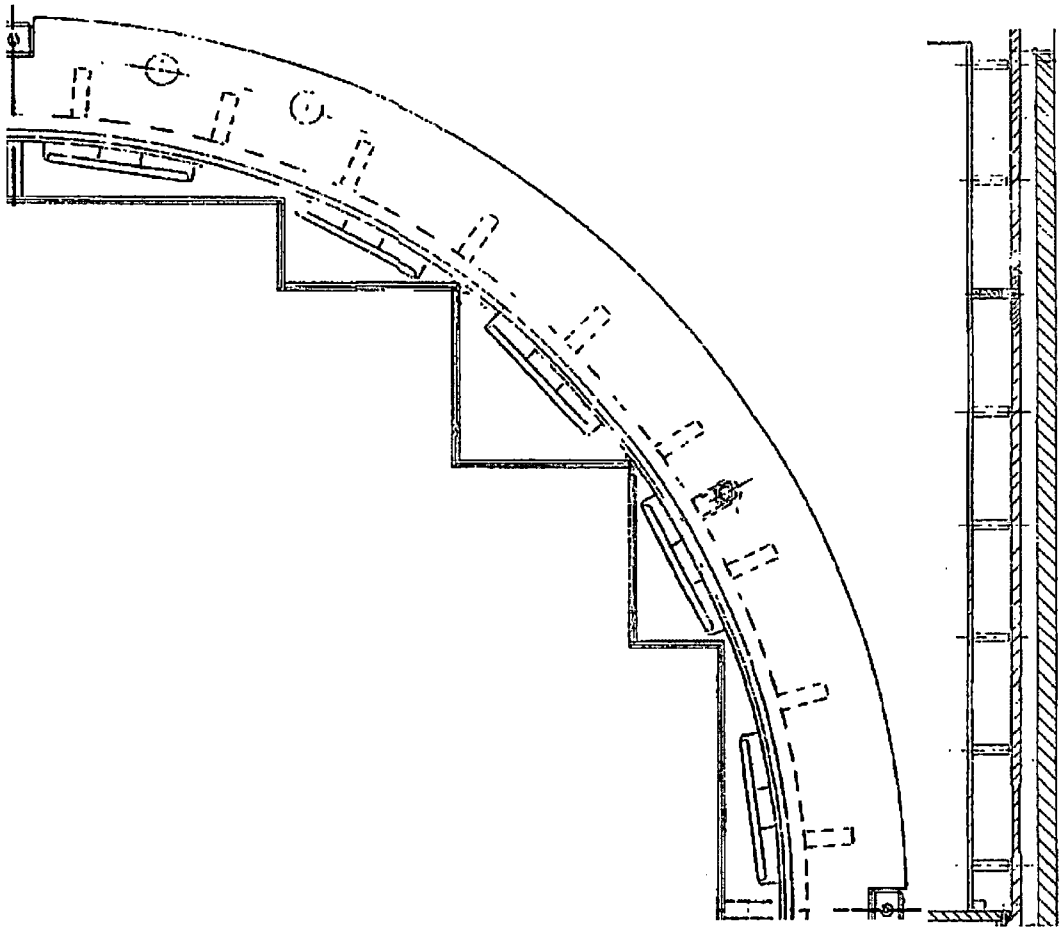

Figure RAI-4.3-5 Palisades Core Shroud Channel and Former Plate Design

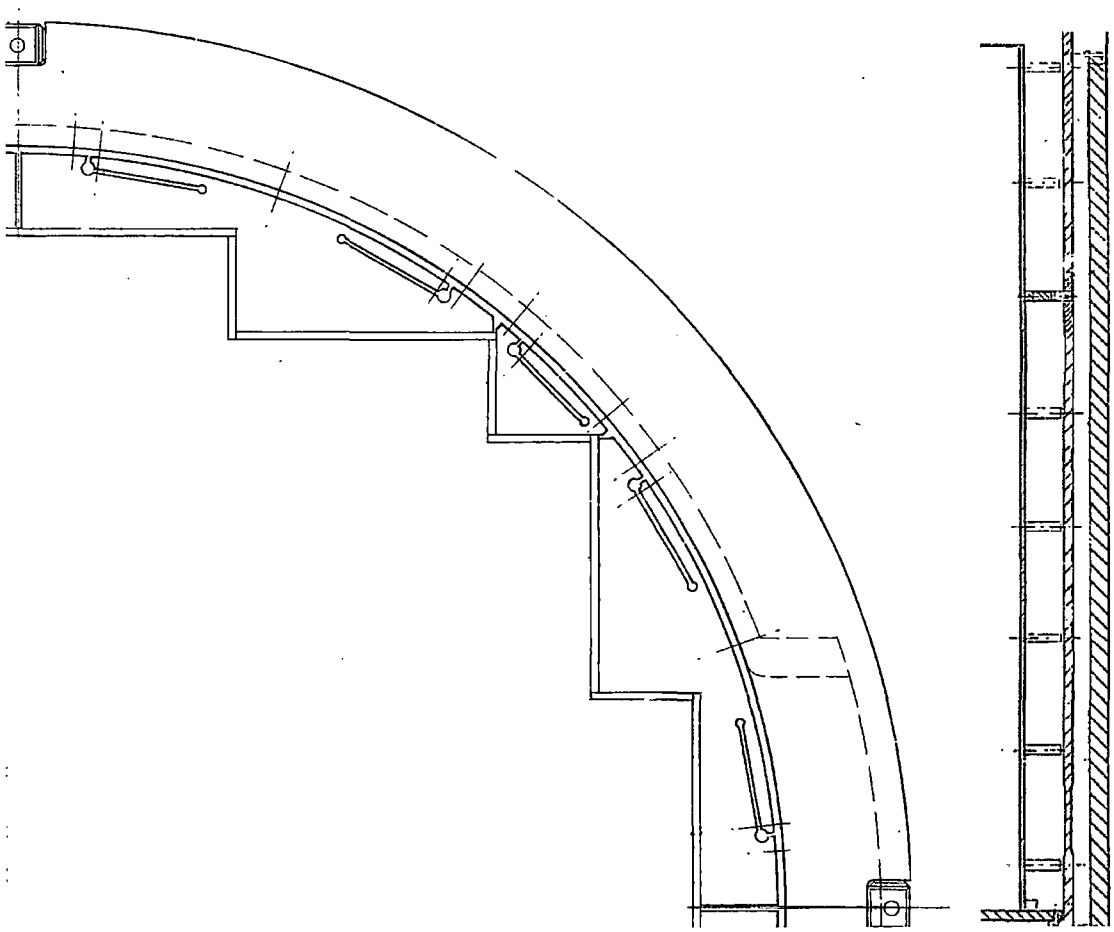

Figure RAI-4.3-6 Fort Calhoun Shroud Channel and Former Plate Design

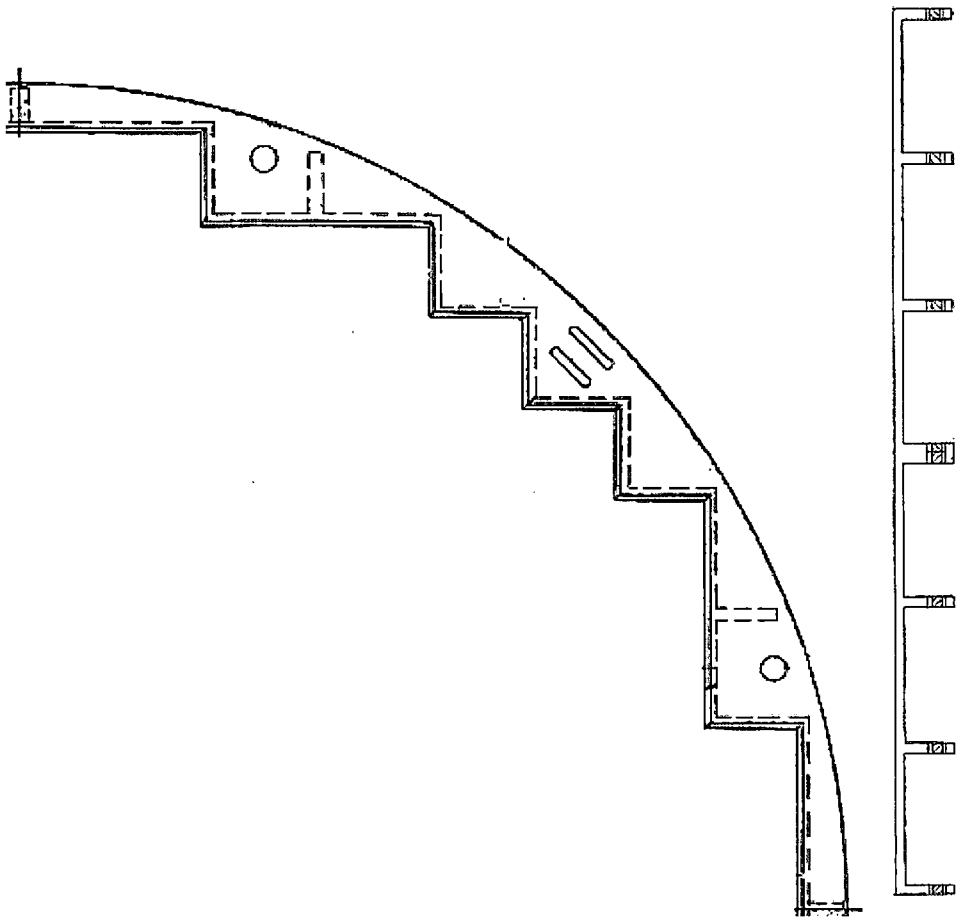

Figure RAI-4.3-7 St. Lucie Unit 1, Calvert Cliffs Units 1 and 2, Millstone Unit 2, and Waterford Unit 3 Shroud Channel and Former Plate Design

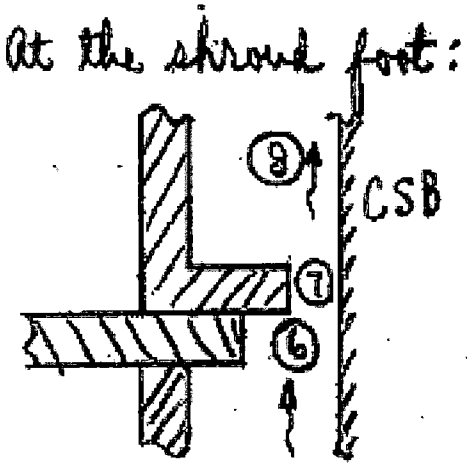

Figure RAI-4.3-8 Shroud Foot at the First Former Plate

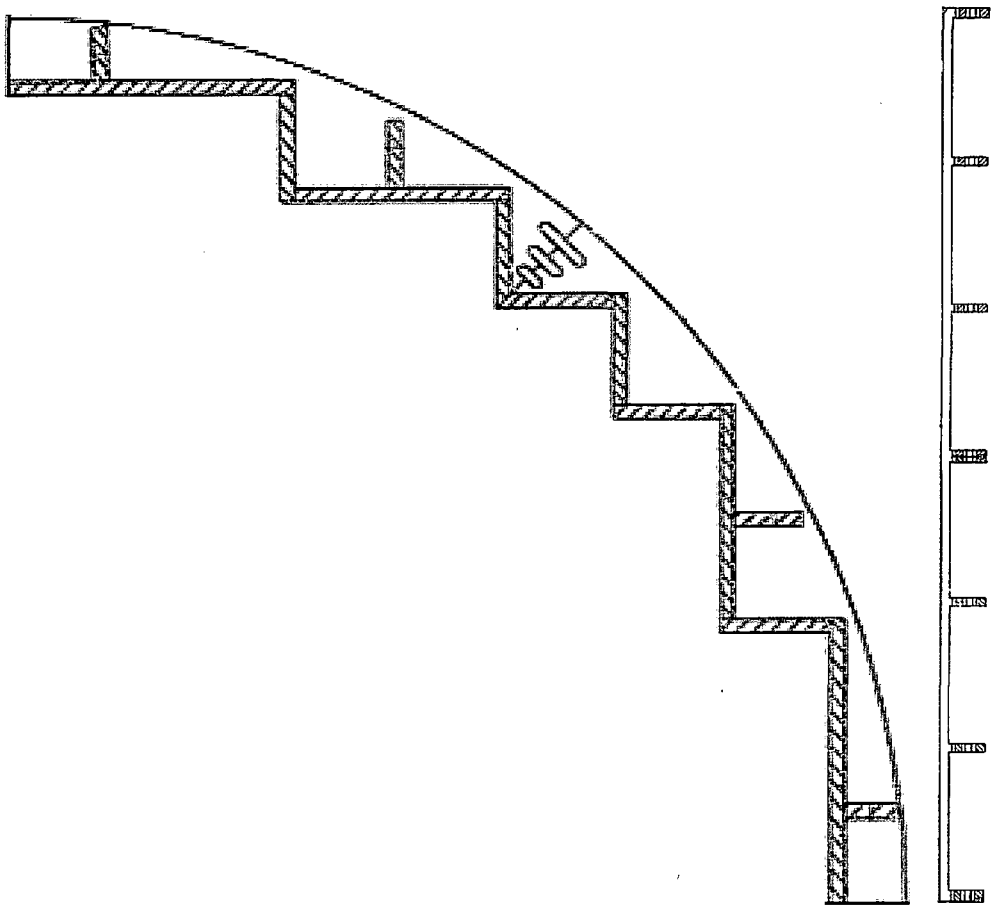

Figure RAI-4.3-9 St. Lucie Unit 2 and Arkansas Nuclear One Unit 2 Shroud Channel and Former Plate Design

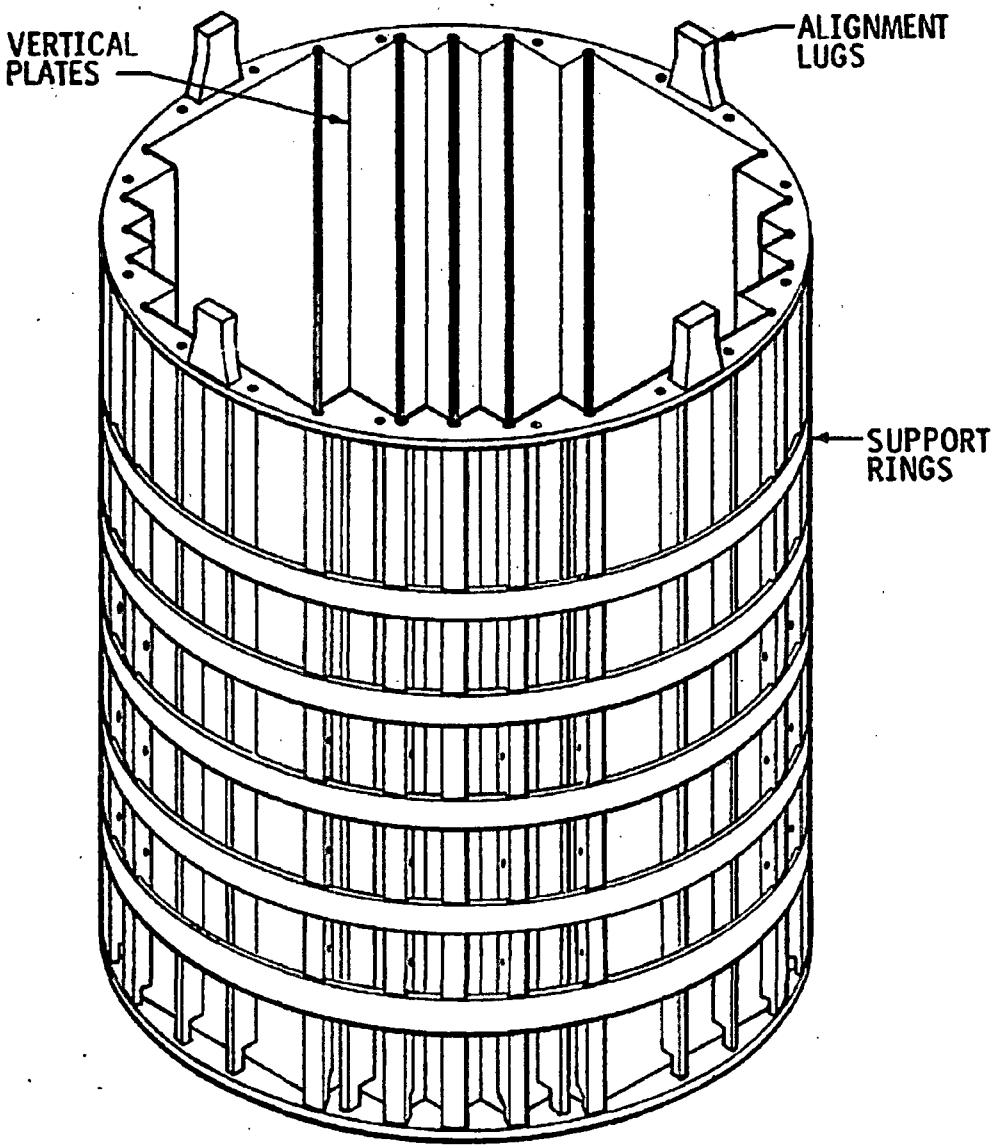

Figure RAI-4.3-10 Palo Verde Units 1, 2, and 3 Core Shroud

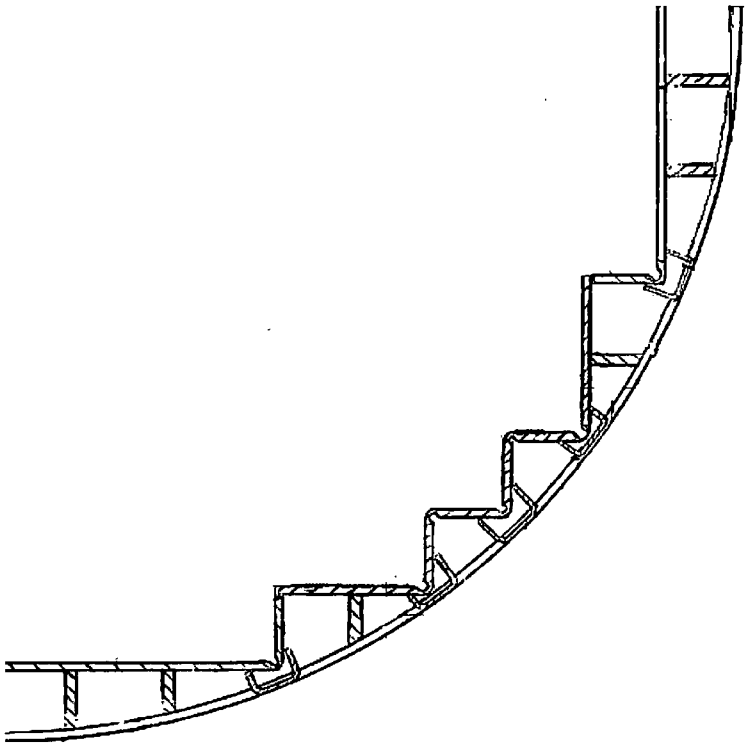

Figure RAI-4.3-11 Palo Verde Units 1, 2, and 3 Core Shroud Cross-Sectional View

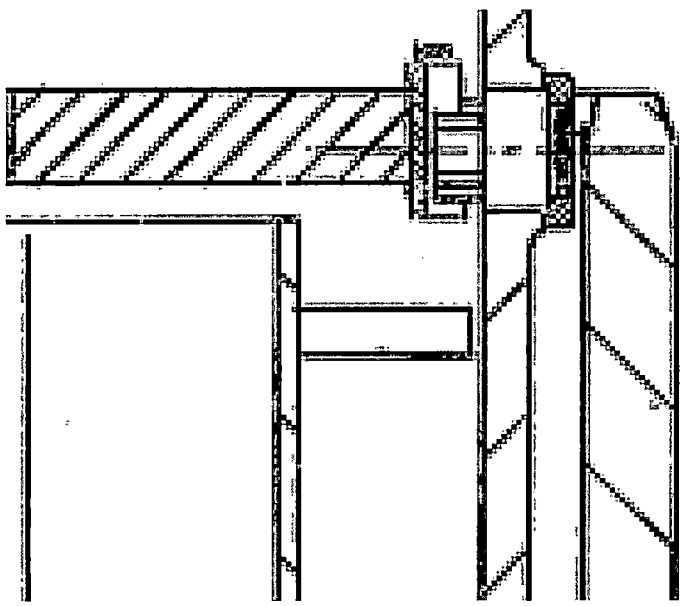

Figure RAI-4.3-12 Core Shroud Outlet Design for Palisades and Fort Calhoun

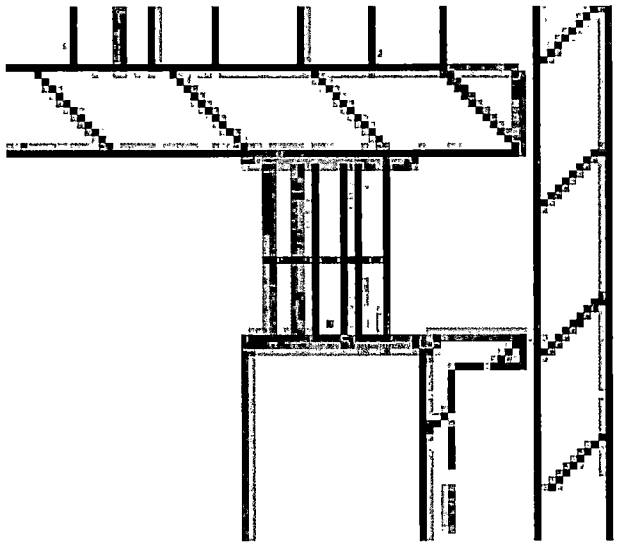

Figure RAI-4.3-13 Core Shroud Outlet Design for St. Lucie Units 1 and 2, Arkansas Nuclear One Unit 2, Calvert Cliffs Units 1 and 2, Millstone Unit 2, and Waterford

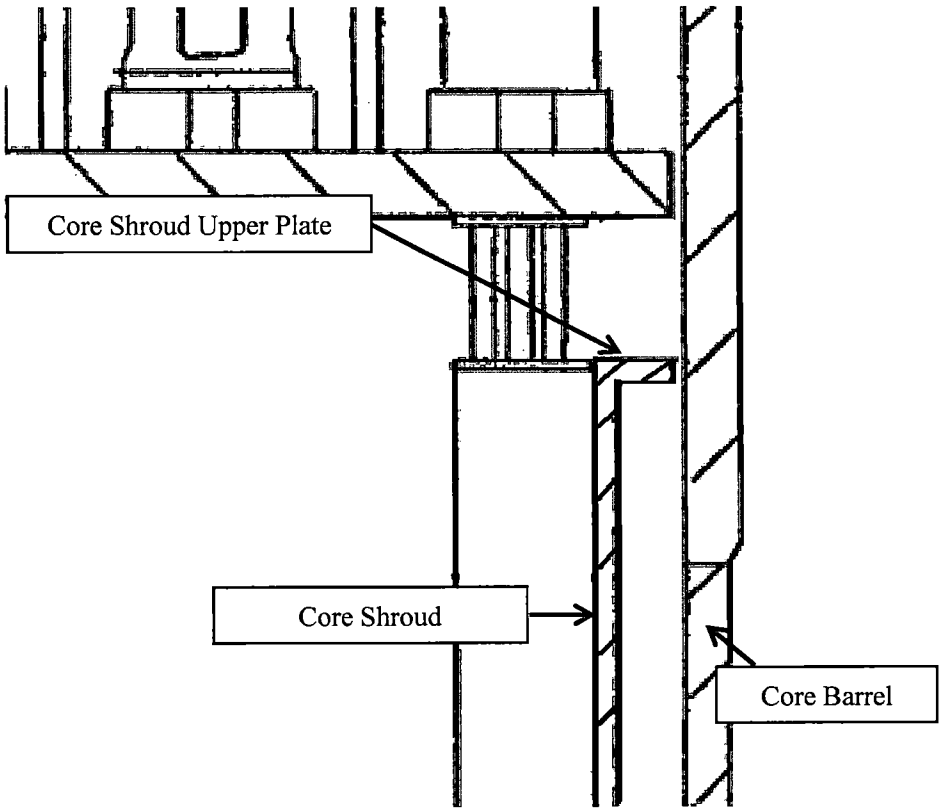

Figure RAI-4.3-14 Combustion Engineering System 80 Core Shroud Outlet

Table RAI-4.3-3 Barrel/Baffle Inlet Geometry, Reference Area, and Loss Coefficient for Combustion Engineering Plants

a,c

Table RAI-4.3-4 Former Plate Geometry and Flow Area for Combustion Engineering Plants

a,c

Table RAI-4.3-5 Former Plate Loss Coefficients and Reference Areas for Combustion Engineering Plants

[

] a,c

Table RAI-4.3-6 Barrel/Baffle Outlet Geometry, Reference Area, and Loss Coefficient for Combustion Engineering Plants

a,c

<table>
<tr><td rowspan="2"></td><td colspan="60"></td></tr>
<tr><td colspan="15"></td><td colspan="15"></td><td colspan="15"></td><td colspan="15"></td></tr>
<tr><td></td><td colspan="15"></td><td colspan="15"></td><td colspan="15"></td><td colspan="15"></td></tr>
<tr><td></td><td colspan="15"></td><td colspan="15"></td><td colspan="15"></td><td colspan="15"></td></tr>
<tr><td></td><td colspan="20"></td><td colspan="20"></td><td colspan="20"></td></tr>
<tr><td></td><td colspan="20"></td><td colspan="20"></td><td colspan="20"></td></tr>
<tr><td></td><td colspan="20"></td><td colspan="20"></td><td colspan="20"></td></tr>
<tr><td></td><td colspan="20"></td><td colspan="20"></td><td colspan="20"></td></tr>
<tr><td></td><td colspan="20"></td><td colspan="20"></td><td colspan="20"></td></tr>
<tr><td></td><td colspan="20"></td><td colspan="20"></td><td colspan="20"></td></tr>
<tr><td></td><td colspan="12"></td><td colspan="12"></td><td colspan="12"></td><td colspan="12"></td><td colspan="12"></td></tr>
<tr><td></td><td colspan="12"></td><td colspan="12"></td><td colspan="12"></td><td colspan="12"></td><td colspan="12"></td></tr>
</table>

Table RAI-4.3-7 Total Barrel/Baffle Channel Resistance for Combustion Engineering Plants

[

] a,c

Table RAI-4.3-8	**Plant Alternate Flow Path Pressure Drop used to Determine Base Plant Alternate Flow Path Resistances used in the GSI-191 Analyses**			
Plant	**Licensed Power (MW)**	**Total Unadjusted $\frac{K}{A^2}$ (ft^{-4})**	**Pressure Drop (psi)**	**Total Adjusted $\frac{K}{A^2}$ (ft^{-4})**
Palisades Nuclear Plant	2565.4	[		] a,c
Fort Calhoun Station, Unit 1	1500			
St. Lucie Plant, Units 1 and 2	2700			
Arkansas Nuclear One, Unit 2	3026			
Calvert Cliffs Nuclear Power Plant, Units 1 and 2	2737			
Millstone Power Station, Unit 2	2700			
Waterford Steam Electrical Station, Unit 3	3716			
Palo Verde Nuclear Generating Station, Units 1, 2, and 3	3990			
S-RELAP5 Plant Model	3458			]

b. Provide a description of the assumptions used in the maximum and minimum BB flow resistance calculations provided in Table 6-3.

Response

The following assumptions were used in the maximum BB flow resistance calculations given in Table 6-3:

- When determining dimensions from plant drawings, nominal values are used unless noted otherwise.
- The BB channel is the only AFP considered in the CE plant GSI-191 TH analyses and the maximum BB resistance is based on the BB channel from the inlet to the outlet.
- As discussed in the Step 1 in the response to RAI-4.3 Item a., assumptions are made when calculating the former plate reference areas such that the areas are minimized. Minimizing the reference areas increase the resistance through the AFP.
- As the BB inlet, former plates, and BB outlet are in series, the total BB channel resistance can be calculated by summing all the individual resistances using Eq. RAI-4.3-8.

The minimum BB flow resistance is no longer used in the GSI-191 thermal-hydraulic analyses, and the value will be removed from Table 6-3.

c. Identify the physical units for the BB flow resistances in Table 6-3.

Response

The physical units for the BB flow resistances in Table 6-3 are ft^{-4}.

d. Describe whether or not the flow passages between the downcomer and upper plenum regions via the hot leg nozzle gaps were modeled. If they were not, provide a justification for the omission.

Response

The mentioned flow passages were not modeled. Neglecting these flow passages maximizes the quantity of debris reaching the core inlet by limiting the quantity that bypasses the core inlet. Neglecting these passages also creates a scenario in which the highest quantity of coolant is required to reach the core through the AFP to effectively remove decay heat.

e. Provide the information requested in Items e, f, g, and h in RAI 4.2 as it applies to the CE plant category. As both AREVA and Westinghouse performed BB flow resistance calculation for CE plant units, all requested information from each vendor for the analyzed plant units should be provided.

Response

i. The name and rated power for each CE unit considered in determining the BB resistances are shown in Table RAI-4.3-1.

ii. The identification numbers of design drawings containing the geometric data to calculate the AFP resistances for each CE unit considered in the GSI-191 TH analyses are shown in Table RAI-4.3-2.

iii. Table RAI-4.3-3 provides the geometry and total resulting flow area for the BB inlet. Tables RAI-4.3-4 and RAI-4.3-5 provide the geometry of all types and sizes of openings that are credited in the former plate resistance calculation for the various CE plant designs. Table RAI-4.3-6 provides the geometry and total resulting flow area for the BB outlet.

iv. Table RAI-4.3-3 provides the loss coefficients and reference areas associated with the BB inlet.

Table RAI-4.3-5 provides the loss coefficients and reference areas associated with the BB channel former plates.

Table RAI-4.3-6 provides the loss coefficients and reference areas associated with the BB outlet.

v. The total unadjusted BB resistances, $\frac{K}{A^2}$, in units ft^{-4} for all CE plants are provided in Table RAI-4.3-8. The table also shows the adjusted BB resistances and the value used in the S-RELAP5 model.

vi. Assumptions related to the way geometric data was treated for calculating resistances and assumptions related to the consideration of any other flow passages are provided in the responses to RAI 4.3b.

vii. The following figures provide the requested information:

- Figure RAI-4.3-1 Combustion Engineering Core Shroud Inlet with Holes in the Lower Core Support Plate
- Figure RAI-4.3-2 Combustion Engineering Core Shroud Inlet with Holes in the Core Support Cylinder
- Figure RAI-4.3-5 Palisades Core Shroud Channel and Former Plate Design

- Figure RAI-4.3-6 Fort Calhoun Shroud Channel and Former Plate Design
- Figure RAI-4.3-7 St. Lucie Unit 1, Calvert Cliffs Units 1 and 2, Millstone Unit 2, and Waterford Unit 3 Shroud Channel and Former Plate Design
- Figure RAI-4.3-8 Shroud Foot at the First Former Plate
- Figure RAI-4.3-9 St. Lucie Unit 2 and Arkansas Nuclear One Unit 2 Shroud Channel and Former Plate Design
- Figure RAI-4.3-10 Palo Verde Units 1, 2, and 3 Core Shroud
- Figure RAI-4.3-11 Palo Verde Units 1, 2, and 3 Core Shroud Cross-Sectional View
- Figure RAI-4.3-12 Core Shroud Outlet Design for Palisades and Fort Calhoun
- Figure RAI-4.3-13 Core Shroud Outlet Design for St. Lucie Units 1 and 2, Arkansas Nuclear One Unit 2, Calvert Cliffs Units 1 and 2, Millstone Unit 2, and Waterford
- Figure RAI-4.3-14 Combustion Engineering System 80 Core Shroud Outlet

f. During the NRC audit of supporting AREVA documents and drawings on March 1-4, 2016, it was found in document [
]" that two different values for the maximum BB flow resistance case, [
], were reported for [ ]. During the audit, it was explained that the values resulted from the calculations performed by AREVA and Westinghouse. This significant difference in resistances is a concern regarding the limiting representative resistances determined for the CE plant category. Provide an explanation for the difference in the BB resistance results for [
]. Since both results may be incorrect, examine the methods used by AREVA and Westinghouse. Identify whether deficiencies in the calculational methodologies or differences in geometrical plant data related to the BB region were involved in both analyses. If deficiencies are discovered, provide a description and results of any changes to the methods for the corrected BB resistance calculation(s). Provide full calculations and final results for [ ] using both methods with applicable modifications. Provide the input derived from geometrical plant data related to the BB region for this unit as used in both analyses.

Response

Both calculations for the [ ]^{a,c} AFP resistance have been reviewed, and an error was discovered in the AREVA calculation. The AREVA calculation identified the BB channel inlet geometry as 16, [ ]^{a,c} holes distributed around the periphery of the lower core plate. This geometry is incorrect, and these holes do not connect the core support region with the BB channel. The correct BB channel inlet geometry is identified in Drawing E-STD-164-012 (Table RAI-4.3-2). This drawing shows 16, [ ]^{a,c} holes in the core support cylinder (Figure RAI-4.3-2) that make up the BB channel inlet in [ ]^{a,c} As shown in Table RAI-4.3-7, the BB inlet resistance is the majority of the total BB channel resistance for [ ]^{a,c} The resistance through the incorrect BB inlet, considered by AREVA is much smaller compared to the correct BB inlet resistance shown in Table RAI-4.3-7. The use of the incorrect BB inlet geometry is what resulted in the large discrepancy between the original AREVA and Westinghouse calculations.

Review of the AREVA calculation also identified discrepancies in the former plate resistance. The AREVA calculation only considered the slots in the former plates and did not account for the gap between the core barrel and former plates. The original Westinghouse calculation considered the slots and the gaps. As such, the former plate resistance calculated by Westinghouse was smaller compared to the AREVA calculation; however, this discrepancy was not as significant as the BB inlet resistance.

In the response to RAI-4.3 Item a., the CE BB channel resistance was recalculated for all CE plants using a consistent methodology. As shown in Table RAI-4.3-7, the revised BB channel resistance calculated for [ ]^{a,c} which is comparable to the original value of [ ]^{a,c} calculated by Westinghouse. The difference between these two values is primarily due to the fact that the original calculation applied a loss coefficient of [ ]^{a,c} as opposed to the revised calculation that applied a value of [ ]^{a,c}

g. Verify that the issues associated with Item f above do not affect the other plant categories.

Response

It has been verified that the issues associated with Item f above do not affect the other plant categories.

References

RAI-4.3-1 NRC Information Digest (NUREG-1350, Volume 26), "Appendix A: U.S. Commercial Nuclear Power Reactors – Operating Reactors."

RAI-4.3-2 CENPD-71, Revision 1, "REVEL a Computer Code to Calculate Nozzle to Nozzle Pressure Drop," April 1988.

RAI-4.4, Vol. 4

Section 6.4, "Babcock and Wilcox [(B&W)] Plant Model," states that "the BB design for all B&W plants is the same" and explains that the BB flow resistance shown in Table 6-4 is representative of all B&W plants. It is also explained that the method and supporting calculations confirming the provided BB flow resistance value are contained in Reference 6-3, which is identified in Section 6.5 and updated with Letter OG-16-42 dated February 12, 2016, as follows.

Reference 6-3: [

]

a. The above identified document appears to be related to the CE plant category. Confirm whether this is the proper reference for B&W plants. If a reference other than Reference 6-3 was used for B&W plants, provide a copy of the document.

b. Include a description of the assumptions used in the calculation of the BB total flow resistance value provided in Table 6-4.

c. Identify the physical units for the BB flow resistance shown in Table 6-4.

d. State whether any other flow passages between the downcomer and upper head/plenum regions were modeled in the analyses. If they were, provide a description of these additional passages and how they are evaluated.

e. Provide the information requested in Items e, f, g, and h in RAI 4.2 as it applies to the B&W plant design category.

f. During the NRC staff audit of AREVA documents and drawings on March 1-4, 2016, the NRC staff encountered difficultly in interpreting, following, and confirming calculations and results pertaining to the BB resistance calculations for the B&W plant design category. Therefore, ensure that the information provided in response to Items a through e above include all necessary clarifying and supporting information to support an independent review of the BB resistance calculation methodology and the results documented for the B&W plant category.

The response to these questions is provided in the B&W submittal

RAI-4.5, Vol. 4

Tables 6-1 through 6-4 provide a summary of key inputs for each plant category. Provide the following information related to the key inputs for the HLB methodology:

a. Justify that the values for the parameters listed in Tables 6-1 through 6-4 are bounding or demonstrate that these values can be considered appropriate and applicable for all of the plant units covered by the TR. If certain key input values have not been validated as bounding, state how the use of the TR methodology will ensure that the applicable acceptance criteria are met for the specific plant application. Include enough information for each key parameter so that the NRC staff can verify that they are bounding for the plants intended to use the TR. Ensure that the information includes, as necessary, plant specific characteristics, operating conditions, licensing basis assumptions (including single failure), regulatory limits, operating procedures, technical specifications limits, uncertainties, and full ranges of the inputs and variables that could affect the evaluation. If it is determined that these parameters are valid for plants using the methodology, how will the plants ensure the variables that can affect these parameters are maintained at acceptable values?

Response

Each parameter for the Westinghouse plant categories in WCAP-17788, Volume 4, Tables 6-1 and 6-2 is discussed in the order they are presented in the tables.

Core Power

The analyzed core power applied to the Westinghouse upflow and downflow plant analyses does not explicitly bound all Westinghouse plants. The values applied to the plant models are appropriate and applicable for all Westinghouse plants covered by the WCAP-17788 methodology. Plant-specific core power was considered when determining the bounding maximum alternate flow path resistances used in the analyses. The response to RAI-4.2 describes the process used to scale the alternate flow path (AFP) resistance accounting for core power. In this fashion, variations in core power for plants considered in each analysis category are accounted for by the modeled AFP resistances. No additional validation is required with regard to core power relative to the AFP resistance during plant-specific implementation of the WCAP-17788 methodology.

Core power was also considered when determining ECCS recirculation flow rates. As described below, each plant implementing the WCAP-17788 methodology will be required to confirm that their plant-specific ECCS recirculation flow rates fall within the range analyzed for each plant category. This confirmation includes consideration for variations in core power between the analyzed value and the plant-specific value.

Number of Loops

The Westinghouse upflow and downflow plant analyses are applicable to both 3- and 4- loop plant designs. 4-loop plants have more fuel assemblies than 3-loop plants, and have higher licensed powers. As power variations between plants is accounted for in the AFP resistance calculations, and the ECCS recirculation flow rate, both 3- and 4-loop plants are covered by the analyses. No additional validation is required with regard to the number of loops during plant-specific implementation of the WCAP-17788 methodology.

Number of Fuel Assemblies

As stated above, Westinghouse 3- and 4- loop plants have a different number of fuel assemblies. The number of fuel assemblies is important when determining the total in-vessel debris load. The parameter K_{max}, is applied uniformly across the entire core inlet such that the resistance due to the accumulation of debris is the same at the inlet to all fuel assemblies. In WCAP-17788, Volume 1, K_{max} is related to a physical fibrous debris mass with units of grams per fuel assembly (g/FA). When implementing the WCAP-17788 methodology, plants should confirm that they are using the correct number of fuel assemblies when comparing their in-vessel debris limits to the quantity of fibrous debris downstream from the sump strainer.

Barrel/Baffle Channel Total Resistance (K/A^2)

The barrel/baffle (BB) channel maximum resistance used in the analyses is bounding for all plants covered by the Westinghouse upflow plant category. The response to RAI-4.2 provides the justification. No additional validation is required with regard to BB resistance during plant-specific implementation of the WCAP-17788 methodology.

Upper Head Spray Nozzle Total Resistance (K/A^2)

The upper head spray nozzle (UHSN) maximum resistance used in the K_{max}, K_{split}, and m_{split} analyses is bounding for all plants included in the Westinghouse downflow plant category. The response to RAI-4.2 provides the justification. No additional validation is required with regard to UHSN resistance during plant-specific use of K_{max}, K_{split}, and m_{split} in the WCAP-17788 methodology.

The UHSN resistance used in the t_{block} analysis does not bound all Westinghouse downflow plants. Table RAI-4.2-24 in the response to RAI-4.2 provides the UHSN resistance used in the Westinghouse downflow plant category t_{block} analysis. When implementing the WCAP-17788 methodology, Westinghouse downflow plants should confirm that the UHSN resistance used to determine t_{block} bounds their plant-specific UHSN resistance. If the plant-specific UHSN resistance is not bounded by the value used in the thermal-hydraulic analysis, additional plant-specific evaluation will be required to justify the earliest time that chemical products can arrive in the reactor vessel.

Total Peaking (F_Q)

See the response to RAI-4.5 Item c. below.

Radial Peaking ($F_{\Delta H}$)

See the response to RAI-4.5 Item c. below.

Axial Peak Power Location

See the response to RAI-4.5 Item c. below.

ECCS Recirculation Flow Rate

When determining the range of ECCS flows used in the thermal-hydraulic analysis, plant-specific single-failure assumptions and pump performance characteristics were not explicitly considered. As described in the response to RAI-4.1, each plant will determine the limiting single-failure assumptions for the GSI-191 hot leg break scenario. Each plant-specific submittal will need to demonstrate that the ECCS recirculation flows used in the thermal-hydraulic analyses bound their specific plant.

When implementing the WCAP-17788 hot leg break methodology, each plant will determine the scenario that leads to the highest quantity of debris reaching the core inlet. The ECCS recirculation flow associated with the worst-case in-vessel debris scenario needs to be compared to the range of ECCS recirculation flow rates analyzed in the thermal-hydraulic analysis. When determining the equivalent ECCS recirculation flow rate, each plant will follow the scaling procedure provided in the Combustion Engineering response to this RAI question. The procedure requires the downcomer volume of the analysis model from the bottom of the cold leg to the bottom of the active fuel. The Westinghouse upflow analysis model has a downcomer volume of 891 ft^3, and the Westinghouse downflow model has a volume of 647 ft^3.

During the injection phase of the transient, cold leg ECCS flow rates were modeled assuming the failure of an entire train of ECCS. This injection flow results in a condition where the downcomer level is below the top of the active fuel upon entry into the recirculation phase of the transient. It has been determined that a low downcomer level results in a longer core uncovery and subsequent fuel heatup when the formation of a debris bed is simulated at the core inlet. This is because there is a delay in which the downcomer must fill before enough driving head is available to force flow through the BB channel and UHSNs to provide cooling via the top of the core. An injection phase ECCS flow rate sensitivity study is presented in the response to RAI-4.24 Item c., which shows that the debris-induced heatup is insensitive to the ECCS injection flow rate. The results of this study, in conjunction with the early application of sump switchover, which was determined to be limiting based on the sump switchover time sensitivity study presented in the response to RAI-4.19 Item b., demonstrate that the ECCS injection flows used in the analyses are appropriate for all Westinghouse plants and no additional validation is required during plant-specific implementation of the WCAP-17788 methodology.

Containment Pressure during Recirculation Phase

As described in WCAP-17788, Volume 4, Section 4.2, the containment pressure is set to 14.7 psia to maximize the break flow rate. This is a representatively limiting lower value for containment pressure following a LOCA for the Westinghouse plants covered by the analyses. No additional validation is required with regard to containment pressure during plant implementation of the WCAP-17788 methodology.

ECCS Temperature after Sump Switchover

The use of saturated ECCS liquid during the recirculation phase is limiting. As described in WCAP-17788, Volume 4, Section 4.2, the use of saturated liquid during the recirculation phase maximizes the core steaming rate and minimizes the reactor coolant system cooldown. A sensitivity study presented in the response to RAI-4.23 demonstrates that the debris-induced peak cladding temperature (PCT) is insensitive to ECCS liquid temperature during the recirculation phase. No additional validation is required with regard to ECCS temperature after sump switchover during plant implementation of the WCAP-17788 methodology.

Sump Switchover Time

As described in the response to RAI-4.1, an early sump switchover time provides the greatest challenge to long-term decay heat removal because debris arrives at the core inlet earlier in the transient when decay heat is higher. The sump switchover time sensitivity study in the response to RAI-4.19 Item b. show that a later switchover time results in a lower debris-induced heatup. A sump switchover time of 20 minutes is a representatively limiting early switchover time for the Westinghouse plants covered by the analyses. No additional validation is required with regard to sump switchover time during plant implementation of the WCAP-17788 methodology.

b. Provide graphs of the physical axial power profiles implemented in the plant design analyses in Sections 8 through 11. Provide each physical axial power profile on a separate plot and for each profile show its nodal approximation based on the core axial nodalization.

   i. Specify the elevation of the axial peak power location associated with the profile described in Table 6-3 for the CE plant design analysis.

Response

The physical axial power profiles along with the core axial continuity cell nodalization used in the Westinghouse upflow and downflow plant analyses are shown on Figure RAI-4.5-1 and Figure RAI-4.5-2, respectively. The physical axial power profiles are approximated based on the core heat transfer nodalization, which is finer than the continuity cell nodalization. The approximated hot rod axial power profiles used in the Westinghouse upflow and downflow plant analyses are shown on Figure RAI-4.5-3 and Figure RAI-4.5-4, respectively. As the figures show, the nodal approximation agrees well with the physical axial power profile. The hot assembly rod, average rod, and low power rod axial power profiles are approximated using the same heat transfer nodalization as the hot rod. The normalized power for each profile is provided in Table RAI-4.5-1.

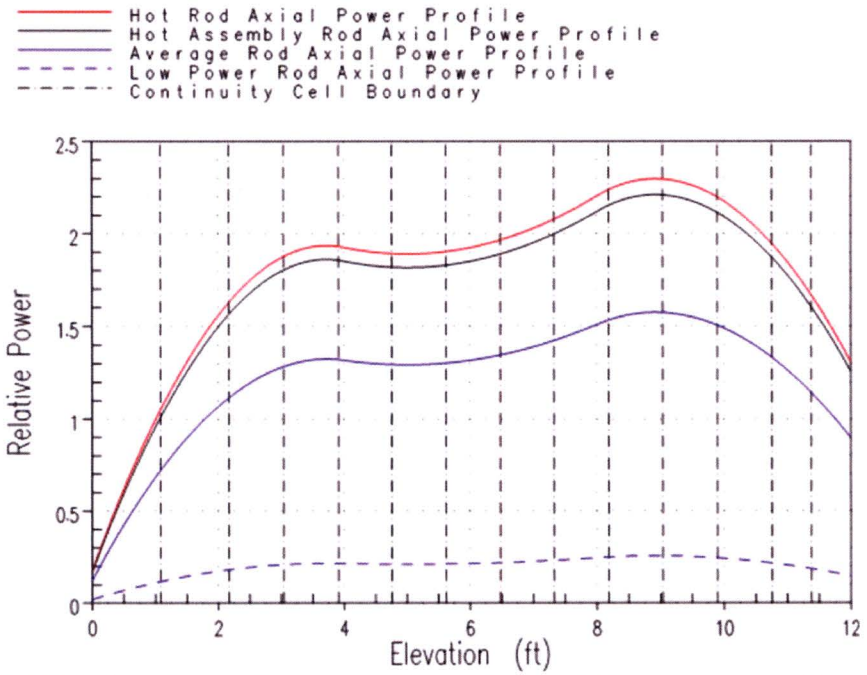

Figure RAI-4.5-1 Axial Power Profiles and Core Fluid Cell Nodalization used for the Westinghouse Upflow Plant Category

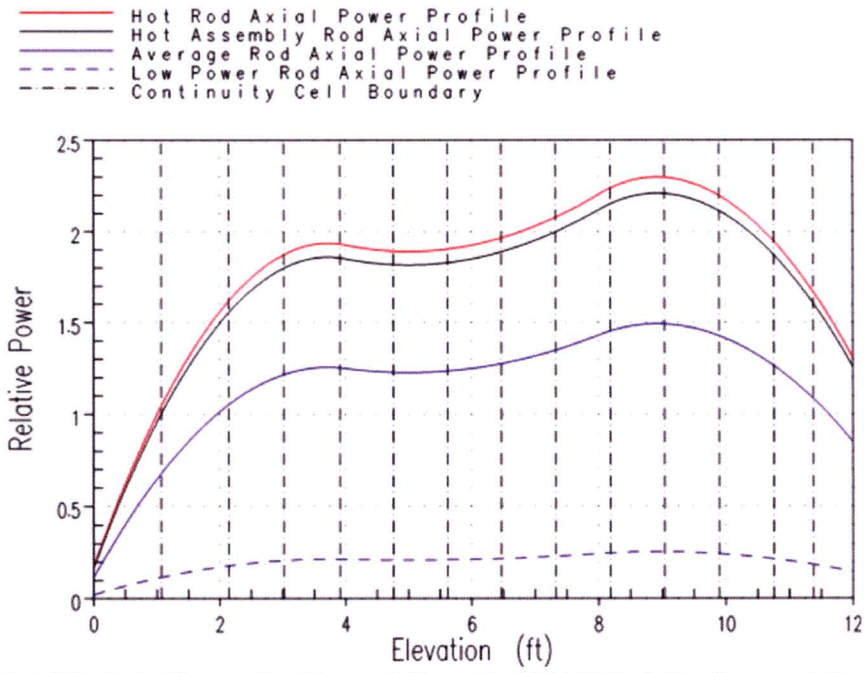

Figure RAI-4.5-2 Axial Power Profiles and Core Fluid Cell Nodalization used for the Westinghouse Downflow Plant Category

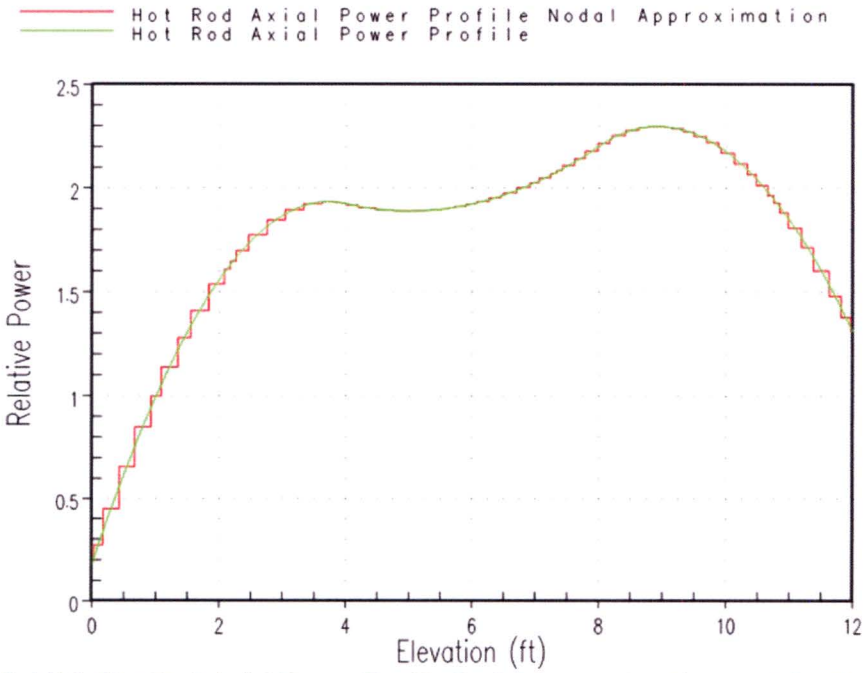

Figure RAI-4.5-3 Hot Rod Axial Power Profile Nodal Approximation used for the Westinghouse Upflow Plant Category

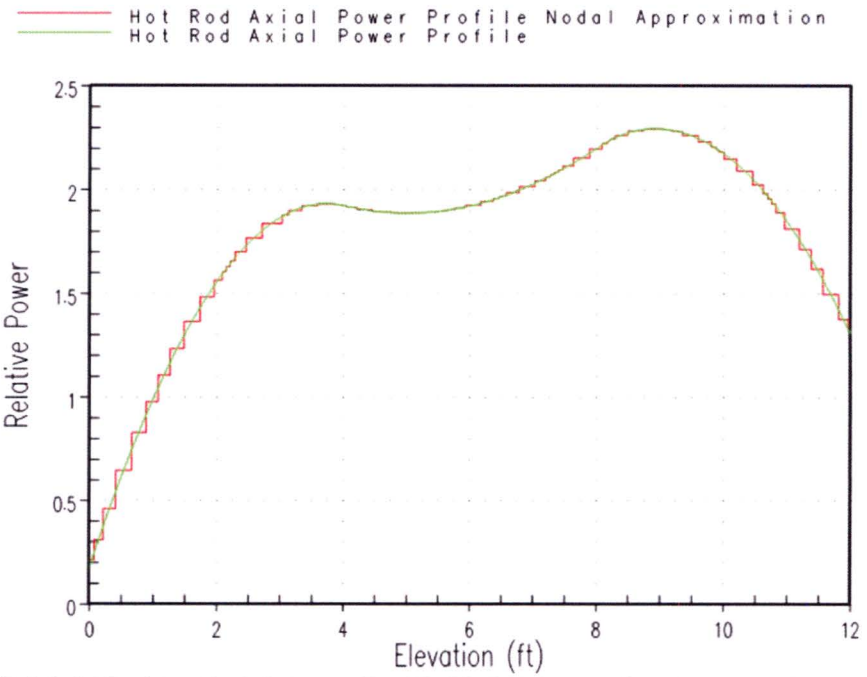

Figure RAI-4.5-4 Hot Rod Axial Power Profile Nodal Approximation used for the Westinghouse Downflow Plant Category

Table RAI-4.5-1 Radial Peaking Factors		
Designation	**Normalized Power**	
	Upflow	**Downflow**
Hot Rod	1.80	1.80
Hot Assembly	1.73	1.73
Average Assemblies	1.23	1.17
Low Power Assemblies	0.20	0.20

c. Clarify the approach to determining the axial power shapes simulated in the LOCA analyses. Explain if any bounding, or otherwise considered appropriate, assumptions were introduced to define the shapes requested in Item a. Explain if any physical axial power shapes, representative of individual units for each of the NSSS plant design categories included in Table 3-1 were considered in analyzing and determining the applicability of the simulated axial power profiles. Describe and justify the basis on which a single axial power profile, applied in the analyses for each plant category, can be considered valid and applicable to reactor core conditions across various units represented by each NSSS design category. An axial power profile applied for the purpose of a small-break LOCA analysis using a model based on 10 CFR Part 50, Appendix K, would represent an acceptable axial power profile on a plant specific basis.

Response

The axial power profiles use a high nuclear enthalpy rise hot channel factor $\left(F_{\Delta H}^{N} = 1.80\right)$, high total peaking factor $\left(F_{Q} = 2.30\right)$, and a skewed to the top power distribution (+13% axial offset (AO)). $F_{\Delta H}^{N}$ is the dominant power profile attribute of interest for long term core cooling (LTCC). The top-skewed power profiles shown in Figures RAI-4.5-1 and RAI-4.5-2 are limiting compared to base load or bottom-skewed power profiles due to the longer time for the quench front to approach the elevations with the highest power and their susceptibility to heatup if the core becomes uncovered or dryout occurs. An axial offset greater than +13% and a total peaking greater than 2.30 can only occur in rare transient (prior to the loss of coolant accident (LOCA)) conditions. Such an axial offset, AO, and F_Q would be temporary and the effects would be limited to the initial stored energy of importance in the short-term LOCA transient but are not indicative of the long-term axial decay heat power distribution of interest for LTCC. Additional justification of the bounding nature of the axial power profiles is as follows:

- Steady-state operation at the Technical Specification (TS) or Core Operating Limits Report (COLR) nuclear enthalpy rise hot channel factor, $F_{\Delta H}^{N}$, is possible and, thus, can 'burn in' and is the appropriate value to model during LTCC. The value modeled in the Westinghouse analyses for both the upflow and downflow plant designs is, $F_{\Delta H}^{N} = 1.80$.

and persist into LTCC. The steady-state depletion total peaking factor, F_Q^{SS}, is the appropriate value to model during LTCC. The value modeled in the Westinghouse analyses for both the upflow and downflow plant designs is, $F_Q^{SS} = 2.30$.

- As with F_Q, steady-state operation is not sustainable with highly skewed axial power profiles and thus, cannot 'burn in' and persist into LTCC. The steady-state depletion axial offset, AO_{SS}, is the appropriate value to model during LTCC. The axial offset value modeled in the Westinghouse analyses for both the upflow and downflow plant designs is, $AO_{SS} = +13\%$.

The power profiles used for the Westinghouse upflow plant and downflow plant analyses are applicable for an individual plant when the following parameters are met:

1. Nuclear enthalpy rise hot channel factor: $F_{\Delta H}^N \leq 1.80$
2. Steady-state depletion total peaking factor: $F_Q^{SS} \leq 2.30$
3. Steady-state depletion axial offset: $AO_{SS} \leq +13\%$

Individual plants will have to verify applicability of the methodology as part of their plant specific submittals. Furthermore, since the above parameters are dependent on the core design, these parameters will need to be reconfirmed for each reload core to demonstrate the continued applicability of the analyses.

RAI-4.6, Vol. 4

The evaluation models (EMs) used for the LOCA T-H computational analyses are described in Section 5. The plant models used to perform the analyses for each plant category presented in Sections 8 through 11 are described in Section 6. Table 1 below summarizes the computer codes and models used in these analyses.

Table 1: Identification of Computer Codes and Plant Models Used in the Thermal-Hydraulic Computational Analyses

Code and Plant Model Used	Plant Category			
	Westinghouse Upflow BB Plant Category	Westinghouse Downflow BB Plant Category	CE Plant Design	B&W Plant Category
System Code	WCOBRA/TRAC MOD7A	WCOBRA/TRAC MOD7A	S-RELAP5	RELAP5/MOD2-B&W
Code Version	Not provided	Not provided	Provided	Provided
EM Topical Report	WCAP-14747 (CQD), WCAP-16009-NP-A (ASTRUM)	WCAP-14747 (CQD), WCAP-16009-NP-A (ASTRUM)	[ ]	[ ]
Code Modified for WCAP-17788 Methodology	Yes (see Section 5.1)	Yes (see Section 5.1)	Yes	No
Base Plant Model	Westinghouse four-loop BE plant model	Westinghouse three-loop BE plant model	CE high-power BE plant model	B&W high-power Appendix K plant model (SBLOCA)

Provide the following information:

a. Identify the code version of WCOBRA/TRAC MOD7A used in the analyses in Sections 8 and 9.

Response

The code version used to analyze the Westinghouse plant categories presented in WCAP-17788, Volume 4, Sections 8 and 9 used WCOBRA/TRAC MOD7A, Revision 8 as the starting point. As described in the response to RAI-4.6 Item c., a unique "single application" version of the code was created to simulate transient core inlet resistance due to the postulated accumulation of debris.

Since the completion of the original analyses documented in Sections 8 and 9, which used the unique single application code version, WCOBRA/TRAC has been updated several times. Revision 9 was created with changes described in LTR-NRC-17-10 (Reference RAI-4.6-1). As part of the WCAP-17788, Volume 4 RAI resolution, additional changes have been made to WCOBRA/TRAC and the latest code version is WCOBRA/TRAC MOD7A Revision 9.1. Revision 9.1 changes include formal implementation of the modeling option to simulate transient core inlet resistance, as described in the response to RAI-4.6 Item c., and a change to reduce the potential for large vessel mass error in long-term core cooling simulations.

WCOBRA/TRAC MOD7A Revision 9.1 was used to address some of the WCAP-17788 Volume 4 RAI questions, and will constitute the code version for the Westinghouse GSI-191 thermal hydraulic analysis EM. The changes made in Version 9 do not significantly impact the results and conclusions of the GSI-191 analysis since they are related to the calculation of high temperature oxidation, and the ASTRUM steady-state calculation. The Version 9.1 changes do not significantly impact the WCAP-17788, Volume 4 analysis results and conclusions since the model update to simulate transient core inlet resistance is equivalent to the model option used by the single application version, and because large vessel mass error was not observed in the WCAP-17788 analysis results.

Reference

RAI-4.6-1 LTR-NRC-17-10, "U.S. Nuclear Regulatory Commission 10 CFR 50.46 Annual Notification and Reporting for 2016," March 7, 2017.

b. Clarify if NRC staff approval of subsequent TRs related to WCOBRA/TRAC, S-RELAP5, and RELAP5/MOD2-B&W can have an impact on the EMs applicability or validity of the T-H analysis results presented in WCAP-17788-P.

Response

NRC staff approval of subsequent Topical Reports (TRs) related to different versions of WCOBRA/TRAC for different applications will not impact this EM's applicability or validity of the GSI-191 analysis results presented in WCAP-17788 Volume 4. In the future, other items may be discovered that require code or EM changes. Once the GSI-191 analyses are approved, then they become part of the Analysis of Record (AOR) for LTCC and would need to be reassessed when a new analysis code issue or error is discovered. Changes to the GSI-191 analyses will be evaluated and addressed appropriately based on the Westinghouse procedures governing errors in codes or results of approved methodologies if some future deviations in the analysis approach is deemed necessary.

c. As seen in Table 1 above, code modifications were made to both WCOBRA/TRAC and S-RELAP5 for the analyses presented in Volume 4 of WCAP-17788-P. Section 5.1 explains that "in order to simulate transient resistance at the core inlet due to the build-up of debris, it was necessary to modify the baseline WCOBRA/TRAC version." Letter OG-16-42 dated February 12, 2016, described a modification of the baseline S-RELAP5 code version to produce "a development version of S-RELAP5" that was used to obtain the updated analyses submitted with OG-16-42 to replace the original results in Section 10 of Volume 4. Describe briefly the code changes and provide the validation and verification results for the "single-application" WCOBRA/TRAC code version and the S-RELAP5 "development version." Confirm that the code modifications were performed in conformance with applicable quality assurance procedures and provide references to related documents for both code modifications.

Response

A code modification was made to WCOBRA/TRAC to simulate resistance due to postulated debris accumulation at the core inlet. The code modification adds logic and input variables that allow the dimensionless form loss coefficient, C_D, at the first node of up to 4 specified channels to be varied with time. The code modification was performed in accordance with the Westinghouse Electric Company Quality Management System (QMS). This system meets the requirements of the United States NRC related to quality control and quality assurance including the requirements set forth in 10CFR50 Appendix B and also the standards set forth in ISO 9001.

As part of the code verification and validation effort, a number of test cases were executed to confirm that the code modification was working as expected. Additionally, a regression test was performed to ensure that the code modification did not lead to any unintended impacts to calculations, and testing was completed to confirm proper diagnostic checks and result output. A simplified model was developed and executed to verify that the code changes to WCOBRA/TRAC were implemented correctly. A schematic of the developed model is shown in Figure RAI-4.6-1. The one-dimensional portion of the model uses a FILL and BREAK component to control the flow and pressure through the three-dimensional portion. FILL component 2 uses a constant velocity flow and BREAK component 11 uses a constant pressure boundary condition. The three-dimensional portion of the model is made up of five channels. Flow enters channel 1 and splits into channel 2, channel 3, and channel 4. This flow split is meant to model a simplified flow split similar to a flow split from the lower plenum to the core channels.

The simulation is run for 90 seconds and the dimensionless loss coefficient was ramped uniformly across the inlet to channels 2, 3, and 4, as shown in Figure RAI-4.6-2. The code input loss coefficient was compared to hand calculations using the following equation:

$$C_D = 2 \cdot \frac{P_1 - P_2 - \rho_1 g h}{\rho_1 v_1^2} \qquad \text{Eq. RAI-4.6-1}$$

Pressure, liquid density, and liquid velocity output from the simple test case are used to calculate the loss coefficient using Eq. RAI-4.6-1. Figure RAI-4.6-3 shows the calculation results. Comparing this figure to Figure RAI-4.6-2 demonstrates that the code input loss coefficients align with expected results.

In a second test case, variable losses were applied across the three channels, as shown in Figure RAI-4.6-4. The impact of the time varying loss coefficients should be reflected in the channel mass flow rates. In this case, the loss coefficients for channels 2, 3, and 4 are varied such that two of the channels remain constant while another channel is being ramped up or down.

As such, the following channel mass flow rate behavior should be observed:

- At 30, 60, and 85-90 seconds, when the loss coefficient values for channels 2, 3, and 4 are all zero, the mass flow rates for each channel should equilibrate.

- During an individual channels ramp period, the mass flow rate for that channel should decrease, and the mass flow rate for the two other channels should increase compared to the equilibrium points. For instance, from 30-60 seconds the Channel 3 loss coefficient is ramped from 0 to 13 and back down to zero. In this period, the Channel 3 mass flow rate should decrease while the loss coefficient is ramped to 13 and then begin to increase back to the equilibrium point as the loss coefficient is decreased back to 0. During that same period, the mass flow rate in Channels 2 and 4 should have the opposite effect, with the mass flow rates increasing due to the increased resistance in Channel 3.

Figure RAI-4.6-5 shows the impact of the time-varying loss coefficients on the channel inlet mass flow rate, and demonstrates that the actual results align with expected results.

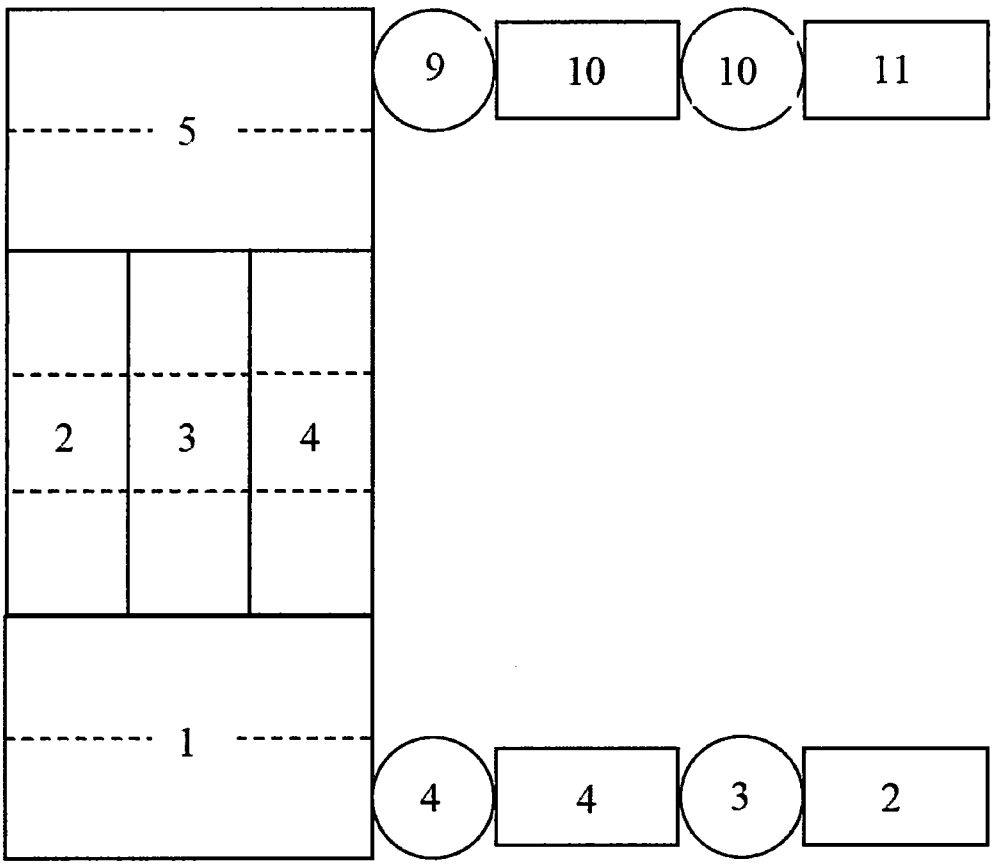

Figure RAI-4.6-1 Validation Test Case Noding Diagram

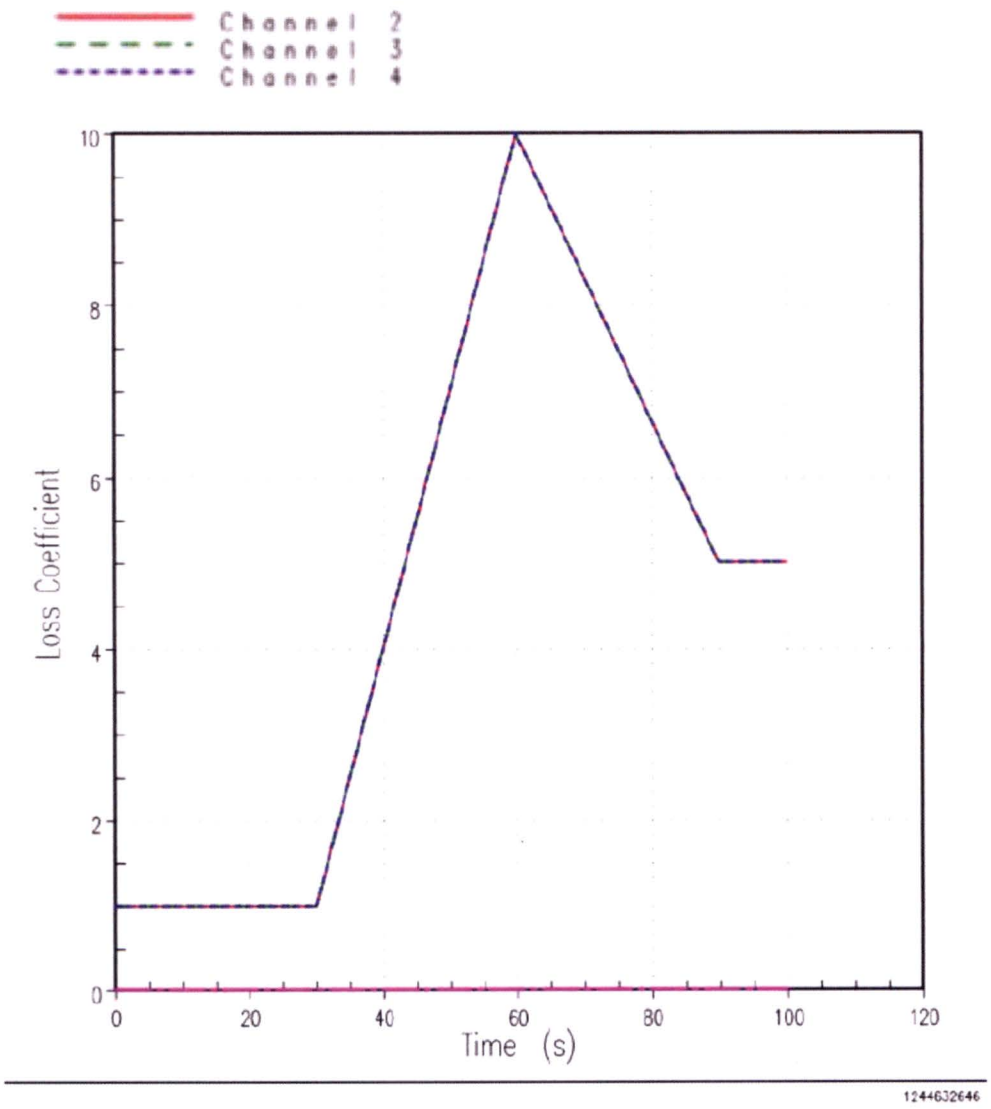

Figure RAI-4.6-2 Uniform WCOBRA/TRAC Loss Coefficient Applied at the Inlet to Channels 2, 3, and 4

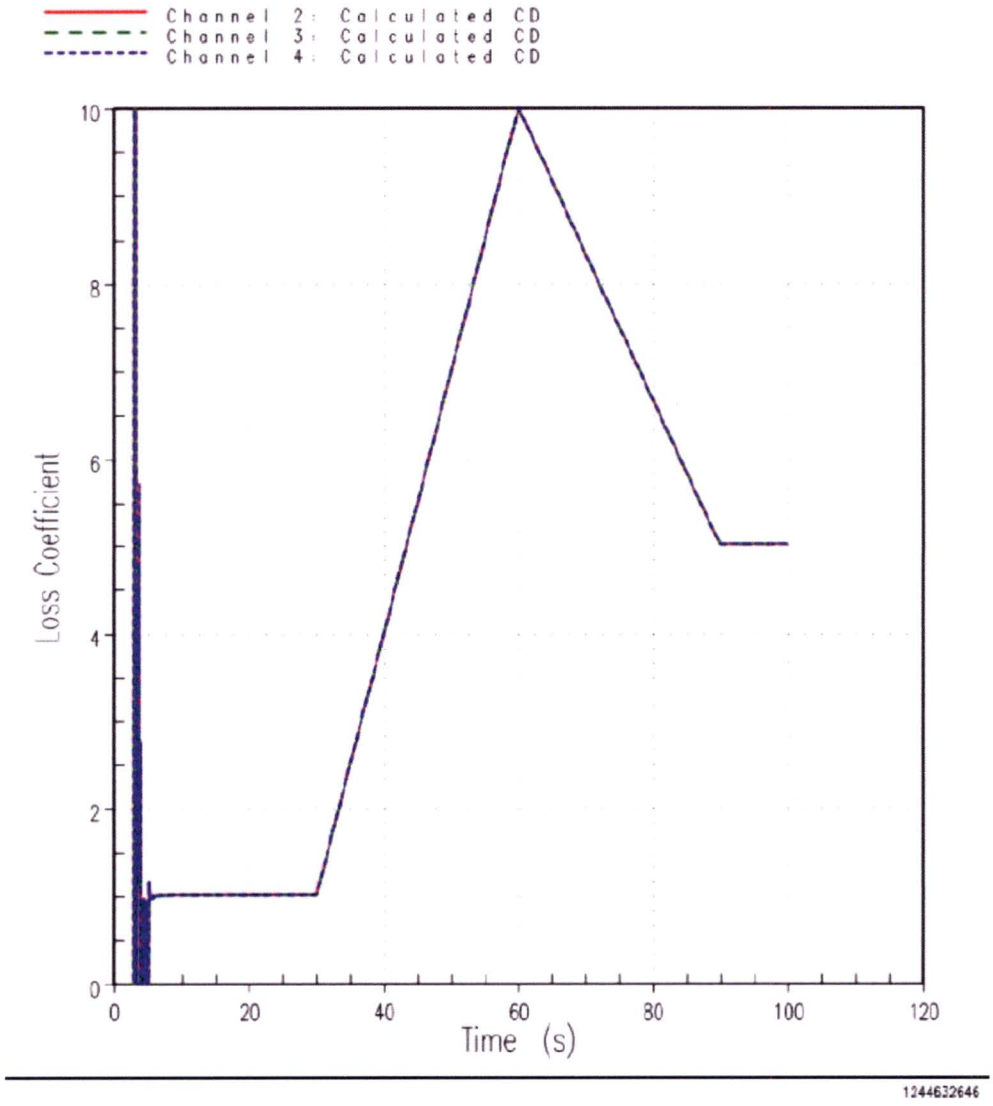

Figure RAI-4.6-3 Calculated Loss Coefficients at the Inlet to Channels 2, 3, and 4

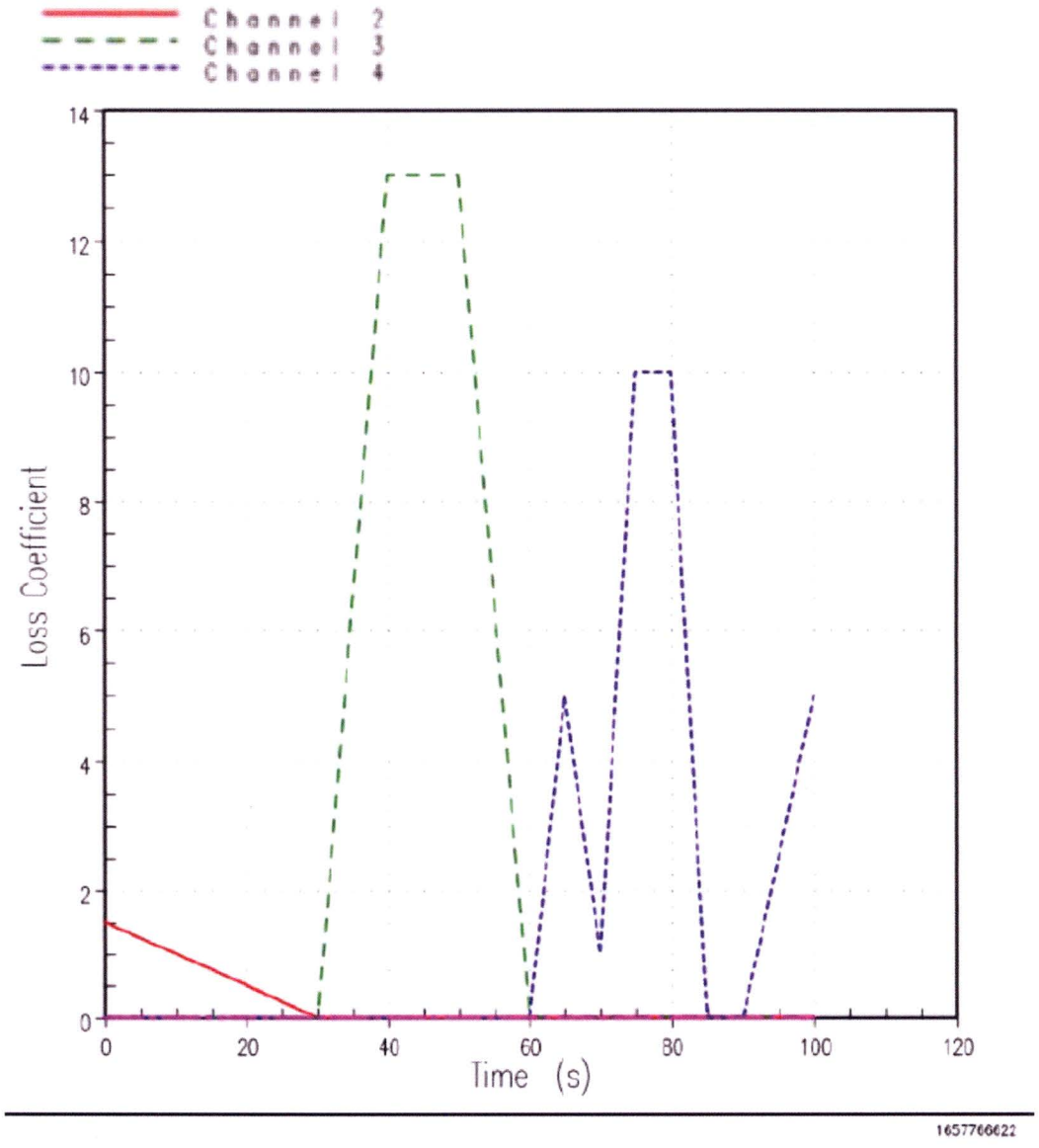

Figure RAI-4.6-4 Non-Uniform WCOBRA/TRAC Loss Coefficients Applied at the Inlet to Channels 2, 3, and 4

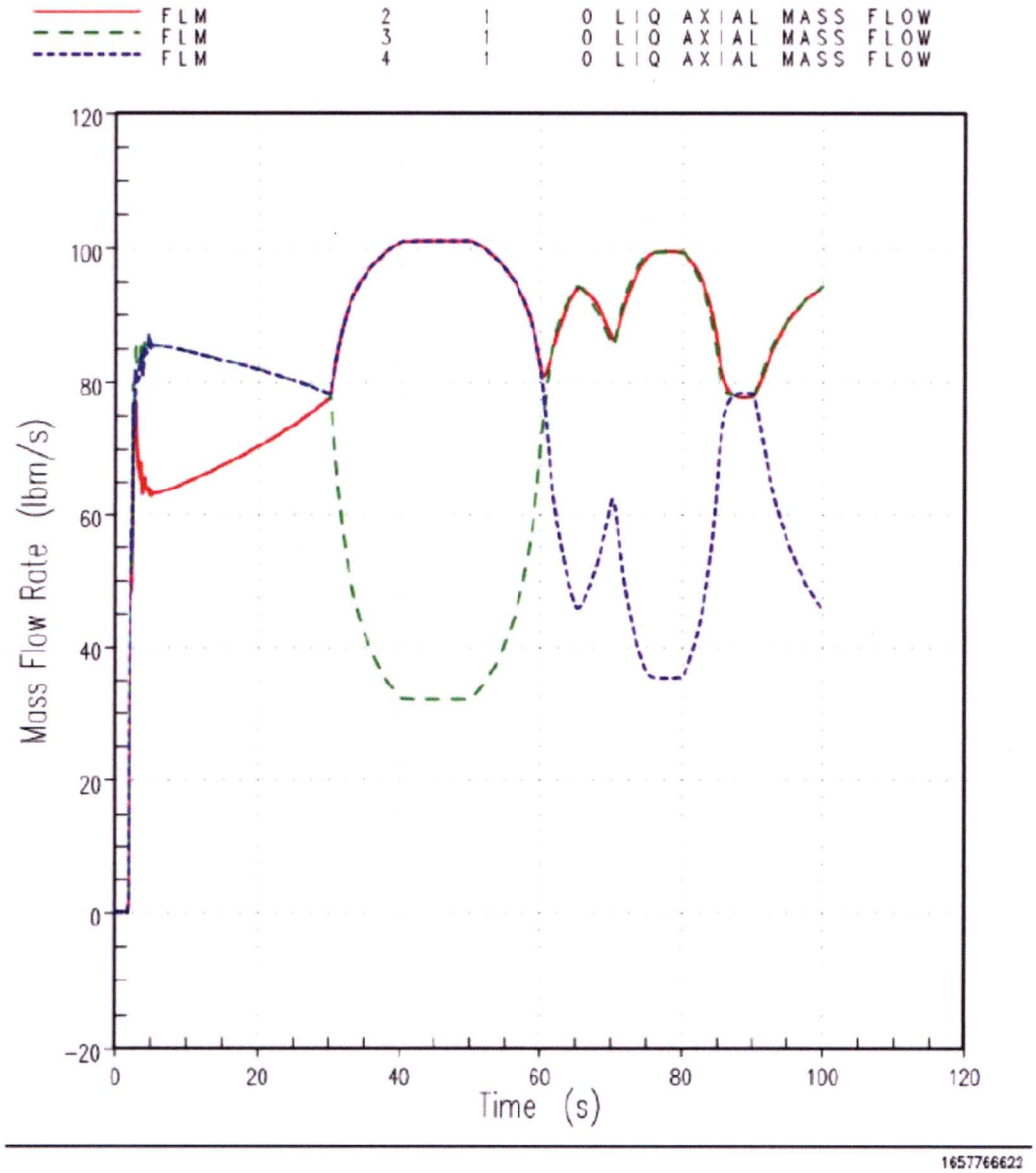

Figure RAI-4.6-5 Mass Flow Rate at the Entrance to the Channels 2, 3, and 4

RAI-4.7, Vol. 4

Section 4 states "it was determined that all computer codes and methods utilized have the ability to accurately predict the RCS response to simulated core inlet blockage during the sump recirculation phase of the post-LOCA transient." Describe the technical basis for this determination for each code methodology used in the analyses. Include identification and description of key governing processes and explain how the code capabilities were evaluated in terms of adequacy for the modeling of such processes. Explain how the code capabilities and accuracy in predicting the system and core response, including important parameters associated with the consequences of core inlet blockage, were evaluated. Include comparisons and assessments using experimental data as applicable.

Response

Regulatory Guide 1.203 (Reference RAI-4.7-1) provides a framework for developing transient and accident analysis methods. Application of the full evaluation model development and assessment process (EMDAP) described therein is not needed for all evaluation models (EMs) submitted for review by the NRC staff. Some EMs submitted for review are relatively minor modifications to existing EMs. Thus, the scope and depth of applying the development process to the EM can be based on a graded approach. The following four attributes of the EM should be considered when determining the extent to which the full model development process may be reduced for a specific application:

(1) Novelty of the revised EM compared to the currently acceptable model

(2) Complexity of the event being analyzed

(3) Degree of conservatism in the EM

(4) Extent of any plant design or operational changes that would require reanalysis

As discussed in the following sections, these attributes are described and reviewed for applicability to the GSI-191 hot leg break (HLB) EM that is applied in Volume 4 of WCAP-17788. This review concludes that a graded EMDAP process is appropriate for development and assessment of the GSI-191 HLB EM. This graded approach will provide the framework for the response to this question, along with other questions related to code applicability and assessment. It is noted that the original development and assessment did not explicitly follow the EMDAP steps; however, the same basic elements contained in the EMDAP were addressed. As such, organizing the original development and assessment effort within the EMDAP is relatively straightforward, and additional assessment effort completed as part of the RAI resolution can easily be incorporated into the EMDAP framework.

For the Westinghouse GSI-191 HLB EM using WCOBRA/TRAC, the technical basis for the adequacy determination is provided using the graded EMDAP. Identification and description of the key governing processes are provided in Element 1 of the EMDAP.

The key processes identified for the GSI-191 HLB scenario include:

- Decay Heat
- Core Inlet Resistance due to Debris
- Core Void Generation/Distribution (Mixture Level)
- Heat Transfer to Single-Phase Vapor
- Upper Plenum Draining and Mixture Level
- Alternate Flow Path Resistance

WCOBRA/TRAC code capabilities were evaluated in terms of adequacy for modeling these key processes by performing assessments using applicable experimental data and making comparisons to known standards and hand calculations, as described in Element 4 of the EMDAP. Code capabilities and accuracy in predicting the system and core response, including the flow split following core inlet blockage and any debris-induced heatups were evaluated using sensitivity studies and engineering judgement, also described in Element 4 of the EMDAP. Completing this process concludes that WCOBRA/TRAC is adequate for analyzing the GSI-191 HLB scenario. A similar approach was taken for the adequacy determination of the other code methodologies presented in WCAP-17788, Volume 4 and the details are provided in the Combustion Engineering and Babcock & Wilcox enclosures.

Evaluation Model Development and Assessment Process

The EM concept establishes the basis for methods used to analyze a particular event or class of events. This concept is described in 10 CFR 50.46 for loss-of-coolant accident (LOCA) analysis. Paragraph (b)(2) provides the definition of an acceptable EM,

> *"An evaluation model is the calculational framework for evaluating the behavior of the reactor system during a postulated loss-of-coolant accident (LOCA). It includes one or more computer programs and all other information necessary for application of the calculational framework to a specific LOCA, such as mathematical models used, assumptions included in the programs, procedure for treating the program input and output information, specification of those portions of analysis not included in computer programs, values of parameters, and all other information necessary to specify the calculational procedure."*

The EMDAP process is broken into the following six basic principles as identified in RG 1.203:

(1) ***Determine requirements for the evaluation model.*** *The purpose of this principle is to provide focus throughout the evaluation model development and assessment process (EMDAP). An important outcome should be the identification of mathematical modeling methods, components, phenomena, physical processes, and parameters needed to evaluate the event behavior relative to the figures of merit described in the SRP and derived from the general design criteria (GDC) in Appendix A to 10 CFR Part 50. The phenomena assessment process is central to ensuring that the EM can appropriately analyze the particular event and that the validation process addresses key phenomena for that event.*

(2) ***Develop an assessment base consistent with the determined requirements.*** *Since an EM can only approximate physical behavior for postulated events, it is important to validate the calculational devices, individually and collectively, using an appropriate assessment base. The database may consist of already existing experiments, or new experiments may be required for model assessment, depending on the results of the requirements determination.*

(3) ***Develop the evaluation model.*** *The calculational devices needed to analyze the events in accordance with the requirements determined in the first principle should be selected or developed. To define an EM for a particular plant and event, it is also necessary to select proper code options, boundary conditions, and temporal and spatial relationships among the component devices.*

(4) ***Assess the adequacy of the evaluation model.*** *Based on the application of the first principle, especially the phenomena importance determination, an assessment should be made regarding the inherent capability of the EM to achieve the desired results relative to the figures of merit derived from the GDC. Some of this assessment is best made during the early phase of code development to minimize the need for later corrective actions. A key feature of the adequacy assessment is the ability of the EM or its component devices to predict appropriate experimental behavior. Once again, the focus should be on the ability to predict key phenomena, as described in the first principle. To a large degree, the calculational devices use collections of models and correlations that are empirical in nature. Therefore, it is important to ensure that they are used within the range of their assessment.*

(5) ***Follow an appropriate quality assurance protocol during the EMDAP.*** *Quality assurance standards, as required in Appendix B to 10 CFR Part 50, are a key feature of the development and assessment processes. When complex computer codes are involved, peer review by independent experts should be an integral part of the quality assurance process.*

(6) ***Provide comprehensive, accurate, up-to-date documentation.*** *This is an obvious requirement for a credible NRC review. It is also clearly needed for the peer review described in the fifth principle. Since the development and assessment process may lead to changes in the importance determination, it is most important that documentation of this activity be developed early and kept current.*

RG 1.203 goes on to break the full EMDAP process into four distinct elements consisting of 20 independent steps as shown in Figure RAI-4.7-1 below. The complexity of the problem should determine the level of detail needed to develop and assess an EM. For simpler events, many of the steps in the process may only need to be briefly addressed. Also, if a new EM only involves an incremental change to an existing EM, the process may be shortened as long as the effect of the change is thoroughly addressed. This instance is referred to as the graded approach to the EMDAP, which is discussed in detail in Section 5 of the *Regulatory Position* Section to RG 1.203. The following section summarizes this approach and identifies how it can be used for the GSI-191 application.

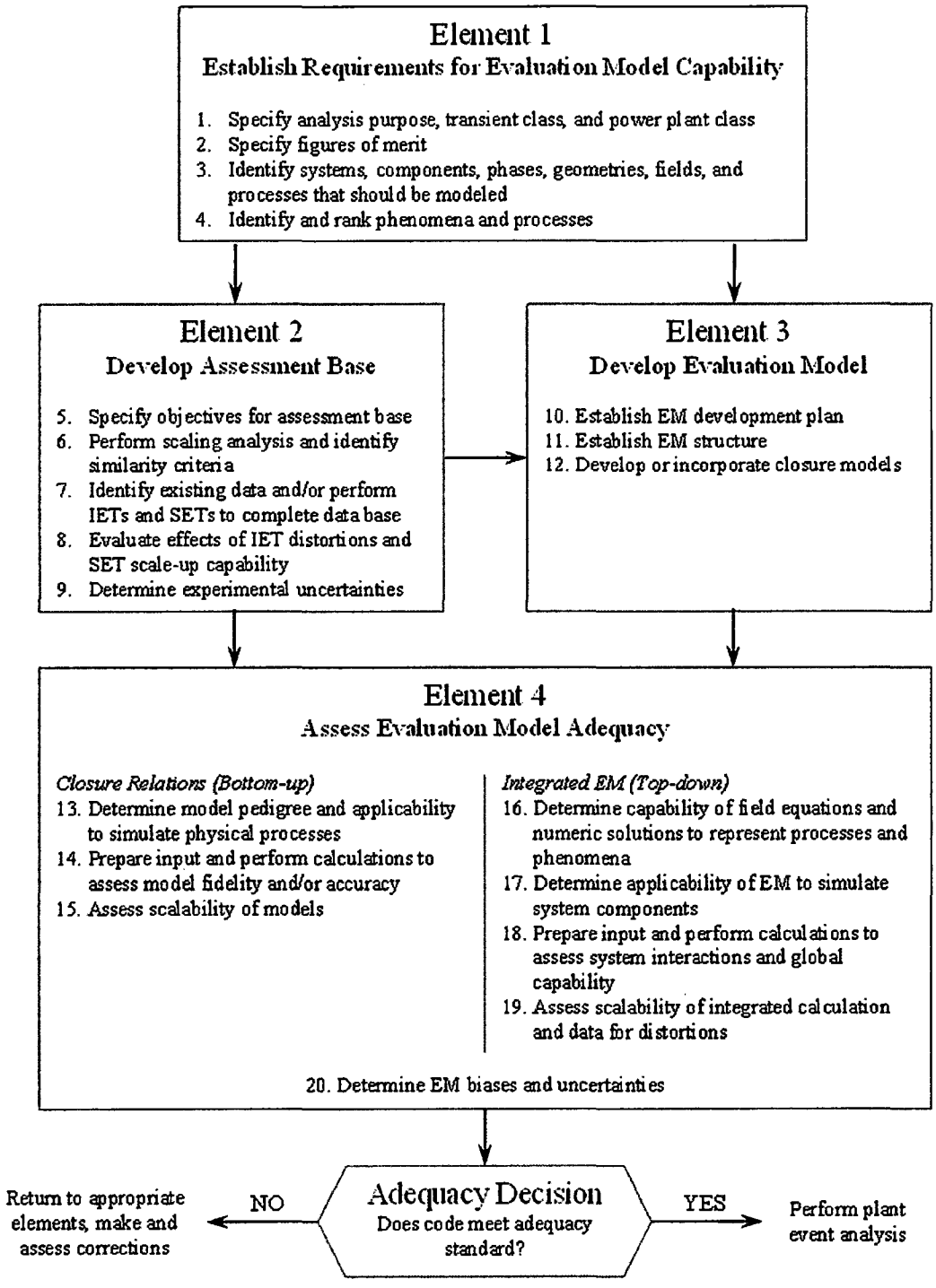

Figure RAI-4.7-1 Elements of EMDAP

Graded Approach to Applying the EMDAP Process to the Westinghouse GSI-191 HLB EM

The following subsections describe each of the graded EMDAP attributes in more detail and provide the justification for applying the graded approach to the Westinghouse GSI-191 HLB EM described in WCAP-17788, Volume 4.

Attribute (1) – Novelty of the Revised EM Compared to the Currently Acceptable Model

Discussion in RG 1.203

The level of effort involved in applying the development and assessment process should be commensurate with the extent of the changes made to an EM. Small changes to a robust, time-tested EM component may not require full application of the EMDAP to the entire EM. For example, consider a change to a simple heat transfer or drag correlation possibly required by an error correction. In this case, scaling would only have to be considered within the context of how well the new model scales to full plant analysis if the model is developed from a reduced-scale test program.

Consideration would also have to be given to how well the assessment cases for the model represent full-scale plant conditions. Implementation testing needs to be performed to show that the new model has been correctly implemented. A small subset of the entire code assessment matrix may be adequate to test the phenomena that are affected by the revised model. Another subset of the code test cases may need to be performed to ensure that other parts of the model are not inadvertently impacted by the changes.

A large model change may require application of the EMDAP on a much larger scale. For example, changing from an equilibrium drift flux model to a two-fluid, non-equilibrium model would be an example of a significant change that would require an extensive development and assessment process for the new EM.

Application to GSI-191

As described in WCAP-17788, Volume 4, Section 5, the WCOBRA/TRAC computer code developed for the ASTRUM best-estimate LOCA method was used as the starting point for the GSI-191 HLB EM, because it represents a robust, time-tested EM that is NRC-approved for licensing basis analysis of the short-term LOCA transient (peak cladding temperature (PCT) and cladding oxidation). WCOBRA/TRAC has been significantly validated and benchmarked to accurately simulate the reactor coolant system (RCS) under LOCA conditions. Most of the models or closure relationships used in WCOBRA/TRAC were developed or available from existing database literature. Although the original development of the WCOBRA/TRAC models or closure relationships did not explicitly consider the long-term core cooling (LTCC) phase of the LOCA transient, models have been evaluated, and sometimes modified or improved, to better simulate the full range of conditions expected in a LOCA transient. The goal was to ensure that the same fundamental correlations apply over the wide range of conditions expected during a large break LOCA. Models are not tailored to a specific scenario or break location. As the existing models, at their fundamental level, are based on the local thermal-hydraulic conditions they are independent of the global system response or time evolution for the GSI-191 HLB scenario.

Use of WCOBRA/TRAC and extension of the methods to simulate the GSI-191 HLB scenario constitutes a minor change to the EM as many of the dominant physical phenomena that govern the GSI-191 HLB scenario have already been assessed as part of the original code development and assessment process. Further, only a minor change to a subset of the code was required to simulate the accumulation of debris at the core inlet.

- Many of the dominant physical phenomena governing the LTCC phase of the LOCA transient have been assessed as part of the original EM assessment process, as described in WCAP-16009-P-A (Reference RAI-4.7-2). As such, only small additions to the original assessment base are required to demonstrate the adequacy of WCOBRA/TRAC for simulating the GSI-191 HLB scenario. These additions include:

  1. Low-pressure separate effects test (SET) data to assess the code's ability to simulate the two-phase mixture level under low-pressure boil-off conditions

  2. Single-phase steam cooling rod bundle data to assess the code's ability to conservatively model heat transfer during a debris-induced core uncovery.

  Details regarding the additions to the existing assessment base are provided in EMDAP Element 2, Element 4, and the responses to RAI-4.8 and RAI-4.9.

- WCOBRA/TRAC required a minor modification to simulate the transient accumulation of debris at the core inlet. The simulation of debris accumulation at the core inlet was completed by increasing the dimensionless flow resistance (K) in the velocity head formulation. The existing equation for velocity head was not changed and the only modification was to the structure of the input such that the form loss could be varied as a function of time. Validation of this code change was completed by constructing simple test cases that could be compared to hand calculations. A regression test was also performed to ensure that the code changes did not lead to any unexpected changes to the code functionality. The response to RAI-4.6 describes the code modification, and verification and validation effort.

- The plant models used in the GSI-191 HLB EM are described in WCAP-17788, Volume 4, Section 6. The models selected represent the plants in one of two plant categories: Westinghouse upflow barrel/baffle plants, and Westinghouse downflow barrel/baffle plants. The base plant models were developed for best-estimate (or realistic) analyses. As such, the non-critical inputs were set to nominal values. Model changes were made based on the critical inputs to bias the model towards more of an Appendix K-type analysis, and to account for variations in the plants contained in each analysis category. The plant models used in the analysis are described in more detail in the response to RAI-4.29, which also describes the changes made to the models for the GSI-191 HLB EM.

- The changes to the plant models are summarized below:

1. Break location. The base models were developed to simulate a cold leg break. For the GSI-191 EM, a HLB is modeled, so the break location was moved. Break location has been assessed as part of the original EM development; thus, assessment of this change is not required.

2. Decay heat model. A best-estimate decay heat model was applied in the base plant models. For the GSI-191 HLB EM, an Appendix K decay heat model (ANS 1971 + 20%) was applied to introduce conservative bias. The response to RAI-4.10 provides the heat generation rate form the decay heat models applied to the GSI-191 HLB EM.

3. Alternate flow path (AFP) flow resistance. The resistance through the AFPs was increased to bound all plants in a given category. The calculation of AFP resistance was completed with hand calculations using the physical plant geometry. Additional margin was added to the AFP resistance applied in the models to account for uncertainties in the calculational method. The details of the AFP calculations are provided in the response to RAI-4.2.

4. Containment pressure. The containment pressure boundary condition applied at the break was minimized to maximize the break flow during the recirculation phase. Output from the simulations verifies that the pressure boundary condition is as expected.

5. Core inlet blockage. A dimensionless form-loss coefficient at the first core node was adjusted to simulate the accumulation of debris during the recirculation phase of the transient. The time and the rate that core inlet resistance is applied are important factors. In the GSI-191 HLB EM, debris arrival is assumed to occur coincident with the sump switchover time, and core inlet resistance is applied over a 1 minute period, which is unrealistically fast.

6. Core power distribution. Power distribution parameters were selected to maximize the potential for core uncovery and cladding heatup during the GSI-191 scenario. The top-skewed core power distribution selected is limiting for the GSI-191 scenario. The core power distribution parameters used in the GSI-191 HLB EM are described in the response to RAI-4.5 Item b.

7. Interfacial drag. A multiplier of 0.8 is applied to the core region axial interfacial drag to reduce the predicted mixture level swell. This was completed to produce two-phase mixture level results that better align with available experimental data. The interfacial drag multiplier was assessed using low-pressure separate effect boil-off data. The basis for the multiplier and the assessment are included in the response to RAI-4.8.

Attribute (2) – Complexity of the Event

Discussion in RG 1.203

The level of effort involved in applying the development process should be commensurate with the complexity of the EM. At first glance, the EMDAP may seem too burdensome to apply to simple events. However, application of the EMDAP to a simple event will automatically result in a simplified process. In simple events, the number of key physical phenomena should also be small, and the code assessment only needs to cover the important phenomena even though the underlying general purpose transient analysis computer program may have models that cover a much wider range of conditions. An example of this is the system evaluation of a pressurized-water reactor pump trip analysis in which the important phenomena may be limited to a few quantities, such as single-phase liquid wall drag and heat transfer, and pump inertia. In this case, very little assessment would need to be performed, and there may be adequate full-scale plant data for the code assessment so there would be no need for a scaling analysis. The other extreme is an EM for a large-break LOCA, where the physical phenomena and the mathematical models are complex and cover a wide range of conditions. An extensive code development process and assessment would be required in this case.

Application to GSI-191

The GSI-191 HLB scenario occurs during the post-LOCA LTCC phase of the transient. This phase of the transient is far less complex than the short-term transient. There are fewer dominant physical phenomena that govern the LTCC transient and the RCS pressure is somewhat stable and low during LTCC (versus the rapid changes seen during the short-term LOCA transient). After core reflood, cladding temperatures have reduced below the minimum film boiling temperature and heat removal is governed by nucleate boiling and convection. With a blockage at the core inlet, the makeup to the core is changed from entering at the core inlet to entering at the core inlet plus through an AFP (i.e., barrel/baffle or upper head spray nozzle). The process of core heat removal does not change. The GSI-191 HLB scenario specification, Figures of Merit, and phenomena identification and ranking table (PIRT) are provided in Element 1 of the EMDAP.

Although complex thermal hydraulic computer programs are used for the GSI-191 HLB analysis, many of the models are not used during the post-LOCA LTCC phase of the transient. For example, the suite of post-critical heat flux (post-CHF) heat transfer correlations is not applicable during LTCC. As such, no assessment of these models is required to demonstrate appropriate extension of these codes into the LTCC period of the transient. The WCOBRA/TRAC models and correlations related to the high ranked processes and phenomena identified in the PIRT require assessment that is focused on the applicability of these models for LTCC.

Attribute (3) – Degree of Conservatism in the Evaluation Model

Discussion in RG 1.203

The intended results of an analysis can be conservative due to a combination of code input and modeling assumptions. The amount of assessment required for a change to an EM may be significantly reduced if the documented degree of conservatism is large or if the new model can be shown to give more conservative results than the previous model. However, conservatism in just one aspect of the EM; that is, a heat transfer correlation cannot be used to justify conservatism in the EM as a whole, because other aspects of the model may be non-conservative and cause the overall model to be non-conservative. The degree of conservatism in the overall EM must be quantified and documented for the particular application in order to justify a reduction in assessment requirements using this argument. Showing the degree of conservatism in an EM for a simple transient may be accomplished by a relatively simple uncertainty analysis, even if the underlying computer code is a large multipurpose code. The key to simplifying the uncertainty analysis is identifying the small number of parameters and physical phenomena that are important in determining the behavior of the accident.

Application to GSI-191

The inputs and boundary conditions to the GSI-191 HLB EM are selected such that a large degree of overall conservatism exists in the analysis results. A conservative decay heat model (10 CFR 50 Appendix K) is applied to maximize the potential for any cladding uncovery and heatup due to the accumulation of debris at the core inlet. The rate of debris accumulation modeled at the core inlet is unrealistically fast such that the potential for core uncovery is again maximized. In addition, other modeling features are applied that further increase the overall conservatism in the EM. This level of documented conservatism reduces the need for extensive assessment and uncertainty analysis.

Attribute (4) – Extent of Plant Design or Operational Changes That Require Reanalysis

Discussion in RG 1.203

The level of effort required to apply the process should be commensurate with the extent of changes made to the plant design or operation. Most changes to plant equipment or operations do not cause the plant to operate outside the range of validity of the EM. In such cases, no additional development and assessment needs to be performed. However, this may not be the case for all changes. Examples of changes that may require additional assessment of the EM are fuel bundle design changes (including grid spacer and intermediate flow mixer design changes), increases in the peak linear heat generation rate, or operational changes that may cause reliance on a different safety grade trip which requires accurate prediction of a quantity not required in the previous analysis. In such cases, a limited application of the EMDAP (similar to that described in Section 5.1) should be sufficient.

Application to GSI-191

The GSI-191 HLB EM was not developed as a result of changes to plant equipment or operations. Therefore, no additional development and assessment needs to be performed to address this attribute. Given the robustness and the overall conservatism contained in the GSI-191 HLB EM, the range of validity is broad and future plant equipment and/or operational changes are not expected to require reanalysis; however, this aspect will need to be assessed on a case-by-case basis. The response to RAI-4.5 discusses checks that must be performed by a plant to verify applicability and specific criteria to be evaluated for change management will be included in the EM implementation guidance currently being developed by the PWR Owners Group.

Conclusions

The four attributes for evaluation of a graded approach to EM development and assessment have been reviewed, and it is concluded that the graded EMDAP in RG 1.203 can be used to assess the adequacy of the GSI-191 HLB EM. The graded EMDAP will also be used as the framework to the response to this question, along with other questions related to code applicability and assessment.

In the following sections, the graded EMDAP is applied to the Westinghouse GSI-191 HLB EM, and it is concluded that the EM is adequate for analyzing the GSI-191 large HLB scenario of interest. The extrapolation of WCOBRA/TRAC for use in the LTCC phase of the post-LOCA transient has been accounted for by applying conservative bias to the critical input parameters such that the uncertainty associated with the modeling of important phenomena is bounded. The magnitude of the applied conservative biases was determined to be acceptable by making additional comparisons to applicable experimental data and performing sensitivity studies. Based on the results of these data comparisons and sensitivity studies, it is concluded that the predicted results are bounding of best-estimate performance. Therefore, the result demonstrates with a high level of probability that the 10 CFR 50.46 long-term cooling acceptance criteria are met, and it is concluded that the GSI-191 HLB EM is adequate.

In Element 1 of the EMDAP, important physical processes and phenomena are defined for the GSI-191 large HLB scenario and Figures of Merit. Each one of these important processes and phenomena were assessed to make the adequacy decision. Each assessment made is summarized as follows:

- Decay Heat – An Appendix K decay heat model was used in the GSI-191 HLB simulations. In Element 4 of the EMDAP, a sensitivity study using a nominal decay heat model was completed. The results of this sensitivity show that the debris-induced heatup that occurs following the application of complete core inlet blockage is virtually eliminated when a nominal decay heat model is applied. The results also demonstrate that the system response to reduced decay heat is as expected. Reduced decay heat results in less boiling and an increased reactor vessel liquid inventory.

- Core Inlet Resistance due to Debris – The timing and rate of the application of core inlet resistance is important to the system response. An early application of core inlet resistance results in a higher potential for a debris induced core uncovery because the decay heat is higher

earlier in the transient. For this reason, the GSI-191 HLB simulations start to apply core inlet resistance coincident with sump switchover time because it is the earliest time that debris can be transported to the RCS. A 1200 second sump switchover time is assumed, which is an early sump switchover time representative of two trains of ECCS in operation. Sensitivity studies completed in the response to RAI-4.19 demonstrate that for the same amount of core inlet resistance, the potential for a debris-induced core uncovery and heatup is greatly reduced when the sump switchover time is increased from 1200 seconds to 1400 seconds.

The rate that core inlet resistance is applied is also important. In the GSI-191 HLB simulations, the core inlet resistance is unrealistically ramped over a 1 minute period. This fast ramp rate bounds any plant-specific ramp rate and is introduced to create a greater potential for a debris-induced core uncovery. Sensitivity studies that apply a more gradual core inlet resistance ramp were completed to assess the conservatism associated with application of a 1 minute core inlet resistance ramp. As presented in Element 4 of the EMDAP, a gradual application of core inlet resistance applied to the upflow plant model results in no core-wide uncovery and the short duration heatups predicted are due to localized dryout at the peak power location. These heatups are shown to be less than 500°F, or approximately 300°F below the acceptance criterion. In this case, a core-wide uncovery does not occur because the downcomer is able to fill as the resistance at the core inlet builds gradually. As such, there is always coolant flow in excess of boil-off reaching the core. Not only is the acceptable core inlet debris load predicted by this gradual ramp rate more than 3 times higher than the defined limit, but the predicted PCT is more than 300°F below the 800°F acceptance criterion. A sensitivity that considers core inlet resistance ramp rate was also completed using the downflow plant model, as described in the response to RAI-4.19. In the downflow plant sensitivity, the core inlet resistance ramp rate was increased from 1 minute to 5 minutes, and the resistance was ramped to the same final value. The study demonstrated similar behavior with regard to the debris-induced heatup. A slower ramp rate allows the downcomer to fill coincident with the buildup of resistance such that a significant core uncovery is not predicted to occur.

- Core Void Generation/Distribution (Mixture Level) – The core mixture level is assessed using SET low pressure boil-off data as described in the response to RAI-4.8. The assessment shows that WCOBRA/TRAC tends to over-predict the core region two-phase mixture level swell by more than 25% in some cases. To offset this effect, the GSI-191 HLB EM applies a multiplier to the axial interfacial drag in the core region. When this multiplier is applied in the experimental assessment, the predicted two-phase mixture level swell falls within ±25% of the measured values. In addition, sensitivity studies were completed to quantify the sensitivity of a predicted debris-induced heatup and the key thermal hydraulic parameters to the value of the axial interfacial drag multiplier. The results of the sensitivity study demonstrated that varying the interfacial drag multiplier from 1.0 to 0.6 had little effect on the debris induced heatup. For the upflow plant model, the variation in debris-induced PCT was approximately 100°F. For the downflow plant, the variation was less than 50°F. This sensitivity study is presented in the response to RAI-4.8.

- Heat Transfer to Single-Phase Vapor – Convection to single-phase vapor is the dominant heat transfer mechanism during a debris-induced core uncovery. The WCOBRA/TRAC single-phase vapor heat transfer package was compared to experimental data from RBHT steam cooling experiments. The results showed good agreement with experimental results from that test program. Figure RAI-4.7-8 shows the single-phase vapor heat transfer correlations used in WCOBRA/TRAC, and compares them to data from RBHT facility single-phase steam cooling tests from NUREG/CR-7152. The WCOBRA/TRAC single-phase vapor heat transfer model conservatively bounds the RBHT data and its uncertainty.

- Upper Plenum Draining - Due to the lower steaming rates encountered in the upper plenum during LTCC, water tends to pool on the upper plenum structures. When resistance is applied to simulate debris accumulation at the core inlet, flow into the core is reduced and a core uncovery can occur if the flow falls below that required to replace boil-off. Liquid draining from the upper plenum into the top of the core will delay core uncovery and limit the magnitude of the uncovery. Also, following complete core inlet blockage, liquid is supplied to the top of the core through the AFPs creating a top-down cooling scenario.

  To confirm that there is good communication between the core region and the upper plenum, the Kutateladze number at the upper core plate was estimated for the WCOBRA/TRAC simulation of partial core inlet blockage (K_{max}). The Kutateladze number for a conservative steaming rate at 1200 seconds post-LOCA was calculated to be less than 2.5. Since the vapor Kutateladze number is less than 3.2, good communication between the core region and the upper plenum is expected. The vapor flow falls below the downflow limit of $Ku_g = 3.2$ after approximately 500 seconds post-LOCA. Therefore, good communication between the core region and the upper plenum is expected throughout LTCC and the GSI-191 HLB scenario.

- Upper Plenum Mixture Level - As described in the response to RAI-4.23, the upper plenum mixture level is important for liquid transport to the break under LTCC conditions. Entrainment is less important because the steaming rates are low such that entrainment rates are diminished. An upper plenum mixture level exists during most of the GSI-191 HLB transient. Under these conditions, the accuracy of the mixture level prediction is less important because there is significant liquid carryover to the break due to natural or forced circulation. Similar to the core mixture level, the upper plenum mixture level is dependent on the flow regime and interfacial drag. Various sensitivity studies completed in this RAI response have demonstrated that the break flow from the reactor vessel side is not significantly sensitive to variations in the upper plenum mixture level. The effect of these studies on break flow is discussed in the response to RAI-4.23 Item i.

- Alternate Flow Path Resistance - The alternate flow path resistances applied in the GSI-191 HLB EM are calculated from physical plant geometry and established methods as described in the response to RAI-4.2. Margin is added to the alternate flow path resistance values to account for uncertainties in the calculation. Before performing transient analysis, the steady-state calculated flow through the alternate flow paths is compared to expected flows under normal operating

conditions to confirm that the calculated steady-state flow through the alternate flow paths is less than the best-estimate calculated flows for normal operation.

The upflow plant steady-state barrel/baffle channel flow is shown in Figure RAI-4.7-9. As the figure shows, the steady state barrel/baffle flow is approximately 10% less than the desired best-estimate flow for the reference plant. Similarly, Figure RAI-4.7-10 shows the upper head spray nozzle flow from the downflow plant steady-state calculation. As shown in the figure, the steady-state upper head spray nozzle flow is more less 20% less than the best-estimate calculated flows for normal operation.

- Non-Condensable Gas Effects – Although not ranked with high importance in the GSI-191 HLB PIRT, the downflow plant model was found to be sensitive to nitrogen gas injection from the accumulators. As described in Element 4 of the EMDAP, cyclic heatup/cooldown behavior following the application of core inlet blockage (K_{max}) in the Westinghouse downflow plant model has been identified and is related to the treatment of non-condensable (NC) gas in WCOBRA/TRAC. The Westinghouse downflow plant model responds differently than the Westinghouse upflow plant model during the accumulator injection phase of the transient, which impacts the response to core inlet blockage. In the downflow plant simulations, the intact loop seals fill with liquid prior to sump recirculation. In the upflow plant simulations, the intact loop seals remain mostly voided until core inlet resistance is applied. It is postulated that open loop seals allow a vent path for nitrogen gas injected from the accumulators to escape the system. In the downflow plant simulation, the plugged loop seals effectively trap nitrogen gas in the downcomer, which impacts the vessel fluid inventory and the response to core inlet resistance. The following observations are made from the downflow K_{max} plant simulations:

  - The downcomer and core levels do not agree. The presence of nitrogen in the downcomer suppresses the liquid level, which increases the core liquid inventory.
  - When core inlet resistance is applied at sump recirculation (K_{max} case), spurious liquid flow at the core inlet is observed. Periodic increases in the core inlet flow correspond to the cooldown behavior observed in the debris-induced PCT response.

The observations may be a result of logic in the simplified NC gas model in the code and may not be physical. WCOBRA/TRAC simplifies the modeling of NC gas by treating the vapor phase as all NC gas or all steam based on the subcooling of the vapor phase. WCOBRA/TRAC also does not have capabilities to model stratified flows accurately in the loop components, which could also be leading to the observed behavior. To complicate matters, there is no applicable experimental data to establish a baseline for the expected system response for this post-LOCA scenario. Specifically, the effect that NC gas has on the system response following core inlet blockage and the transport and venting behavior during the GSI-191 large hot leg break scenario.

To better understand the NC gas effect, Westinghouse performed simulations in which the accumulator nitrogen gas was removed from the models. The accumulators were modeled as a FILL component so that the liquid injection could be modeled without the presence of nitrogen. Simulation results confirmed that if the intact loop seals plug, nitrogen gas in the downcomer

tends to suppress the downcomer liquid level and increase the core liquid inventory prior to sump switchover. Under this condition, the application of core inlet blockage results in a less severe debris-induced PCT. It has been determined that this effect does not significantly impact the Westinghouse upflow plant analysis because the intact loop seals do not plug and nitrogen gas can vent from the system. It has also been determined that the downflow t_{block} analysis is not adversely impacted because the NC gas effect diminishes as the transient extends longer into long-term core cooling. The downflow plant K_{split} and m_{split} analyses are also not adversely impacted because of the slower application of core inlet blockage in these cases does not result in a debris-induced heatup. Since it has been determined that not including accumulator nitrogen gas in the downflow K_{max} analysis results in a more severe debris-induced heatup, a reanalysis was performed to define a new value of K_{max} which meets the PCT acceptance criteria of 800°F. The Westinghouse downflow plant category K_{max} (Case 2B) analysis results documented in WCAP-17788, Volume 4 will be updated to reflect the reanalysis. WCAP-17788, Volume 1 will also be updated to reflect the revised K_{max} value and acceptable core inlet debris loadings for the Westinghouse downflow plant category. The reanalysis is described below.

The Westinghouse downflow plant category K_{max} reanalysis (Case 2B) applies a core inlet resistance of 4.75×10^5. The original K_{max} analysis applied a value of 6×10^5. The accumulators are modeled as FILL components and the UHSN resistance is increased to bound all plants as described in the response to RAI-4.2. The reanalysis results meet the WCAP-17788, Volume 4 acceptance criteria.

Application of Graded Evaluation Model Development and Assessment Process to the Westinghouse GSI-191 Hot Leg Break Analysis with Simulated Core Inlet Blockage

As discussed in the previous sections, a graded EMDAP process is appropriate for development and assessment of the GSI-191 Hot Leg Break Evaluation Model. In this section, the four elements of the EMDAP process are discussed for the Westinghouse GSI-191 Hot Leg Break Evaluation Model.

Element 1 – Establish Requirements for Evaluation Model Capability

Step 1: Specify Analysis Purpose, Transient Class, and Power Plant Class

The analysis purpose of the GSI-191 Hot Leg Break Evaluation Model (EM) is to evaluate the adequacy of reactor vessel alternate flow paths (AFPs) at maintaining long-term core cooling (LTCC) during sump recirculation and the postulated formation of a highly-resistive debris bed at the core inlet following a double-ended guillotine (DEG) hot leg break (HLB) loss-of-coolant accident (LOCA). This HLB scenario description is not applicable to Westinghouse 2-loop PWRs with upper plenum injection. Refer to Section 8 of WCAP-17788, Volume 1 for the Westinghouse 2-loop scenario description. The AFPs considered in the analysis are:

1. Barrel/Baffle (BB) channel for Westinghouse upflow-design plants
2. Upper head spray nozzles (UHSNs) for Westinghouse downflow-design plants

The starting point for development of the GSI-191 HLB EM is the Realistic Large-Break LOCA Evaluation Model Using the Automated Statistical Treatment of Uncertainty Method (ASTRUM), documented in WCAP-16009-P-A (Reference RAI-4.7-2). The analysis purpose of the ASTRUM EM is the evaluation of the short-term large break LOCA transient to demonstrate compliance with GDC 35 as required by 10 CFR 50.46 (b)(1),(b)(2), and (b)(3). The break type considered in the ASTRUM EM is either a DEG, or a split break, defined as a partial tear. A break in the cold leg piping between the reactor coolant pump and the reactor vessel inlet nozzle has been concluded to be the most limiting location for this analysis purpose.

The GSI-191 HLB scenario progression is described as follows:

- **Blowdown, Refill and Reflood** – The blowdown, refill and reflood periods of the scenario are characterized by complex thermal hydraulic phenomena that are considered in the ASTRUM EM. During the short-term LOCA transient, large breaks in the hot leg do not result in core flow reversal during blowdown. Consequently, there is sufficient flow to remove the core stored energy. All accumulators are functional, and no safety injection is spilled directly to containment. The refill and reflood periods are not realized as distinct processes, because the combined resistance to flow of the pump and steam generator to the break opposite the vessel side is much higher than the vessel side. Safety injection follows the path of least resistance and preferentially flows through the core to the broken hot leg. Because of the overall pressure gradient developed by the postulated break at the core outlet, processes such as counter current flow and emergency core cooling (ECC) bypass in the downcomer are not important in large HLB scenarios. During the reflood period, a larger driving head in the downcomer is maintained and reflood occurs almost immediately. As a result, short-term peak cladding temperature (PCT)

is lower in HLB scenarios.

- **Post-Reflood, Prior to Debris Accumulation** – Following reflood, the reactor coolant system (RCS) transitions to a quasi-steady state. The RCS pressure will remain close to containment pressure. The ECCS pumps coolant from the refueling water storage tank (RWST) and injects it into the cold legs. Coolant flows into the core through the downcomer, boils in the inner region of the core, and a two-phase mixture flows upwards into the upper plenum and out of the hot leg break. Any coolant injected into the cold legs in excess of boil-off will flow through the reactor vessel and out of the break as part of the two-phase mixture. Because the entire ECCS flow enters the core, heat removal begins to transition from a boiling heat transfer regime into forced single-phase convection regime. This period establishes the initial conditions for the debris accumulation periods.

- **Debris Accumulation, Partial Core Inlet Blockage** – The switchover to sump recirculation triggers the start of the debris accumulation periods. The containment sump coolant source can contain debris. Sump strainers are installed to capture debris and limit the quantity that enters the ECCS and transports to the reactor vessel. Debris sources are divided into three categories: (1) fibrous debris; (2) particulate debris; (3) chemical product debris. Fibrous and particulate debris are present in the sump pool at the time switchover occurs. Chemical product debris is delayed until later in the transient because it takes time for the chemical products to form.

  The partial core inlet debris accumulation period is characterized by the arrival of fibrous and particulate debris in the reactor vessel. It is postulated that the debris will initially accumulate at the core inlet. A uniform resistance across the entire core inlet is assumed in the GSI-191 HLB EM. The resistance is large enough such that core inlet flow is reduced but not completely stopped. The increased core inlet resistance leads to a transient RCS response. As the pressure drop across the core region increases, the downcomer liquid level will increase to balance the increased pressure loss due to postulated core inlet debris accumulation. As core inlet resistance continues to increase, the downcomer level will continue to increase. Eventually, the driving head in the downcomer becomes large enough to activate the AFP(s). Activation of the AFP(s) is defined as the time when ECCS flow entering the reactor vessel begins to bypass the core inlet and flow through the AFP(s). The BB channel is the first AFP to activate, followed by the UHSNs. After activation of the AFPs, ECCS coolant splits between the core inlet, AFP(s), intact loop steam generators, and the broken loop steam generator to the break. The flow resistance through each path determines the magnitude of the flow through each path.

  If the rate of debris accumulation during the partial core inlet blockage period is faster than the rate that the downcomer liquid level can increase, flow into the core can drop below boil-off. In this case, a debris-induced heatup is possible. If core inlet flow drops below boil-off, liquid inventory from the upper plenum will drain into the core. Once the upper plenum liquid inventory is depleted, the core will uncover and a heatup will occur. The heatup will subside as the downcomer driving head increases such that the combined flow through the core inlet and AFPs exceeds boil-off, allowing the core mixture level to recover.

- **Debris Accumulation, Complete Core Inlet Blockage** – As the transient progresses, chemical products form inside containment that can be transported through the ECCS into the reactor vessel. Collection of chemical products in an established fibrous debris bed at the core inlet can result in complete core inlet blockage in which flow through the core inlet stops completely. Following complete core inlet blockage, the AFPs are the only flow path for coolant from the ECCS to enter the core region and provide decay heat removal (before hot leg recirculation is initiated).

  The potential for a debris-induced heatup following the application of complete core inlet blockage depends on the partial core inlet blockage period. If the resistance applied at the core inlet during the partial core inlet blockage period is high enough to activate the AFP(s), then the potential for a debris-induced heatup following the application of complete core inlet blockage is diminished since there is a pre-established flow path to provide coolant to the core region. However, if the resistance applied during the partial core inlet blockage period is not high enough to activate the AFP prior to complete core inlet blockage, a debris-induced heatup is possible. In this case, flow through the core inlet ceases and there is a time period associated with filling the downcomer in which the driving head is not sufficient to activate the AFP. During this period, a short duration core uncovery and heatup is possible. As the downcomer driving head increases, flow through the AFP will increase until flow to the core region is again in excess of boil-off. The mixture level in the core will increase, and the heatup will subside.

The RCS response to complete core inlet blockage is illustrated in Figure RAI-4.7-2 through Figure RAI-4.7-7. The figures provide screenshots of simulation results showing the RCS void fraction from an upflow plant analysis that applies complete core inlet blockage 143 minutes post-LOCA. Partial core inlet blockage is not applied in this case so that the activation of the AFPs can be realized.

Figure RAI-4.7-2 shows the RCS void distribution at the time of the application of complete core inlet blockage. As the figure shows, the core is covered with a two-phase mixture and the mixture level extends into the upper plenum. The downcomer collapsed liquid level is just below the top of the active fuel, and the pump suction and crossover legs are partially filled with liquid. The hot leg piping, steam generators, and upper head remain highly voided.

Figure RAI-4.7-3 shows the RCS void distribution 1.5 minutes after the application of complete core inlet blockage. As the figure shows, the core mixture level has reduced below the top of the active fuel and the upper plenum liquid inventory is draining into the core. The downcomer liquid level has extended beyond the top of the active fuel, and the barrel/baffle channel is beginning to fill with liquid.

Figure RAI-4.7-4 shows the RCS void distribution 3.5 minutes after the application of complete core inlet blockage. As the figure shows, the downcomer liquid level has extended beyond the cold leg elevation and the pump suction and crossover legs are completely liquid solid. The steam generator outlet plenums are also starting to fill with liquid. The barrel/baffle channel is also nearly liquid solid and flow from the barrel/baffle channel outlet is beginning to recover the core mixture level.

Figure RAI-4.7-5 shows the RCS void distribution 5 minutes after the application of complete core inlet

blockage. As the figure shows, the core two-phase mixture level has recovered due to flow from the barrel/baffle channel. The downcomer liquid level continues to increase. As does the liquid level in the steam generators. The upper plenum liquid inventory has also recovered.

Figure RAI-4.7-6 shows the RCS void distribution 10 minutes after the application of complete core inlet blockage. As the figure shows, the downcomer liquid level has reached the upper head spray nozzle elevation. The steam generator liquid level has also continued to increase, and some liquid is spilling over the broken loop steam generator to the break.

Figure RAI-4.7-7 shows the RCS void distribution 75 minutes after the application of complete core inlet blockage. As the figure shows, liquid flooded the upper head to the guide tube elevation and the upper head spray nozzle AFP has been established. All the steam generators have established liquid levels that allow for some spillover. The core and upper plenum liquid inventory has increased consistent with the additional flow reaching the core and upper plenum regions via the upper head spray nozzle and intact hot legs.

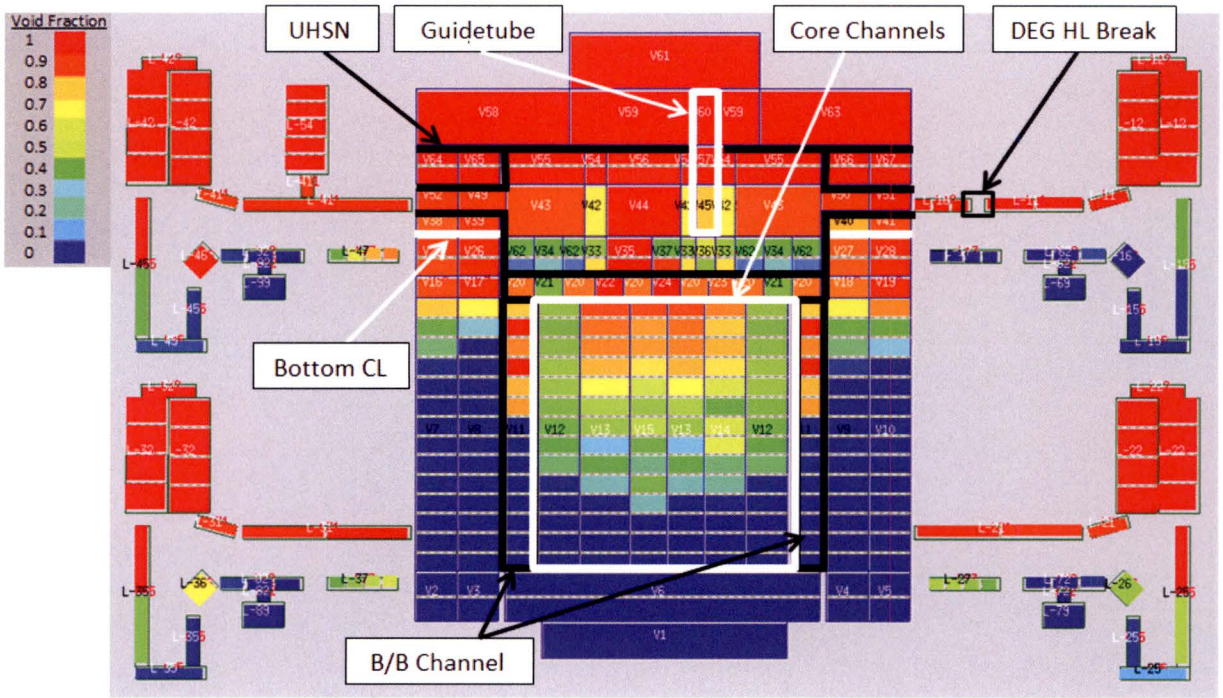

Figure RAI-4.7-2 RCS void distribution before the application of core inlet blockage

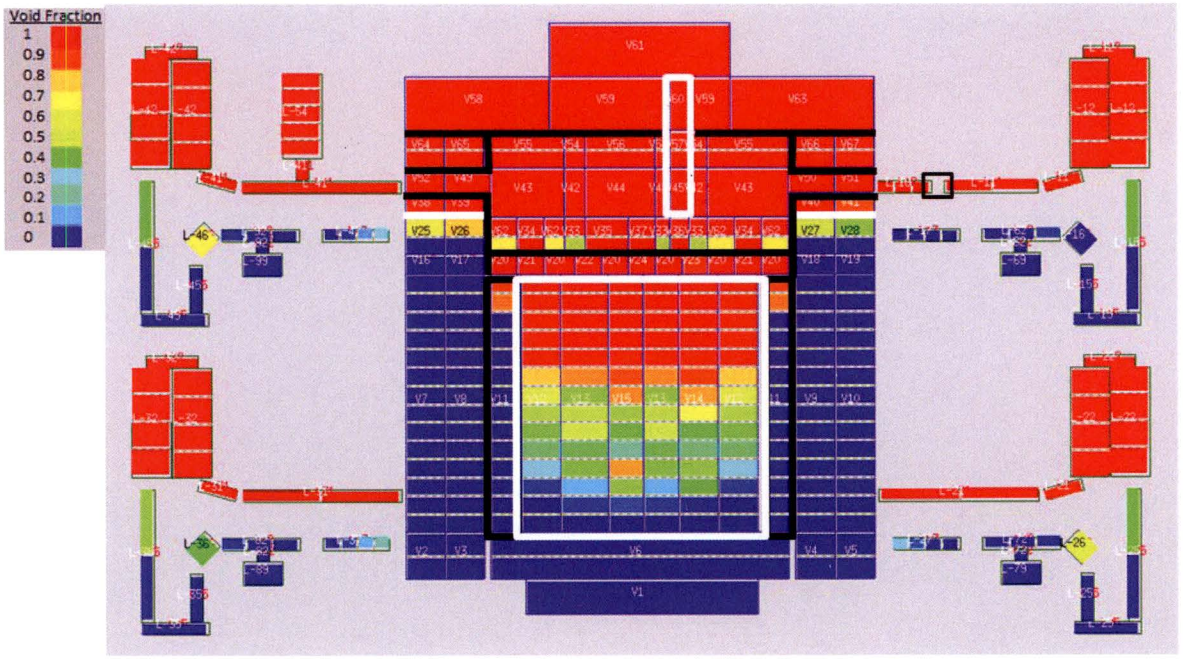

Figure RAI-4.7-3 RCS void distribution 1.5 minutes after the application of core inlet blockage

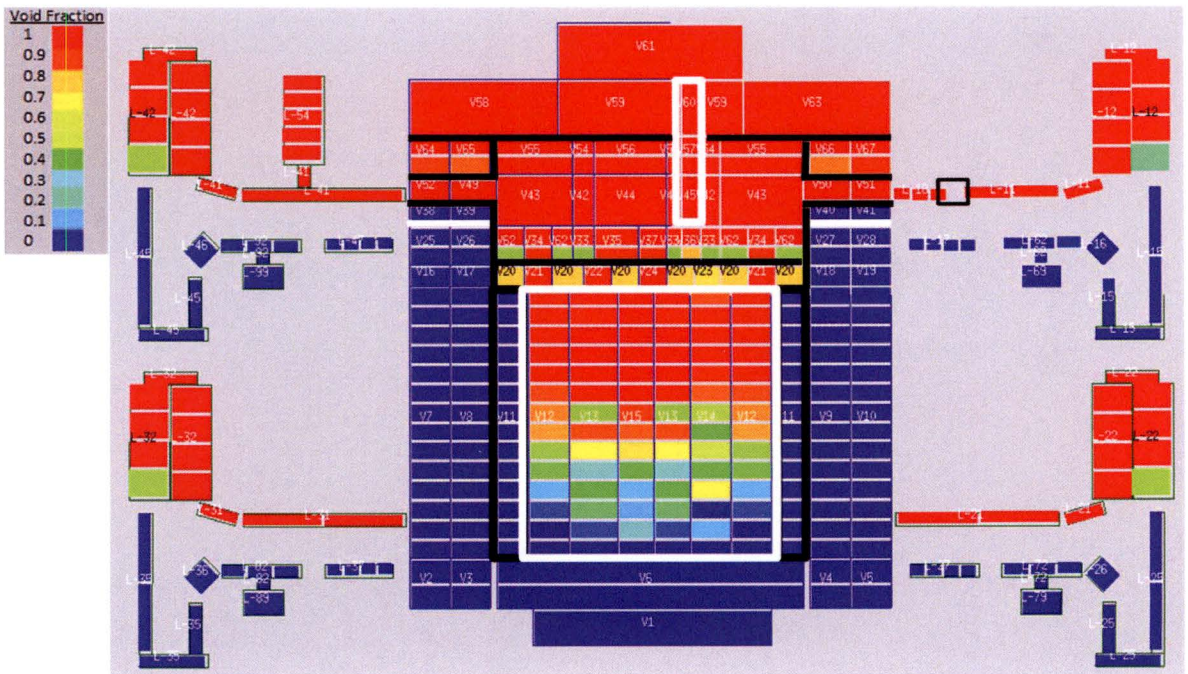

Figure RAI-4.7-4 RCS void distribution 3.5 minutes after the application of core inlet blockage

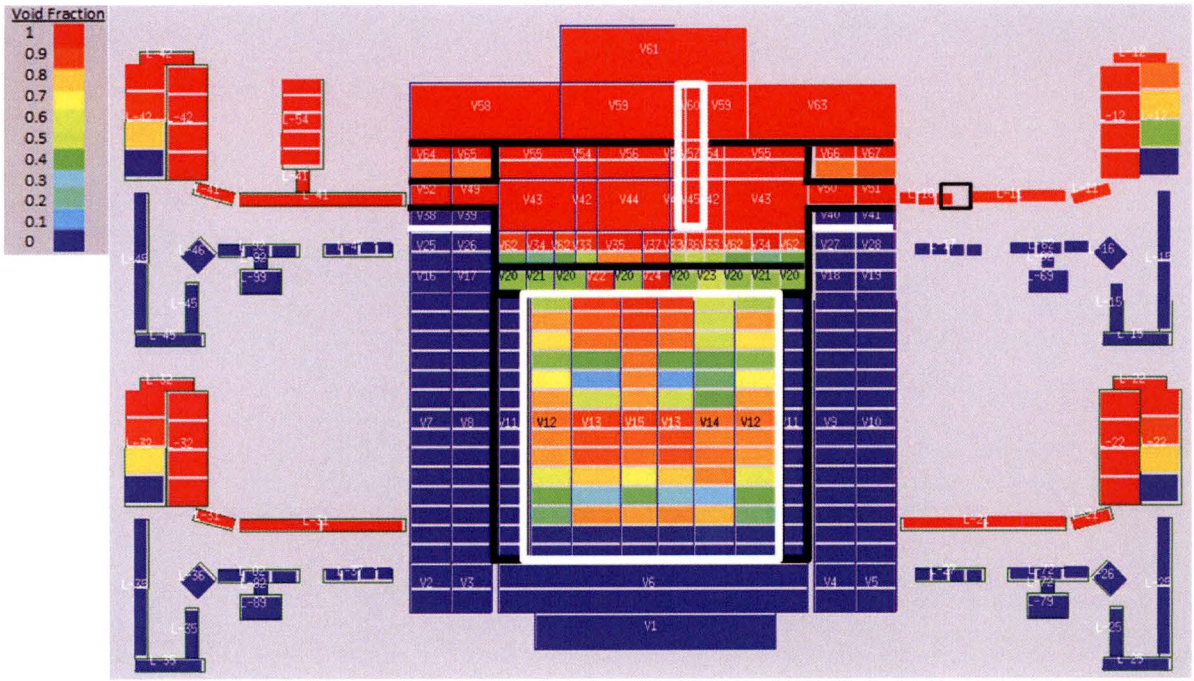

Figure RAI-4.7-5 RCS void distribution 5 minutes after the application of core inlet blockage

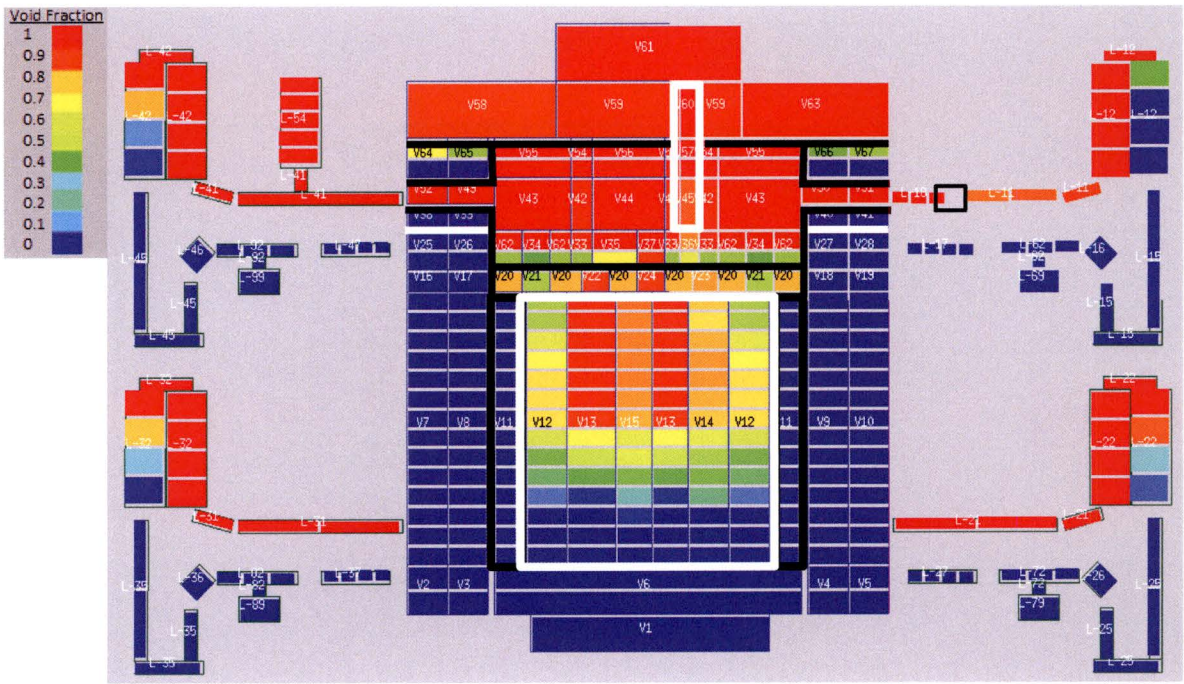

Figure RAI-4.7-6 RCS void distribution 10 minutes after the application of core inlet blockage

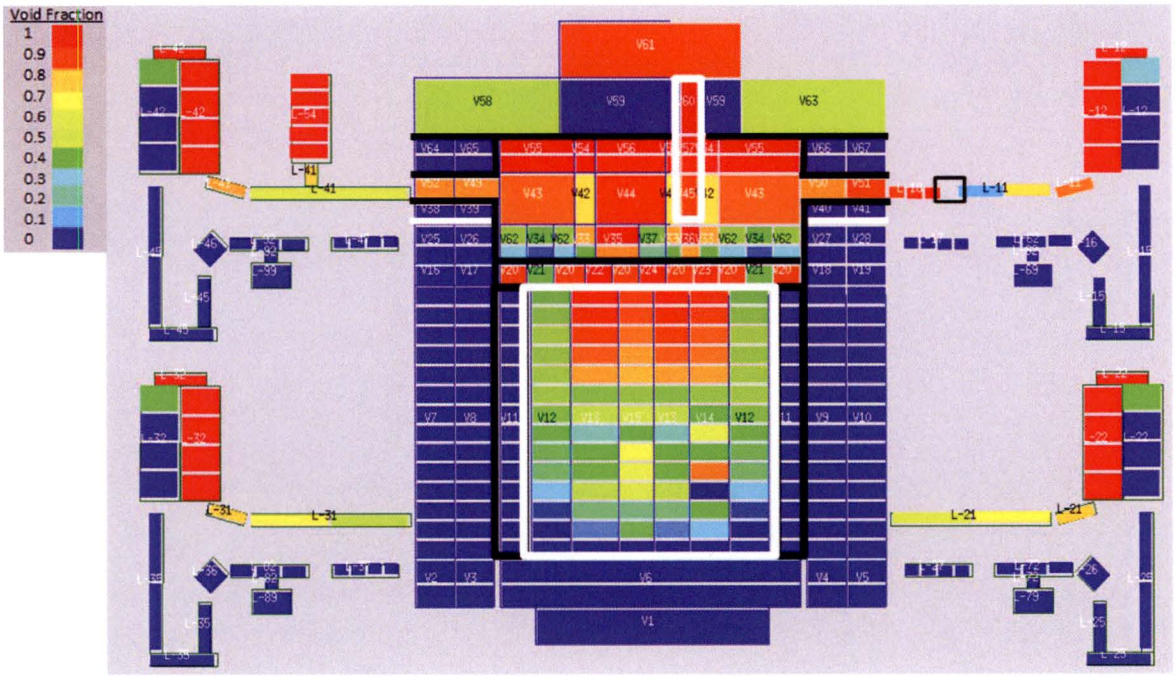

Figure RAI-4.7-7 RCS void distribution 75 minutes after the application of core inlet blockage

Four output parameters from the GSI-191 HLB EM are used in the overall WCAP-17788 in-vessel debris methodology. The simulations model the evolution of debris collection at the core inlet to determine the following four parameters:

1. The minimum time that complete core inlet blockage can occur (t_{block}).

2. The maximum resistance at the core inlet that can occur prior to reaching complete core inlet blockage (K_{max}).

3. The resistance at the core inlet that begins to divert flow into the AFP (K_{split}).

4. The flow split between the core inlet and the AFP after K_{split} (m_{split}).

Evaluations are performed to determine the above parameters and show that the cladding temperature remains below 800°F and that excessive boric acid concentration does not occur in the core. The analysis is performed separately for Westinghouse upflow-design plants and Westinghouse downflow-design plants. The analyses use single plant models that are representative of all plants contained in each of the two plant categories.

The analyses consider the effect of the limiting single failure on ECCS performance. The minimum safety injection (SI) flow rate and maximum SI delay times are used based on plant technical specification limits from the base plant models selected for each plant category. The base plant models and the

changes made for the GSI-191 HLB EM are identified and described in the response to RAI-4.29. The limiting single failure takes into account the effect of containment pressure. Failure of an entire safety train would result in the loss of one or several containment spray and fan cooling units, reducing containment cooling, and increasing containment pressure, which will reduce cladding temperatures during a debris-induced secondary heatup by increasing the reactor vessel liquid inventory. The inputs to the containment pressure are skewed in order to obtain a conservative (low) pressure transient such that cladding temperatures during any calculated debris-induced secondary heatup are maximized.

The ECCS performance assumptions applied during the recirculation phase of the accident are disconnected from those applied during the injection phase of the accident transient. In the simulations, an early sump switchover time is applied that is representative of two trains of safety injection during the refueling water storage tank (RWST) injection phase (i.e., no single failure). An early sump switchover time is more limiting for GSI-191 scenarios since the decay heat is higher and RCS liquid inventory is lower. A range of ECCS recirculation flows considering both single- and two-trains of ECCS in operation are considered in the EM.

As these are generic analyses intended to represent a number of Westinghouse plants, plant-specific considerations are necessary to address GDC 35 and should be addressed by each utility when implementing the WCAP-17788 in-vessel debris methodology as part of their GL 2004-02 supplemental responses. Each plant will have to justify applicability of the methodology as part of their plant-specific submittal. Each plant will need to determine their limiting GSI-191 scenario relative to debris accumulation in the reactor vessel, considering appropriate single-failure assumptions. Once the limiting GSI-191 in-vessel debris accumulation scenario is defined, a plant will need to demonstrate that it falls within the bounds of the WCAP-17788 methodology. The response to RAI-4.5 provides details regarding the confirmation checks that each utility must complete to justify applicability of the GSI-191 HLB EM.

Step 2: Specify Figures of Merit

Two Figures of Merit are considered in the GSI-191 HLB EM:

1. Decay Heat Removal (DHR) - DHR requires that sufficient coolant be supplied to the core such that the core temperature is maintained at an acceptably low level. For previous GSI-191 evaluations, the maximum allowable PCT during a debris-induced secondary heatup is 800°F. This conservative limit will be retained.

2. Boric Acid Precipitation Control (BAPC) - BAPC requires that boron concentrations in the reactor vessel remain below the solubility limit. For the GSI-191 HLB scenario with core inlet blockage, BAPC requires demonstration of adequate break quality to flush boron from the reactor vessel and demonstration of adequate mixing within the reactor vessel to ensure effectiveness of the flushing flow.

These two Figures of Merit are identical to the two acceptance criteria defined in Section 2.5 of WCAP-17788, Volume 4.

Step 3: Identify Systems, Components, Phases, Geometries, Fields, and Processes that Must be Modeled

This step identifies the GSI-191 HLB EM characteristics by performing hierarchical decomposition of the reactor coolant system. In order from top to bottom, the following ingredients at each hierarchical level characterize the GSI-191 HLB EM:

System: Reactor Coolant System

Components: Reactor Vessel, Steam Generators, Reactor Coolant Pumps, Break, Loop Piping

Constituents/Phases: Water/Liquid and Vapor, Structures/Solid

Geometries: Heated Rod Bundle/Cylindrical Fuel Rod, Unheated Structures, Single- and Two-Phase Flow

Fields: Continuous Liquid, Dispersed Liquid, Continuous Vapor

Processes: The key processes for the GSI-191 HLB scenario are provided in Step 4 of the EMDAP process.

Step 4: Identify and Rank Phenomena and Processes

The phenomena identification and ranking table (PIRT) process has been completed for the GSI-191 HLB scenario. The PIRT was developed following the approach outlined in Boyack (Reference RAI-4.7-3). First, a list of plausible phenomena was prepared using the existing LOCA PIRTs for short-term LOCA analysis as the starting point. Next, new phenomena associated with the GSI-191 HLB scenario were added to the list. The phenomena were then ranked for importance through the various periods identified for the GSI-191 HLB scenario. The GSI-191 HLB PIRT does not include all processes and phenomena considered in the short-term LOCA PIRTs since many of the short-term LOCA processes and phenomena are of low importance or not-applicable to the GSI-191 HLB scenario. In general, processes and phenomena determined to be of high importance, relevant to the EM, or discussed in the WCAP-17788, Volume 4 RAI response are included.

Relative rankings in the GSI-191 HLB PIRT were assigned the following criteria:

H = The process is considered to have high importance. Accurate modeling of the process during the particular period is considered to be crucial to the correct prediction of the transient.

M = The process is considered to have medium importance. The process must be modeled with sufficient detail to obtain accuracy in the simulation; however, the process is expected to have less impact on the overall results than those ranked high.

L = The process is not considered to be very important during the transient. The phenomena needs to be modeled in the code (or accounted for in the EM), but inaccuracies in modeling these processes are not considered likely to have a significant impact on the overall transient results.

N/A = The process is considered insignificant, or does not occur at all. This process need not be modeled or be taken into consideration, as it has an insignificant impact on the results.

The PIRT process considers the period after reflood but prior to debris accumulation at the core inlet, the period when partial core inlet blockage exists, and the period when complete core inlet blockage exists. Partial core inlet blockage is characterized by blockages in which flow through the core inlet can still exist, and is related to the K_{max}, K_{split}, and m_{split} analyses. Complete core inlet blockage is characterized by blockages in which there is no flow through the core inlet, and is related to the t_{block} analyses. A description of the scenario progression, and the important periods is provided in Step 1 of the EMDAP above. The Figures of Merit considered in the PIRT are identified in Step 2. The blowdown, refill and reflood periods are addressed by the previous PIRT developed for short-term LOCA analysis in WCAP-16009-P-A.

Process / Phenomena	Ranking		
	Prior to Debris Accumulation	**Partial Core Inlet Blockage**	**Complete Core Inlet Blockage**
Fuel Rod			
Decay Heat – The fuel rod heat generation rate during the GSI-191 HLB scenario is dominated by the decay of fission products. Decay heat is the main driver of a debris-induced heatup and is assigned a ranking of high (H) through all periods.	H	H	H
Initial Stored Energy – The stored energy is the total energy of the fuel rods, and its spatial distribution, at the initiation of the LOCA transient. The stored energy is most important during the early periods of a large break LOCA transient, since the resulting pellet temperature distribution undergoes a readjustment that determines the heatup of the clad after critical heat flux (CHF) is reached. For the GSI-191 HLB scenario, the fuel rod stored energy is assigned a low (L) ranking for the entire scenario since the stored energy has been removed during the short-term LOCA phase.	L	L	L
Clad Oxidation – At high temperatures the zirconium base metal in the clad undergoes an exothermic reaction with steam. [ ]^{a,c} For the GSI-191 HLB scenario, clad oxidation is assigned a low (L) ranking for the entire scenario since clad temperatures do not reach the temperature necessary for the clad to react with steam. During the short-term LOCA phase, clad oxidation is also assigned a ranking of low (L) since high clad temperatures are not reached during large HLB scenarios.	L	L	L
Core			
Core Inlet Resistance due to Debris Accumulation – The application of core inlet resistance due to the postulated accumulation of debris increases the pressure drop across the core and governs the amount of flow through the core inlet for a given downcomer driving head. The time that core inlet resistance is applied is important since the heat generation rate is decaying as the transient progresses. Switchover to sump recirculation is the earliest time that debris can arrive in the reactor vessel. The rate of debris accumulation is also important. As core inlet resistance increases the pressure drop across the core, liquid level in the downcomer will increase to balance the pressure difference between the core and the downcomer. A fast debris accumulation rate can result in a debris-induced core uncovery and heatup because there is a	N/A	H	H

Process / Phenomena	Ranking		
	Prior to Debris Accumulation	Partial Core Inlet Blockage	Complete Core Inlet Blockage
delay associated with filling the downcomer to balance the pressure increase across the core. The magnitude of core inlet resistance is also an important factor. Partial core inlet resistance does not completely block the core inlet. At relatively low core inlet resistances, there is enough driving head to allow flow in excess of the steaming rate through the core inlet. As core inlet resistance is increased, a point can be reached where flow through the core inlet reduces below boil-off. Under this condition, flow through the AFPs is required to compensate the reduction in flow through the core inlet such that decay heat removal is maintained. As core inlet resistance continues to increase, the core inlet becomes completely blocked and flow is eliminated completely. Under this condition, flow through the AFPs in excess of the steaming rate is required to maintain decay heat removal. A ranking of not applicable (N/A) is assigned to the prior to debris accumulation period since debris is not entering the reactor vessel. The process is assigned a ranking of high (H) during the partial and complete core inlet blockage periods since the accumulation of debris can result in a debris-induced secondary heatup.			
Heat Transfer to a Covered Core – The heat transfer regimes of saturated and subcooled nucleate boiling, in addition to single-phase convection to liquid, encompass heat transfer to a covered core. Heat transfer in the covered core region is high, and the rate of vapor generation is equal to that generated by decay heat. No temperature excursion is expected while saturated and subcooled nucleate boiling is sustained. This process is assigned a low (L) ranking throughout the transient. The reason is that given the high heat transfer coefficients, an accurate prediction is not required.	L	L	L
Heat Transfer to an Uncovered Core – Heat transfer to an uncovered core is governed by convection to single-phase vapor. Post-CHF heat transfer regimes like inverted annular and dispersed flow film boiling are not applicable because clad temperatures remain below the minimum film boiling temperature. Prior to debris accumulation, the process is assigned a ranking of not applicable (N/A) since the core remains covered during this period. During the core inlet blockage phases, the process is assigned a ranking of high (H) since debris accumulation has the potential to uncover the core during these periods.	N/A	H	H

Process / Phenomena	Ranking		
	Prior to Debris Accumulation	**Partial Core Inlet Blockage**	**Complete Core Inlet Blockage**
Radiation Heat Transfer – Radiation heat transfer is the surface-to-surface thermal radiation heat transfer in the core. This heat transfer process is assigned a ranking a low (L) for the GSI-191 scenario since the radiative heat flux is low when the fuel temperatures are low.	L	L	L
Void Generation / Void Distribution – The void generation and distribution refer to the generation and distribution of steam and their effect on the mixture level. For the GSI-191 HLB scenario, the mixture level largely determines the potential for, and the severity of a debris-induced secondary heatup. The void generation and distribution also influence circulation patterns in the core. These processes are assigned a ranking of medium (M) prior to debris accumulation because liquid flow into the core is sufficient to maintain a mixture level above the active fuel. The processes are assigned a ranking of high (H) during the core inlet blockage periods because the mixture level reduces during the application of core inlet blockage making the mixture level prediction more important.	M	H	H
Entrainment/De-Entrainment – Entrainment/de-entrainment describes the axial entrainment of liquid at the two-phase mixture level and de-entrainment at elevations above the two-phase mixture level. For the GSI-191 HLB scenario, debris accumulation at the core inlet can reduce the two-phase mixture level below the top of the active fuel, leading to a debris-induced heatup. Entrainment from the two-phase mixture level and de-entrainment above the two-phase mixture level provides a means of cooling during the debris-induced heatup. Prior to the accumulation of debris, the process is assigned a ranking of low (L) since the two-phase mixture level remains above the top of the active fuel. The process is assigned a medium (M) ranking during the partial core inlet blockage period and a ranking of low (L) during the complete core inlet blockage period. The higher ranking during the partial core inlet blockage period is to identify that entrainment rates will be higher when steaming rates are higher. Entrainment rates diminish due to the decreased steaming rates, which is why the ranking is lower than entrainment and de-entrainment processes during the short-term.	L	M	L

Process / Phenomena	Ranking		
	Prior to Debris Accumulation	**Partial Core Inlet Blockage**	**Complete Core Inlet Blockage**
Three-Dimensional Flow/Natural Circulation – The importance of distinguishing between several core channels of different geometries is recognized in the Westinghouse methodology. The hardware in the reactor upper plenum can affect the amount of flow the fuel assemblies receive following activation of the AFPs and flow delivered to the core from the upper plenum and upper head. These hardware effects have to be modeled to accurately predict the flow split for the different assemblies, because there will be different flows entering the top of the channels. The presence of a low-power zone on the edge of the core provides an easier flow path from the upper plenum to the lower plenum. As a result, liquid in the upper plenum can more easily bypass the center regions of the core and drain down the low-power region. This effect must be modeled, or otherwise the flow from the upper plenum into the center region of the core may be overestimated. The process is assigned a ranking of low (L) prior to debris accumulation and during the partial core inlet blockage periods. A ranking of medium (M) is assigned during complete core inlet blockage. The higher ranking assigned during complete core inlet blockage is to recognize that flow through the AFP is the only source of coolant for decay heat removal. Therefore, modeling of the flow split from the upper plenum to the top of the core is more important during this period.	L	L	M
Flow Resistance – Cross-flows between parallel channels can be a contributing factor affecting code prediction of local fuel conditions, including PCT, due to their impact on fluid velocities, void fraction, and two-phase flow patterns. In addition, potential effects on the axial flows due to possible localized accumulation of debris at the locations of spacer grids in regions above the core inlet can increase flow resistance. This process is assigned a ranking of low (L) for all periods, because the open lattice designs of PWR fuel assemblies promote cross-flow between parallel channels.	L	L	L

Process / Phenomena	Ranking		
	Prior to Debris Accumulation	Partial Core Inlet Blockage	Complete Core Inlet Blockage
Upper Plenum			
Draining/Fallback – Liquid draining from the upper plenum region, or falling back during core uncovery, can contribute to core cooling and delay a debris-induced heatup. These processes are assigned a ranking of low (L) prior to debris accumulation, as flow through the core remains upward, and large void fractions in the core are not expected. A high (H) ranking is assigned to these processes during the core inlet blockage periods as a significant amount of liquid can drain into the core region if the application of core inlet resistance leads to a loss of liquid inventory in the core.	L	H	H
Counter-current Flow Limitation – The amount of liquid that can drain from the upper plenum may be limited by counter-current flow limitation (CCFL) phenomena, wherein the steam upflow is sufficient to limit or prevent draining. This process is assigned a ranking of low (L) for all periods since the steam velocity in the upper plenum is expected to be less than the critical steam velocity required for the onset of CCFL.	L	L	L
Entrainment/De-Entrainment – Depending on the steam velocities in the upper plenum, droplets can be entrained into the hot legs, and potentially out of the break. De-entrainment on the upper plenum structures will result in the build-up of a pool, and steam flow from the core can also re-entrain liquid from the pool. The processes have a low (L) ranking prior to core inlet blockage, because the two-phase level is generally high enough such that most of the liquid is transported to the hot leg break as a low void fraction mixture through natural or forced circulation, rather than by entrainment in the steam flow. During the core inlet blockage periods, it is possible that the two-phase mixture level drops below the hot leg elevations, and entrainment is the only mechanism that transports liquid to the hot leg break. After the two-phase mixture level recovers, the processes become less important. The ranking for the partial core inlet blockage period is assigned a ranking of medium (M), and the ranking during the complete core inlet blockage period is low (L). The higher ranking during the partial core inlet blockage phase is to identify the fact that the steaming rate is higher, which results in a higher potential for entrainment.	L	M	L

Process / Phenomena	Ranking		
	Prior to Debris Accumulation	**Partial Core Inlet Blockage**	**Complete Core Inlet Blockage**
Mixture Level/Phase Separation – this phenomenon is related to the upper plenum liquid inventory throughout the transient, as it affects draining and fallback to the core, and liquid carryover to the break. This phenomenon is assigned a ranking of high (H) for all periods, since the upper plenum mass inventory is substantial enough to produce a significant mixture region, which leads to the amount of liquid carryover to the break.	H	H	H
Hot Assembly Location – The specific geometries of the hardware that exists in the upper plenum will result in different flows into the assemblies following the application of core inlet blockage when flow through the AFPs to the upper plenum is present. The process is assigned a ranking of low (L) prior to debris accumulation because the two-phase mixture level is above the top of the active core and flow redistribution effects due to different resistances at the upper core plate will have little effect on cooling at the PCT location. The process is assigned a ranking of medium (M) during the core inlet blockage periods because top-down cooling can affect the duration and magnitude of a debris induced heatup in which the PCT occurs in the hot assembly.	L	M	M
Upper Head			
Draining/Filling/Mixture Level – The liquid inventory in the upper head initially drains through the guide tubes, until depressurization causes flashing in this region. The two-phase mixture will continue to drain through the guide tubes and UHSNs until the upper head is mostly voided. The upper head will remain voided until debris blockage at the core inlet causes the downcomer to fill. Once the downcomer has filled to the UHSN elevation, liquid will flow into the upper head, and will eventually drain into the guide tubes once the upper head mixture level reaches the guide tube elevation. This is the primary AFP for the Westinghouse downflow plant category. The processes are ranked low (L) prior to debris accumulation since the upper head remains voided prior to the application of core inlet blockage. The processes is also ranked low (L) during the partial core inlet blockage period since flow in excess of the steaming rate can still flow through the core inlet. The process is ranked medium (M) during the complete core inlet blockage period since this is the primary AFP for the downflow plant model.	L	L	M

Process / Phenomena	Ranking		
	Prior to Debris Accumulation	Partial Core Inlet Blockage	Complete Core Inlet Blockage
Hot Leg			
Entrainment/De-Entrainment – Steam flows in the broken loop hot leg are high enough to generate entrained liquid. The processes have a low (L) ranking for all periods, because the two-phase level is generally above the bottom of the hot legs, and most of the liquid is transported through the broken loop hot leg as a low void fraction mixture through natural or forced circulation, rather than by entrainment in the steam flow.	L	L	L
Flow Direction – Flow direction refers to the direction of liquid flow in the intact hot legs. When the mixture level is above the hot leg elevation, liquid can flow into the intact hot legs. Core inlet blockage can cause the intact steam generators to spillover, and liquid flows into the upper plenum through the intact hot legs. The process is assigned a ranking of low (L) for all periods before complete core inlet blockage and a ranking of medium (M) for the complete core blockage period because it takes high levels of core inlet resistance for ECCS flow to spillover the intact steam generators.	L	L	M
Steam Generator			
Primary Side Heat Transfer/Boiling – For large breaks, the steam generator (SG) secondary side is a heat source (i.e., secondary-to-primary heat transfer), not a heat sink, due to the rapid depressurization of the primary side. Without core inlet blockage, this process has a low (L) ranking since the SGs remain highly voided and there is little heat transfer. Core inlet blockage causes ECCS to fill the SGs. If boiling occurs it affects the amount of liquid carryover into the hot legs. A ranking of low (L) is assigned to the partial blockage period and the complete blockage period is assigned a ranking of medium (M) to identify the increased importance following complete core inlet blockage. This process is important for the downflow plant type because the high upper head spray nozzle resistance promotes ECCS flow filling into the SGs.	L	L	M
Secondary Side Cooldown Behavior – For large breaks, the SG secondary side cooldown is limited by the relief valve capacity, and the steam generators will remain a heat source throughout the transient. As the secondary side cooldown has some effect on the primary side heat transfer, the process is assigned a ranking of low (L) prior to debris accumulation and during	L	L	M

Process / Phenomena	Ranking		
	Prior to Debris Accumulation	Partial Core Inlet Blockage	Complete Core Inlet Blockage
partial core inlet blockage. The process is assigned a medium (M) during the complete core inlet blockage period for its effect on primary side heat transfer.			
Flow Regime/Liquid Carryover – This process is important for the downflow plant type because the high upper head spray nozzle resistance promotes ECCS flow filling into the SGs. Liquid carryover through the intact SGs provides liquid to the upper plenum following complete core inlet blockage. The process is assigned a ranking of low prior to core inlet blockage and during partial core inlet blockage. The process is assigned a ranking of medium (M) during complete core inlet blockage because of its importance for the downflow plant category.	L	L	M
Multi-Tube Behavior – The SG U-tubes are different lengths. Depending on the mixture level, some tubes may spill liquid to the hot side of the SG tubes, while higher tubes may remain voided. Significant SG spillover is predicted during complete core inlet blockage; therefore, it is assigned a ranking of medium (M) for the complete core blockage period, and low (L) for the other periods.	L	L	M
Pump/Pump Suction Piping/Loop Seal			
Flow Split/Resistance – This process is important because following core inlet blockage, ECCS injected into the cold legs will split between the vessel and the cold leg loop piping. This flow split determines the quantity of flow to the vessel versus through the broken/intact loops. The process is ranked low (L) prior to debris accumulation because the path of least resistance is through the vessel to the break. The process is ranked medium (M) during the core inlet blockage periods because the simulation of core inlet resistance will result in a flow split.	L	M	M
Loop Seal Plugging/Filling – Loop seal plugging is relevant to the GSI-191 HLB scenario during the short-term phase because the loop seals provide a vent path for nitrogen gas injected from the accumulators to reach the break. If the loop seals plug before nitrogen gas is vented, the nitrogen effectively becomes trapped in the cold leg downcomer region. This can affect the reactor vessel liquid inventory. The timing and rate of the loop piping to fill with liquid also influences how quickly the downcomer fills past the cold leg elevation following the application of core inlet blockage. These processes are assigned a ranking of medium (M) during the Prior to Debris Accumulation and Partial Core Inlet Blockage Periods, and a	M	M	L

Process / Phenomena	Ranking		
	Prior to Debris Accumulation	Partial Core Inlet Blockage	Complete Core Inlet Blockage
ranking of low (L) during the Complete Core Inlet Blockage Period because the majority of nitrogen gas has vented from the system and the loop piping has filled with liquid by this point in time.			
Cold Leg/Safety Injection			
Interfacial Heat Transfer (Condensation) – This is condensation of steam in the cold leg, and is of high importance during the refill periods of large cold leg break scenarios as the ECCS liquid is no longer bypassed in the refill period. For large hot leg break scenarios, the condensation process is of less importance because there is less steam flow in the cold legs because of the hot side break location. This process also diminishes as the transient progresses because the accumulators end their injection and the lower ECCS flows continue. For these reasons, this process is assigned a ranking of low (L) in all periods.	L	L	L
Non-condensable Gas Effects – In the cold leg, this process refers to the effect that nitrogen has on condensation in the cold leg. The rankings for this effect generally follow those assigned for condensation, and are ranked low (L) for all periods.	L	L	L
Downcomer			
Condensation – Under large hot leg break conditions, condensation during the short-term LOCA is less important because ECC bypass and downcomer penetration phenomena are less relevant. The condensation process in the downcomer also diminishes following the application of core inlet because the downcomer becomes liquid solid. For these reasons, this process is ranked low (L) during all periods.	L	L	L
Non-condensable Gas Effects - Under large hot leg break conditions, nitrogen gas from the accumulators cannot as readily be evacuated from the system as they would during a large cold leg break LOCA. If the loop seals plug nitrogen gas can accumulate in the downcomer, and affect the reactor vessel liquid inventory prior to and after partial core inlet blockage when the downcomer is filling. For this reason, a ranking of medium (M) is applied prior to and during partial core inlet blockage. The process is assigned a ranking of low (L) during complete core inlet because nitrogen gas has been vented from the downcomer by this time.	M	M	L

Process / Phenomena	Ranking		
	Prior to Debris Accumulation	**Partial Core Inlet Blockage**	**Complete Core Inlet Blockage**
Reactor Vessel Internals/Vessel Wall Stored Energy – This is the effect of the heat release to the fluid from the downcomer metal structures. For large cold leg break LOCA, the important hot wall effects occur only during the reflood phase when the flows through the downcomer are low and the injection water is hotter due to condensing steam and has a greater opportunity to boil. Under large hot leg break conditions, flows through the downcomer are greater and condensation of steam is not as great, thus reducing the potential to boil. The boiling effect will reduce the effective downcomer driving head, but following the application of core blockage, the downcomer will become liquid solid. The process is assigned a ranking of medium (M) prior to debris accumulation to acknowledge the potential to boil and reduce driving head. The process is assigned a ranking of low (L) during the debris accumulation periods.	M	L	L
Mixture Level/Void Fraction – This refers to the two-phase mixture level in the downcomer. Prior to debris accumulation, boiling in the downcomer can reduce the mixture level in the downcomer. Following debris accumulation at the core inlet, the downcomer mixture level establishes the driving force for core inlet and barrel/baffle flow in the Westinghouse upflow plant model. In the downflow plant model, the downcomer level determines when flow begins to enter the upper head spray nozzles. For these reasons, the downcomer mixture level is assigned a ranking of medium (M) in all phases.	M	M	M
Downcomer Boiling – Downcomer boiling occurs when stored energy from the reactor vessel metal mass is released to the liquid in the downcomer. Most of the metal mass is released during the short-term phase of the LOCA, and the process is assigned a ranking of low (L) during all periods.	L	L	L
Break			
Critical Flow – Critical flow is no longer present during the period of interest for the GSI-191 scenario.	N/A	N/A	N/A
Containment Pressure - The containment pressure establishes the boundary condition for the break and influences the amount of break flow during the GSI-191 scenario. The containment pressure is assigned a ranking of medium (M) during all periods.	M	M	M

Process / Phenomena	Ranking		
	Prior to Debris Accumulation	**Partial Core Inlet Blockage**	**Complete Core Inlet Blockage**
AFP (BB/UHSNs)			
Flow Resistance – The AFP resistance affects the flow through the AFP following core inlet blockage and determines the flow split between the core and the AFP. The process is ranked low (L) prior to core inlet blockage because flow through the AFP is not required to replace boil-off. The process is assigned a ranking of medium (M) during partial core inlet blockage because core inlet flow remains in excess of boil-off. The process is assigned a ranking of high (H) during the complete core inlet blockage period to identify the increased importance of AFP resistance during this period.	L	M	H

Summary of High Ranked Phenomena

The list of dominant processes and phenomena identified by the PIRT process for the GSI-191 HLB scenario is provided in this section. Important phenomena identified for the blowdown, refill, and reflood periods of the LOCA transient are discussed as well. Although the GSI-191 EM was used to simulate the entire event, the blowdown, refill, and reflood periods were simulated only inasmuch to provide the initial and boundary conditions for the long-term core cooling phases. In other words, the GSI-191 EM was not as interested in accurately calculating PCT during the short-term, and the focus was on creating an appropriate starting point for the long-term simulation.

Blowdown/Refill/Reflood Periods

- Break flow
- Initial stored energy/fuel rod
- Core heat transfer
- Entrainment

Bypassing of ECC is not included as a dominant phenomenon since the GSI-191 EM is focused on a large hot leg break LOCA. Steam binding is also not important during large hot leg break LOCAs because there is minimal steam flow through the steam generators. Cold leg/downcomer condensation and non-condensable gas/accumulator nitrogen are also not identified as dominant phenomena during hot leg break LOCAs because the steam flow in these regions is not sufficient to induce significant condensation. Break path resistance is also less important for hot leg break scenarios since the path from the reactor vessel to the break is shorter and less complex.

Prior to Debris Accumulation Period

- Decay Heat
- Core Void Generation/Distribution (Mixture Level)
- Upper Plenum Mixture Level

Partial Core Inlet Blockage Period

- Decay Heat
- Core Inlet Resistance due to Debris
- Core Void Generation/Distribution (Mixture Level)
- Heat Transfer to Single-Phase Vapor
- Upper Plenum Draining and Mixture Level

Complete Core Inlet Blockage Period

- Decay Heat
- Core Inlet Resistance due to Debris
- Core Void Generation/Distribution (Mixture Level)
- Heat Transfer to Single-Phase Vapor
- Upper Plenum Draining and Mixture Level
- Alternate Flow Path Resistance

Element 2 – Develop Assessment Base

Step 5: Specify Objectives for Assessment Base

Develop an assessment base that considers the highly ranked phenomena identified by the PIRT. The majority of the assessment base comes from the ASTRUM EM because there is little experimental data relevant to the GSI-191 HLB scenario. Several separate effect tests (SETs) have been added to the ASTRUM assessment base for assessing the GSI-191 HLB EM. The new SETs include: G-1 and G-2 low pressure boil-off tests and the rod bundle heat transfer (RBHT) facility single-phase vapor heat transfer tests.

The objectives of the assessment base are consistent with the ASTRUM EM:

- The assessment base should include separate effects experiments to assess empirical correlations and other closure models.
- The assessment base should include integral system tests to assess system interactions and global code capability.
- Simple Test Problems to illustrate fundamental calculational device capability and comparison to hand calculations.

Step 6: Perform Scaling Analysis and Identify Similarity Criteria

No new scaling analyses or similarity criteria are developed for the GSI-191 EM. The ASTRUM EM scaling basis applies to the GSI-191 HLB EM:

- Full-length, power-to-volume scaling basis applied for most LOCA experiments. This scaling rationale captures the majority of the LBLOCA phenomena.
- Multi-dimensional downcomer phenomena and upper plenum entrainment/de-entrainment behavior cannot be well-represented by full-height, power-to-volume scaled experiments.

Step 7: Identify Existing Data and/or Perform Integral Effects Tests (IETs) and Separate Effects Tests (SETs) To Complete the Database

The following list of existing experiments applies to the dominant phenomena identified for the GSI-191 HLB EM. The ASTRUM EM assessment base includes many more experiments, as described in WCAP-16009-P-A. Only experiments related to the dominant phenomena identified for the GSI-191 HLB EM are summarized in this step. Extrapolating the use of the existing assessment base into the long-term core cooling phase of the LOCA transient is discussed in Element 4.

SETs	Test Feature(s) / Process(s)
G-2	Forced Reflood, Multiple Power Shapes, Low-Pressure, Rob Bundle Geometries / Core Heat Transfer, Core Entrainment
FLECHT LFR	
FLECHT Skewed	
FLECHT SEASET	
FEBA	
NRU	Forced Reflood, Low-pressure, Skewed Power Shape, Nuclear Rods, Rod Bundle / Core Heat Transfer, Fuel Rod Decay Heat, Entrainment
Achilles	Gravity Reflood w/ Nitrogen Injection, Low-pressure, Rod Bundle / Heat Transfer, Entrainment
GE CCFL	Saturated CCFL, Low-pressure, Rod Bundle / UP Drain Distribution
UPTF 29B	Full-scale UP, Low-pressure / Entrainment,/De-entrainment, Mixture Level
UPTF 20	Full-scale UPI, Low-pressure / Entrainment, UP Drain Distribution, Mixture Level
G-1 and G-2 Low Pressure Boil-off	Low-pressure, Rod Bundle / Core Heat Transfer, Mixture Level Swell, Void Generation/Distribution
RBHT Single-Phase Steam Cooling Tests	Low-pressure, Rob Bundle / Single-phase Vapor Heat Transfer
IETs	
CCTF	Gravity Reflood, Low-pressure, Rod Bundle / Loop Flows/Flow Split, Core Heat Transfer, Core and UP Entrainment/Mixture Levels
SCTF	Forced and Gravity Reflood, Low-pressure, Radial Power, Rod Bundle / Core Heat Transfer, Core and UP Entrainment
LOFT	Nuclear Core, Scaled PWR, Low-pressure / Heat Transfer, Entrainment, Mixture Levels
CCTF 72, 76	Gravity Reflood, Low-pressure, UPI, Rod Bundle / Core Heat Transfer, Entrainment, UP Drain Dist.

Step 8: Evaluate Effects of IET Distortions and SET Scaleup Capability

Section 18 of WCAP-12945-P-A (Reference RAI-4.7-4) evaluated the effect of using scaled-down experiments in some instances to assess highly ranked models and phenomena. Of particular interest for the GSI-191 HLB EM are scale effects on the important upper plenum processes and phenomena. Westinghouse used the full-scale Upper Plenum Test Facility (UPTF) data to examine scaling trends in these processes and phenomena. Prediction of the UPTF full-scale test results indicated a scale effect, with WCOBRA/TRAC under-predicting the de-entrainment as facility size increased to full scale. Comparison of the Slab Core Test Facility (SCTF) and Cylindrical Core Test Facility (CCTF) upper plenum mass retention with that of UPTF also indicated a scale effect, [

]^{a,c}

The effect of scale on heated rod bundle PCT predictions was also examined in WCAP-12945-P-A. No scale effects were observed. This assessment is applicable to the debris-induced PCT predictions made in the GSI-191 EM.

The addition of the low-pressure G-1 and G-2 boil-off tests and the RBHT steam cooling tests will not introduce any additional scale bias as their design is based on full-height power-to-volume scaling with rod bundle geometries. This experimental setup has been demonstrated in WCAP-12945-P-A not to lead to scale bias.

Step 9: Determine Experimental Uncertainties as Appropriate

The existing assessment base experimental uncertainties and their treatment are discussed in the ASTRUM EM.

The largest source of uncertainty associated with the G1 and G2 low pressure boil-off tests can be attributed to heat losses. Heat losses were not accounted for in the development of the facility model used to perform the assessment provided in the response to RAI-4.8. As heat losses were not accounted for in the facility model, the predicted mixture level swell is expected to trend higher than the experimental data, which is the case. The uncertainty associated with the G1 and G2 low pressure mixture level data is accounted for in the GSI-191 EM by performing sensitivity studies to understand the impact to the key output parameters K_{max}, t_{block}, K_{split}, and m_{split}. The study is presented in the response to RAI-4.8 and shows that the output parameters are not significantly sensitive to the predicted two-phase mixture level.

The largest source of uncertainty associated with the RBHT steam cooling data can be attributed to thermal radiative heat transfer. Experimental temperature measurements taken during these tests reflect combined convective and thermal radiative heat transfer; therefore, to calculate a "true" convective heat transfer coefficient the radiative heat flux for each rod surface must be calculated and subtracted from the total measured rod heat flux. An evaluation of the RBHT steam cooling thermal radiative heat transfer was completed in Reference RAI-4.7-5, and concluded that for most of the steam cooling experiments, the radiative heat transfer from rods at least two rows from the flow housing wall (inner 3x3 rods) represents less than 10% of the total measured rod heat flux at the peak temperature location. For rods one row from the flow housing wall (5x5 peripheral rods) the radiative heat flux represents less than 20% of the total heat flux. Steam cooling data from the inner 3x3 rod bundle is used for the GSI-191 EM assessment such that uncertainty associated with the thermal radiation heat transfer is minimized, and the uncertainty is accounted for in the assessment by reducing the values of the experimental heat transfer coefficients by 10%. Additional, the RBHT steam cooling data provided in NUREG/CR-7152 (Reference RAI-4.7-6) includes uncertainty values determined through a single point uncertainty analysis. This uncertainty is included in the assessment.

Element 3 – Develop Evaluation Model

Step 10: Establish an Evaluation Model Development Plan

The development plan established for the GSI-191 HLB EM aligns with the graded EMDAP approach.

- Determine Requirements for the EM – The GSI-191 HLB EM requirements are established in Element 1 of the EMDAP.
- Identify Assessment Base – New SET additions to the WCOBRA/TRAC assessment base are identified in Element 2 of the EMDAP.
- Develop the EM – The GSI-191 HLB EM is described in Element 3 of the EMDAP.
    - Select Appropriate Codes – WCOBRA/TRAC is selected for the GSI-191 HLB EM, and contains all the necessary models and closure relations required to adequately simulate the GSI-191 large HLB scenario.
    - Identify any Required Code Modifications – A code upgrade is made to simulate core inlet resistance due to the accumulation of debris.
    - Selection of Plant Models (Bin PWR Fleet) – Assessment of AFP capability to adequate remove decay heat following core inlet blockage requires that the Westinghouse PWR fleet be binned into two categories: (1) upflow barrel/baffle plants, and (2) downflow barrel/baffle plants.
    - Identify any Required Model Modifications – Plant model modifications are required to address plant-specific differences between plants in a given plant category. Other modifications are made to skew the best-estimate plant models to more of an Appendix K type model.
- Assess the Adequacy of the EM – The GSI-191 HLB EM assessment is provided in Element 4 of the EMDAP.
    - Existing Assessments – Assessments completed for the previous EM are justified as being applicability to GSI-191 HLB EM.
    - New Assessments – A limited set of new SET assessments are performed to demonstrate adequate code prediction of several high ranked phenomena.
    - Perform Sensitivity Studies – Plant sensitivity studies are performed to help quantify uncertainty and conservatism bias in the GSI-191 HLB EM.
    - Peer Review – The GSI-191 HLB EMDAP process was peer reviewed by WCOBRA/TRAC code developers and LOCA subject matter experts.
- Quality Assurance – The GSI-191 HLB EM was developed and assessed under the Westinghouse Quality Management System, which complies with 10 CFR Part 50, Appendix B.

- Documentation – Adequate and up-to-date documentation exists for the GSI-191 HLB EM including WCOBRA/TRAC Theory and Input Manuals, Transient Description, Objectives, Output Requirements, Acceptance Criteria (Figures of Merit), Key Physical Processes and Phenomena, Methodology/Code Changes, Assumptions and Critical Inputs, Description of Computer Codes and Plant Models, Results, Assessment of Uncertainty/Conservative Bias.

Step 11: Establish Evaluation Model Structure

Code: WCOBRA/TRAC MOD7A R9.1 version for GSI-191 HLB EM. The response to RAI-4.6 describes the code modification made for the GSI-191 HLB EM. The code change allows for the modeling of transient core inlet flow resistance to simulate the accumulation of debris.

Systems and Components: Analyze the behavior of all RCS components identified in Step 3 above. Loop components modeled as 1-D control volumes. Reactor vessel components modeled as 3-D control volumes. The ASTRUM EM has the capability to model all important systems and components.

Constituents and Phases: Analyze the behavior of all constituents and phases identified in Step 3 above. The ASTRUM EM has the capability to model all important constituents and phases.

Field Equations: The codes use a two-fluid, three-field representation of flow in the vessel components. The three fields are a vapor field, a continuous liquid field, and an entrained liquid drop field. Each field uses a separate set of continuity, momentum, and energy equations with one exception. A common energy equation is used by the continuous liquid and entrained liquid drop fields. The 1-D components are represented by a two-phase, five-equation, drift flux model. The formulation consists of two equations for the conservation of mass, two equations for the conservation of energy, and a single equation for the conservation of momentum.

Closure Relations: Closure for the field equations requires specification of the relative velocities (1-D components using drift flux formulation), interfacial heat and mass transfer, and other thermodynamic and constitutive relationships. The ASTRUM EM includes all the necessary closure relations.

WCOBRA/TRAC Numerics: The numerics are described in Section 2-6 of WCAP-16009-P-A and are unchanged for the GSI-191 HLB EM.

Step 12: Develop or Incorporate Closure Models

WCOBRA/TRAC closure models are described in Sections 3-6 of WCAP-16009-P-A. In this step, the closure models necessary to sufficiently model the processes and phenomena identified for the GSI-191 HLB EM are summarized. References identified as bracketed years in this section are provided in Sections 3 through 6 of WCAP-16009-P-A.

The additional feature to model core inlet resistance due to the accumulation of debris is described in the response to RAI-4.6.

WCOBRA/TRAC Flow Regime Maps – Three flow regime maps to determine the type of two-phase flow in the RCS are used by WCOBRA/TRAC. Two flow regime maps are used in the vessel. The "hot wall" flow regime map is used when the wall temperature exceeds the critical heat flux temperature. The "normal wall" flow regime map is used when the wall temperature is below the critical heat flux temperature. A third flow regime map similar to the vessel normal wall map is used for 1-D components. The flow regime maps are used to determine interfacial area for transport of properties across the two-phase interfaces.

Vessel Component Normal Wall Flow Regimes – Section 3-2, WCAP-16009-P-A

The vessel component normal wall flow regime is used when the wall surface temperature is below the critical heat flux temperature, which is defined as [ ]^{a,c} The normal wall flow regimes are: small bubble, small to large (slug) bubble, churn-turbulent, and film/drop. In the GSI-191 HLB scenario these are the primary flow regimes that exist following core quench.

Vessel Component Hot Wall Flow Regimes – Section 3-2, WCAP-16009-P-A

The hot wall flow regime map is primarily used during the short-term transient to model the post-CHF blowdown, refill, and reflood periods. However, when local heatups are predicted to occur due to dryout (i.e., void fraction = 1.0), a top-down recovery of liquid introduces several of the hot wall flow regimes. The hot wall flow regimes include; the subcooled inverted annular flow regime, the inverted liquid slug flow regime, the dispersed droplet flow regime, the falling film flow regime, and the top deluge flow regime. The falling film and top deluge flow regimes are the only applicable hot wall flow regimes applicable to the LTCC phase of the GSI-191 HLB scenario, and only occur for a short time during the recovery from the debris-induced heatup. When local dryout occurs at the peak power location, liquid recovery may be from the top down. If the momentum cell above the cell with dryout contains no surfaces with a temperature greater than T_{CHF} and the void fraction is above [ ]^{a,c} the falling film flow regime is assumed. The top deluge flow regime is similar to the falling film flow regime except that the top deluge is assumed when the void fraction is less than [ ]^{a,c} The top deluge flow regime consists of large liquid slugs having diameters equal to the flow channel hydraulic diameter.

1-D Component Flow Regimes – Section 3-4, WCAP-16009-P-A

The flow regime map assumes the existence of four flow regimes; bubbly, slug, churn, and annular mist. The same map is used for both vertical and horizontal flows. In addition, the slug flow regime does not occur if the total mass flux is greater than [ ]^{a,c}

WCOBRA/TRAC Wall Heat Transfer Models – These models and correlations determine the temperature response of the fuel, cladding, and structural components of a PWR during normal operations and postulated LOCA transients. Separate heat transfer packages are used for the vessel and the 1-D components. Only the pre-CHF heat transfer models are important to the GSI-191 scenario following core quench. The pre-CHF heat transfer packages are similar for both the vessel and 1-D components. During a debris-induced heatup and recovery, a small window of transition boiling may occur.

Vessel Component Wall Heat Transfer Models – Section 6-2, WCAP-16009-P-A

The vessel heat transfer package consists of a library of heat transfer correlations and the selection logic to determine which correlation is appropriate for a given set of hydrodynamic conditions. The heat transfer correlations and selection logic produce a continuous boiling curve. The following list gives the heat transfer regimes used in the vessel components. Post-CHF heat transfer regimes are not included.

- Single-Phase Liquid Convection – The WCOBRA/TRAC vessel heat transfer routines employ two correlations to calculate the heat transfer coefficients to single-phase liquid. The correlations depend on if the flow is laminar or turbulent.

- Saturated Nucleate Boiling – When the wall temperature is greater than saturation but less than the temperature at the critical heat flux and liquid is present, the Chen (1963) correlation is used.

- Subcooled Nucleate Boiling – The Chen correlation, though developed for saturated boiling, may be extended into the subcooled region. The Chen correlation superimposes a forced convective and nucleate boiling component. For subcooled boiling the forced convective heat flux is computed using subcooled liquid properties.

- Single-Phase Vapor Convection – The WCOBRA/TRAC vessel component uses a set of four correlations to determine the heat transfer coefficients for convection to single-phase vapor. The maximum value of these four correlations is chosen as the heat transfer coefficient. The correlations are described in more detail in the response to RAI 4.9.

1-D Component Wall Heat Transfer Models – Section 6-3, WCAP-16009-P-A

This section describes the models and correlations used in WCOBRA/TRAC to determine the heat transfer coefficients in the 1-D components. The heat transfer coding logic in WCOBRA/TRAC for the 1-D components is from the TRAC-PD2 package released by Los Alamos (Liles et al., 1981). The expressions and coding for this package are in the metric system of units. While the heat transfer logic in TRAC-PD2 can generate a full boiling curve with all the heat transfer regimes being modelled, the loops

quickly void during the transient and are primarily filled with vapor during the LTCC period; so heat transfer rates are low, and single phase vapor convection is dominant. The exception is after the application of core inlet blockage which causes the ECCS flow to back-up into the cold side piping and steam generators. The steam generators remain a hot source during the transient. For this situation, the nucleate boiling model is important. Also, post-CHF heat transfer correlations are not important during the LTCC period of the transient since wall temperatures in the 1-D components have reduced below the CHF temperature.

- Single-Phase Liquid Natural Convection – Conventional heat transfer correlations are used for single-phase flow situations. The code has logic to determine natural convection, forced laminar convection or turbulent flow forced convection.

- Single-Phase Liquid Forced Convection – Heat transfer coefficients for both laminar and turbulent flows.

- Nucleate Boiling – The Chen correlation (1963) is used in the nucleate boiling heat transfer regime.

- Convection to Single-Phase Vapor – Heat transfer to single-phase vapor is selected as the larger of the McAdams (1954) turbulent natural convection heat transfer coefficient or the forced convection heat transfer coefficient using the Dittus-Boelter equation (1930).

Vessel Component Entrainment and De-entrainment Models – The drag between the vapor and continuous liquid results in either liquid entrainment, where the liquid moves from the continuous liquid field to the entrained liquid field due to the interfacial shear forces of the vapor acting on the liquid, or liquid de-entrainment caused by the entrained liquid interacting with the continuous liquid in the form of liquid film on structures. For liquid de-entrainment, the liquid moves from the entrained phase to the continuous liquid phase. The models for the different entrainment and de-entrainment mechanisms will be discussed below.

Entrainment of liquid drops from the continuous liquid phase can occur under a variety of conditions. The physical models used to determine the average net mass rate of entrainment and the entrained drop size will be different for each condition. Entrainment mechanisms that may have a significant influence on reactor thermal hydraulics include entrainment from liquid films, entrainment resulting from vapor bubbling through liquid pools, and entrainment resulting from vapor flow across structures such as the upper plenum internals of a PWR. All of the aforementioned entrainment mechanisms are applicable to the GSI-191 HLB scenario following core quench, although the magnitude of entrainment is decreased due to the lower decay heat.

Entrainment in Film Flow – Section 4-6-2, WCAP-16009-P-A

[

]^{a,c}

Core Entrainment During Debris-Induced Uncovery – Section 4-6-3, WCAP-16009-P-A

This entrainment model in the ASTRUM EM is applicable to bottom reflood scenarios and is available for channels with heated structures only. During a debris-induced uncovery, the two-phase mixture level will fall below the top of the active fuel. Although steaming rates are lower during the long-term core cooling period of the transient, entrainment from the two-phase pool surface will occur. This limited droplet entrainment is beneficial since it enhances heat transfer downstream of the pool surface, and influences the location of dryout on the fuel rods.

The primary mechanism for entrainment during a debris-induced core uncovery is the formation of droplets formed by bubbles breaking through the surface of the liquid. This entrainment mechanism tends to generate smaller entrainment fractions compared to breakup entrainment mechanisms governed by surface instabilities. Due to the lower steaming rates during long-term core cooling, the entrained liquid will not transport with the steam phase as readily, and will fall back to the pool surface. Also, de-entrainment rates of the fuel rod surface above the mixture level is expected to be enhanced during a debris-induced heat since cladding temperatures are below the rewet temperature.

In WCOBRA/TRAC, entrainment in the core near the mixture level is based on a model developed by Kataoka and Ishii (1983) assuming vapor bubbling through a liquid pool.

Entrainment During Top-Down Cooling – Section 4-6-4, WCAP-16009-P-A

This entrainment model in the ASTRUM EM is applicable to top-down reflood scenarios. Following core inlet blockage and the activation of the alternate flow paths, liquid draining from the upper plenum is supplied to the top of the core. Due to the lower steaming rates encountered in the upper plenum during long-term core cooling water tends to pool on the upper plenum structures and drain, or fall, into the core. This mechanism is especially important during the debris-induced core uncovery. Prior to the uncovery, liquid in the upper plenum drains into the top of the core, and entrainment will influence the rate of draining along with the drain distribution. The same is true during the debris-induced recovery phase, especially following complete core inlet blockage when all coolant is being provided to the top of the core.

The entrainment model for this mechanism is dependent on droplet size. Droplets falling into the core would be determined from drops which are formed at the fuel nozzle or top spacer grid as liquid falls through the holes. Under conditions with low vapor-to-liquid velocities, the interfacial drag is small and droplets are expected to remain large in size. Therefore, a drop size model was developed to calculate the size of droplets which would be formed as the liquid flows through the hardware at the top of the core. The model was developed by Wallis (1969) for a single drop falling through an area restriction, or orifice.

De-entrainment in Film Flow – Section 4-6-6, WCAP-16009-P-A

Liquid film flow can exist on any structural surface which is in the wetted wall regime, such as the reactor upper plenum structures, vessel wall, core barrel wall, the fuel rods, and other structures. The deposition of entrained drops on this liquid film occurs as a result of random turbulent motions that impart transverse velocity to the drops, bringing them into contact with the solid surfaces or liquid films within the flow channel. The rate at which this occurs has been correlated by Cousins et al. (1965) using a drop concentration gradient diffusion model in which the concentration at the wall is assumed to be zero. The model is a function of the physical geometry, void fraction, and fluid properties.

Crossflow De-entrainment – Section 4-6-7, WCAP-16009-P-A

Entrained liquid carried into the reactor upper plenum during the GSI-191 HLB scenario can de-entrain on the reactor structures as the two-phase mixture flows across these structures and out of the broken hot leg. This cross flow de-entrainment will result in creating liquid films on the structures which can flow downward to the liquid pool on the horizontal upper core plate. The model used in WCOBRA/TRAC employs de-entrainment fractions obtained in the upper plenum de-entrainment experiments of Dallman and Kirchner (1980).

De-entrainment at Area Changes – Section 4-6-8, WCAP-16009-P-A

Droplets will de-entrain at area changes on the wetted wall flow regimes by contacting the walls or surfaces of the reduced area channel for axial and lateral flow. The droplets are assumed to de-entrain anytime the area changes, regardless of if the actual area is normal or inclined toward the flow. These drops will then form liquid films on those surfaces which will drain. WCOBRA/TRAC uses a simple area ratio to de-entrain a fraction of the droplet field where an abrupt area reduction occurs in the reactor vessel.

De-entrainment at Solid Surfaces and Liquid Pools – Section 4-6-9, WCAP-16009-P-A

Entrained liquid flow is assumed to de-entrain under the following additional conditions:

- Flow of entrained droplets into a cell with a solid surface at the opposite cell face.
- Flow of entrained droplets into a cell which is in a bubbly flow regime.

For the above cases, [

]^{a,c}

Vessel Component Momentum Transfer Models – The momentum equations used for the WCOBRA/TRAC vessel component have been described in Section 2 of WCAP-16009-P-A. There are specific terms in these equations that model the wall-to-fluid drag for each phase and the vapor-to-liquid drag. The constitutive relationships which characterize the wall and interphase drag account for the wall friction force on the fluid, as well as the interfacial forces which occur as a result of momentum exchange between the phases flowing together within a channel. The interfacial drag models and correlations used in WCOBRA/TRAC are flow regime dependent. These expressions for the interfacial drag force also assume that the force is proportional to the square of the relative velocity between the phases. In the WCOBRA/TRAC vessel model, there exist two liquid fields such that different expressions are used to calculate the interfacial drag term for the entrained droplet and the continuous liquid fields within a computational cell.

As mentioned above, the interfacial drag relationships are flow regime dependent. Thus, the interfacial area, liquid content, and resulting frictional relationship between phases will change as the flow regime changes. As a result, the interfacial drag relationship will depend on the cell void fraction and the total mass flux through the cell at any one time. The flow regimes used in WCOBRA/TRAC have been discussed above and the interfacial drag models and their basis for each flow regime are summarized below.

Since the WCOBRA/TRAC vessel component interfacial drag uses the formation of two separate liquid fields, entrained and continuous film flow, this permits the use of more basic, microscopic models to describe the interfacial drag. In addition, the use of two liquid fields permits more accurate modelling of the reactor vessel geometric details such details such as spacer grids, top and bottom nozzles (tie plates), downcomer, lower plenum, and complex flow passages in the upper core plate and structures. More detailed modelling of these geometries allows the code to calculate, more accurately, a variety of hydraulic conditions such as countercurrent flow, flooding, entrainment, and de-entrainment.

Vessel Component Wall Shear Models – Section 4-2, WCAP-16009-P-A

The vessel momentum equations described in Section 2-3-3-2, WCAP-16009-P-A define the wall drag coefficient in units, which, when multiplied by the new time phasic velocity, will yield force per unit length on the phase. However, the phasic mass flow rates are the actual solution variables. The wall shear stress components for axial and lateral flow in the vessel are a function of the wall drag coefficient, and the phasic density, volume fraction and velocity.

Vessel Component Form Loss – Section 4-3, WCAP-16009-P-A

The WCOBRA/TRAC vessel component models a form loss as defined in Section 4-2. The form loss coefficient is directly input into the code for both axial and lateral flows. The user has two options when modelling an unrecoverable pressure loss coefficient that has been adjusted for the area changes: to model the true area change, or to use the nominal area and input a loss coefficient that has been adjusted for the area change.

In the GSI-191 HLB EM, area changes due to structures within the AFP (e.g., barrel/baffle channel) are modelled using the nominal AFP area and a form loss coefficient adjusted to that area. Core inlet resistance due to the accumulation of debris is also modelled in this fashion. As described in the response to RAI-4.6, a code modification was made such that the core inlet form loss coefficient could be varied as a function of time. The code modification ramps the dimensionless form loss coefficient at the first core node of up to 4 specified channels. The loss coefficient values are normally specified along with the index number of the nodes corresponding to the vertical location of the loss.

Vessel Interfacial Shear Models – Section 4-4, WCAP-16009-P-A

Flow regime maps are used in the vessel component of WCOBRA/TRAC. The normal or cold wall flow regime map is used unless there is a structure in the computational cell that has a surface temperature in excess of the critical heat flux temperature. If heated rods exist in the computational cell with temperatures in excess of the critical heat flux temperature, [

]^{a,c} Conversely, if the wall temperature is below the critical heat flux temperature, the code will use the cold wall flow regime with a liquid film on the wall. The vessel momentum equations require the interfacial drag coefficient in units which, when multiplied by the new time velocity difference between the phases, will yield force per unit length for that phase. During the numerical solution, these coefficients are divided by the appropriate phasic densities, when the phasic mass flowrate is solved for. The average interfacial drag force per unit length between the vapor and continuous liquid and between the vapor and entrained liquid are defined in terms of a flow regime dependent interfacial drag coefficient and the relative velocity between the phases.

As local dryouts at the peak power location may occur in the GSI-191 HLB scenario when core inlet resistance is applied, a liquid film is formed on the rods above the dryout. The interfacial drag relationships on the film above a localized dryout are the same as those for annular film flow except that the interfacial friction uses the Wallis (1969) friction factor. [

]^{a,c}

When the walls are hot and a large amount of liquid flows downward into a computational cell, the flow regime is called top deluge. This flow regime is similar to the liquid slug regime for upflow. The top deluge flow regime can be present during the recovery from a dryout when liquid is being supplied to the top of the core via an AFP. The top deluge interfacial drag is calculated based on a droplet drag coefficient that uses a vapor Reynolds number in the cell based on local vapor properties. The low vapor fraction for this regime implies that the liquid is filling most of the channel. Note that the velocity used in the interfacial drag calculation is the relative velocity between the continuous liquid and the vapor, rather than the entrained liquid to vapor, since the liquid slugs are modelled by the continuous liquid field. Again, the model represents large liquid slugs or chunks which would nearly fill the channel and would capture any small droplets in the channel.

Vessel Component Intercell Drag – Section 4-5, WCAP-16009-P-A

WCOBRA/TRAC calculates an additional interfacial drag force for interfacial shear that occurs at mesh cell boundaries. These interfaces are detected by changes in void fraction between adjacent cells, and can occur on either horizontal or vertical cell boundaries.

The intercell drag model is used to help calculate counter current flow limitation (CCFL) situations where there is liquid flowing downward against vapor upflow. The intercell drag models are applied between channels where liquid can pool, such as on top of the upper core plate in the reactor upper plenum, and channels representing vapor jets through holes in the upper core plate, for example. The intercell drag models will calculate a drag force on the pooled liquid in the adjacent cell as well as the reaction force on the vapor jet.

Decay Heat Models - WCOBRA/TRAC decay heat models used in the GSI-191 HLB EM include the ANSI/ANS 5.1-1971 and ANSI/ANS 5.1-1979 standards. Design analysis is completed using the Appendix K decay heat model (ANSI/ANS 5.1-1971 + 20%). Sensitivity studies are completed using the nominal ANSI/ANS 5.1-1979 standard as part of the uncertainty assessment completed in Step 20 of the EMDAP.

Element 4 – Assess Evaluation Model Adequacy

Steps 13, 14, and 15: Closure Relations (Bottom-up Assessment)

Most of the models or closure relationships used in the ASTRUM EM were developed or available from existing database literature. In a few instances, specialized models have been developed using specific SET data. Although the original development of the WCOBRA/TRAC models or closure relationships did not explicitly consider the LTCC phase of the LOCA transient, models have been evaluated, and sometimes modified, to better simulate the full range of conditions expected in a LOCA transient. The goal was to ensure that the same fundamental correlations apply over the wide range of conditions expected during a large break LOCA. Models are not tailored to a specific scenario or break location. As the existing models, at their fundamental level, are based on the local thermal-hydraulic conditions they are independent of the global system response or time evolution for the GSI-191 HLB scenario. As such, model ranges of applicability and scalability concerns have been addressed with a specific focus of extending the use of these models into the LTCC phase of the transient and accounting for additional uncertainties related to phenomena important for the GSI-191 EM, like two-phase mixture level under low pressure boil-off conditions, which was not assessed in the ASTRUM EM development.

Sections 11 through 16 of WCAP-12945-P-A described WCOBRA/TRAC simulations of separate and integral effects tests. These test simulations provide a comprehensive validation of the code logic for the short-term LOCA transient (blowdown, refill, and reflood). A wide range of test facilities and conditions were selected for simulation, not only to establish code applicability, but to provide a means of isolating and assessing individual model and correlation packages. Tests in the assessment matrix were selected so as to validate the code's ability to model the important phenomena that occur during a LOCA in a PWR. For phenomena that have not been assessed by the ASTRUM EM, or for new GSI-191 EM features (i.e., transient resistance due to debris accumulation at the core inlet), new assessments are performed to assess model fidelity and accuracy. These additional assessments are described below.

References identified as bracketed years in this section are provided in Sections 3 through 6 of WCAP-16009-P-A.

Decay Heat Model

The decay heat models used in the GSI-191 HLB EM are based on ANS Decay Heat Standards. The decay heat models used by WCOBRA/TRAC have been verified. In the response to RAI-4.10, the WCOBRA/TRAC heat generation rate calculated by the EM analysis is compared to the Appendix K Decay Heat Standard.

Core Inlet Resistance Due to Debris

The modeling of core inlet resistance is described in the response to RAI-4.6. Simple test cases were prepared to validate and verify that the model is functioning as expected. The pressure drop across the core inlet created by the application of resistance was compared to hand calculations and shown to be accurate.

Core Void Generation/Distribution (Mixture Level Swell)

Following complete core reflood during the GSI-191 large hot leg break scenario, the two-phase mixture level in the inner reactor vessel is characterized by the pressure balance between the liquid level in the downcomer and the collapsed liquid level in the core region. Because vapor generation from decay heat is initially high, regions in the vessel can achieve a significant void fraction. As the transient progresses into the LTCC phase, vapor generation reduces due to the reduction in decay heat. The two-phase mixture level depends on the interfacial shear exerted by the vapor on the liquid, and as a result, the mixture level can be significantly higher than the collapsed liquid level. The difference between the two-phase mixture level and the collapsed liquid level is a measure of the mixture level swell. Using this definition, a swell of zero corresponds to a two-phase mixture level which is the same as the collapsed liquid level.

Prediction of the mixture level swell and tracking of the mixture level are important during the GSI-191 scenario and is ranked high in the PIRT provided in Step 3. When resistance due to debris accumulation at the core inlet is modeled, the flow to the core is reduced. As more liquid boils away, the mixture level can eventually drop into the core. While sufficient cooling is maintained below the mixture level, dryout occurs above the mixture level. Heat transfer above the mixture level is governed by single-phase convection to the vapor. This relatively poor heat transfer mode causes the cladding temperature above the mixture level to increase rapidly. Thus, adequate prediction of the two-phase mixture level in the active core region is vital to the prediction of the cladding temperature during a post-quench debris-induced heatup.

Mixture level swell is the process that determines the vertical position of the two-phase interfaces in the system; above the interface the mixture is essentially single-phase vapor. [

]^{a,c}

The flow regime maps used by WCOBRA/TRAC are described in Section 3 of WCAP-16009-P-A, and the models and correlations for wall drag, interfacial drag, and entrainment are described in Section 4. These models are important for determining the void fraction distribution within the core region. The pedigree and applicability to the GSI-191 scenario are discussed for each of these models in the following sections.

WCOBRA/TRAC Flow Regime Maps

The WCOBRA/TRAC flow regime and flow regime transition models and correlations are consistent with experimental observations and well-known models and correlations available in the literature. The models and correlations have been verified as part of the ASTRUM methodology by comparison to SET

and IET data. WCOBRA/TRAC contains all the flow regime maps necessary to simulate the GSI-191 scenario.

The model for the small bubble regime is based on motion of an individual bubble in a flow stream. Therefore, no scale bias is introduced. The transition point from bubbly flow to slug flow is close to the theoretical transition, which is also scale independent. Therefore, although there is little information on flow pattern transitions for large diameter pipes, the transition point appears to be generally applicable. In the application of WCOBRA/TRAC to PWRs, typical fuel assemblies have a hydraulic diameter of approximately 0.5 in, which is within the range of tube diameters that were used in determining the transition point between the bubbly and slug flow. The flow regime tests thus provide reasonable assurance that the transition boundary between bubbly and slug flow is appropriate for flow in a reactor core under LTCC conditions. Simulations of experimental tests of differing scale using WCOBRA/TRAC are reported in Volumes 2 and 3 of WCAP-12945-P-A. The agreement between predicted and test data indicates that flow regime transition criteria assumed in WCOBRA/TRAC are sufficiently accurate for the GSI-191 HLB analysis.

The effect of scale on the small bubble transition boundary completed by Chow et al. (1989) was also considered in the ASTRUM EM. In that study, the WCOBRA/TRAC normal wall flow regime map was assessed by comparing it to the vertical flow regime map by Taitel, Bornea, and Dukler (1980). The Taitel-Bormea-Dukler map was found to have a small scale dependence on hydraulic diameter for the bubbly flow boundaries. The WCOBRA/TRAC flow regime boundary between small bubble and the small to large bubble regime, obtained by assuming steady flow conditions, relative velocity obtained from a force balance, and using the interfacial shear models described in Step 12 above, agree well with the Taitel-Bormea-Dukler map. As the only scale dependence identified was on hydraulic diameter, the flow regime is appropriate for the GSI-191 HLB EM.

The small to large bubble regime, similar to the small bubble regime, is based on the behavior of a single bubble in a flow field. The use of mesh cell volume to determine the large bubble size, however, indicates that noding selection can influence calculations for this regime. Chow et al. (1989), however, found the small to large bubble flow regime boundaries in WCOBRA/TRAC to be relatively scale independent. That finding is consistent with the Taitel-Bormea-Dukler map, which shows no scale dependence for the slug flow regime. Therefore, the WCOBRA/TRAC small to large bubble regime does not contribute to scale bias, and is applicable to the GSI-191 HLB EM, which used the same mesh cell volume as the ASTRUM EM.

The model of churn-turbulent flow regime was assessed by Chow et al. (1989). The transition boundaries of the churn-turbulent flow regime were found to be relatively insensitive to scale, and can be applied to the GSI-191 HLB EM.

The model for film/drop flow regime was assessed by Chow et al. (1989). The transition boundary between the film/drop regime and the churn-turbulent regime was found to be somewhat dependent on scale. The GSI-191 HLB EM uses the same mesh cell size as the ASTRUM EM. Since the scale effect on the transition boundary was found to be acceptable for the ASTRUM EM, it is also acceptable for the GSI-191 HLB EM.

Vessel Component Wall Shear and Interfacial Drag

The WCOBRA/TRAC vessel wall shear models use a system of consistent correlations for the friction and form loss components for axial and lateral flow. The WCOBRA/TRAC use of an entrained liquid field in addition to a continuous liquid field results in partitioning the form losses by each fraction of the flow for the total loss. This particular feature of the vessel wall shear models has been verified on full-scale, two-phase flow experiments on simulated reactor hardware, and is applicable to the GSI-191 scenario. The form loss coefficients are used inputs to the calculation and are dependent on the geometry and the method of modelling the area changes in the model, making them appropriate for LTCC simulation. Interfacial shear is modeled using correlation consistent with the literature, and are based on local conditions. The models have been verified over a broad range of conditions, and are applicable to LTCC.

The wall friction models, as defined in WCOBRA/TRAC, are scale independent. The friction factor relationships agree with existing friction factor relationships found in textbooks (Vennard, 1961). The laminar friction factor is obtained from a momentum balance in laminar flow and the turbulent relationship agrees with the smooth pipe data of Nikuradse (1933). The key assumption is the void fraction weighting of the form losses. The WCOBRA/TRAC wall friction model has been compared to the two-phase flow data in complex geometries for different experiments. In these experiments, the static pressures as well as the local void fraction were measured for channels with multi-hole plates. The WCOBRA/TRAC predicted pressure drop and void fractions are in excellent agreement with test data, for both the frictional pressure losses as well as the form losses. In Volumes 2 and 3 of WCAP-12945-P-A, heated wall pressure drop comparisons are also shown for rod bundle experiments and again indicate good agreement with the test data.

The formulation for interfacial drag used in the small bubble regime is scale independent, since it is based on an individual bubble in the flow stream. Therefore, no scale dependence or bias would be introduced into the calculation by this model. Since the small bubble regime would be only a small region in the reactor core, before the flow regime would transition to other regimes, the noding selection used could influence the size of this regime and how it is weighted with other regimes. There is a small region of bubbly flow in the FLECHT-SEASET, FLETCH, and FEBA reflood heat transfer experiments. These effects are examined in Section 12 of WCAP-12945-P-A and should not influence the GSI-191 HLB calculations since the same noding approach is used in the code assessment as is used in the GSI-191 HLB calculations.

The noding selection could also influence the interfacial drag in the small-to-large bubble flow regime. The verification of this model with noding similar to the noding used in the GSI-191 HLB EM is given in Section 12 of WCAP-12945-P-A. It indicates that the model, in conjunction with other models for bubble size and void fraction, represents the measured void fraction from the FLECHT-SEASET experiments below the quench front. Since these experiments preserve full-scale core geometry, potential scaling bias is eliminated.

The model for interfacial drag in the churn-turbulent flow regime has some scale dependence. Ishii (1977) attempted to compensate for the interaction effects of one bubble or groups of bubbles on each

other through adjustments of the effective viscosity. A comparison of the void fraction predicted by WCOBRA/TRAC and the FLECHT-SEASET pressure drop data below the quench front shows good agreement, as shown in Section 12 of WCAP-12945-P-A.

The interfacial drag in the film/drop flow regime is determined using correlations developed from a broad range of experimental data. The Wallis friction factor used for film flow has been examined for horizontal and vertical flow from pipe sizes ranging from 1 inch to 3 inch diameters. The Hanstock and Hanratty film friction model has also been compared to vertical film flow data on diameter tubes ranging from 0.503 inches to 2.5 inches over a range of different fluid velocities and pressures. The comparison of their correlation to data provides a good fit over a range of scales. WCOBRA/TRAC has been compared to annular pressure drop data on full-scale reactor internals. The agreement between the measured pressure drop, pressure distribution, and void fraction with the WCOBRA/TRAC prediction is excellent, indicating the models used in this flow regime do not have a scale bias.

Based on WCOBRA/TRAC simulations of the G-1 and G-2 loop experiments, in addition to the simulation of CCTF Run 76, both of which predicted a falling film regime near the top of the heater rods after they had quenched, scale bias is not expected in the interfacial drag model for the falling film flow regime. The G-1 and G-2 loop tests used full-size, full-height test bundles, and the CCTF facility modelled a full-height core. Since these tests are full- and/or large-scale, there should be no scaling concerns regarding the interfacial drag model for the falling film flow regime.

The top deluge interfacial drag model is similar to the liquid slug model for upflow. The basic correlations that are used are scale dependent because they depend on the channel hydraulic diameter. Experiments with upper head injection will result in lower void fractions in the upper portion of the test bundle such that WCOBRA/TRAC will be in the top deluge flow regime for a portion of the transient. Since these experiments have been performed on prototypical rod bundles with different rod array sizes at full-scale there are no scaling effects that need to be considered. The agreement of the test data with the WCOBRA/TRAC predictions for heat transfer is reasonable and indirectly shows that the proper interfacial area and drag is calculated for this flow regime.

Entrainment During Debris-Induced Uncovery

The basic formulation for entrainment has no scale dependent parameters, and the droplet Weber numbers come from FLECHT reflood experiment which were performed using prototypical geometries, flow, pressure, and powers. Droplet Weber numbers during LTCC conditions are expected to be lower than during reflood conditions because the dominant entrainment mechanism during LTCC is the breakup of bubbles pushing through the pool surface. Lower steaming rates during LTCC also limit the height that droplets can be transported above the top of the pool surface. The aggregate effect is a lower entrainment fraction closer to the pool surface. The entrainment model has been shown to have similar dependence to the gas flux and pool height as the entrainment models of Kataoka and Ishii (1983), which considers the bubble breakup mechanism.

Additional Assessment of WCOBRA/TRAC Mixture Level Predictions

Several experimental tests have been conducted under low pressure boil-off thermal-hydraulic conditions to measure the effects of various parameters on mixture level swell. [

]^{a,c}

An additional experimental assessment was made using G1 and G2 test data in the response to RAI-4.8. Based on the G1 and G2 experimental assessment using WCOBRA/TRAC, it is determined that the use of the 0.8x nominal interfacial drag is appropriate for the GSI-191 thermal hydraulic analysis. The sensitivity study presented also demonstrates that the interfacial drag multiplier has only a minimal impact on the key parameters output from the GSI-191 thermal hydraulic analysis.

Heat Transfer to Single-Phase Vapor

The GSI-191 TH PIRT in Step 3 identifies convection to single-phase vapor as the most important heat transfer mechanism. As this heat transfer regime exist in reflood separate effects tests, previous assessments made against low pressure, low reflood rate tests provide reasonable assessment of this heat transfer model for the GSI-191 scenario. Section 12 of WCAP-12945-P-A describes simulations of reflood heat transfer separate effect tests. The noding used in these simulations is consistent with the GSI-191 HLB EM noding.

The WCOBRA/TRAC heat transfer models are well-known from the literature. They have been validated over a broad range of conditions and have physical bases. The correlations have been verified as part of the ASTRUM methodology by comparison to SET and IET data. WCOBRA/TRAC contains all the heat transfer models necessary to simulate the GSI-191 scenario.

Each of the four correlations used to calculate the single-phase vapor heat transfer coefficient to vapor scale by using an appropriate characteristic length. In WCOBRA/TRAC, the channel hydraulic diameter is used for the characteristic length. The McAdams correlation (1954) is not affected by choice of the characteristic length since that term cancels out of the expression for the heat transfer coefficient. The hydraulic diameter affects the calculation of the natural convection heat transfer coefficient only through its use in the Reynolds number in the selection logic to determine the appropriate heat transfer mode. Therefore, the scale dependence of the McAdams (1954) correlation is not large.

The correlation by Wong and Hochreiter (1981) was developed directly from experimental data from a

full-scale rod bundle. Therefore, the only scale dependence concern is over the application of this correlation to rod bundle arrays different from the 17x17 rod bundle used to generate the experimental data on which this correlation is based. Therefore, the set of equations used by WCOBRA/TRAC to calculate single-phase vapor heat transfer is not strongly dependent on scale.

Additionally, the WCOBRA/TRAC single-phase vapor heat transfer package was compared to experimental data from RBHT steam cooling experiments. The results showed good agreement with experimental results from that test program. Figure RAI-4.7-8 shows the single-phase vapor heat transfer correlations used in WCOBRA/TRAC, and compares them to data from RBHT facility single-phase steaming cooling tests from NUREG/CR-7152 (Reference RAI-4.7-6). The RBHT data is taken from heater rods D3, D4, and C4, which are all in the inner 3x3 rod bundle, at a bundle elevation of 110 in. The WCOBRA/TRAC single-phase vapor heat transfer model conservatively bounds the RBHT data and its uncertainty. The RBHT heat transfer is also reduced by 10% to account for the radiative heat transfer component inherent to the experimental heat transfer coefficients.

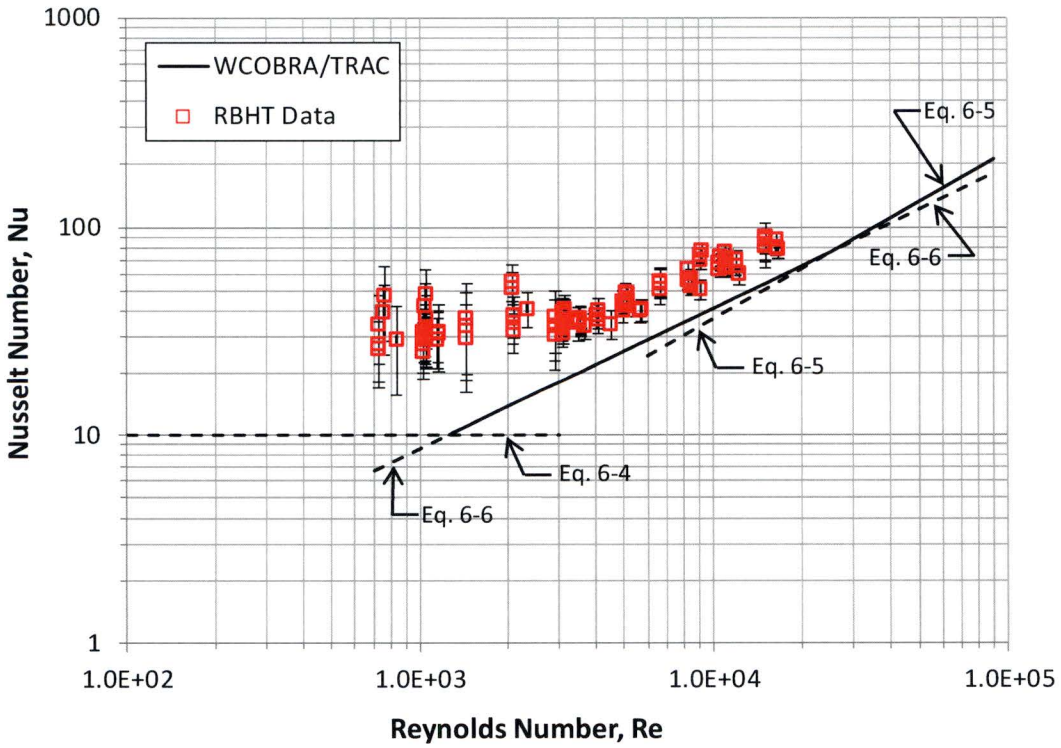

Figure RAI-4.7-8 WCOBRA/TRAC Single-Phase Vapor Heat Transfer Correlations Compared to RBHT Steam Cooling Data (NUREG/CR-5172)

Upper Plenum Draining

Due to the lower steaming rates encountered in the upper plenum during LTCC water tends to pool on the upper plenum structures. When resistance is applied to simulate debris accumulation at the core inlet, flow into the core is reduced and a core uncovery can occur if the flow falls below that required to replace boil-off. Liquid draining from the upper plenum into the top of the core will delay core uncovery and limit the magnitude of the uncovery. Also, following complete core inlet blockage, liquid is supplied to the top of the core through the AFPs creating a top-down cooling scenario.

Good communication between the core region and the upper plenum is necessary for adequate top-down cooling. The vapor flow through the upper core plate is an important parameter in determining the counter current flow limitation (CCFL) condition at the upper core plate and whether the liquid in the upper plenum is allowed to drain back into the core. The vapor Kutateladze number (Ku_g) is an indicator for the CCFL limit. If the vapor flow is sufficiently high (beyond no liquid downflow limit of $Ku_g = 3.2$), the core would behave as in the boil-off situation immediately following the application of core inlet resistance. If Ku_g is less than 3.2, liquid can fall back from the upper plenum into the core region. Note that even if Ku_g is less than this limit, the liquid downflow may still be retarded such that the void fraction below such a flow restriction could be higher than the void fraction in the upper plenum.

To confirm that there is good communication between the core region and the upper plenum, the Kutateladze number at the upper core plate was estimated for the WCOBRA/TRAC simulation of partial core inlet blockage (K_{max}). The Kutateladze number for a conservative steaming rate at 1200 seconds post-LOCA was calculated to be less than 2.5. Since the vapor Kutateladze number is less than 3.2, good communication between the core region and the upper plenum is expected. The vapor flow falls below the downflow limit of $Ku_g = 3.2$ after approximately 500 seconds post-LOCA. Therefore, good communication between the core region and the upper plenum is expected throughout LTCC and the GSI-191 HLB scenario.

Upper Plenum Mixture Level

As described in the response to RAI-4.23, the upper plenum mixture level is important for liquid transport to the break under LTCC conditions. Entrainment is less important because the steaming rates are low such that entrainment rates are diminished. An upper plenum mixture level exists during most of the GSI-191 HLB transient. Under these conditions, the accuracy of the mixture level prediction is less important because there is significant liquid carryover to the break due to natural or forced circulation. Similar to the core mixture level, the upper plenum mixture level is dependent on the flow regime and interfacial drag. Various sensitivity studies completed in this RAI response have demonstrated that the break flow from the reactor vessel side is not significantly sensitive to variations in the upper plenum mixture level. The effect of these studies on break flow is discussed in the response to RAI-4.23 Item i.

During a debris-induced core uncovery, liquid drains from the upper plenum and the mixture level is suppressed for a short period of time. Under suppressed upper plenum two-phase mixture level conditions, transport of continuous liquid to the break due to circulation is lost, and entrainment is the only mechanism available to transport liquid to the break. Section 18 of WCAP-12945-P-A concludes

entrainment models is small-scale experiments which isolate each phenomenon. The entrainment rate formulation is mesh cell length dependent. However, this dependence reflects the length of the surfaces with films which are generating the entrained liquid. Other parameters in the entrained model are local flow, interfacial friction, and channel geometry. These models have been verified against different scaled experiments, as shown in Volume 3 of WCAP-12945-P-A, which have structures similar to a PWR upper plenum such that the entrainment and de-entrainment from and on these structures should be prototypical.

As the only scale distortion identified was the mesh cell length dependence, the conclusions are applicable to the GSI-191 HLB EM since the same upper plenum noding scheme is applied. Further, since the LTCC steaming rates are lower than that required to generate significant entrainment rates, and because the duration of upper plenum mixture level suppression is short, the effect of the entrainment/de-entrainment distortion identified in WCOBRA/TRAC is less significant for the GSI-191 HLB scenario.

Alternate Flow Path Resistance

The loss coefficients that are normally used in codes like WCOBRA/TRAC are derived from full-scale and scaled experimental test data, and in many cases are standardized and available in handbooks of hydraulic resistance (Crane, 1969). For specific nuclear reactor geometries and area changes in the reactor vessel, loss coefficients and unrecoverable pressure drop information is obtained from scale model experiments. These experimental loss coefficients and pressure drops are used as a guide to adjust the form loss coefficients in regions of the vessel where the geometries are complex.

The WCOBRA/TRAC method of applying the form loss coefficients is verified by comparing the WCOBRA/TRAC steady-state flow and pressure distributions to calculated PWR steady-state conditions. WCOBRA/TRAC has also been compared to single-phase and two-phase pressure drop experiments on prototypical reactor internals hardware which contained restrictive multi-hole plates. The comparisons of WCOBRA/TRAC predictions with pressure drop and void fraction data was excellent, as shown in Volumes 2 and 3 of WCAP-12945-P-A.

The alternate flow path resistances applied in the GSI-191 HLB EM are calculated from physical plant geometry, and established methods as described in the response to RAI-4.2. Margin is added to the alternate flow path resistance values to account for uncertainties in the calculation. Before performing transient analysis, the steady-state calculated flow through the alternate flow paths is compared to expected flows under normal operating conditions to confirm that the calculated steady-state flow through the alternate flow paths is less than the design bypass flow calculated by THRIVE for normal operation.

The upflow plant steady-state barrel/baffle channel flow is shown in Figure RAI-4.7-9. As the figure shows, the steady state barrel/baffle flow is approximately 10% less than the desired best-estimate flow for the reference plant. Similarly, Figure RAI-4.7-10 shows the upper head spray nozzle flow from the downflow plant steady-state calculation. As shown in the figure, the steady-state upper head spray nozzle flow is more less 20% less than the best-estimate calculated flows for normal operation.

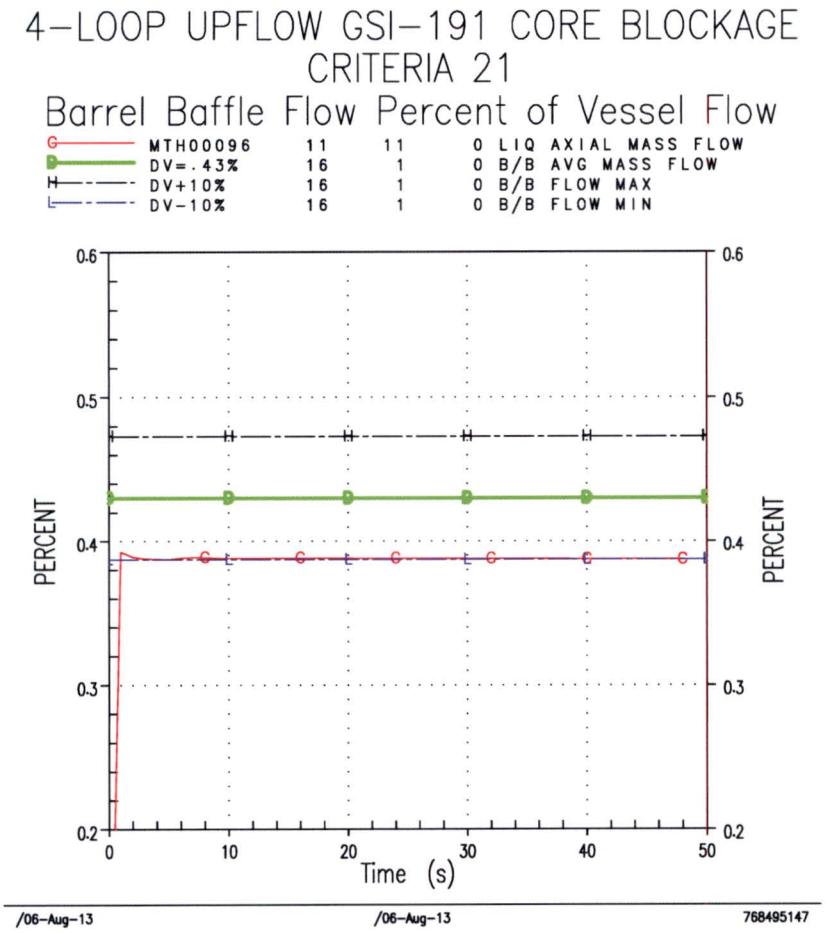

Figure RAI-4.7-9 Calculated Steady-State Barrel/Baffle Channel Flow

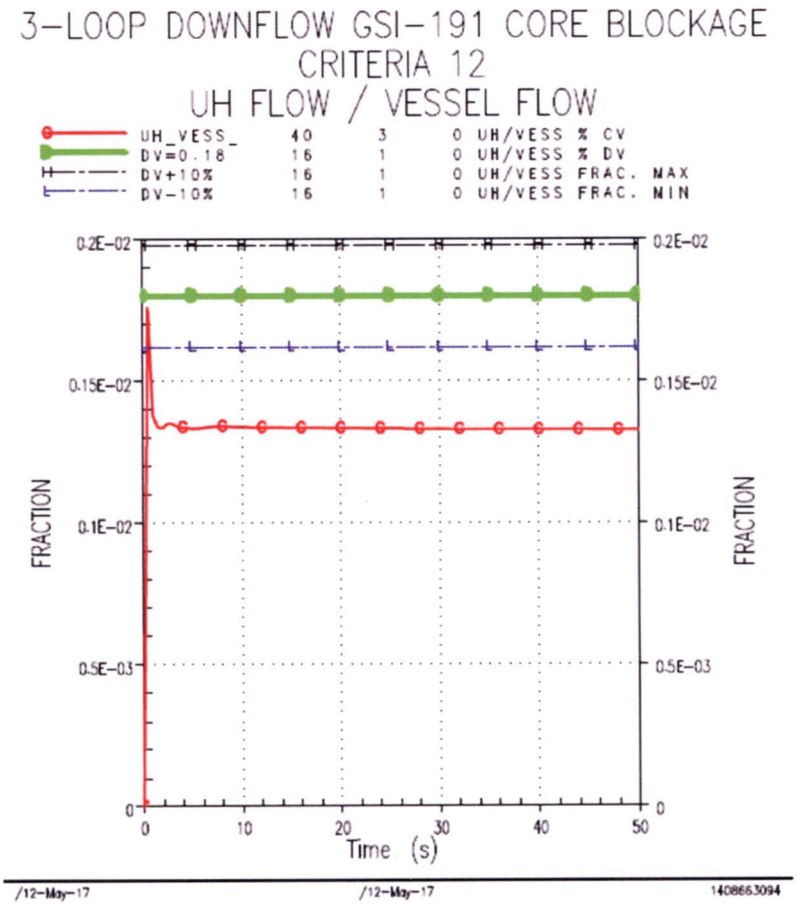

Figure RAI-4.7-10 Calculated Steady State Upper Head Spray Nozzle Flow

Steps 16, 17, 18, and 19: Integrated EM (Top-down Assessment)

WCOBRA/TRAC Field Equations

Section 2 of WCAP-16009-P-A describes the WCOBRA/TRAC conservation equations and numerical solution method. No changes to the WCOBRA/TRAC conservation equations or solution method were made for the GSI-191 HLB EM. The governing equations for the vessel and the one-dimensional components use different representations of two-phase flow and are discussed separately. Sections 2-2 and 2-3 describe the conservation equations and the three-dimensional computational cell structure used in the vessel component, while Sections 2-4 and 2-5 discuss the one-dimensional components. The numerical solution methods for the vessel component and the one-dimensional components, the timestep size selection, and convergence criteria are described in Sections 2-6 and 2-7.

WCOBRA/TRAC-TF2 uses a two-fluid, three-field representation of flow in the vessel component. The three fields are a combined-gas field (steam and non-condensables), a continuous liquid field and an entrained liquid drop field. Each field in the vessel uses a set of three dimensional continuity, momentum, and energy equations with one exception. A common energy equation is used by both the continuous liquid and the entrained liquid drop fields.

The one-dimensional components consist of all the major components in the primary system, such as pipes, pumps, valves, steam generators, accumulators, and the pressurizer. The one-dimensional components are represented by a two-phase, five equation drift flux model. This formulation consists of two equations for the conservation of mass, two equations for the conservation of energy, and a single equation for conservation of momentum. Closure for the field equations requires specification of the interfacial friction, interfacial heat and mass transfer, and other thermodynamic and constitutive relationships.

This representation of the conservation equations is an industry-standard for thermal-hydraulic system codes which can account for non-equilibrium effects between the vapor and liquid phases. The ASTRUM EM determined the formulation to be capable of representing the processes and phenomena important to large break LOCA. Since the GSI-191 EM introduces no new processes or phenomena, the field equations in WCOBRA/TRAC are adequate for the GSI-191 HLB scenario.

Modeling of Systems and Components

All U.S. designed light water PWRs have the same fundamental design. The functions of the major system components such as the reactor vessel, steam generators, and pumps are the same, and most have similar design features. Differences between PWR systems are primarily due to loop design, the ECCS configuration, and the AFP design. Operating Westinghouse units, for example, have loop designs that are 2x2 (two-loop), 3x3 (three-loop), and 4x4 (four-loop), while Combustion Engineering (CE) units and Babcock and Wilcox (B&W) units have a 2x4 loop arrangement. With the exception of size, and the B&W once-through steam generator, individual loop flow paths in each type of system are similar.

The reactor vessel internals for various PWRs are also similar. There are differences in the detailed

internal structures of the various regions however. In some older Westinghouse plants for example, the lower support plate is curved while in other plants it is flat. Within the core, there are differences in fuel design. Some plants have a thermal shield in the downcomer, while others have a neutron pad attached to the core barrel. B&W plants include vent valves in their core barrels. The upper plenums and upper heads contain control rod guide tubes and support structures that may have slightly different designs and arrangements.

Most PWRs in the U.S. have an emergency core cooling system (ECCS) configuration that includes high and low head pumped safety injection, in addition to accumulators for passive injection. The injection location for most plants is the cold legs. Several two-loop plants are equipped with an upper plenum injection (UPI) system.

All U.S. PWRs have flow paths in the reactor vessel that may allow fluid to bypass the heated core during normal operations. Examples include flow through the barrel/baffle channel and/or flow through the upper head spray nozzles. The B&W, CE, and a portion of the Westinghouse fleet have upflow BB designs that provide a direct flow path between the lower support region and the upper plenum. Westinghouse standard upflow plants and B&W plants have pressure relief holes (LOCA holes) that allow direct communication between the barrel/baffle and core periphery as well. Conversely, Westinghouse downflow plants have limited flow paths between the lower support region and the upper plenum. Westinghouse plants also have upper head spray nozzles (UHSNs) that are a credited AFP. The spray nozzles provide a flow path between the top of the downcomer and upper head. Both the barrel/baffle channel and the UHSNs may provide a path for coolant to reach the core in the event that the core inlet becomes blocked with debris. In this context, these paths are termed AFPs as they provide an alternate path for coolant to reach the core other than the core inlet.

The WCOBRA/TRAC code options, models, and inputs have the inherent capability to model the major systems and components important to LOCA analysis. The GSI-191 HLB EM introduces no new systems or components that require applicability evaluation.

Additional Assessments

Due to the lack of new applicable IET or large scale facility test data relevant to the GSI-191 HLB scenario, no new IET assessments are made for the GSI-191 EM. Assessment of system interactions and global capability is made using engineering judgement and sensitivity studies, as discussed in Step 20.

Step 20: Determine Evaluation Model Biases and Uncertainties

As many of the physical models and plant parameters included in the ASTRUM EM uncertainty analysis are related to short-term LOCA analysis, they are not considered in the GSI-191 HLB EM. The response to RAI-4.28 identifies the important physical models and parameters considered by the ASTRUM EM that should be considered in the GSI-191 HLB EM uncertainty assessment. The important physical models and parameters are consistent with those identified by the PIRT provided in Step 4.

Table RAI-4.7-1 summarizes the physical models and plant parameters considered in the GSI-191 EM uncertainty assessment. The extrapolation of WCOBRA/TRAC for use in the LTCC phase of the post-LOCA transient has been accounted for by applying conservative bias to important parameters such that the uncertainty associated with the modeling of important phenomena is bounded. The impact of the applied conservative biases was determined to be acceptable by making additional comparisons to applicable experimental data and performing sensitivity studies. Based on the results of these data comparisons and sensitivity studies, it is concluded that the predicted results are bounding of best-estimate performance. Therefore, the result demonstrates with a high level of probability that the 10 CFR 50.46 long-term cooling acceptance criteria are met, and it is concluded that the GSI-191 HLB EM is adequate.

Table RAI-4.7-1 Physical models and plant parameters considered in GSI-191 uncertainty assessment

Physical Models	Plant Parameters
Core mixture level	Alternate flow path resistance
Upper plenum drain distribution and mixture level	Decay heat
	Debris accumulation rate
Single-phase vapor heat transfer coefficient	Core power and distribution
	Sump switchover time
	Safety injection water flow rate and temperature

Base Plant Models for Sensitivity Studies

The base plant model selected for the Westinghouse upflow analysis is a high-power, four-loop plant with a T-hot upper head configuration. The base plant model was developed for BE PCT and clad oxidation analysis. Since the base plant model was developed for BE analysis, many of the model non-critical inputs are set to nominal values. For this reason, some changes were made to bias the model toward an Appendix K analysis. Doing so has added conservatism to the model to account for uncertainties associated with the LTCC phase of the post-LOCA transient.

The base plant model selected for the Westinghouse downflow analysis is a high-power, three-loop plant with a T-hot upper head configuration. The base plant model was developed for BE PCT and clad oxidation analysis. Since the base plant model was developed for BE analysis, many of the model inputs are set to nominal values. For this reason, some changes were made to bias the model toward an Appendix K analysis. Doing so has added conservatism to the model to account for uncertainties

associated with the LTCC phase of the post-LOCA transient.

The model changes made for the GSI-191 analyses are described in the response to RAI-4.29. The baseline simulation cases used for the sensitivity studies are described in Section 8 and 9 of WCAP-17788, Volume 4.

Decay Heat Sensitivity

Sensitivity studies using Westinghouse upflow plant Case 1B and downflow plant Case 1A to show the sensitivity to the decay heat model have been completed. The sensitivity matrix is shown in Table RAI-4.7-2.

Table RAI-4.7-2 Decay Heat Sensitivity Study

Case	Decay Heat Model	Plant Model
Case 1B (base case)	ANSI/ANS 1971 + 20%	Upflow
1	ANS 5.1-1979 Nominal	Upflow
Case 1A (base case)	ANSI/ANS 1971 + 20%	Downflow
1	ANS 5.1-1979 Nominal	Downflow

A comparison of the ANSI/ANS 1971 + 20% (Appendix K) and the ANS 5.1-1979 nominal decay heat models is shown in Figure RAI-4.7-11. The upflow plant sensitivity results for PCT prediction, core average collapsed level, downcomer collapsed liquid level, and reactor vessel water mass are shown in Figure RAI-4.7-12 through Figure RAI-4.7-15. The downflow plant sensitivity results for PCT prediction, core average collapsed level, downcomer collapsed liquid level, and reactor vessel water mass are shown in Figure RAI-4.7-16 through Figure RAI-4.7-19.

Figure RAI-4.7-12 and Figure RAI-4.7-16 show that the recirculation phase PCT sensitivity for both plant types is considerably different using the ANS 1979 model. The debris-induced heatup is eliminated when modeling a nominal value of decay heat relative to the Appendix K prescribed model. Figure RAI-4.7-13 and Figure RAI-4.7-17 show that the core average collapsed liquid level (CLL) is affected by the decay heat model. This is expected since the lower nominal decay heat generates less void in the core thus resulting in a higher core average CLL. The downcomer CLL shown in Figure RAI-4.7-14 and Figure RAI-4.7-18 is only affected to the degree necessary to balance the CLL in the core. The reactor vessel water mass shown in Figure RAI-4.7-15 and Figure RAI-4.7-19 are only affected to the extent expected due to the higher core and downcomer CLLs for the nominal decay heat model.

The results of this sensitivity show that the debris-induced heatup that occurs following the application of complete core inlet blockage is virtually eliminated when a nominal decay heat model is applied. The results also demonstrate that the system response to reduced decay heat is as expected. Reduced decay heat results in less boiling and an increased reactor vessel liquid inventory.

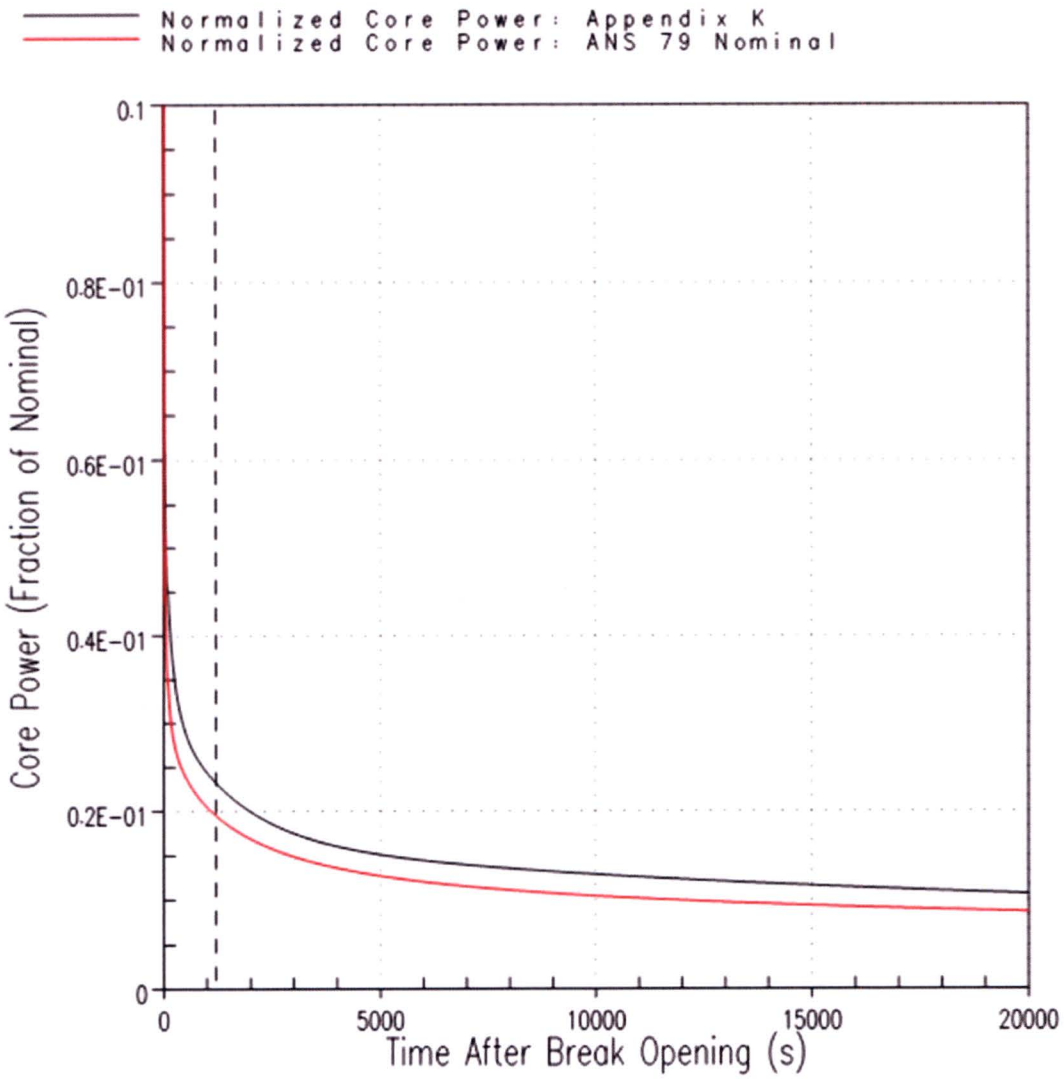

Figure RAI-4.7-11 Decay Heat Sensitivity Normalized Core Power Comparison

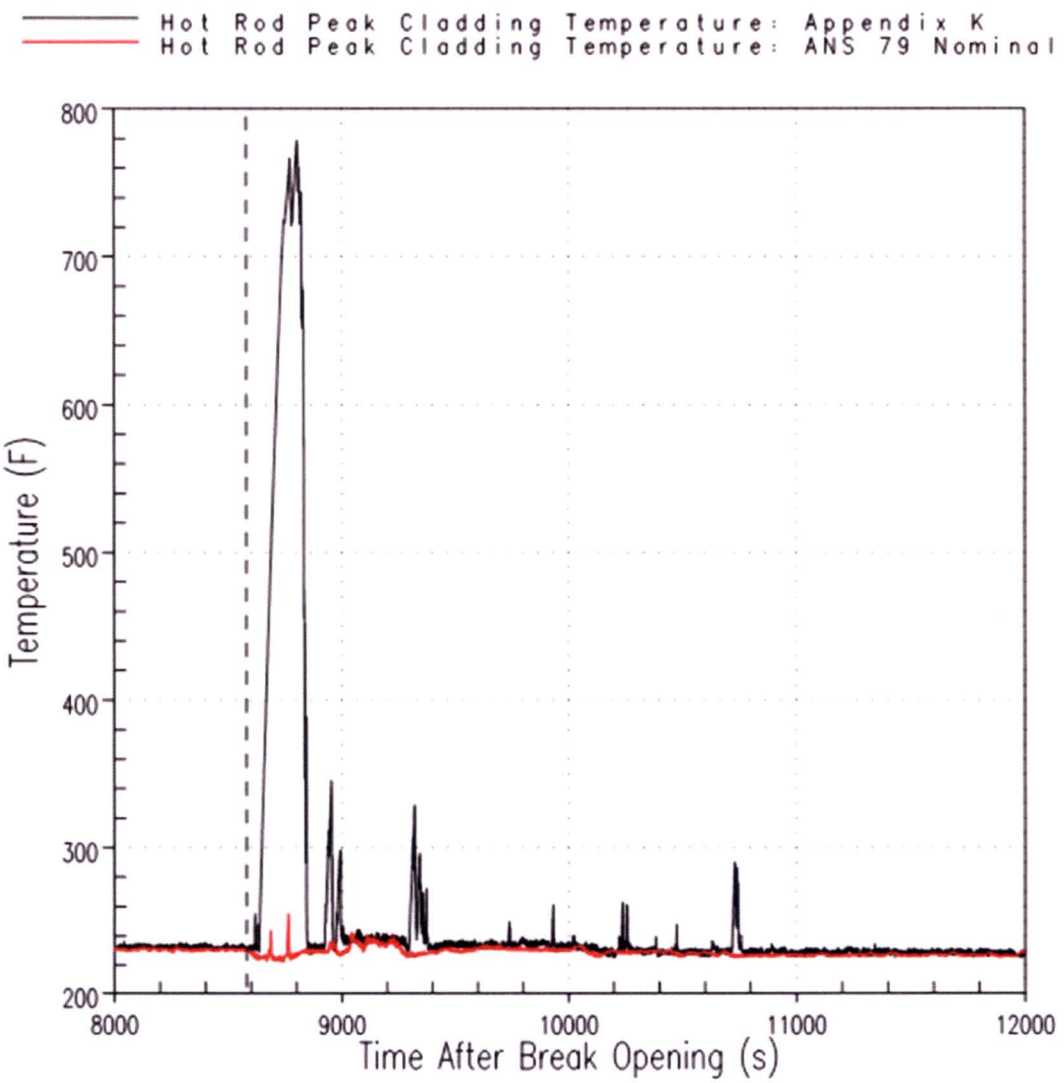

Figure RAI-4.7-12 Westinghouse Upflow Plant Decay Heat Sensitivity PCT Results

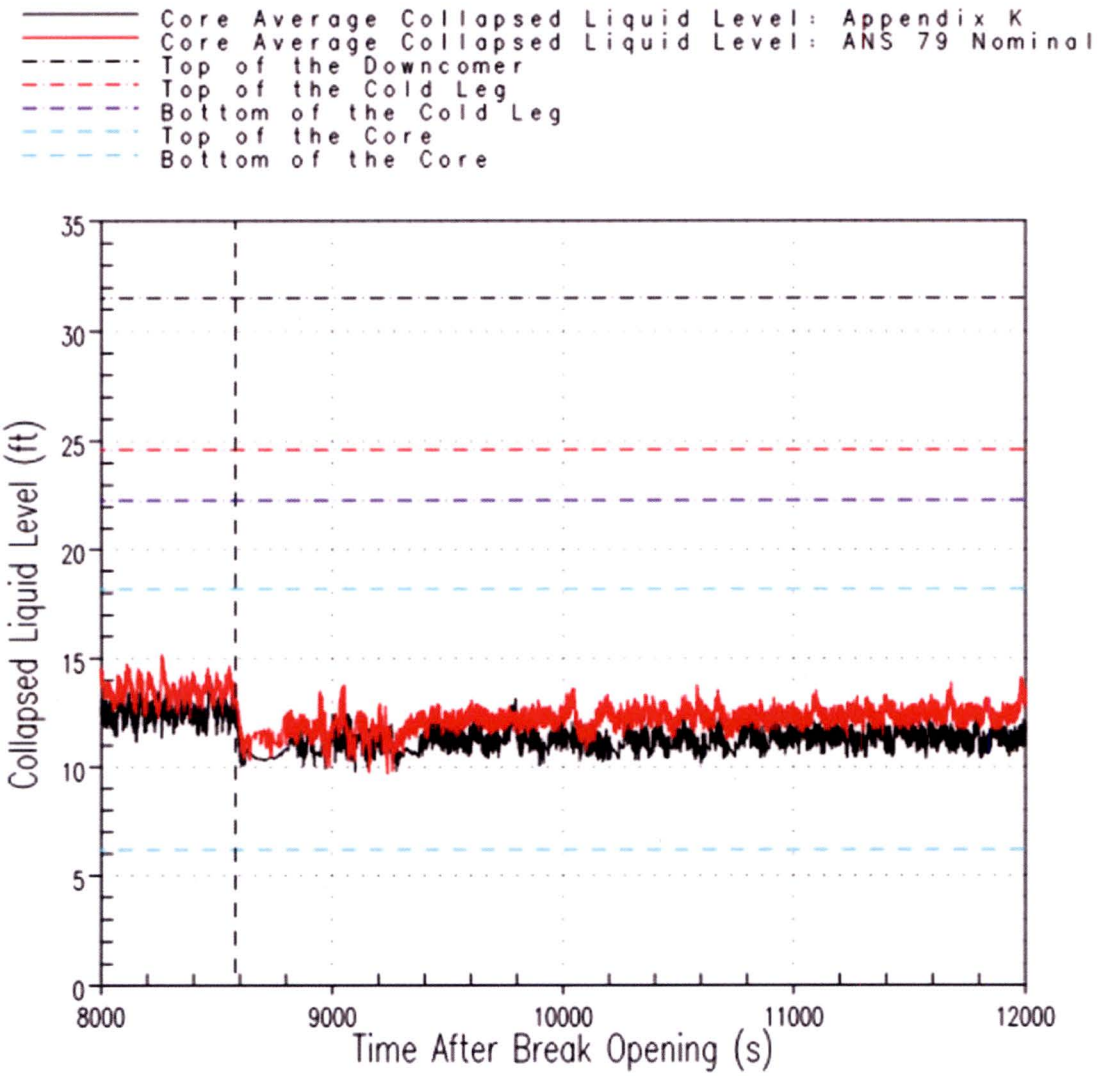

Figure RAI-4.7-13 Westinghouse Upflow Plant Decay Heat Sensitivity Core Average Collapsed Liquid Level Results

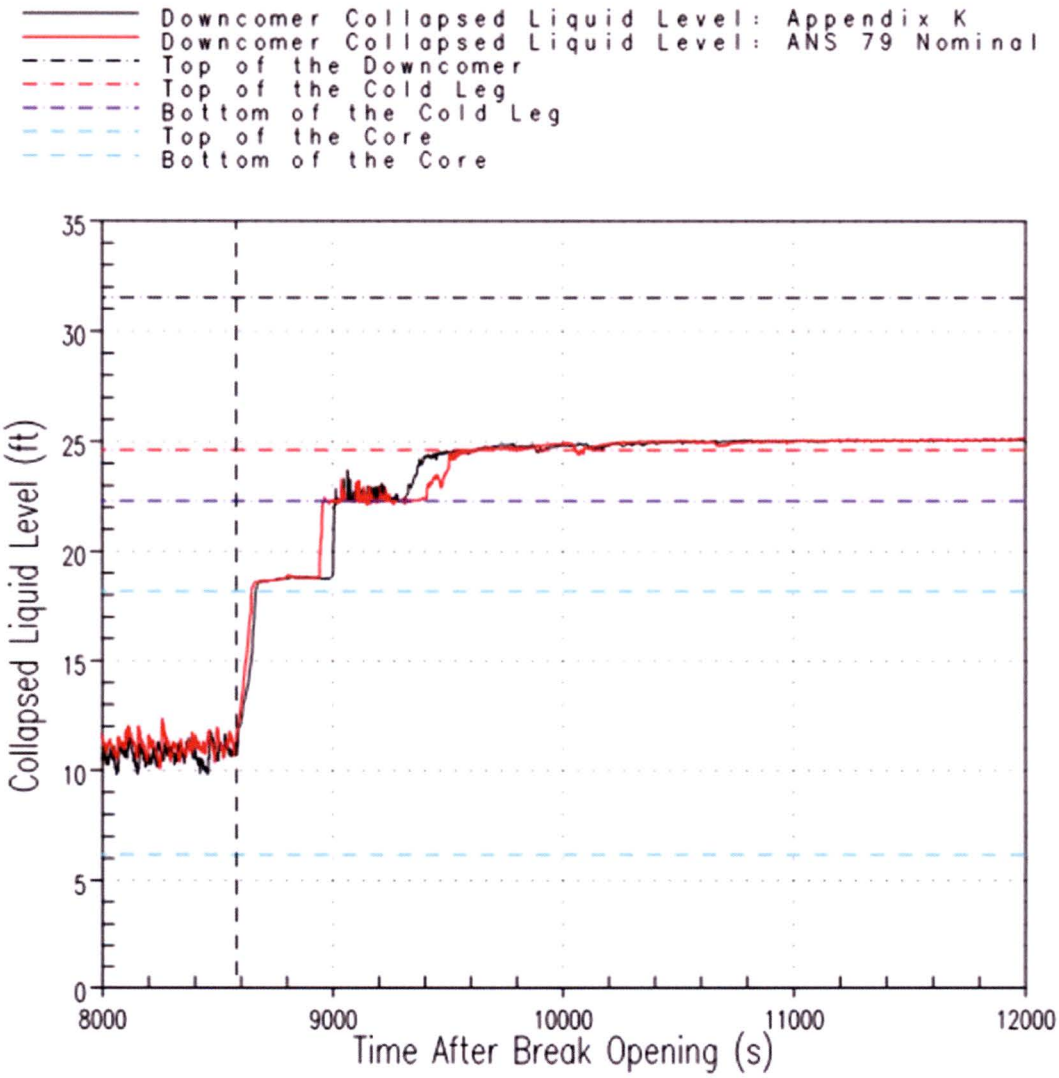

Figure RAI-4.7-14 Westinghouse Upflow Plant Decay Heat Sensitivity Downcomer Collapsed Liquid Level Results

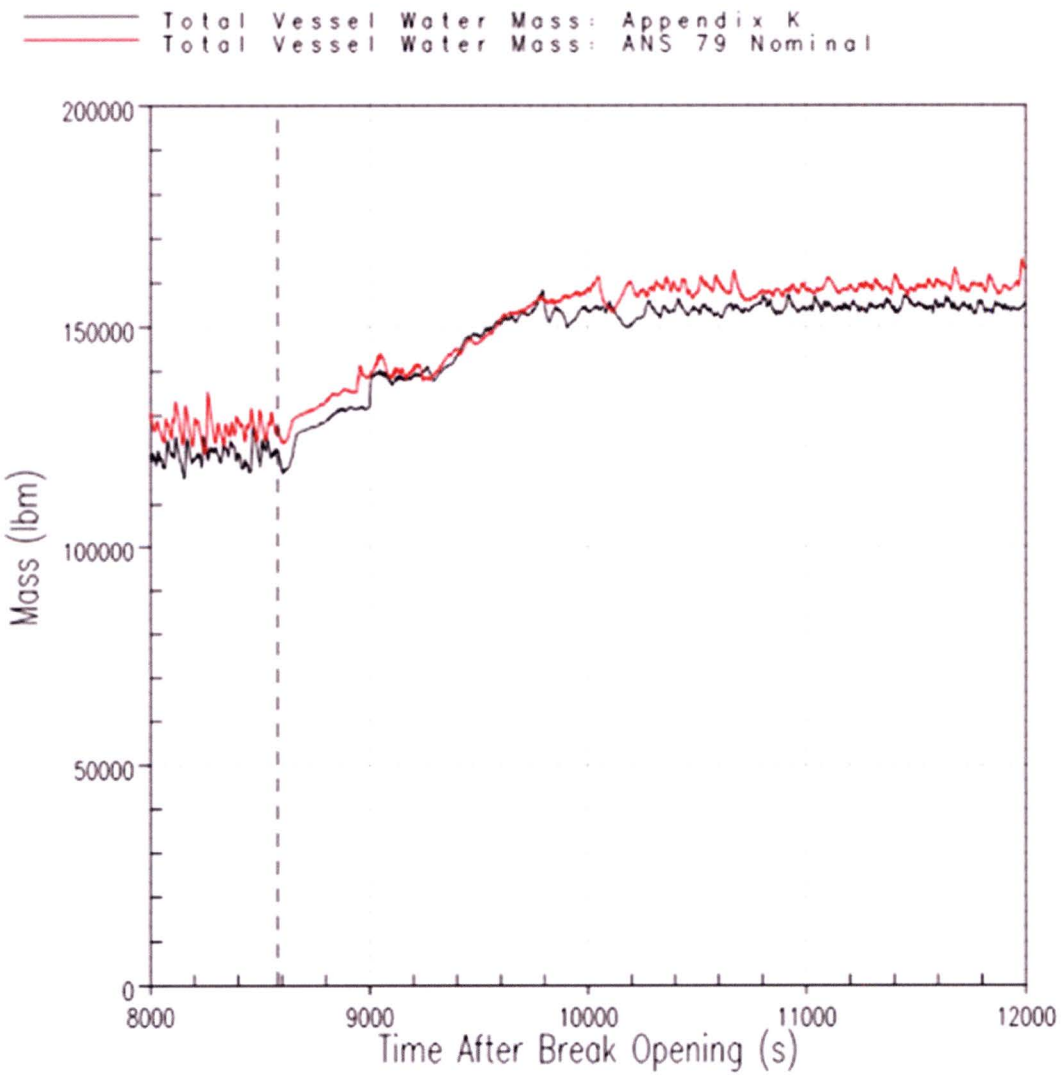

Figure RAI-4.7-15 Westinghouse Upflow Plant Decay Heat Sensitivity Reactor Vessel Water Mass Results

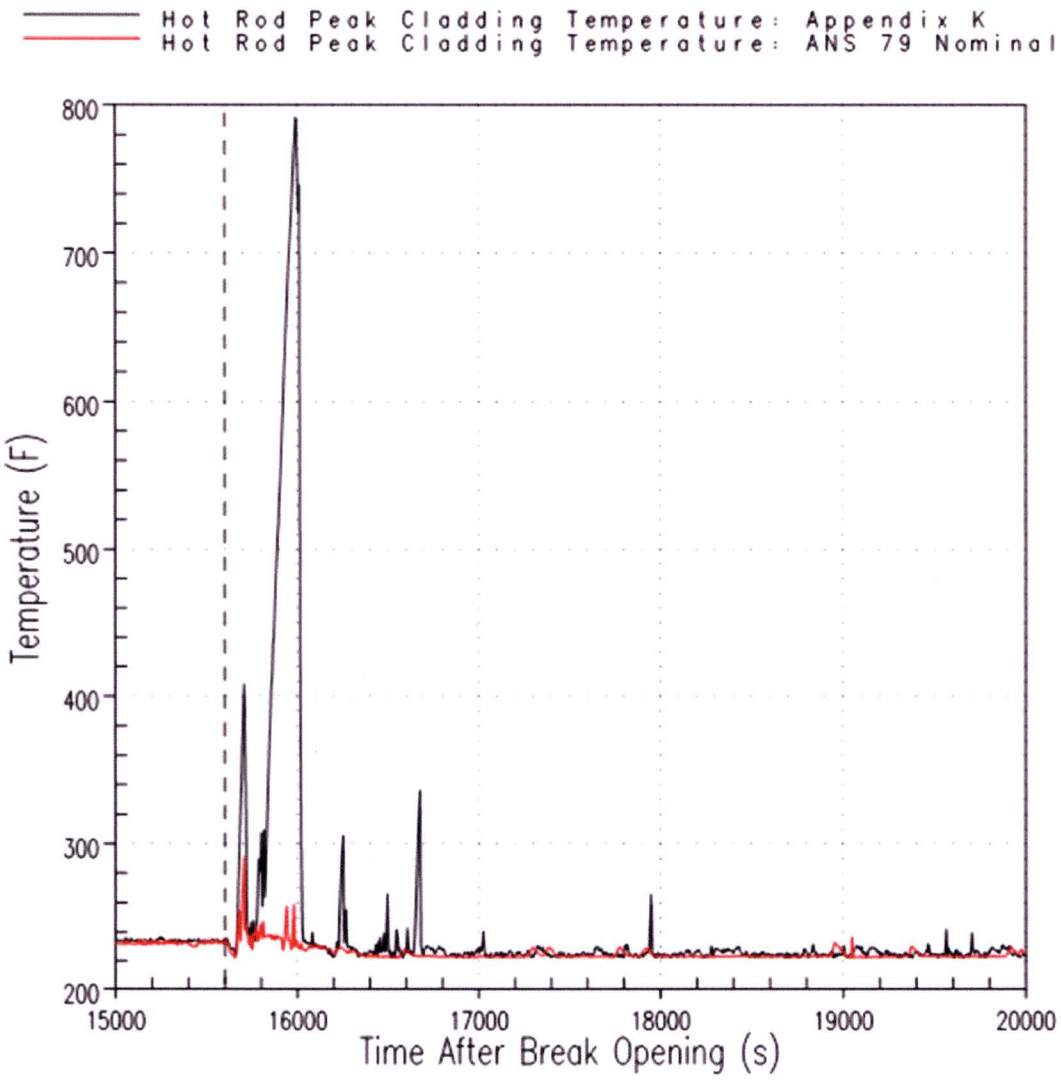

Figure RAI-4.7-16 Westinghouse Downflow Plant Decay Heat Sensitivity PCT Results

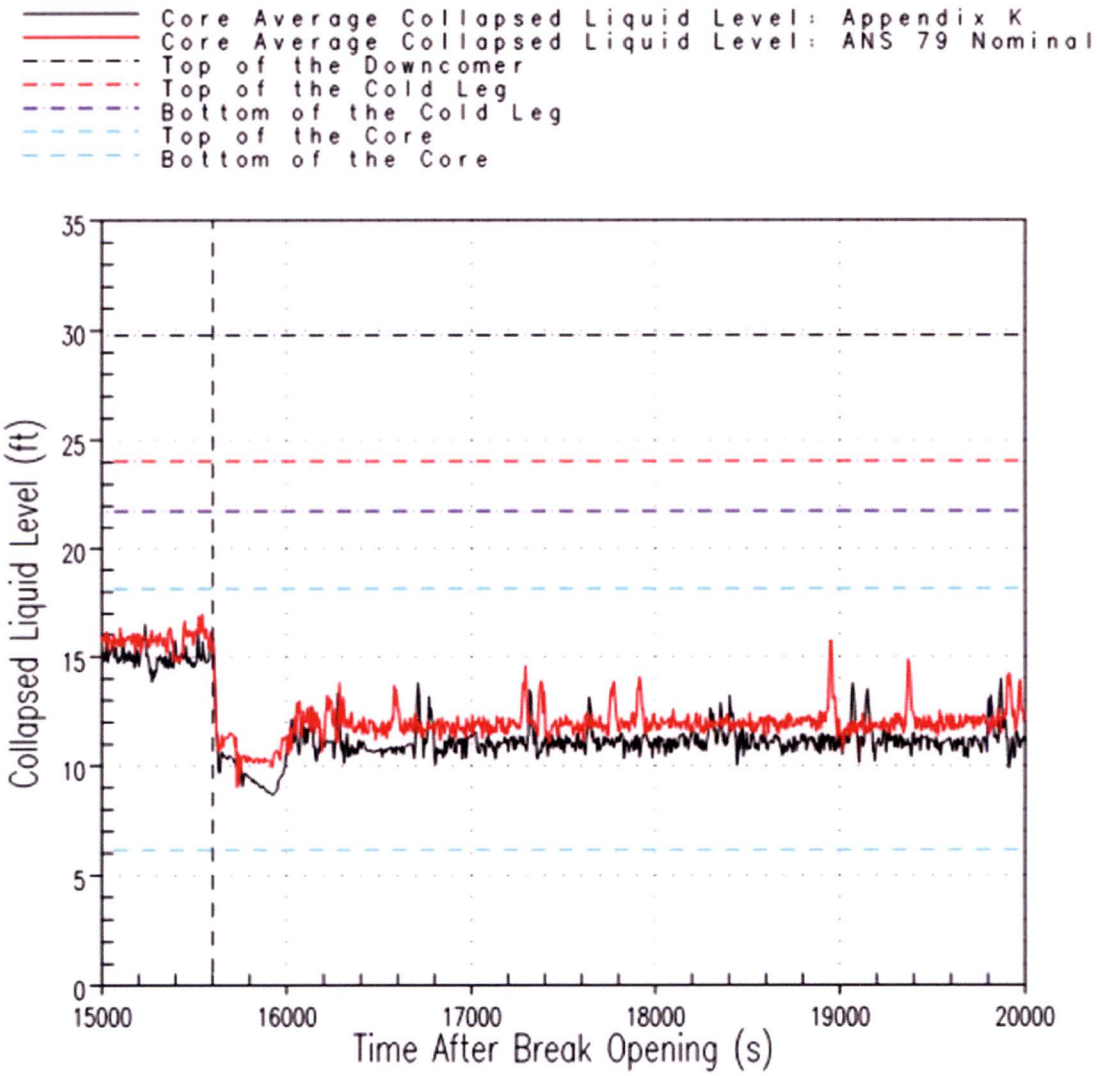

Figure RAI-4.7-17 Westinghouse Downflow Plant Decay Heat Sensitivity Core Average Collapsed Liquid Level Results

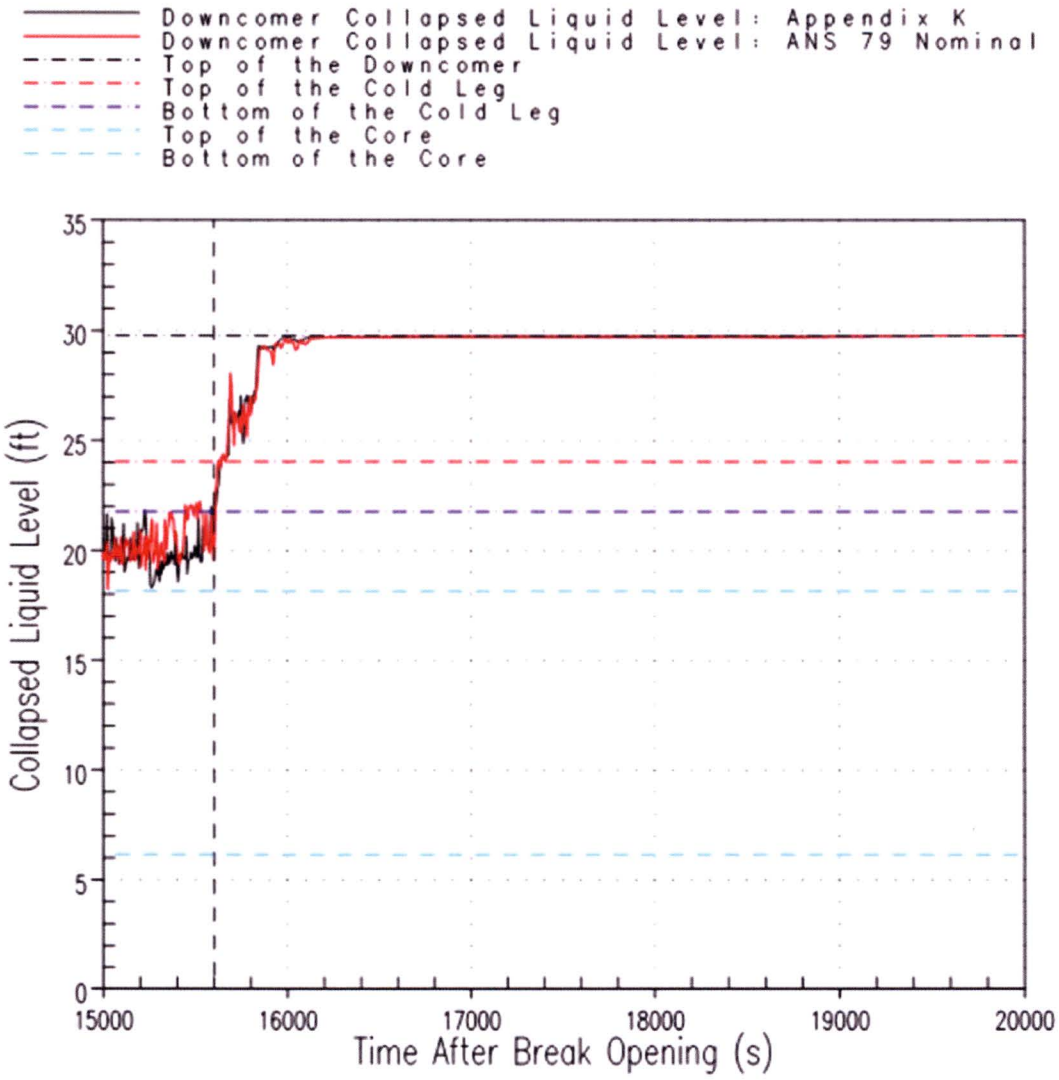

Figure RAI-4.7-18 Westinghouse Downflow Plant Decay Heat Sensitivity Downcomer Collapsed Liquid Level Results

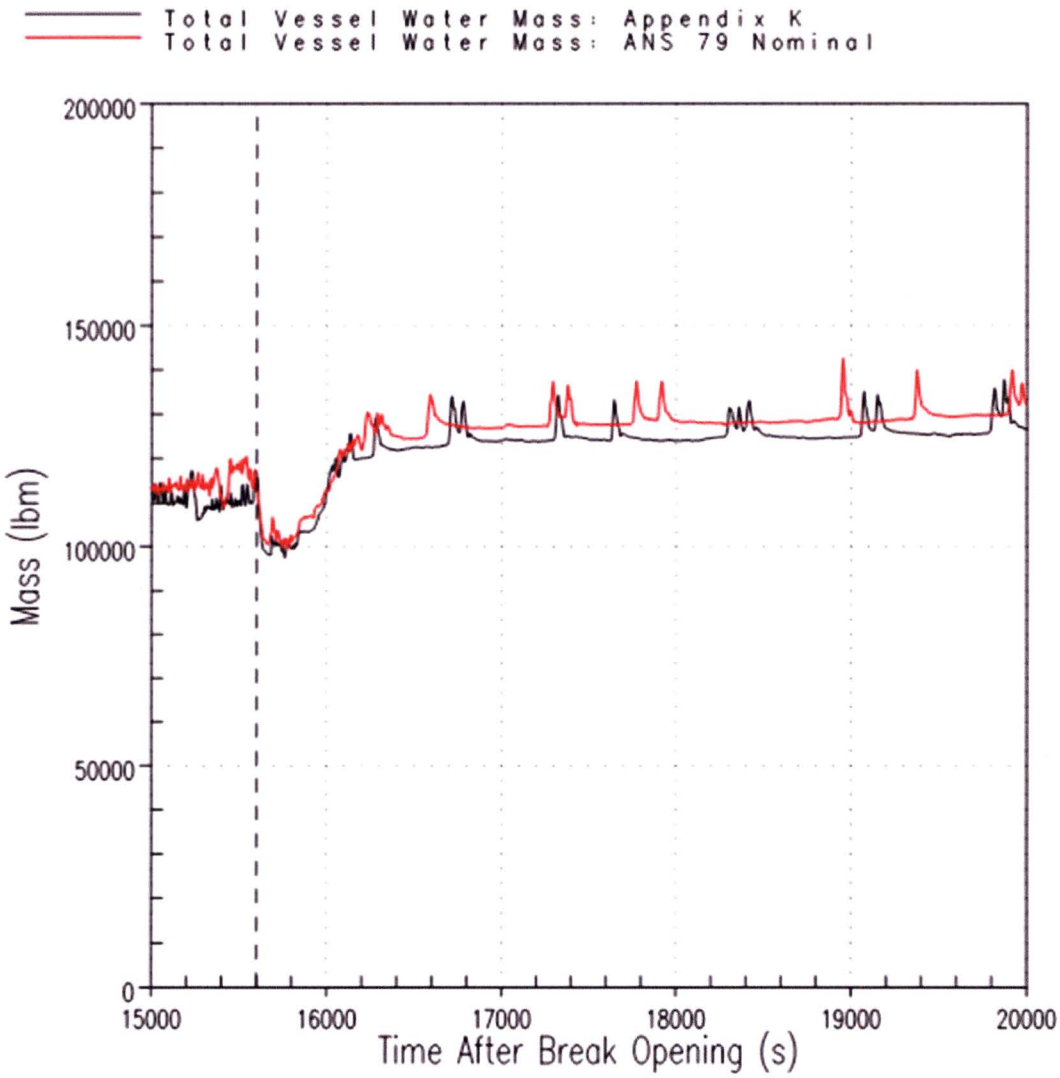

Figure RAI-4.7-19 Westinghouse Downflow Plant Decay Heat Sensitivity Reactor Vessel Water Mass Results

Debris Accumulation Rate Study

Results from a debris accumulation rate sensitivity study are presented to quantify the conservatism contained in the method used to define the core inlet debris limit. The sensitivity is performed using a Westinghouse upflow barrel/baffle plant model and the debris limits presented are applicable to a Westinghouse upflow plants fueled with Westinghouse fuel.

Figure RAI-4.7-20 shows the core inlet resistance transient for two cases; instantaneous blockage and gradual blockage. The instantaneous blockage case is the simulation used to determine the WCAP-17788 methodology parameter defined as K_{max}. At 1200 seconds, which is the time ECCS alignment to the containment sump is assumed to occur, the core inlet resistance is ramped over a 1 minute period (defined as instantaneously) from K = 0 to $5.5x10^5$. This stepwise approach to core inlet resistance is non-realistic, and is applied such that any, more gradual, realistic accumulation rate of debris will be bounded. When compared to head loss testing results, this dimensionless resistance equates to 50.6 grams per fuel assembly (g/FA) of fiber for Westinghouse upflow plants fueled with Westinghouse fuel. This is the core inlet debris load limit used by the WCAP-17788 methodology for the hot leg break scenario.

Also shown in the figure is a gradual core inlet debris transient, which is more realistic in terms of the timing of debris arrival at the core inlet. At 1200 seconds a linear ramp is applied to the core inlet dimensionless resistance. After two hours, the linear ramp is terminated at a resistance of $4x10^6$. Based on extrapolation of the head loss test data, this dimensionless resistance equates to approximately 163 g/FA of fiber, or over 3 times the debris limit defined for this plant category.

Figure RAI-4.7-21 shows debris-induced heatup results from the two simulations. The acceptance criterion for successful results is PCT < 800°F. As the figure shows, both simulations meet the acceptance criterion; however, the PCT trends observed in the figure are different. In the instantaneous blockage case, a short duration secondary heatup is predicted to occur shortly after the application of core inlet resistance. This heatup is due to a lack of flow reaching the core and core wide dryout and uncovery extending roughly one-quarter into the heated core. Flow through the simulated core inlet debris bed, and through the barrel/baffle channel, is governed by the available driving head in the downcomer. At 1200 seconds when the stepwise core inlet resistance is applied, the downcomer driving head is not sufficient to supply flow in excess of boil-off through the core inlet and/or barrel/baffle channel. As such, the coolant inventory in and above the heated core boils and the core uncovers from the top down. As the transient progresses, coolant supplied by the ECCS fills the downcomer, and eventually sufficient driving head exists to recover the core coolant inventory such that the cladding temperature returns to levels just above the liquid saturation temperature. This trend in PCT is a result of the bounding nature in which core inlet resistance is applied.

In the case of gradual application of core inlet resistance, no core-wide uncovery occurs and the short duration heatups predicted are due to localized dryout at the peak power location. These heatups are shown to be less than 500°F, or approximately 300°F below the acceptance criterion. In this case, a core-wide uncovery does not occur because the downcomer is able to fill as the resistance at the core inlet builds gradually. As such, there is always coolant flow in excess of boil-off reaching the core. This is a better representation of a realistic transient and can be used to quantify the conservatism, or margin, associated with the core inlet debris limit defined for the WCAP-17788 in-vessel hot leg break

methodology. Not only is the acceptable core inlet debris load predicted by this gradual ramp rate more than 3 times higher than the defined limit, but the predicted PCT is more than 300°F below the 800°F acceptance criterion.

A sensitivity that considers core inlet resistance ramp rate was also completed using the downflow plant model, as described in the response to RAI-4.19. In the downflow plant sensitivity, the core inlet resistance ramp rate was increased from 1 minute to 5 minutes, and the resistance was ramped to the same final value. The study demonstrated similar behavior with regard to the debris-induced heatup. A slower ramp rate allows the downcomer to fill coincident with the buildup of resistance such that a significant core uncovery is not predicted to occur.

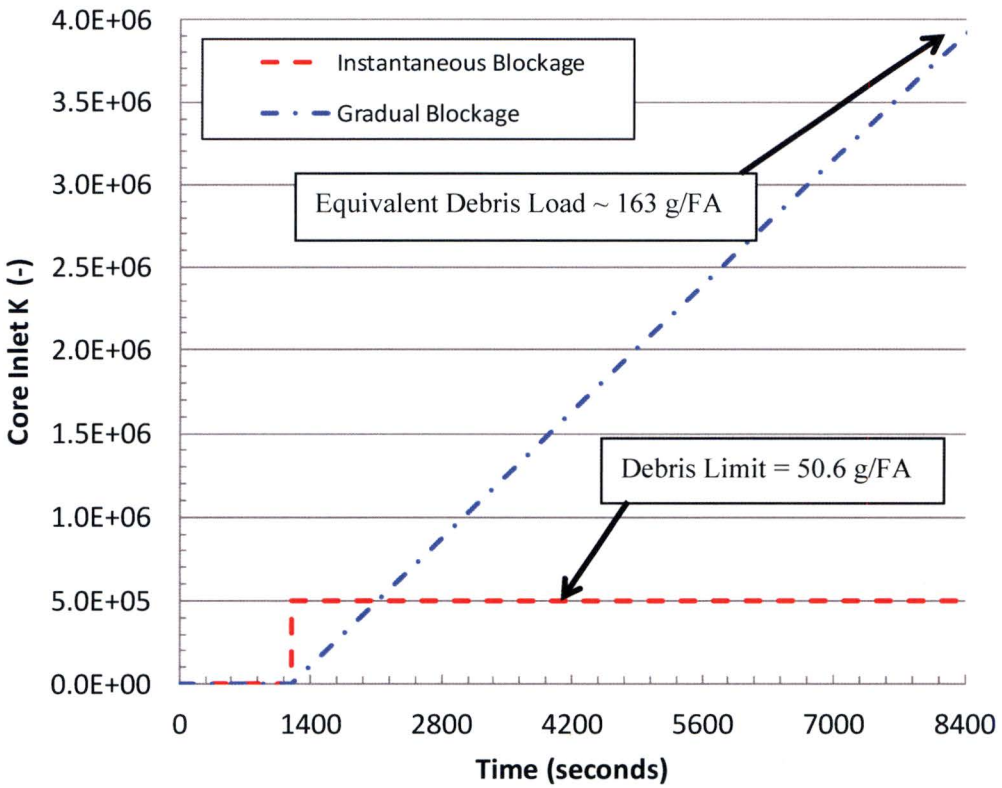

Figure RAI-4.7-20 Core inlet resistance transients from Westinghouse upflow plant analysis: instantaneous blockage case used to determine debris limit versus realistic gradual blockage case

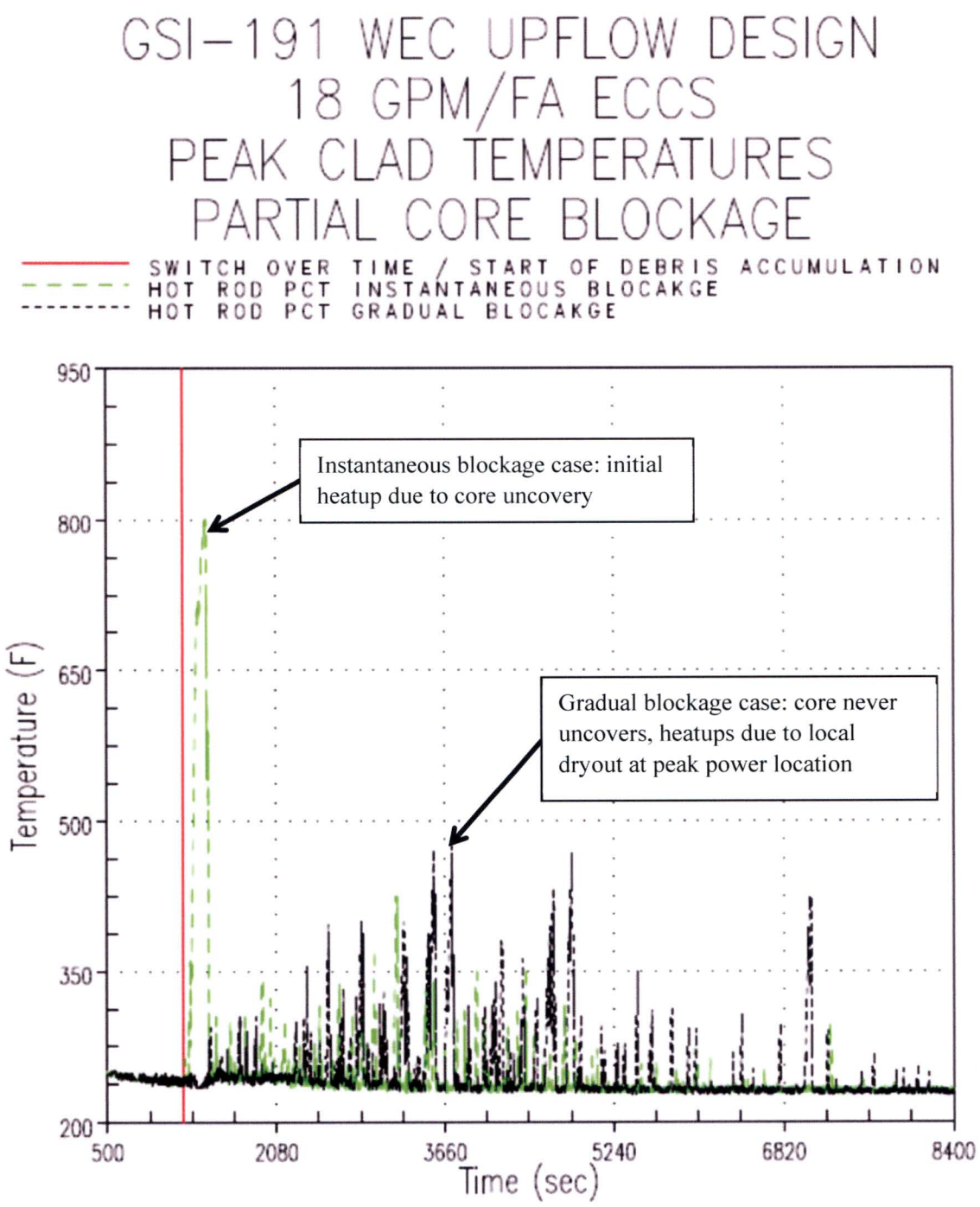

Figure RAI-4.7-21 Peak clad temperature results from Westinghouse upflow plant analysis: instantaneous blockage case used to determine debris limit versus realistic gradual blockage case

Non-Condensable Gas Effects

The cyclic heatup/cooldown behavior following the application of core inlet blockage (K_{max}) in the Westinghouse downflow plant model has been identified and is related to the treatment of non-condensable (NC) gas in WCOBRA/TRAC. The Westinghouse downflow plant model responds differently than the Westinghouse upflow plant model during the accumulator injection phase of the transient, which impacts the response to core inlet blockage. In the downflow plant simulations, the intact loop seals fill with liquid prior to sump recirculation. In the upflow plant simulations, the intact loop seals remain mostly voided until core inlet resistance is applied. It is postulated that open loop seals allow a vent path for nitrogen gas injected from the accumulators to escape the system. In the downflow plant simulation, the plugged loop seals effectively trap nitrogen gas in the downcomer, which impacts the vessel fluid inventory and the response to core inlet resistance. The following observations are made from the downflow K_{max} plant simulations:

- The downcomer and core levels do not agree. The presence of nitrogen in the downcomer suppresses the liquid level, which increases the core liquid inventory.
- When core inlet resistance is applied at sump recirculation (K_{max} case), spurious liquid flow at the core inlet is observed. Periodic increases in the core inlet flow correspond to the cooldown behavior observed in the debris-induced PCT response.

The observations may be a result of logic in the simplified NC gas model in the code and may not be physical. WCOBRA/TRAC simplifies the modeling of NC gas by treating the vapor phase as all NC gas or all steam based on the subcooling of the vapor phase. WCOBRA/TRAC also does not have capabilities to model stratified flows accurately in the loop components, which could also be leading to the observed behavior. To complicate matters, there is no applicable experimental data to establish the expected system response for this post-LOCA scenario. Specifically, the effect that NC gas has on the system response following core inlet blockage and the transport and venting behavior during the GSI-191 large hot leg break scenario.

To better understand the NC gas effect, Westinghouse performed simulations in which the accumulator nitrogen gas was removed from the models. The accumulators were modeled as a FILL component so that the liquid injection could be modeled without the presence of nitrogen. Simulation results confirmed that if the intact loop seals plug, nitrogen gas in the downcomer tends to suppress the downcomer liquid level and increase the core liquid inventory prior to sump switchover. Under this condition, the application of core inlet blockage results in a less severe debris-induced PCT. It has been determined that this effect does not significantly impact the Westinghouse upflow plant analysis because the intact loop seals do not plug and nitrogen gas can vent from the system. It has also been determined that the downflow t_{block} analysis is not adversely impacted because the NC gas effect diminishes as the transient extends longer into long-term core cooling. The downflow plant K_{split} and m_{split} analyses are also not adversely impacted because of the slower application of core inlet blockage in these cases does not result in a debris-induced heatup. Since it has been determined that not including accumulator nitrogen gas in the downflow K_{max} analysis results in a more severe debris-induced heatup, a reanalysis is performed to define a new value of K_{max} which meets the PCT acceptance criteria of 800°F. The Westinghouse downflow plant category K_{max} (Case 2B) analysis results documented in WCAP-17788, Volume 4 will be updated to reflect the reanalysis. WCAP-17788, Volume 1 will also be updated to reflect the revised K_{max} value and acceptable core inlet debris loadings for the Westinghouse downflow plant category. The

reanalysis is described below.

Westinghouse Downflow Plant Category K_{max} Reanalysis

The Westinghouse downflow plant category K_{max} reanalysis (Case 2B) applies a core inlet resistance of $4.75x10^5$. The original K_{max} analysis applied a value of $6x10^5$. The accumulators are modeled as FILL components and the UHSN resistance is increased to bound all plants as described in the response to RAI-4.2. The reanalysis results meet the WCAP-17788, Volume 4 acceptance criteria.

Figure RAI-4.7-22 shows the mass flow rate in one of the accumulator lines. As the figure shows, the case without accumulator nitrogen injection reasonably represents the liquid mass injection from the accumulator. The mass flow rate in the other two accumulator lines is similar.

Figures RAI-4.7-23 and RAI-4.7-24 show the void fraction in the horizontal section of an intact loop crossover leg and the broken loop crossover leg, respectively. As shown in Figure RAI-4.7-23, the intact crossover legs remain voided until after the application of core blockage when nitrogen from the accumulators is not included in the model. As shown in Figure RAI-4.7-24, the broken loop crossover leg in the original simulation has a short period after accumulator injection in which nitrogen from the accumulators is venting, as indicated by the non-zero void fraction.

The debris-induced PCT is shown in Figure RAI-4.7-25, and shows that the debris-induced heatup behavior is less oscillatory than the original analysis. The reanalysis debris-induced PCT is also more severe, but meets the PCT acceptance criterion of 800°F with the reduced core inlet resistance.

The downcomer and hot assembly channel collapsed liquid levels are shown in Figures RAI-4.7-26 and RAI-4.7-27, respectively. Not modeling nitrogen from the accumulators eliminates the downcomer liquid suppression prior to sump recirculation. It takes longer for the downcomer to fill above the cold leg elevation in the simulation without nitrogen gas because the intact loop seals need to fill. The hot assembly collapsed liquid level is significantly lower in the simulation without nitrogen from the accumulators during the injection phase and at the time of sump switchover. This indicates that the core liquid inventory is less at the time core inlet blockage is applied, which can explain why the debris-induced PCT is impacted.

The results from this simulation resolve the issues observed in the original K_{max} simulation and result in a more limiting debris-induced heatup. The revised simulation uses a higher UHSN resistance, which bounds all downflow plants. The core inlet debris limit is lower, as shown in Table RAI-4.7-3.

Table RAI-4.7-3 Downflow Plant Revised Core Inlet Debris Limits

Fuel Type	Original K_{max}	Debris Limit (g/FA)	Revised K_{max}	Debris Limit (g/FA)
Westinghouse Fuel	$6x10^5$	54.3	$4.75x10^5$	49.6
AREVA Fuel		20.9		20.4

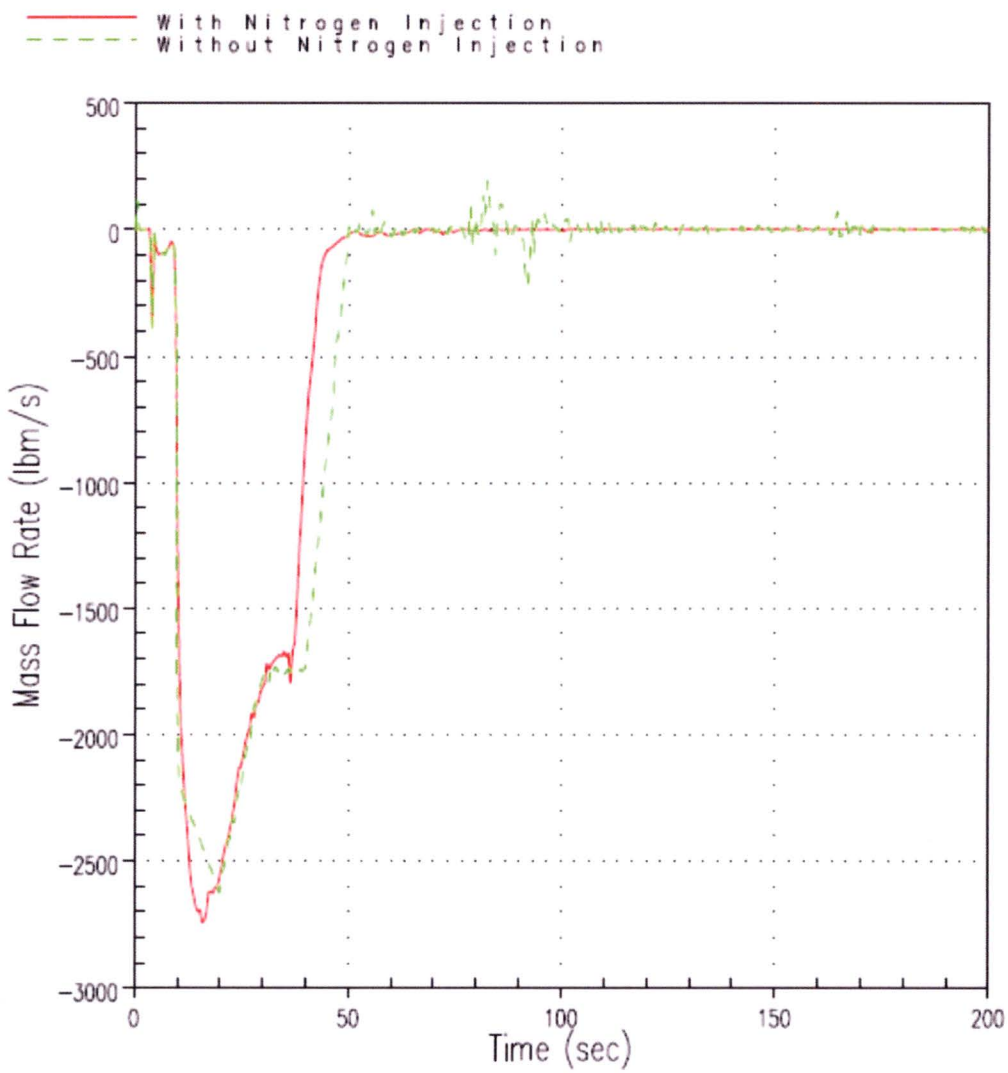

Figure RAI-4.7-22 Mass Injection from One Accumulator

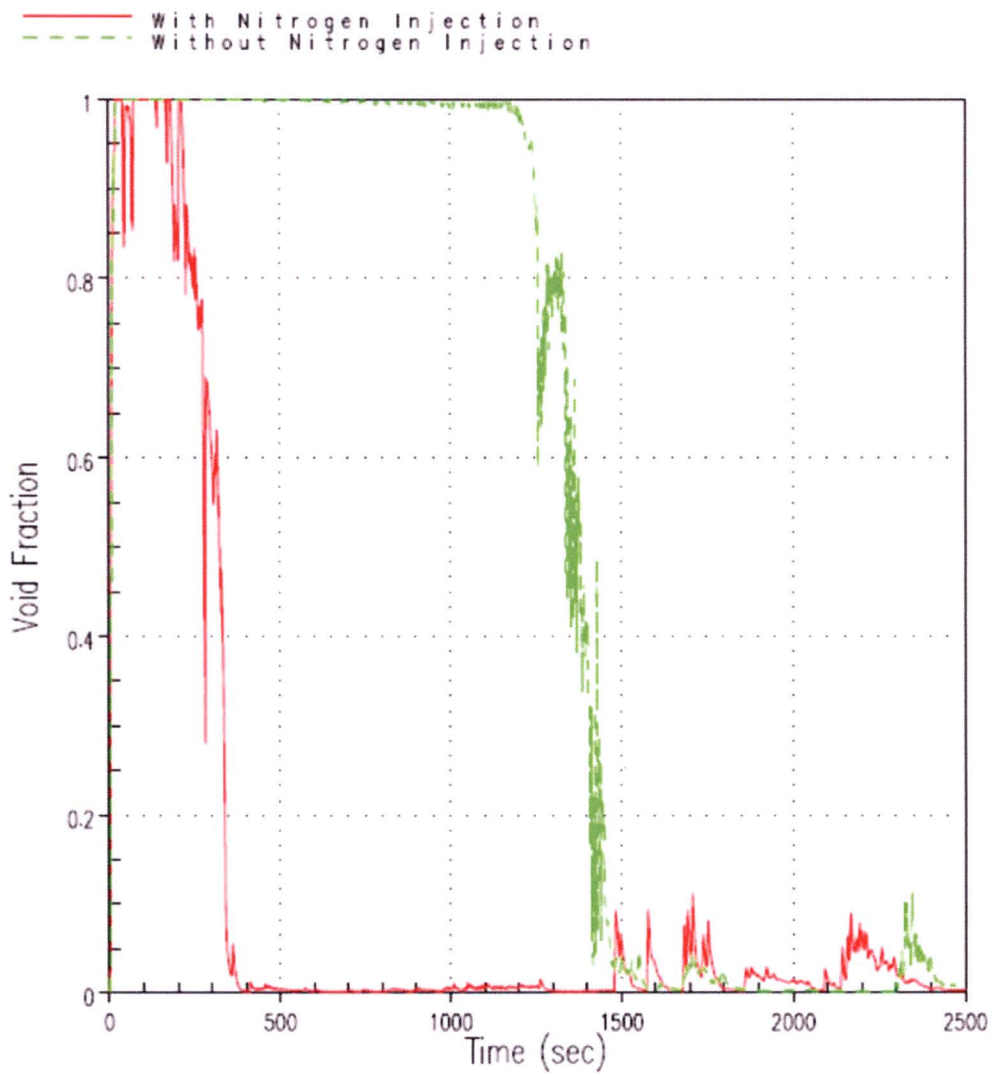

Figure RAI-4.7-23 Void Fraction in the Horizontal Section of an Intact Loop Crossover Leg

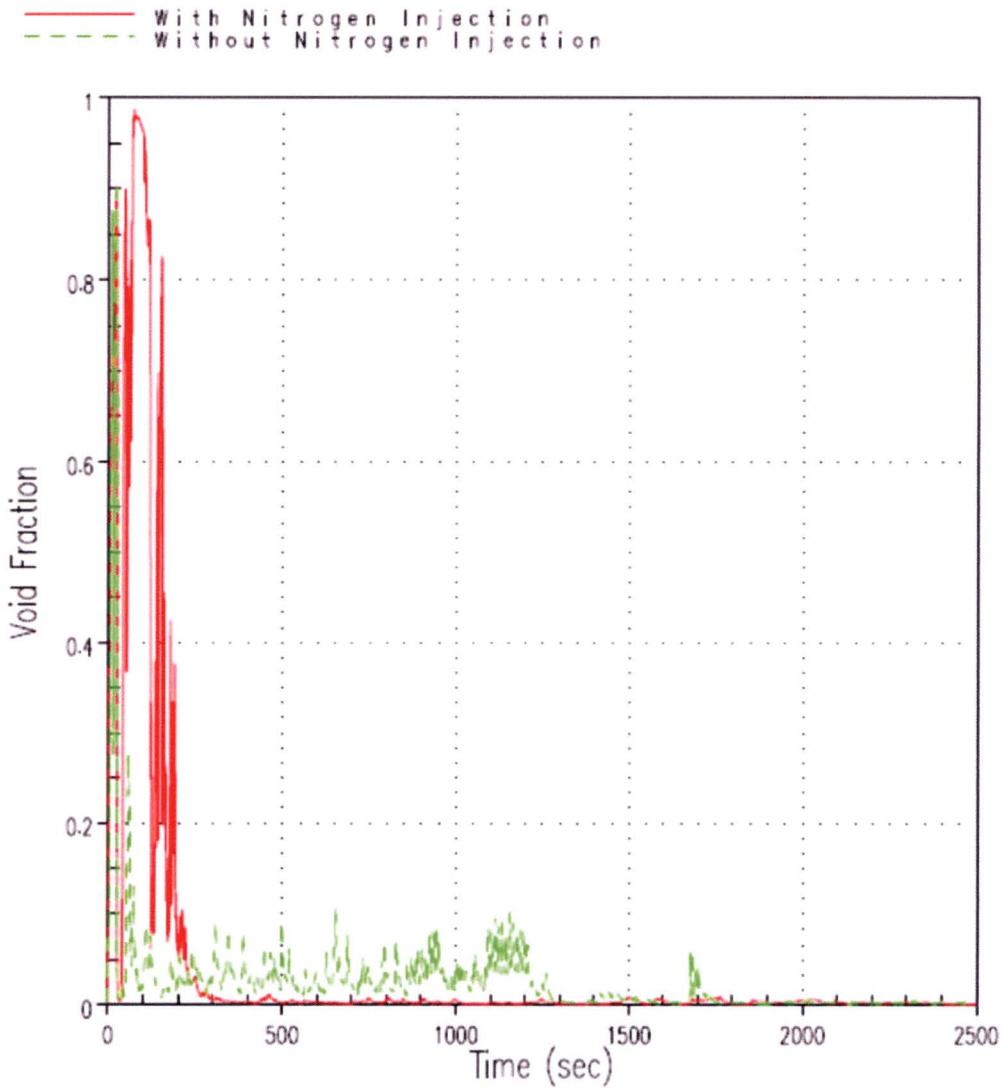

Figure RAI-4.7-24 Void Fraction in the Horizontal Section of the Broken Loop Crossover Leg

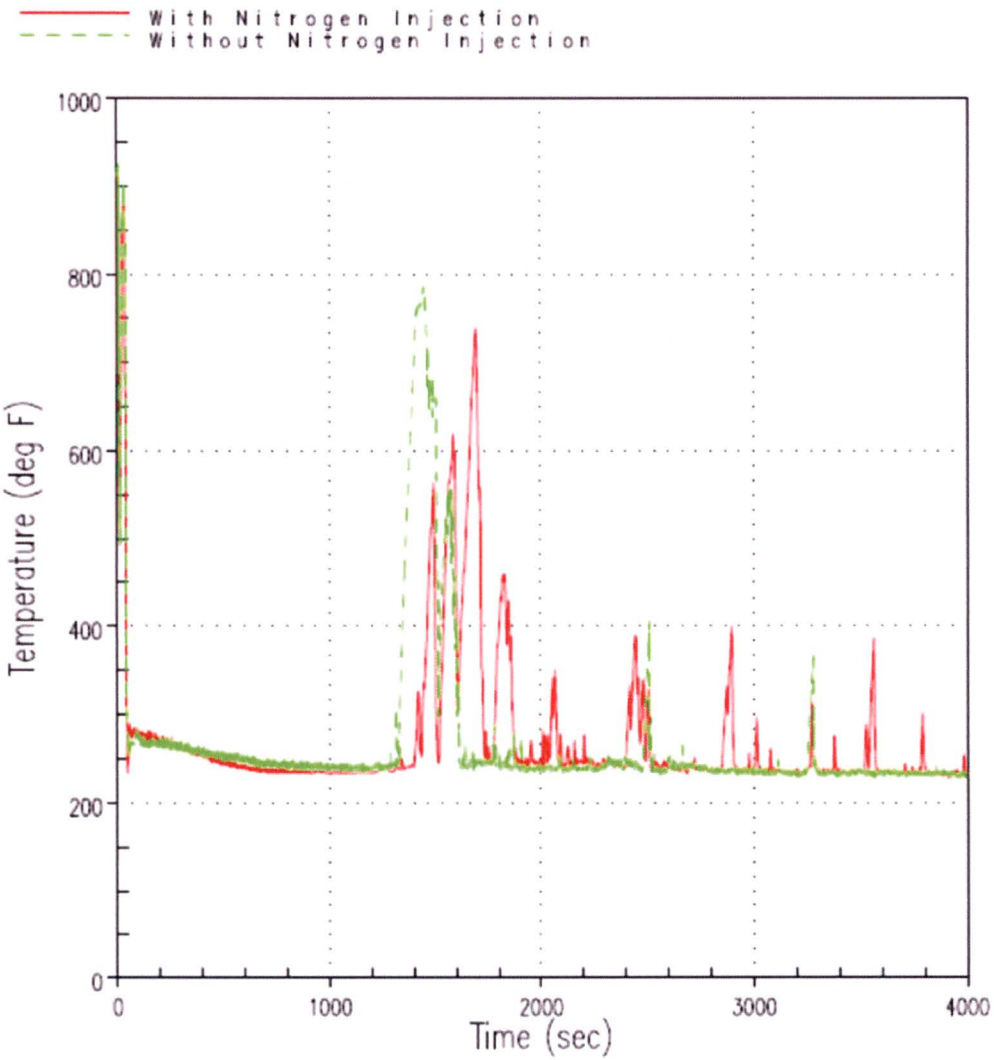

Figure RAI-4.7-25 Debris-Induced PCT Response

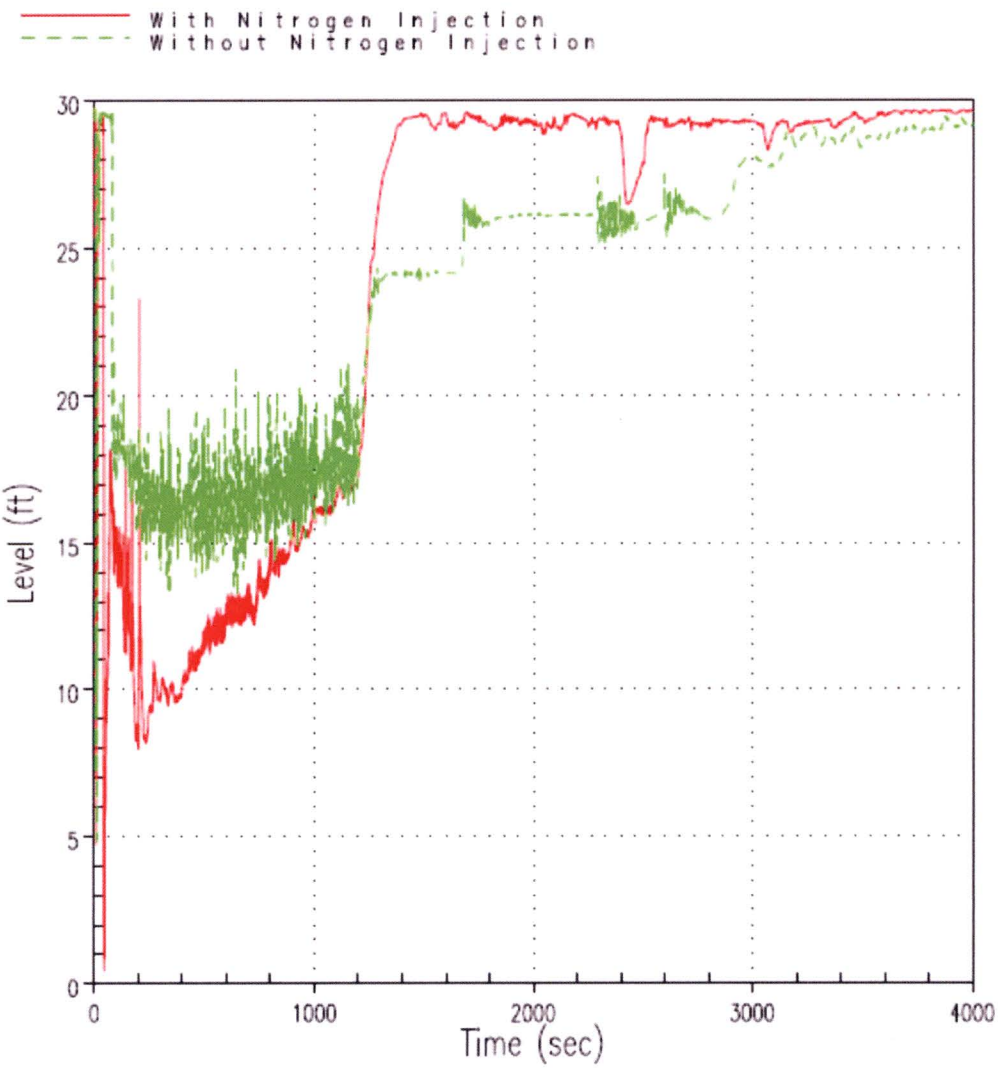

Figure RAI-4.7-26 Downcomer Collapsed Liquid Level

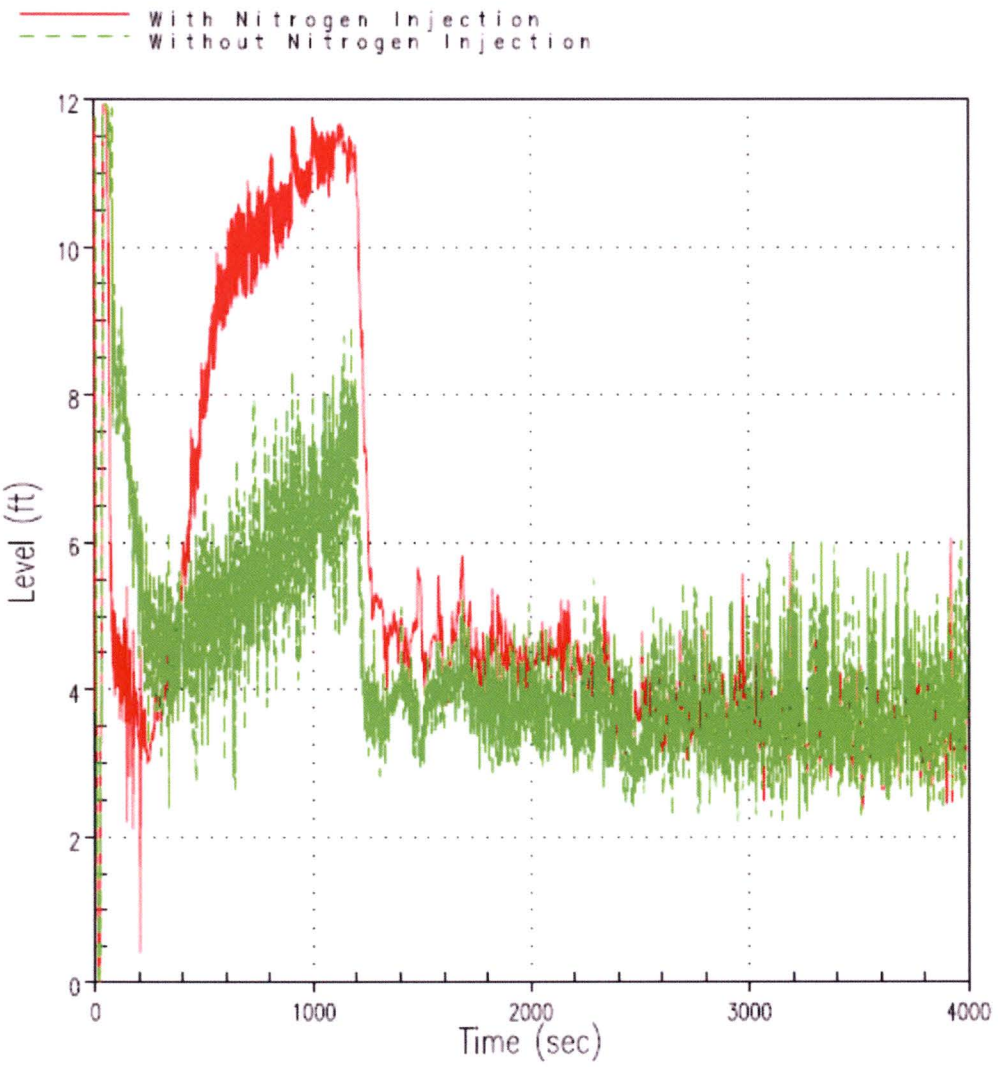

Figure RAI-4.7-27 Hot Assembly Channel Collapsed Liquid Level

Interfacial Drag Sensitivity Study

In the response to RAI-4.8, sensitivity studies using Westinghouse upflow plant Case 2B and downflow plant Case 2B were completed to investigate whether the axial interfacial drag multiplier has a significant impact on the output parameters t_{block}, K_{max}, K_{split}, and m_{split}. The sensitivity results demonstrate that critical core parameters like void fraction, mixture level, and debris-induced PCT are minimally affected by the axial interfacial drag multiplier. Results indicate that the debris-induced heatup is more sensitive to local variability in the void fraction rather than the global core void distribution. Other indicators like downcomer collapsed liquid level, upper head spray nozzle flow and liquid carryover through the break are also minimally affected by the drag multiplier. It is concluded that the axial interfacial drag multiplier does not have a significant impact on t_{block}, K_{max}, K_{split}, and m_{split}.

Subcooling Sensitivity Study

Varying the ECCS subcooling is another approach to varying the upper plenum mixture level and liquid inventory since increased subcooling will reduce the steaming rate, and thus, the upper plenum void fraction. The response to RAI-4.16 Item d. presents a sensitivity study in which the injection phase ECCS subcooling is varied, and the response to RAI-4.23 Item i. presents a study in which the ECCS recirculation phase subcooling is varied. The results of these sensitivity studies show that ECCS subcooling does not significantly affect the liquid discharge from the break. The parameters K_{max}, t_{block}, K_{split}, and m_{split} are also not significantly impacted by ECCS subcooling.

Sump Switchover Time

Sump switchover is the time that debris begins to transport from the containment sump to the reactor vessel. Earlier arrival of debris will result in the greatest potential for a debris-induced heatup because decay heat is higher. Sensitivity studies provided in the response to RAI-4.19 demonstrate that earlier sump switchover times are limiting in terms of debris-induced heatup.

References

RAI-4.7-1 Regulatory Guide 1.203, "Transient and Accident Analysis Methods," December 2005.

RAI-4.7-2 WCAP-16009-P-A, "Realistic Large-Break LOCA Evaluation Methodology Using the Automated Statistical Treatment Of Uncertainty Method (ASTRUM)," January 2005.

RAI-4.7-3 NUREG/CR-5249, "Quantifying Reactor Safety Margins: Application of Code Scaling, Applicability, and Uncertainty (CSAU) Evaluation Methodology to a Large-Break, Loss-of-Coolant Accident," 1989.

RAI-4.7-4 WCAP-12945-P-A, "Code Qualification Document for Best Estimate LOCA Analysis," March 1998.

RAI-4.7-5 Spring, J. P., "COBRA-TF Analysis of RBHT Steam Cooling Experiments," August 2008.

RAI-4.7-6 NUREG/CR-7152, "Rod Bundle Heat Transfer Facility – Steady-state Steam Cooling Experiments," May, 2014.

RAI-4.8, Vol. 4

Adequate prediction of the two-phase mixture level swell under core pool boiling conditions at atmospheric or close to atmospheric pressures during the long term core cooling (LTCC) phase of a PWR LOCA is of primary importance for demonstrating adequate core cooling in association with core inlet blockage. Sections 6.1 and 6.2 state "it is known that the version of WCOBRA/TRAC utilized tends to over predict two-phase mixture level swell in the core under low pressure pool boiling conditions (Reference 6-1). To account for this, a multiplier on the core axial interfacial drag is applied consistent with the approach taken in Reference 6-1." Reference 6-1 is listed in Section 6.5 as follows.

Reference 6-1: WCAP-15644-P, Rev. 2 (Proprietary) and WCAP-15644-NP, Rev. 2 (Non-Proprietary), "AP1000 Code Applicability Report," March 2004.

Revised Section 7.1.1, "Debris Collection at the Core Inlet," of WCAP-17788-P Vol. 1, provided with Letter CAW-15-4339 dated November 24, 2015, further clarifies that an "interfacial drag multiplier of 0.8 x nominal" was used to analyze a double-ended cold leg break in a three-loop Westinghouse plant "consistent with Westinghouse NSSS analyses in WCAP-17788, Volume 4." Sections 8 through 11 of Vol. 4 provide no information relative to the capabilities of the other codes used for the analyses to predict two-phase mixture level swell in the core under low pressure pool boiling conditions. Also, Reference 6-1 has not been approved by the NRC.

a. Provide assessment results that demonstrate the codes used for the analyses documented in Sections 8 through 11 adequately predict two-phase mixture level swell under core pool boiling conditions at pressures close to atmospheric. These results should be based on level swell test data relevant to the analyzed plant conditions. Provide figures comparing code predictions to low pressure test data. Include tables identifying the test facilities, test runs, test flow conditions, measured void fractions, and predicted void fractions for the code assessments performed.

Response

See the response to RAI-4.8 Item b.

b. Clarify whether the "interfacial drag multiplier of 0.8 x nominal" identified in revised Section 7.1.1 was used in the HLB LOCA analyses in WCAP-17788-P Vol. 4 performed with WCOBRA/TRAC. If the multiplier was used in the analyses presented in Vol. 4:

   i. Describe the basis for determining the multiplier value.
   ii. Provide data assessments and the established range for this multiplier.
   iii. Demonstrate the applicability of the multiplier value to near-atmospheric pressure conditions
   iv. Explain whether the multiplier has a significant impact on t_{block}, K_{max}, K_{split}, and m_{split}. Use results of sensitivity studies, if necessary, to demonstrate the acceptability of the results in Section 8 and 9 in this regard.

Response

The "interfacial drag multiplier of 0.8 x nominal" identified in revised WCAP-17788, Volume 1, Section 7.1.1 was used in the GSI-191 thermal-hydraulic analyses in WCAP-17788-P, Volume 4 that were performed with WCOBRA/TRAC.

Following complete core reflood during the GSI-191 large hot leg break scenario, the two-phase mixture level in the inner reactor vessel is characterized by the pressure balance between the liquid level in the downcomer and the collapsed liquid level in the core region. Because vapor generation from decay heat is initially high, regions in the vessel can achieve a significant void fraction. As the transient progresses into the long-term core cooling (LTCC) phase, vapor generation reduces due to the reduction in decay heat. The two-phase mixture level depends on the interfacial shear exerted by the vapor on the liquid, and as a result, the mixture level can be significantly higher than the collapsed liquid level. The difference between the two-phase mixture level and the collapsed liquid level is a measure of the mixture level swell. Using this definition, a swell of zero corresponds to a two-phase mixture level which is the same as the collapsed liquid level.

Prediction of the mixture level swell and tracking of the mixture level are important during the GSI-191 scenario and are ranked high in the PIRT provided in the response to RAI-4.7. When resistance due to debris accumulation at the core inlet is modeled, the flow to the core is reduced. As more liquid boils away, the mixture level can eventually drop into the core and a debris-induced core uncovery may occur. While sufficient cooling is maintained below the mixture level, dryout occurs above the mixture level. Heat transfer above the mixture level is governed by single-phase convection to the vapor. This relatively poor heat transfer mode causes the cladding temperature above the mixture level to increase rapidly. Thus, conservative prediction of the two-phase mixture level in the active core region is vital to a conservative prediction of core uncovery and fuel cladding temperature during a debris-induced heatup.

Mixture level swell is the process that determines the vertical position of the two-phase interfaces in the system; above the interface the mixture is essentially single-phase vapor. [

]^{a,c}

Several experimental tests have been conducted under low pressure boil-off thermal-hydraulic conditions to measure the effects of various parameters on mixture level swell. [

]^{a,c}

The models and correlations used by WCOBRA/TRAC for wall and interfacial drag are described in WCAP-16009-P-A (Reference RAI-4.8-1), Section 4, and the flow regime maps are described in Section 3. These models are used to determine the void fraction distribution within a region.

[

]^{a,c}

There are several separate effects experimental tests that provide data on the mixture level in a rod bundle under low pressure boil-off conditions representative of the GSI-191 large hot leg break scenario. Two such experimental facilities were modeled with WCOBRA/TRAC, and these experimental tests were simulated to determine the predictive capability of the code. The tests were as follows:

- The Westinghouse G-1 Core Uncovery Tests, WCAP-9764 (Reference RAI-4.8-2)
- The Westinghouse G-2 Core Uncovery Tests, EPRI NP-1692 (Reference RAI-4.8-3)

These tests include runs at low pressures typical of the GSI-191 large break hot leg break scenario, and provide information on the cladding heatup elevation, mixture level, and mass inventories for uncovered rod bundles.

A series of G1 and G2 boil-off tests at near atmospheric pressure were simulated with WCOBRA/TRAC. The level swell calculated from the data and the corresponding value from the WCOBRA/TRAC results was compared. Results show that the nominal interfacial drag model has the tendency to over predict the level swell, in some cases by more than 25%.

A sensitivity study considered varying the interfacial drag coefficient. Results indicate that by setting the drag multiplier to 0.8 most data is captured within a ±25% band.

G1 test runs 28, 35, 38, 58, 59 and 61 and G2 test runs 728, 729, 730, 732, 733, and 734 were selected to validate the WCOBRA/TRAC interfacial drag models used to perform the GSI-191 thermal hydraulic analysis. G1 represents a prototypical 15x15 PWR assembly and contains 480 heater rods. The G1 heated length is 12 ft. G2 represents a 17x17 PWR assembly and contains 336 heater rods. The G2 heated length is 13.7 ft. Both considered an approximate chopped cosine power shape.

Once WCOBRA/TRAC G1 and G2 models were obtained, the G1 and G2 low pressure boil-off tests were simulated. [

]^{a,c} As liquid started to boil in the heated section, a mixture level was established in proximity to the top of the bundle. As the transient proceeded, steam exited the top of the bundle and some liquid was injected by gravity from the downcomer region. During the transient, both the liquid level in the downcomer and the mixture level in the heated region slowly decreased.

At each given time, the location of the mixture level Z_{mix} is defined by examining the rod temperature axial distribution. The rod surface temperature is close to saturation below the mixture level and suddenly increases significantly above the saturation temperature above the mixture level.

The average void fraction below the mixture level is related to a parameter called swell 'S' defined as follows:

$$S = \frac{Z_{mix} - Z_{sat}}{Z_{CLL} - Z_{sat}} = \frac{1}{1 - \bar{\alpha}} \qquad \text{Eq. RAI-4.8-1}$$

Z_{sat} is defined as the location where the heat transfer mode changes from subcooled boiling to nucleate boiling and Z_{CLL} is defined as the location of the collapsed liquid level. The predicted swell ratio (S) was compared with the observed test value. The same test series was repeated with two values of interfacial drag multipliers; 1.0 and 0.8.

The observed values of Z_{mix} and Z_{CLL} for each test were taken from Appendix B of WCAP-9764 (Reference RAI-4.8-2) for G1 and Volume 2 of EPRI NP-1692 (Reference RAI-4.8-3) for G2. [

]^{a,c} The heatup time is defined as the time when the clad temperature undergoes the first significant heatup. The required values of Z_{CLL} and Z_{sat} are then determined at the heatup time. Z_{CLL} is read directly from the WCOBRA/TRAC output and Z_{sat} is taken as the elevation where the heat transfer mode changes from subcooled nucleate boiling to nucleate boiling.

The test conditions are summarized in Table RAI-4.8-1. Figure RAI-4.8-1 summarizes results from the G1 and G2 simulations with nominal and 20% reduced interfacial drag, respectively.

Table RAI-4.8-1 G1 and G2 Experimental Test Conditions used in WCOBRA/TRAC Simulations

Facility	Test	Test Time (s)	Inlet Flow (lbm/s)	Pressure (psia)	Bundle Power (kW)	Inlet Enthalpy (Btu/lbm)
G1	28	368	0.363	14.7	500	130
G1	35	430	0.704	14.7	1000	100
G1	38	365	0.356	14.7	500	110
G1	58	365	0.751	14.7	1000	165
G1	61	910	0.337	14.7	500	155
G1	61	670	0.259	14.7	500	155
G2	728	100	0.42	50	600	250
G2	728	200	0.42	50	600	241
G2	728	400	0.42	50	600	241
G2	728	500	0.27	50	600	241
G2	728	600	0.27	50	600	241
G2	729	500	0.16	50	250	233
G2	729	700	0.16	50	250	233
G2	729	1000	0.16	50	250	233
G2	729	1500	0.13	50	250	233
G2	730	40	0.59	50	900	250
G2	730	150	0.59	50	900	243
G2	732	1000	0.16	15.1	250	176
G2	732	1500	0.16	15.1	250	176
G2	733	300	0.38	15.8	600	173
G2	733	400	0.38	15.8	600	173
G2	733	500	0.38	15.8	600	173
G2	734	50	0.64	16.1	900	183
G2	734	100	0.64	16.1	900	181
G2	734	150	0.64	16.1	900	178
G2	734	200	0.64	16.1	900	176

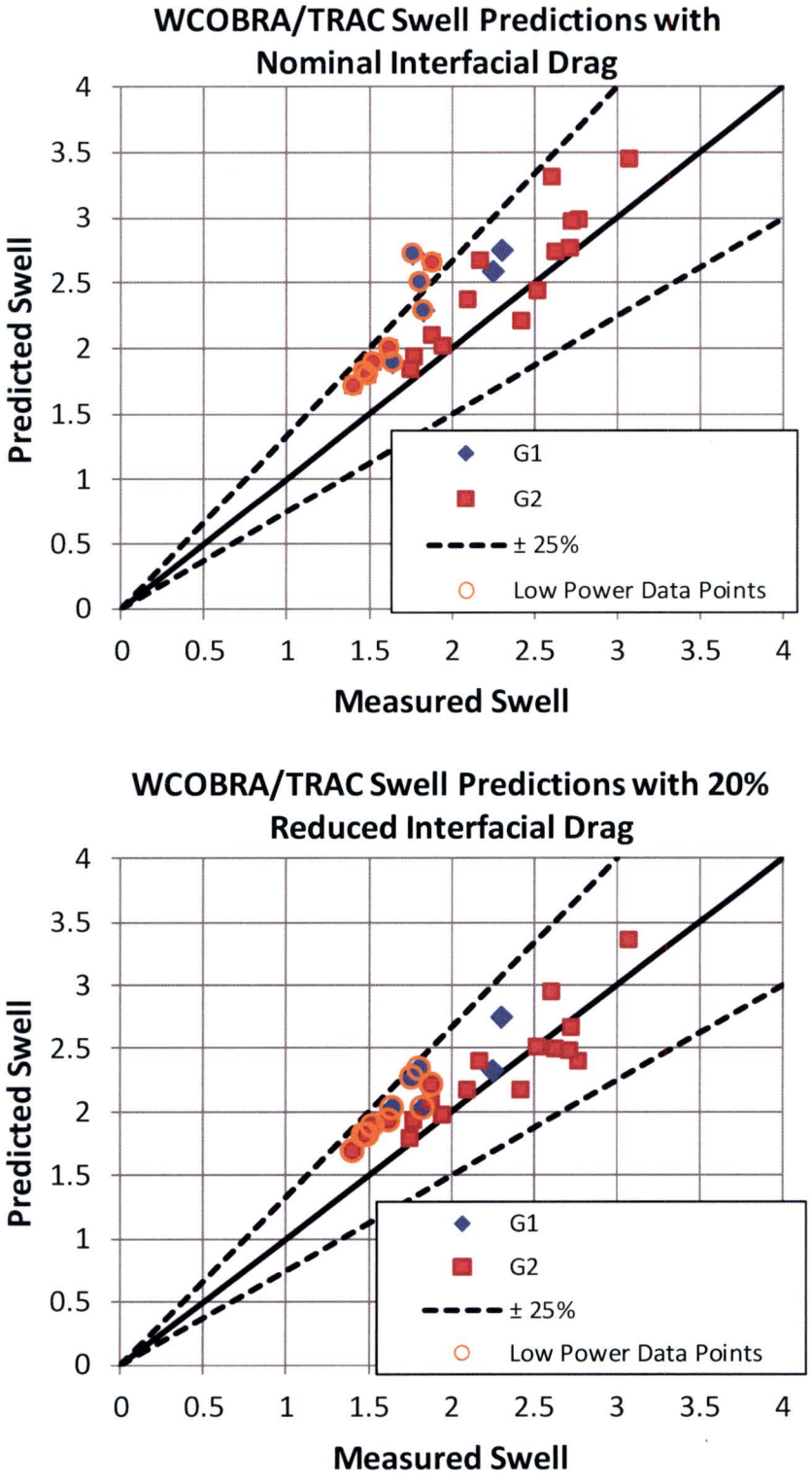

Figure RAI-4.8-1 Results from the WCOBRA/TRAC G1 and G2 Simulations

Sensitivity Studies

Sensitivity studies using Westinghouse upflow plant Case 2B and downflow plant Case 2B to show the sensitivity to the axial interfacial drag multiplier (XDRAG) have been completed. The sensitivity matrix is shown in Table RAI-4.8-2.

Table RAI-4.8-2 Axial Interfacial Drag Sensitivity Study

Case	Drag Multiplier (XDRAG)	Plant Model
Case 2B (base case)	0.8	Upflow
1	1.0	Upflow
2	0.6	Upflow
Case 2B (base case)	0.8	Downflow
3	1.0	Downflow
4	0.6	Downflow

Westinghouse Upflow Plant Sensitivity Results

The axial interfacial drag multiplier is expected to influence the axial void distribution. Figure RAI-4.8-2 shows the hot assembly void fraction at a core elevation of 103 in. As the figure indicates, the oscillation in void fraction makes it difficult to distinguish any trends. Integrating the void fraction makes it possible to understand the effect the drag multiplier has on void fraction. Figure RAI-4.8-3 shows the integrated hot assembly void fraction at a core elevation of 103 in. As the figure indicates, decreasing the drag multiplier tends to decrease the void fraction. Figure RAI-4.8-4 and Figure RAI-4.8-5 show the integrated hot assembly void fraction at core elevations of 73 in. and 42 in., respectively. Review of the figures shows similar behavior; decreasing the drag multiplier tends to decrease the void fraction. The figures also demonstrate that the void fraction is more sensitive to the drag multiplier at lower core elevations where the void fraction is smaller. This result indicates that the drag multiplier has a larger effect on the void distribution in bubbly flow regimes than it would have in churn turbulent or dispersed flow regimes.

As the previous figures showed that decreasing the axial interfacial drag multiplier tends to decrease the void fraction, reducing the drag multiplier is expected to increase the core collapsed liquid level. The core average collapsed liquid level from the drag multiplier sensitivity study is shown in Figure RAI-4.8-6. In Figure RAI-4.8-6, the x-axis has a range of 1000-2000 seconds to highlight the period of interest, which is when core inlet resistance is applied that leads to the core uncovery and subsequent heatup. Similar to void fraction, it is difficult to distinguish any trends from this figure. The integrated core average collapsed liquid level in shown in Figure RAI-4.8-7. The x-axis in Figure RAI-4.8-7 is extended to 5000 seconds to better illustrate the effect that interfacial drag has on core average collapsed liquid level. As indicated by the figure, decreasing the drag multiplier tends to increase the collapsed liquid level, consistent with the trends in void fraction.

The parameters t_{block} and K_{max} are governed by the ability to effectively remove decay heat from the core. As such, the peak cladding temperature (PCT) during the predicted debris-induced secondary heatup is chosen as the indicator (figure of merit) for determining the impact of the axial interfacial drag multiplier on these parameters. The upflow plant sensitivity for PCT prediction is shown in Figure RAI-4.8-8. In Figure RAI-4.8-8, the x-axis has a range of 1000-2000 seconds to highlight the period of interest, which is when core inlet resistance is applied that leads to the core uncovery and subsequent heatup. As the figure indicates, the debris-induced PCT has a span of approximately 100°F. This relatively minor sensitivity to the drag multiplier is expected considering the void fraction results, which demonstrate that the drag multiplier has only a small effect on the void distribution in higher void fraction flow regimes where the core uncovery and subsequent debris-induced heatup occurs. Figure RAI-4.8-8 also shows that the debris-induced heatup does not behave monotonically like the void fraction and collapsed liquid level. This behavior indicates that the debris-induced heatup is more sensitive to the local void fraction at the PCT location than the global core void distribution. That is, variations in the local void fraction at the PCT location drive variations in the heatup more so than the axial interfacial drag multiplier, which influences the global core void distribution. If the void fraction at and around the PCT location tends to be higher during the heatup, the magnitude of the heatup will tend to be higher. Conversely, if the void fraction tends to be lower, the magnitude of the heatup will tend to be lower.

The parameter K_{split} is driven by the downcomer collapsed liquid level. As resistance due to the accumulation of debris at the core inlet builds, the downcomer collapsed liquid level increases. When the downcomer driving head overcomes the losses through the barrel/baffle channel, K_{split} is reached and flow begins to bypass the core inlet through the barrel/baffle channel. Figure RAI-4.8-9 shows the downcomer collapsed liquid level sensitivity to the axial interfacial drag multiplier. In Figure RAI-4.8-9, the x-axis has a range of 1000-2000 seconds to highlight the period of interest, which is when core inlet resistance is applied that leads to the core uncovery and subsequent heatup. As the figure indicates, the downcomer collapsed liquid level is only minimally impacted by variations to the drag multiplier. As such, the axial interfacial drag multiplier will not significantly impact the parameter K_{split}.

The parameter m_{split} is governed by the fraction of flow bypassing the core inlet through the barrel/baffle channel. Figure RAI-4.8-10 shows the barrel/baffle exit integrated liquid flow sensitivity to the axial interfacial drag multiplier. As the figure indicates, the barrel/baffle exit flow is not significantly affected by changes to the drag multiplier. As such, the parameter m_{split} will not be significantly impacted by the axial interfacial drag multiplier.

The liquid carryover from the reactor vessel through the break is also an important parameter. Figure RAI-4.8-11 shows the integrated liquid flow through the broken loop hot leg nozzle, which shows that the amount of liquid carryover through the nozzle is only minimally impacted by the axial interfacial drag multiplier. Figure RAI-4.8-12 shows the reactor vessel water mass, which is also only minimally impacted by the axial interfacial drag multiplier. In Figure RAI-4.8-12, the x-axis has a range of 1000-2000 seconds to highlight the period of interest, which is when core inlet resistance is applied that leads to the core uncovery and subsequent heatup.

The sensitivity results presented above for the Westinghouse upflow plant demonstrate that critical core parameters like void fraction, mixture level, and debris-induced heatup are minimally affected by

the axial interfacial drag multiplier. Results indicate that the debris-induced heatup is more sensitive to local variability in the void fraction than the global core void distribution. Other indicators like downcomer collapsed liquid level, barrel/baffle exit flow and liquid carryover through the break are also minimally affected by the drag multiplier. It is concluded that the axial interfacial drag multiplier does not have a significant impact on t_{block}, K_{max}, K_{split}, and m_{split} for the Westinghouse upflow plant analysis.

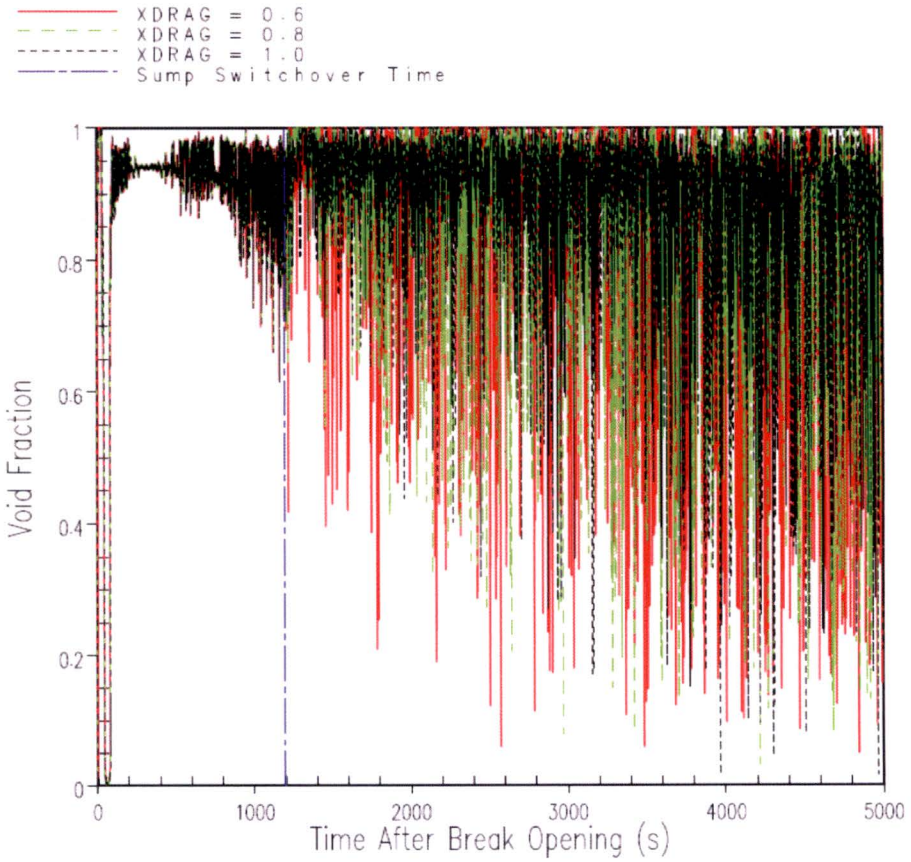

Figure RAI-4.8-2 Westinghouse Upflow Plant Interfacial Drag Sensitivity Hot Assembly Void Fraction at a Core Elevation of 103 in. Results

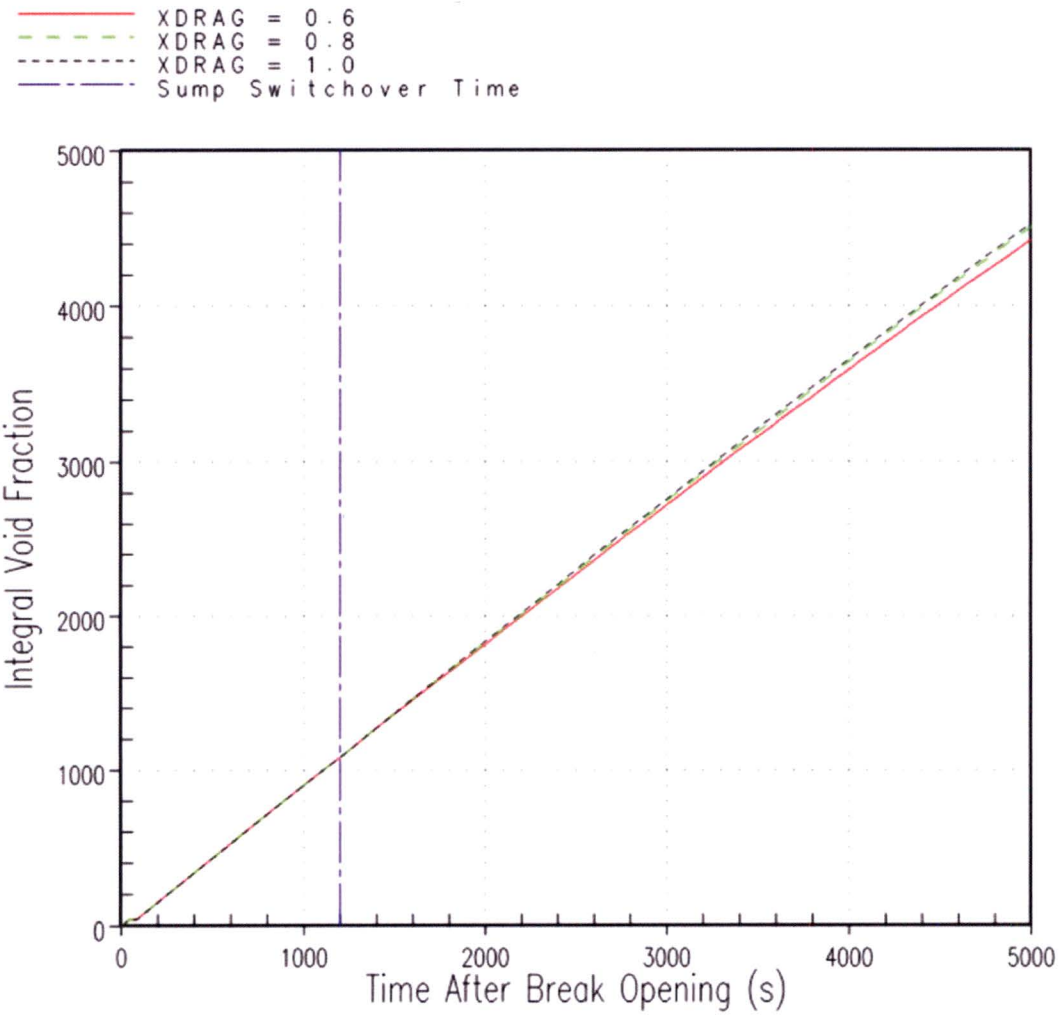

Figure RAI-4.8-3 Westinghouse Upflow Plant Interfacial Drag Sensitivity Hot Assembly Integrated Void Fraction at a Core Elevation of 103 in. Results

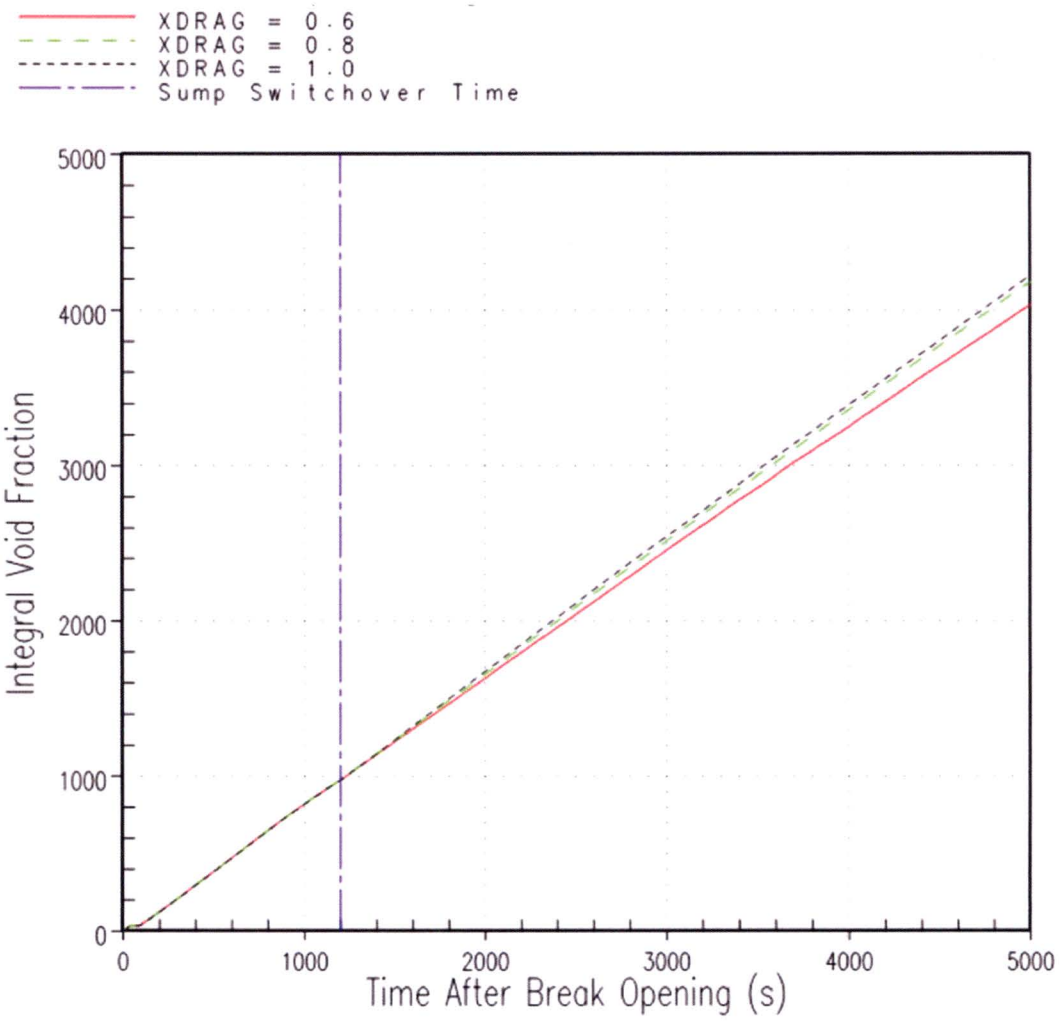

Figure RAI-4.8-4 Westinghouse Upflow Plant Interfacial Drag Sensitivity Hot Assembly Integrated Void Fraction at a Core Elevation of 73 in. Results

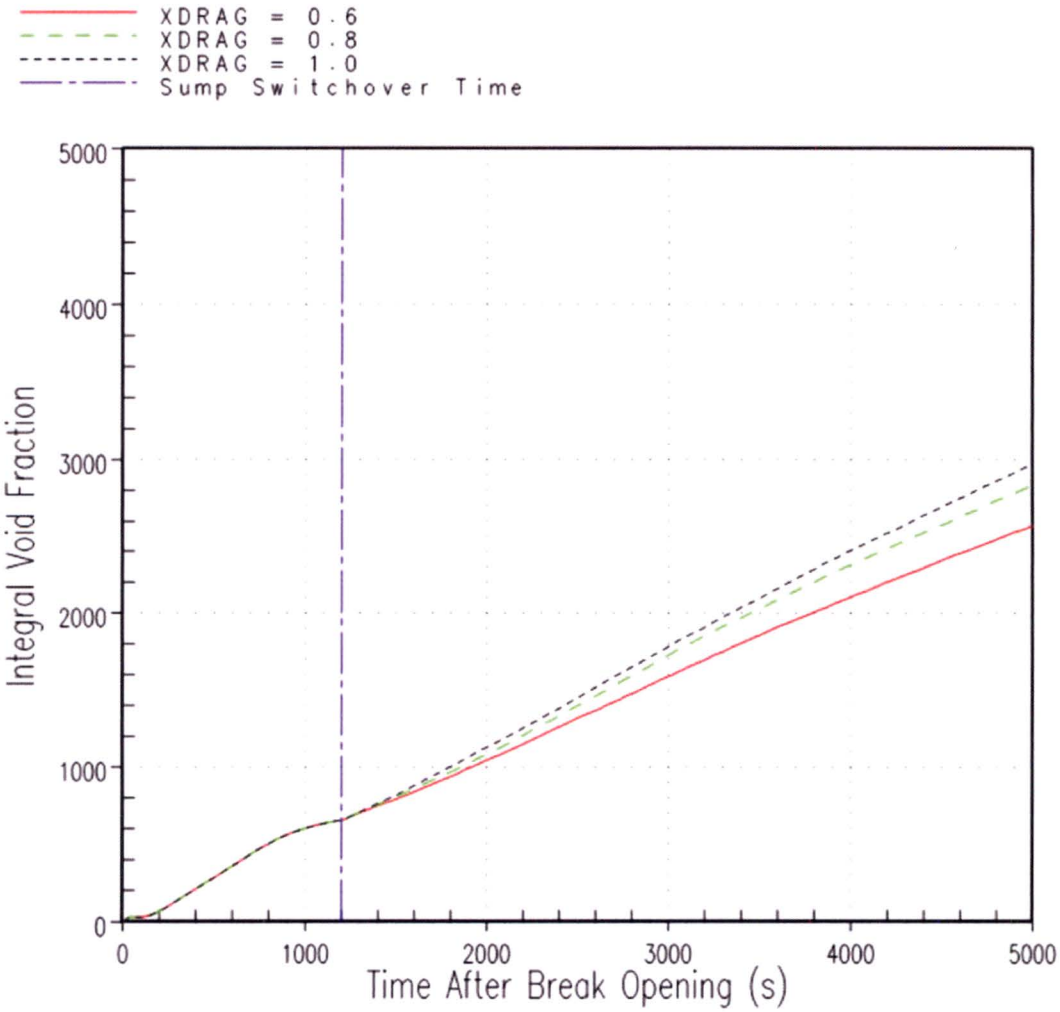

Figure RAI-4.8-5 Westinghouse Upflow Plant Interfacial Drag Sensitivity Hot Assembly Integrated Void Fraction at a Core Elevation of 42 in. Results

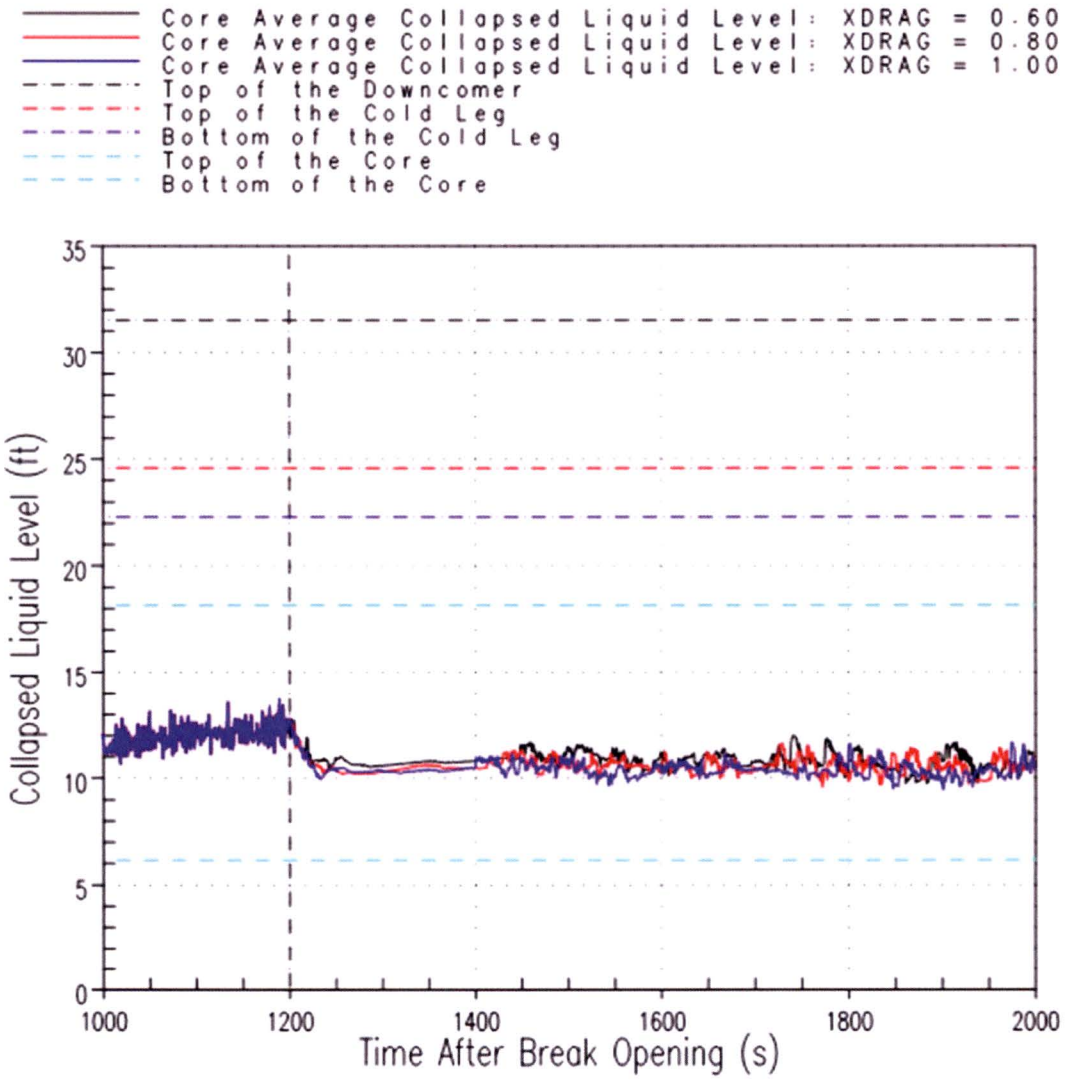

Figure RAI-4.8-6 Westinghouse Upflow Plant Interfacial Drag Sensitivity Core Average Collapsed Liquid Level Results

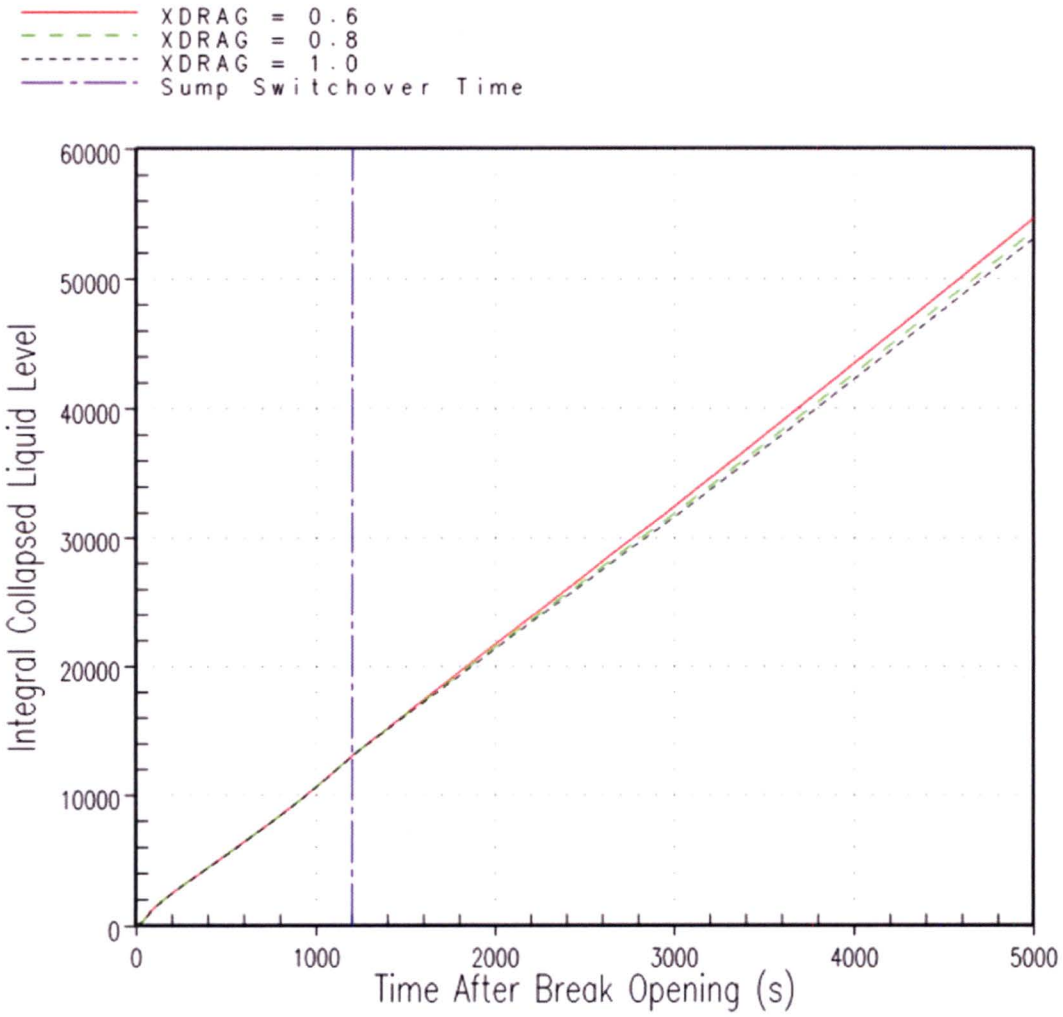

Figure RAI-4.8-7 Westinghouse Upflow Plant Interfacial Drag Sensitivity Core Average Integrated Collapsed Liquid Level Results

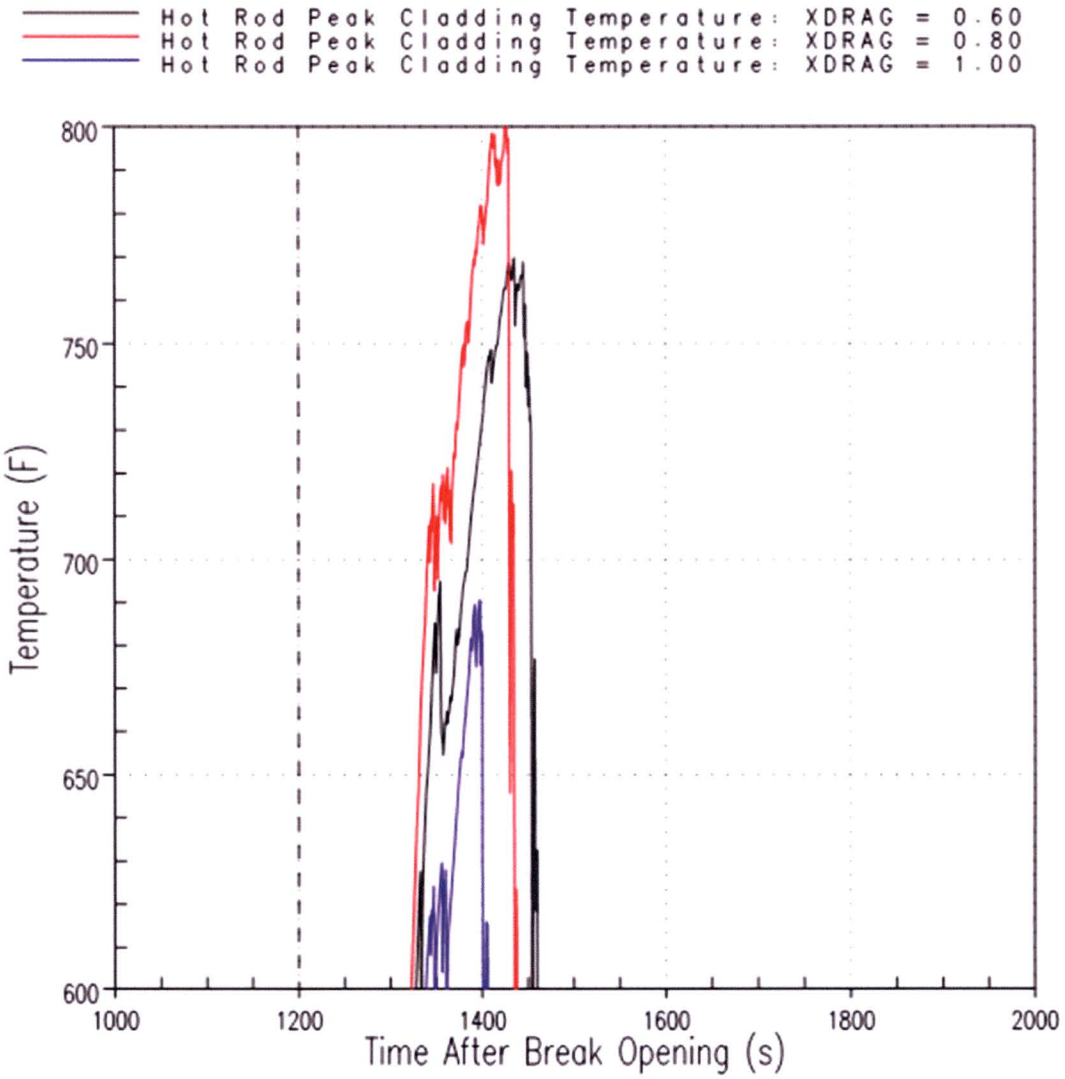

Figure RAI-4.8-8 Westinghouse Upflow Plant Axial Interfacial Drag Sensitivity Debris-Induced Heatup Results

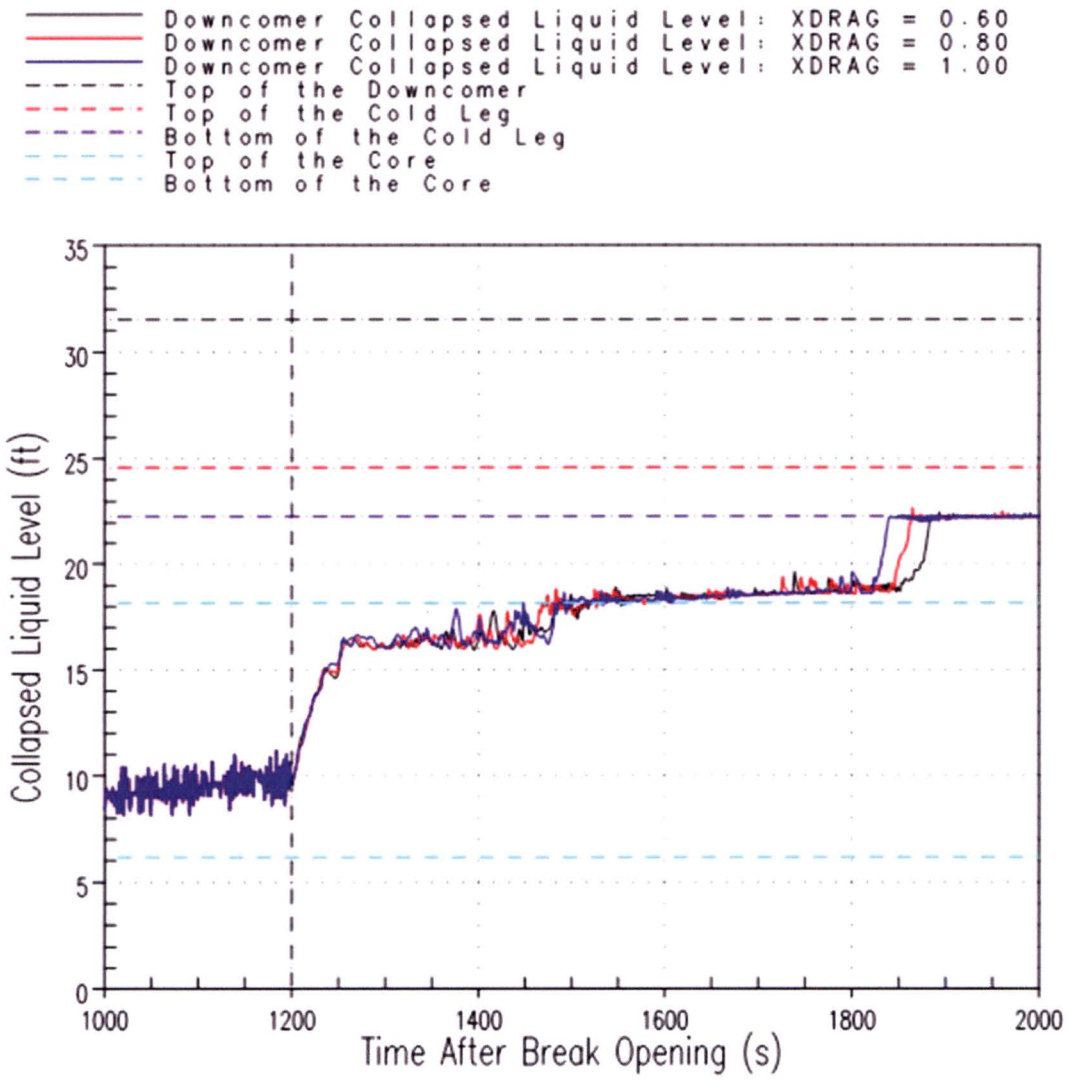

Figure RAI-4.8-9 Westinghouse Upflow Plant Interfacial Drag Sensitivity Downcomer Collapsed Liquid Level Results

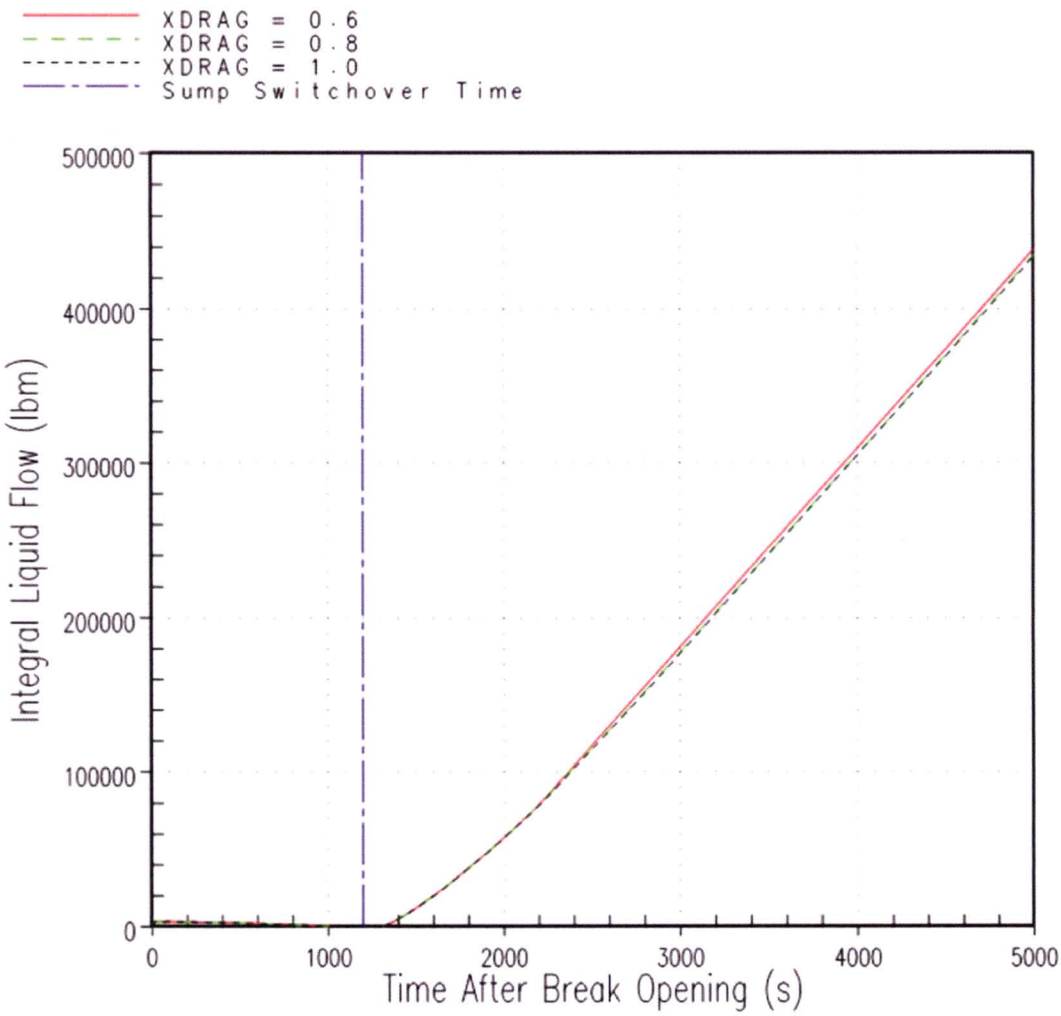

Figure RAI-4.8-10 Westinghouse Upflow Plant Interfacial Drag Sensitivity Barrel/Baffle Exit Integrated Liquid Flow Results

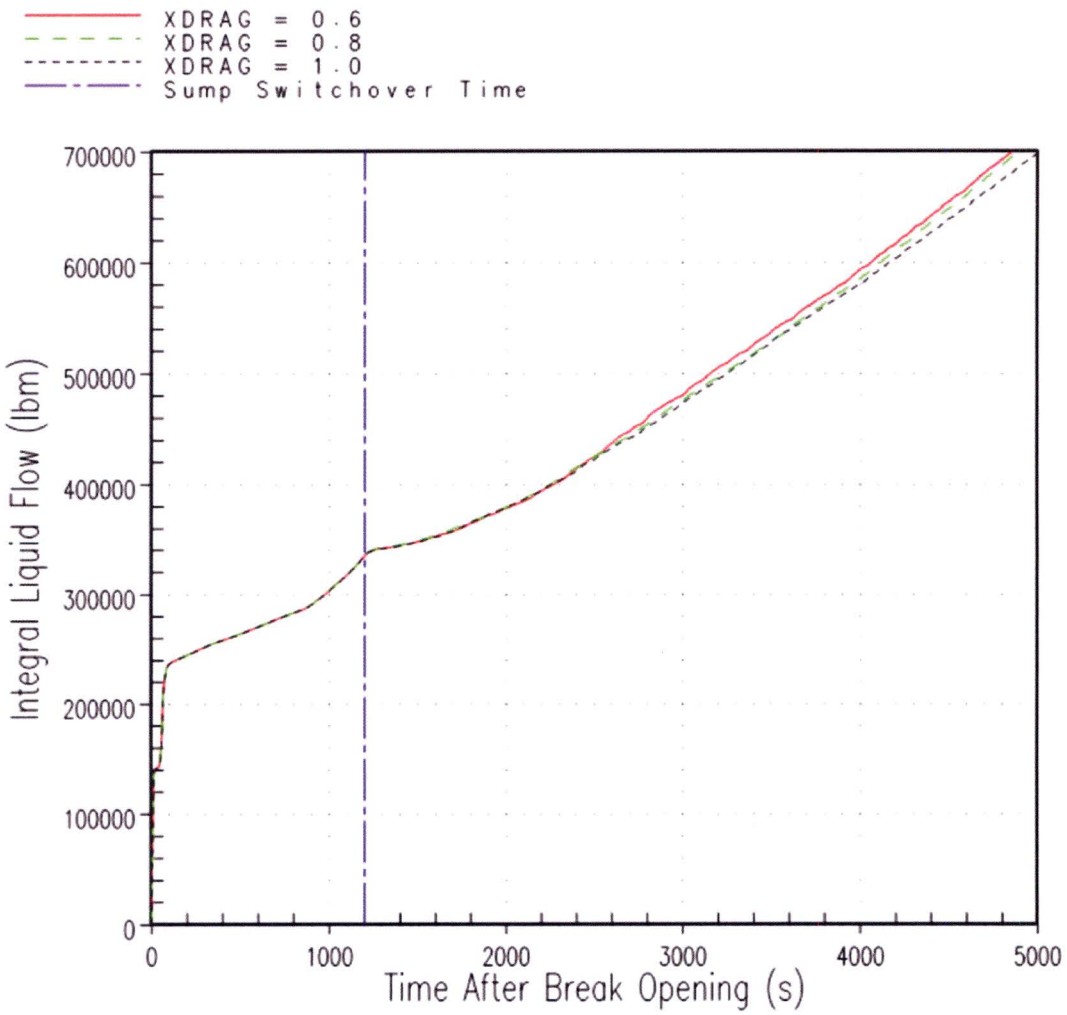

Figure RAI-4.8-11 Westinghouse Upflow Plant Interfacial Drag Sensitivity Broken Loop Hot Leg Nozzle Integrated Liquid Flow Results

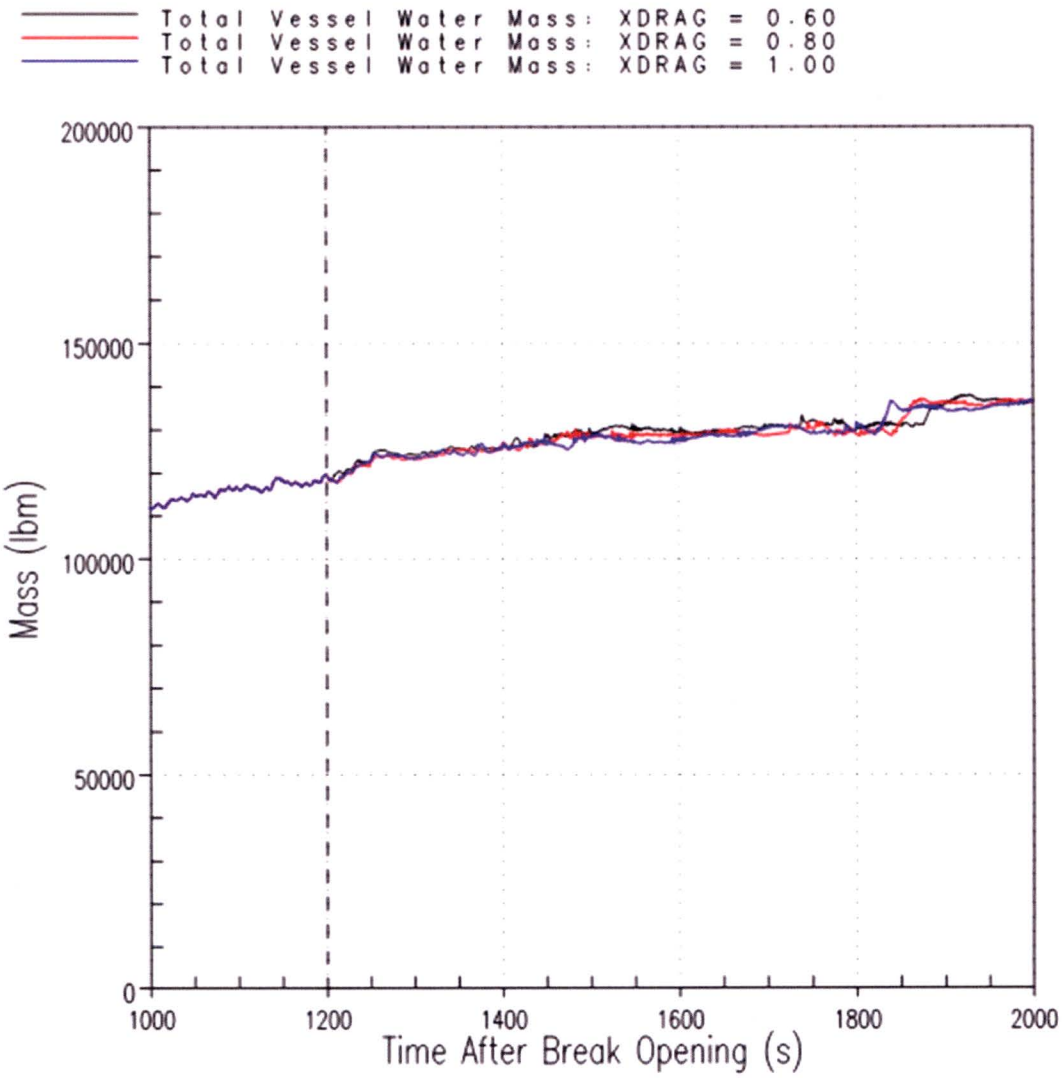

Figure RAI-4.8-12 Westinghouse Upflow Plant Interfacial Drag Sensitivity Reactor Vessel Water Mass Results

Westinghouse Downflow Plant Sensitivity Results

The Westinghouse downflow plant is expected to have a similar sensitivity to the axial interfacial drag multiplier as was observed for the Westinghouse upflow plant category. Figure RAI-4.8-13 shows the hot assembly void fraction at a core elevation of 103 in. Similar to the upflow plant sensitivity, the oscillation in void fraction makes it difficult to distinguish any trends. Integrating the void fraction makes it possible to understand the effect of the drag multiplier. Figures RAI-4.8-14, RAI-4.8-15 and RAI-4.8-16 show the integrated hot assembly void fraction at core elevations of 103 in., 73 in. and 42 in., respectively. Review of the figures indicates similar behavior as was seen in the upflow plant sensitivity; decreasing the drag multiplier tends to decrease the void fraction. The figures also demonstrate that the void fraction is more sensitive to the drag multiplier at lower core elevations where the void fraction is smaller. This result indicates that the drag multiplier has a larger effect on the void distribution in bubbly flow regimes than it would have on churn turbulent or dispersed flow regimes.

As the previous figures showed that decreasing the axial interfacial drag multiplier tended to decrease the void fraction, reducing the drag multiplier is expected to increase the core collapsed liquid level. The core average collapsed liquid level from the drag multiplier sensitivity study is shown in Figure RAI-4.8-17. Similar to void fraction, it is difficult to distinguish any trends from this figure. The integrated core average collapsed liquid level in shown in Figure RAI-4.8-18. As indicated by the figure, decreasing the drag multiplier tends to increase the collapsed liquid level, consistent with the trends in void fraction. This trend is also consistent with that seen in the upflow plant sensitivity study.

The parameters t_{block} and K_{max} are governed by the ability to effectively remove decay heat from the core. As such, the PCT during the predicted debris-induced secondary heatup is chosen as the indicator (figure of merit) for determining the impact the axial interfacial drag multiplier has on these parameters. The downflow plant sensitivity for PCT prediction is shown in Figure RAI-4.8-19. As the figure indicates, the debris-induced PCT has a span of less than 50°F, which is less than the span observed in the upflow plant sensitivity study. This relatively minor sensitivity to the drag multiplier is expected considering the void fraction results, which demonstrate that the drag multiplier has only a small effect on the void distribution in higher void fraction flow regimes where the core uncovery and subsequent debris-induced heatup occurs.

The parameter K_{split} is driven by the downcomer collapsed liquid level. As resistance due to the accumulation of debris at the core inlet builds, the downcomer collapsed liquid level increases. When the downcomer liquid level reaches the upper head spray nozzles, the point of K_{split} is reached and flow begins to bypass the core inlet through the upper head. Figure RAI-4.8-20 shows the downcomer collapsed liquid level sensitivity to the axial interfacial drag multiplier. As the figure indicates, the downcomer collapsed liquid level is only minimally impacted by variations to the drag multiplier. As such, the axial interfacial drag multiplier will not significantly impact the parameter K_{split}.

The parameter m_{split} is governed by the fraction of flow bypassing the core inlet through the upper head spray nozzles. Figure RAI-4.8-21 shows the upper head spray nozzle integrated liquid flow sensitivity to the axial interfacial drag multiplier. As the figure indicates, the upper head spray nozzle

flow is not significantly affected by changes to the drag multiplier. As such, the parameter m_{split} will not be significantly impacted by the axial interfacial drag multiplier.

The liquid carryover from the reactor vessel through the break is also an important parameter. Figure RAI-4.8-22 shows the integrated liquid flow through the broken loop hot leg nozzle, which shows that the amount of liquid carryover through the nozzle is only minimally impacted by the axial interfacial drag multiplier. Figure RAI-4.8-23 shows the reactor vessel water mass, which is also only minimally impacted by the axial interfacial drag multiplier.

The sensitivity results presented above for the Westinghouse downflow plant demonstrate that critical core parameters like void fraction, mixture level, and debris-induced PCT are minimally affected by the axial interfacial drag multiplier. Results indicate that the debris-induced heatup is more sensitive to local variability in the void fraction than the global core void distribution. Other indicators like downcomer collapsed liquid level, upper head spray nozzle flow and liquid carryover through the break are also minimally affected by the drag multiplier. It is concluded that the axial interfacial drag multiplier does not have a significant impact on t_{block}, K_{max}, K_{split}, and m_{split} for the Westinghouse downflow plant analysis.

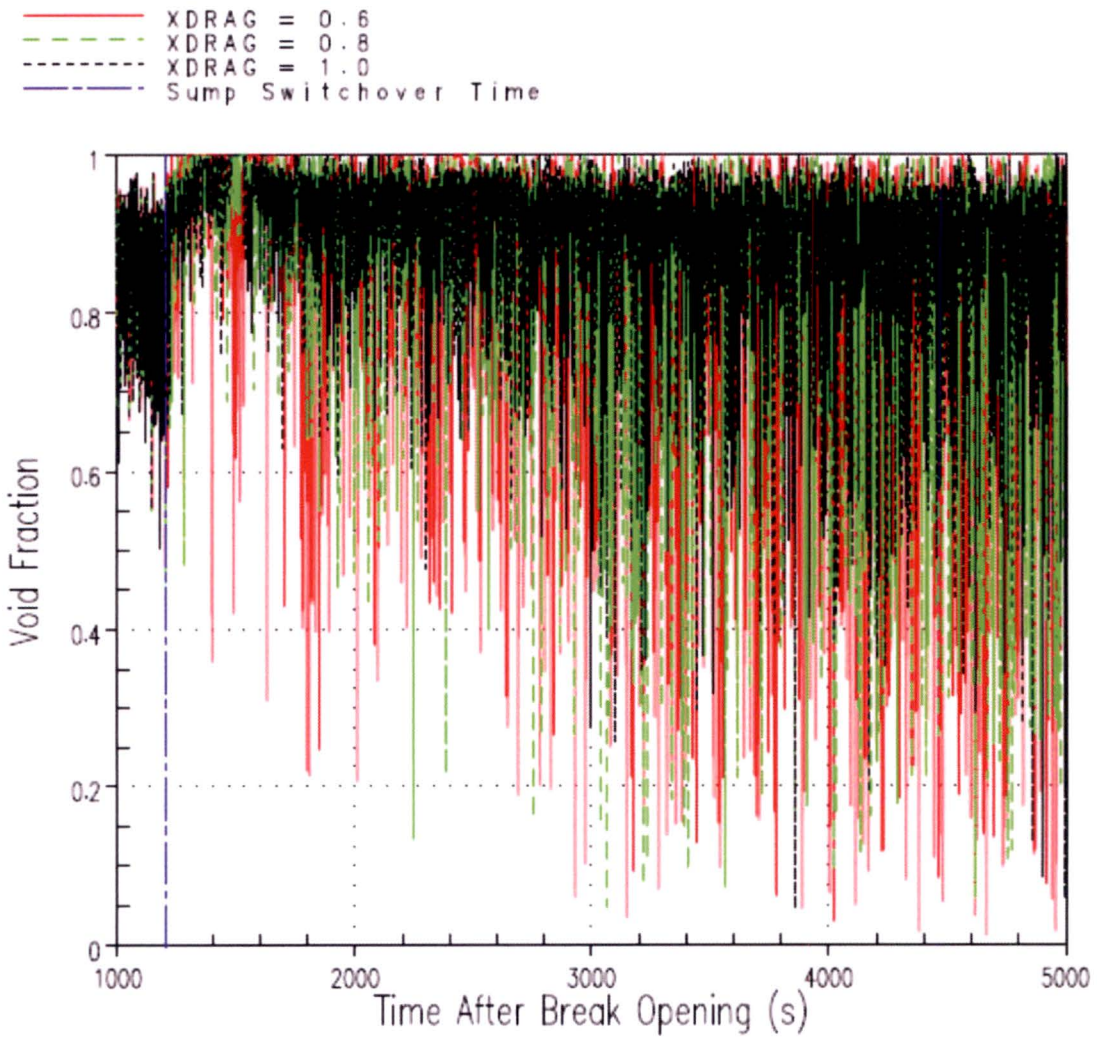

Figure RAI-4.8-13 Westinghouse Downflow Plant Interfacial Drag Sensitivity Hot Assembly Void Fraction at a Core Elevation of 103 in. Results

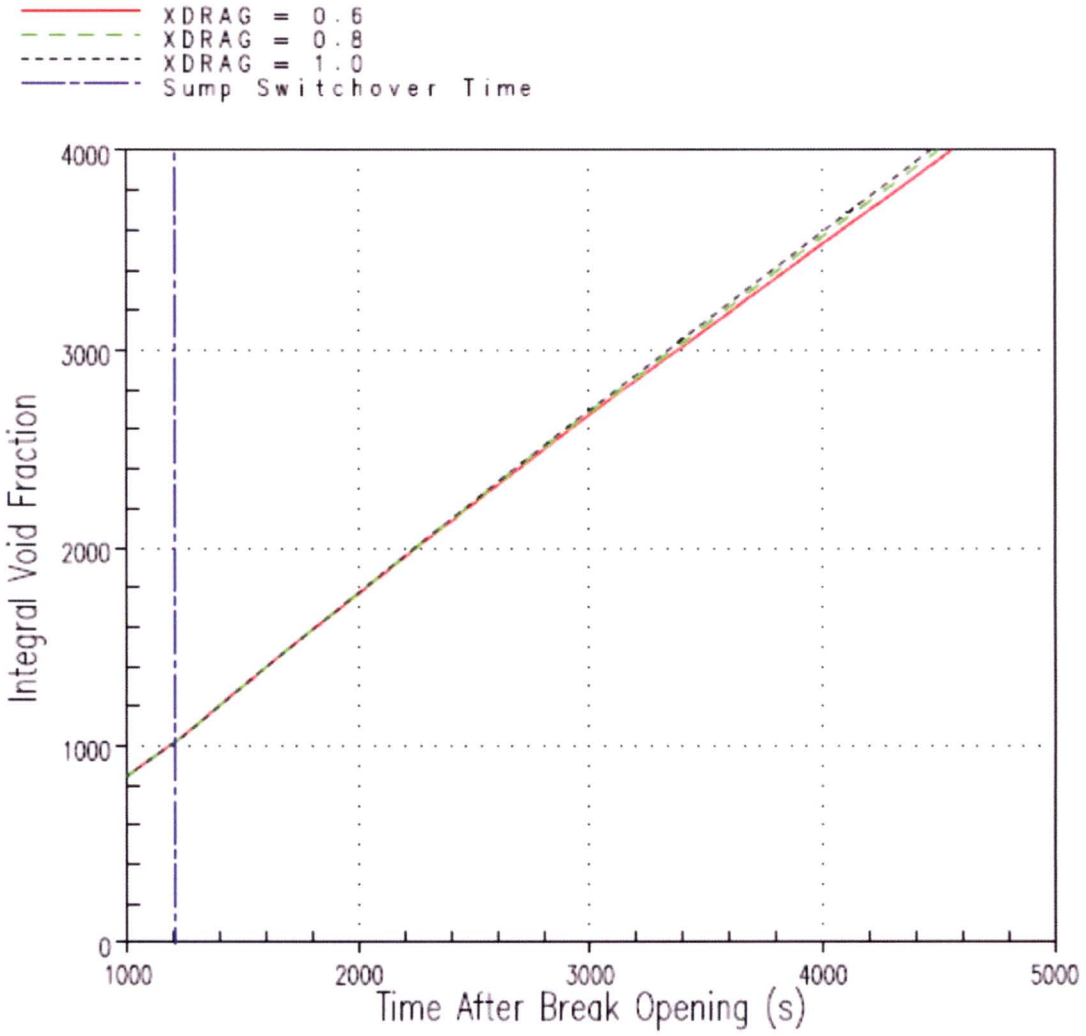

Figure RAI-4.8-14 Westinghouse Downflow Plant Interfacial Drag Sensitivity Hot Assembly Integrated Void Fraction at a Core Elevation of 103 in. Results

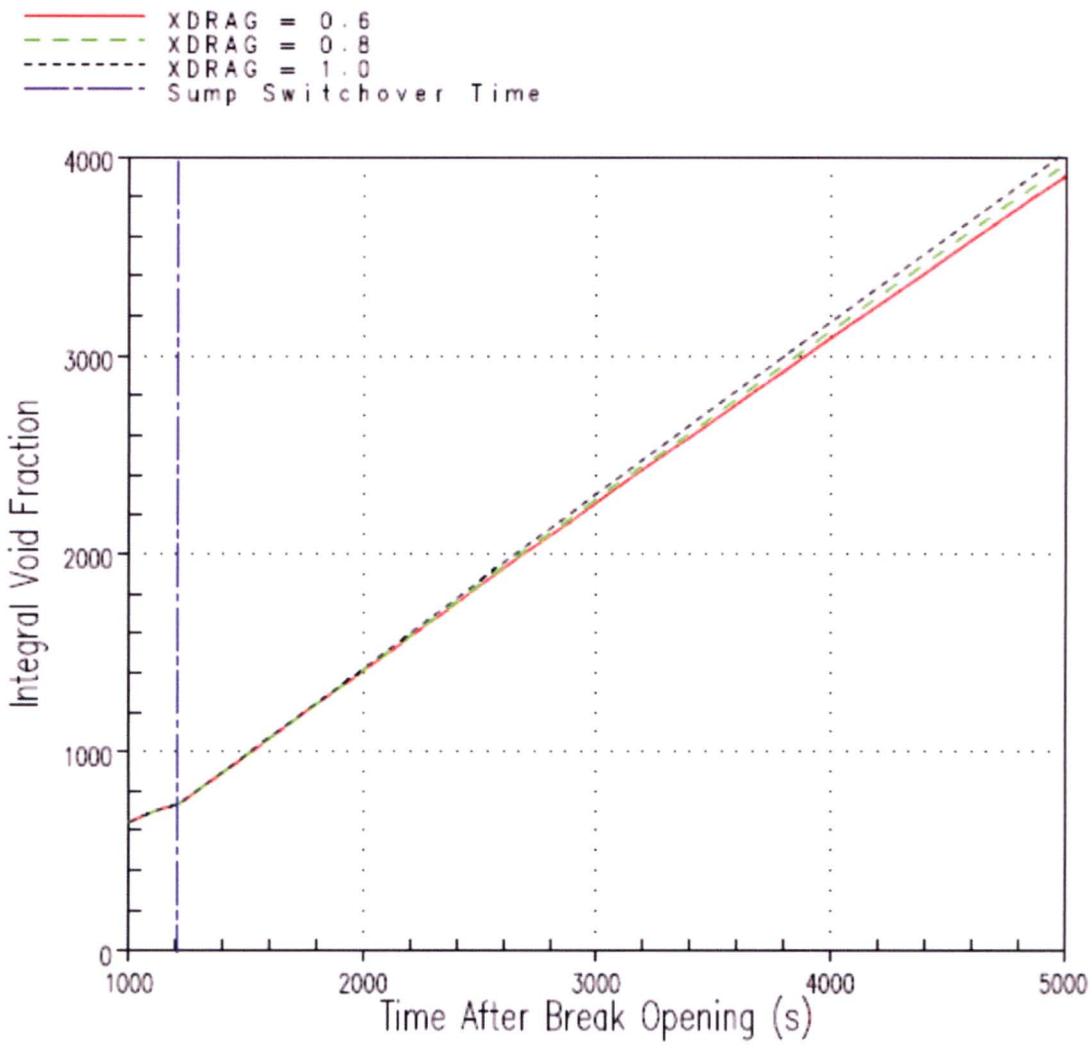

Figure RAI-4.8-15 Westinghouse Downflow Plant Interfacial Drag Sensitivity Hot Assembly Integrated Void Fraction at a Core Elevation of 73 in. Results

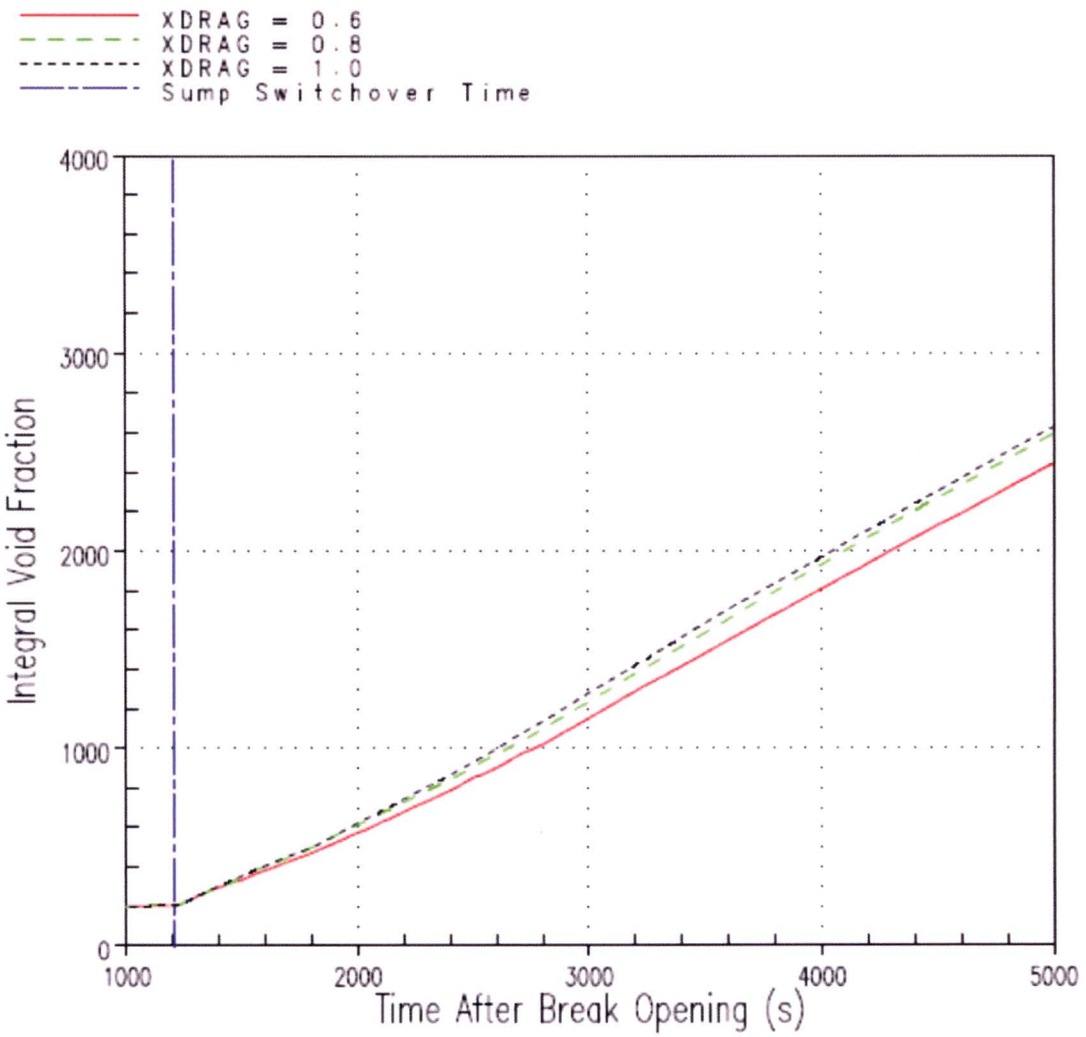

Figure RAI-4.8-16 Westinghouse Downflow Plant Interfacial Drag Sensitivity Hot Assembly Integrated Void Fraction at a Core Elevation of 42 in. Results

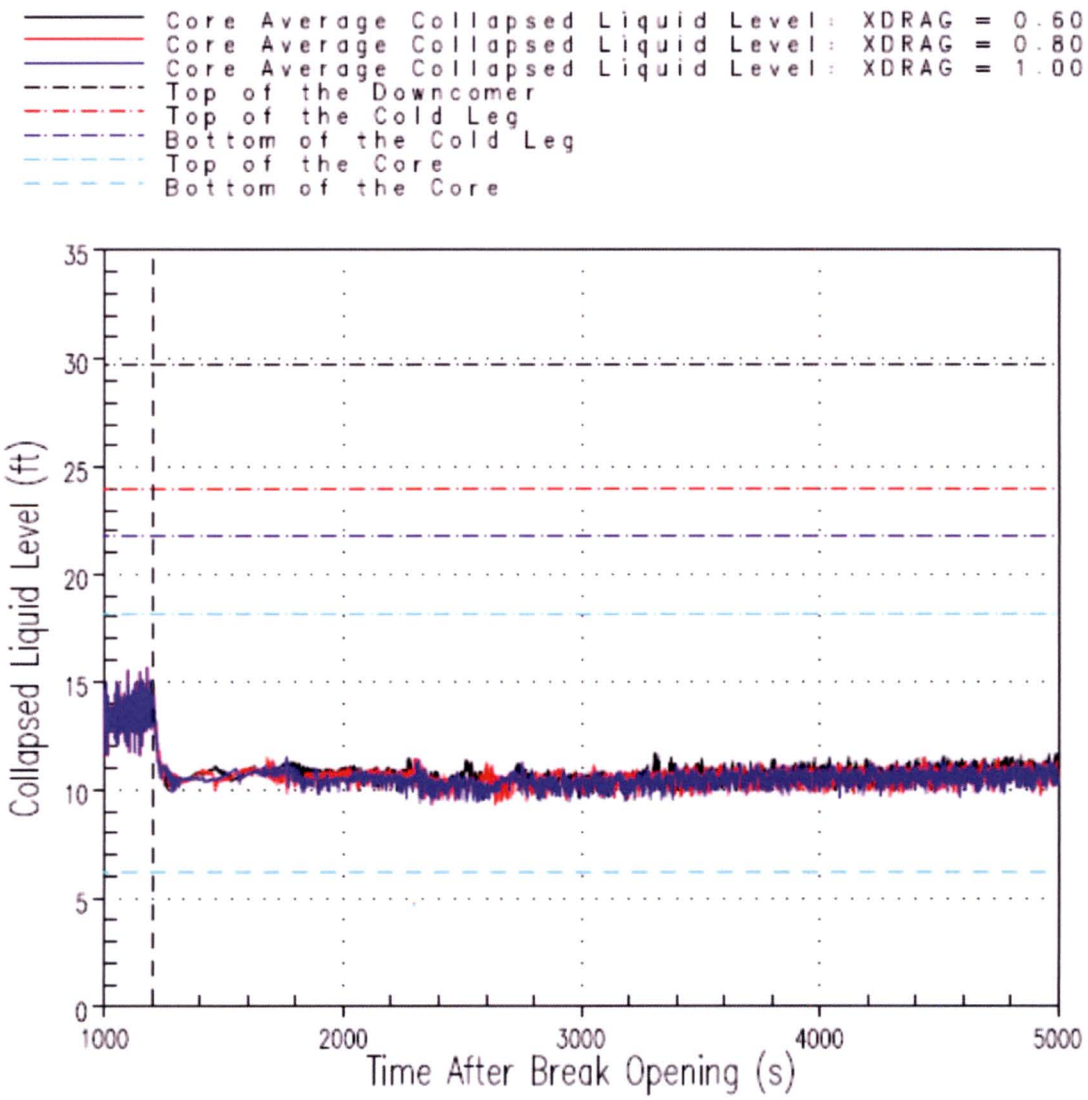

Figure RAI-4.8-17 Westinghouse Downflow Plant Interfacial Drag Sensitivity Core Average Collapsed Liquid Level Results

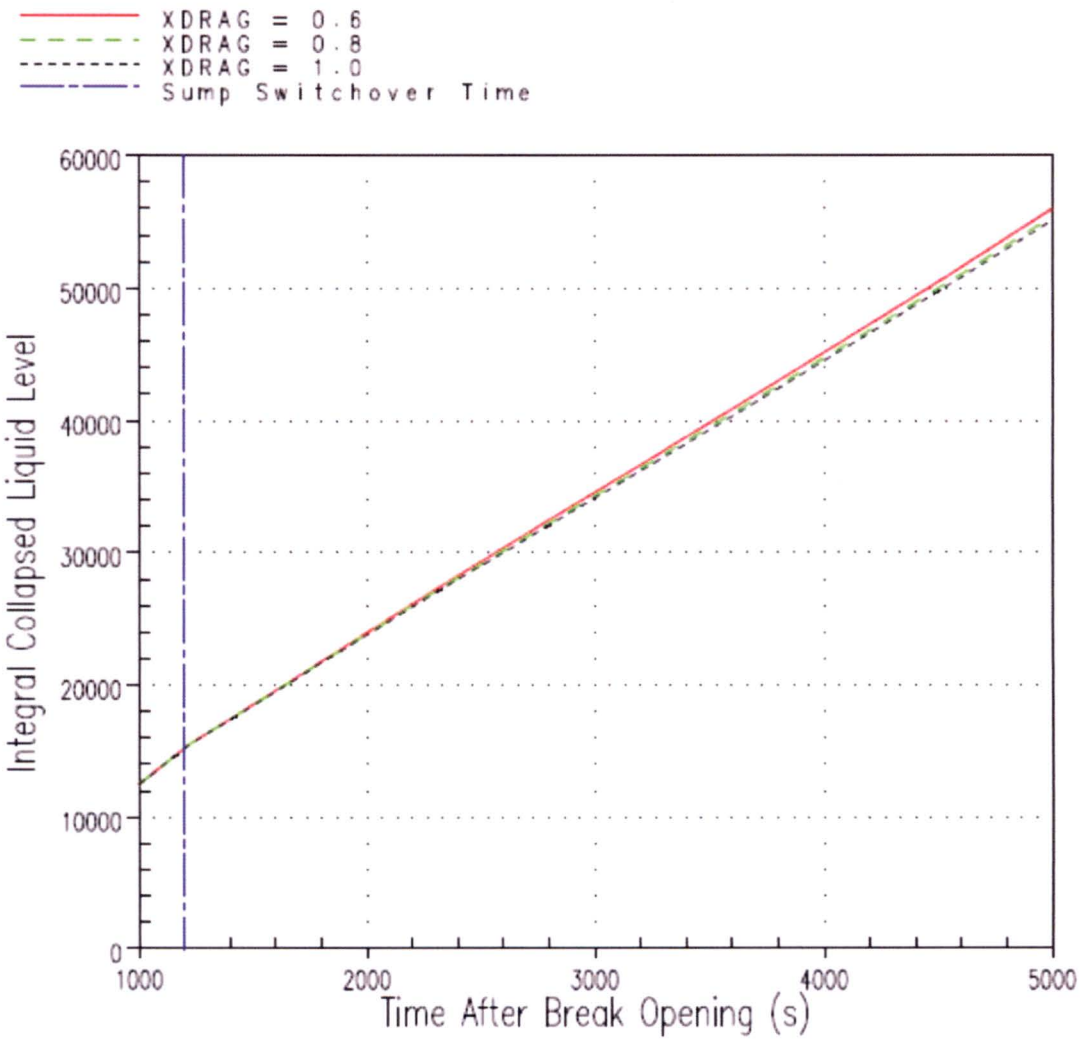

Figure RAI-4.8-18 Westinghouse Downflow Plant Interfacial Drag Sensitivity Core Average Integrated Collapsed Liquid Level Results

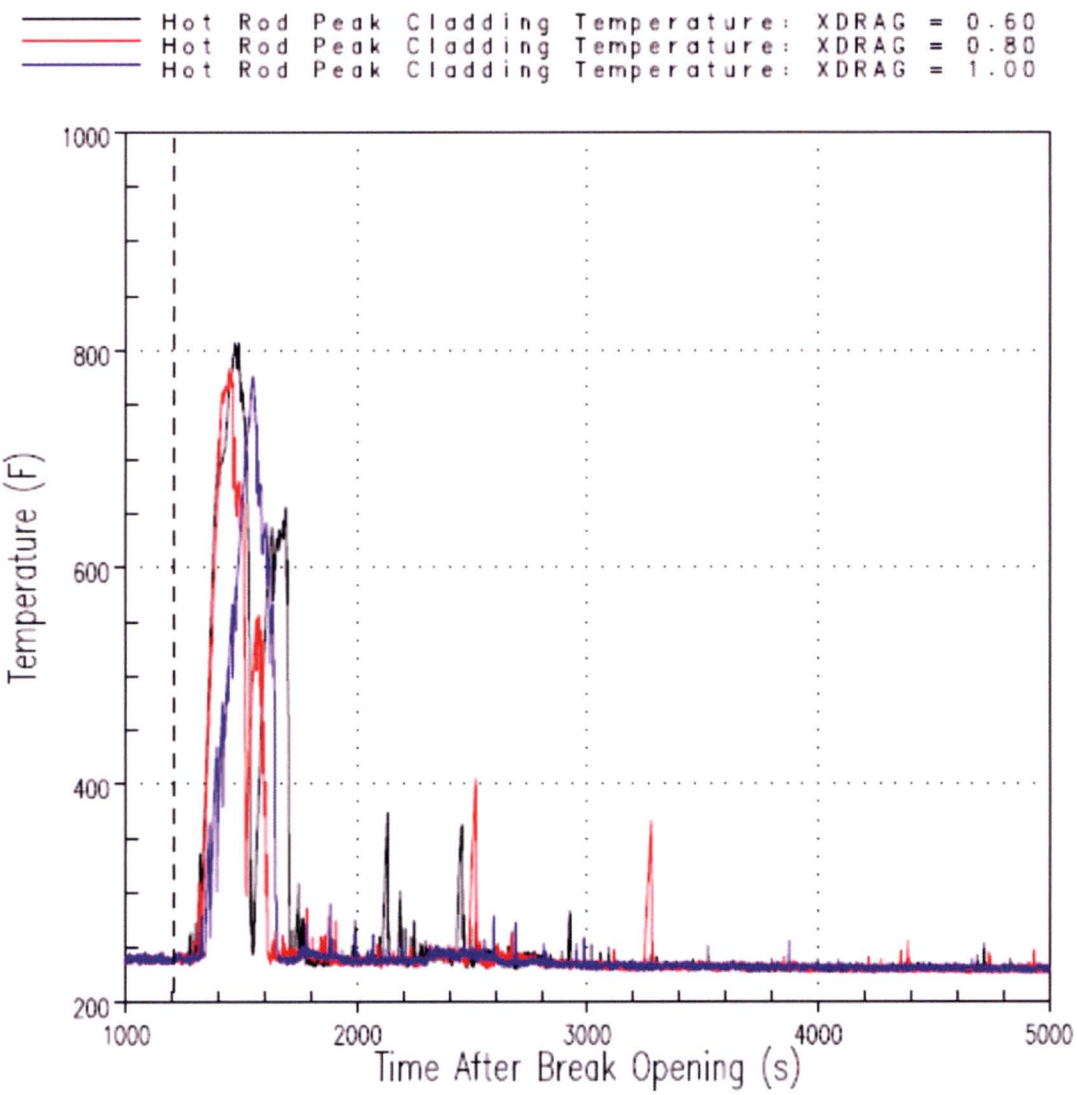

Figure RAI-4.8-19 Westinghouse Downflow Plant Axial Interfacial Drag Sensitivity Debris-Induced Heatup Results

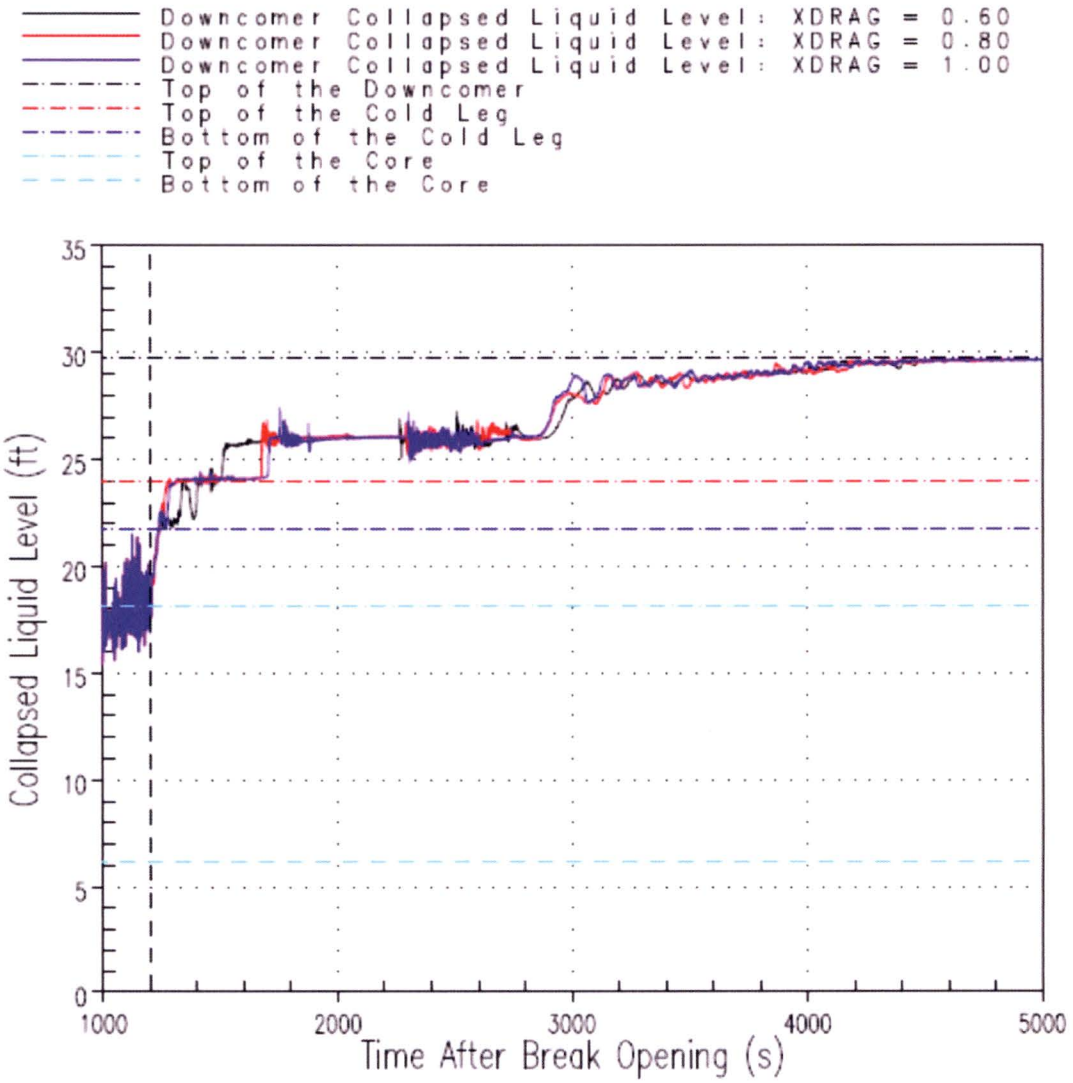

Figure RAI-4.8-20 Westinghouse Downflow Plant Interfacial Drag Sensitivity Downcomer Collapsed Liquid Level Results

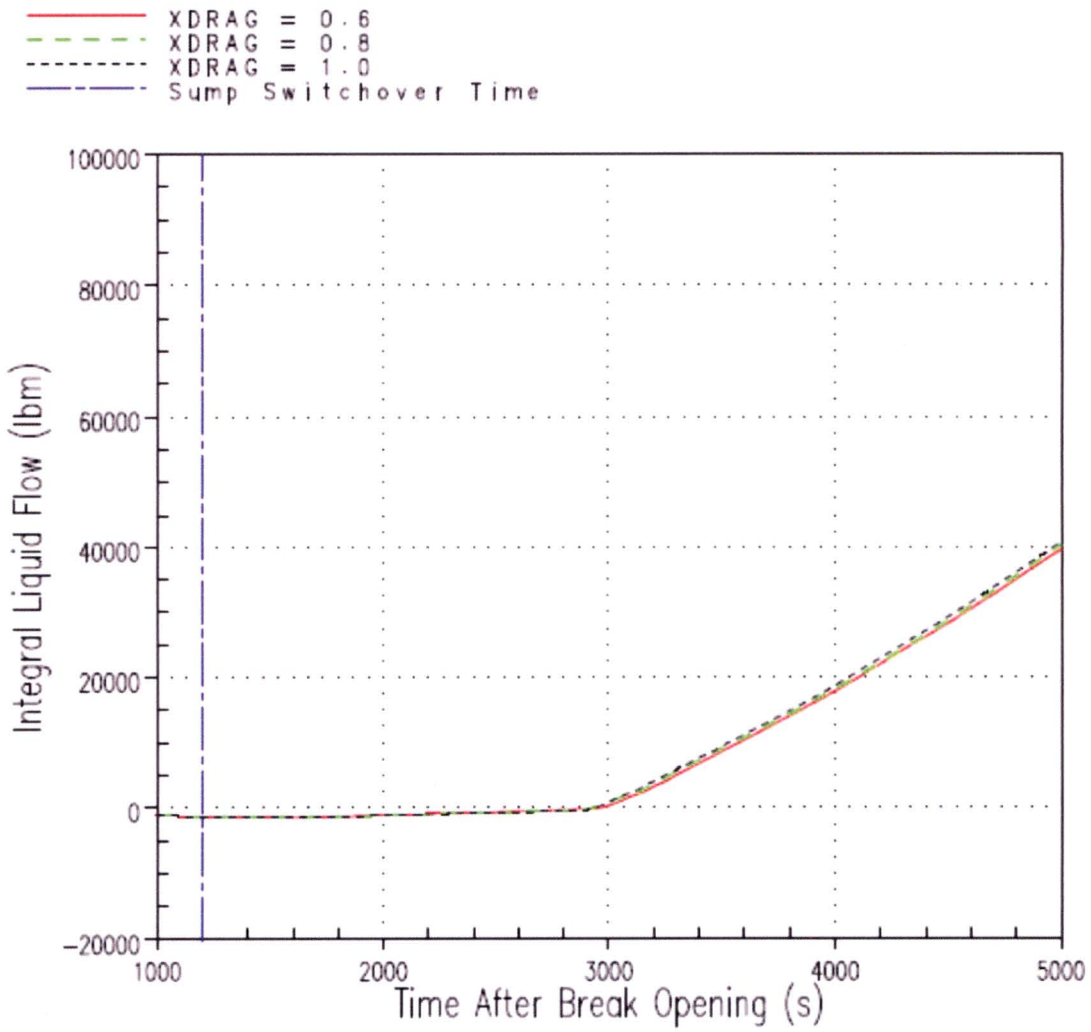

Figure RAI-4.8-21 Westinghouse Downflow Plant Interfacial Drag Sensitivity Upper Head Spray Nozzle Integrated Liquid Flow Results

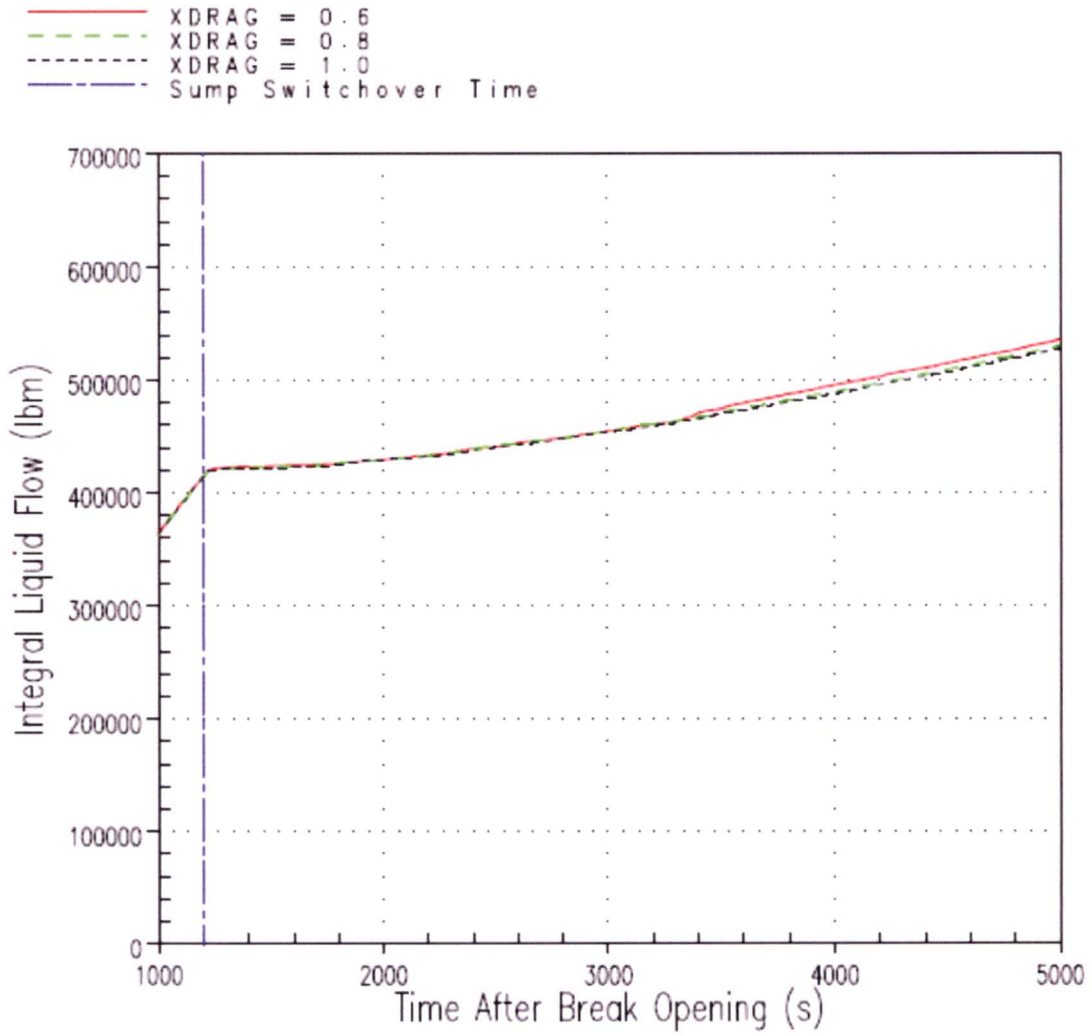

Figure RAI-4.8-22 Westinghouse Downflow Plant Interfacial Drag Sensitivity Broken Loop Hot Leg Nozzle Integrated Liquid Flow Results

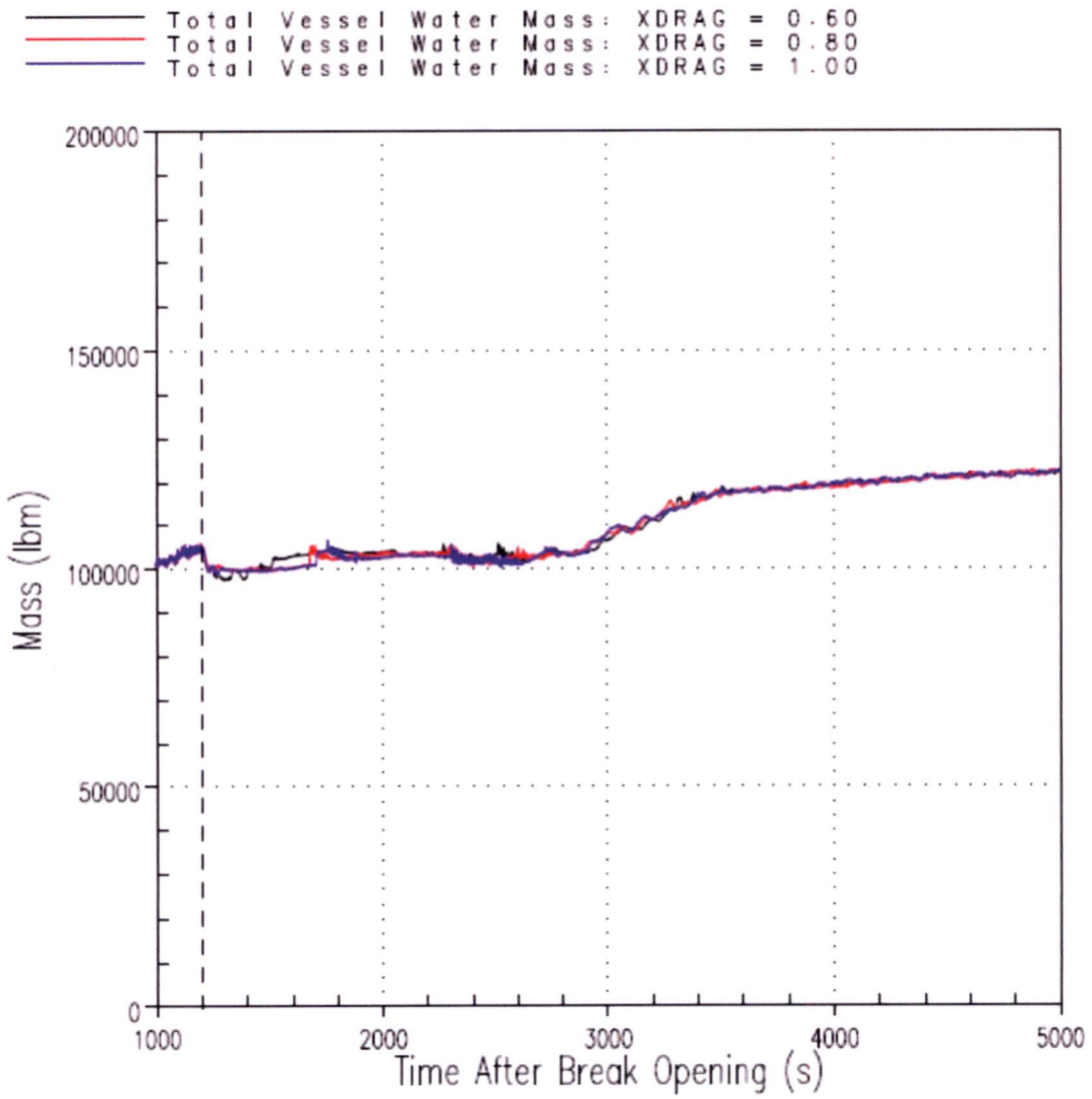

Figure RAI-4.8-23 Westinghouse Downflow Plant Interfacial Drag Sensitivity Reactor Vessel Water Mass Results

Conclusions

Based on the G1 and G2 experimental assessment using WCOBRA/TRAC, it is determined that the use of the 0.8x nominal interfacial drag is appropriate for the GSI-191 thermal hydraulic analysis. The sensitivity study presented also demonstrates that the interfacial drag multiplier has only a minimal impact on the key parameters output from the GSI-191 thermal hydraulic analysis.

References

RAI-4.8-1 WCAP-16009-P-A, "Realistic Large-Break LOCA Evaluation Methodology Using the Automated Statistical Treatment Of Uncertainty Method (ASTRUM)," January 2005.

RAI-4.8-2 WCAP-9764, "Documentation of the Westinghouse Core Uncovery Tests and the Small Break Evaluation Model Core Mixture Level Model," 1980.

RAI-4.8-3 EPRI NP-1692, Volumes 1 and 2, Research Project 1760-1, "Heat Transfer Above the Two-Phase Mixture Level Under Core Uncovery Conditions in a 336-Rod Bundle," 1981.

c. Explain how interfacial drag was treated in the codes used for the CE and B&W analyses in Sections 10 and 11, respectively. Provide the information requested in Item b above as it applies to the EMs used for the analyses of the CE and B&W design categories.

The response to this question is provided in the CE and B&W submittals

RAI-4.9, Vol. 4

Sections 8 through 11 provide LOCA T-H analysis results for determining the earliest transient point in time, t_{block}. T_{block} is defined so that the acceptance criteria for maintaining LTCC would be satisfied should complete core inlet blockage occur at or after this point in time following a HLB LOCA. Figures 8-16 (Case 1B), 9-15 (Case 1A), 10-13 (Case 1), and 11-9 (Case 1) show the core peak cladding temperature (PCT) responses following the application of complete core inlet blockage with temperature excursions being observed in Figures 8-16 and 9-15. Provide the following information in a table format (where applicable) for the limiting analyses. For example, Case 1B in Section 8 and Case 1A in Section 9 for each plant category. Include the axial void fraction profile results (Item c) in separate tables. If a parameter exhibits an oscillatory behavior within the vicinity of the time point of interest, include the parameter's variation range along with the observed predicted value itself.

a. Provide the following prediction results relative to the PCT excursions:

   i. Time of PCT (relative to break opening)

   ii. PCT

   iii. The core channel and axial elevation associated with the PCT location

Response

See the Response to RAI-4.9 Item b.

b. Provide the following results relative to the axial elevation in the channel where the PCT was observed and the timing of PCT:

   i. Fuel rod local linear heat generation rate

   ii. Predicted two-phase flow regime

   iii. Vapor/liquid mass flow rates and mass fluxes for predicted continuous/dispersed flow fields (axial and cross-flow)

   iv. Vapor/liquid phase velocities for predicted continuous/ dispersed flow fields (axial and cross-flow)

   v. Wall heat transfer mode

   vi. Fuel rod heat transfer fluxes to continuous/dispersed flow fields (clarify if any radiation heat transfer of significance was predicted)

   vii. Heat transfer coefficients to continuous/dispersed flow fields.

Response

The information requested in Item a. and Item b. is provided in Table RAI-4.9-1. Radiation heat transfer tends to be an important mode of heat transfer only when the rod temperatures become very high (> 2000°F). As the maximum rod temperatures during these transients remain below 800°F, the rod to single phase vapor heat transfer due to radiation is not significant. It is estimated that the rod to vapor heat transfer due to radiation is less than 5% of the total heat transfer.

Table RAI-4.9-1 T/H Analysis Results for Determining t_{block}

Item	Parameter	Upflow Case 1B		Downflow Case 1A	
a.i	Time of PCT, s	8803.5		15,990	
a.ii	PCT, °F	780		792	
a.iii	Core Channel and Elevation of PCT, ft	Channel 15 - 10.48		Channel 13 - 9.42	
b.i	Fuel rod linear heat generation rate, kW/ft	0.154		0.146	
b.ii	Two-phase flow regime	Single-phase vapor		Single-phase vapor	
b.iii	Mass flow rate, lbm/s	Axial[1]	Lateral[2]	Axial[1]	Lateral[2]
	vapor	0.2	0	0.2	0
	dispersed liquid	0	0	0	0
	continuous liquid	0	0	0	0
	Mass flux, $lbm/s \cdot ft^2$	Axial[1]	Lateral[2]	Axial[1]	Lateral[2]
	vapor	0.5	0	0.5	0
	dispersed liquid	0	0	0	0
	continuous liquid	0	0	0	0
b.iv	Velocity, ft/s	Axial[1]	Lateral[2]	Axial[1]	Lateral[2]
	vapor	22	-1	14	0
	dispersed liquid	0	0	0	0
	continuous liquid	0	0	0	0
b.v	Heat transfer mode	Single-phase vapor		Single-phase vapor	
b.vi	Heat flux, $Btu/hr \cdot ft^2$	3300		1500	
b.vii	Heat transfer coefficient, $Btu/hr \cdot ft^2 \cdot$ °F				
	vapor	12		13	
	liquid	0		0	

Table RAI-4.9-1 T/H Analysis Results for Determining t_{block} (cont'd)			
Item	**Parameter**	**Upflow Case 1B**	**Downflow Case 1A**
c.	Axial void distribution	Figures RAI-4.9-1 and RAI-4.9-2	Figures RAI-4.9-3 and RAI-4.9-4
	Two-phase mixture level, ft	8.52	6.68
1. Positive direction is up 2. Positive direction is into the hot assembly			

c. Provide the axial void fraction distribution in the channel where the PCT was observed at the time when the PCT occurred and corresponding predicted two-phase mixture level in the channel.

Response

The axial void distribution in the hot assembly channel at the time the PCT occurs is presented as Figure RAI-4.9-1 for Upflow Case 1B and Figure RAI-4.9-3 for Downflow Case 1A. Since the calculated void fraction can exhibit oscillatory behavior, the range of values (maximum, average, and minimum) over a 10 second interval centered on the PCT time is presented as Figure RAI-4.9-2 for Upflow Case 1B and Figure RAI-4.9-4 for Downflow Case 1A. The predicted two-phase mixture level is provided in Table RAI-4.9-1.

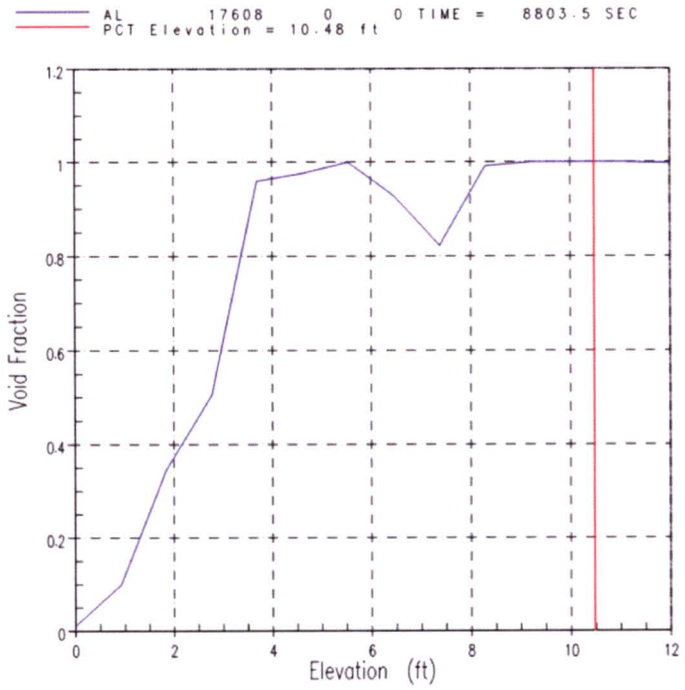

Figure RAI-4.9-1 Upflow Case 1B Axial Void Distribution at Time PCT Occurs (8803.5 s)

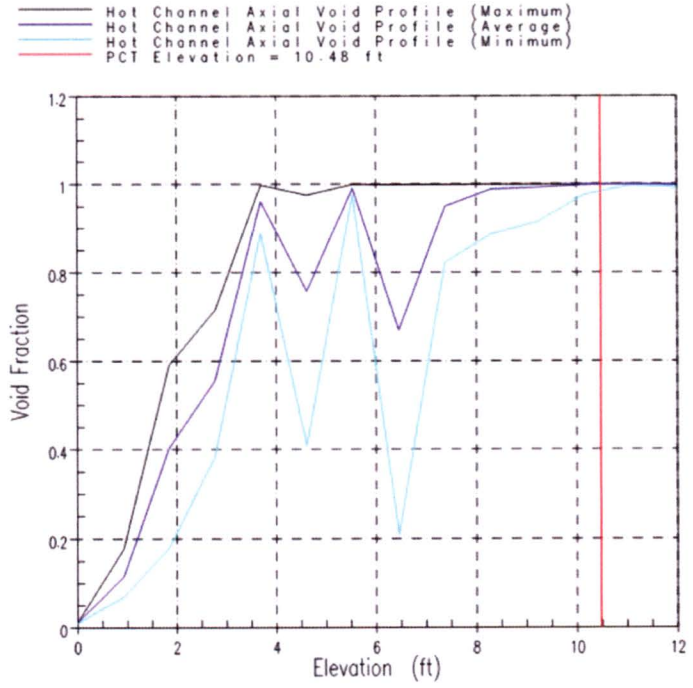

Figure RAI-4.9-2 Upflow Case 1B Axial Void Distribution Range near PCT Time

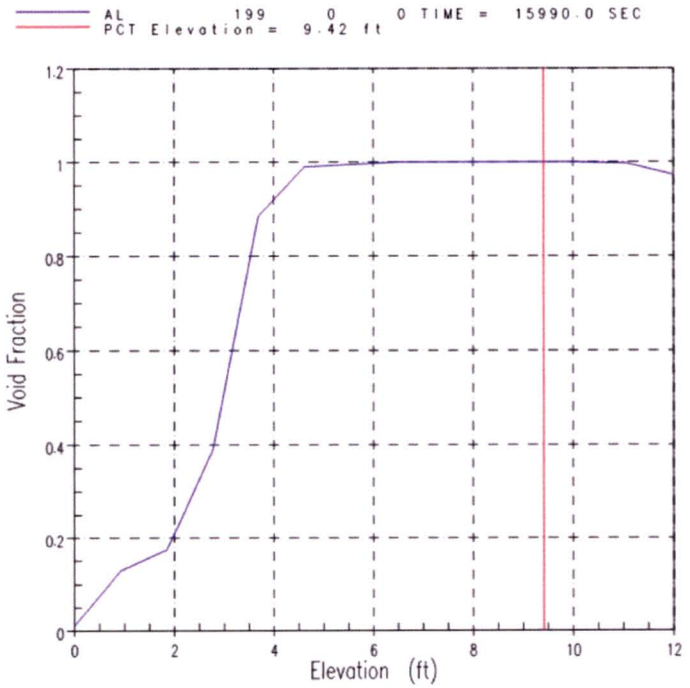

Figure RAI-4.9-3 Downflow Case 1A Axial Void Distribution at Time PCT Occurs (15,990 s)

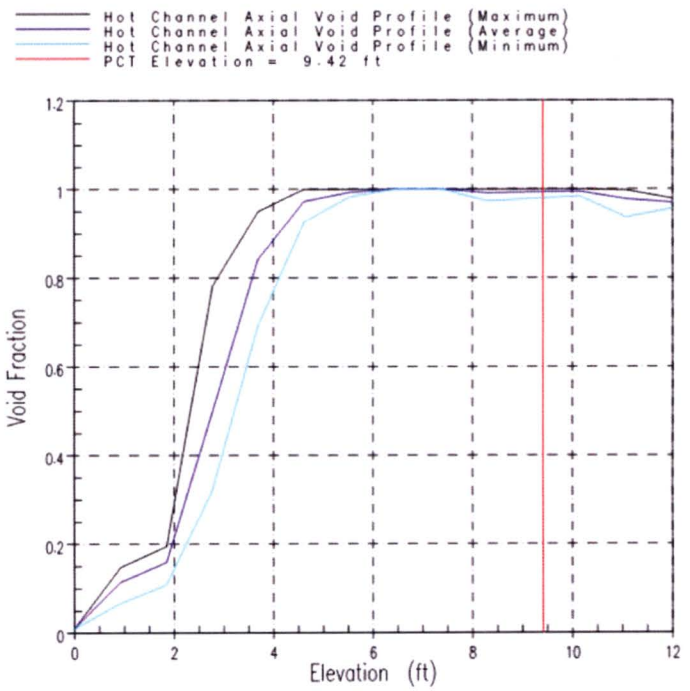

Figure RAI-4.9-4 Downflow Case 1A Axial Void Distribution Range near PCT Time

d. Identify the closure heat transfer correlations associated with the heat transfer regimes identified as controlling with regard to the PCT values in Figures 8-16 and 9-15. Provide the ranges of applicability of these correlations and compare them against the predicted core limiting T-H parameters.

Response

As shown in the response to RAI-4.9 Item b., convection to single-phase vapor is the controlling heat transfer regime with regard to the peak cladding temperature (PCT) during the debris-induced secondary heatup. In WCOBRA/TRAC, heat transfer to single-phase is assumed when the vapor fraction is greater than [ ]^{a,c} A set of four correlations are used to determine the heat transfer coefficients for convection to single-phase vapor, as described in WCAP-16009-P-A, Section 6-2-1 (Reference RAI-4.9-1). These correlations are the McAdams correlation for turbulent natural convection, a constant Nusselt number value for laminar forced convection, the Dittus-Boelter equation, and an expression proposed by Wong and Hochreiter for turbulent forced convection.

The WCOBRA/TRAC single-phase vapor heat transfer package extends from a turbulent free convection regime (McAdams correlation) to a fully turbulent forced convection regime (Dittus-Boelter). As shown in the response to RAI-4.9 Item b., the vapor phase velocity in the hot channel at the time of PCT is on the order of 15 – 25 ft/s. Assuming a slightly superheated vapor phase at atmospheric conditions (T = 300°F, P = 14.7 psia), the resulting Reynolds number for the rod bundle geometry is on the order of 1900 – 3200, which is in the laminar to transition to fully turbulent regimes for rod bundle geometries. The WCOBRA/TRAC single-phase vapor heat transfer package is valid for these regimes.

e. Identify the constitutive correlations for computing void fraction and any predicted entrained droplets/liquid film fields, as applicable, associated with the two-phase flow regime predicted at the PCT location and time of its occurrence. Provide their ranges of applicability and compare them against the predicted core limiting T-H parameters.

Response

As shown in the response to RAI-4.9 Item b., single-phase vapor is the controlling flow regime with regard to the PCT during the debris-induced secondary heatup. In WCOBRA/TRAC, single-phase vapor is assumed when the vapor fraction is greater than [ ]^{a,c} WCOBRA/TRAC vessel components solve a two-fluid, three-field model for flow of a two-phase steam-water mixture, which can contain a non-condensable in the vapor phase. The three fields are a vapor field, a continuous liquid field and an entrained liquid drop field. Each field uses a set of three dimensional continuity, momentum, and energy equations with one exception. A common energy equation is used by both the continuous liquid and entrained liquid drop fields. The effects of one phase on another are accounted for by the interaction terms appearing in the governing equations. The void fraction of each phase is one of the primary dependent variables appearing in the field equations solved by WCOBRA/TRAC. Reference RAI-4.9-1, Sections 2-2 and 2-3 include a detailed discussion of the two-fluid field equations and Section 2-6 describes the solution methods. The momentum transfer

models, and the interfacial heat and mass transfer models are described in Reference RAI-4.9-1, Sections 4 and 5, respectively.

Reference

RAI-4.9-1 WCAP-16009-P-A, "Realistic Large-Break LOCA Evaluation Methodology Using the Automated Statistical Treatment Of Uncertainty Method (ASTRUM)," January 2005.

RAI-4.10, Vol. 4

Provide plots showing the heat generation rates from the decay heat models that were used in the LOCA T-H analyses documented in Sections 8 through 11. Show the decay heat rates as a function of transient time with time zero corresponding to the break opening. Display the decay heat rate in relative dimensionless units using a linear scale with a range from null to 1.2. Plot the time axis in a logarithmic scale in units of seconds. Use a common time range that starts at one second after break opening and ends when the longest analyzed LOCA transient case ends.

Response

Figure RAI-4.10-1 shows the heat generation rates for the Westinghouse upflow and downflow plant categories. The figure also shows the Appendix K Decay Heat Model (1971 ANS Infinite + 20%) for fission product decay. WCOBRA/TRAC models initial stored energy, fission heat using a point kinetics model, actinide decay heat, heat generated from cladding chemical reactions, and fission product decay heat. During the early phases of the transient (< 50 seconds) the first four heat sources modeled by WCOBRA/TRAC increase the overall heat generation rate beyond that predicted by the Appendix K model for fission product decay. However, as the transient progresses, these heat sources diminish and the primary contributor to heat generation is the decay of fission products. This is seen in Figure RAI-4.10-1, which shows that the WCOBRA/TRAC heat generation rates compare well with the Appendix K Decay Heat Model, which only accounts for fission product decay, after approximately 50 seconds.

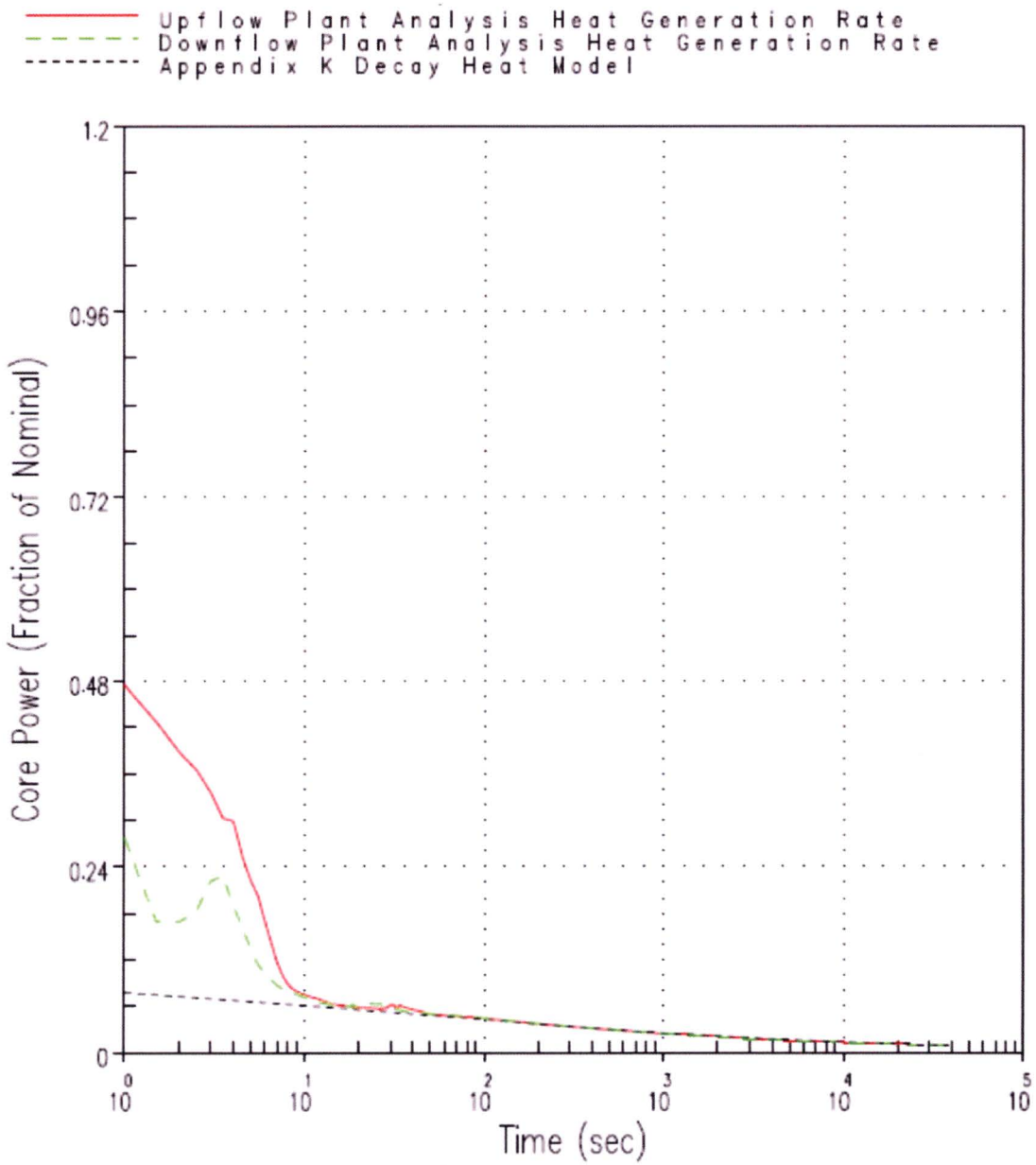

Figure RAI-4.10-1 Heat Generation Rates from the Westinghouse Upflow and Downflow Plant Categories

RAI-4.11, Vol. 4

Section 5.4 states that "the analysis completed by AREVA using S-RELAP5 produced results that compared reasonably well to those predicted by WCOBRA/TRAC, which are described in Section 9." The section also explains that "the plant and transient condition analyzed was identical to that used by Westinghouse;" however, "the plant models used for each analysis were developed independently following different methods and techniques." Section 5.4 concludes that "irrespective of the computer codes and methods used, the resulting code predictions are expected to be consistent."

a. Define the simulated LOCA transient and provide a summary description of the analyses. Provide a table that documents and compares key inputs and modeling features for both studies and explain how this information relates to key inputs provided in Table 6-2 for the Westinghouse downflow plant design analysis.

b. Provide comparisons of key results from the analyses. Explain any significant discrepancies between the results from the studies and provide an assessment of the degree of conservatism reflected in each of the analyses. Discuss how differences in the prediction results relative to t_{block}, K_{max}, K_{split}, and/or m_{split} could be caused or explained by differences in the applied methodologies, plant model features (such as core nodalization), assumed key inputs, and other relevant conditions.

c. Provide references for the technical documents containing the calculation notebooks documenting the analyses in Items a and b and confirm that the analyses were quality assured.

The response to these questions is provided in the CE submittal

RAI-4.12, Vol. 4

The UPI plants were not considered as part of the analysis due to their ECCS configurations. Provide justification that plants with the UPI configurations do not require T-H analyses to demonstrate that the acceptance criteria defined in WCAP-17788 are satisfied and that the TR is applicable to their specific plant designs including applicable ECCS features.

Response

WCAP-17788 Volume 1 Section 8 describes the method used for UPI plants to demonstrate that the acceptance criteria defined in WCAP-17788 are satisfied. UPI plants do not require core inlet limits derived from the TH analyses (K_{max}) since the UPI core inlet limit is 15 g/FA, based on WCAP-16793-NP-A, Rev. 2 (Reference RAI-4.12-1). Since the 15g/FA core inlet limit is applied, the core inlet cannot block completely after the arrival of chemical effects. As such, t_{block} is not needed for UPI plant analysis. UPI plants also do not credit AFPs, so K_{split} and m_{split} are not needed.

Reference

RAI-4.12-1 WCAP-16793-NP-A, Revision 2, "Evaluation of Long-Term Cooling Considering Particulate, Fibrous and Chemical Debris in the Recirculating Fluid," July 2013.

RAI-4.13, Vol. 4

Figure 8-13 shows the mid-core velocity in the BB channel going from negative, interpreted as downward, to about zero very rapidly before switchover time. The plotted BB inlet velocity remains stable at near zero or around a slightly negative value throughout the exhibited part of the transient while the BB exit velocity remains stable at a low negative value. In addition, the BB exit velocity is large in magnitude compared to the BB inlet velocity. Provide an explanation for this behavior.

Response

During the transient presented in WCAP-17788-P/NP, Volume 4, Section 8.2.1, the BB channel is not liquid solid. WCAP-17788-P/NP, Volume 4, Figure 8-8 provides the BB channel collapsed liquid level during the transient. The figure shows that the BB channel has a collapsed liquid level of approximately 3 ft at 500 seconds. As the transient progresses, the BB channel collapsed liquid level increases consistent with the downcomer collapsed liquid level. Figure RAI-4.13-1 shows the BB inlet, mid-plane (mid-core), and exit liquid velocities with the y-axis extended to show the complete behavior of the mid-core BB channel velocity. As seen in the figure, the mid-core velocity is relatively constant at -1.5 ft/s (the negative indicates downflow). The rapid change in liquid velocity is representative of the mid-core BB cell filling with liquid. The time that the mid-core velocity changes is consistent with the time that the BB channel collapsed liquid level reaches the mid-core elevation.

Liquid from the upper plenum region drains into the top of the BB channel and serves as the source for filling the BB channel. This is illustrated in Figure RAI-4.13-1, or WCAP-17788-P/NP, Volume 4, Figure 8-13, which shows that flow into the top of the BB channel is downward, while there is very little net flow at the BB inlet. The downward liquid velocity at the mid-core is considerably larger in magnitude compared to the BB exit velocity because the mid-core cell contains increased resistance due to the presence of a former plate. To illustrate this, Figure RAI-4.13-2 was generated, which shows the BB channel liquid velocity at the mid-core (Cell 7) and the two adjacent cells (Cell 6 and Cell 8). As the figure indicates, the liquid velocity magnitudes in the adjacent cells are less than the Cell 7 liquid velocity and are more comparable to the magnitude of the BB channel exit velocity.

To illustrate the filling of the BB channel with liquid near the mid-core elevation, the void fraction of Cells 6, 7, and 8 are presented in Figure RAI-4.13-3. As the figure indicates, Cell 6 fills with liquid first, followed by Cell 7, then Cell 8. Even though the velocities in these cells are considerably different due to the presence of a former plate within Cell 7, the liquid mass flow rates shown in Figure RAI-4.13-4 are consistent with the filling behavior.

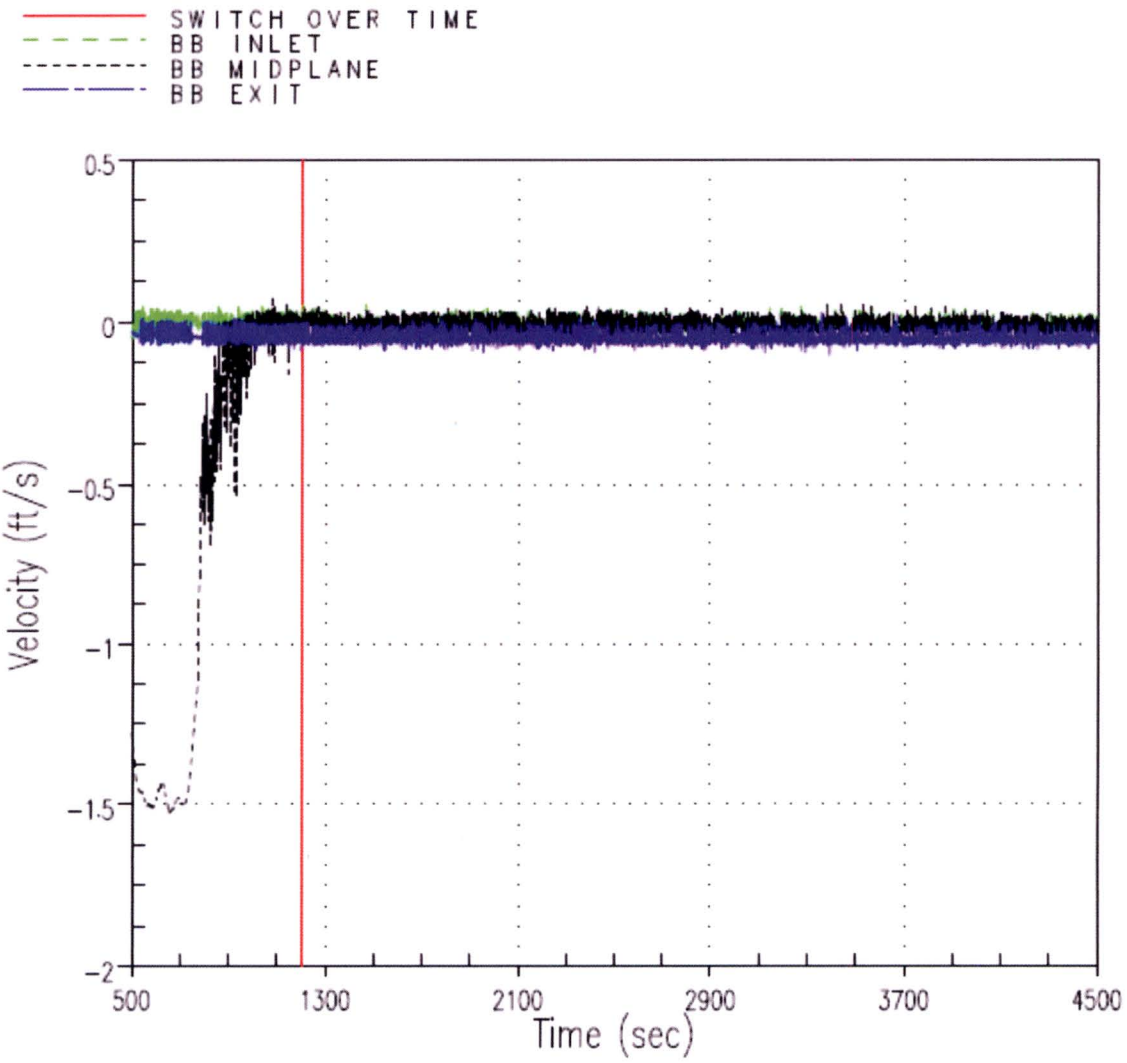

Figure RAI-4.13-1 Barrel/Baffle Channel Inlet, Mid-plane, and Exit Liquid Velocities

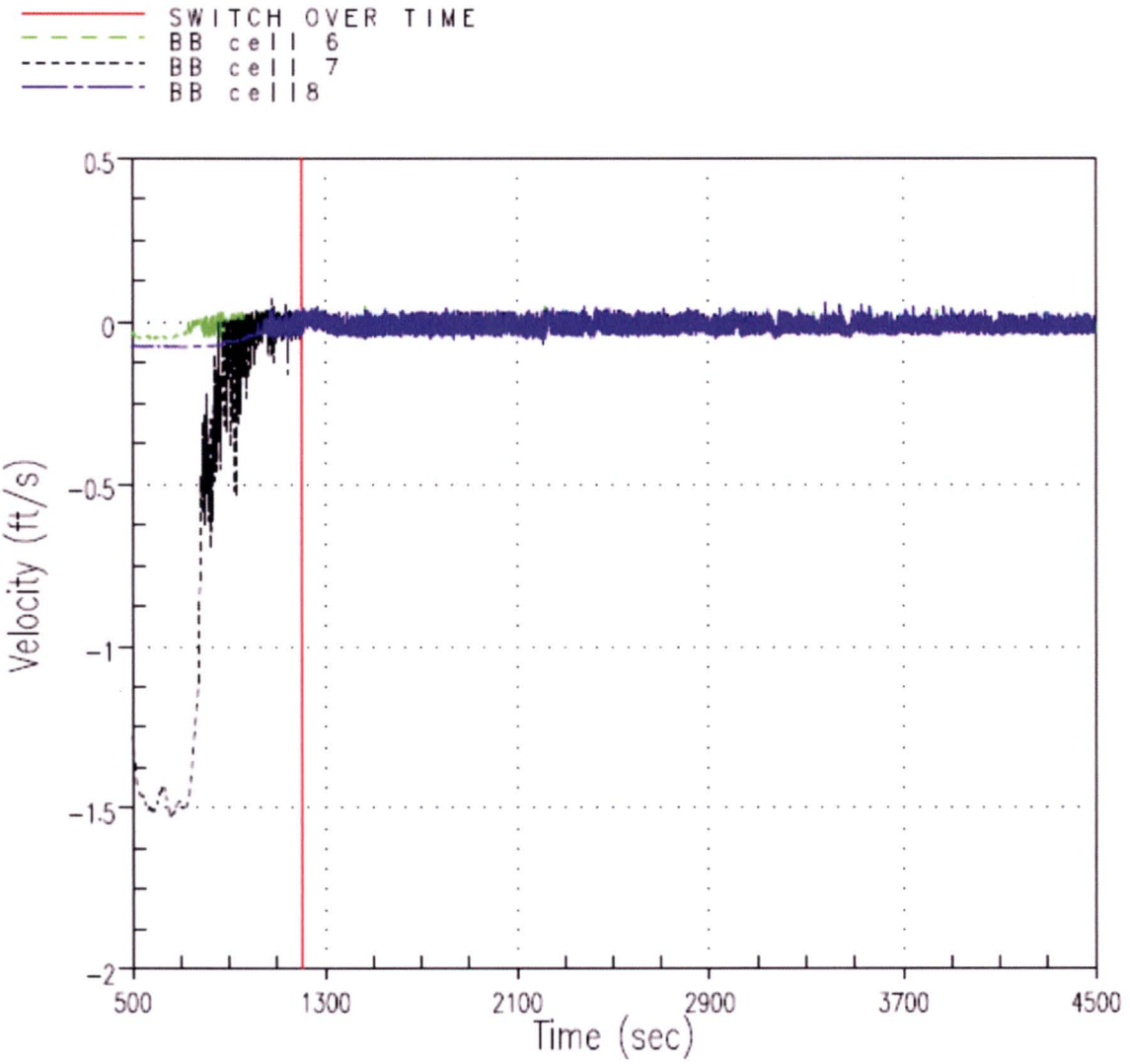

Figure RAI-4.13-2 Barrel/Baffle Channel Liquid Velocities from Cells 6, 7, and 8

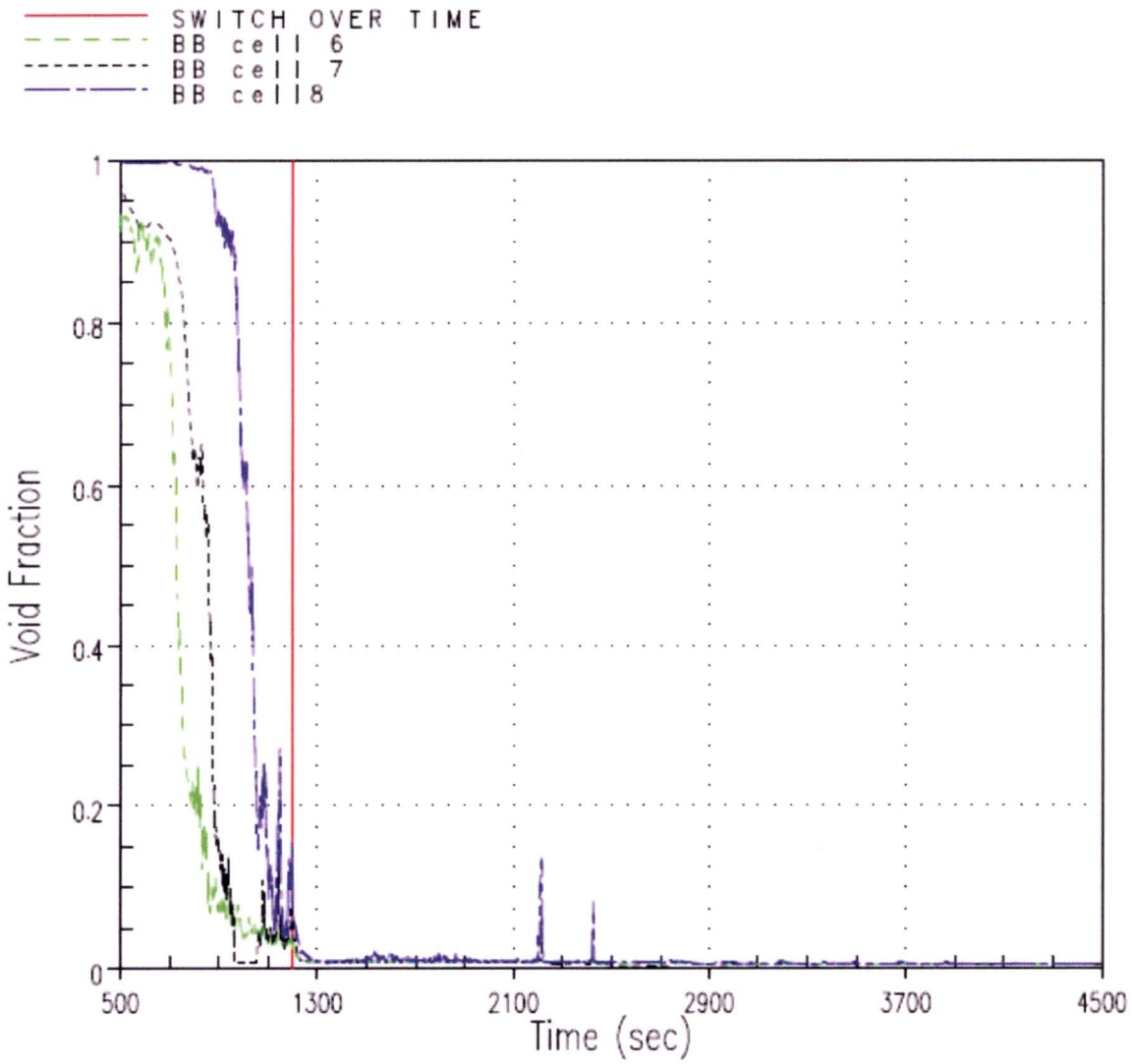

Figure RAI-4.13-3 Barrel/Baffle Channel Void Fraction from Cells 6, 7, and 8

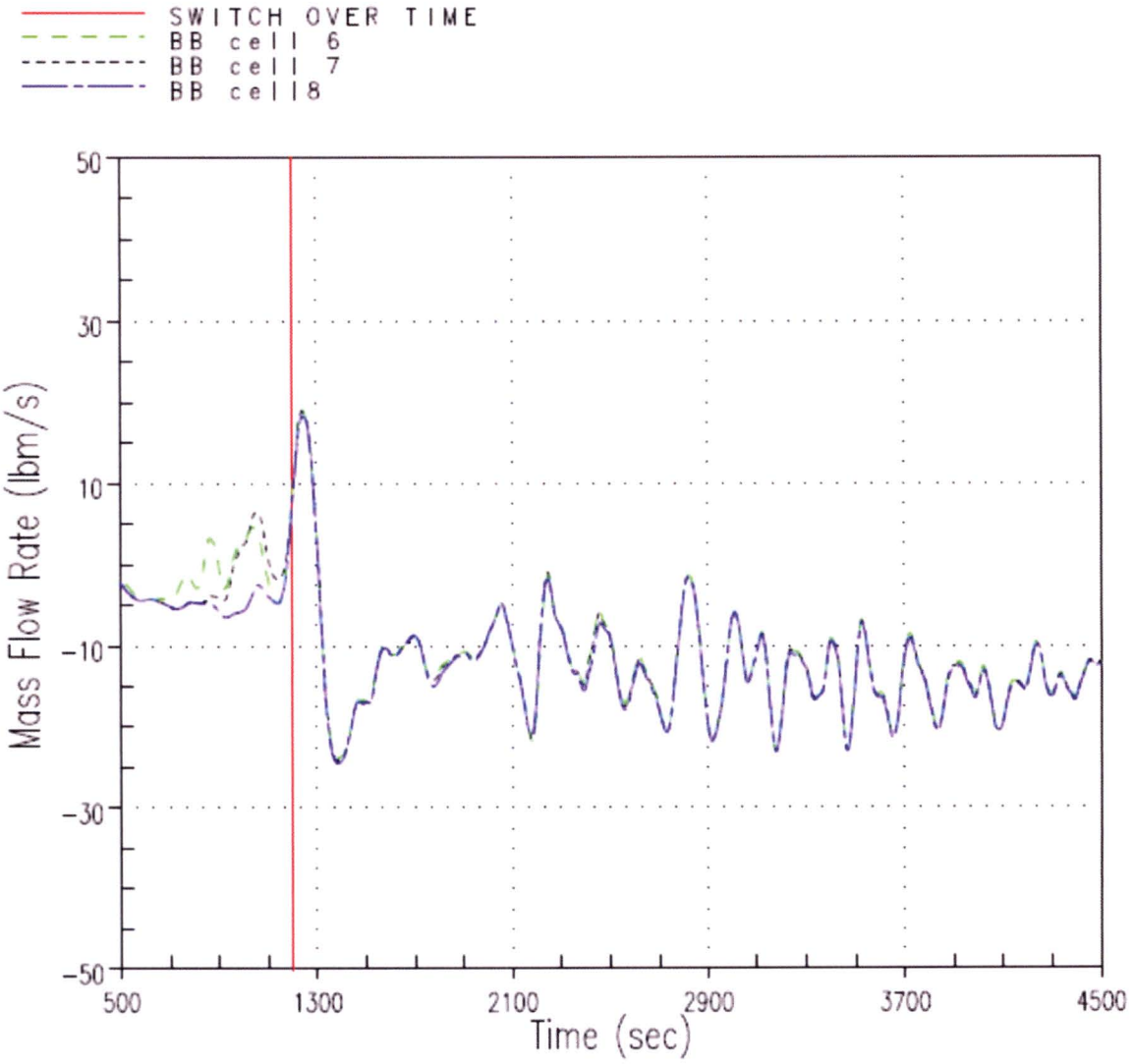

Figure RAI-4.13-4 Barrel/Baffle Channel Mass Flow Rate from Cells 6, 7, and 8

RAI-4.14, Vol. 4

Figures 8-16 and 8-25 show a spike in PCT occurring while the downcomer fills. Once the flow begins exiting the BB region, the core begins to cool again and PCT decreases. Were the potential range of flow rates for downcomer fill considered in the analyses? Explain how the analysis accounts for potential uncertainties or variability in the downcomer fill time. If the analysis does not account for such uncertainty/variability, explain how the behavior (PCT spike) would be affected by different downcomer fill times.

Response

The downcomer volume for Westinghouse plants is proportional to the number of reactor coolant loops and the power-to-volume ratio is similar between 3- and 4- loop plants. Given the proportionality of the downcomer volume, the downcomer fill time and associated uncertainties are effectively embodied in the ECCS flow rate modeled in the analyses. The nominal range of the ECCS recirculation flow rate modeled in the thermal-hydraulic analyses is 18 gpm/FA to 40 gpm/FA for the upflow plants and 12 gpm/FA to 40 gpm/FA for the downflow plants based on a survey of plant design data conducted early in the development of the methodology. These values represent the maximum expected flow such as having all ECCS trains in operation but with ECCS pump head loss degradation consistent with the degradation mechanisms assumed ECCS performance used in the short-term LOCA analyses. However, the actual range may vary depending on plant-to-plant downcomer design variations and current ECCS performance capability.

The methodology is applicable for plants whose ECCS recirculation flow rate lies within the range of 18 gpm/FA to 40 gpm/FA for the upflow plants and 12 gpm/FA to 40 gpm/FA for the downflow plants as adjusted for downcomer design variations and ECCS performance capability to account for variability in these parameters. Plants that fall below this range will need to evaluate the effect since a slower downcomer fill time would be expected to result in a higher calculated PCT. Plants that are above this range would not need to evaluate the difference since a faster downcomer fill time would be expected to result in a lower calculated PCT. Variations in downcomer volume are accounted for in the required ECCS recirculation flow check, as described in the response to RAI-4.5.

RAI-4.15, Vol. 4

Provide the results of Figures 9-9 and 9-10 on the same graph. Normalize the integrated mass flow on an average channel basis so that a meaningful comparison can be made.

Response

The results of WCAP-17788-P/NP, Volume 4, Figures 9-9 and 9-10, normalized on a per fuel assembly basis, are provided in Figure RAI-4.15-1.

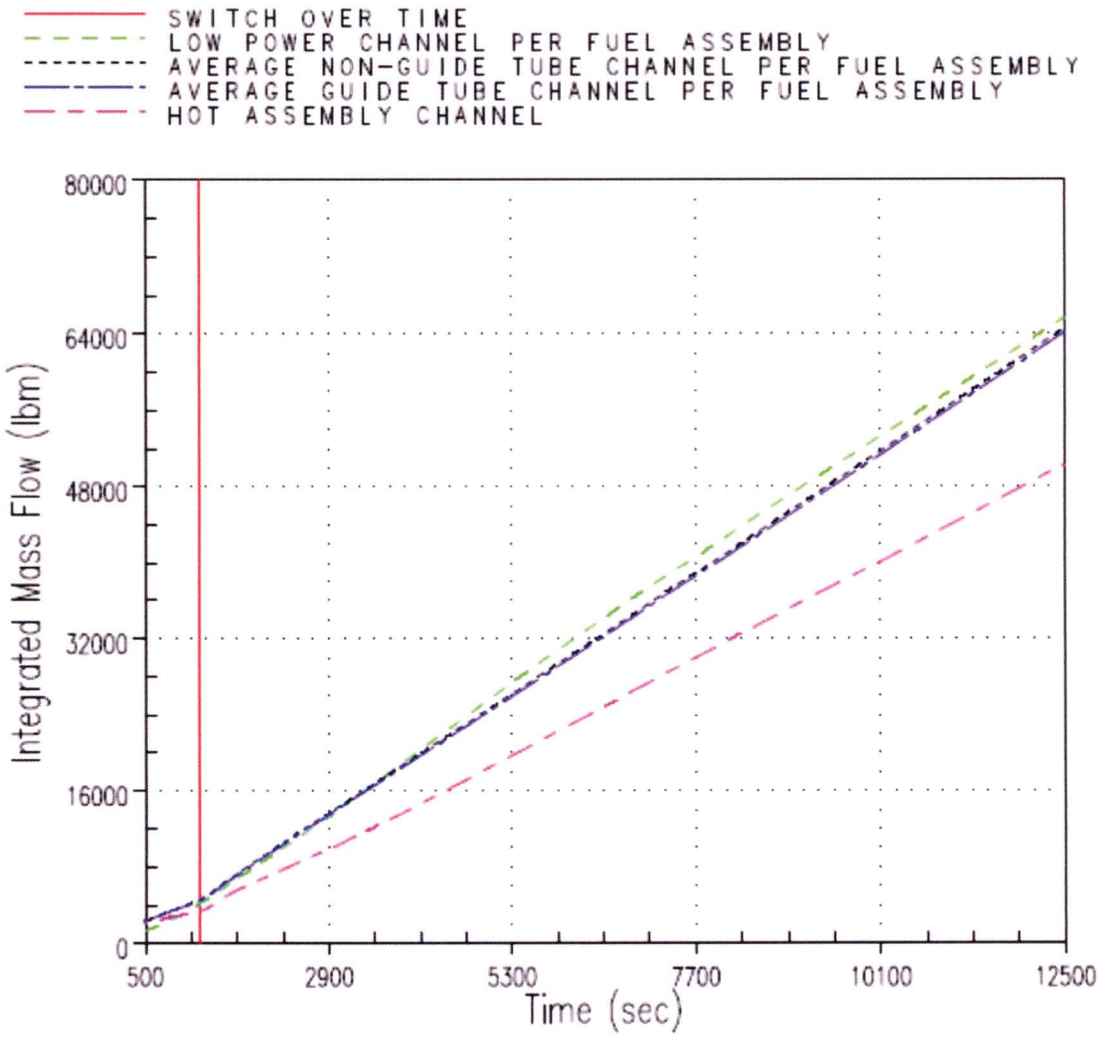

Figure RAI-4.15-1 Integrated Core Inlet Mass Flow

RAI-4.16, Vol. 4

Assumption 6 in Section 4.1 states that "ECCS temperature during sump recirculation will be set at or near saturation temperature at containment pressure" and explains that "neglecting the presence of subcooling is conservative because it maximizes the steaming rate in the core and minimizes the cooldown rate of the reactor vessel (RV) and steam generators (SGs)." Tables 6-1 through 6-4 include the parameter "ECCS temperature during recirculation phase" as a key input. The CE plant category stands apart in the sense that this input is set at a temperature of 212 °F with the "containment pressure during recirculation phase" specified as "dynamically calculated" according to Table 6-3. During the NRC audit of the AREVA T-H analyses for the CE plant category, it was clarified that S-RELAP5 was used in a coupled mode with the ICECON containment code to calculate the containment backpressure.

a. Identify contributing physical processes that are dependent on the degree of ECCS fluid temperature subcooling and explain the effects associated with these processes with regard to core cooling. In addition to core steaming, explain whether processes such as condensation, downcomer boiling, liquid entrainment, and boiling in SG tube bundles (if engaged) were considered among such processes. State whether these effects are considered conservative or non-conservative and provide justifications for the conclusions.

Response

The physical processes applicable to Westinghouse plants are provided in the response to RAI-4.7. The processes that have dependence on the ECCS fluid temperature include the void generation (steaming rate), entrainment, mixture level, steam generator primary side boiling, condensation and downcomer boiling. Of these processes, void generation and upper plenum mixture level are ranked high during all periods of the GSI-191 scenario. Entrainment is ranked medium during the partial core uncovery period, and steam generator boiling is ranked medium for the downflow plant during the complete core blockage period. Condensation and downcomer boiling are ranked low during all periods of the GSI-191 scenario. The justification for these rankings is provided in the response to RAI-4.7.

A sensitivity study presented in the response to RAI-4.23 Item i., demonstrates that the key thermal-hydraulic output parameters are not significantly influenced by the degree of ECCS subcooling during sump recirculation. With regard to void generation, the sensitivity study shows that the presence of ECCS fluid subcooling during the recirculation phase of the transient reduces core voiding and increases the reactor vessel liquid inventory. The upper plenum mixture level is increased which increases the break flow. For these high ranked processes, applying a saturated ECCS fluid temperature during sump recirculation is conservative, as supported by the sensitivity study results.

As ECCS fluid subcooling tends to reduce the void generation, the steam rates will be reduced which is expected to reduce the amount of liquid entrainment. Reduced liquid entrainment tends to retain more liquid in the core region during a debris-induced uncovery, which is a benefit to core cooling. As such, it is considered conservative to model the ECCS recirculating fluid at a saturated

temperature. With regard to steam generator boiling, the process is ranked medium during the complete core blockage period in the downflow plant category because the intact steam generators are a potential alternate flow path that can provide liquid to the core region following complete core inlet blockage. Enhanced boiling in the steam generators due to saturated fluid from the ECCS can increase the liquid carryover through the steam generators due to mixture level swell and entrainment. Considering this process by itself, it is non-conservative to model the ECCS fluid with a saturated temperature because flow through the intact steam generators following complete core inlet blockage is increased. However, this effect is overwhelmed by the effect subcooling has on increasing the reactor vessel liquid inventory. Further, the complete blockage analysis for the downflow plant category shows that sufficient flow through the UHSNs is present such that adequate core cooling is maintained without credit from liquid spillover through the intact steam generators.

As condensation and downcomer boiling are low ranking process for the GSI-191 scenario, their sensitivity to ECCS fluid subcooling was not investigated in detail. However, ECCS fluid subcooling would lead to greater condensation potential and reduced downcomer boiling, both of which would increase reactor vessel liquid inventory and improve core cooling. As such, both of these processes are expected to be conservatively accounted for by modeling the ECCS recirculating flow at saturated temperature.

The effect of ECCS fluid temperature during the injection phase of the transient is discussed in the response to RAI-4.16 Item d.

b. Identify the coupled S-RELAP5/ICECON methodology by providing a reference to the technical document that describes it. Explain whether the methodology was validated and assessed for applications similar to the LOCA analyses documented in Vol. 4 for the CE plant category. Clarify whether the coupled code methodology and/or application analyses obtained with this methodology have been reviewed and/or approved by NRC. Provide the key inputs and assumptions relative to the containment model. Explain which of these input parameters were modeled in a bounding manner along with the ranges considered in determining the input values for the parameters.

The response to this question is provided in the CE submittal

c. In order to assess the effect from the major assumption regarding the ECCS temperature subcooling, the NRC staff recommends performing two re-analyses for Cases 1 and 2 documented in Section 10 using S-RELAP5 in a stand-alone mode. For the purpose of these re-analyses it is suggested that an "ECCS temperature during recirculation phase" of 212 °F along with a "containment pressure during recirculation phase" of 14.7 psia consistent with the key inputs applied for the Westinghouse upflow and downflow plant categories is used. Verify that there is little impact on the K_{max} and t_{block} results compared to the results documented in Section 10.

The response to this question is provided in the CE submittal

d. Tables 6-1 through 6-4 do not provide information regarding the ECCS temperatures prior to sump switch over (SSO). Section 9.3 states that "during transfer to sump recirculation, the ECCS coolant temperature is set to 212 °F." Explain how the ECCS temperatures prior to SSO were defined for the purposes of the analyses and provide the values used for the analyses in Sections 8, 10, and 11. Clarify whether the ECCS temperature prior to SSO should also be considered a contributing factor for the purposes of the T-H analyses in Vol. 4 and justify the response. Describe the effects that the ECCS temperature assumption prior to sump switchover can have on other processes (i.e., voiding, swelling, etc.) if it is found to have a significant impact on the results.

Response

The upflow plant analyses in Section 8 used an injection phase ECCS temperature of 76°F. The downflow plant analyses in Section 9 used an injection phase ECCS temperature of 90°F. For both plant categories, the recirculation phase ECCS temperature was 212°F. The injection phase ECCS temperature modeled in the analyses is the nominal value typically based on the arithmetic average of the Technical Specification minimum and maximum refueling water storage tank (RWST) surveillance requirements.

A sensitivity study was performed to determine if this parameter could be a contributing factor to the debris-induced secondary heatup. The sensitivity used the Westinghouse upflow plant model Case 2B as the base case. In the sensitivity, the injection phase ECCS temperature was increased to 90°F and 120°F; thus reducing the subcooling in both cases while remaining in a typical range of RWST water temperature. The case matrix is shown in Table RAI-4.16-1.

Table RAI-4.16-1 Upflow Plant Injection Phase ECCS Subcooling Sensitivity Study

Case	Injection Phase ECCS Temperature (°F)	Recirculation Phase ECCS Temperature (°F)
Case 2B (base case)	76	212
1	90	212
2	120	212

The upflow plant sensitivity results for void fraction, debris-induced heatup prediction, downcomer collapsed liquid level, barrel/baffle channel exit liquid flow, and broken loop hot leg nozzle liquid flow are shown in Figure RAI-4.16-1 through Figure RAI-4.16-7.

Figure RAI-4.16-1, Figure RAI-4.16-2, and Figure RAI-4.16-3 show the integrated void fraction at core elevations of 103 in., 73 in., and 42 in., respectively. The figures show that the void fraction at 103 in. is not impacted by the ECCS injection temperature. At lower elevations, a lower ECCS temperature prior to sump switchover tends to reduce core boiling, as indicated by the smaller slope of the integral curves. This behavior is most pronounced in Figure RAI-4.16-3, which is the 42 in. core elevation. When sump switchover is reached, and the ECCS temperature is increased to 212°F, the slopes of the integrated void fraction remain similar in all cases.

Figure RAI-4.16-4 shows that the recirculation phase debris-induced PCT sensitivity. In Figure RAI-4.16-4, the x-axis has a range of 1000-2000 seconds to highlight the period of interest, which is when core inlet resistance is applied that leads to the core uncovery and subsequent heatup. As indicated by the figure, decreasing the ECCS injection temperature tends to slightly delay the time PCT is reached, but the span in sensitivity is less than 10°F. The recirculation phase PCT is relatively insensitive to the injection phase ECCS temperature.

Figure RAI-4.16-5 shows that the injection phase downcomer collapsed liquid level is somewhat sensitive to the ECCS injection temperature but the sensitivity is diminished during the recirculation phase. In Figure RAI-4.16-5, the x-axis has a range of 1000-2000 seconds to highlight the period of interest, which is when core inlet resistance is applied that leads to the core uncovery and subsequent heatup. The figure indicates that increasing the ECCS injection temperature tends to reduce the downcomer collapsed liquid level.

Figure RAI-4.16-6 shows the barrel/baffle channel exit integrated flow, which indicates that the bypass flow through the barrel/baffle channel is only minimally impacted by ECCS injection temperature. Figure RAI-4.16-7 shows that the liquid carryover to the break through the hot leg nozzle is also only minimally impacted by the ECCS injection temperature.

Given the lack of sensitivity of the void fraction, debris-induced heatup PCT, downcomer collapsed liquid level, barrel/baffle exit liquid flow, and the broken loop hot leg nozzle liquid flow to the injection phase ECCS temperature, this parameter is not considered a significant contributor to the T-H analysis results. Further, given that the sensitivity to ECCS injection temperature diminishes shortly after switchover to sump recirculation, its importance for the purposes of long-term core cooling (LTCC) analyses is even less significant. As such, a similar sensitivity study is not completed for the Westinghouse downflow plant category.

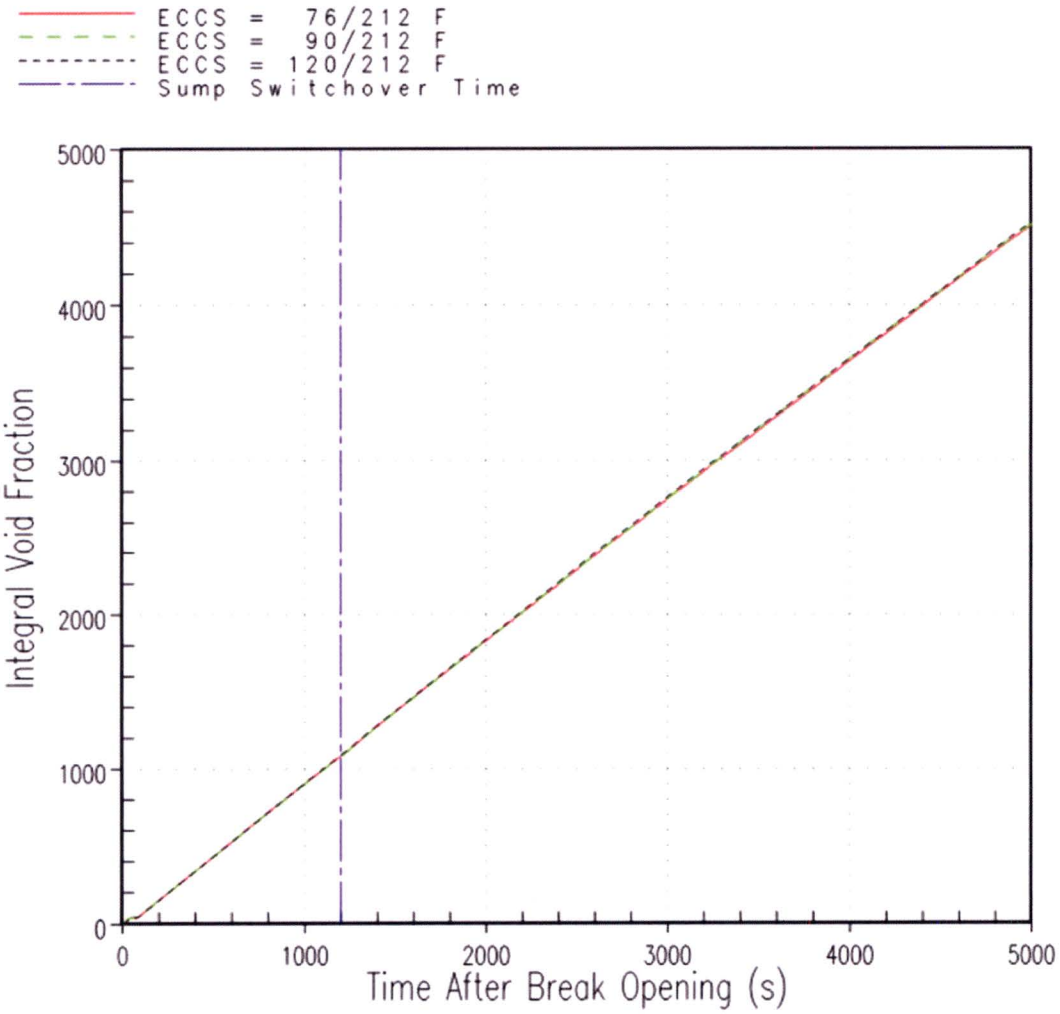

Figure RAI-4.16-1 Westinghouse Upflow Plant Injection Phase ECCS Subcooling Sensitivity Hot Assembly Integrated Void Fraction at a Core Elevation of 103 in. Results

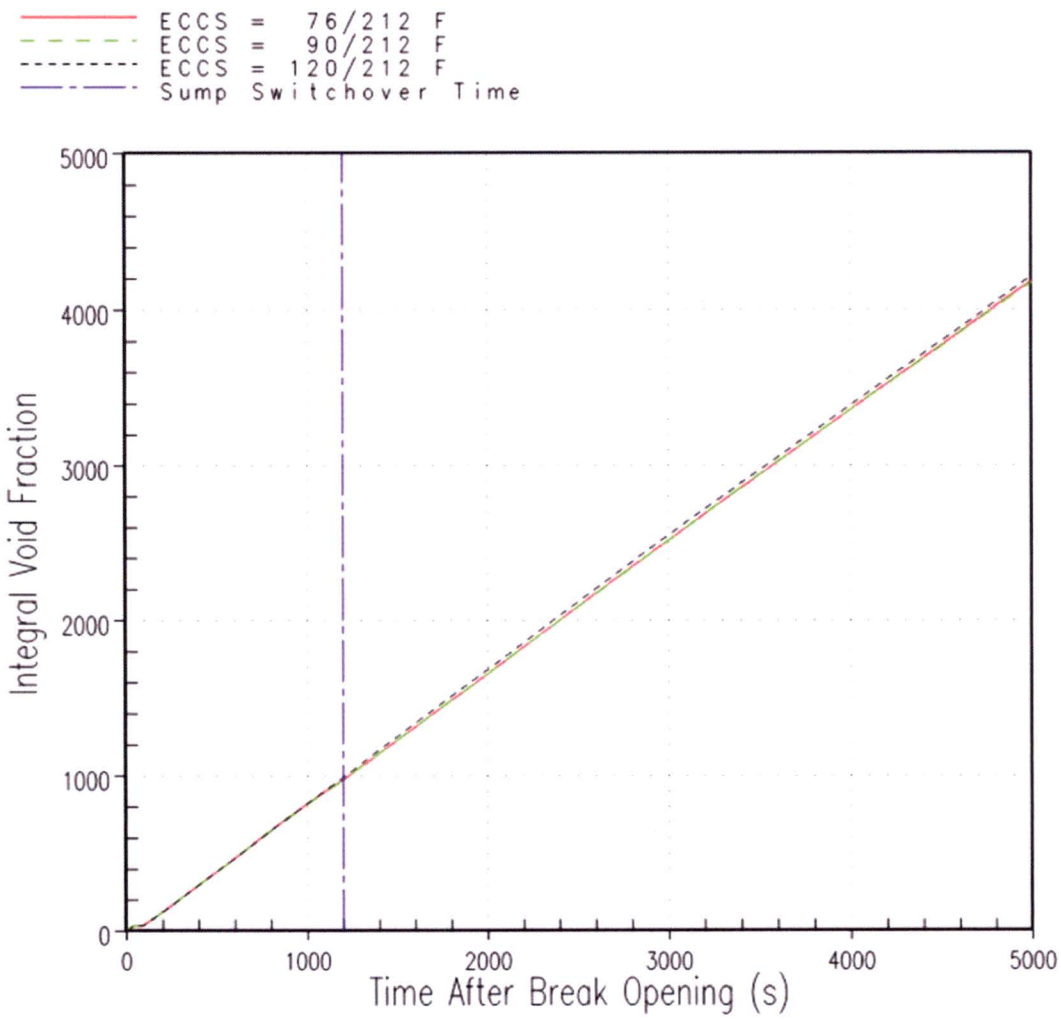

Figure RAI-4.16-2 Westinghouse Upflow Plant Injection Phase ECCS Subcooling Sensitivity Hot Assembly Integrated Void Fraction at a Core Elevation of 73 in. Results

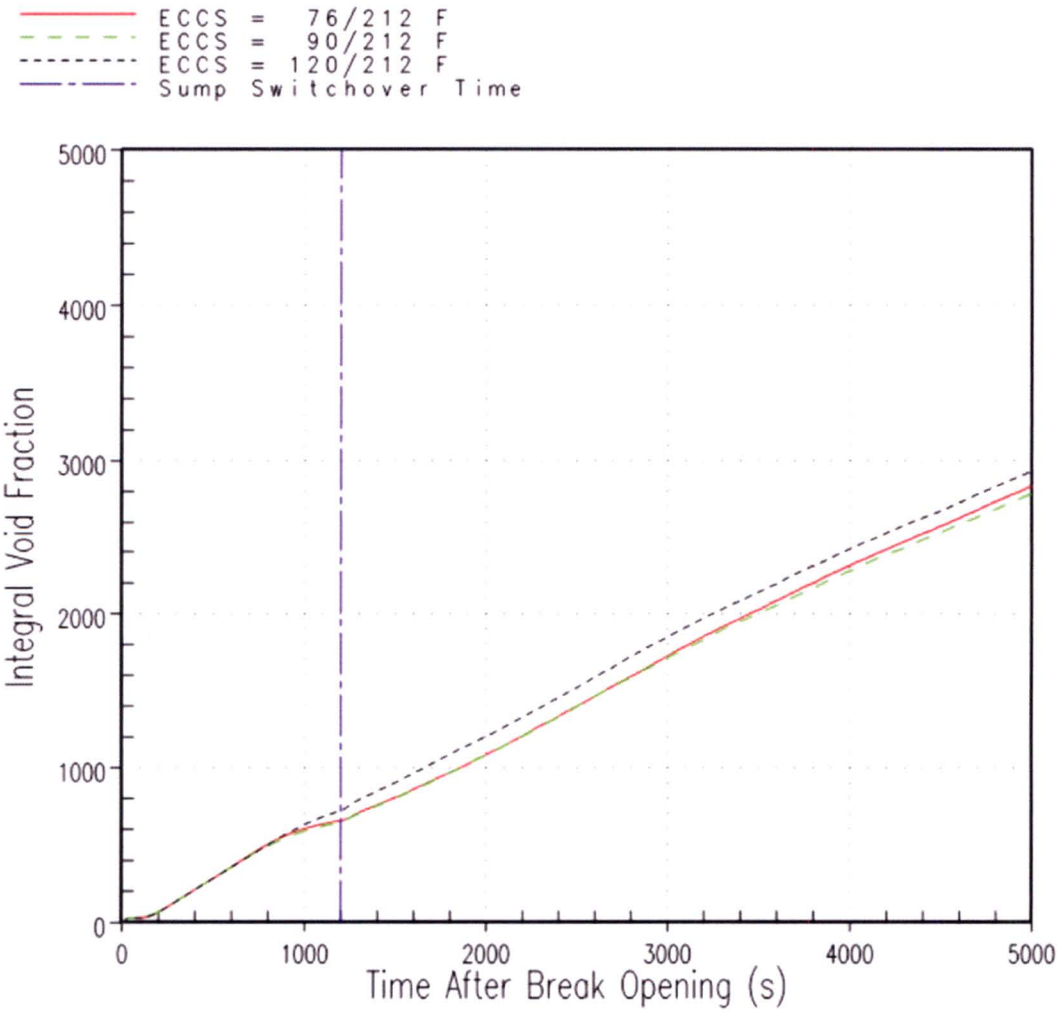

Figure RAI-4.16-3 Westinghouse Upflow Plant Injection Phase ECCS Subcooling Sensitivity Hot Assembly Integrated Void Fraction at a Core Elevation of 42 in. Results

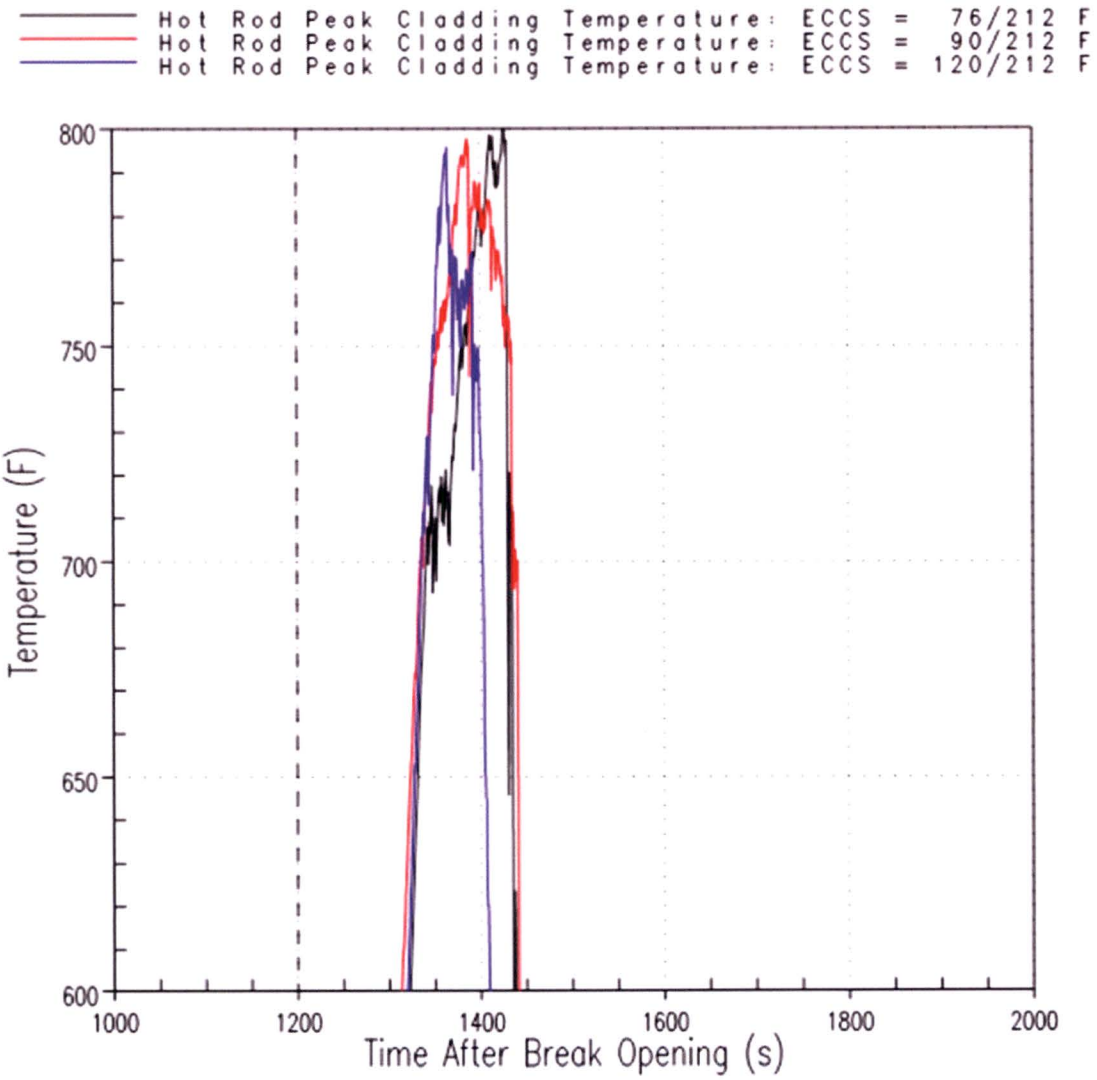

Figure RAI-4.16-4 Westinghouse Upflow Plant Injection Phase ECCS Subcooling Sensitivity Debris-Induced PCT Results

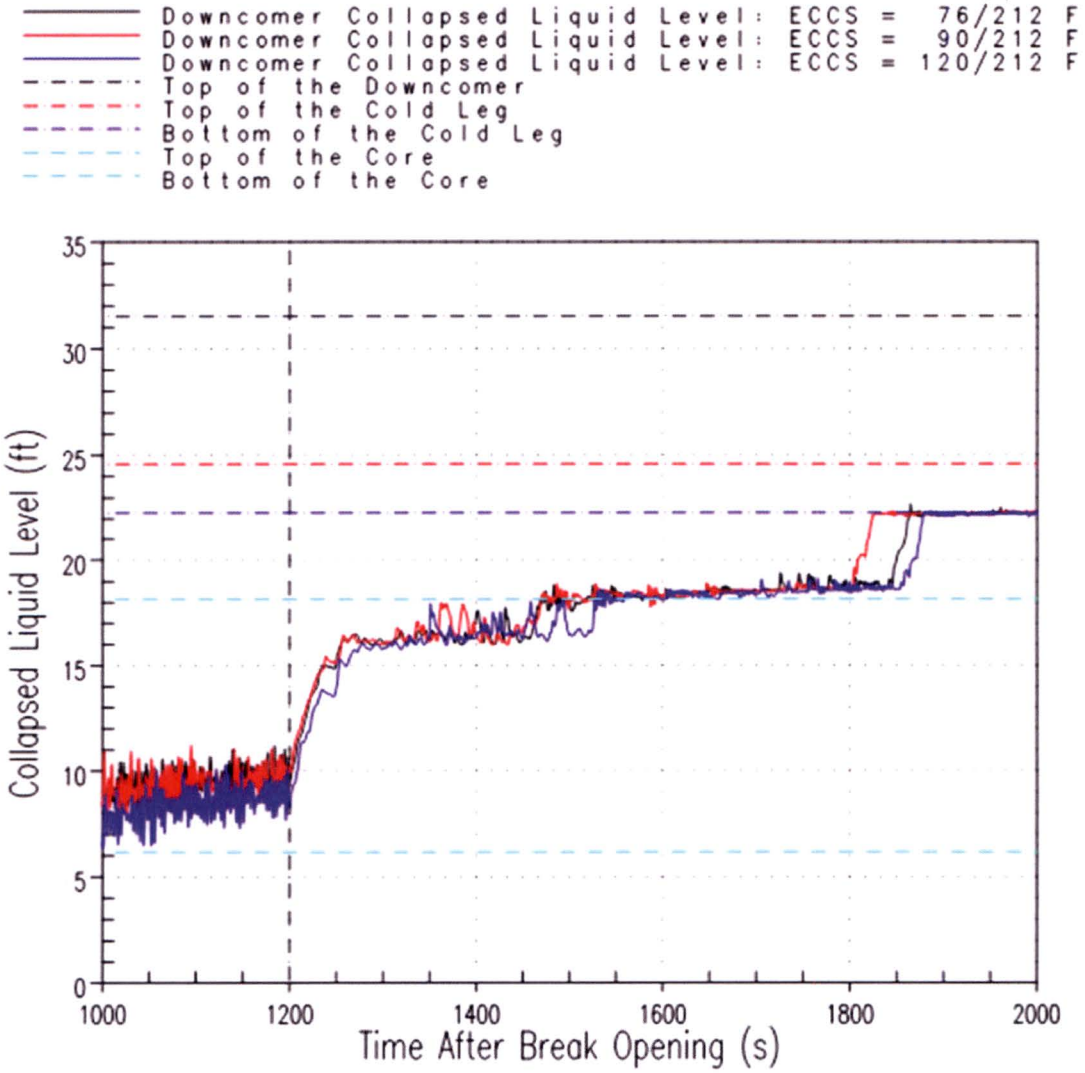

Figure RAI-4.16-5 Westinghouse Upflow Plant Injection Phase ECCS Subcooling Sensitivity Downcomer Collapsed Liquid Level Results

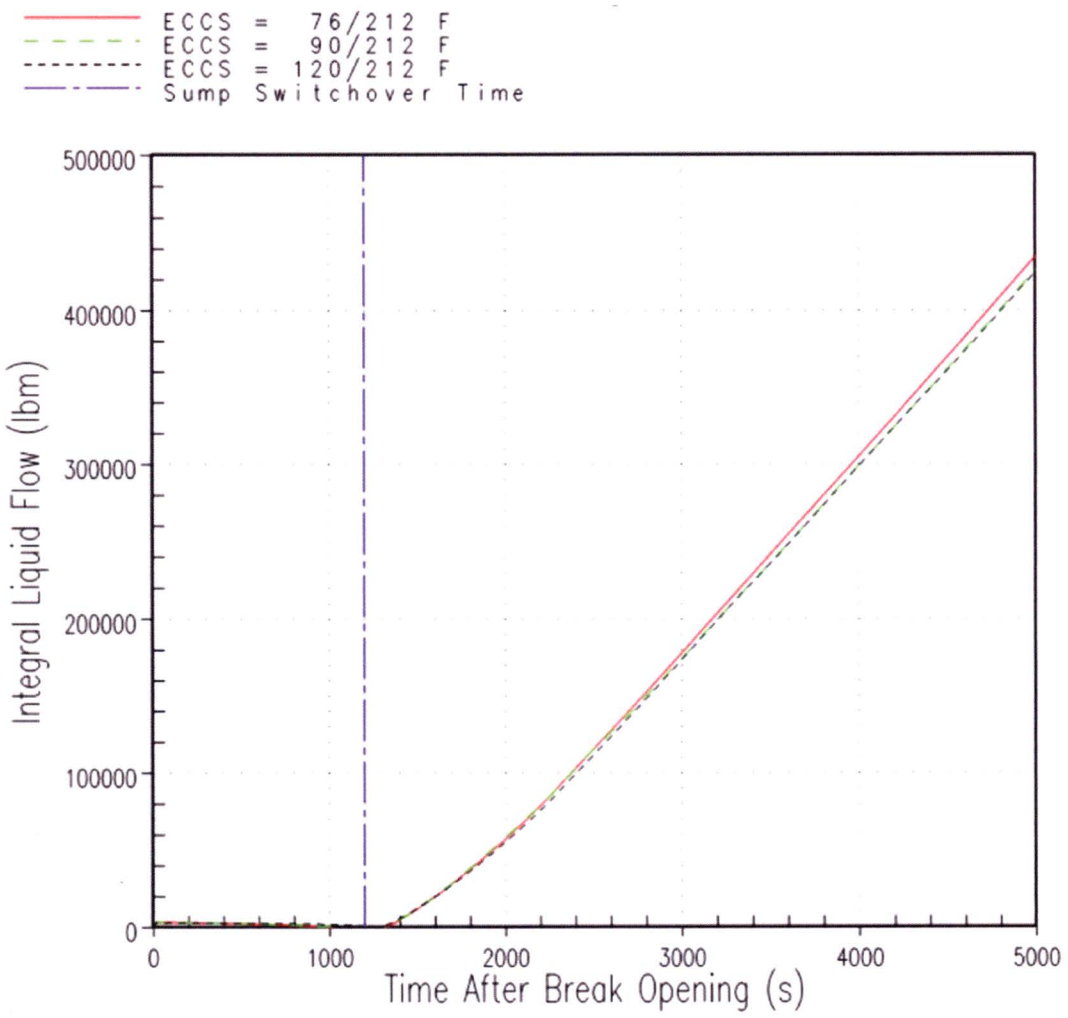

Figure RAI-4.16-6 Westinghouse Upflow Plant Injection Phase ECCS Subcooling Sensitivity Barrel/Baffle Channel Exit Integrated Liquid Flow Results

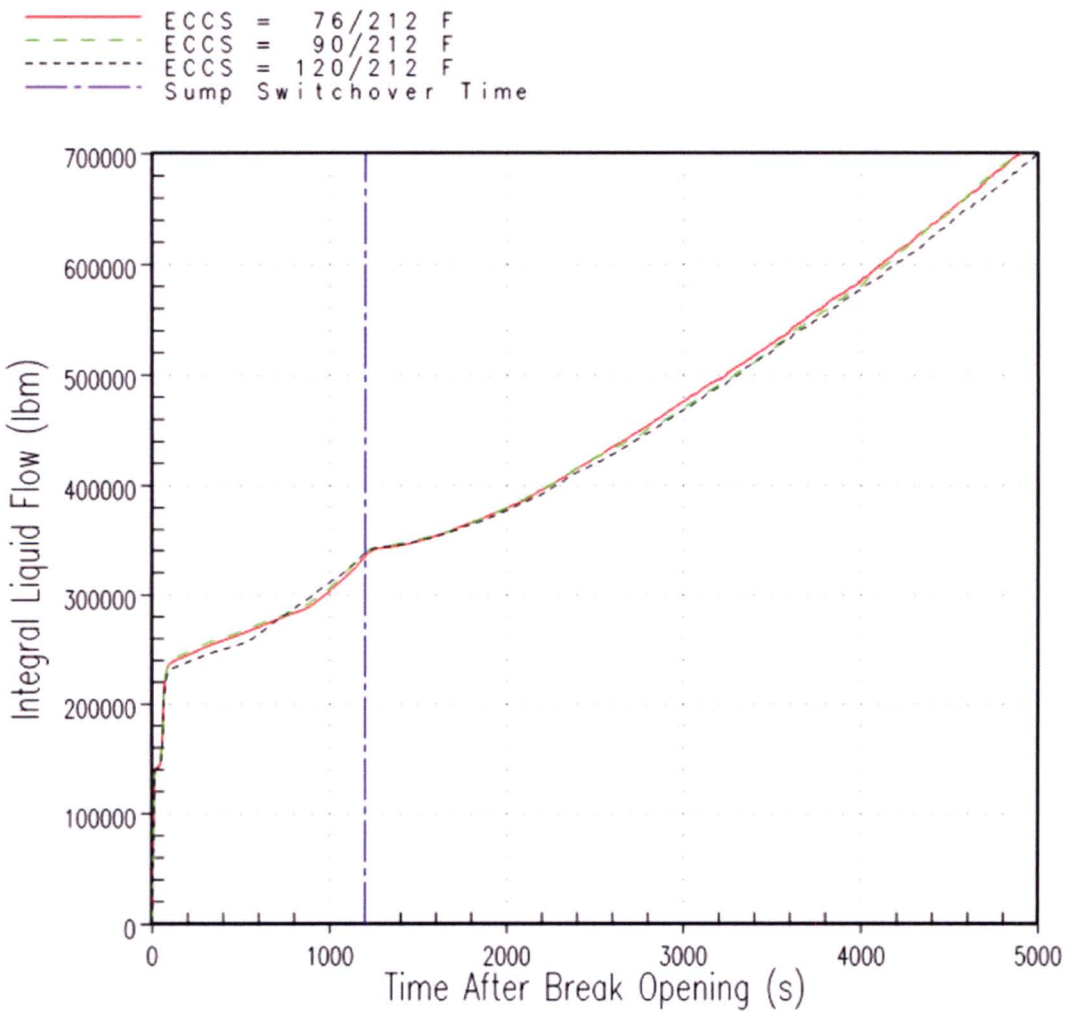

Figure RAI-4.16-7 Westinghouse Upflow Plant Injection Phase ECCS Subcooling Sensitivity Broken Loop Hot Leg Nozzle Integrated Liquid Flow Results

RAI-4.17, Vol. 4

Section 8.2.2 presents T-H results for Case 1B. Case 1B is presented because it represents the limiting time of complete core blockage, t_{block}, for the Westinghouse upflow plant category. In discussing the quantity identified as "reactor vessel fluid mass," shown in Figure 8-17, it is stated that "when complete core inlet blockage is applied, the RV inventory increases quickly, which can be credited to filling of the downcomer." The explanation for the inventory increase following the simulated core inlet blockage appears implausible if the result in Figure 8-17 represents the fluid mass within the entire RV volume. Since a stable ECCS liquid injection rate is expected during the period discussed in the above citation, the increase in accumulated fluid mass in the RV should be attributed to a reduction in the mass rate at which fluid exits the RV though the break, as suggested by the "break exit quality" shown in Figure 8-24, rather than by accumulation of mass in any sub-region within the entire RV control volume. The same observation applies to a similar statement in Section 8.2.3 that "when partial core inlet blockage is applied, the RV inventory increases quickly, which can be credited to filling of the downcomer." This explanation was provided with regard to the predicted "reactor vessel fluid mass" shown in Figure 8-26 for Case 2B, which was used to determine K_{max}. For Case 2B, the corresponding "break exit quality" response appears in Figure 8-34. To understand the role of entrainment and driving processes in the results:

a. Explain what causes the increase in the RV inventories shown in Figures 8-17 and 8-26. Provide updates to the explanations provided in the text of Sections 8.2.2 and 8.2.3, as appropriate.

Response

As shown in WCAP-17788, Volume 4, Figure 8-17, the reactor vessel (RV) fluid mass increases from approximately 122,500 lbm at 8580 sec. to 152,500 lbm at 9750 sec., which is an increase in fluid mass of 30,000 lbm, or 500 ft^3 of saturated liquid at atmospheric pressure. WCAP-17788, Volume 4, Figure 8-19 shows the downcomer liquid level. Following complete core inlet blockage, the downcomer liquid level increases from approximately 11 ft at 8580 sec. to 25 ft at 9750 sec. The downcomer area of a Westinghouse 4-loop plant is on the order of 35 ft^2. This indicates that the downcomer liquid volume has increased by approximately 490 ft^3, which is comparable to the increase in RV fluid volume shown in WCAP-17788, Volume 4, Figure 8-17.

Further, comparing the trends in Figures 8-17 and 8-19, it is seen that there are two consistent periods in which the downcomer fill rate and the RV fluid mass increase slows. The first period (8750 – 9000 sec.) is associated with the downcomer liquid level reaching the bottom of the cold leg, at which point, liquid has to fill the cold leg loop piping before the downcomer can fill further. The second period (9000 – 9250 sec.) occurs when the cold side liquid level reaches the steam generator outlet plenum, which must fill before the downcomer can continue to fill. As such, the increase in RV fluid mass is because the downcomer has filled with liquid.

The downcomer liquid level is governed by the manometric pressure balance between the downcomer and the inner RV. If the pressure between the downcomer and the inner RV is constant, then the amount of ECCS injection entering the downcomer will equal the amount of liquid leaving the RV

through the break, and the RV fluid mass will be in a quasi-steady-state. If the pressure balance between the two channels changes, then the downcomer level will change until the pressures equilibrate and the ECCS injection entering the downcomer again equals the flow leaving the RV through the break. This pressure balance change happens when complete core inlet blockage is applied. The pressure drop across the inner reactor vessel increases. As such, the liquid level in the downcomer must increase to offset the increased pressure drop.

Given the above discussion, the increase in RV inventory is because the downcomer liquid level increases. The increased pressure drop across the inner reactor vessel due to the application of complete core inlet blockage is what causes the downcomer level to increase, and thus the RV fluid inventory to increase.

b. Define the parameter "break exit quality" shown in Figures 8-24 and 8-34. Explain whether the same definition applies to any T-H quantity labeled as "quality" throughout Vol. 4. Otherwise, provide definitions and clarifications.

Response

Break exit quality, x, is defined as:

$$x = \frac{\dot{m}_v}{\dot{m}_v + \dot{m}_l}. \qquad \text{Eq. RAI-4.17-1}$$

Where,

$\dot{m}_v$ = vapor phase mass flow rate,

$\dot{m}_l$ = liquid phase mass flow rate.

Eq. RAI-4.17-1 is used to calculate any quantity labeled as "quality" throughout WCAP-17788, Volume 4.

This definition is consistent throughout WCAP-17788, Volume 4.

c. Provide plots showing the following sets of parameters for Cases 1B and 2B in Section 8.

i. Mass flow rates of liquid, steam, and total (liquid and steam) fluid discharges through each opening of the double-ended guillotine (DEG) break

ii. ECCS liquid mass flow rates injected into each cold leg and the total ECCS liquid mass flow rate injection into the reactor coolant system

iii. Liquid mass flow rates entering the RV through each cold leg nozzle and the total liquid flow for all cold leg nozzles

iv. Mass flow rates of liquid and steam entering the RV through each intact hot leg nozzle and the total (liquid and steam) flow rate for all intact hot leg nozzles

v. Steam flow quality defined as a ratio of the steam mass flow rate to the total (liquid and steam) mass flow rate for the RV-side opening of the DEG break

Response

See the response to Item d.

d. Present plots that show integrals for the identified mass flow rates requested in Item c above (liquid, steam, and/or total liquid and steam, as relevant).

Response

The figures are summarized in Table RAI-4.17-1.

Table RAI-4.17-1 Listing of RAI 4.17 Item c and Item d Figures

Figure No.	Description
RAI-4.17-1	Case 1B – Mass Flow Rates through the Vessel Side of the DEG Break
RAI-4.17-2	Case 1B – Integrated Mass Flow through the Vessel Side of the DEG Break
RAI-4.17-3	Case 1B – Break Exit Quality – Vessel Side of DEG Break
RAI-4.17-4	Case 1B – Mass Flow Rates through the SG Side of the DEG Break
RAI-4.17-5	Case 1B – Integrated Mass Flow through the SG Side of the DEG Break
RAI-4.17-6	Case 1B – ECCS Mass Flow Rates Injected into Cold Legs
RAI-4.17-7	Case 1B – Integrated ECCS Mass Flow Injected into Cold Legs
RAI-4.17-8	Case 1B – Mass Flow Rates Entering Reactor Vessel at Cold Leg Nozzles
RAI-4.17-9	Case 1B – Integrated Mass Flow Entering Reactor Vessel at Cold Leg Nozzles
RAI-4.17-10	Case 1B – Mass Flow Rates Entering Reactor Vessel through Intact Hot Leg Nozzles
RAI-4.17-11	Case 1B – Integrated Mass Flow Entering Reactor Vessel through Intact HL Nozzles
RAI-4.17-12	Case 2B – Mass Flow Rates through the Vessel Side of the DEG Break
RAI-4.17-13	Case 2B – Integrated Mass Flow through the Vessel Side of the DEG Break
RAI-4.17-14	Case 2B – Break Exit Quality – Vessel Side of DEG Break
RAI-4.17-15	Case 2B – Mass Flow Rates through the SG Side of the DEG Break
RAI-4.17-16	Case 2B – Integrated Mass Flow through the SG Side of the DEG Break
RAI-4.17-17	Case 2B – ECCS Mass Flow Rates Injected into Cold Legs
RAI-4.17-18	Case 2B – Integrated ECCS Mass Flow Injected into Cold Legs
RAI-4.17-19	Case 2B – Mass Flow Rates Entering Reactor Vessel at Cold Leg Nozzles
RAI-4.17-20	Case 2B – Integrated Mass Flow Entering Reactor Vessel at Cold Leg Nozzles
RAI-4.17-21	Case 2B – Mass Flow Rates Entering Reactor Vessel through Intact Hot Leg Nozzles
RAI-4.17-22	Case 2B – Integrated Mass Flow Entering Reactor Vessel through Intact HL Nozzles

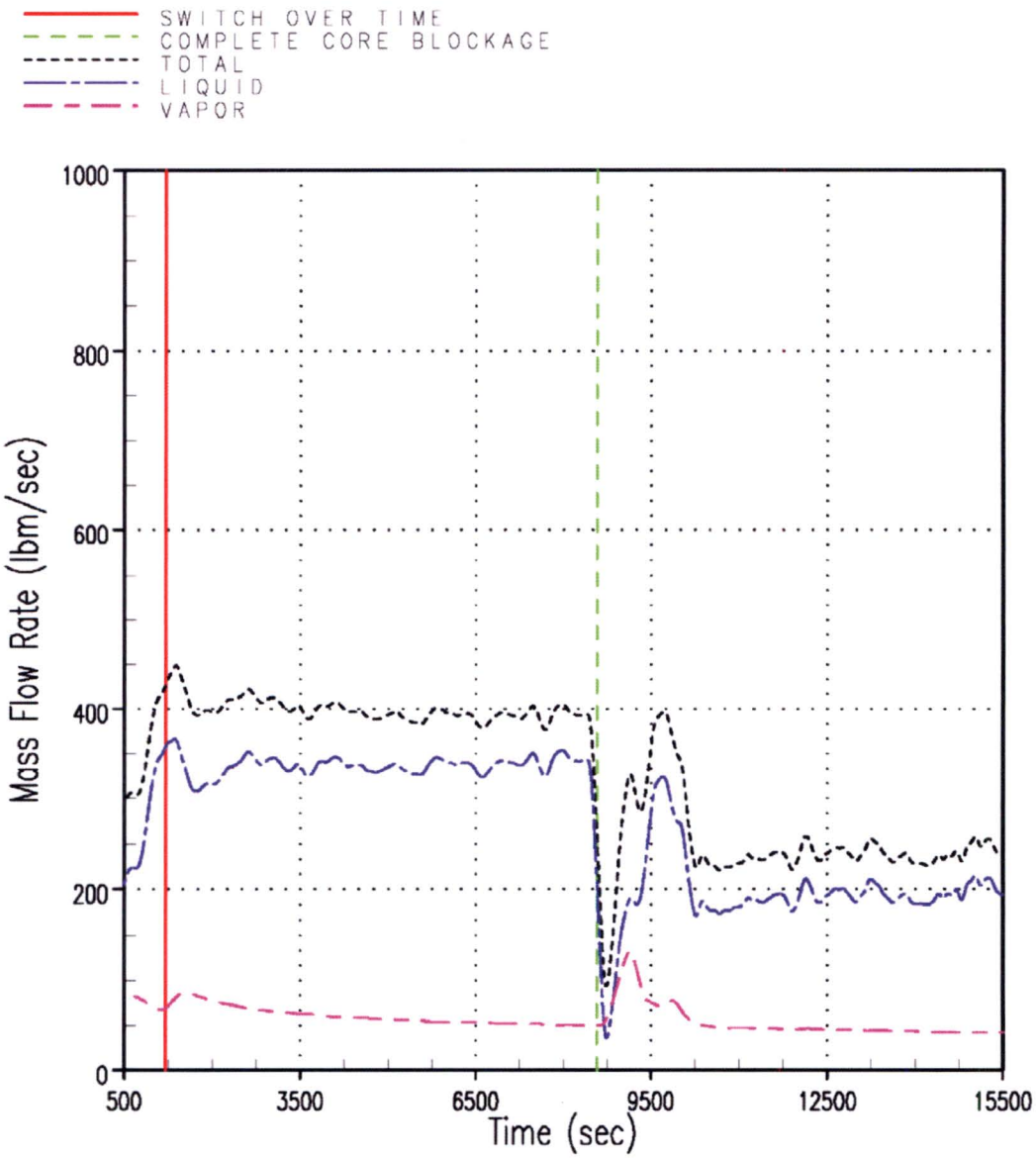

Figure RAI-4.17-1 Case 1B – Mass Flow Rates through the Vessel Side of the DEG Break

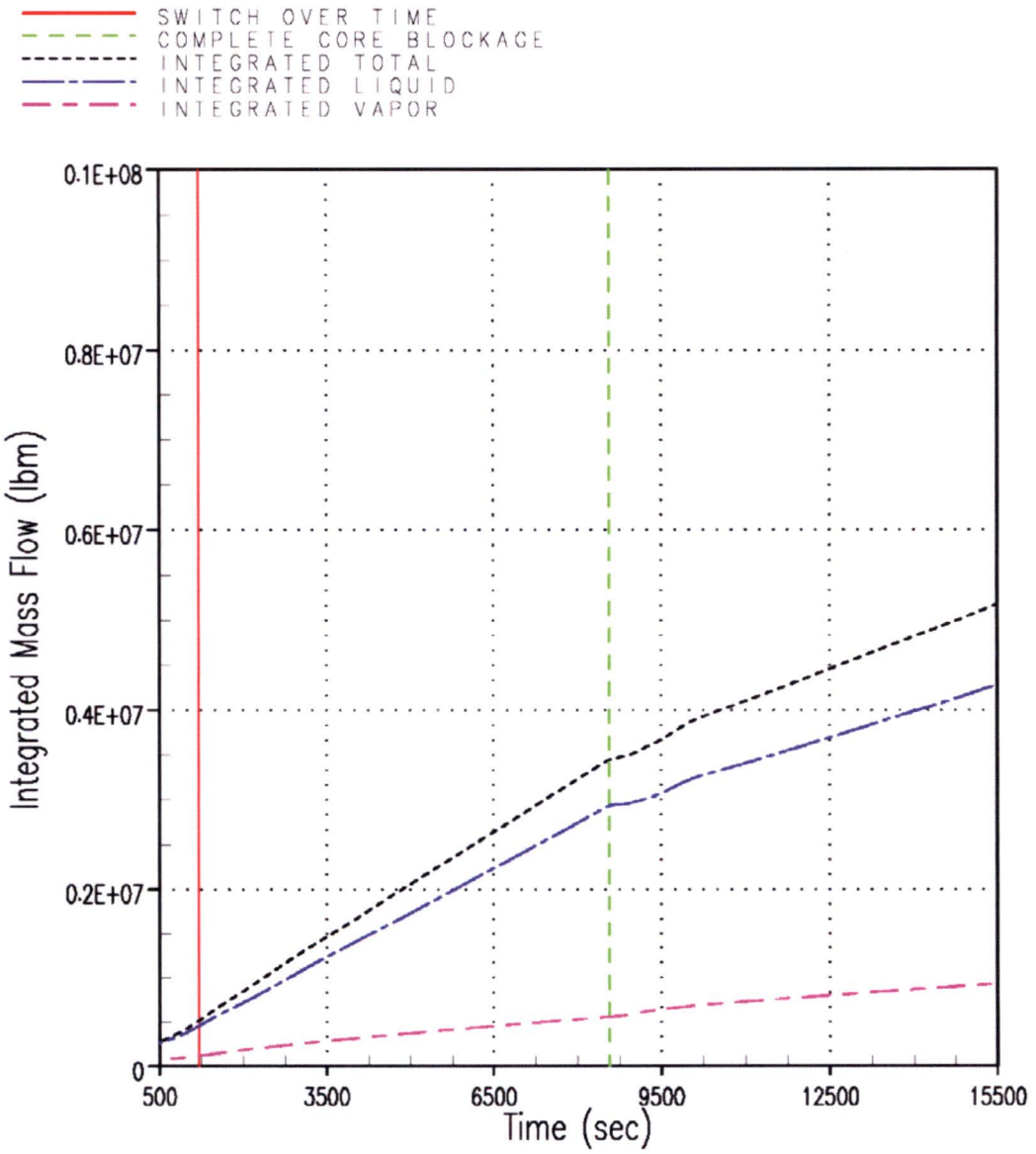

Figure RAI-4.17-2 Case 1B – Integrated Mass Flow through the Vessel Side of the DEG Break

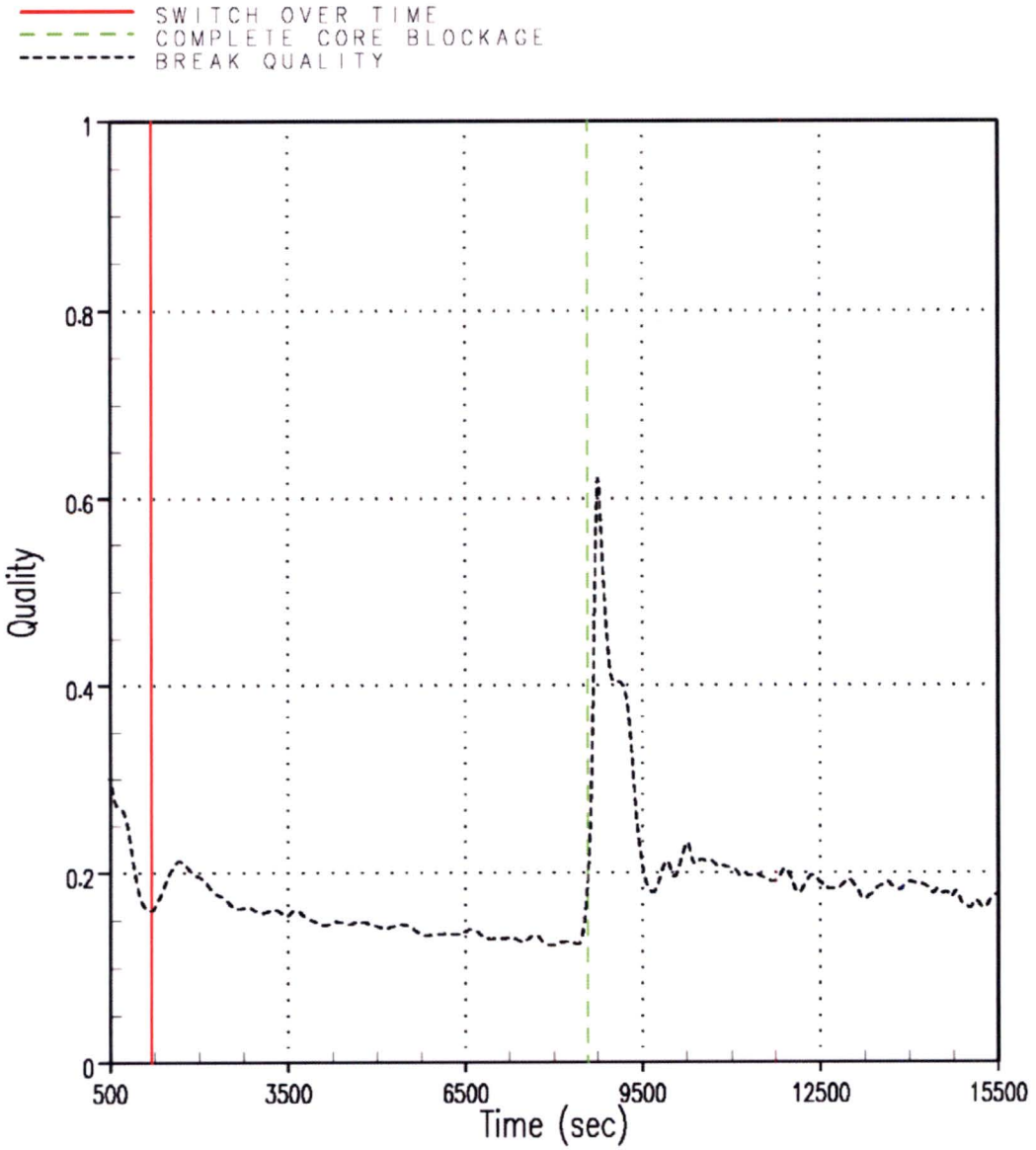

Figure RAI-4.17-3 Case 1B – Break Exit Quality – Vessel Side of DEG Break

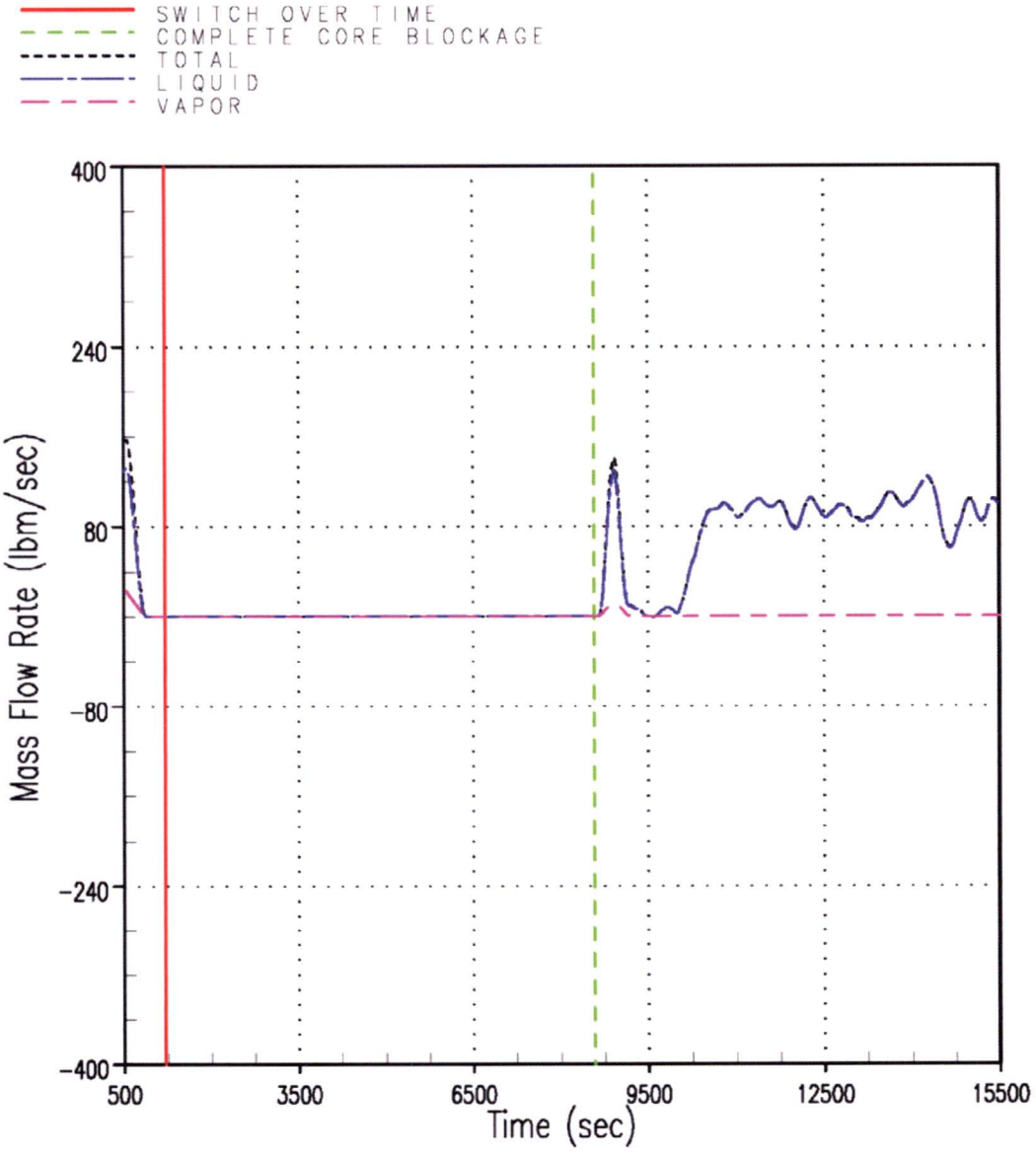

Figure RAI-4.17-4 Case 1B – Mass Flow Rates through the SG Side of the DEG Break

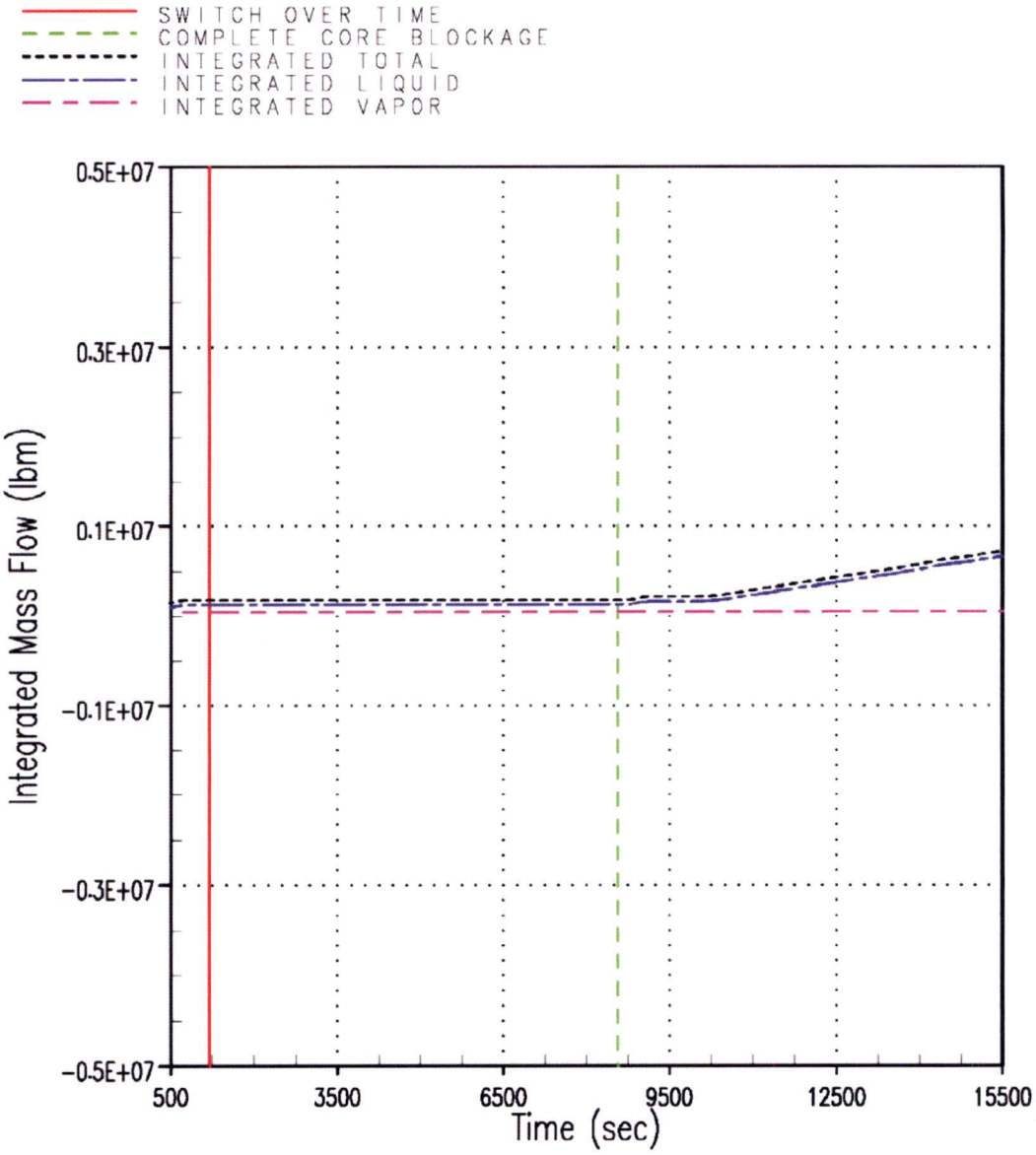

Figure RAI-4.17-5 Case 1B – Integrated Mass Flow through the SG Side of the DEG Break

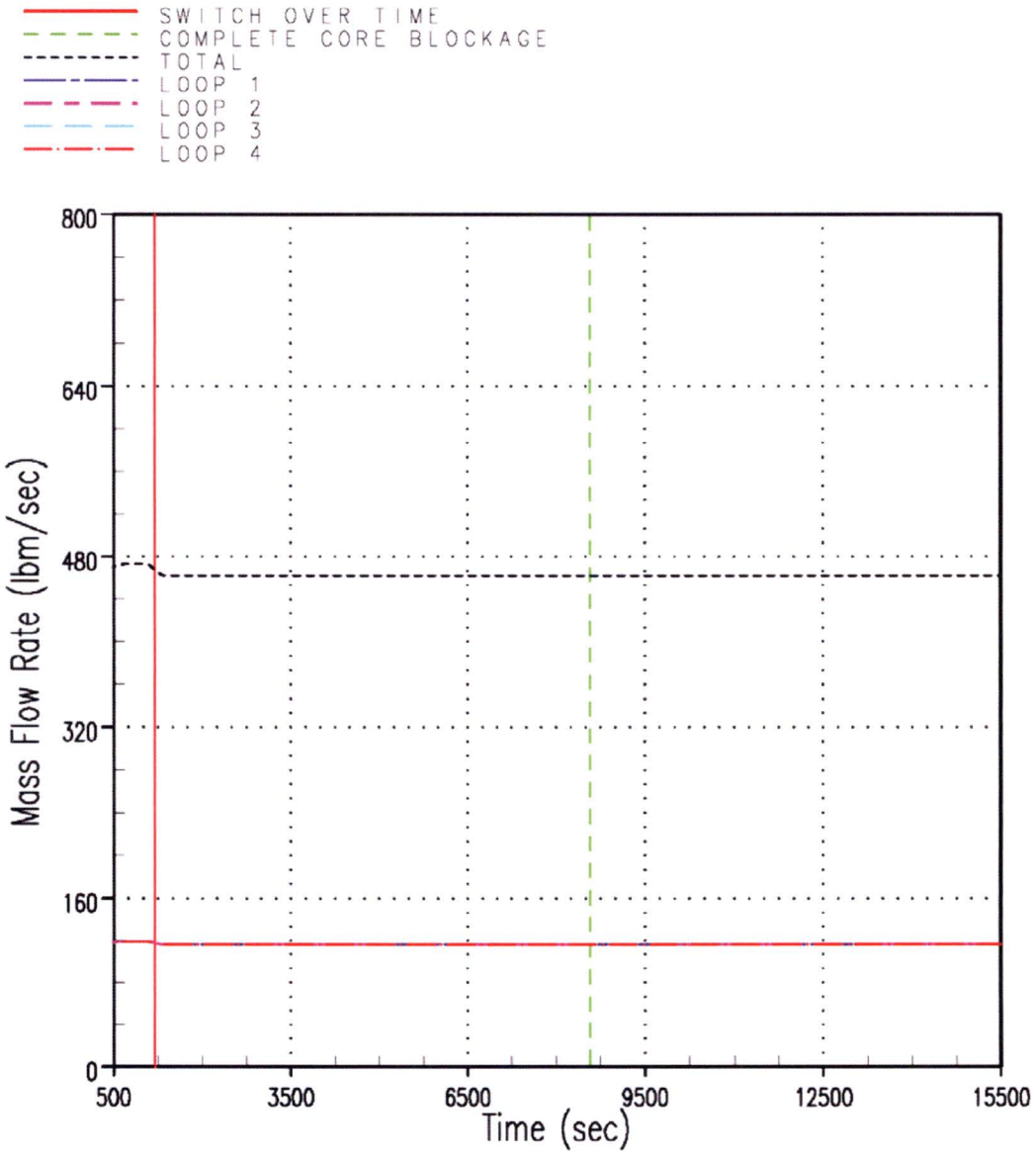

Figure RAI-4.17-6 Case 1B – ECCS Mass Flow Rates Injected into Cold Legs

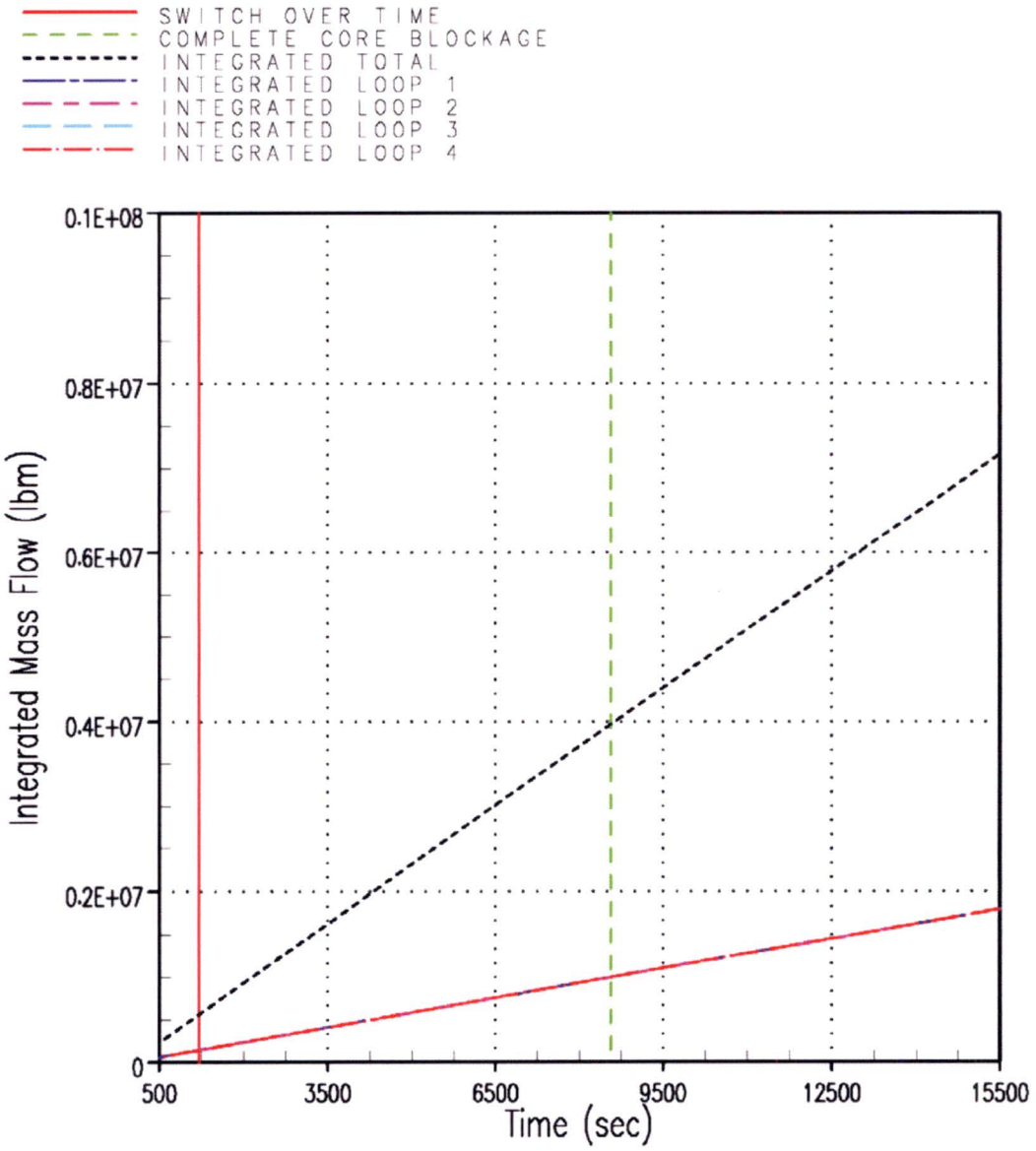

Figure RAI-4.17-7 Case 1B – Integrated ECCS Mass Flow Injected into Cold Legs

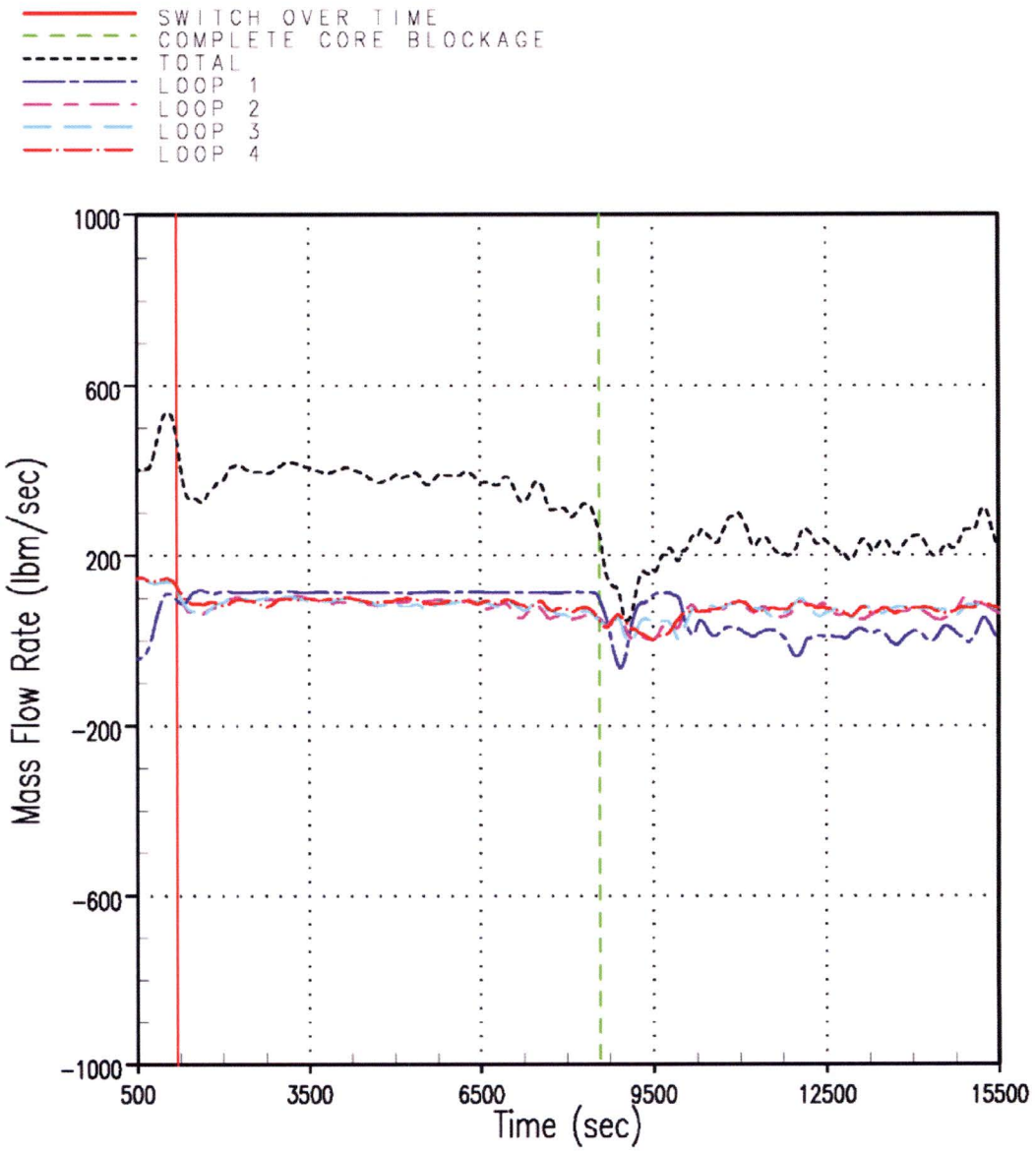

Figure RAI-4.17-8 Case 1B – Mass Flow Rates Entering Reactor Vessel at Cold Leg Nozzles

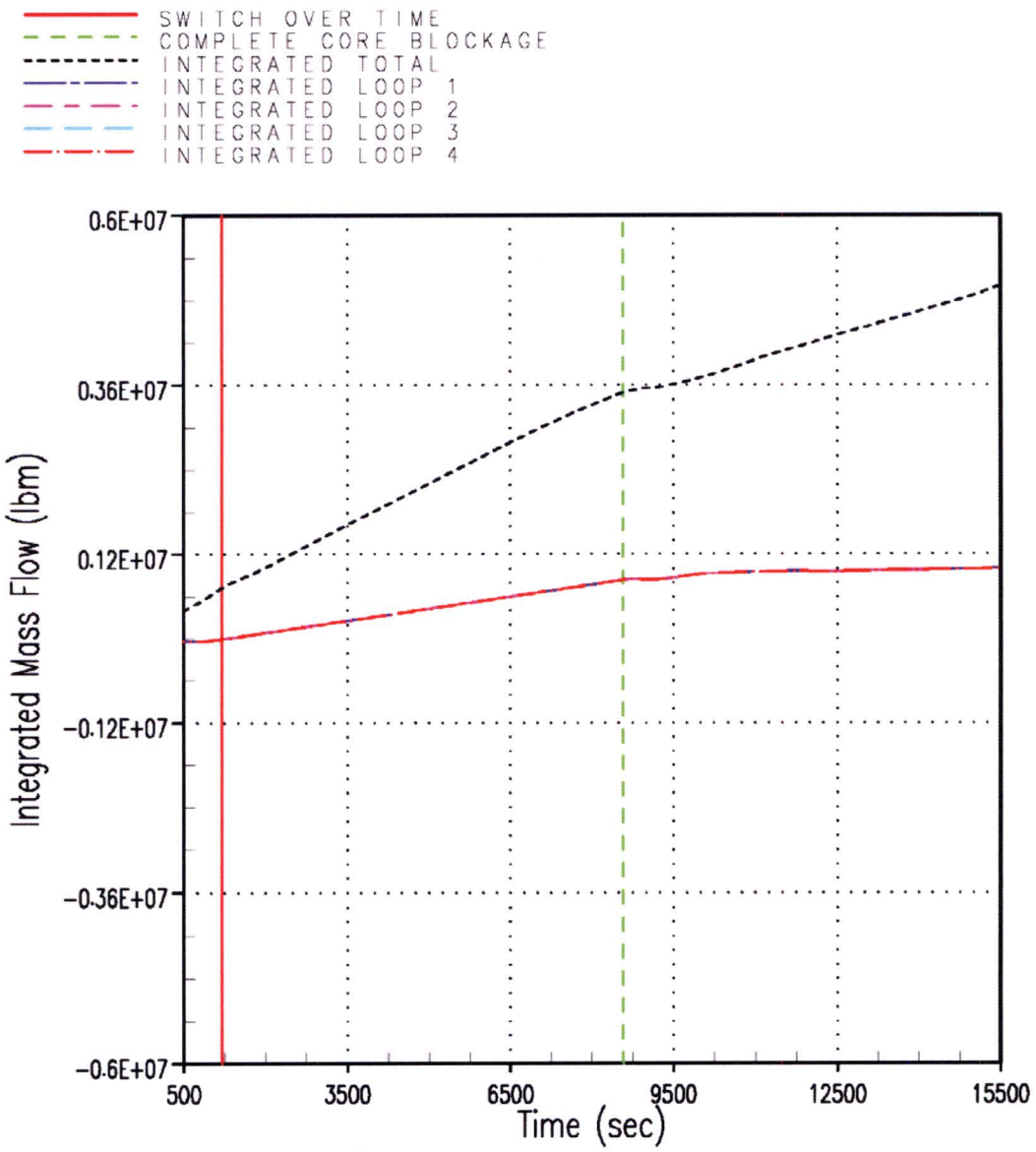

Figure RAI-4.17-9 Case 1B – Integrated Mass Flow Entering Reactor Vessel at Cold Leg Nozzles

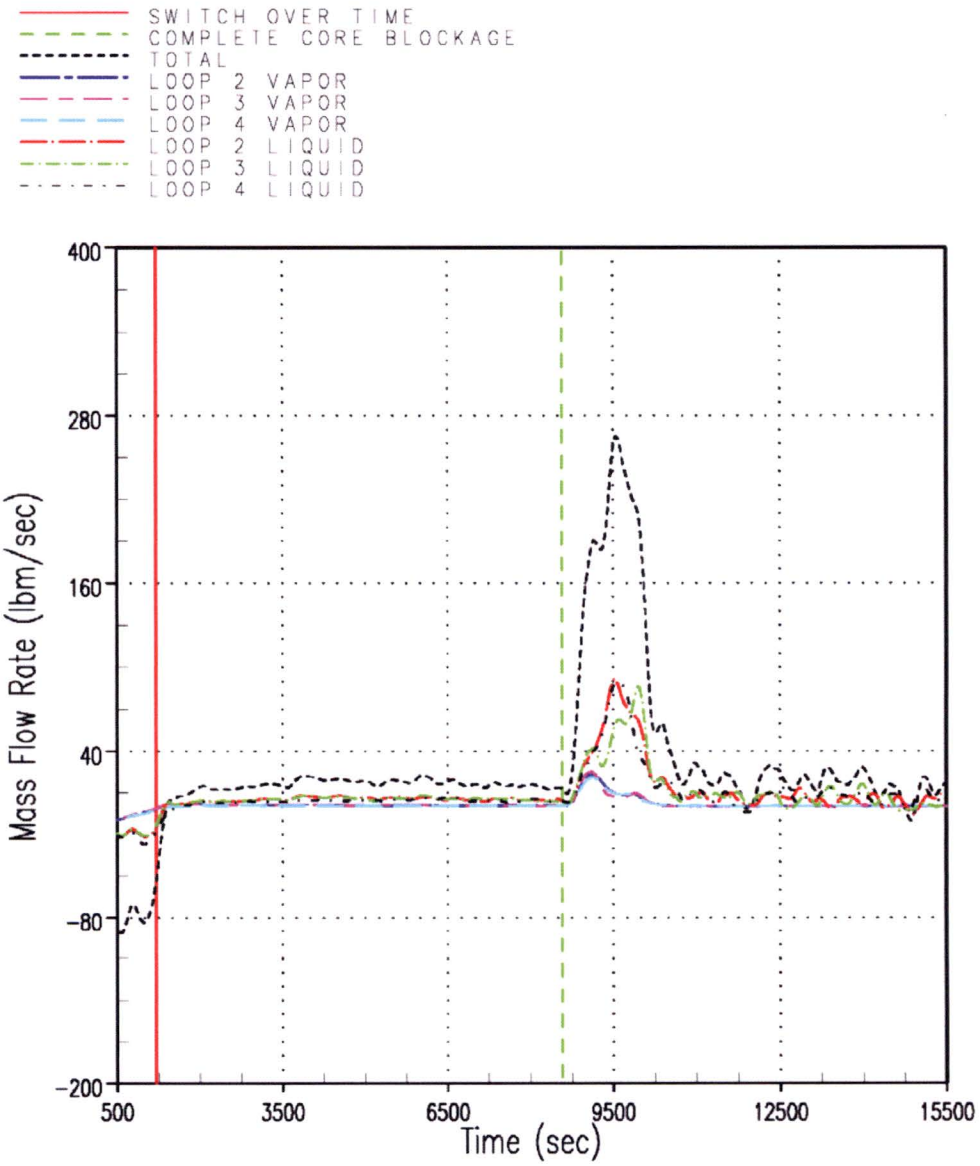

Figure RAI-4.17-10 Case 1B – Mass Flow Rates Entering Reactor Vessel through Intact Hot Leg Nozzles

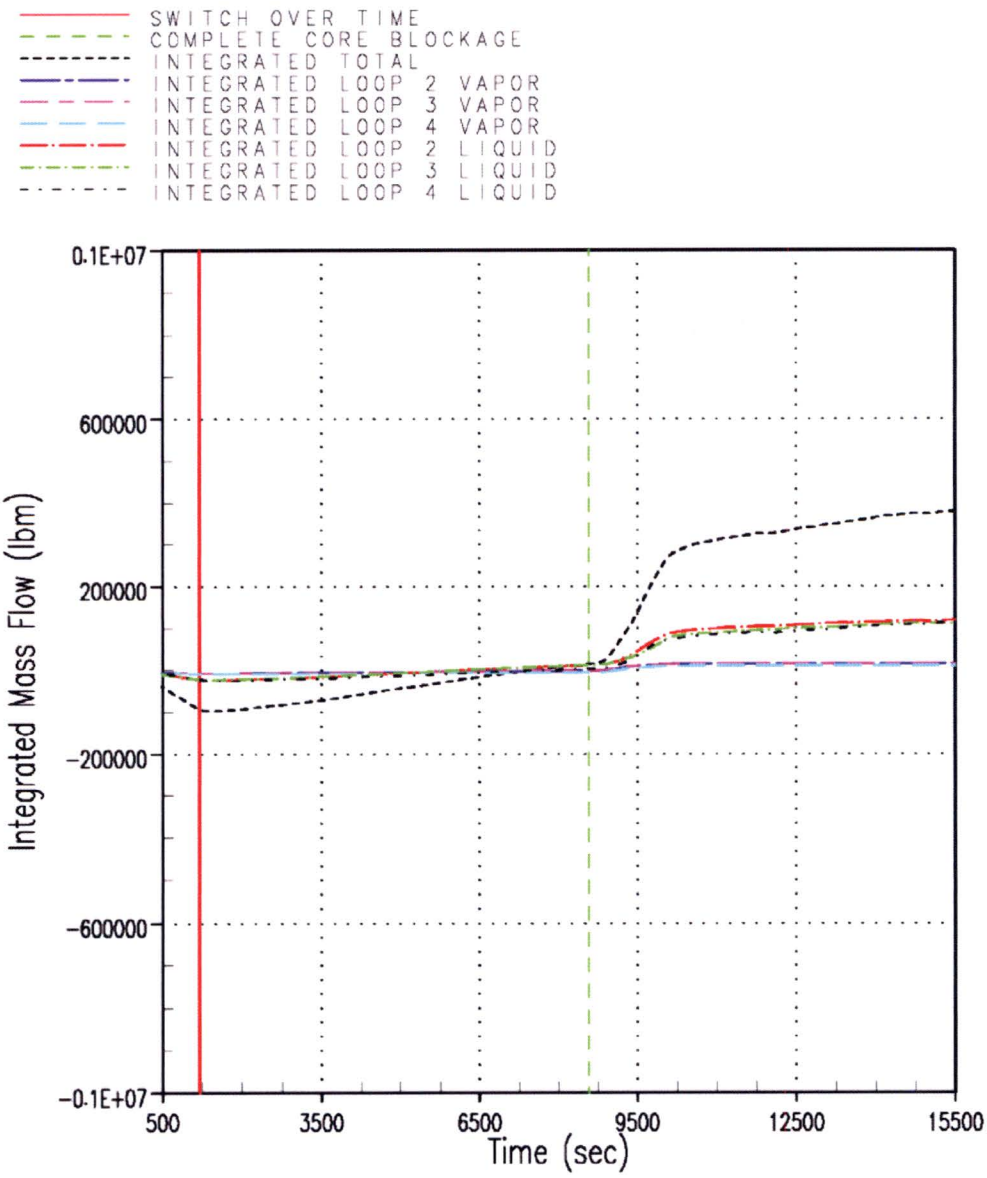

Figure RAI-4.17-11 Case 1B – Integrated Mass Flow Entering Reactor Vessel through Intact HL Nozzles

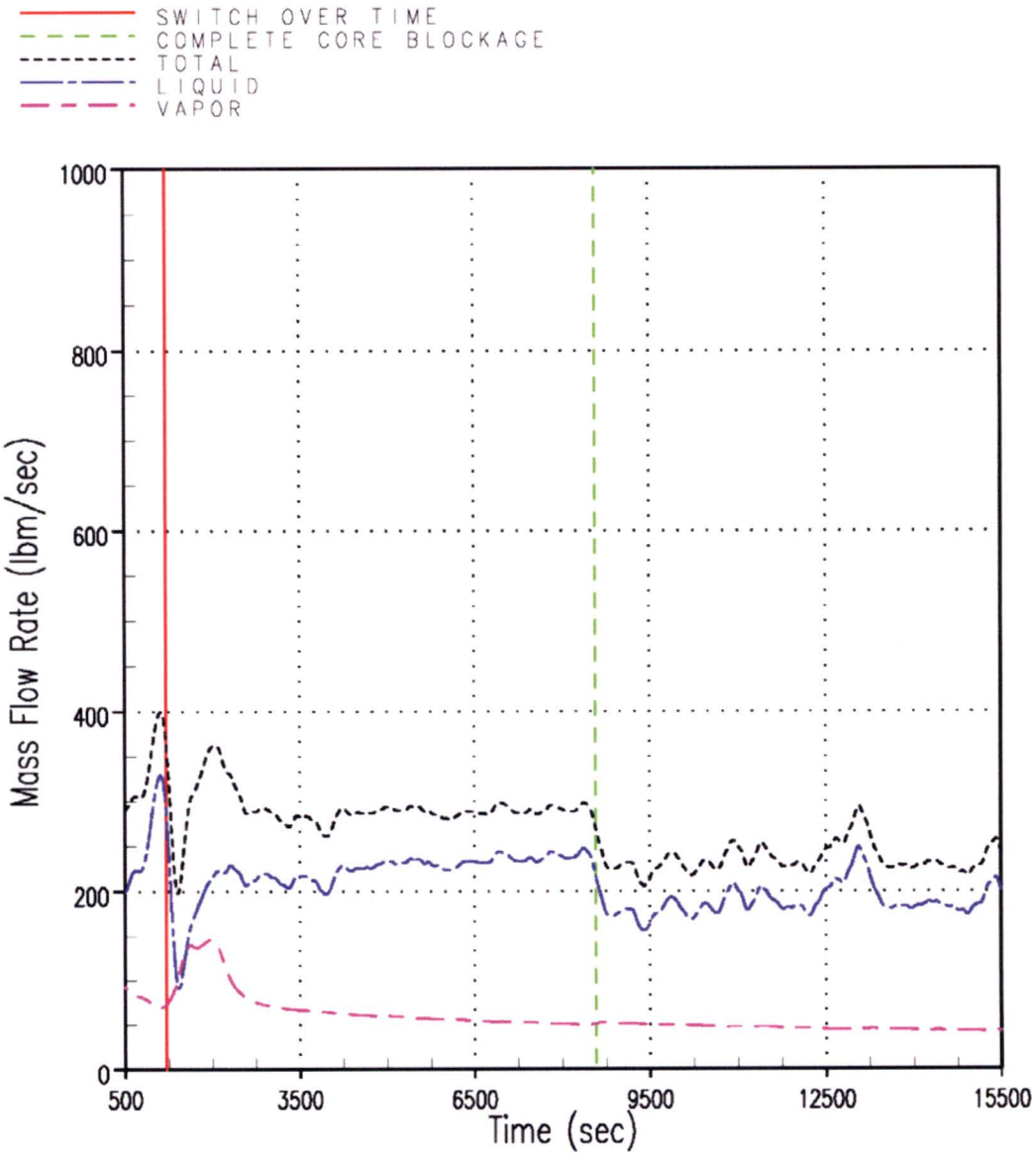

Figure RAI-4.17-12 Case 2B – Mass Flow Rates through the Vessel Side of the DEG Break

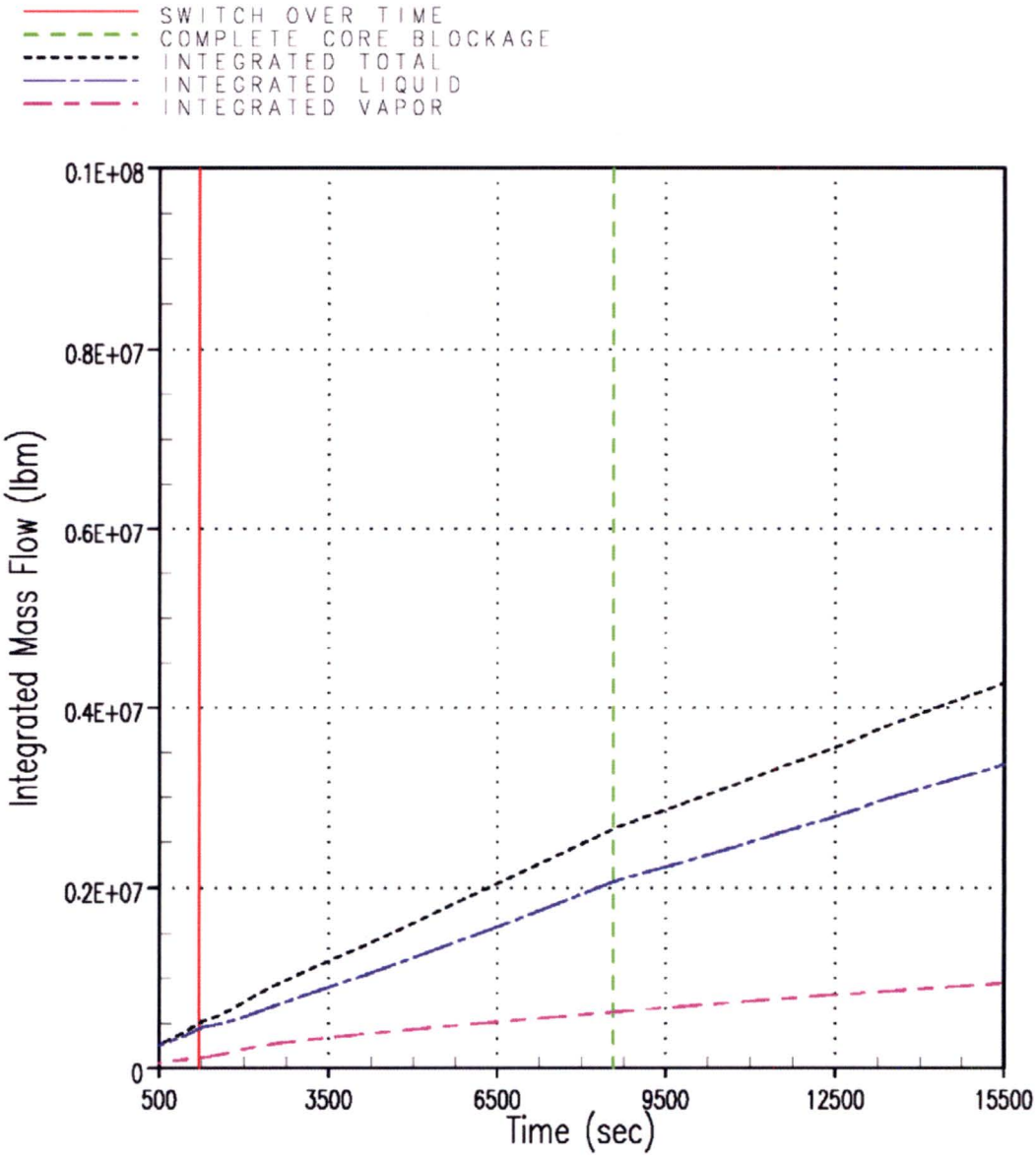

Figure RAI-4.17-13 Case 2B – Integrated Mass Flow through the Vessel Side of the DEG Break

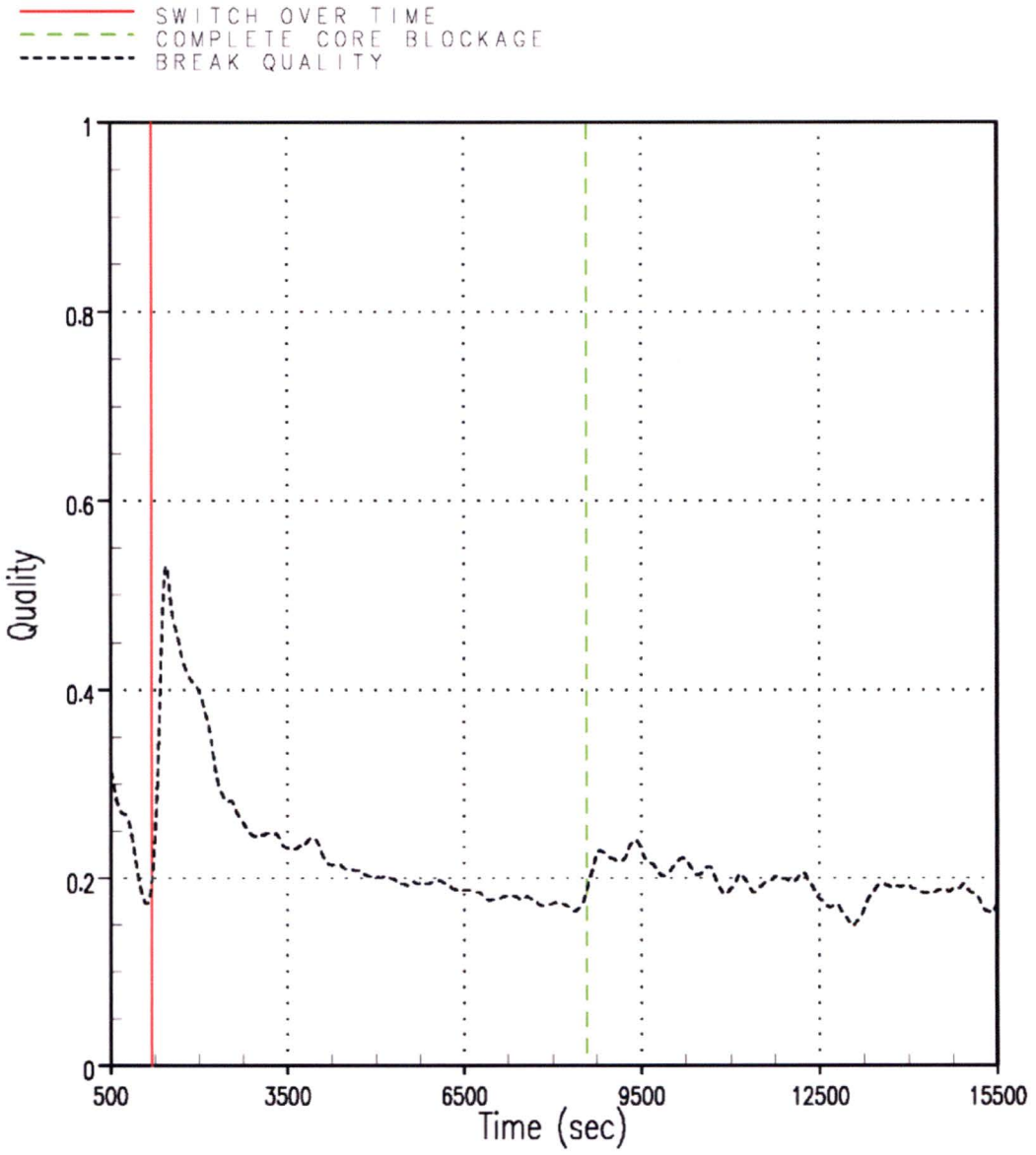

Figure RAI-4.17-14 Case 2B – Break Exit Quality – Vessel Side of DEG Break

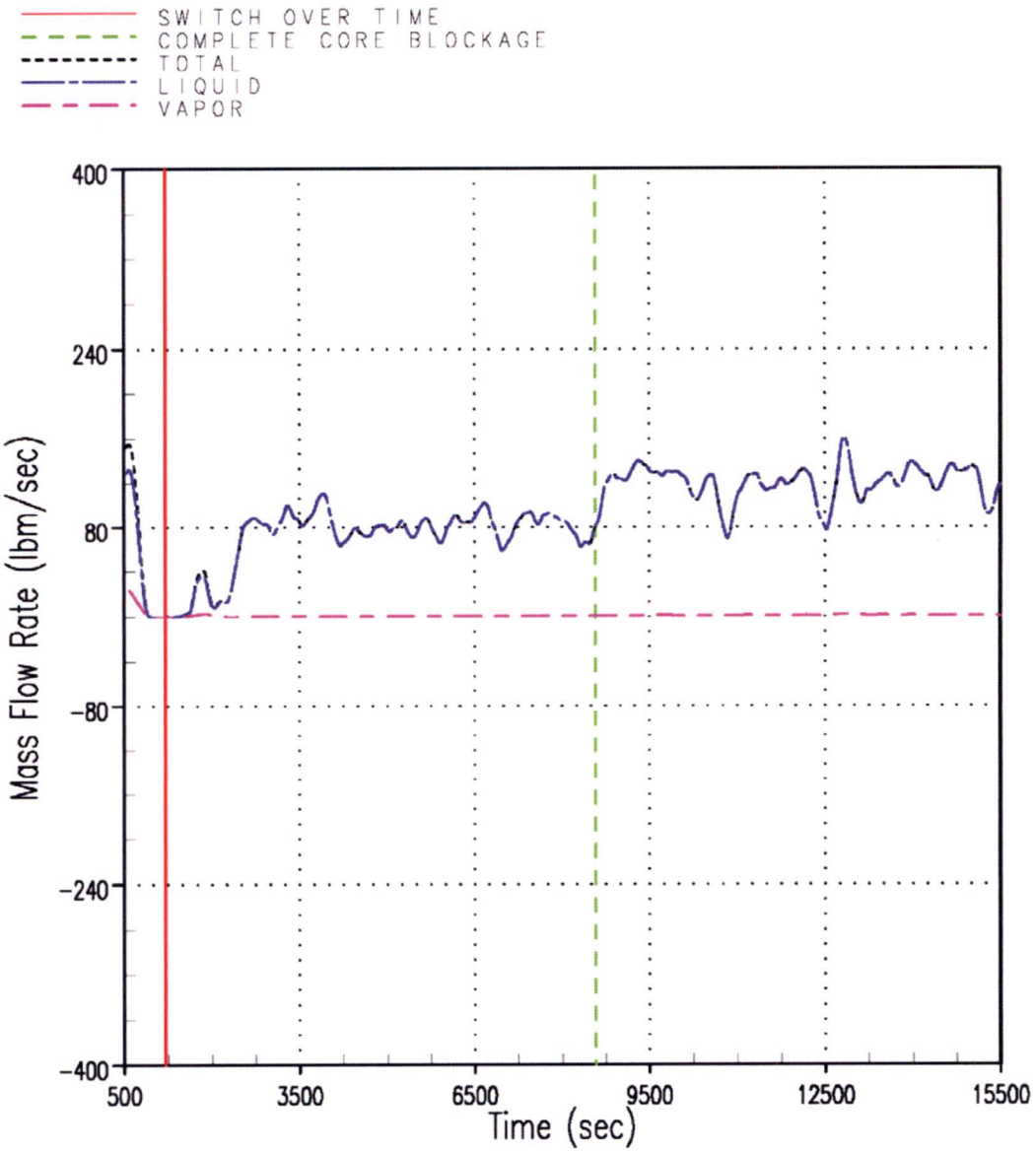

Figure RAI-4.17-15 Case 2B – Mass Flow Rates through the SG Side of the DEG Break

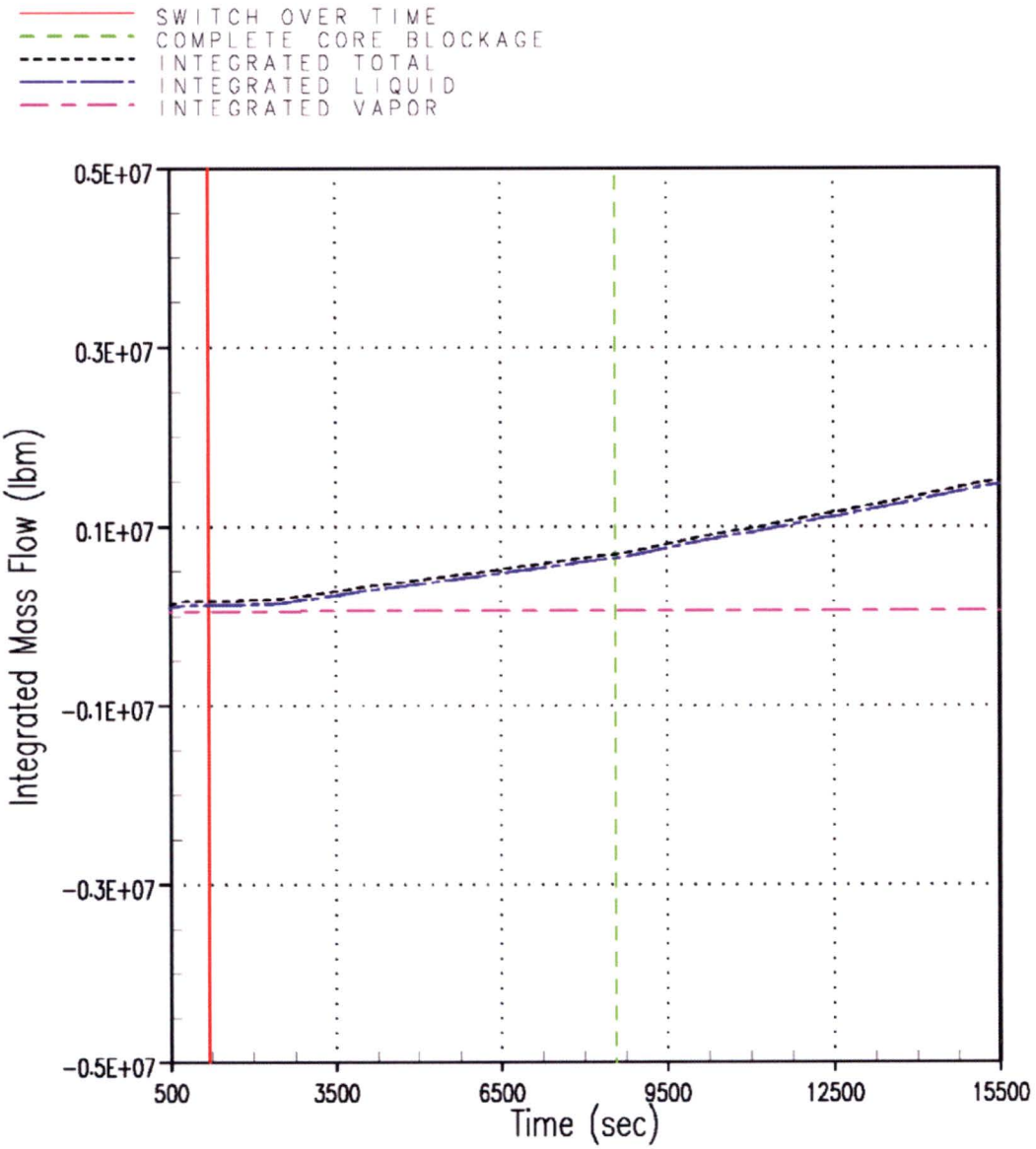

Figure RAI-4.17-16 Case 2B – Integrated Mass Flow through the SG Side of the DEG Break

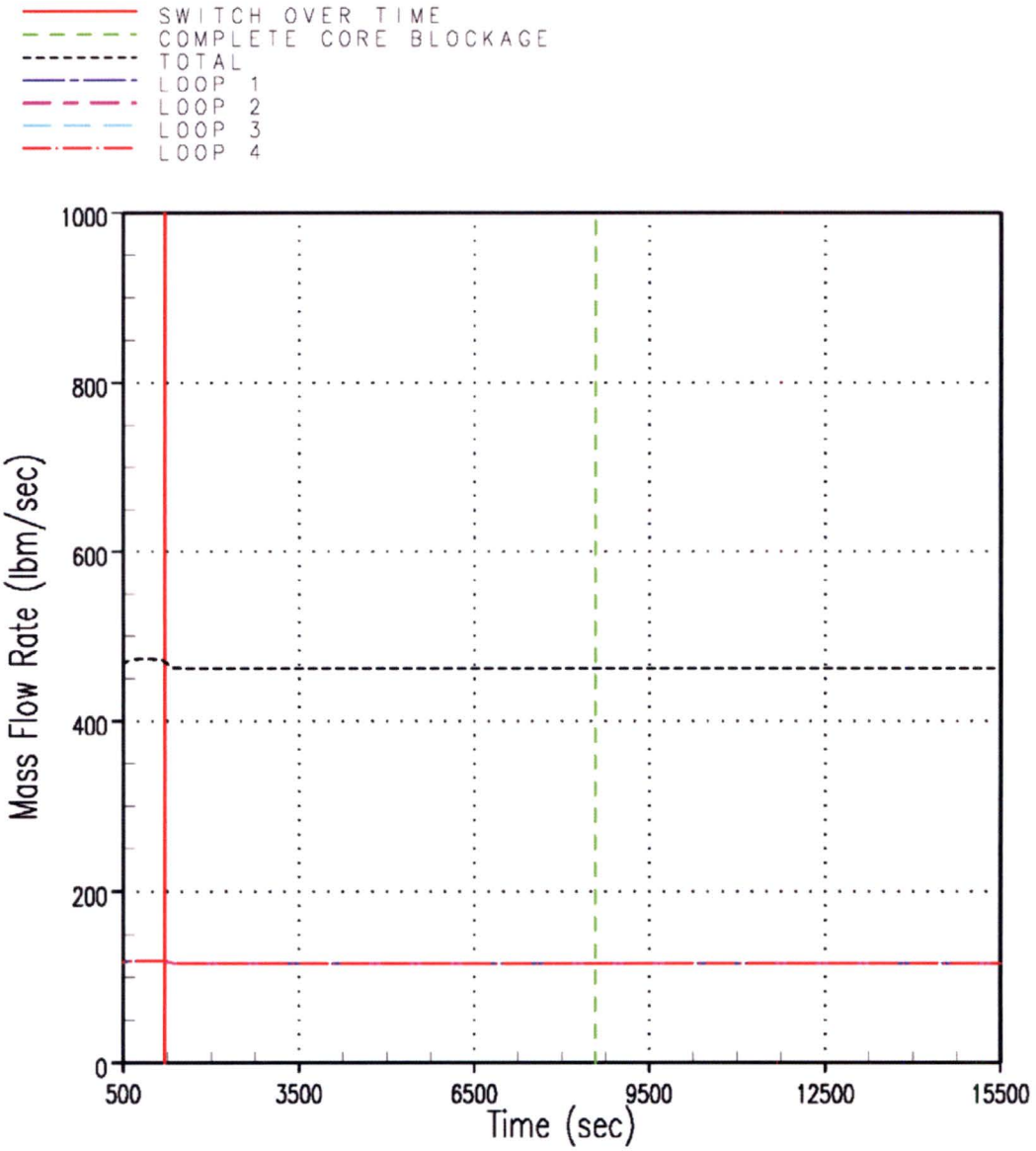

Figure RAI-4.17-17 Case 2B – ECCS Mass Flow Rates Injected into Cold Legs

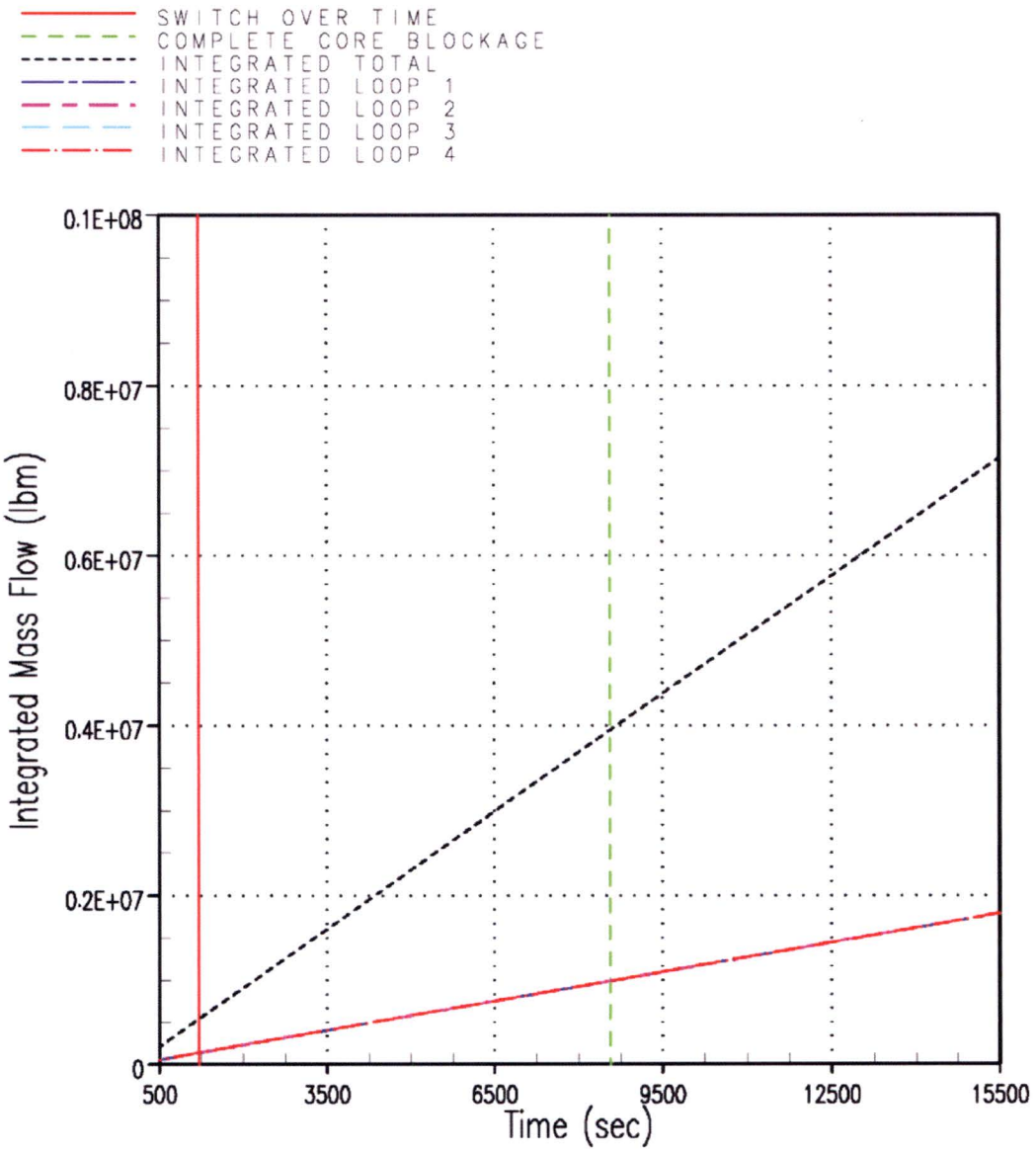

Figure RAI-4.17-18 Case 2B – Integrated ECCS Mass Flow Injected into Cold Legs

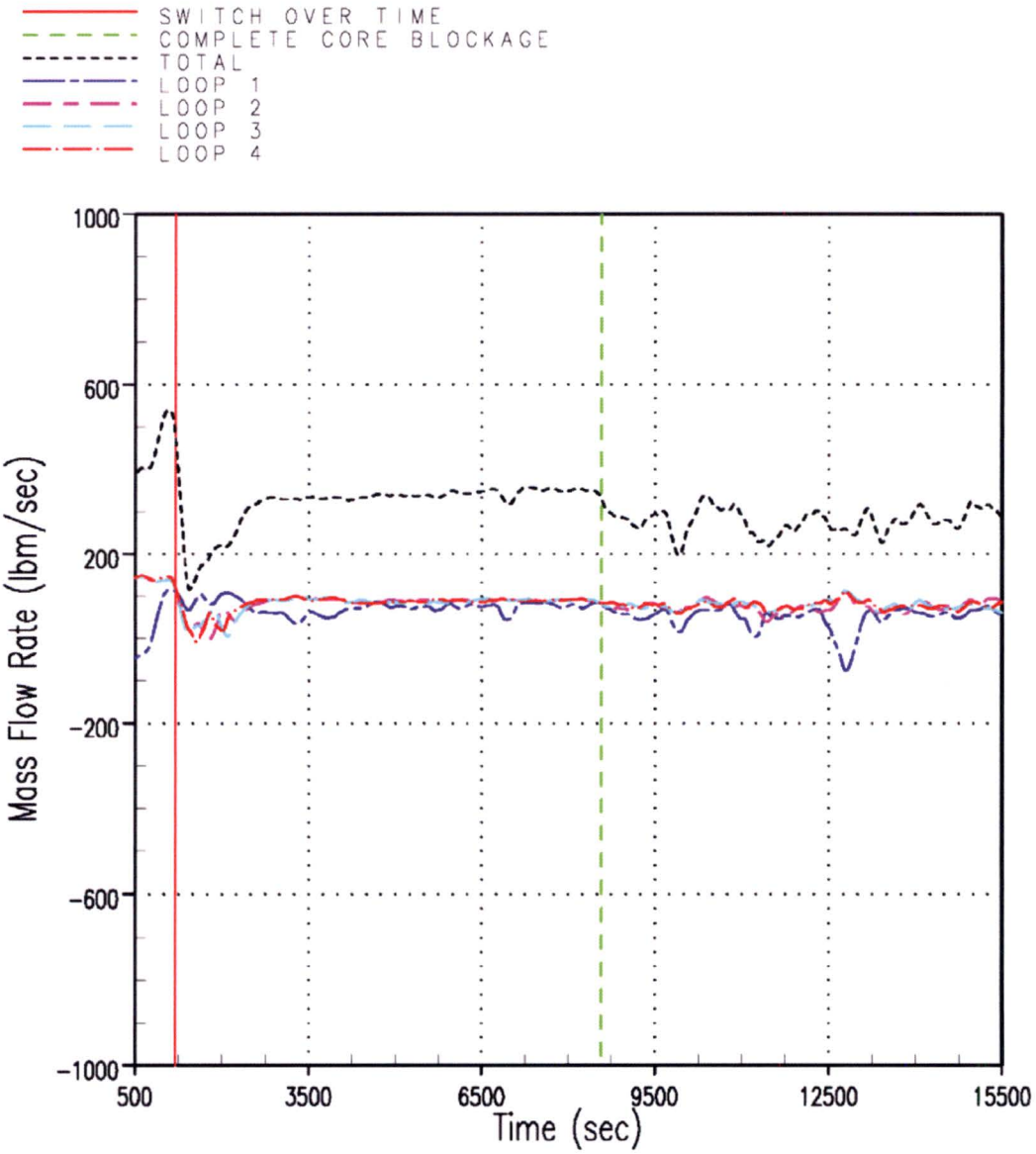

Figure RAI-4.17-19 Case 2B – Mass Flow Rates Entering Reactor Vessel at Cold Leg Nozzles

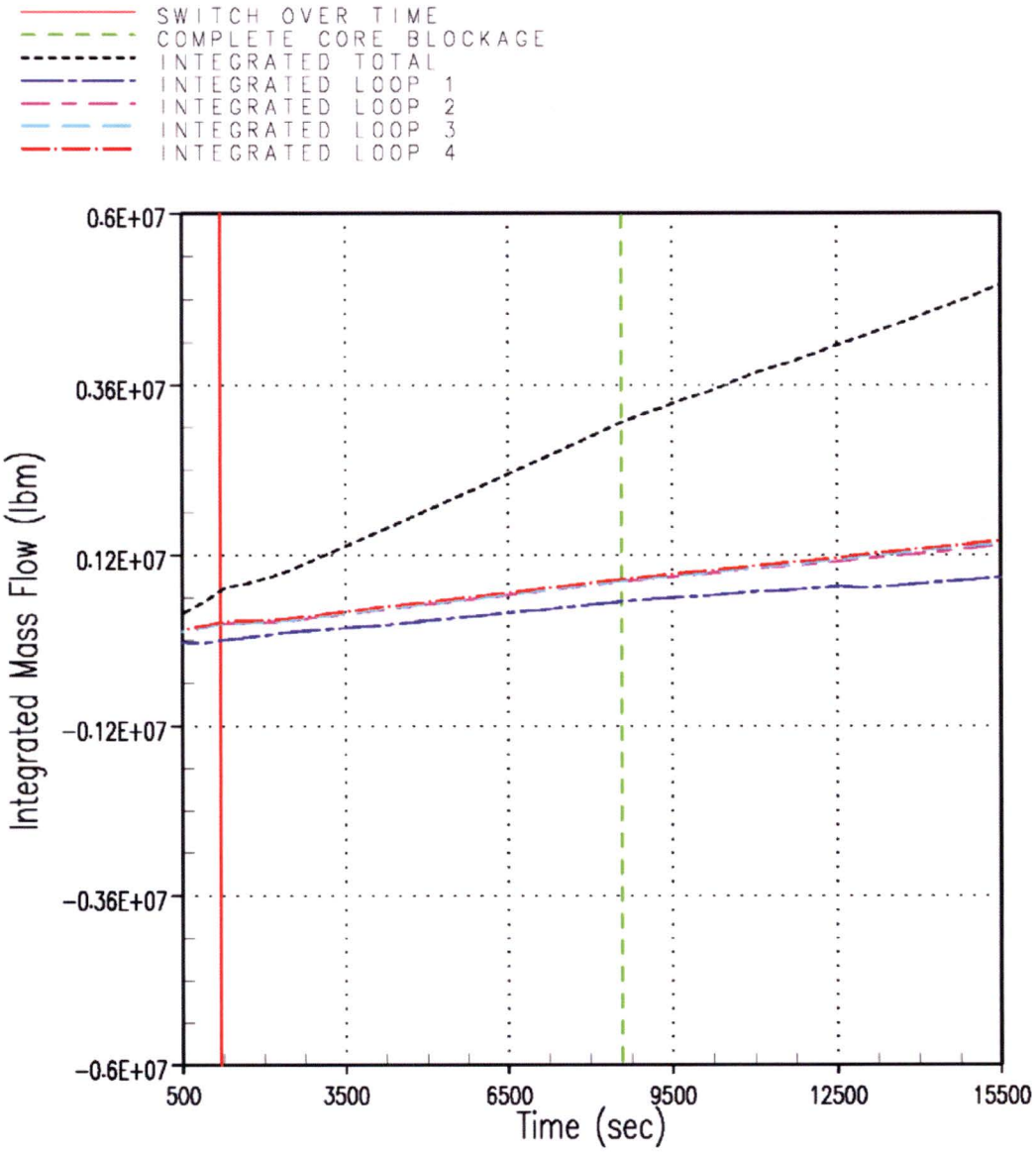

Figure RAI-4.17-20 Case 2B – Integrated Mass Flow Entering Reactor Vessel at Cold Leg Nozzles

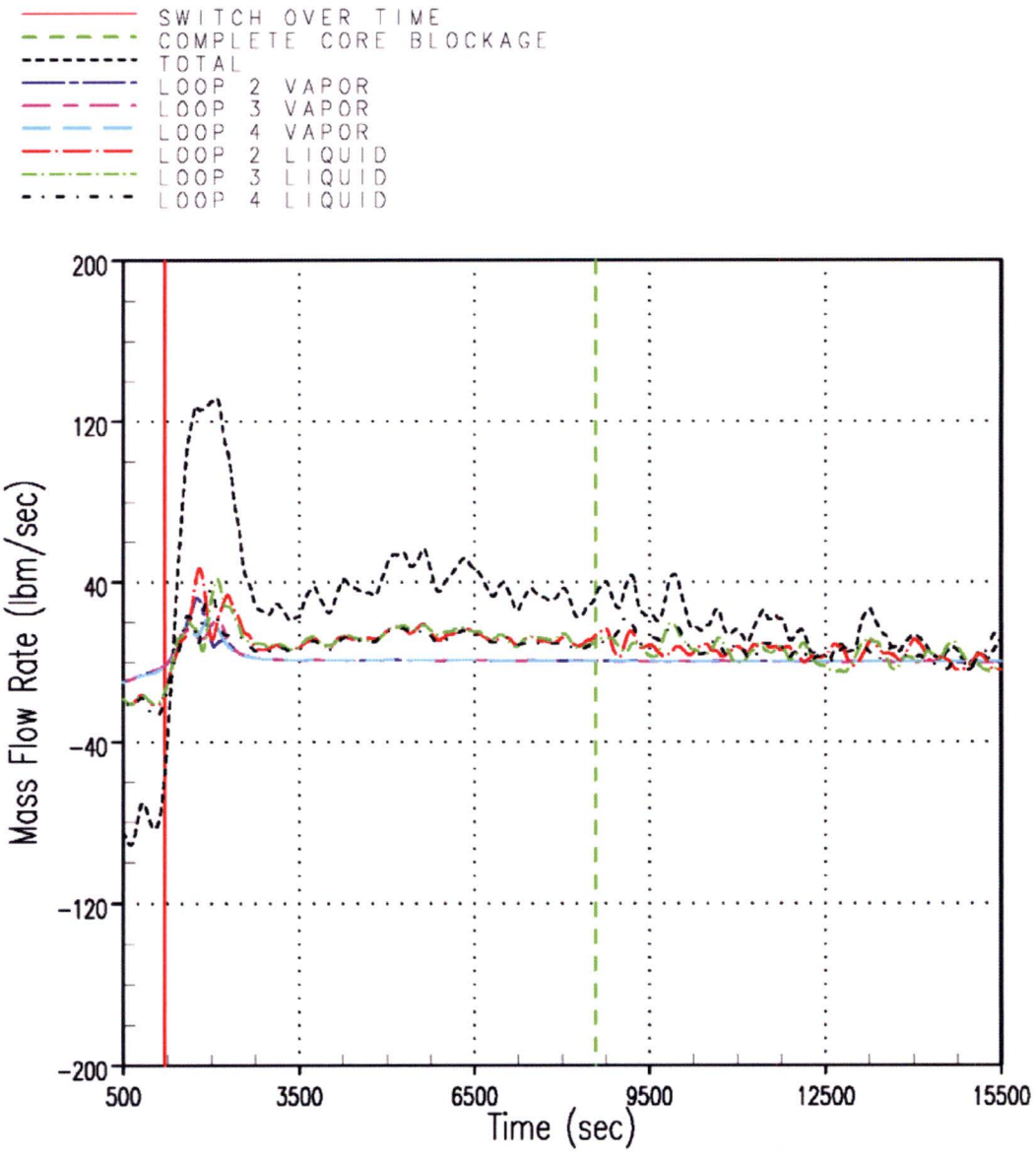

Figure RAI-4.17-21 Case 2B – Mass Flow Rates Entering Reactor Vessel through Intact HL Nozzles

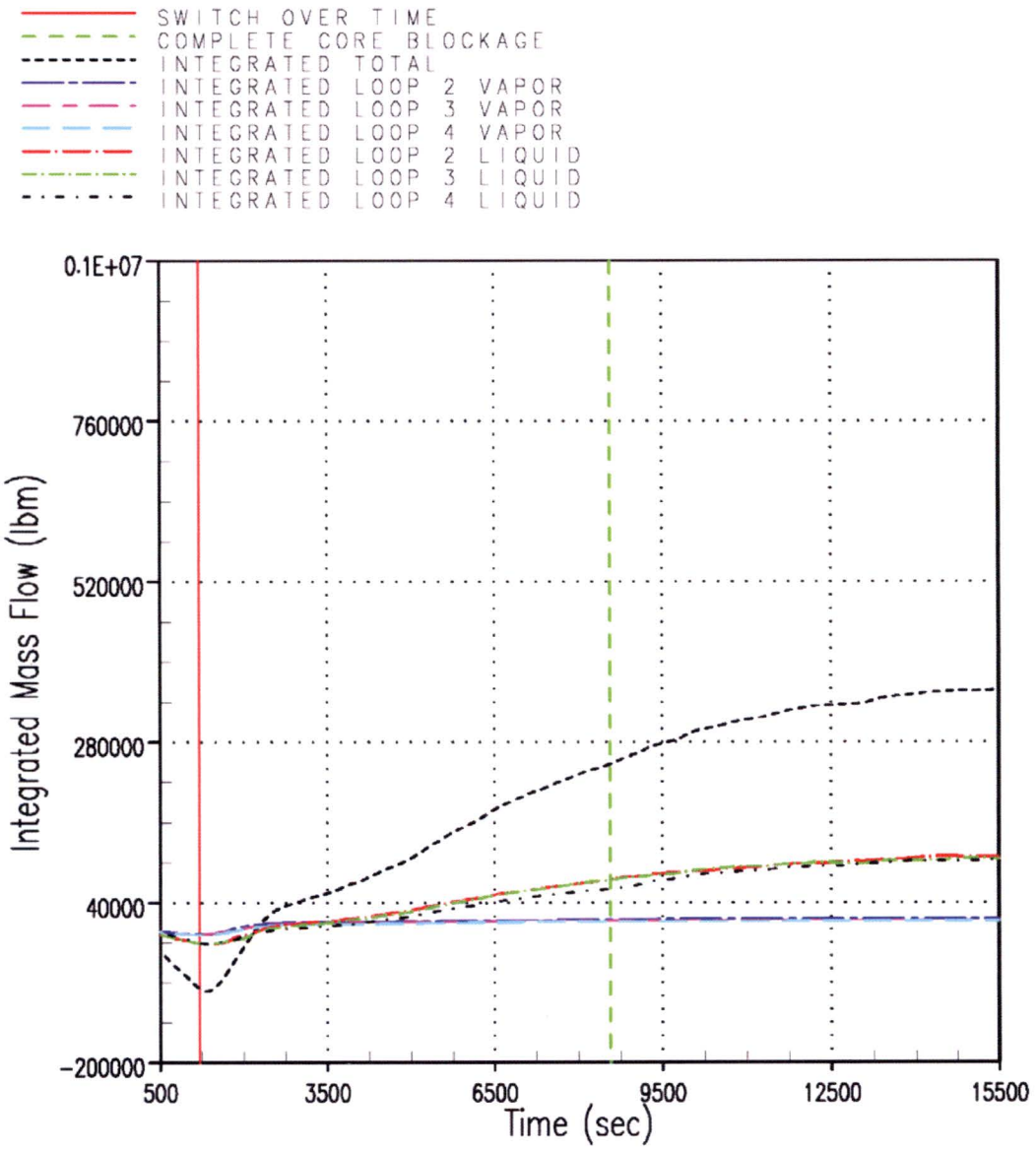

Figure RAI-4.17-22 Case 2B – Integrated Mass Flow Entering Reactor Vessel through Intact HL Nozzles

RAI-4.18, Vol. 4

The HLB T-H cases analyzed for the Westinghouse upflow plant category presented in Section 8 include Case 5, which simulated debris blockage for determination of K_{split} and m_{split} at an ECCS recirculation flow rate of 8 gallons per minute per fuel assembly (gpm/FA). As seen in Figure 8-44, following the SSO time, the downcomer and BB collapsed liquid levels decrease relatively rapidly and drop by about 8 ft and 3 ft, respectively, and reach their minimum levels at about 2,100 seconds before starting a gradual recovery. In contrast to all remaining cases presented in Section 8 (Cases 0A, 1B, 2B, 1, and 3), the result for Case 5 shows the predicted downcomer collapsed liquid level decreasing below the BB collapsed liquid level over a period of about 1,800 seconds. Explain the physical processes leading to this prediction based on the code results for this case. Specifically, explain whether liquid entrainment is among the processes. If necessary, implement modeling changes that correct any unacceptable code behavior and present updated results for Case 5.

Response

Before explaining the behavior, it is noted that the K_{split}/m_{split} cases have been revised in the response to RAI 4.20. The alternate flow path (AFP) resistance was changed from a minimum to a maximum value. The same behavior observed in the original upflow Case 5 (WCAP-17788, Volume 4, Figure 8-44) is seen in the revised case, as shown in Figure RAI-4.18-1.

The RAI is asking to explain two trends; (1) the rapid drop in the downcomer and barrel/baffle (BB) channel collapsed liquid levels at the start of sump recirculation, and (2) the trend that the downcomer collapsed liquid level drops below the BB liquid level.

With regard to the drop in downcomer and BB channel collapsed liquid level, this behavior is related to the change in the emergency core cooling (ECCS) boundary condition at the switchover to sump recirculation. Figure RAI-4.18-2 shows the ECCS flow rate and flow temperature. As the figure indicates, the ECCS flow rate drops from approximately 18 gpm/FA to 8 gpm/FA, and the subcooling is eliminated at the start of sump recirculation. This enhances boiling in the lower core region, as indicated by the hot channel void fraction shown in Figure RAI-4.18-3, and reduces the core collapsed liquid level, as shown in Figure RAI-4.18-4. Figure RAI-4.18-4 also shows the BB and downcomer collapsed liquid levels, which drop consistent with the core collapsed liquid level, as expected.

Figure RAI-4.18-4 also illustrates the behavior related to the RAI's second question, which is why the downcomer collapsed liquid level reduces below the BB channel collapsed liquid level. This behavior can be traced to the ECCS flow split at the cold leg injection points. Since this is a hot leg break ECCS flow can reach the reactor vessel, or it can reach the crossover legs. Without core inlet resistance due to the accumulation of debris, the majority of the ECCS flow enters the reactor vessel, flows through the core, and exits at the hot leg break. When core inlet resistance is applied, the flow split at the ECCS injection points is affected. The ECCS flow split for this case is shown in Figure RAI-4.18-5, which provides the total ECCS flow, the ECCS flow rate of coolant entering the downcomer from the cold legs, and the ECCS flow rate of coolant entering the crossover legs. As the figure indicates, the flow rate to the downcomer decreases and the flow rate to the crossover legs increases. This change in flow split, and

reduction in flow to the downcomer is consistent with the time that the downcomer collapsed liquid level decreases below the inner vessel (core and BB channel) collapsed liquid level. The downcomer liquid level recovers when the ECCS flow from the cold legs to the downcomer recovers.

To understand why the ECCS flow split behavior in the cold legs occurs, the cross over leg void fraction is plotted, as shown in Figure RAI-4.18-6. As the figure shows, the broken loop cross over leg is filled with liquid prior to sump switchover, but the intact loops cross over legs remain highly voided. After core inlet resistance is applied, the intact loop crossover legs begin to fill with liquid, consistent with the reduction in flow to the reactor vessel and the reduction in core collapsed liquid level.

This behavior explains why the downcomer liquid level reduces, and can be explained by a simple parallel circuit analogy. The magnitude of flow in a parallel circuit is governed by the resistance in each flow path. Before sump switchover, and the application of core inlet blockage, the path of least resistance through the system (ECCS injection point to the break) is through the reactor vessel. Mass injected into the system is approximately equal to mass out of the system. This is confirmed in Figure RAI-4.18-7, which compares the total ECCS flow rate to the break flow rate. When core inlet resistance is applied, the resistance through this flow path increases. As a result, the ECCS flow begins to fill the intact loops crossover legs, which have a lower resistance. However, as the crossover legs fill with liquid, the resistance increases, and the flow transfers back to going through the reactor vessel to the break.

Review of Figure RAI-4.18-7 also shows that the liquid carryover from the vessel to the break (entrainment) decreases below the ECCS injection rate during the time that the downcomer liquid level is below the core liquid level, and flow to the reactor vessel is reduced. This demonstrates that the behavior observed is not governed by the liquid carryover (entrainment process), but rather the carryover behavior is governed by the downcomer liquid level. For the short period of time that the downcomer liquid level drops below the inner reactor vessel liquid level, the driving head is not sufficient to maintain the level of liquid carryover seen prior to the reduction in downcomer liquid level. Liquid from the inner reactor vessel wants to reverse and flow into the downcomer to balance the pressure. When the downcomer level recovers, the driving head is sufficient to again maintain liquid carryover to the break that is comparable to the total ECCS recirculation flow.

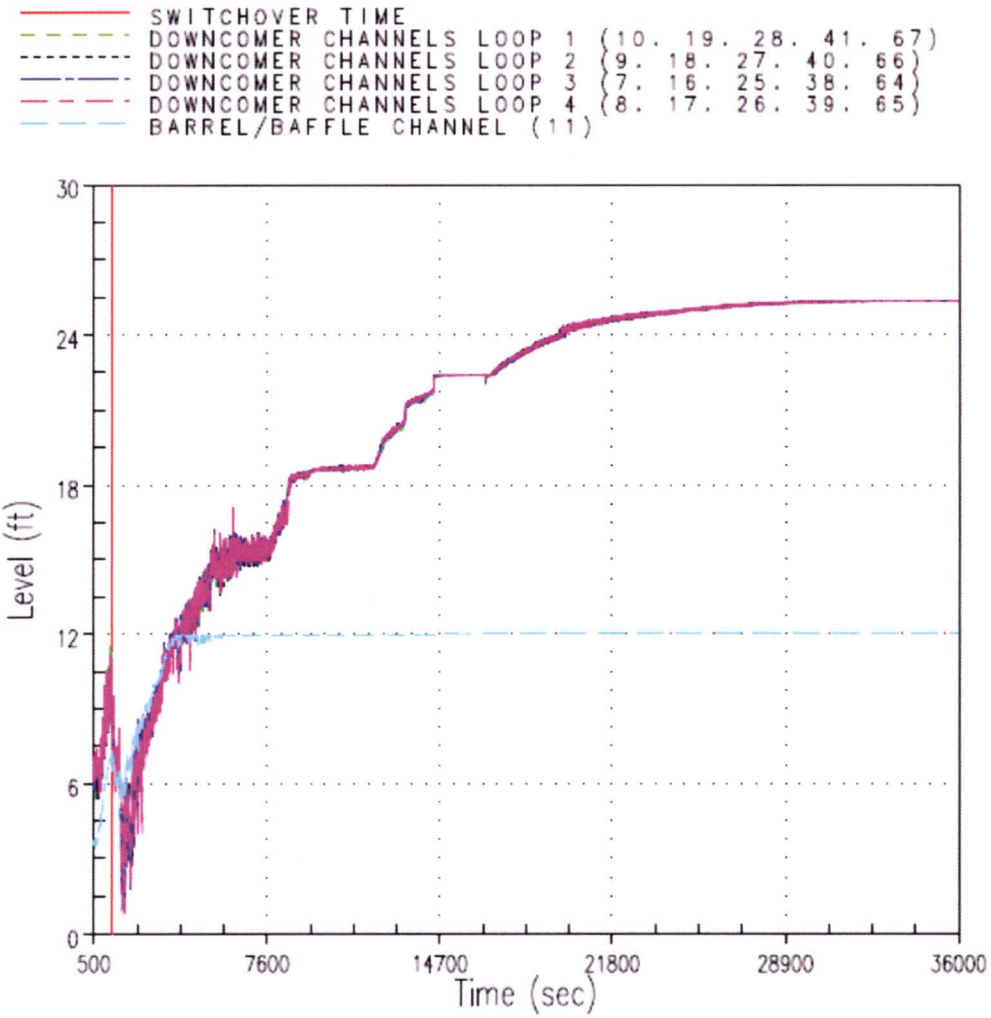

Figure RAI-4.18-1 Upflow Barrel/Baffle Case 5 – Downcomer and Barrel/Baffle Collapsed Liquid Levels

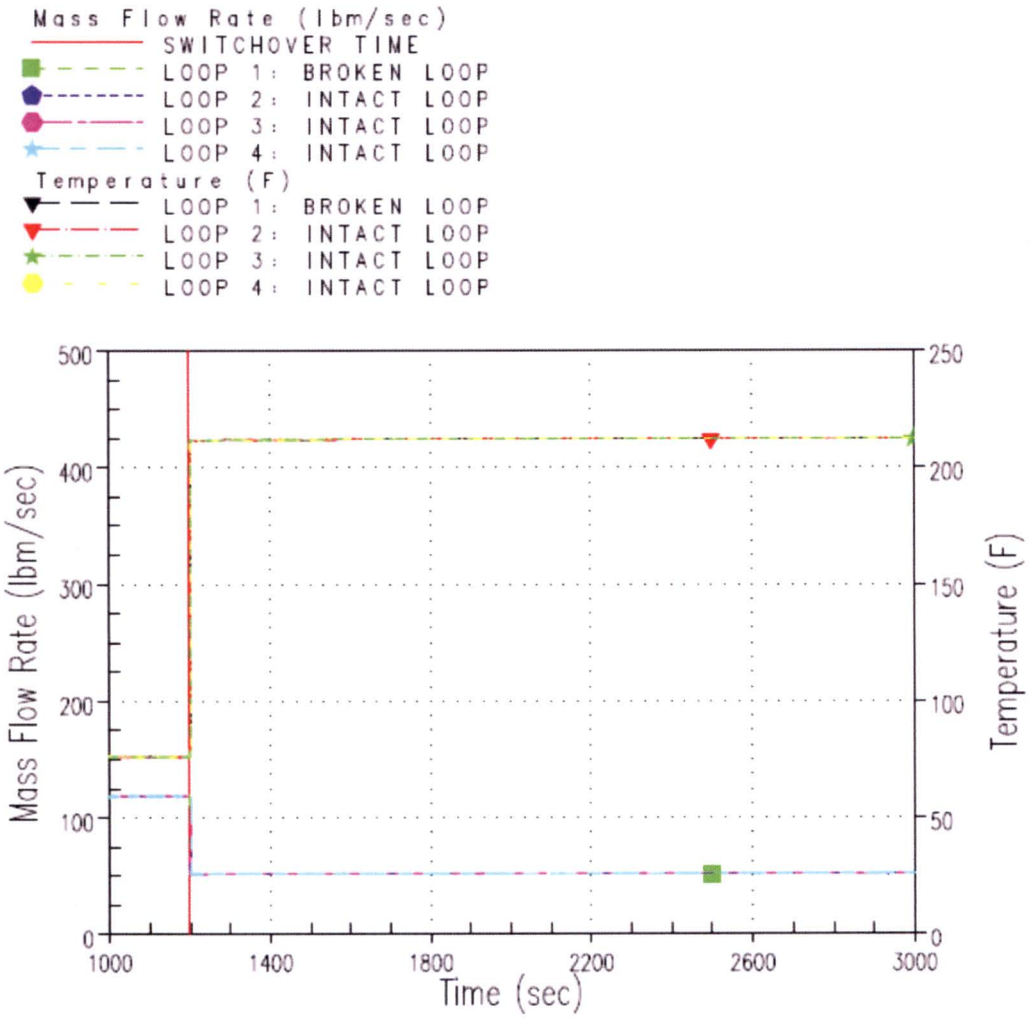

Figure RAI-4.18-2 ECCS Flow Rate and Temperature from Upflow Case 5

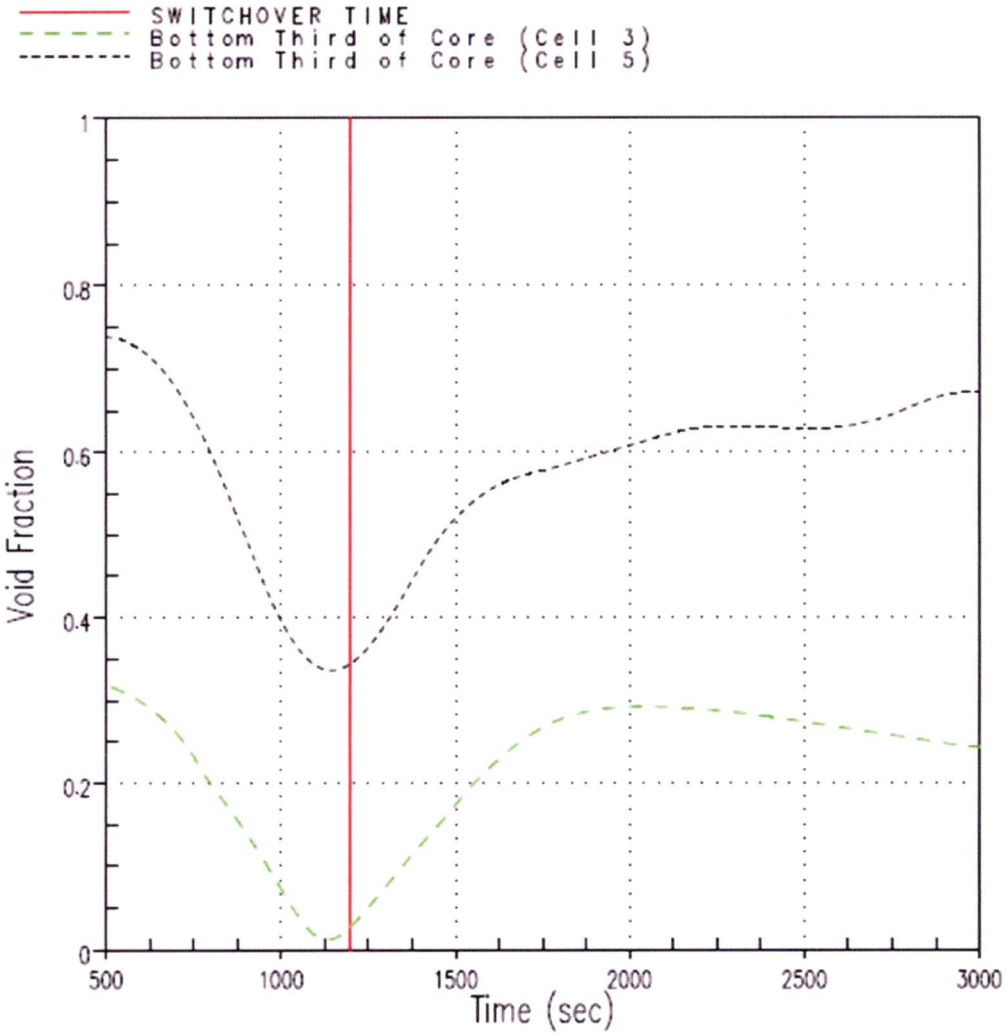

Figure RAI-4.18-3 Void Fraction in the Hot Assembly in the Lower Third of the Core

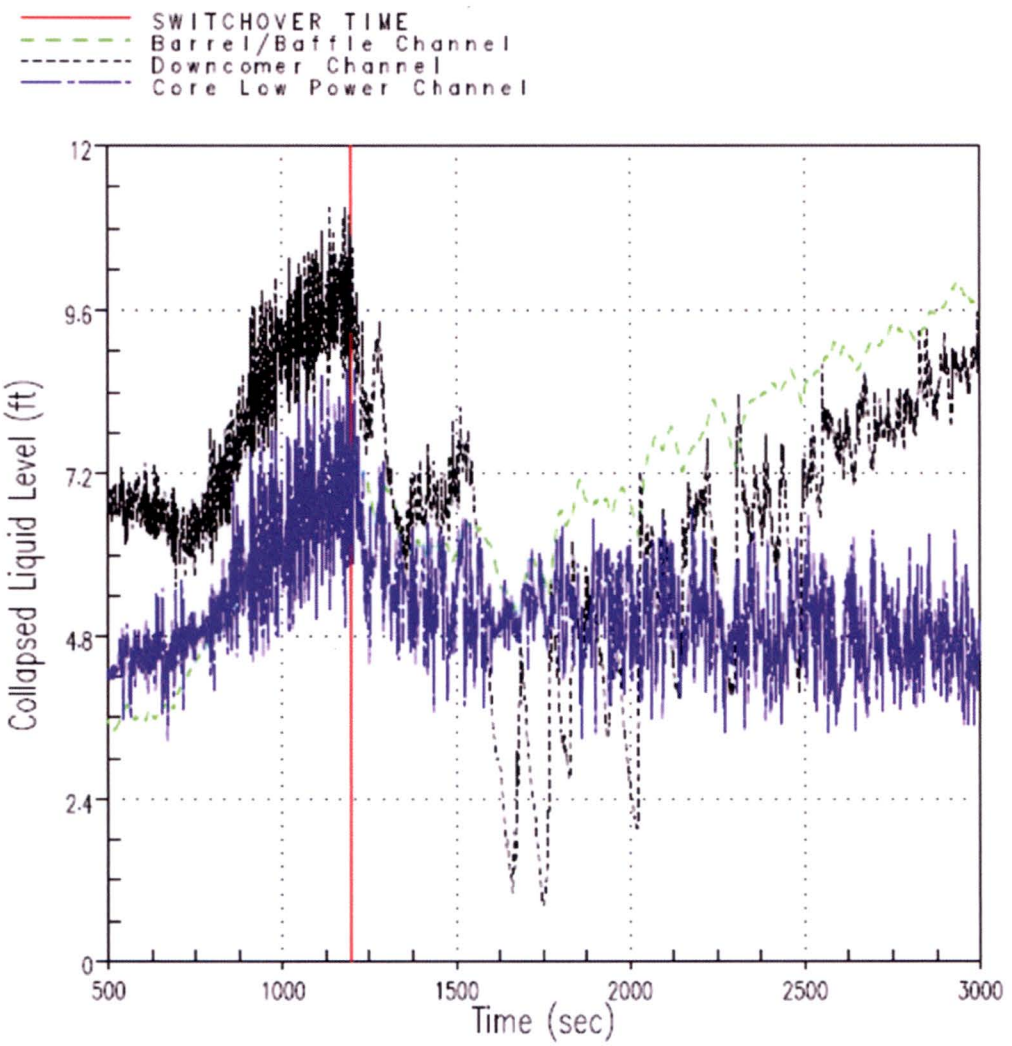

Figure RAI-4.18-4 Barrel/Baffle Channel, Downcomer, and Core Channel Collapsed Liquid Levels

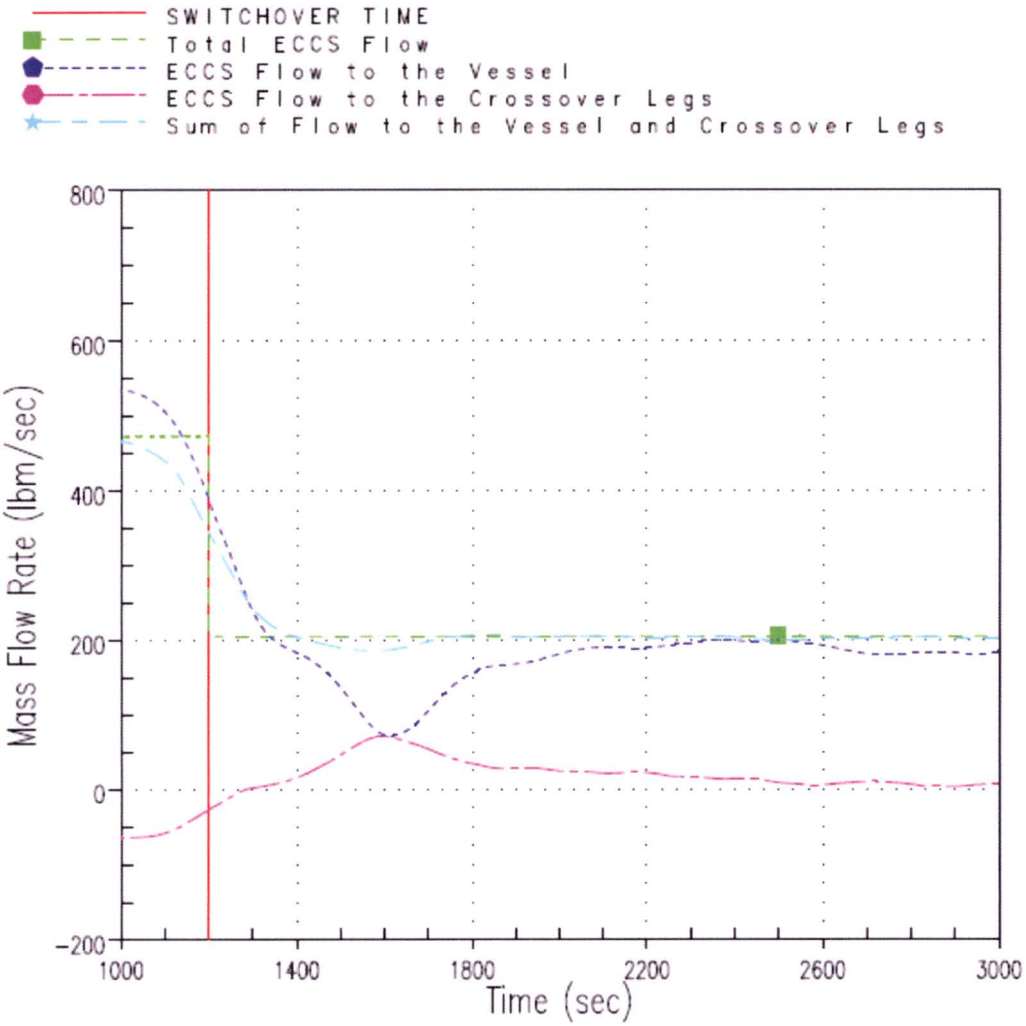

Figure RAI-4.18-5 ECCS Flow Split in the Cold Legs

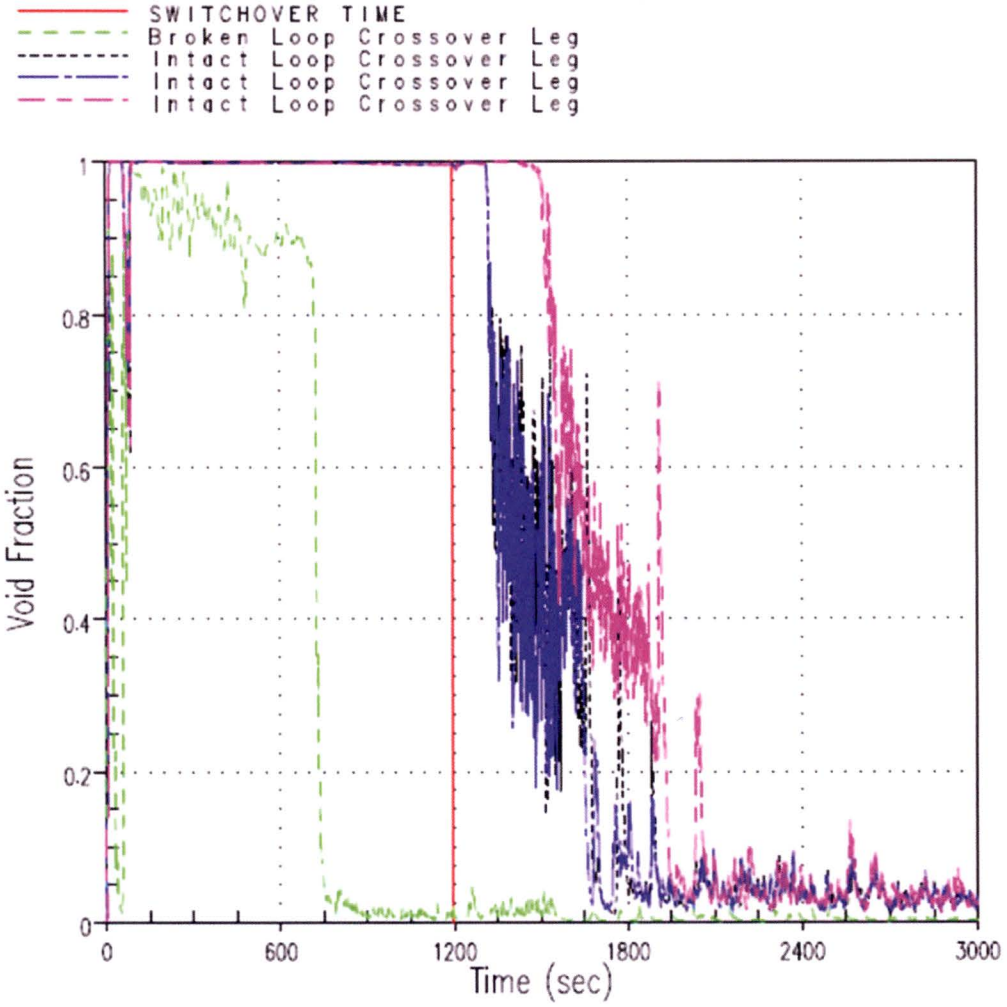

Figure RAI-4.18-6 Crossover Leg Void Fraction

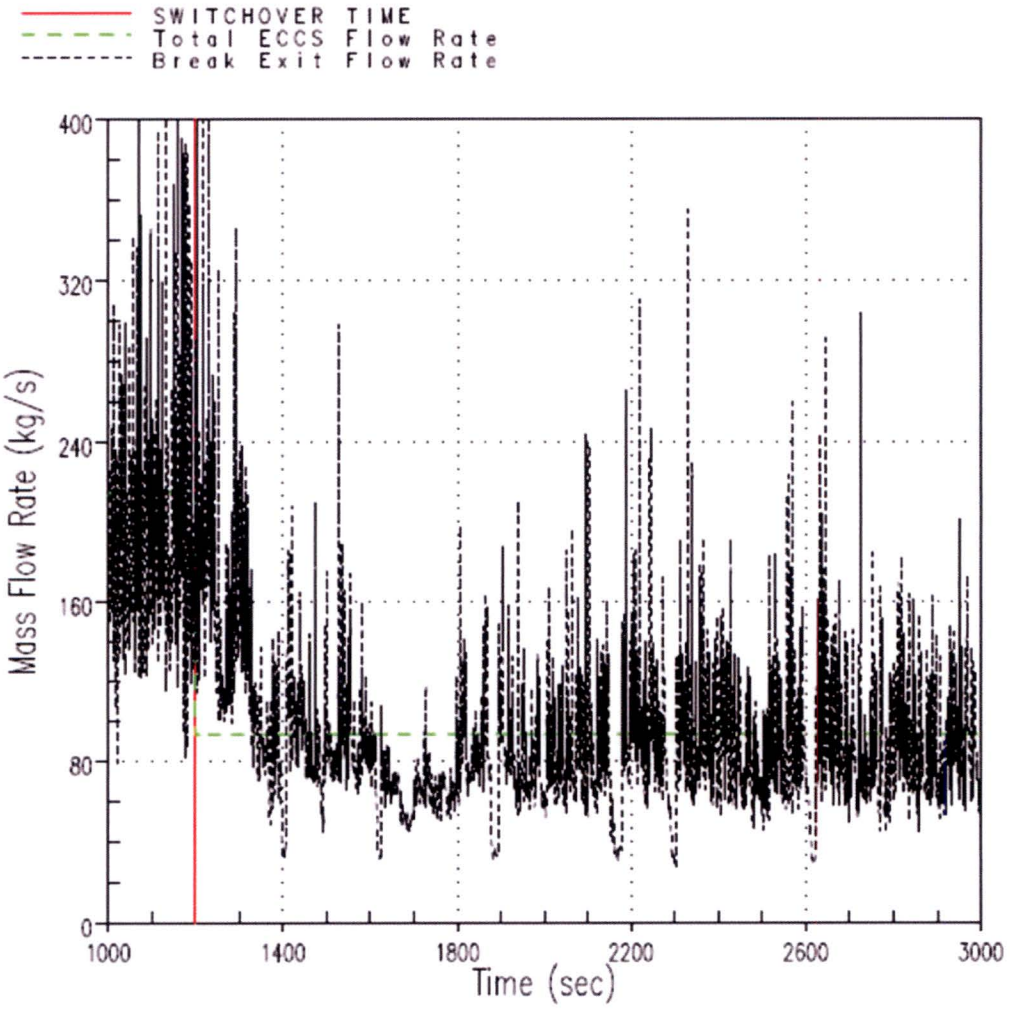

Figure RAI-4.18-7 Total ECCS Flow Rate Compared to Break Exit Flow Rate

RAI-4.19, Vol. 4

The HLB T-H results for the Westinghouse upflow plant category presented in Section 8 include calculations for a single case without debris simulation (Case 0A) and five additional cases that simulate debris for determining t_{block} (Case 1B), K_{max} (Case 2B), and K_{split} and m_{split} (Cases 1, 3, and 5). Regardless of whether debris was simulated or not, the results exhibit a common response as reflected in the plots of collapsed liquid levels for the downcomer, BB, hot assembly, and some plots of predicted RV fluid masses. The response takes place around and following the SSO time. It is characterized by an initial increase in the magnitude of these parameters, which reach maximum levels followed by a relatively rapid decrease. From the predicted collapsed liquid levels, this response is seen taking place around 100 seconds following SSO at 1,300 seconds for Case 0A (Figure 8-7), and within about one minute of the SSO time for Cases 1B (Figure 8-18), 2B (Figure 8-27; it is not easily seen in Figure 8-28 due to core blockage simulated coincidently with SSO), 1 (Figure 8-36, over a shorter timeframe than in the other noted figures due to the high ECCS flow), 3 (Figure 8-40), and 5 (Figure 8-44). A similar response also occurs in Figure 8-17, which illustrates the effect on a predicted RV fluid mass (note that the response is masked in Figure 8-26 due to core blockage simulated coincidently with SSO).

A similar observation applies to the results presented in Section 9 for the Westinghouse downflow plant category. Figures 9-6, 9-7, 9-17, 9-18, 9-29, 9-33, and 9-37 illustrate the response on predicted collapsed levels and Figures 9-16 and 9-22 show predicted RV fluid masses.

a. Explain the physical processes leading to this behavior based on the code results for the analyzed cases. This response reflects the system manometric balances and related contributing pressure losses experienced across the core inlet and other simulated flow passages and regions. Describe the effects of each process and explain whether the observed impact from such effects was considered acceptable. Specifically, explain whether liquid entrainment is among such processes. If liquid entrainment has an effect, analyze the degree to which it had an effect on key results from the simulated cases and justify the acceptability of the results.

Response

As the RAI notes, cases in which core inlet blockage is applied (Case 2B, and Cases 1, 3, and 5 to some extent) at sump switchover mask the system response in question. For this reason, the no blockage case (Case 0A) and the t_{block} case (Case 0B) from the Westinghouse upflow plant category will be used to explain the observed behavior. Case 0A was completed using a 40 gpm/FA recirculation flow rate. Figure RAI-4.24-1 shows the emergency core cooling system (ECCS) flow rate and flow temperature for this case. As the figure shows, the ECCS recirculation flow rate increases relative to the injection phase flow rate. The ECCS flow subcooling is also removed when switchover to sump recirculation occurs. Case 1B was completed using an 18 gpm/FA recirculation flow rate. Figure RAI-4.24-13 shows the ECCS flow rate and flow temperature for this case. As the figure shows, the ECCS recirculation flow rate decreases relative to the injection flow rate. Consistent with the high recirculation flow cases, the ECCS flow subcooling is also removed when sump switchover occurs.

Following reflood, the core is covered with a two phase mixture, the ECCS flow is in excess of boil-off, the ECCS flow is subcooled, and the decay heat is continually decreasing. Under these conditions, boiling in the core is decreasing and the core collapsed liquid level is expected to increase. When ECCS flow is increased, core boiling is further suppressed. WCAP-17788, Volume 4, Figure 8-7 shows the hot assembly core channel collapsed liquid level for Case 0A and shows that the collapsed liquid level increases to approximately 9 feet before beginning to drop again. WCAP-17788, Volume 4, Figure 8-18 shows the hot assembly channel collapsed liquid level from Case 1B and shows that the collapsed liquid level increases to approximately 7 feet before beginning to decrease. The higher peak collapsed liquid level observed in Case 0A is due to the increased ECCS recirculation flow rate.

A reduction in ECCS flow subcooling has the opposite effect and enhances boiling in the core region. This results in higher core voiding and a subsequent reduction in the collapsed liquid level. As shown in WCAP-17788, Volume 4, Figure 8-7, the hot assembly channel collapsed liquid level in Case 0A reduces to a value of approximately 5 feet. Comparatively, the hot assembly collapsed liquid level in Case 0B (WCAP-17788, Volume 4, Figure 8-18) drops to approximately 4 feet. The collapsed liquid level in Case 1B drops to a lower value because the ECCS recirculation flow rate is less. The hot assembly channel collapsed liquid level continues to increase 60 – 100 seconds beyond sump switchover because it takes a finite period of time for the saturated ECCS coolant to reach the reactor vessel core.

The manometric pressure balance between the inner reactor vessel and the downcomer leads to similar behavior in the barrel/baffle (BB) channel and the downcomer channels.

Liquid entrainment is dependent on the steaming rate in the core. As the steaming rate increases, local vapor velocities increase and the entrainment rate increases. However, the entrained liquid must be able to exit the core to influence the collapsed liquid level. The amount of liquid entrainment from the core region is dependent on the distance from the two-phase pool surface and the top of the core, and more liquid will de-entrain on surfaces with longer distances to the core exit. From the perspective of the GSI-191 analyses, a smaller liquid inventory in the core region and upper plenum will result in a more severe core uncovery and heatup transient when debris resistance is applied at the core inlet. This is the reasoning for removing the subcooling and using low recirculation flow rates in the analyses that determine the output parameters K_{max}, and t_{block}. As described in the response to RAI-4.7, WCOBRA/TRAC is also known to over-predict entrainment rates and under-predict de-entrainment. This known code conservatism, in conjunction with the conservative ECCS boundary conditions applied during the recirculation phase of the transient reduce the liquid inventory in the core and the upper plenum and creates a condition that leads to a higher potential for core uncovery when resistance due to the accumulation of debris at the core inlet is applied.

b. The maximum resistance, K_{max}, results for the Westinghouse upflow and downflow plant categories are obtained from analyses in which the core blockage is applied simultaneously with SSO. The NRC staff needs assurance that K_{max} results are not affected by processes associated with the above described system response occurring around the SSO time. The NRC staff recommends performing a re-analyses for the cases presented in Sections 8 (Case 2B) and 9 (Case 2B) used to determine K_{max} with the only change being that the core inlet blockage is applied 200 seconds following the SSO time instead of coincidently with the SSO time.

Response

As described in the response to RAI-4.19 Item a., the system response occurring at the sump switchover time is related to the change in ECCS fluid flow rate and enthalpy. The K_{max} results for each Westinghouse plant category are completed using the minimum ECCS recirculation flow rate considered in the analyses. In the upflow plant category the recirculation flow rate is 18 gpm/FA, which is approximately the same as the injection flow rate. In the downflow plant category the recirculation flow rate is 12 gpm/FA, which is less than the injection flow rate. Since the ECCS fluid change in the downflow plant analysis at sump switchover is more drastic, the system response will be affected more. For this reason, the suggested sensitivity study is performed with the downflow plant model, and any effect on the K_{max} results due to the system response occurring around sump switchover observed in this study will capture the effect expected in the upflow plant model.

In addition to performing the suggest reanalysis in which the core inlet resistance is applied following sump switchover, several simulations are performed in which the sump switchover time is delayed with core inlet blockage applied coincidently with the sump switchover time. In all cases the value of K_{max} is set to 4.75×10^5. Table RAI-4.19-1 provides the simulation matrix. As the table shows, Cases 1 and 2 extend the sump switchover time and the application of core inlet resistance 200 and 400 seconds beyond the base case. The core inlet resistance ramps to K_{max} over a 60 second period in these cases. In Case 3, the sump switchover time is the same as the base case and the start of core inlet resistance is delayed 200 seconds after sump switchover. In this case the resistance is ramped over a 300 second period.

For Case 3 to achieve a debris-induced heatup that was below the base PCT, it was necessary to extend the ramp time. This was expected considering that the core collapsed liquid level is reduced due to the ECCS flow rate reduction following sump switchover. Performing the case in this manner demonstrates that the sensitivity to core inlet resistance ramp rate greatly outweighs the sensitivity to the change in core liquid inventory due to the reduction in ECCS flow rate at the time of sump switchover. A 300 second ramp time still bounds any realistic plant time to reach an equivalent resistance of K_{max} at the core inlet, and the debris-induced heatup predicted in this case is shown to be significantly less severe than the base case.

Table RAI-4.19-1	Sump Switchover and Debris Arrival Time Sensitivity Study Matrix		
Case	**Sump Switchover Time (sec)**	**Start of Core Inlet Resistance (sec)**	**Resistance Ramp Time (sec)**
Base Case (Case 2B)	1200	1200	60
1	1400	1400	60
2	1600	1600	60
3	1200	1400	300

The debris-induced PCT, downcomer collapsed liquid level, and hot assembly collapsed liquid level for the base case and the three sensitivity studies are shown in Figure RAI-4.19-1, Figure RAI-4.19-2, and Figure RAI-4.19-3, respectively.

Figure RAI-4.19-1 shows that the debris-induced PCT is the highest in the base case simulation. As the sump switchover time, and the application of core inlet resistance, is extended (Cases 1 and 2) the PCT reduces. The figure also shows that the case with delayed core inlet and an extended ramp (Case 3) results in a lower PCT compared to the base case.

Figure RAI-4.19-2 shows that the downcomer collapsed liquid levels behave as expected. In the cases that apply core inlet resistance coincident with sump switchover, the downcomer liquid level increases when resistance is applied. The case with delayed core inlet resistance also increases when resistance is applied, only that the liquid level is lower due to the reduction in ECCS flow rate which occurs prior to the application of core inlet resistance. The rate that the level increases is also slower in this case, consistent with the slower ramp rate.

Figure RAI-4.19-3 shows that the hot assembly collapsed liquid level behaves similarly. The level drops when core inlet resistance is applied in the cases that apply the resistance coincident with sump switchover. In the case with delayed core inlet resistance, the level drops at sump switchover, consistent with the reduction in ECCS flow rate. When core inlet resistance is applied in this case there is little change to the level, which is consistent with the minimal debris-induced heatup caused by the slower ramp of resistance.

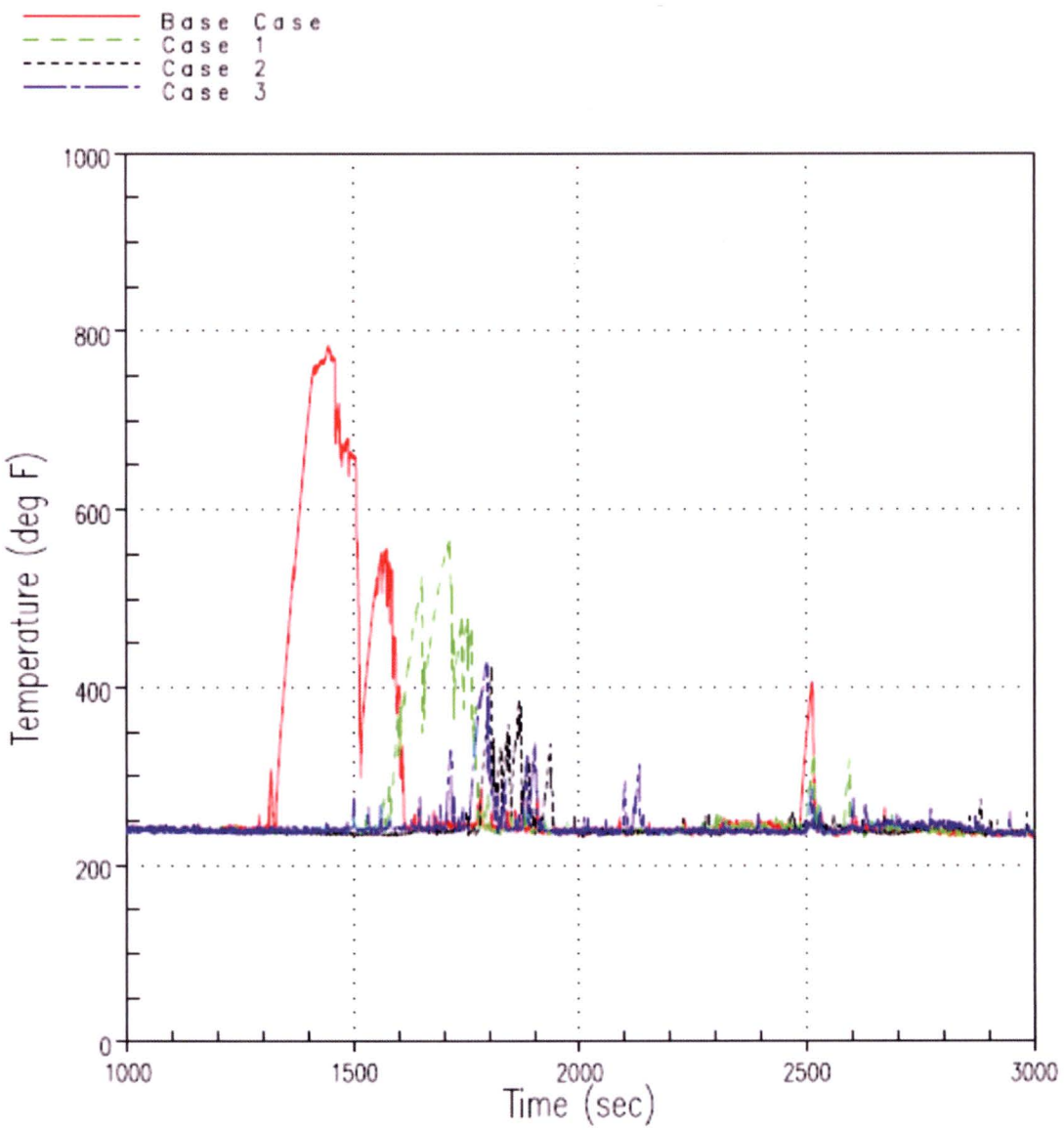

Figure RAI-4.19-1 Westinghouse Downflow Plant Debris-Induced Heatup Results

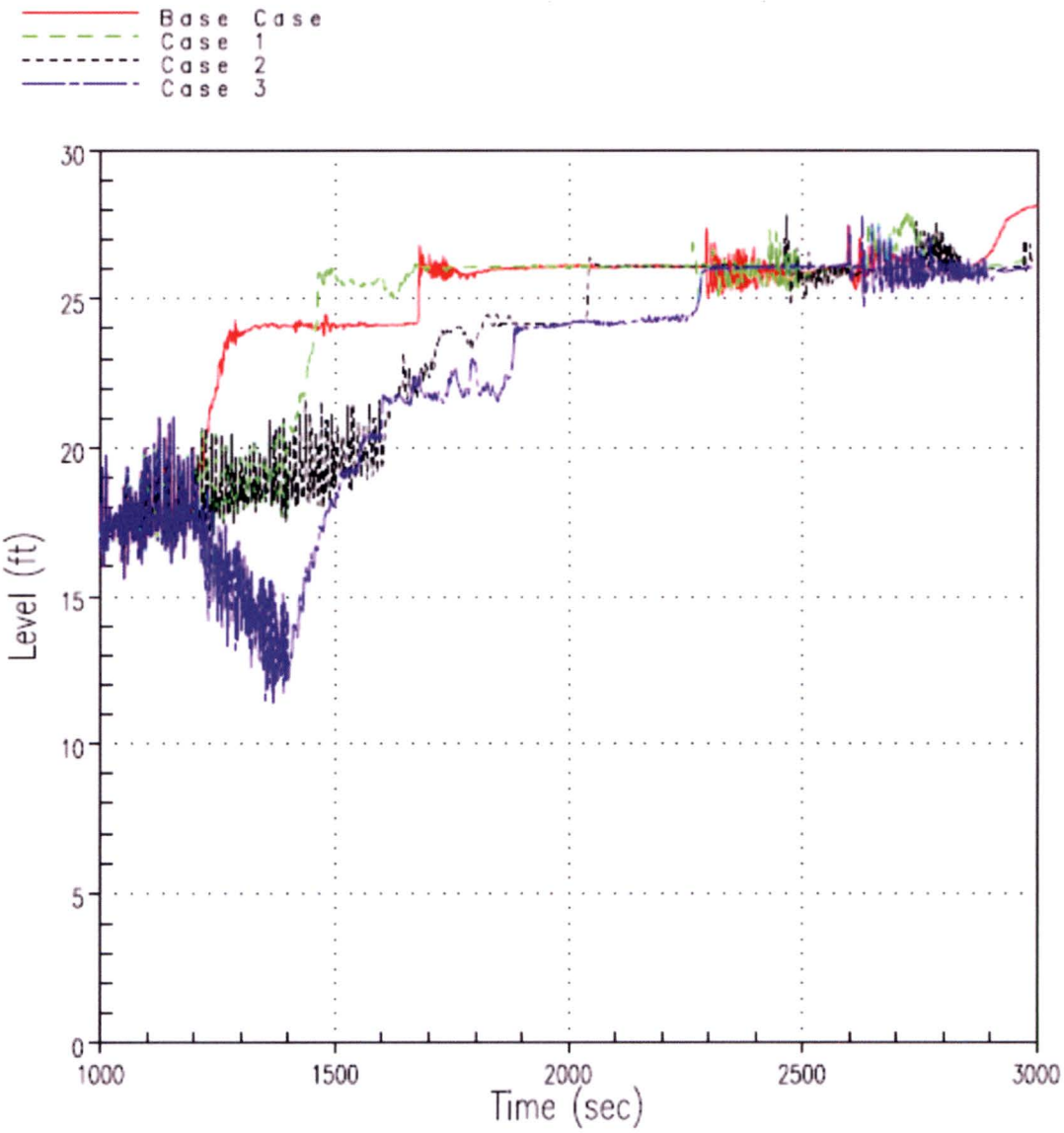

Figure RAI-4.19-2 Westinghouse Downflow Plant Downcomer Collapsed Liquid Level Results

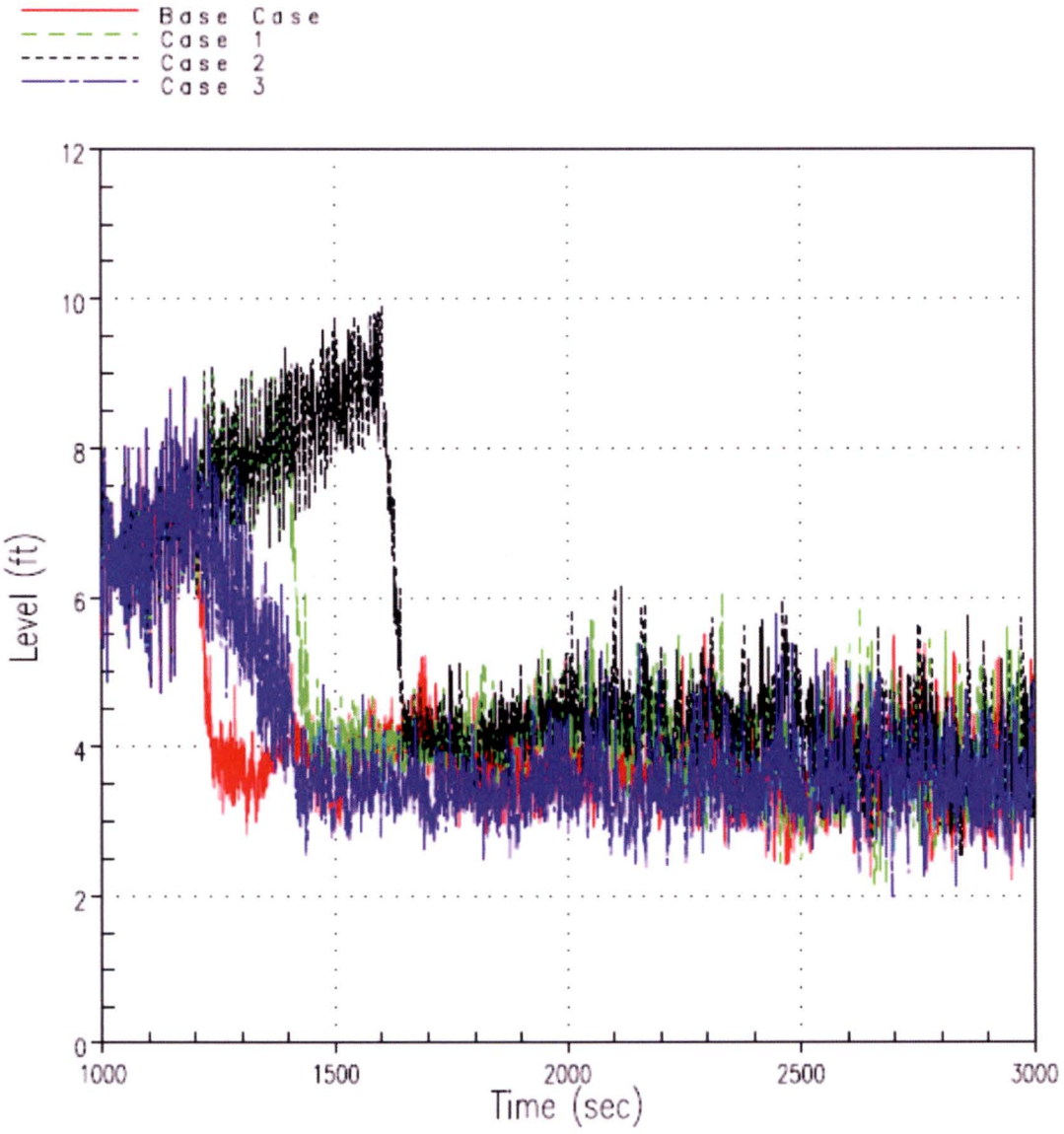

Figure RAI-4.19-3 Westinghouse Downflow Plant Hot Assembly Collapsed Liquid Level Results

RAI-4.20, Vol. 4

The T-H analyses for the large HLB LOCA scenario are used to determine four key parameters, t_{block}, K_{max}, $K_{split,}$ and m_{split}, which are used as inputs to the overall HLB methodology described in Volume 1.

Implementing the high-level process outlined in Figure 4-2, "Overview of Hot Leg Break Methodology," Section 6.5 provides an algorithm that uses K_{split} and m_{split} for calculating in-vessel fiber loads and verifying that they comply with the applicable limits for core inlet, in-core, and total RV fiber. In particular, the core inlet fiber load is used to determine the core inlet resistance, based on the subscale head loss testing in Vol. 6, so that it can be compared against the applicable K_{max} limit as the accident progresses. This important check is performed in Step 10 of the algorithm. As stated in Step 10, "if the core inlet K factor is greater than K_{max} before the time of t_{block}, then the calculation does not meet the acceptance criteria defined by the TH analyses." The core inlet flow and fiber load after SSO are calculated using both K_{split} and m_{split}. When the core inlet resistance is less than or equal to K_{split}, the flow into the RV passes only through the core inlet where it deposits fiber. When the core inlet resistance is greater than K_{split}, the flow into the RV is split between the core inlet and the alternate flow path (AFP) based on m_{split}. The current core inlet resistance is compared against K_{split} at Step 9 of the algorithm.

The K_{split} and m_{split} critical inputs are determined in Vol. 4 from T-H analyses, which were performed using minimum BB flow resistances "for all plant categories with an upflow BB configuration." Section 4.2 states that "selecting the minimum resistance will minimize the resistance due to debris (and hence the amount of debris at the core inlet) that will begin to divert flow to the AFP." It explains that "minimizing the debris at the core inlet required to divert flow to the AFP will maximize the amount of debris predicted to bypass the core inlet and transport to the core region through the AFP." Section 4.2 further explains that a minimum UHSN resistance "will be applied for cases that are used to determine K_{split} and m_{split}" for the Westinghouse downflow plant category.

Explain if the use of maximum AFP flow resistances result in a conservative mass of debris at the core inlet for all cases. Evidently, using thus determined K_{split} and m_{split} parameters will result in the earliest time of flow diversion through the AFPs and the maximum fraction of ensuing ECCS flow through the AFPs, which will maximize the predicted amount of debris transported to the core region and minimize the amount of debris accumulated at the core inlet. Accordingly, the calculated core inlet debris amount can allow the calculation process to continue, unless stopped due to exceeding the in-core or total RV fiber limits, both of which can be significantly higher than the core inlet fiber limit, and eventually produce an acceptable overall analysis outcome without detecting possible violation of the applicable core inlet debris limit. Therefore, the generic HLB methodology, using the K_{split} and m_{split} critical inputs established in Vol. 4, could result in non-conservative results for the Westinghouse upflow, Westinghouse downflow, and CE plant categories.

It is possible that an approach based on maximized, as opposed to minimized, AFP resistances for the determination of K_{split} and m_{split} can be considered for implementation in the HLB methodology for assuring satisfaction of the core inlet fiber limit. Provide additional information to justify how the HLB methodology described in WCAP-17788 can be applied to assure satisfaction of the established core inlet

fiber based on the t_{block}, K_{max}, K_{split}, and m_{split} results established in Vol. 4. The justification could include sensitivity studies where AFP resistance is minimized for each plant category and plant-specific guidance on this matter.

Response

The thermal hydraulic (TH) analyses for the large hot leg break (HLB) loss-of-coolant accident (LOCA) scenario are used to determine four key parameters, t_{block}, K_{max}, K_{split}, and m_{split}, which are used as inputs to the overall HLB methodology described in WCAP-17788, Volume 1. These parameters are dependent on the alternate flow path (AFP) resistance. The response to RAI-4.2 provides the AFP resistances for the Westinghouse pressurized water reactor (PWR) fleet operating in the US, which is broken into two plant categories. For the Westinghouse upflow plant category, the barrel/baffle (BB) channel is the AFP considered in the HLB TH analyses. For the Westinghouse downflow plant category, the upper head spray nozzles (UHSNs) are the AFP considered. Review of the response to RAI-4.2 indicates that there is variance in the AFP resistance for both Westinghouse plant categories.

As described in WCAP-17788-P, Volume 4, Section 4.2, using a maximum AFP resistance in the TH analyses is appropriate for determining t_{block} and K_{max}, because a higher AFP resistance will require the largest driving head to force flow through the AFP and into the core region, resulting in the worst-case scenario for defining t_{block} and K_{max}. The base analyses for the Westinghouse plant categories described in WCAP-17788, Volume 4 used bounding high AFP resistances as input to calculate t_{block} and K_{max}. Therefore, no additional work is required to justify the value of these parameters relative to the AFP resistance.

The original analyses for determining K_{split} and m_{split} were performed using bounding low AFP resistances. The original intent of this selection was to maximize the amount of debris that would be transported to the heated core region, such that the in-core debris limit would be challenged. As a consequence, this would limit the amount of debris accumulation at the core inlet by bypassing debris through the AFP earlier in the transient and at a higher rate. If the in-vessel debris limit is indeed limited by the in-core debris loading, the selection of a low AFP resistance would be correct. However, since the total in-vessel fibrous debris limit is set equal to the in-core fibrous debris limit, the core inlet debris limit, K_{max} prior to t_{block} will be the limiting factor. As such, a maximum bounding AFP resistance should be used to determine K_{split} and m_{split} to maximize the amount of debris calculated to accumulate at the core inlet.

Based on the above discussion, the K_{split} / m_{split} analyses were revised for the Westinghouse upflow plant categories using the maximum AFP resistances determined in the response to RAI-4.2. The AFP resistance was the only value changed in the base plant models described in WCAP-17788, Volume 4, Sections 6.1 and 6.2, for the upflow and downflow plant categories respectively. Another shortcoming identified in the original K_{split} / m_{split} analyses was that the core inlet loss coefficient at the end of the simulations was much less than the K_{max} value. As a result, the original curve fit provided for m_{split} had to be extrapolated beyond the analyses range. This was also corrected in the revised analyses by extending the simulation end time and core inlet resistance ramp rates. Table RAI-4.20-1 and Table RAI-4.20-2

show the case matrices for the Westinghouse upflow and downflow revised K_{split} / m_{split} analyses, respectively.

Figure RAI-4.20-1 shows the revised K_{split} curve as a function of emergency core cooling system (ECCS) flow rate for the Westinghouse upflow plant category, and compares it to the original curve. The figure indicates that AFP resistance tends to increase the value of K_{split} for a given flow rate. Also provided in Figure RAI-4.20-1 is the revised curve fit that will be used for the HLB in-vessel debris methodology. As the figure indicates, the curve fit was selected such that a higher K_{split} is calculated using the curve fit than what is predicted by the TH analyses. A higher K_{split} value will delay debris bypass and increase the amount of debris accumulation at the core inlet. The revised curve fit also only covers the range of flow rates considered in the TH analyses, and is only valid over the range of ECCS recirculation flows analyzed.

Figure RAI-4.20-2 shows the revised m_{split} data plotted as a function of K-K_{split} for the Westinghouse upflow plant category, and compares it to the original curve fit. As expected, the value of m_{split} is reduced when the AFP resistance is increased. Two m_{split} curve fits are developed for use in the HLB in-vessel debris methodology. The first curve fit is applicable to ECCS recirculation flow rates greater than or equal to 18 gpm/FA, and is shown in Figure RAI-4.20-3. The second curve fit is applicable to ECCS recirculation flow rates less than 18 gpm/FA, and is shown in Figure RAI-4.20-4. Both figures indicate that the curve fits calculate m_{split} values that fall below the TH analysis predictions, in most instances. Using a lower m_{split} value will reduce debris bypass and maximize debris accumulation at the core inlet.

Figure RAI-4.20-5 shows the revised K_{split} curve as a function of emergency core cooling system (ECCS) flow rate for the Westinghouse downflow plant category, and compares it to the original curve. The figure indicates that AFP resistance tends to increase the value of K_{split} for a given flow rate. Also provided in Figure RAI-4.20-5 is the revised curve fit that will be used for the HLB in-vessel debris methodology. Similar to the upflow plant category, the curve fit was selected such that a higher K_{split} is calculated using the curve fit than what is predicted by the TH analyses.

Figure RAI-4.20-6 shows the revised m_{split} data plotted as a function of K-K_{split} for the Westinghouse downflow plant category, and compares it to the original curve fit. As expected, the value of m_{split} is reduced when the AFP resistance is increased. A single m_{split} curve fit is developed for use in the HLB in-vessel debris methodology. The curve fit is applicable to the full range of ECCS recirculation flow rates analyzed (8 – 40 gpm/FA), and is shown in Figure RAI-4.20-7. The figure indicates that the curve fit calculates m_{split} values that fall below the TH analysis predictions.

WCAP-17788, Volumes 1 and 4 will be updated to reflect the revised K_{split}/m_{split} analyses.

Table RAI-4.20-1 Case Matrix for the Upflow Barrel/Baffle Plant Simulations				
CASE	SUMP RECIRCULATION FLOW RATE (GPM/FA)	CORE BLOCKAGE (LINEAR RAMP)		
		LOSS COEFFICIENT	INITIATION TIME (S)	END TIME (S)
1	40	$6.25x10^4$/hr	1200	30 000
2	30	$6.25x10^4$/hr	1200	30 000
3	18	$6.25x10^4$/hr	1200	30 000
4	12	$6.25x10^4$/hr	1200	30 000
5	8	$6.26x10^4$/hr	1200	36 000

Table RAI-4.20-2 Case Matrix for the Downflow Barrel/Baffle Plant Simulations				
CASE	SUMP RECIRCULATION FLOW RATE (GPM/FA)	CORE BLOCKAGE (LINEAR RAMP)		
		LOSS COEFFICIENT	INITIATION TIME (S)	END TIME (S)
1	40	$7.5x10^4$/hr	1200	30 000
2	30	$7.5x10^4$/hr	1200	30 000
3	18	$7.5x10^4$/hr	1200	30 000
4	12	$7.5x10^4$/hr	1200	30 000
5	8	$7.5x10^4$/hr	1200	30 000

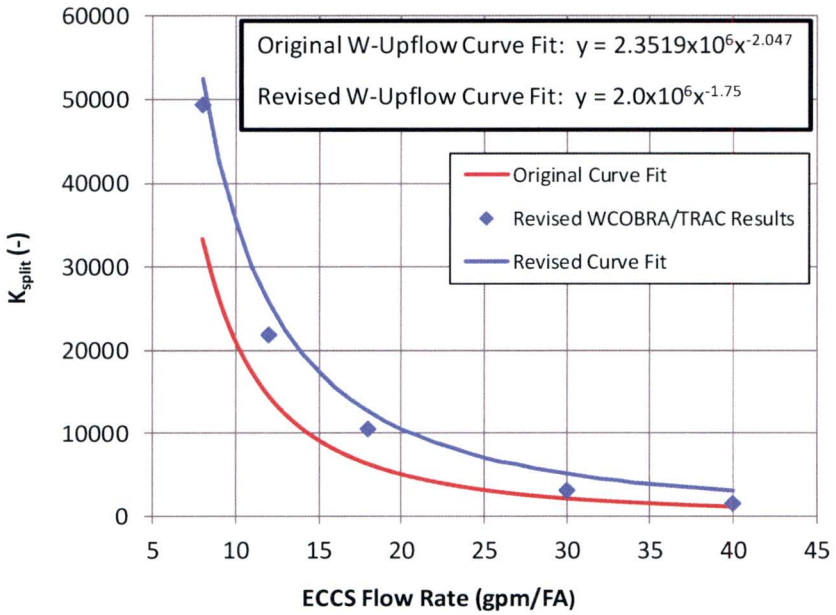

Figure RAI-4.20-1 Westinghouse Upflow Barrel/Baffle Plant Category – Revised K_{split} Curve Compared to the Original Curve Fit

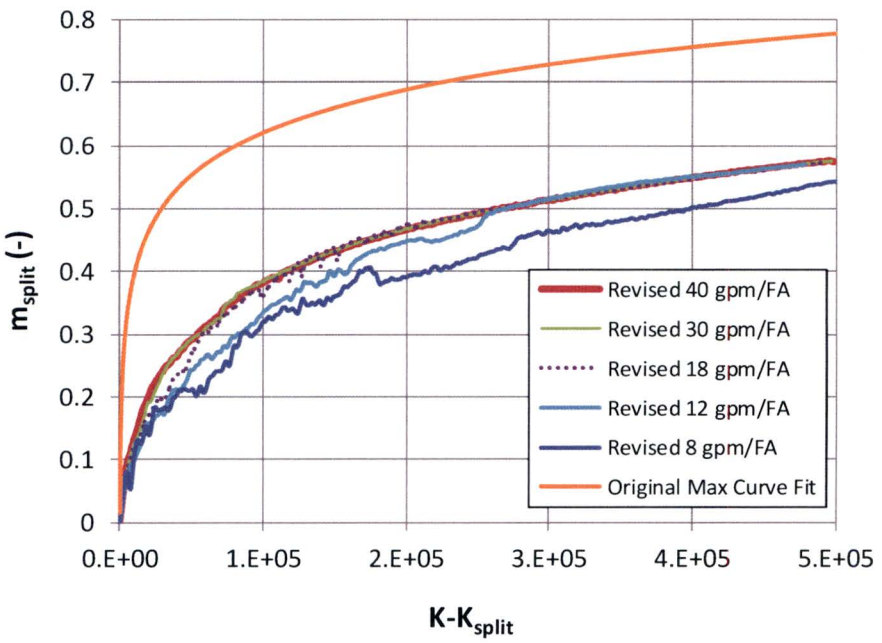

Figure RAI-4.20-2 Westinghouse Upflow Barrel/Baffle Plant Category – Revised m_{split} Curves Compared to the Original Curve Fit

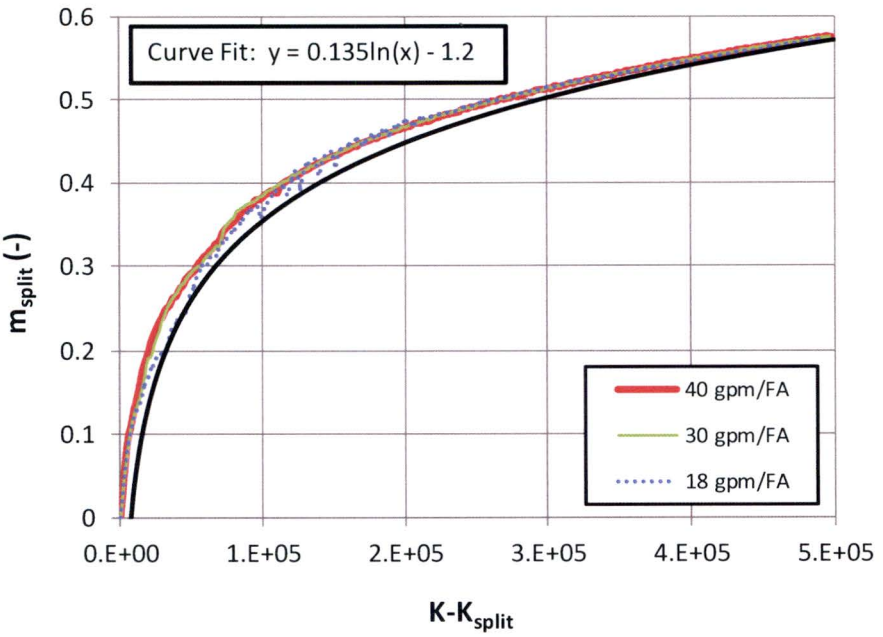

Figure RAI-4.20-3 Westinghouse Upflow Barrel/Baffle Plant Category – Revised m_{split} Curves and Curve Fit for ECCS Recirculation Flows Greater Than or Equal to 18 gpm/FA

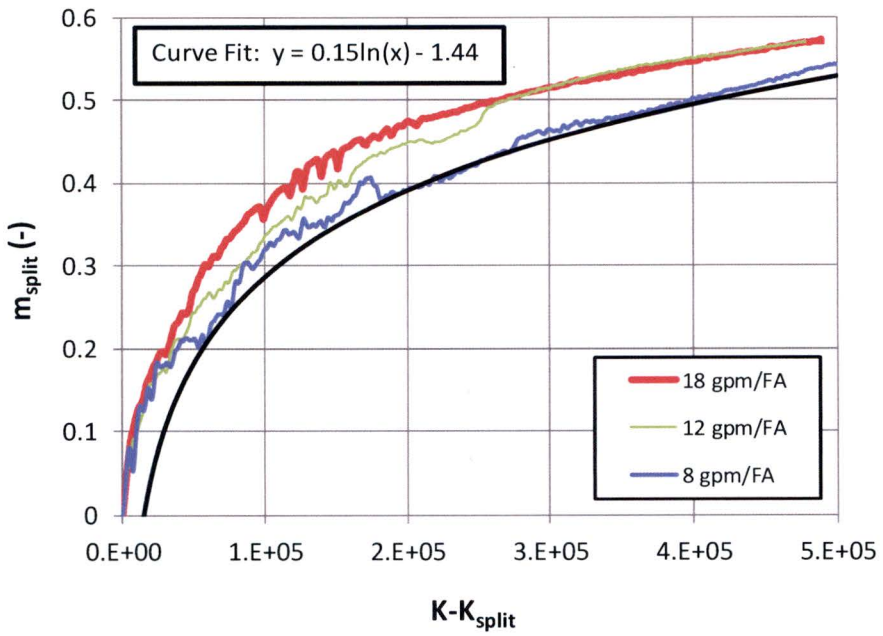

Figure RAI-4.20-4 Westinghouse Upflow Barrel/Baffle Plant Category – Revised m_{split} Curves and Curve Fit for ECCS Recirculation Flows Less Than 18 gpm/FA

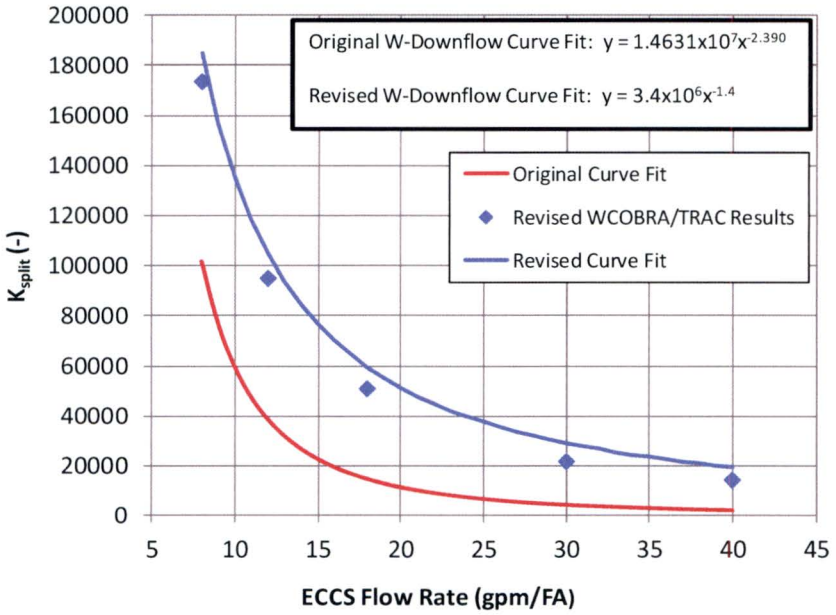

Figure RAI-4.20-5 Westinghouse Downflow Barrel/Baffle Plant Category – Revised K_{split} Curve Compared to the Original Curve Fit

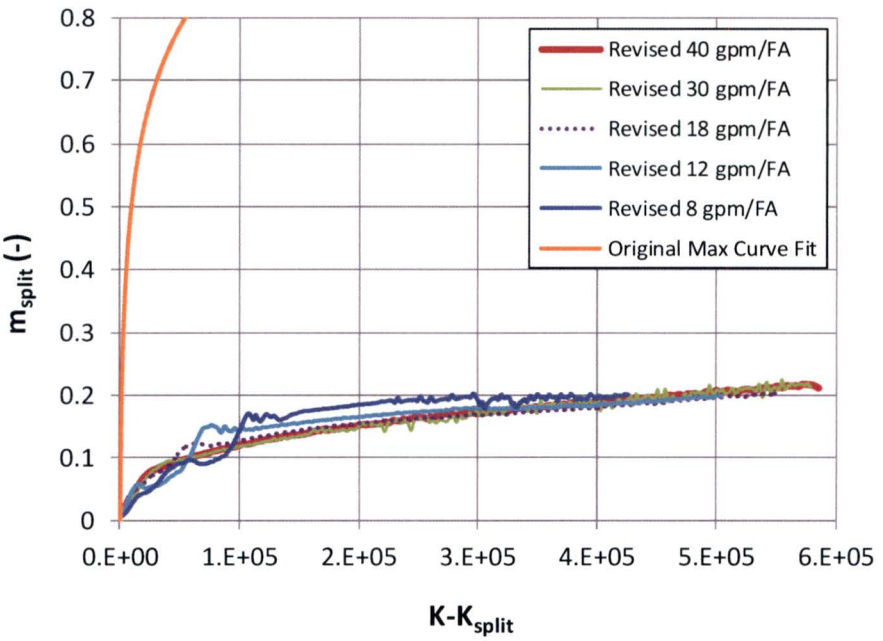

Figure RAI-4.20-6 Westinghouse Downflow Barrel/Baffle Plant Category – Revised m_{split} Curves Compared to the Original Curve Fit

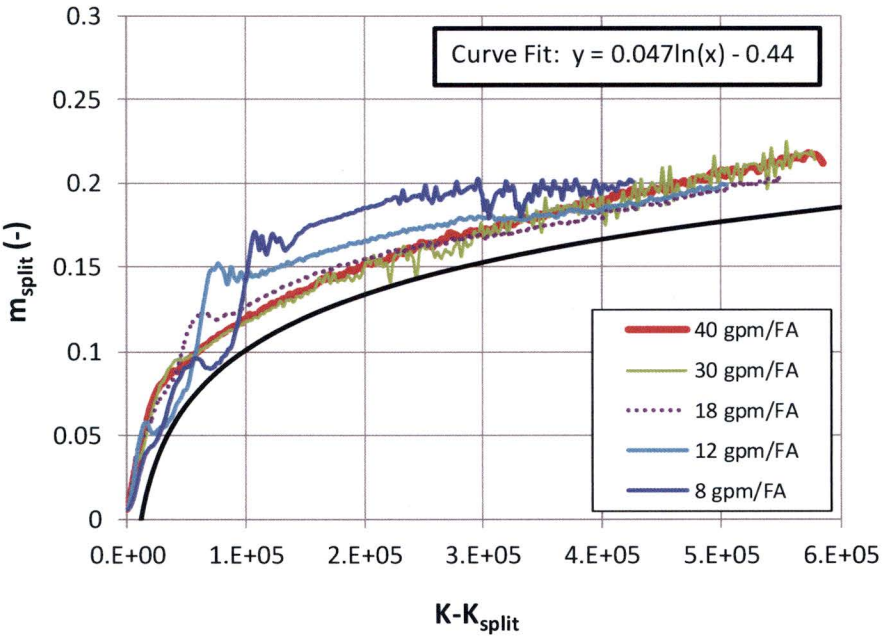

Figure RAI-4.20-7 Westinghouse Downflow Barrel/Baffle Plant Category – Revised m_{split} Curves and Curve Fit

RAI-4.21, Vol. 4

The T-H analyses determine four key parameters, t_{block}, K_{max}, K_{split}, and m_{split}, which are used as input to the overall methodology described in Vol. 1. The K_{split} results are presented in Figures 8-4, 9-3, 10-4, and 11-3 and the m_{split} results are presented in Figures 8-5, 9-4, 10-5, and 11-4 in Vol. 4. Fitting curves to the predicted K_{split} and some m_{split} results are shown in each of these plots. The same plots are reproduced in Figures 6-1 through 6-8 in Volume 1.

The T-H analyses do not provide a basis for extrapolation or interpolation of the calculated K_{split} results as a function of the ECCS recirculation flow rate. Provide the applicability of extrapolating the calculated K_{split} values outside of the analyzed range of ECCS rates for the fitting expressions in Figures 8-4, 9-3, 10-4, and 11-3. Justify the ability to interpolate the expressions to reproduce the calculated K_{split} values between the calculated points.

Similar to the case with the calculated K_{split} inputs, the m_{split} results and the supporting T-H analyses in Vol. 4 do not provide a basis for justifiable extrapolation or interpolation of the calculated m_{split} results documented as a function of the core inlet resistance reduced by K_{split} and the ECCS flow rate. Provide the basis for extrapolating the calculated m_{split} results beyond the maximum core inlet resistances analyzed for each assumed ECCS rate to produce the m_{split} results shown in Figures 8-5, 9-4, 10-5, and 11-4. For the Westinghouse upflow category, the largest core inlet resistance of about 4.0×10^4 was reached in the case of 8 gpm/FA, whereas the applicable K_{max} is 5.0×10^5; for the Westinghouse downflow category the largest core inlet resistance of about 1.2×10^5 was reached in the case of 8 gpm/FA whereas the applicable K_{max} is 6.0×10^5; for the CE category the largest core inlet resistance of about 5.4×10^5 was reached in the case of 800 gpm, whereas the applicable K_{max} is 6.5×10^6; and for the B&W category, a core inlet resistance of about 1.8×10^4 was reached for each ECCS rate, whereas the applicable K_{max} is 1.0×10^8. Figures 8-5 and 9-4 each document two fitting expressions for the cases with the lowest and highest ECCS rates for the Westinghouse upflow and downflow categories, whereas Figures 10-5 and 11-4 each show a single fitting curve presumably intended to bound the calculated m_{split} results. Describe how the m_{split} results can be justifiably interpolated to obtain a valid m_{split} input at ECCS flow rates that do not match any of the values analyzed for the Westinghouse upflow and downflow categories (8, 12, 18, 30, and 40 gpm/FA) or for the B&W category (7.5, 12.5, 17.5, 22.5, 27.5, and 43.5 gpm/FA). Also, the significant degree of scatter in the plotted m_{split} points in Figure 10-5 makes the information on the plot hard to interpret.

The NRC staff needs confidence that reliable and valid K_{split} and m_{split} inputs were obtained. If such assurance is not reached generically, additional T-H calculations to produce applicable K_{split} and m_{split} inputs, including supporting analyses, will be requested on an as-needed plant-specific basis.

Response

With regard to K_{split}, extrapolating beyond the range of ECCS flow rates analyzed is not recommended and would require additional justification if a licensee chooses to do so. The revised K_{split} curves for the Westinghouse plant categories, presented in Figure RAI-4.20-1, and Figure-4.20-5, were revised so that the fit does not extend beyond the range of flow analyzed. If it is necessary to analyze a flow rate outside

the range of ECCS flows analyzed for K_{split}. It would be acceptable to select a value that falls within the range of flows analyzed. For example, if the analyzed flow rate was 45 gpm/FA, the K_{split} value calculated using the curve fit for a 40 gpm/FA flow rate would be acceptable. This approach is justified since the trend in K_{split} as a function of ECCS flow rate is well understood. As the flow rate increases, the value of K_{split} will decrease because the downcomer will increase more quickly, which increases the driving head, and reduces the time required to activate the AFP. In this case, selecting a K_{split} value at 40 gpm/FA would be conservative. Interpolating between explicit K_{split} points determined from the analysis is acceptable since enough analyses were performed such that an accurate trend in K_{split} was captured. In addition, the curve fits for K_{split} were selected such that any minor variations at different flow rates would still fall under the curve. With regard to m_{split}, the revised analyses presented in the response to RAI-4.20 were extended to K_{max} to alleviate the extrapolation concern. Interpolation between ECCS flow rates in the m_{split} results is not recommended, and would require additional justification if a licensee choses to do so. The revised m_{split} curves provided in the response to RAI-4.20 are intended to cover all ECCS flow rates analyzed.

RAI-4.22, Vol. 4

The small-break LOCA analysis approach applied for the B&W plant category and the plant analysis results for a 0.5 ft^2 small HLB LOCA presented in Section 11 may not meet the requirements of 10 CFR 50.46(a)(1)(i), which states, "ECCS cooling performance must be calculated in accordance with an acceptable evaluation model and must be calculated for a number of postulated loss-of-coolant accidents of different sizes, locations, and other properties sufficient to provide assurance that the most severe postulated loss-of-coolant accidents are calculated." Specifically, it is questionable whether the RCS T-H conditions, predicted at the time of core inlet blockage and thereafter for a 0.5 ft^2 small HLB LOCA, remain applicable to a DEG HLB LOCA, which represents the limiting scenario as stated in the TR. The three arguments provided in Section 6.4 of Vol. 4 in support of the selected 0.5 ft^2 break size do justify extrapolation of the calculated small-break LOCA results to a full-size DEG HLB LOCA transient considered as the limiting scenario.

Provide additional LOCA calculation results for the B&W plant design category, including results for predicted safety criteria, figures of merit, and supporting analysis results, which demonstrate quantitatively that the requirements of 10 CFR 50.46(a)(1)(i) are met. T-H LOCA calculations should be performed using applicable and appropriately assessed EMs.

Response

The response to these questions is provided in the B&W submittal

RAI-4.23, Vol. 4

To assist the NRC staff evaluation of liquid discharge through the break for the large HLB LOCA scenario, provide the following information for each of the four analyzed plant categories for the limiting break size.

a. Identify key transport mechanisms of liquid discharge through each side of the break that can occur during transient phases of relevance to the T-H analyses. Explain how liquid transport mechanisms caused by liquid spillover under elevated two-phase mixture levels in the reactor upper plenum due to carry-out of dispersed liquid by entrainment under depressed mixture level conditions are accounted for and modeled in the applied codes. Describe whether the liquid transport models are reflective of and dependent on the upper plenum two-phase mixture level and explain how the performance of these models, in terms of their accuracy and sensitivity, depends on the code capabilities to predict the two-phase mixture levels in the reactor upper plenum under conditions representative of the LTCC phase of a large HLB LOCA.

Response

On the steam generator (SG) side of the break, there are a limited number of liquid transport mechanisms of liquid discharge through the break after the initial blowdown phase. There are two main liquid transport mechanisms on the SG side of the break.

The first mechanism can only transport a limited amount of liquid. The first liquid transport mechanism is due to the fact that the SGs are modeled as heat sources during the event. If liquid enters the cold leg side of the broken loop SG due to the added resistance at the core inlet, the hot walls of the tubes will create steam, which can potentially carry liquid up to the top of the u-tubes and out to the break. This process is likely overestimated in the simulations as the SG model has a coarse noding in the u-tubes as it is not designed to be refilled during the transient. The code tends to homogenize the fluid in the nodes and the liquid could be spread over this large surface area and generate more steam than in reality. This liquid transport mechanism is time-limited since the steam production removes energy from the SG secondary side. The secondary side will eventually cool as this process continues and the mechanism will eventually cease to exist once the secondary side temperature approaches the primary side temperature.

The second liquid transport mechanism is when the resistance to the core and alternate flow path is high, and the ECCS flow exceeds what can enter the core and alternate flow path with the given available elevation head, the ECCS can eventually fill the SG u-tubes (after going through the first liquid transport mechanism phase) and the excess ECCS can spill over the top of the u-tubes and exit to the break.

The majority of the flow entering the loops will enter the broken loop and transport through the broken loop SG to the break, because the pressure drop through this broken loop is lower. Some liquid may also sporadically flow through the intact SGs, driven by the two transport mechanisms described above, mix with fluid in the upper plenum and then exit the break on the reactor vessel side

of the break. The response to RAI-4.30 shows that the liquid transported through the intact SGs is small compared to the liquid flow through the core inlet, barrel/baffle, upper head spray nozzles, and broken loop SG.

On the reactor vessel side of the break, the liquid transport mechanisms are more complex. In the short-term phase (prior to sump switchover) droplet entrainment can exist due to high steam velocities. As the decay heat reduces, the steam velocities reduce and the magnitude of droplet entrainment diminishes. Prior to the blockage, the two-phase mixture level in the upper plenum is high and liquid is transported to the hot leg break as a low void fraction mixture through natural or forced circulation, rather than by entrainment in the steam flow. As core inlet resistance is applied, or the ECCS flow rate is reduced, the upper plenum two-phase mixture level drops and the transport of liquid due to natural or forced circulation diminishes. If the upper plenum two-phase mixture level continues to fall, like during a debris-induced core uncovery, the circulation transport mechanism will be lost completely. During this period of suppressed upper plenum mixture level, some liquid will continue to be entrained to the break as steam sweeps across the top of the mixture levels but at a lower rate. As the downcomer level builds in order to overcome the higher core inlet resistance, the mixture level will begin to recover until it reaches near the bottom of the hot leg and natural or forced circulation becomes the dominant transport mechanism again.

As described above, the upper plenum mixture level is important for liquid transport to the break under LTCC conditions. Entrainment is less important because the steaming rates are low such that entrainment rates are diminished. An upper plenum mixture level exists during most of the GSI-191 hot leg break transient. Under these conditions, the accuracy of the mixture level prediction is less important because there is significant liquid carryover to the break due to natural or forced circulation. Various sensitivity studies completed in this RAI response have demonstrated that the break flow from the reactor vessel side is not significantly sensitive to variations in the upper plenum mixture level. The effect of these studies on break flow is discussed in the response to RAI-4.23 Item i. Section 18 of WCAP-12945-P-A (Reference RAI-4.23-1) concludes that [

]^{a,c}

b. Describe code assessments, including analyses and results, which demonstrate the capability of the codes used in the T-H analyses to adequately predict transport mechanisms that result in liquid discharge through the break during LTCC. Consideration should be given to contribution from mechanisms accounting for both entrainment and deposition (de-entrainment) of liquid that can take place in participating RV regions including the upper plenum and connected broken hot leg piping. Include information identifying test facilities, test runs, and test conditions used in the code assessments. Provide comparisons of code predictions against relevant test data, as available.

Response

As described in the response to RAI-4.23 Item a., entrainment rates diminish during LTCC because of the reduced steaming rates. Two-phase mixture level is the primary factor that results in liquid discharge from the break during the GSI-191 scenario.

A number of code assessments have been completed to validate the core region void distributions and mixture level swell. With respect to LTCC, the most applicable are the G1 and G2 assessments presented in the response to RAI-4.8. Assessment results demonstrate that WCOBRA/TRAC tends to slightly over-predict the mixture level swell. Similar models are used to predict the two-phase mixture level in the upper plenum and the same over-prediction of mixture level would be expected, since the upper plenum region does not apply the interfacial drag multiplier as the core region. Over-prediction of the two-phase mixture level would tend to increase the liquid carryover through the break.

WCOBRA/TRAC assessments of upper plenum de-entrainment and carryover are presented in Section 15-2-3 of WCAP-12945-P-A (Reference RAI-4.23-1). Simulations were performed for several tests that provided information on flows in the upper plenum. Applicable simulations for short-term LOCA assessment included the UPTF simulations of Tests 10B and 29B, and the CCTF, SCTF, and LOFT tests. Two simulations were performed for tests in which the main purpose was to determine the amount of upper plenum de-entrainment and carryover. The UPTF Tests 10B and 29B simulated the conditions in the upper plenum during reflood, and provided measurements of liquid level above the tie plate. The UPTF upper plenum was full-scale in both height and cross section.

Applicable experimental data at LTCC conditions is not available, so extension of the previous assessment must be justified. Of particular interest is UPTF Test 29B, since the simulated steaming rates were some of the lowest for the UPTF testing. As described in Section 14-4-15 of WCAP-12945-P-A, the objective of UPTF Test 29B was to extend the range of flow conditions examined in Test 10B. Test 29B was composed of six subphases, and the lowest steaming rate simulated in the test was [ ]^{a,c}

For each phase of UPTF Test 29B, a mass balance was performed based on test measurements by MPR Associates (1990), and the mass distribution estimated. As described in Section 15-2-3 of WCAP-12945-P-A, [

]^{a,c}

In addition to UPTF 29B, UPTF Test 10B and SCTF Runs 604, 620, 621 and 623 were simulated and the predicted upper plenum inventories were compared to test data. WCOBRA/TRAC was found to generate results that were in very good agreement with the measurements, indicating that the models for entrainment and de-entrainment adequately represent these processes in the upper plenum.

c. Explain if any special liquid entrainment models, modeling options, and related flags were available in the applied codes and if any such features were activated in the T-H analyses to account for liquid entrainment. Examples of such modeling features can be related to special upper plenum entrainment models, mixture level models, and related special interfacial drag models. State whether any break flow multipliers were applied in the analyses. Provide the multiplier values, and explain if the selected inputs were examined for impact on the predicted break liquid discharge.

Response

In the event of a postulated large break loss-of-coolant accident (LBLOCA) in a PWR, the rate of depressurization of the primary loop is dominated by the rate of fluid discharge at the break. During the blowdown phase of the LOCA, the discharge will be choked (critical flow). Following the blowdown phase of the LOCA, break flow transitions from a critical flow to a post-critical flow (i.e., unchoked flow) on both sides of the double-ended guillotine (DEG) break and remains unchoked for the rest of the transient. As such, the upper plenum liquid inventory, and mixture level determines the break flow.

No special entrainment models, modeling options, or related flags were activated in the Westinghouse plant thermal hydraulic analysis within the upper plenum region of the models. The interfacial drag multiplier, which impacts mixture level, was set to 0.8 in the core region of the models. As provided in the response to RAI-4.8, the sensitivity of break flow to the core region interfacial drag multiplier was shown to be minimal.

As described in Section 4-8 of WCAP-16009-P-A (Reference RAI-4.23-2), there are two critical flow models available in WCOBRA/TRAC. The model used for the GSI-191 thermal-hydraulic analysis is taken from TRAC-PF1/MOD1. The TRAC-PF1/MOD1 two-phase, two-component, choked flow model was developed from first principals using the characteristic analysis approach. The TRAC-PF1/MOD1 subcooled choked flow model is a modified form of the Burnell model. Section 4-8-2 of WCAP-16009-P-A provides the model basis, the WCOBRA/TRAC as coded model, and scaling considerations. A break flow multiplier of unity is used in the GSI-191 analysis.

As described in Section 4-8-3 of WCAP-16009-P-A WCOBRA/TRAC applies a post critical flow model that is applied during the transition from choked to unchoked flow. This model helps to reduce large oscillations in break flow rates observed in large cold leg break LOCA simulations during the transition period. After the system has completely depressurized during refill, the transition period ends, and control of the break flow is returned to the normal momentum equations using phase slip and the full pipe area.

d. Identify key models used and the underlying correlations related to the predicted break liquid discharges. Provide the ranges of applicability of these correlations, and compare them against the conditions predicted in the analyses documented in Sections 8 through 11. Provide the information in a table format for each of the cases analyzed to determine t_{block} and K_{max} in Section 8 (Cases 1B and 2B), Section 9 (Cases 1A and 2B), Section 10 (Cases 1 and 2), and Section 11.

Response

Reference to the key models and correlations related to the predicted break liquid discharges are provided in the response to RAI-4.23 Item c. The reactor coolant system to containment pressure differential decreases rapidly for a DEG break such that the break flow becomes unchoked during the refill phase of the LOCA, which is well before sump recirculation. The period of interest for the cases documented in Section 8 and 9 of WCAP-17788, Volume 4 is after sump recirculation, when the flow is unchoked. For unchoked flow, WCOBRA/TRAC calculates break flow using the momentum equations with phase slip and the full pipe area. The containment pressure during the sump recirculation phase is a constant 14.7 psia. There are no limitations on the range of applicability for the momentum equation calculation of break flow at this pressure.

e. If not provided elsewhere, include plots showing the following sets of parameters for the cases documented in Sections 8 through 11 as a function of transient time:

i. Mass flow rates of liquid, steam, and total fluid (liquid and steam) discharges through each opening of the DEG break. Include integrals of the identified break mass flow rates.
ii. Two-phase mixture level on the core side of the RV
iii. Steam flow quality calculated as a ratio of the steam mass flow rate to the total (liquid and steam) mass flow rate for the RV-side opening of the DEG break
iv. Predicted pressure difference between the upper plenum cell connected to the broken hot leg pipe and the containment backpressure.

Response

Table RAI-4.23-1 provides a listing of the figures provided in the subsequent pages of this letter.

Table RAI-4.23-1	**Listing of RAI-4.23 Item e. Figures**
Section 8	
Figure No.	**Description**
RAI-4.23-1	Case 0A – Mass Flow Rates through the Vessel Side of the DEG Break
RAI-4.23-2	Case 1B – Mass Flow Rates through the Vessel Side of the DEG Break
RAI-4.23-3	Case 1 – Mass Flow Rates through the Vessel Side of the DEG Break
RAI-4.23-4	Case 3 – Mass Flow Rates through the Vessel Side of the DEG Break
RAI-4.23-5	Case 5 – Mass Flow Rates through the Vessel Side of the DEG Break
RAI-4.23-6	Case 0A – Integrated Mass Flow through the Vessel Side of the DEG Break
RAI-4.23-7	Case1B – Integrated Mass Flow through the Vessel Side of the DEG Break
RAI-4.23-8	Case 1 – Integrated Mass Flow through the Vessel Side of the DEG Break
RAI-4.23-9	Case 3 – Integrated Mass Flow through the Vessel Side of the DEG Break
RAI-4.23-10	Case 5 – Integrated Mass Flow through the Vessel Side of the DEG Break
RAI-4.23-11	Case 0A – Break Exit Quality – Vessel Side of DEG Break
RAI-4.23-12	Case 1B – Break Exit Quality – Vessel Side of DEG Break

Table RAI-4.23-1	Listing of RAI-4.23 Item e Figures (cont'd)
Figure No.	**Description**
RAI-4.23-13	Case 1 – Break Exit Quality – Vessel Side of DEG Break
RAI-4.23-14	Case 3 – Break Exit Quality – Vessel Side of DEG Break
RAI-4.23-15	Case 5 – Break Exit Quality – Vessel Side of DEG Break
RAI-4.23-16	Case 0A – Mass Flow Rates through the SG Side of the DEG Break
RAI-4.23-17	Case 1B – Mass Flow Rates through the SG Side of the DEG Break
RAI-4.23-18	Case 1 – Mass Flow Rates through the SG Side of the DEG Break
RAI-4.23-19	Case 3 – Mass Flow Rates through the SG Side of the DEG Break
RAI-4.23-20	Case 5 – Mass Flow Rates through the SG Side of the DEG Break
RAI-4.23-21	Case 0A – Integrated Mass Flow through the SG Side of the DEG Break
RAI-4.23-22	Case 1B – Integrated Mass Flow through the SG Side of the DEG Break
RAI-4.23-23	Case 1 – Integrated Mass Flow through the SG Side of the DEG Break
RAI-4.23-24	Case 3 – Integrated Mass Flow through the SG Side of the DEG Break
RAI-4.23-25	Case 5 – Integrated Mass Flow through the SG Side of the DEG Break
RAI-4.23-26	Case 0A – Hot Assembly CLL
RAI-4.23-27	Case 0A – UP Outer Global CLL
RAI-4.23-28	Case 0A – UP Inner Global CLL
RAI-4.23-29	Case 0A – UP Open Hole / Support Column / etc CLL
RAI-4.23-30	Case 0A – UP / Upper Head Guide Tube CLL
RAI-4.23-31	Case 1B – Hot Assembly CLL
RAI-4.23-32	Case 1B – UP Outer Global CLL
RAI-4.23-33	Case 1B – UP Inner Global CLL
RAI-4.23-34	Case 1B – UP Open Hole / Support Column / etc CLL
RAI-4.23-35	Case 1B – UP / Upper Head Guide Tube CLL
RAI-4.23-36	Case 1 – Hot Assembly CLL
RAI-4.23-37	Case 1 – UP Outer Global CLL
RAI-4.23-38	Case 1 – UP Inner Global CLL
RAI-4.23-39	Case 1 – UP Open Hole / Support Column / etc CLL
RAI-4.23-40	Case 1 – UP / Upper Head Guide Tube CLL
RAI-4.23-41	Case 3 – Hot Assembly CLL
RAI-4.23-42	Case 3 – UP Outer Global CLL
RAI-4.23-43	Case 3 – UP Inner Global CLL
RAI-4.23-44	Case 3 – UP Open Hole / Support Column / etc CLL
RAI-4.23-45	Case 3 – UP / Upper Head Guide Tube CLL
RAI-4.23-46	Case 5 – Hot Assembly CLL
RAI-4.23-47	Case 5 – UP Outer Global CLL
RAI-4.23-48	Case 5 – UP Inner Global CLL
RAI-4.23-49	Case 5 – UP Open Hole / Support Column / etc CLL
RAI-4.23-50	Case 5 – UP / Upper Head Guide Tube CLL

Table RAI-4.23-1	Listing of RAI-4.23 Item e Figures (cont'd)
Figure No.	**Description**
RAI-4.23-51	Case 0A – Delta P between Upper Head Channel Connection to Broken HL and Containment Backpressure
RAI-4.23-52	Case 1B – Delta P between Upper Head Channel Connection to Broken HL and Containment Backpressure
RAI-4.23-53	Case 1 – Delta P between Upper Head Channel Connection to Broken HL and Containment Backpressure
RAI-4.23-54	Case 3 – Delta P between Upper Head Channel Connection to Broken HL and Containment Backpressure
RAI-4.23-55	Case 5 – Delta P between Upper Head Channel Connection to Broken HL and Containment Backpressure
RAI-4.23-56	Case 2B – Mass Flow Rates through the Vessel Side of the DEG Break
RAI-4.23-57	Case 2B – Integrated Mass Flow through the Vessel Side of the DEG Break
RAI-4.23-58	Case 2B – Break Exit Quality – Vessel Side of DEG Break
RAI-4.23-59	Case 2B – Mass Flow Rates through the SG Side of the DEG Break
RAI-4.23-60	Case 2B – Integrated Mass Flow through the SG Side of the DEG Break
RAI-4.23-61	Case 2B – Hot Assembly CLL
RAI-4.23-62	Case 2B – UP Outer Global CLL
RAI-4.23-63	Case 2B – UP Inner Global CLL
RAI-4.23-64	Case 2B – UP Open Hole / Support Column / etc CLL
RAI-4.23-65	Case 2B – UP / Upper Head Guide Tube CLL
RAI-4.23-66	Case 2B – Delta P between Upper Head Channel Connection to Broken HL and Containment Backpressure
Section 9	
RAI-4.23-67	Case 0A – Mass Flow Rates through the Vessel Side of the DEG Break
RAI-4.23-68	Case 0A – Integrated Mass Flow through the Vessel Side of the DEG Break
RAI-4.23-69	Case 0A – Break Exit Quality – Vessel Side of DEG Break
RAI-4.23-70	Case 0A – Mass Flow Rates through the SG Side of the DEG Break
RAI-4.23-71	Case 0A – Integrated Mass Flow through the SG Side of the DEG Break
RAI-4.23-72	Case 1A – Mass Flow Rates through the Vessel Side of the DEG Break
RAI-4.23-73	Case 1A – Integrated Mass Flow through the Vessel Side of the DEG Break
RAI-4.23-74	Case 1A – Break Exit Quality – Vessel Side of DEG Break
RAI-4.23-75	Case 1A – Mass Flow Rates through the SG Side of the DEG Break
RAI-4.23-76	Case 1A – Integrated Mass Flow through the SG Side of the DEG Break
RAI-4.23-77	Case 2B – Mass Flow Rates through the Vessel Side of the DEG Break
RAI-4.23-78	Case 2B – Integrated Mass Flow through the Vessel Side of the DEG Break
RAI-4.23-79	Case 2B – Break Exit Quality – Vessel Side of DEG Break
RAI-4.23-80	Case 2B – Mass Flow Rates through the SG Side of the DEG Break
RAI-4.23-81	Case 2B – Integrated Mass Flow through the SG Side of the DEG Break
RAI-4.23-82	Case 0A – Hot Assembly CLL
RAI-4.23-83	Case 0A – UP Global CLL
RAI-4.23-84	Case 0A – UP Low Power CLL

Table RAI-4.23-1	Listing of RAI-4.23 Item e Figures (cont'd)
Figure No.	**Description**
RAI-4.23-85	Case 0A – UP / Upper Head Guide Tube CLL
RAI-4.23-86	Case 0A – UP Open Hole / Support Column / etc CLL
RAI-4.23-87	Case 1A – Hot Assembly CLL
RAI-4.23-88	Case 1A – UP Global CLL
RAI-4.23-89	Case 1A – UP Low Power CLL
RAI-4.23-90	Case 1A – UP / Upper Head Guide Tube CLL
RAI-4.23-91	Case 1A – UP Open Hole / Support Column / etc CLL
RAI-4.23-92	Case 2B – Hot Assembly CLL
RAI-4.23-93	Case 2B – UP Global CLL
RAI-4.23-94	Case 2B – UP Low Power CLL
RAI-4.23-95	Case 2B – UP / Upper Head Guide Tube CLL
RAI-4.23-96	Case 2B – UP Open Hole / Support Column / etc CLL
RAI-4.23-97	Case 0A – Delta P between Upper Head Channel Connection to Broken HL and Containment Backpressure
RAI-4.23-98	Case 1B – Delta P between Upper Head Channel Connection to Broken HL and Containment Backpressure
RAI-4.23-99	Case 2B – Delta P between Upper Head Channel Connection to Broken HL and Containment Backpressure
RAI-4.23-100	Case 1 – Mass Flow Rates through the Vessel Side of the DEG Break
RAI-4.23-101	Case 3 – Mass Flow Rates through the Vessel Side of the DEG Break
RAI-4.23-102	Case 5 – Mass Flow Rates through the Vessel Side of the DEG Break
RAI-4.23-103	Case 1 – Integrated Mass Flow through the Vessel Side of the DEG Break
RAI-4.23-104	Case 3 – Integrated Mass Flow through the Vessel Side of the DEG Break
RAI-4.23-105	Case 5 – Integrated Mass Flow through the Vessel Side of the DEG Break
RAI-4.23-106	Case 1 – Break Exit Quality – Vessel Side of DEG Break
RAI-4.23-107	Case 3 – Break Exit Quality – Vessel Side of DEG Break
RAI-4.23-108	Case 5 – Break Exit Quality – Vessel Side of DEG Break
RAI-4.23-109	Case 1 – Mass Flow Rates through the SG Side of the DEG Break
RAI-4.23-110	Case 3 – Mass Flow Rates through the SG Side of the DEG Break
RAI-4.23-111	Case 5 – Mass Flow Rates through the SG Side of the DEG Break
RAI-4.23-112	Case 1 – Integrated Mass Flow through the SG Side of the DEG Break
RAI-4.23-113	Case 3 – Integrated Mass Flow through the SG Side of the DEG Break
RAI-4.23-114	Case 5 – Integrated Mass Flow through the SG Side of the DEG Break
RAI-4.23-115	Case 1 – Hot Assembly CLL
RAI-4.23-116	Case 1 – UP Global CLL
RAI-4.23-117	Case 1 – UP Low Power CLL
RAI-4.23-118	Case 1 – UP / Upper Head Guide Tube CLL
RAI-4.23-119	Case 1 – UP Open Hole / Support Column / etc CLL
RAI-4.23-120	Case 3 – Hot Assembly CLL
RAI-4.23-121	Case 3 – UP Global CLL

Table RAI-4.23-1	Listing of RAI-4.23 Item e Figures (cont'd)
Figure No.	**Description**
RAI-4.23-122	Case 3 – UP Low Power CLL
RAI-4.23-123	Case 3 – UP / Upper Head Guide Tube CLL
RAI-4.23-124	Case 3 – UP Open Hole / Support Column / etc CLL
RAI-4.23-125	Case 5 – Hot Assembly CLL
RAI-4.23-126	Case 5 – UP Global CLL
RAI-4.23-127	Case 5 – UP Low Power CLL
RAI-4.23-128	Case 5 – UP / Upper Head Guide Tube CLL
RAI-4.23-129	Case 5 – UP Open Hole / Support Column / etc CLL
RAI-4.23-130	Case 1 – Delta P between Upper Head Channel Connection to Broken HL and Containment Backpressure
RAI-4.23-131	Case 3 – Delta P between Upper Head Channel Connection to Broken HL and Containment Backpressure
RAI-4.23-132	Case 5 – Delta P between Upper Head Channel Connection to Broken HL and Containment Backpressure

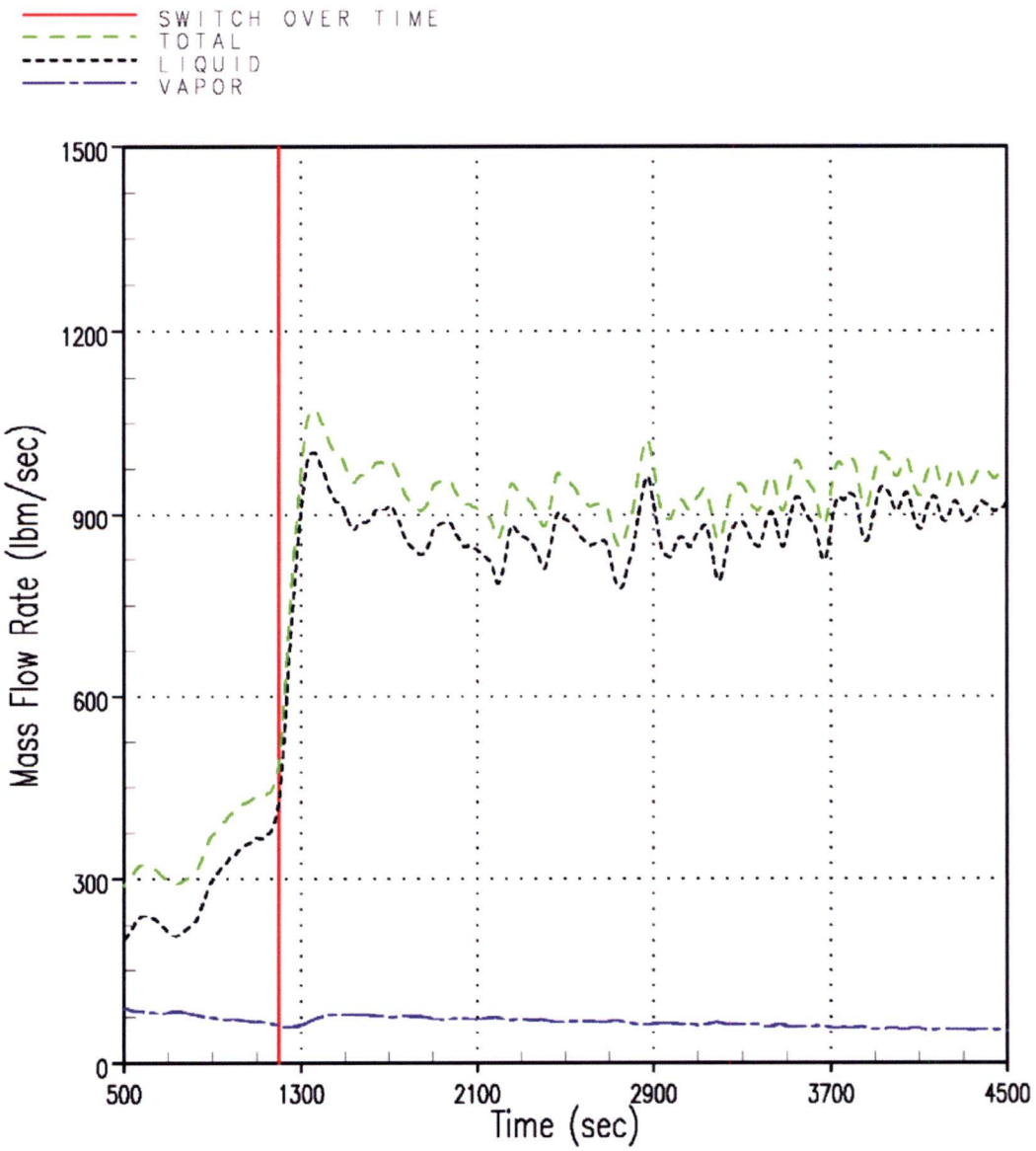

Figure RAI-4.23-1 Case 0A – Mass Flow Rates through the Vessel Side of the DEG Break

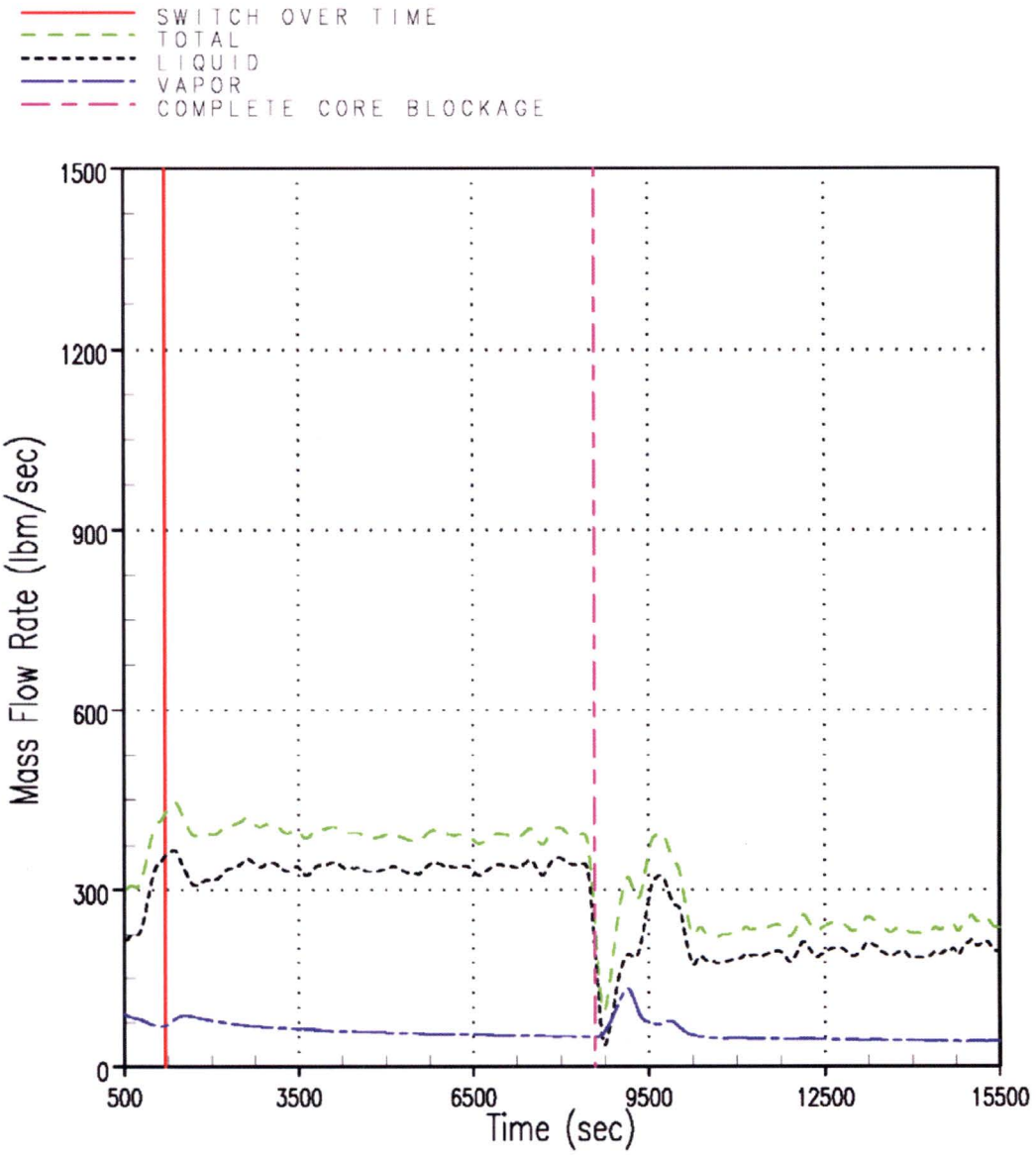

Figure RAI-4.23-2 Case 1B – Mass Flow Rates through the Vessel Side of the DEG Break

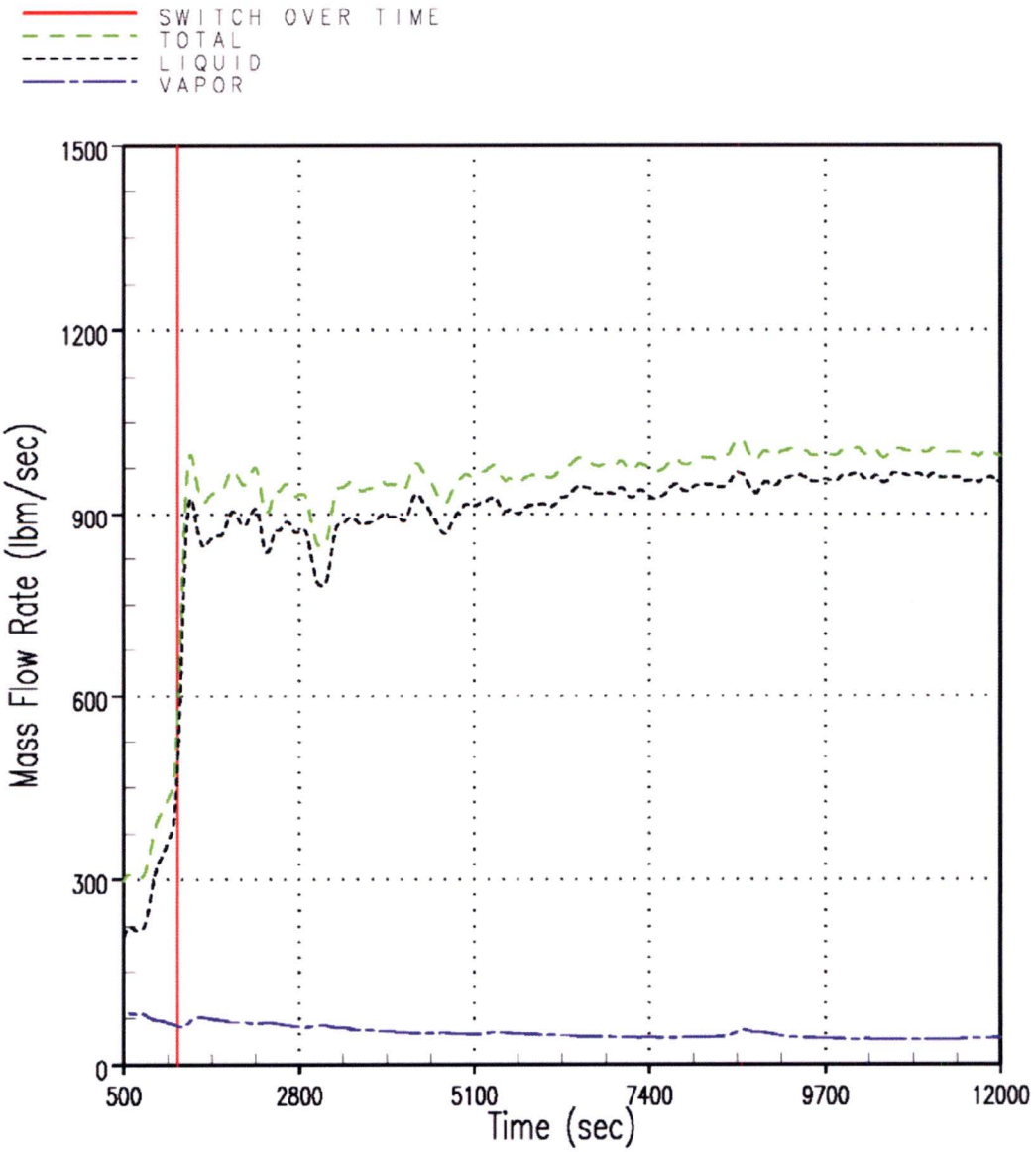

Figure RAI-4.23-3 Case 1 – Mass Flow Rates through the Vessel Side of the DEG Break

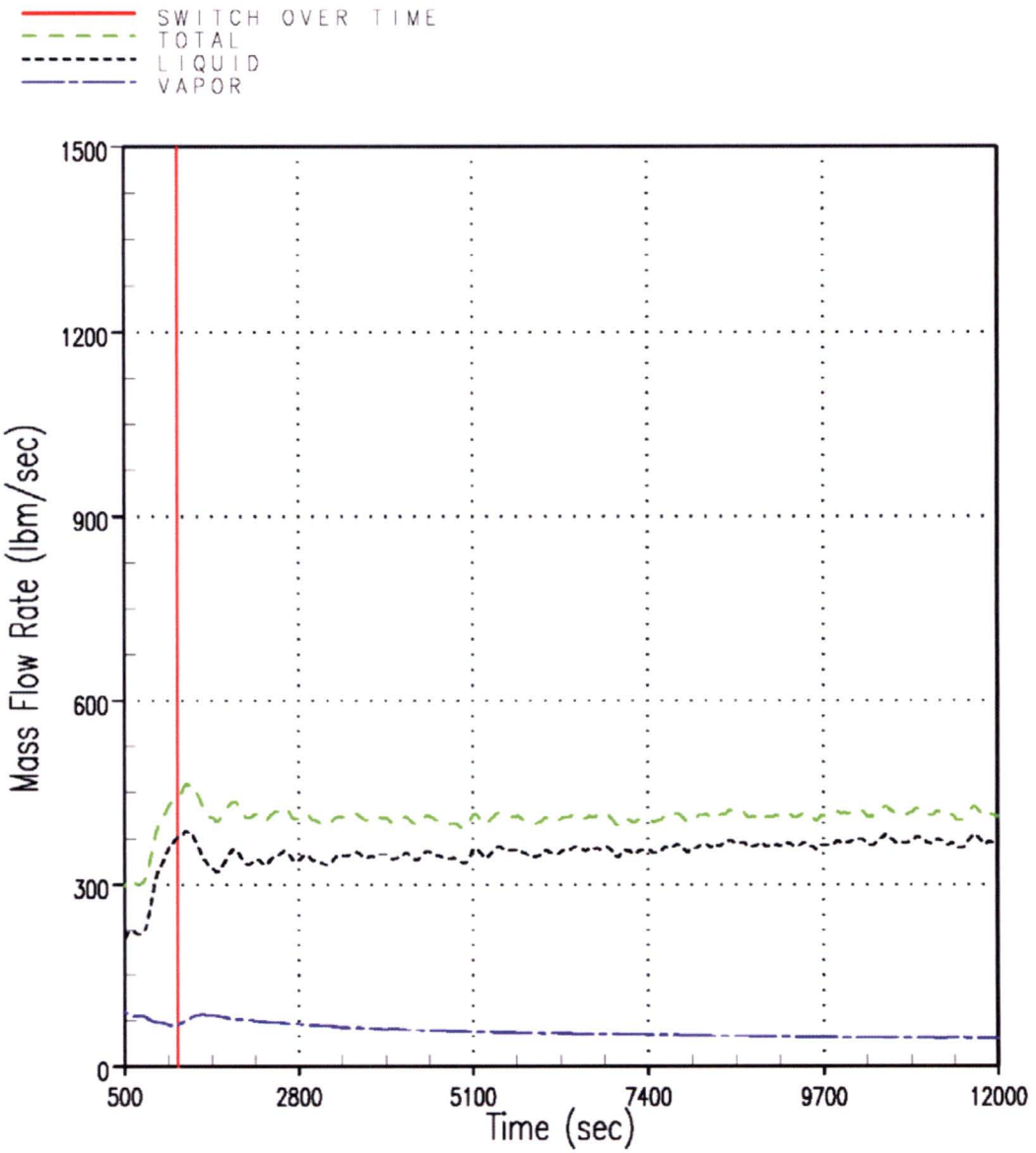

Figure RAI-4.23-4 Case 3 – Mass Flow Rates through the Vessel Side of the DEG Break

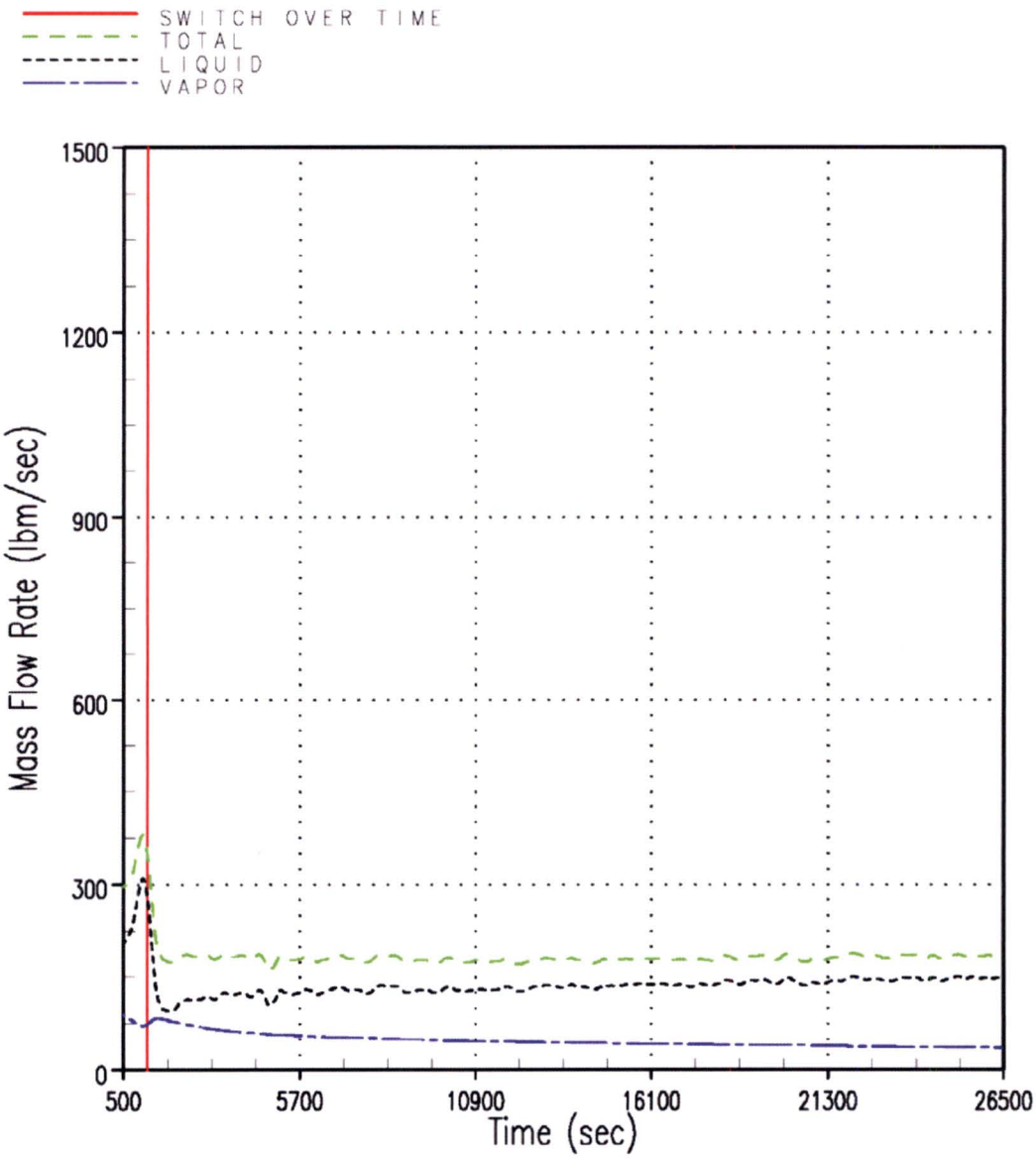

Figure RAI-4.23-5 Case 5 – Mass Flow Rates through the Vessel Side of the DEG Break

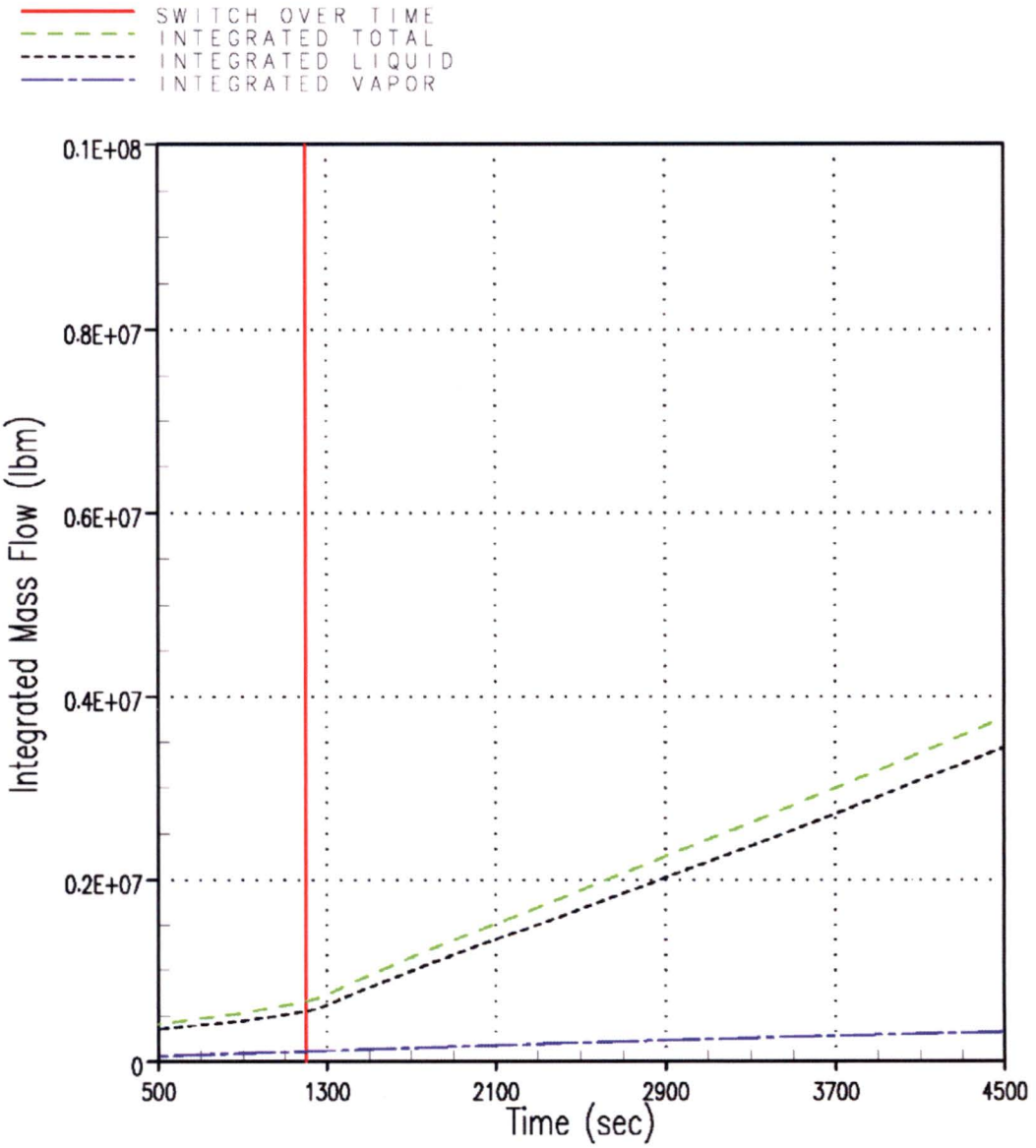

Figure RAI-4.23-6 Case 0A – Integrated Mass Flow through the Vessel Side of the DEG Break

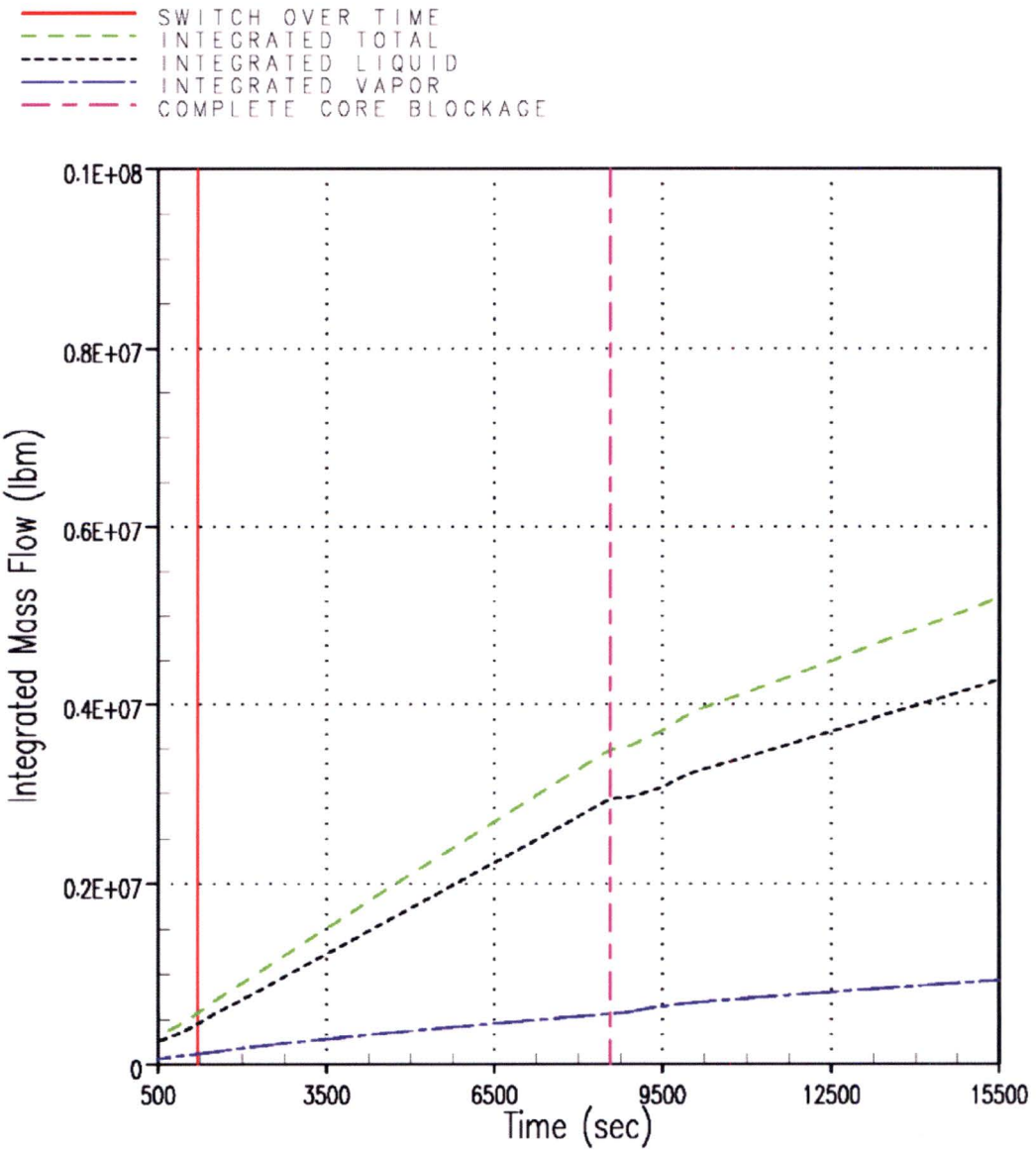

Figure RAI-4.23-7 Case1B – Integrated Mass Flow through the Vessel Side of the DEG Break

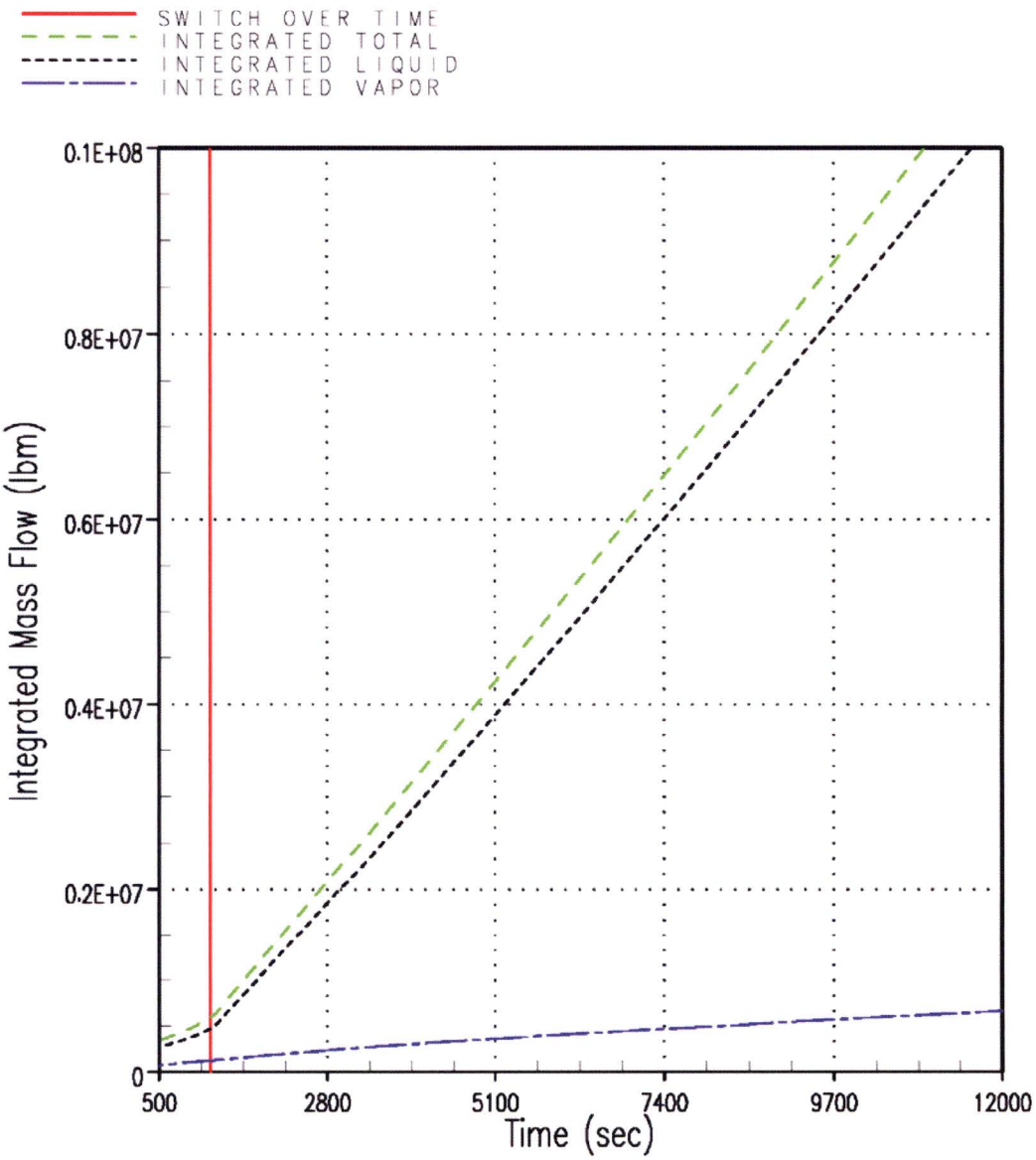

Figure RAI-4.23-8 Case 1 – Integrated Mass Flow through the Vessel Side of the DEG Break

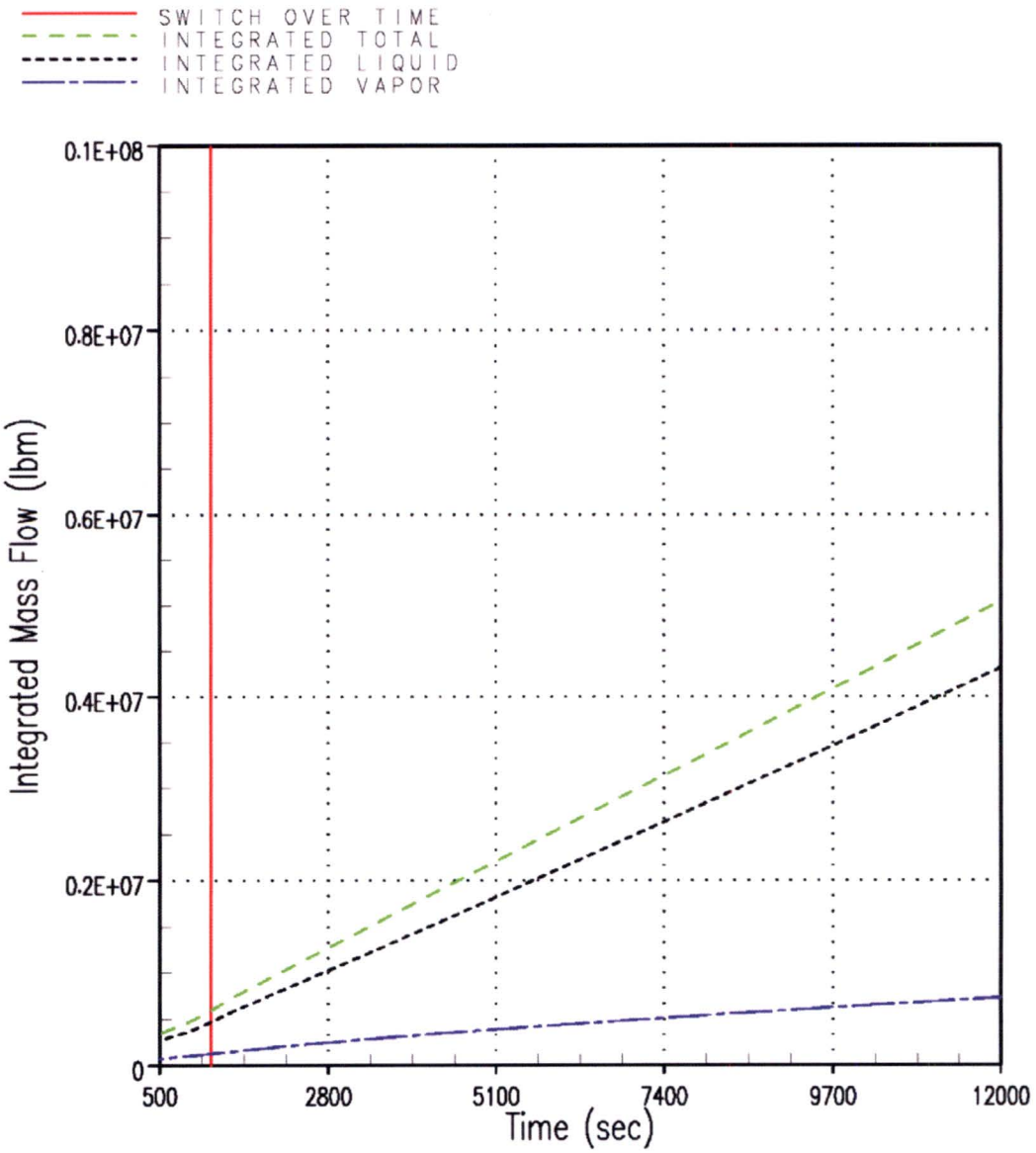

Figure RAI-4.23-9 Case 3 – Integrated Mass Flow through the Vessel Side of the DEG Break

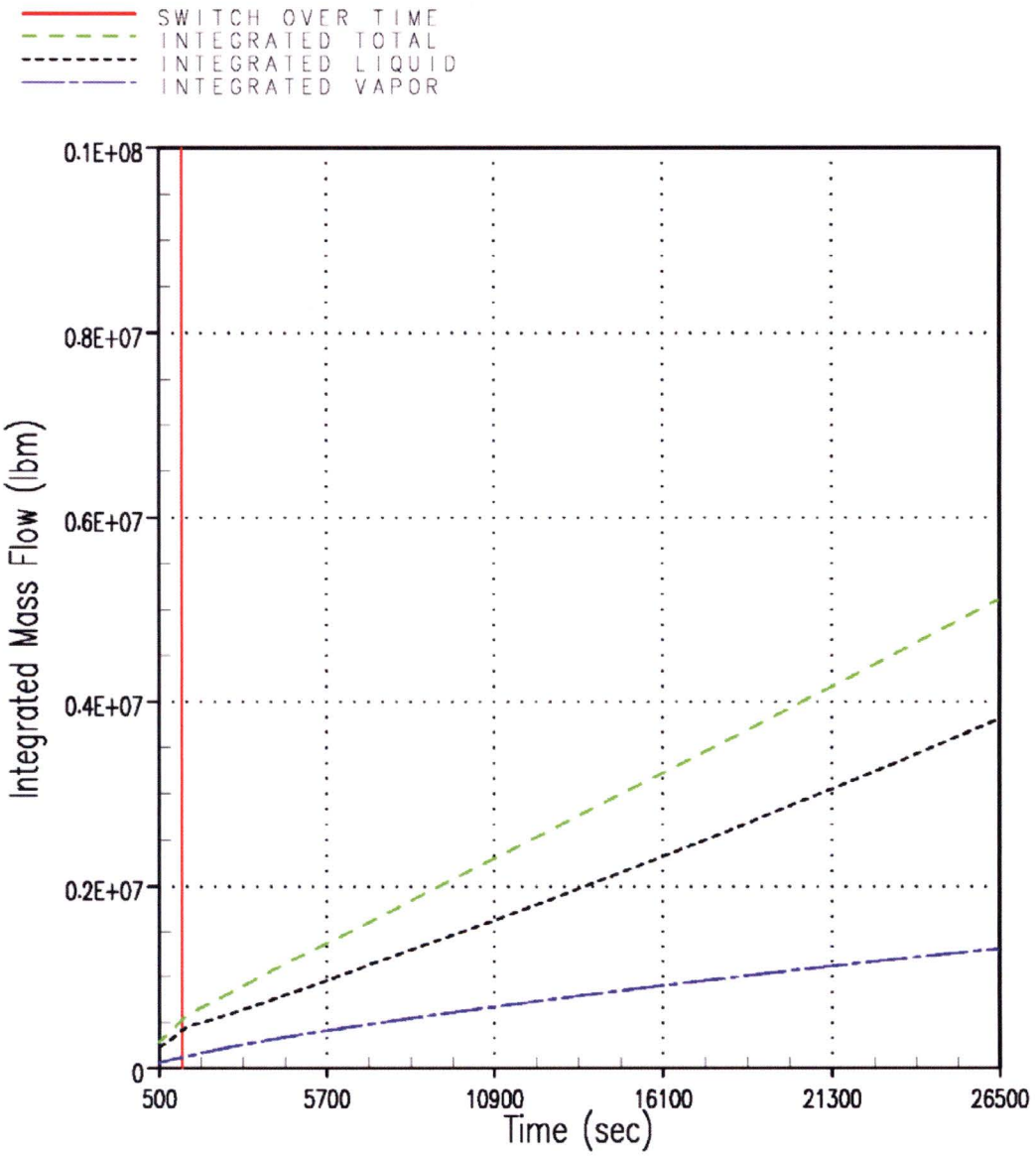

Figure RAI-4.23-10 Case 5 – Integrated Mass Flow through the Vessel Side of the DEG Break

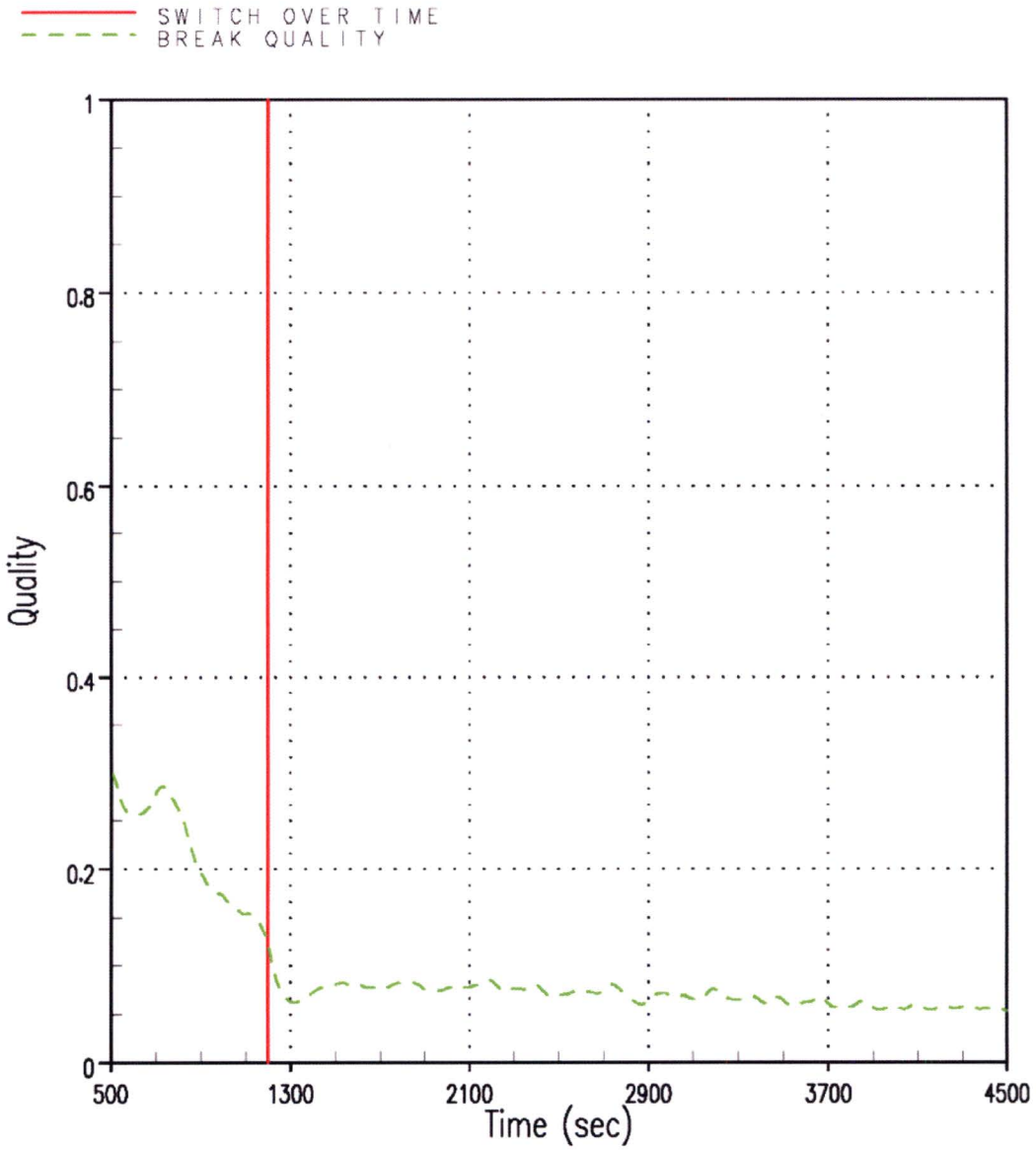

Figure RAI-4.23-11 Case 0A – Break Exit Quality – Vessel Side of DEG Break

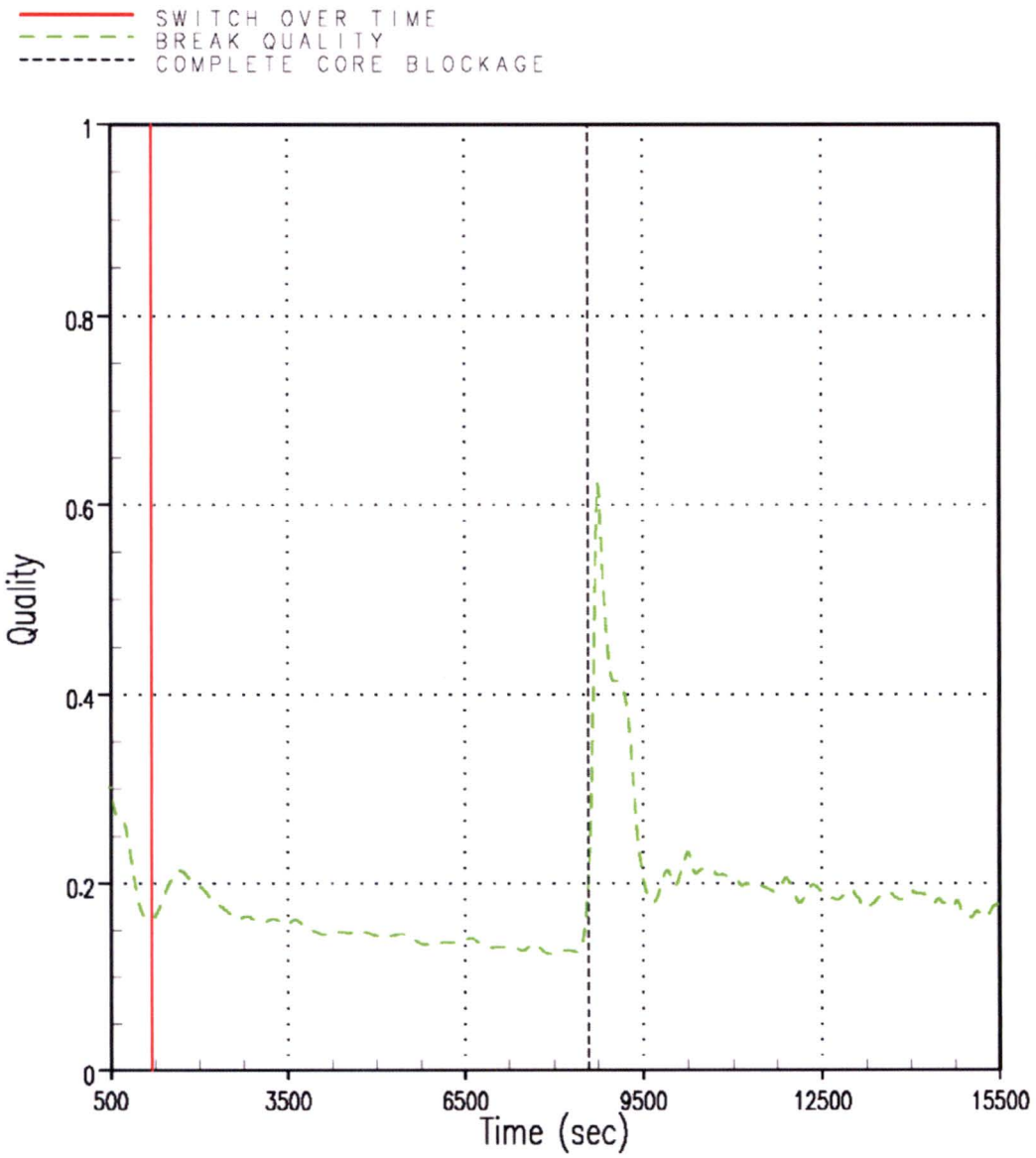

Figure RAI-4.23-12 Case 1B – Break Exit Quality – Vessel Side of DEG Break

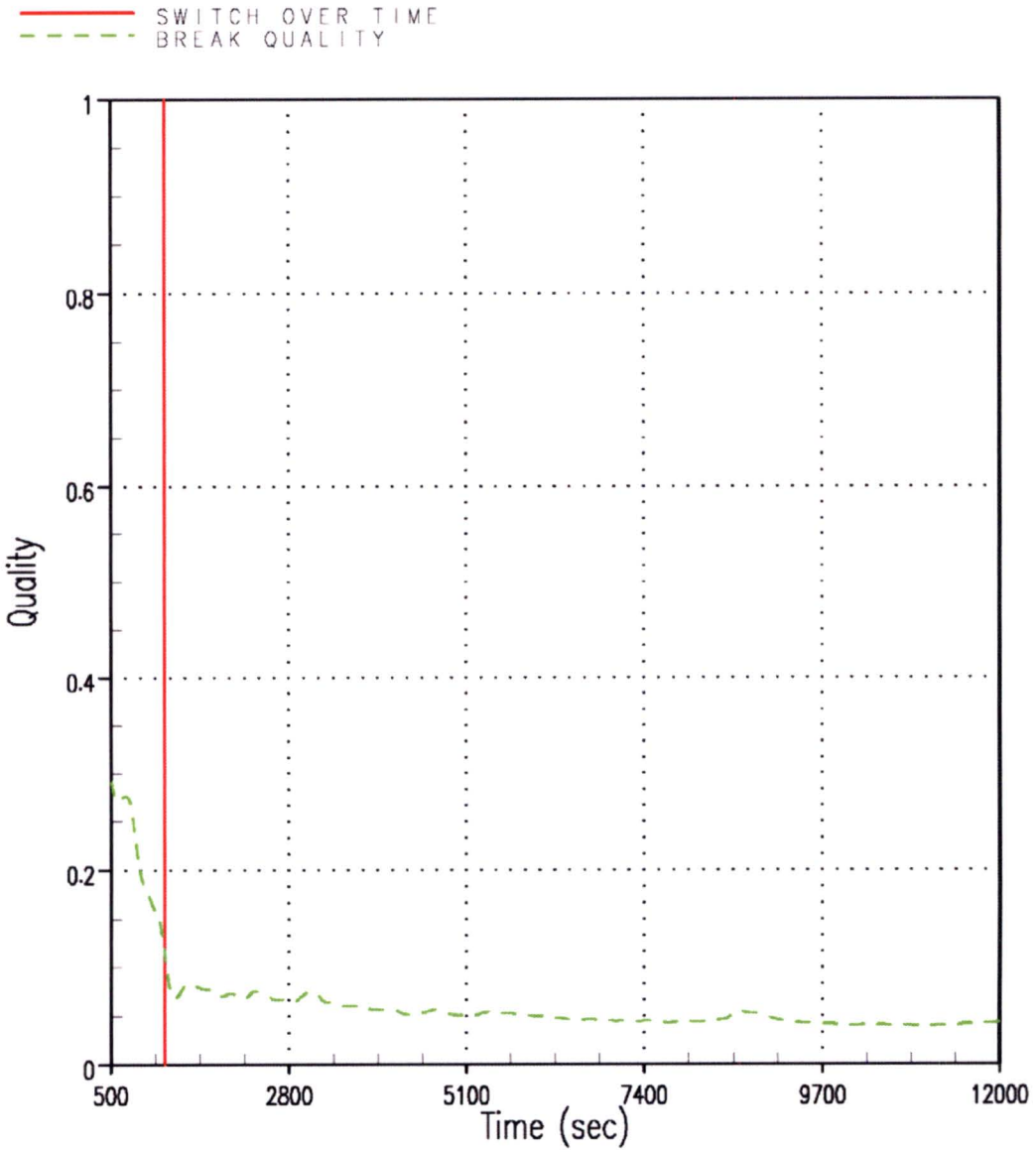

Figure RAI-4.23-13 Case 1 – Break Exit Quality – Vessel Side of DEG Break

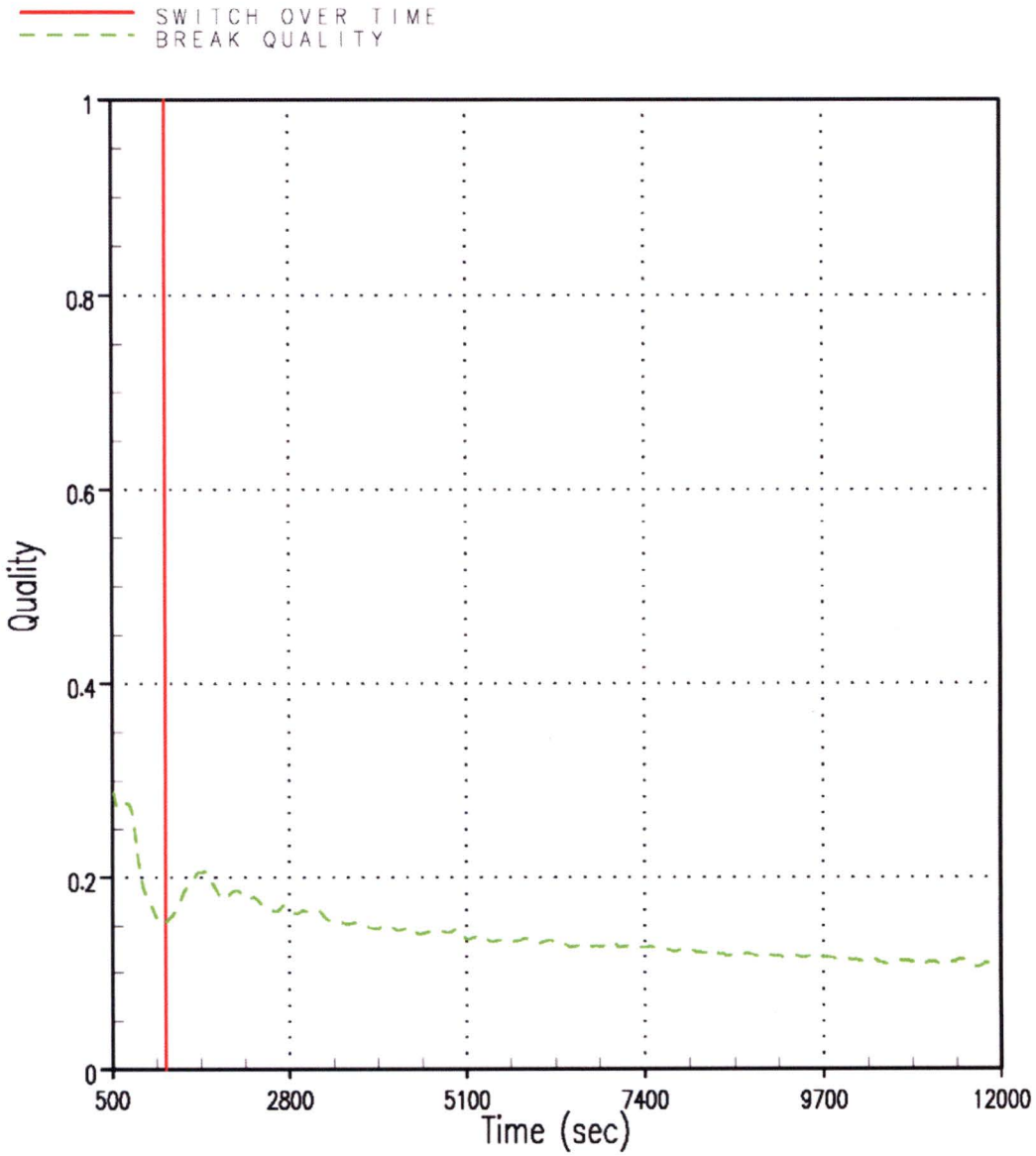

Figure RAI-4.23-14 Case 3 – Break Exit Quality – Vessel Side of DEG Break

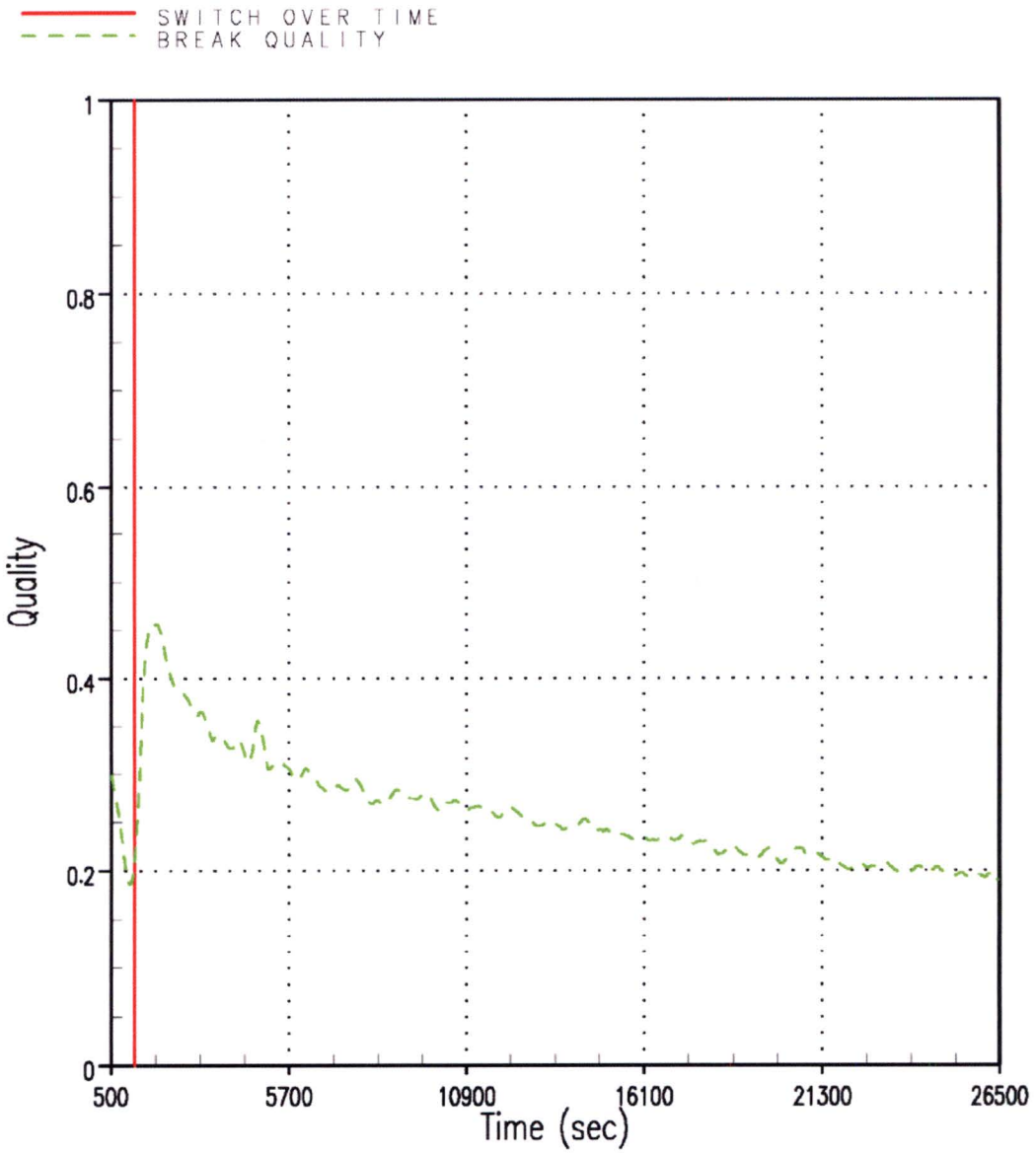

Figure RAI-4.23-15 Case 5 – Break Exit Quality – Vessel Side of DEG Break

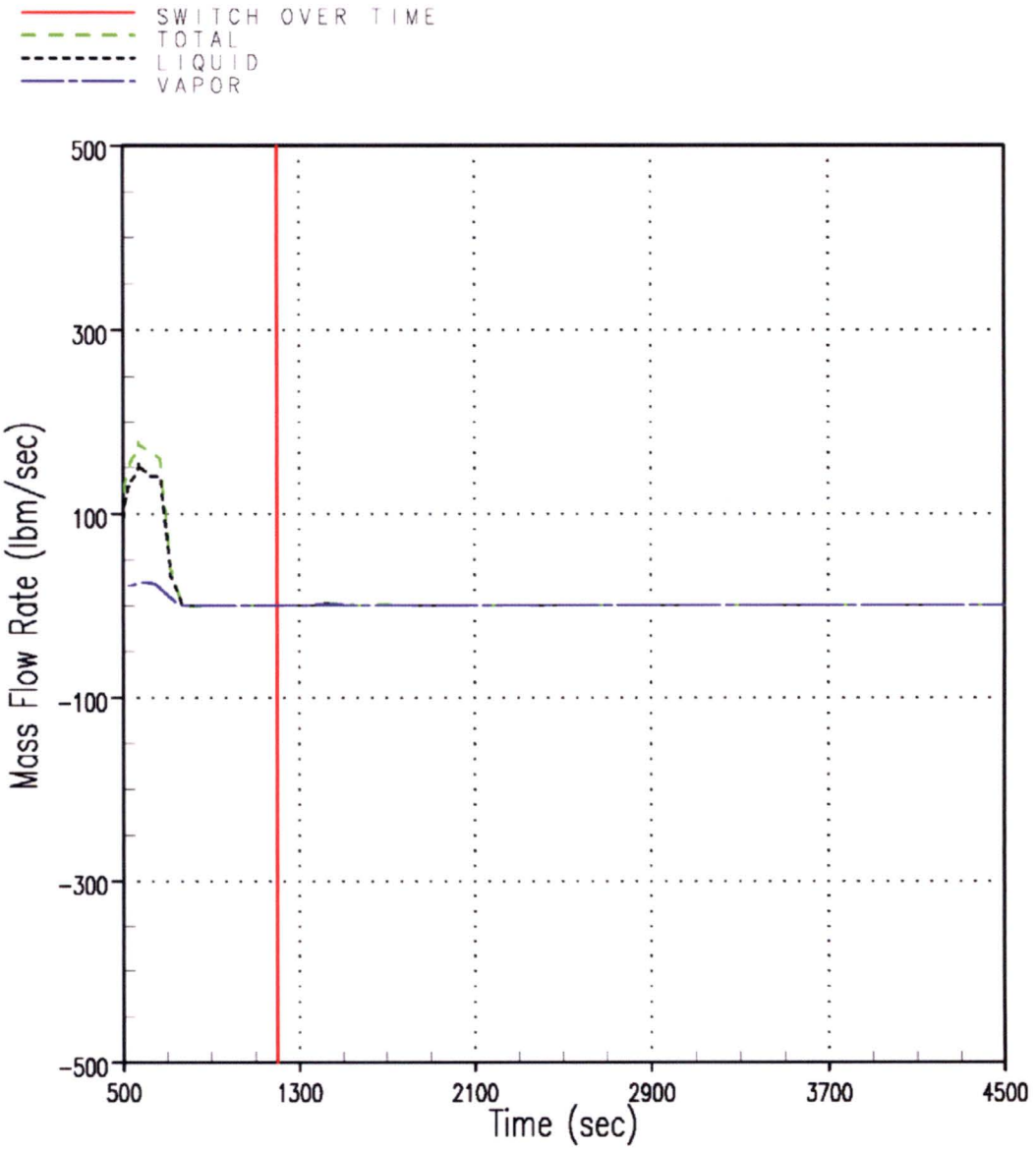

Figure RAI-4.23-16 Case 0A – Mass Flow Rates through the SG Side of the DEG Break

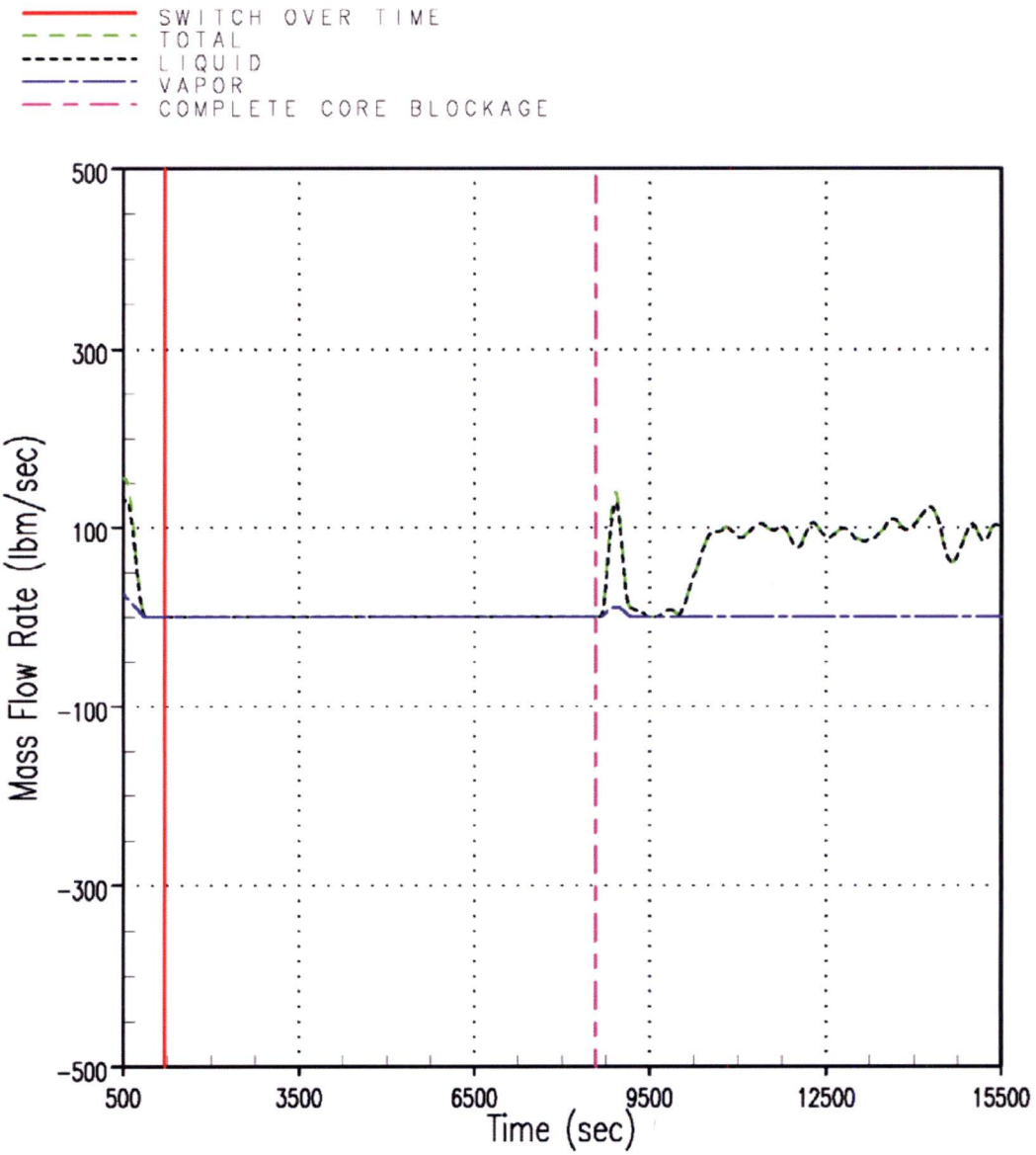

Figure RAI-4.23-17 Case 1B – Mass Flow Rates through the SG Side of the DEG Break

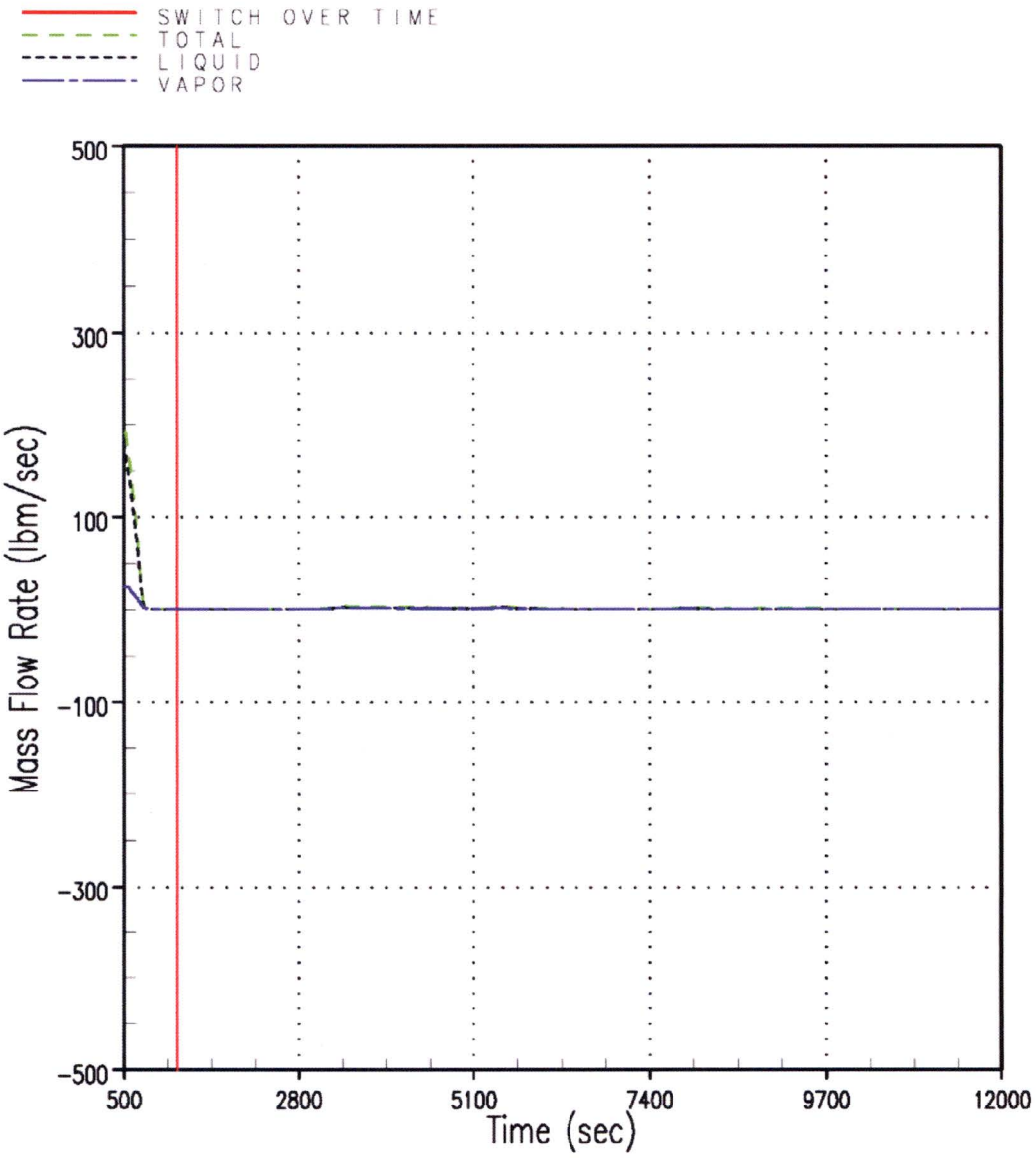

Figure RAI-4.23-18 Case 1 – Mass Flow Rates through the SG Side of the DEG Break

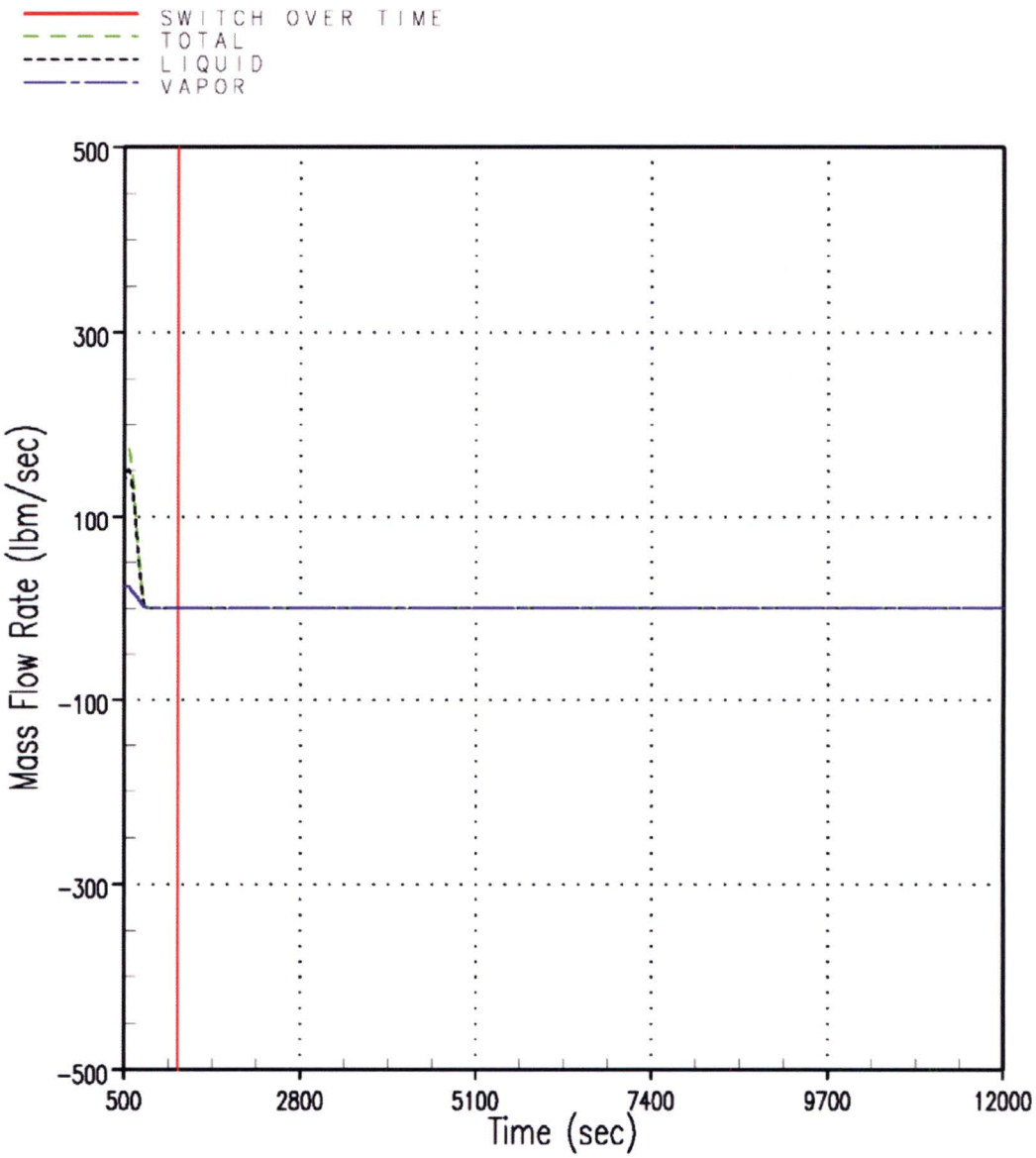

Figure RAI-4.23-19 Case 3 – Mass Flow Rates through the SG Side of the DEG Break

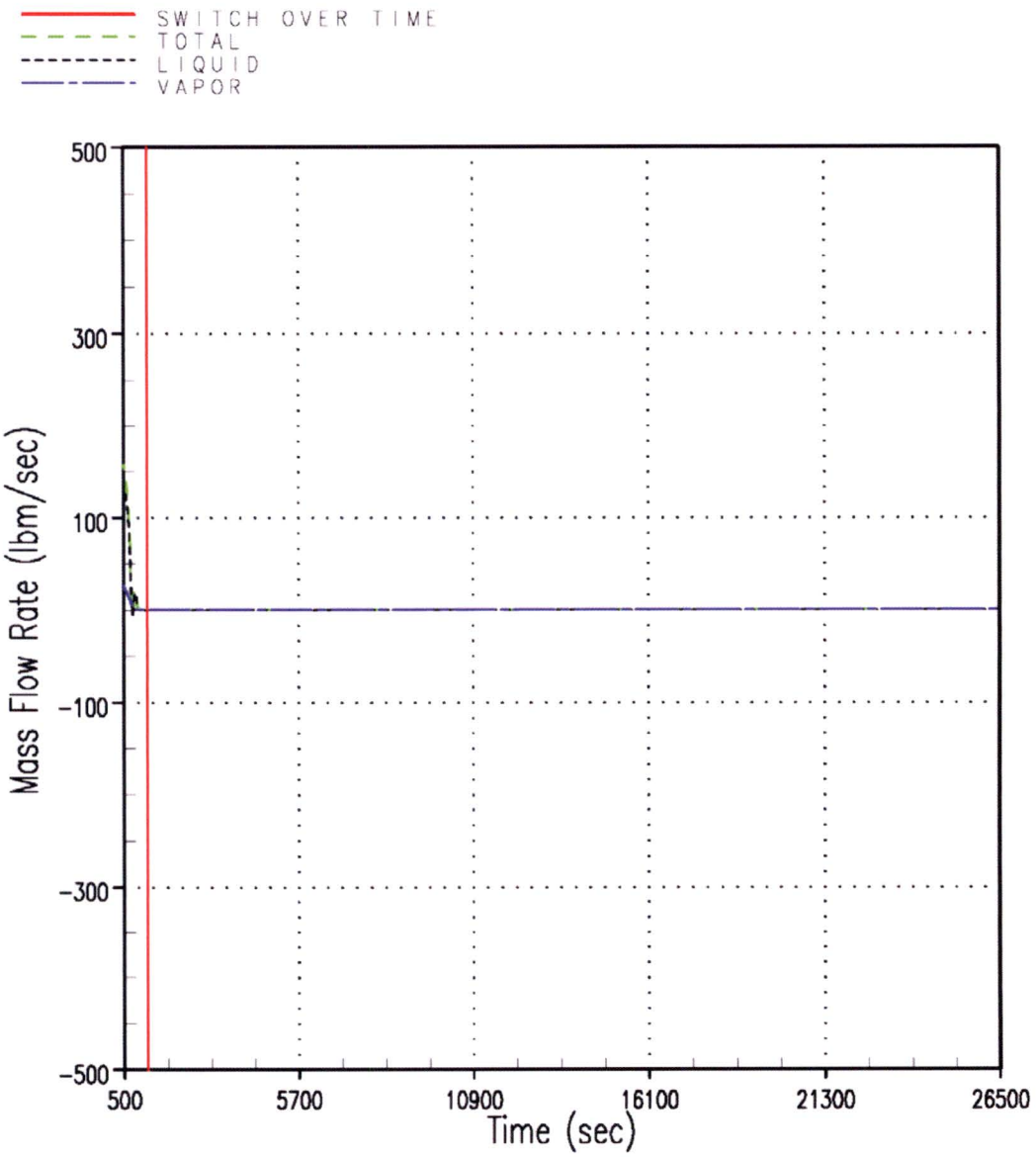

Figure RAI-4.23-20 Case 5 – Mass Flow Rates through the SG Side of the DEG Break

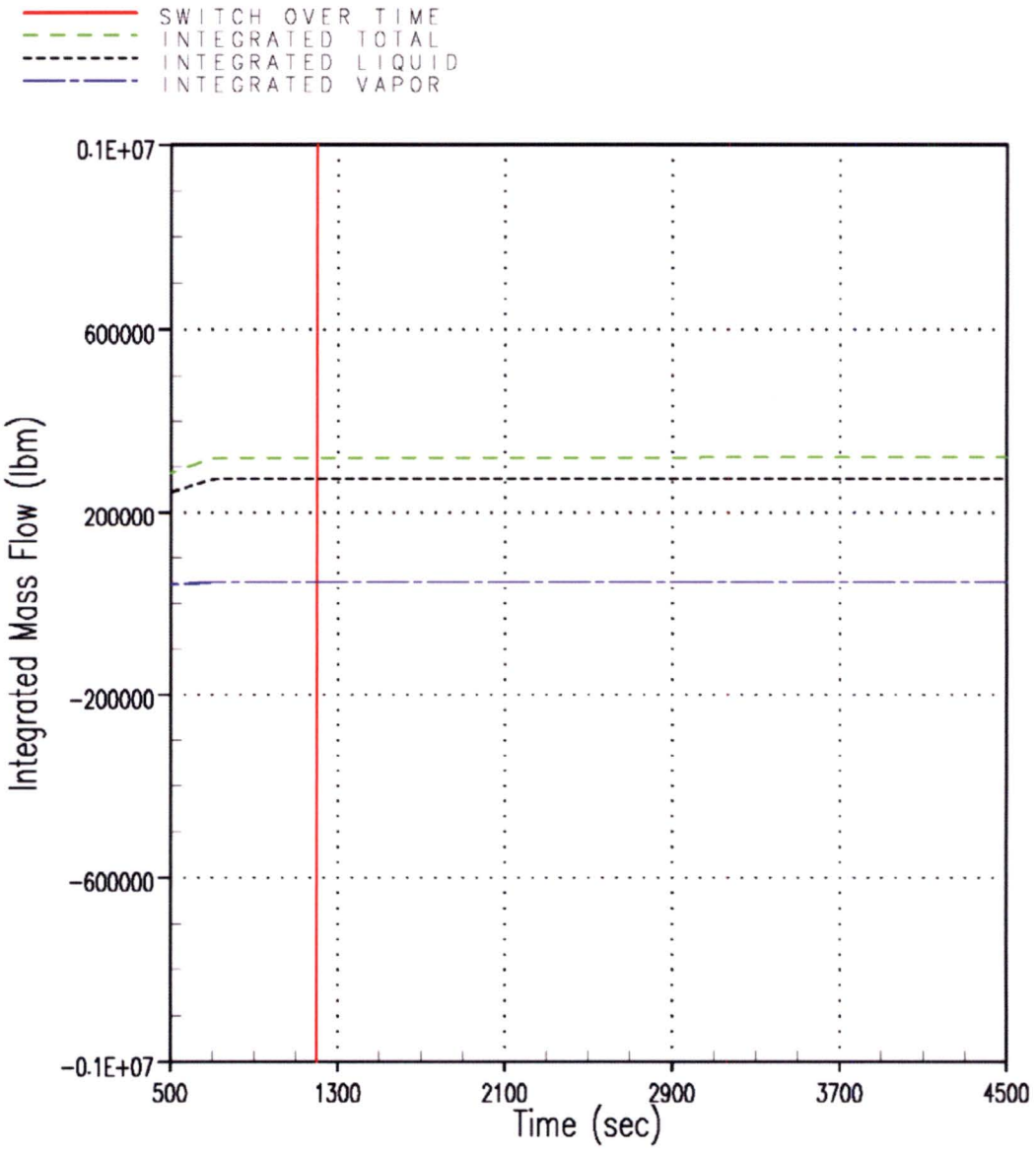

Figure RAI-4.23-21 Case 0A – Integrated Mass Flow through the SG Side of the DEG Break

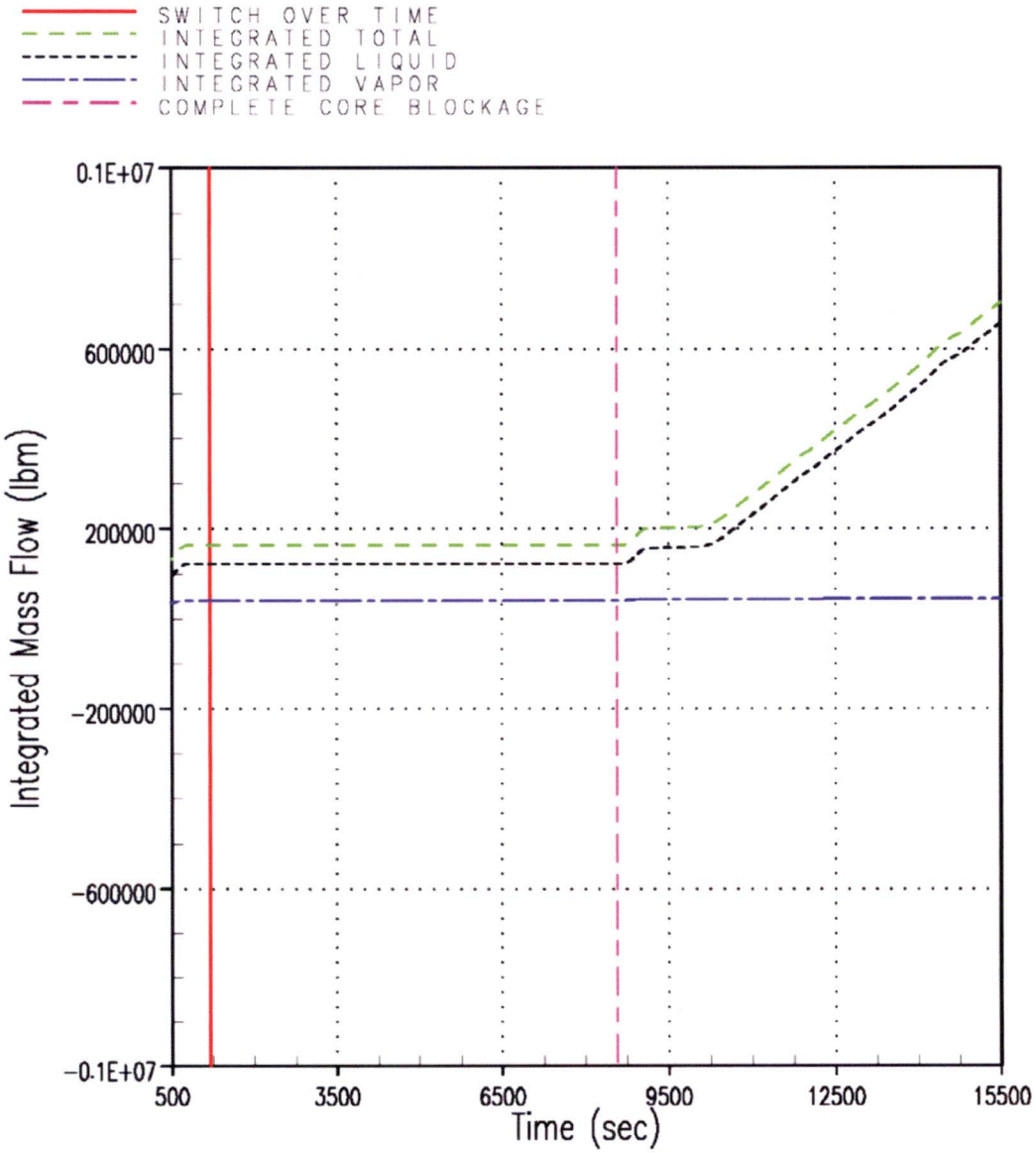

Figure RAI-4.23-22 Case 1B – Integrated Mass Flow through the SG Side of the DEG Break

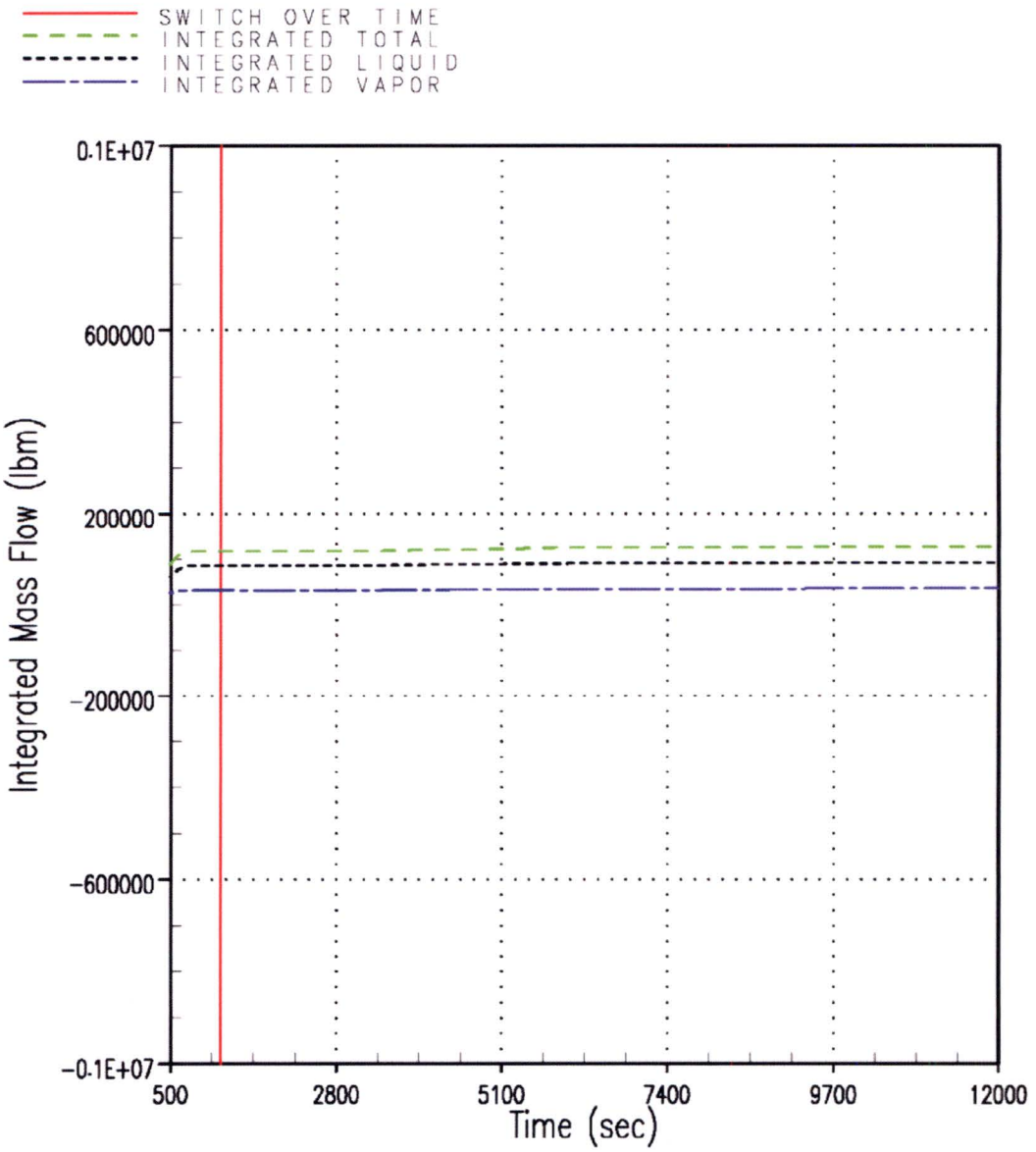

Figure RAI-4.23-23 Case 1 – Integrated Mass Flow through the SG Side of the DEG Break

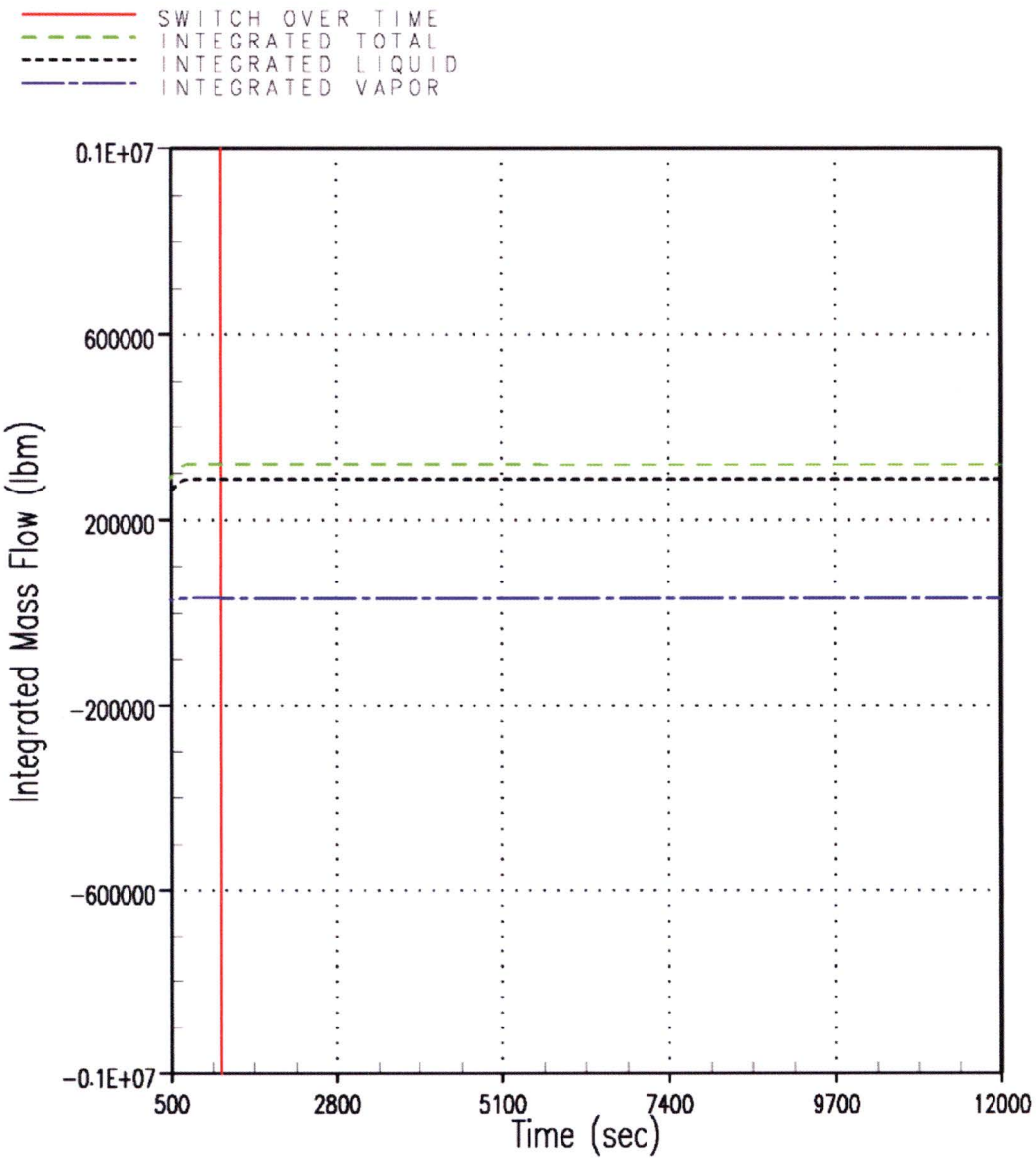

Figure RAI-4.23-24 Case 3 – Integrated Mass Flow through the SG Side of the DEG Break

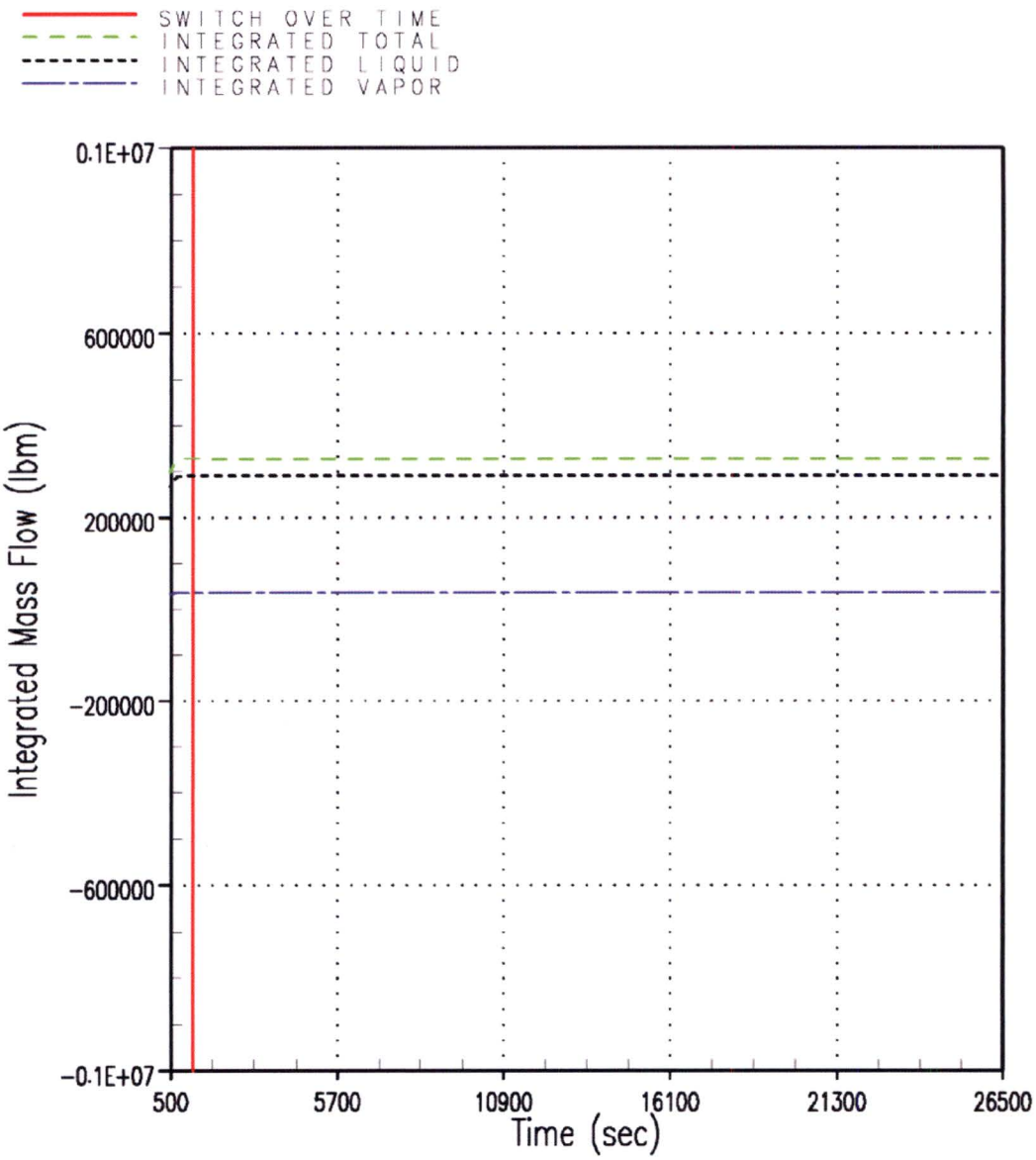

Figure RAI-4.23-25 Case 5 – Integrated Mass Flow through the SG Side of the DEG Break

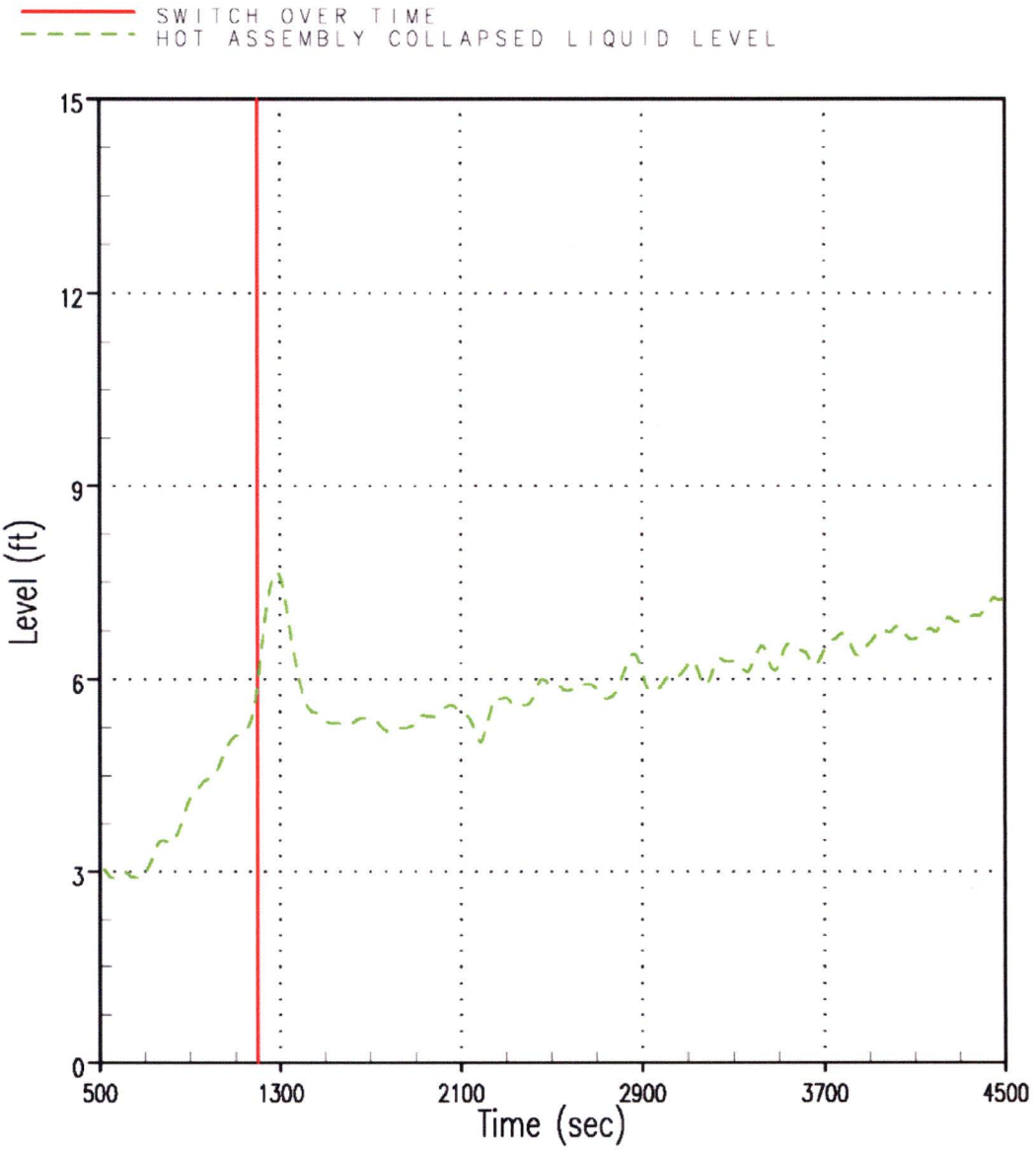

Figure RAI-4.23-26 Case 0A – Hot Assembly CLL

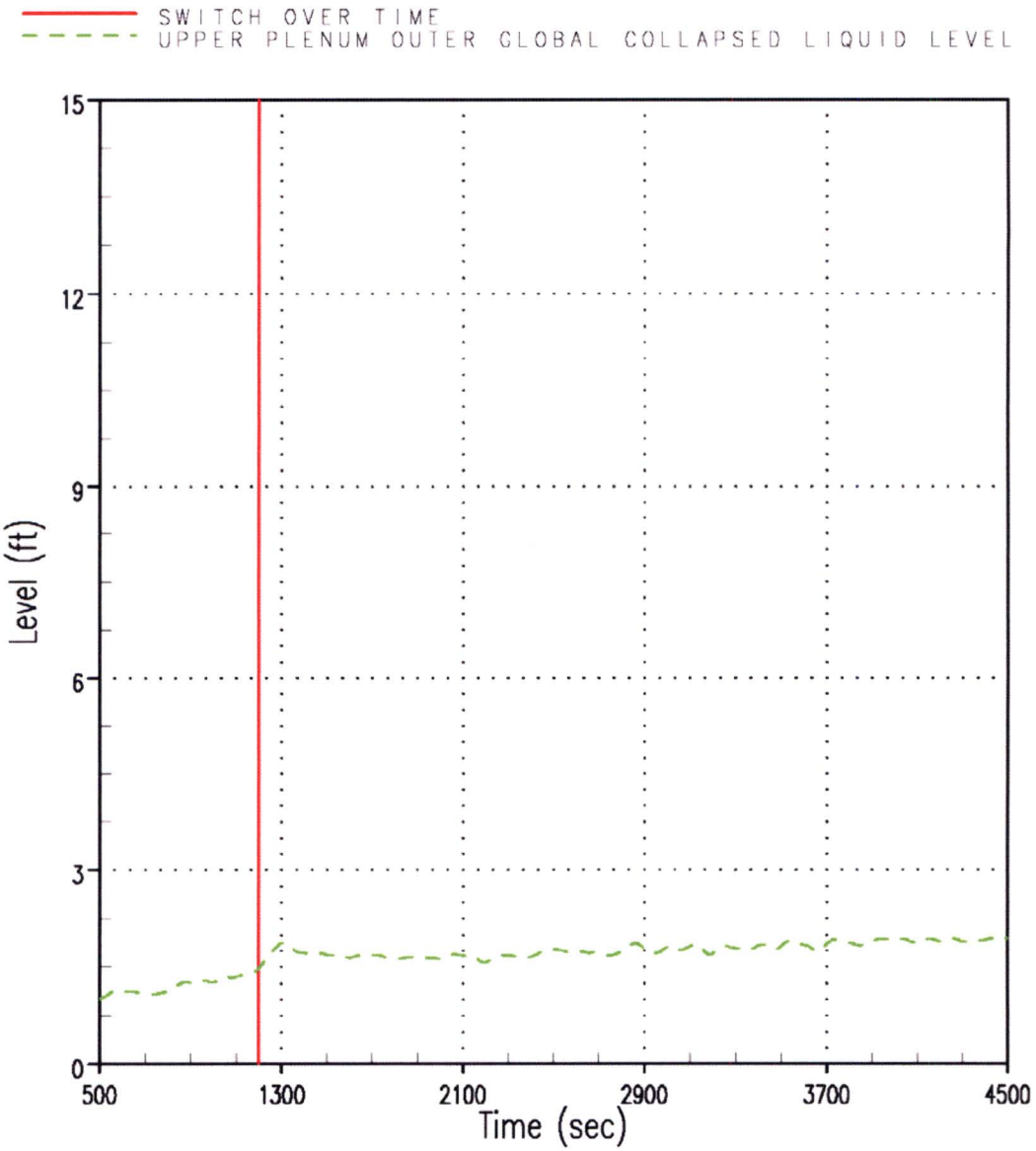

Figure RAI-4.23-27 Case 0A – UP Outer Global CLL

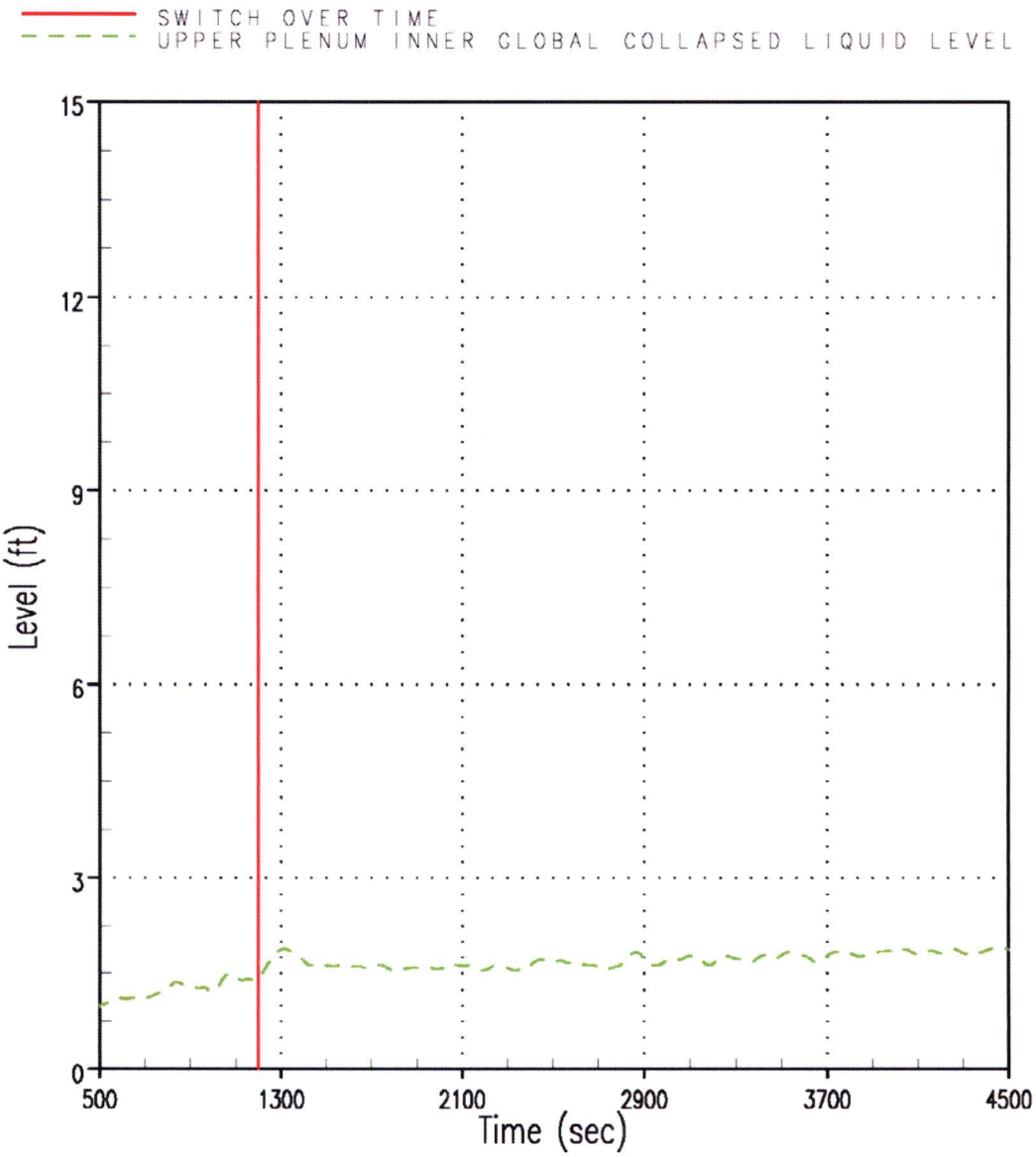

Figure RAI-4.23-28 Case 0A – UP Inner Global CLL

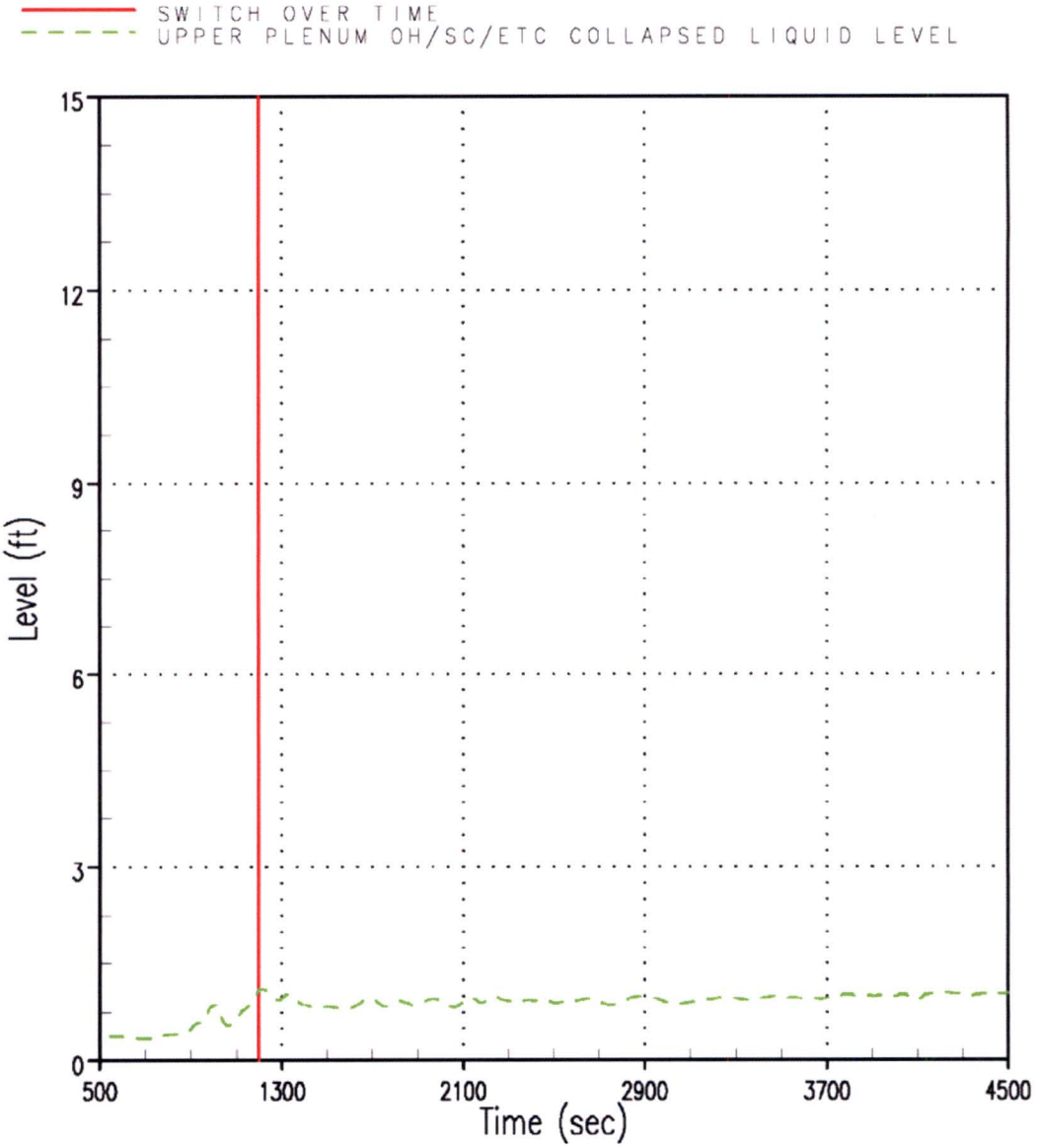

Figure RAI-4.23-29 Case 0A – UP Open Hole / Support Column / etc CLL

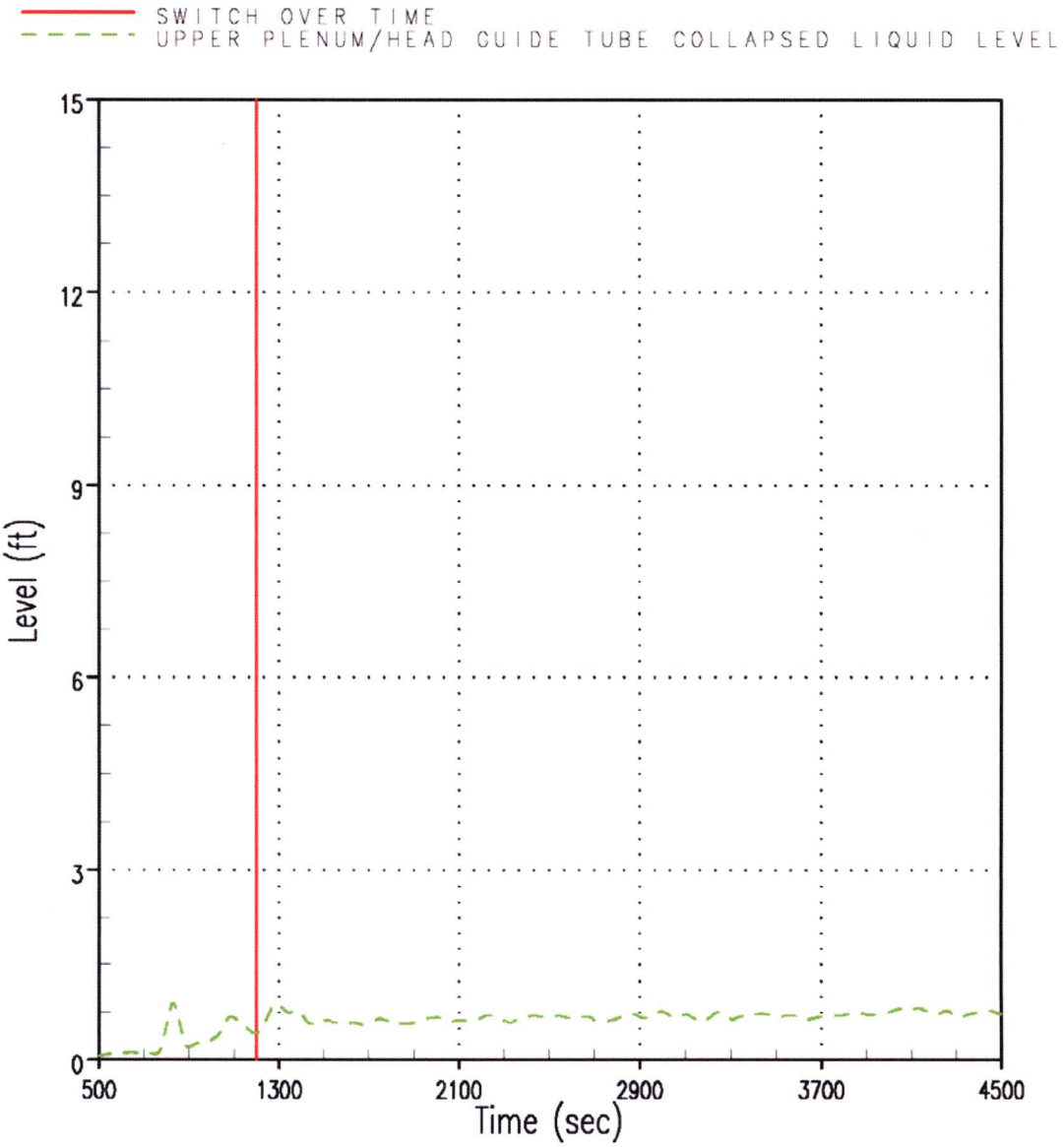

Figure RAI-4.23-30 Case 0A – UP / Upper Head Guide Tube CLL

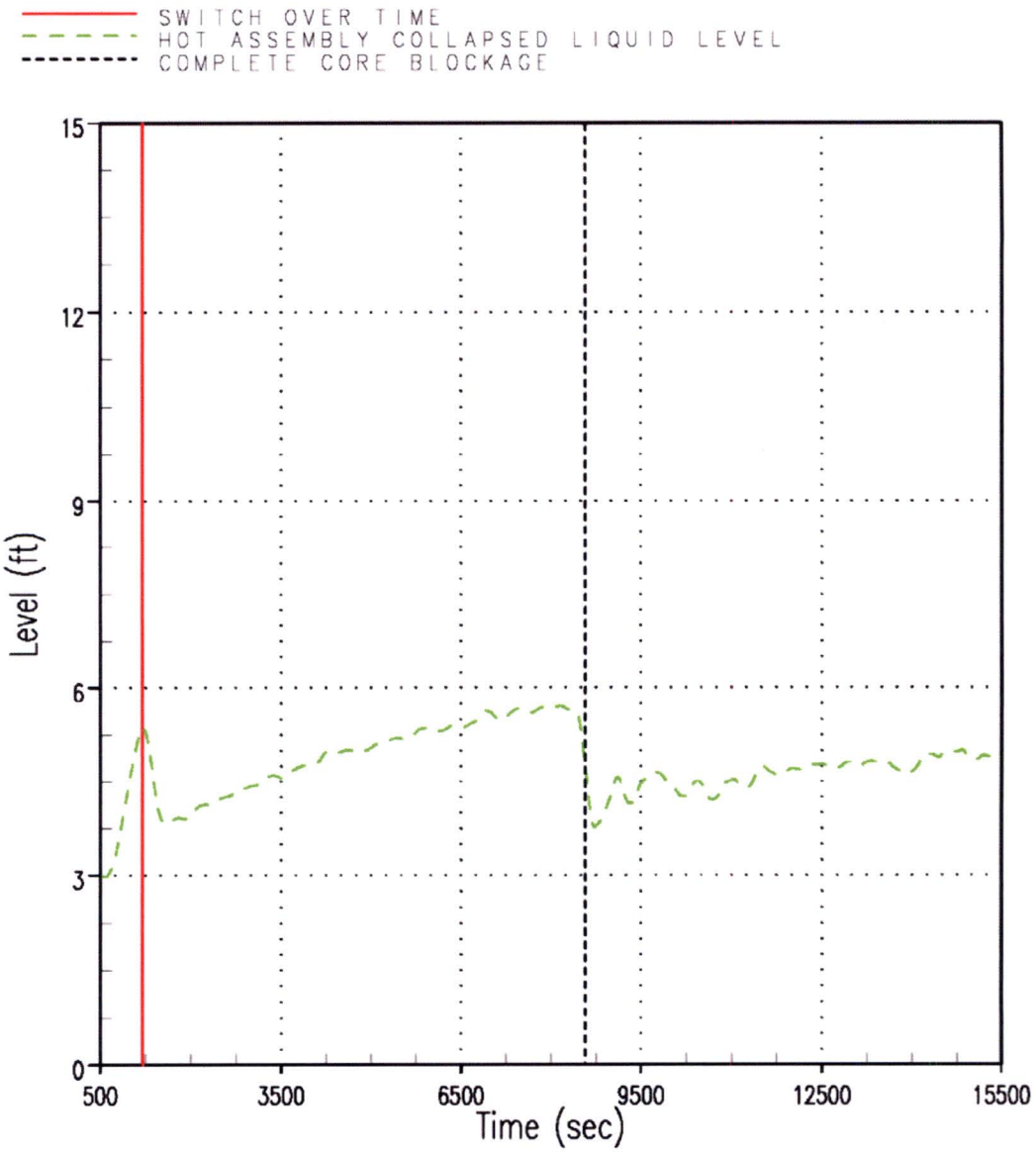

Figure RAI-4.23-31 Case 1B – Hot Assembly CLL

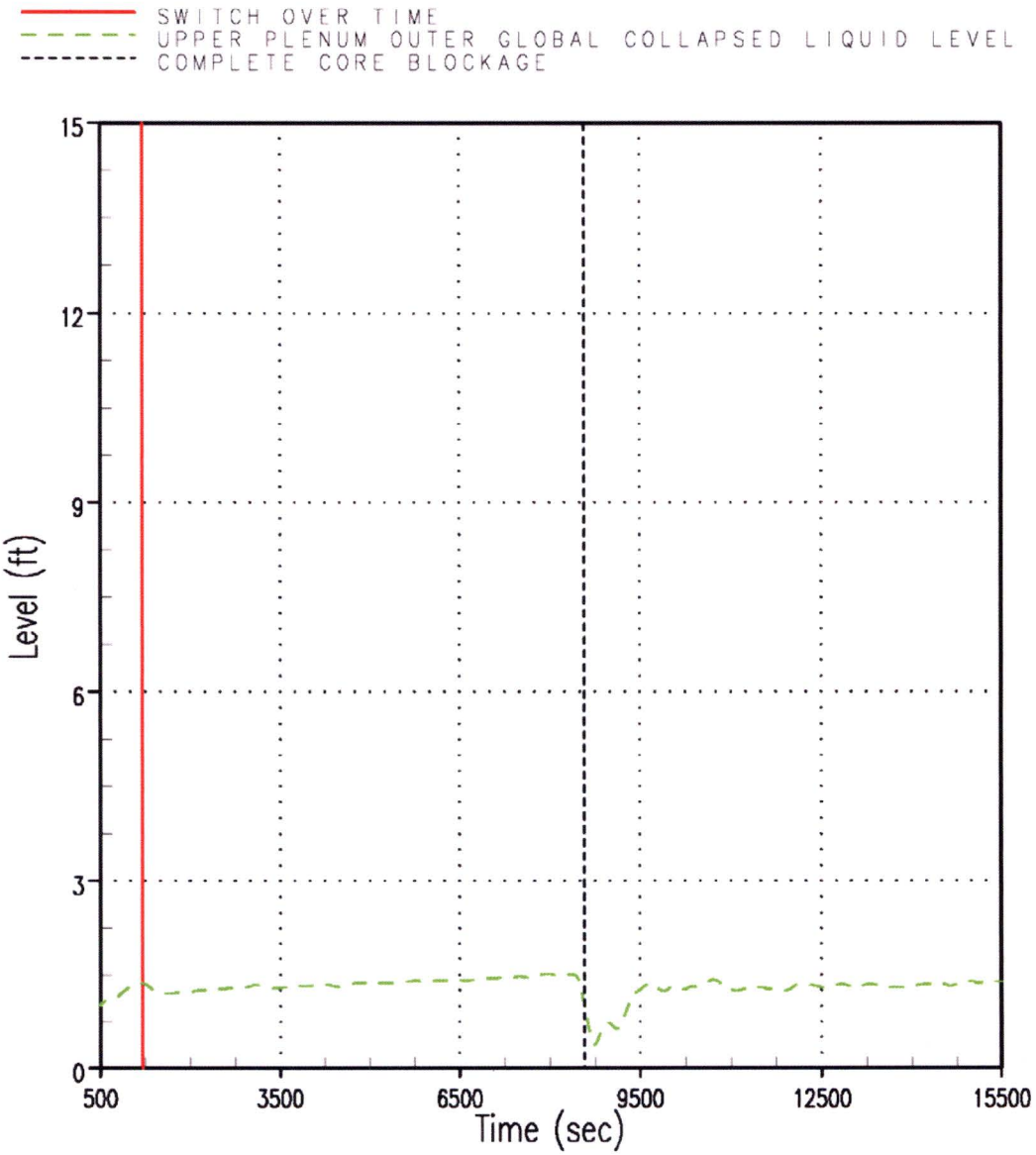

Figure RAI-4.23-32 Case 1B – UP Outer Global CLL

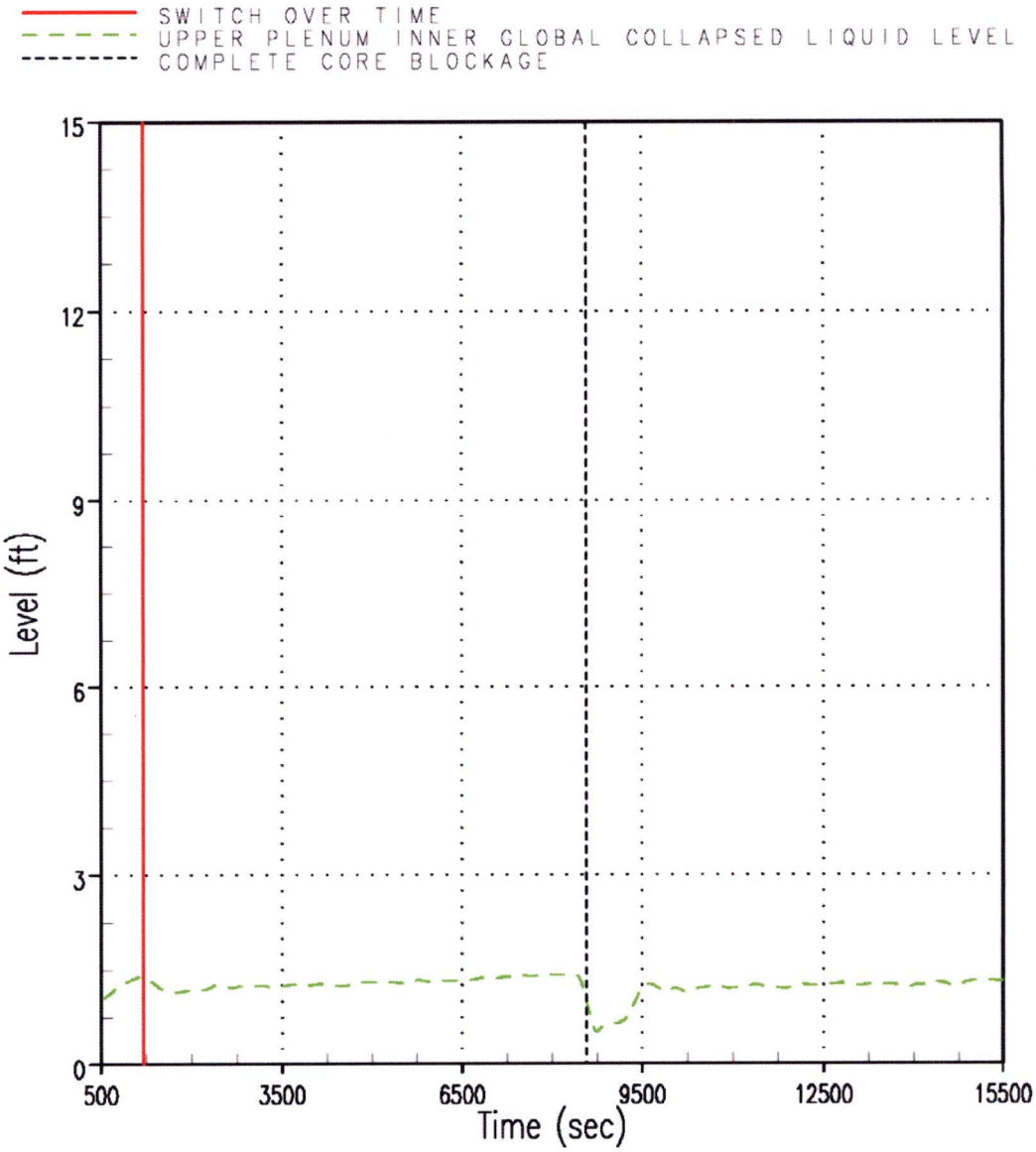

Figure RAI-4.23-33 Case 1B – UP Inner Global CLL

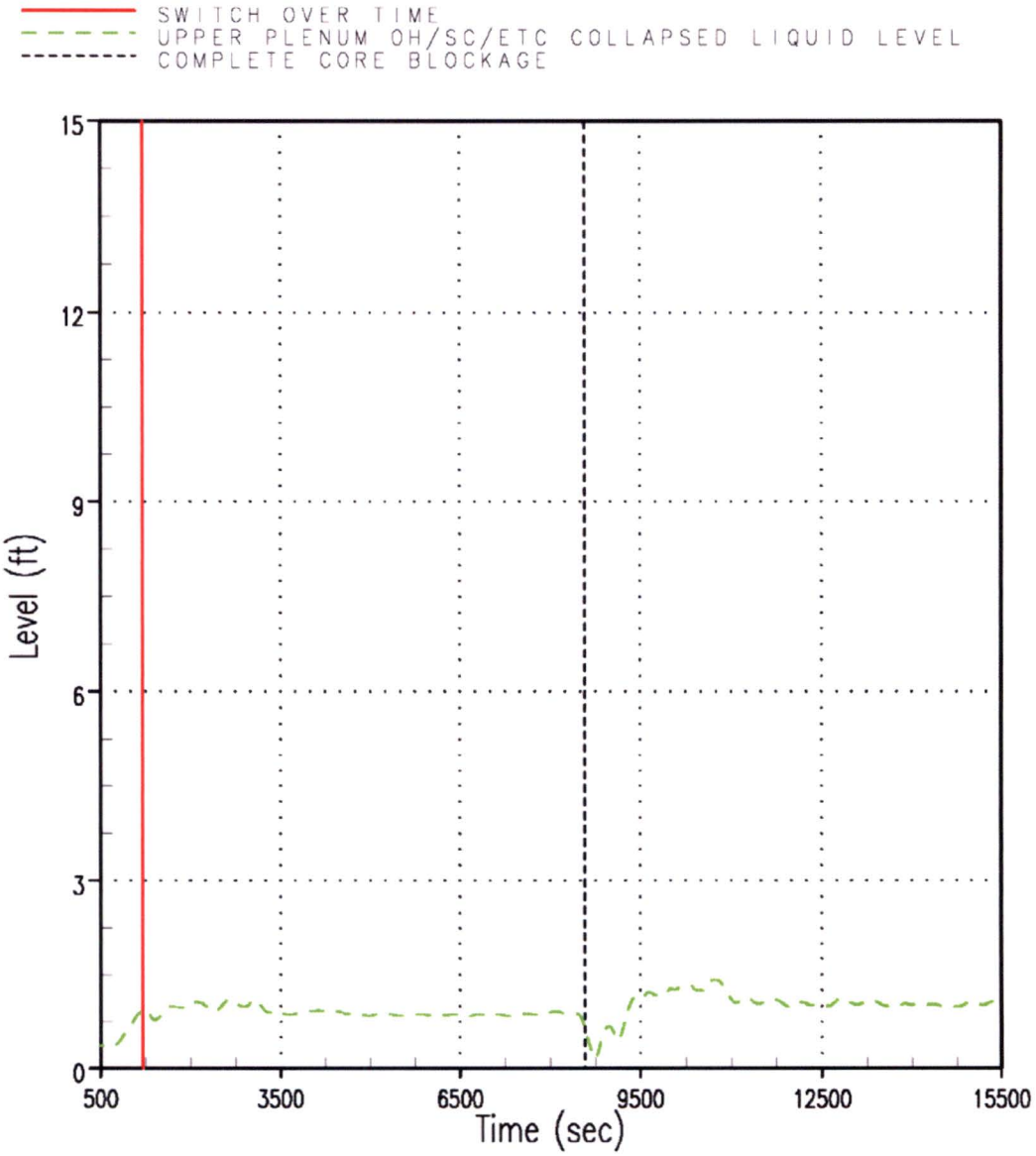

Figure RAI-4.23-34 Case 1B – UP Open Hole / Support Column / etc CLL

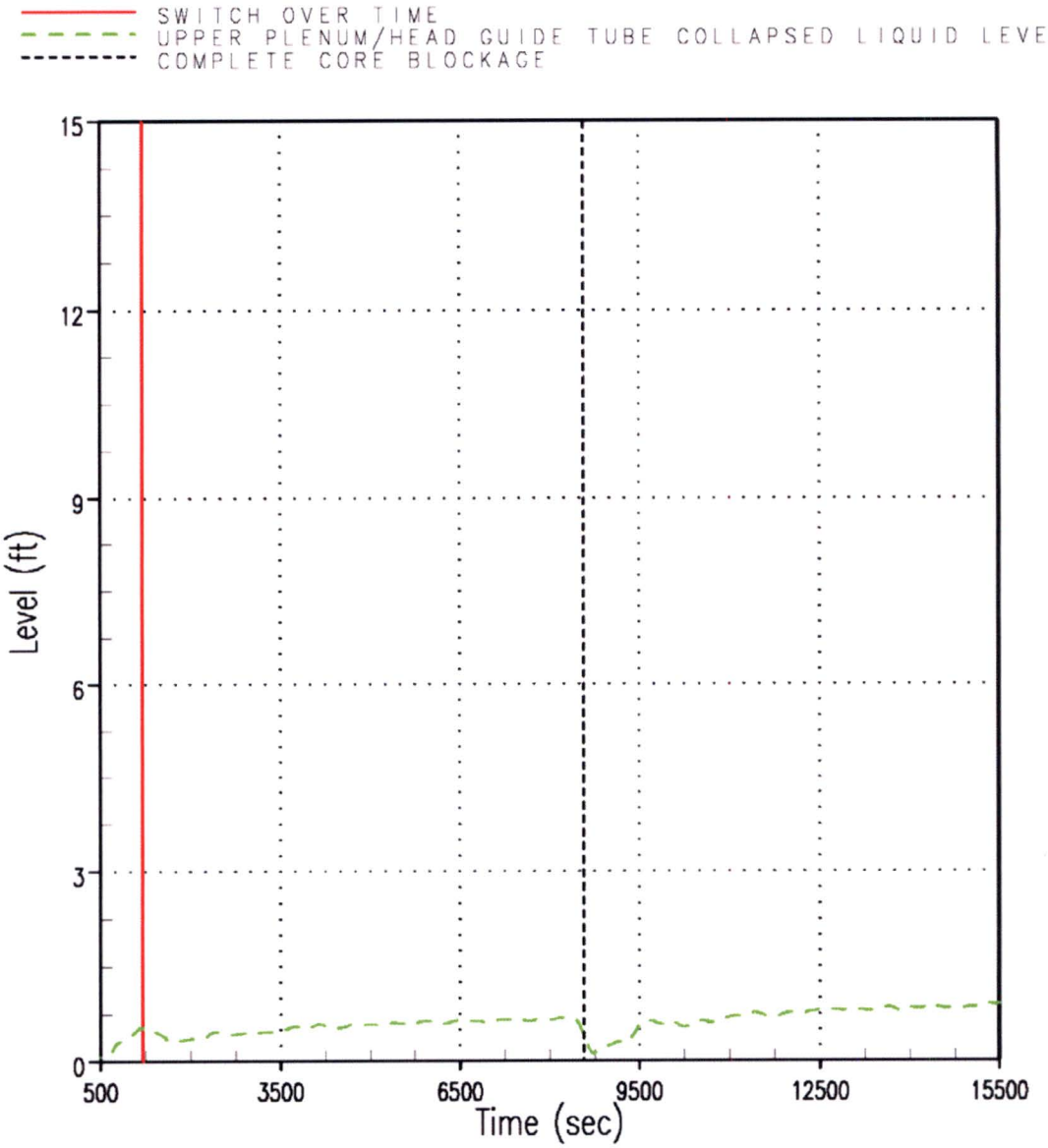

Figure RAI-4.23-35 Case 1B – UP / Upper Head Guide Tube CLL

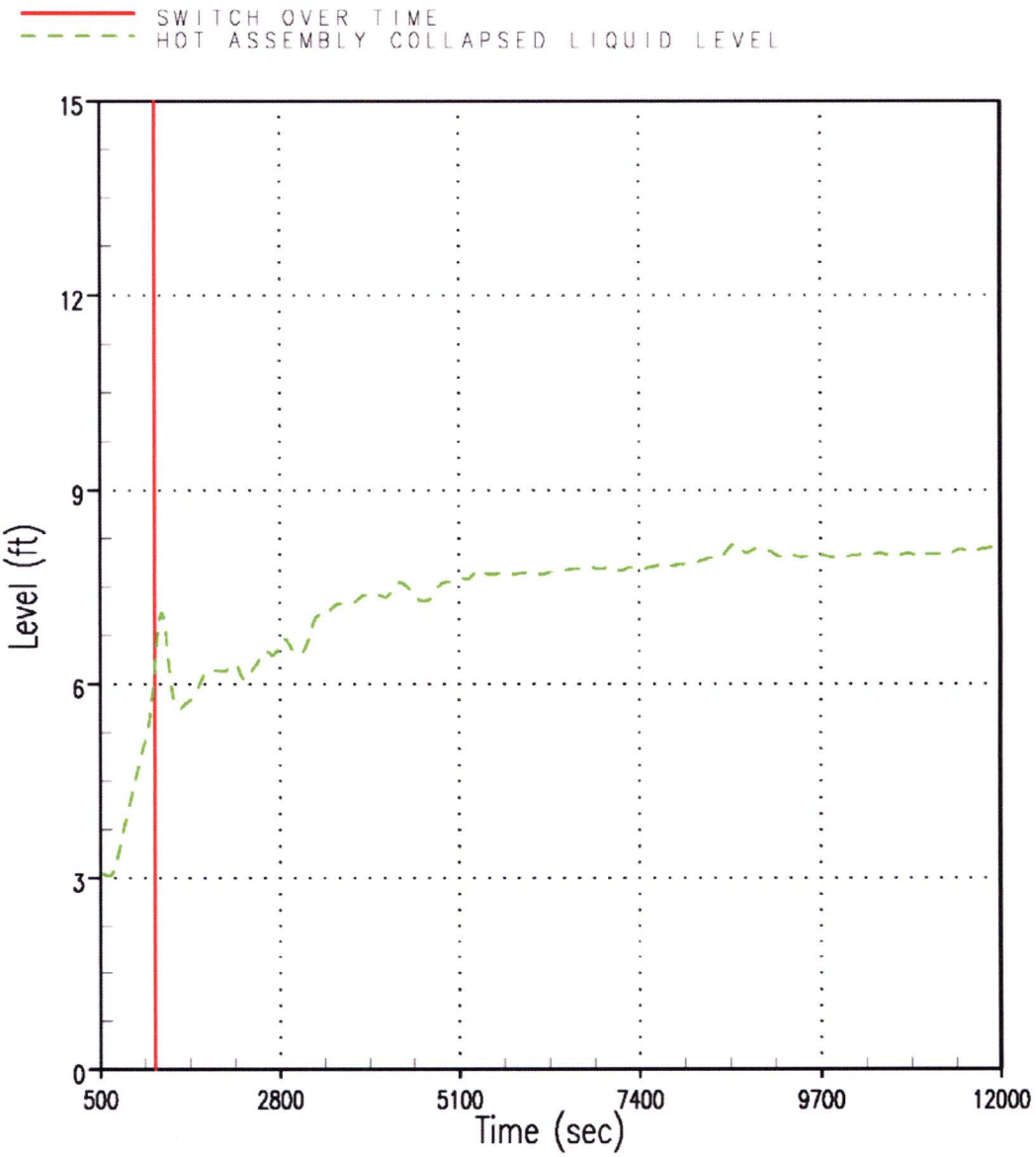

Figure RAI-4.23-36 Case 1 – Hot Assembly CLL

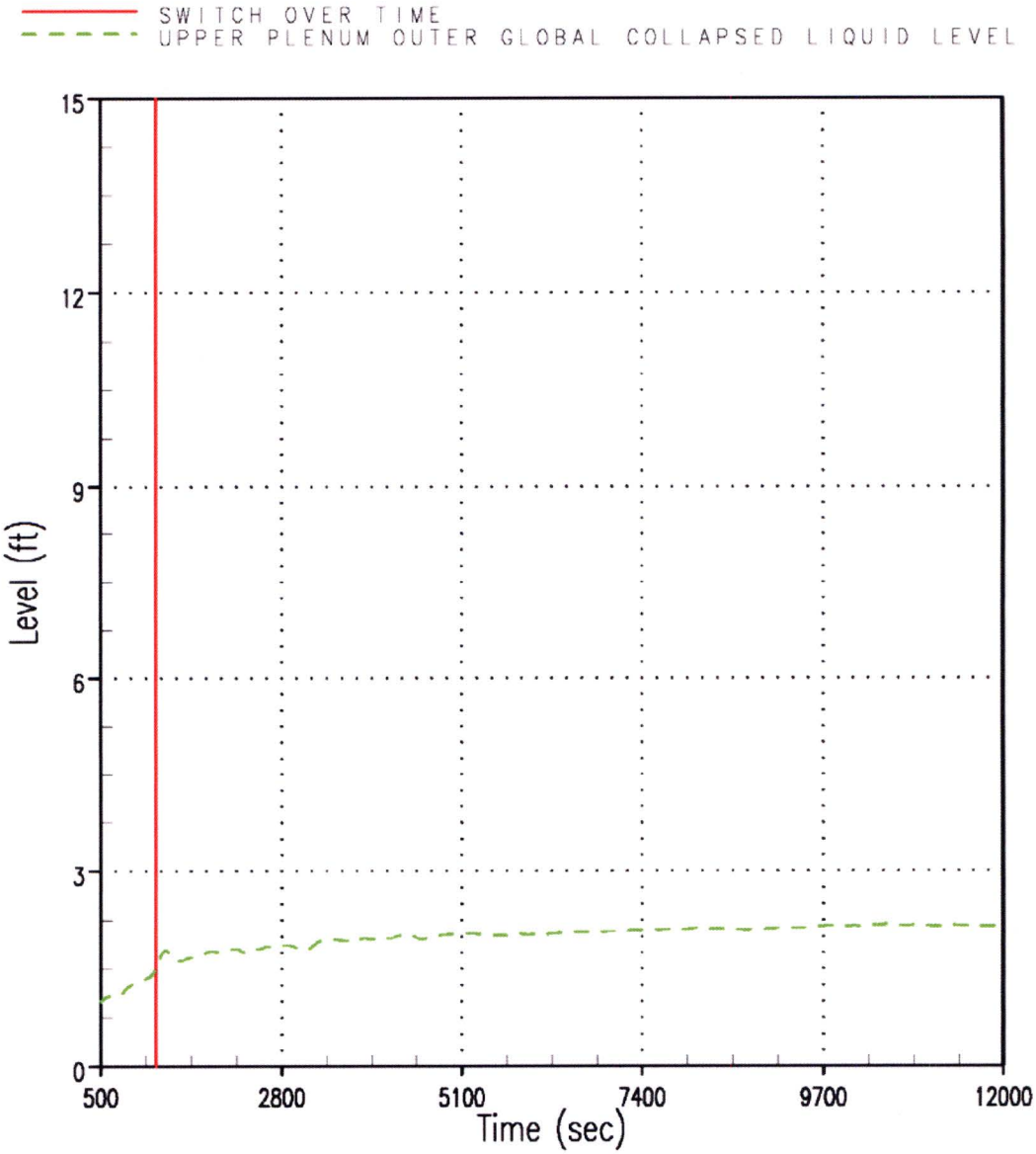

Figure RAI-4.23-37 Case 1 – UP Outer Global CLL

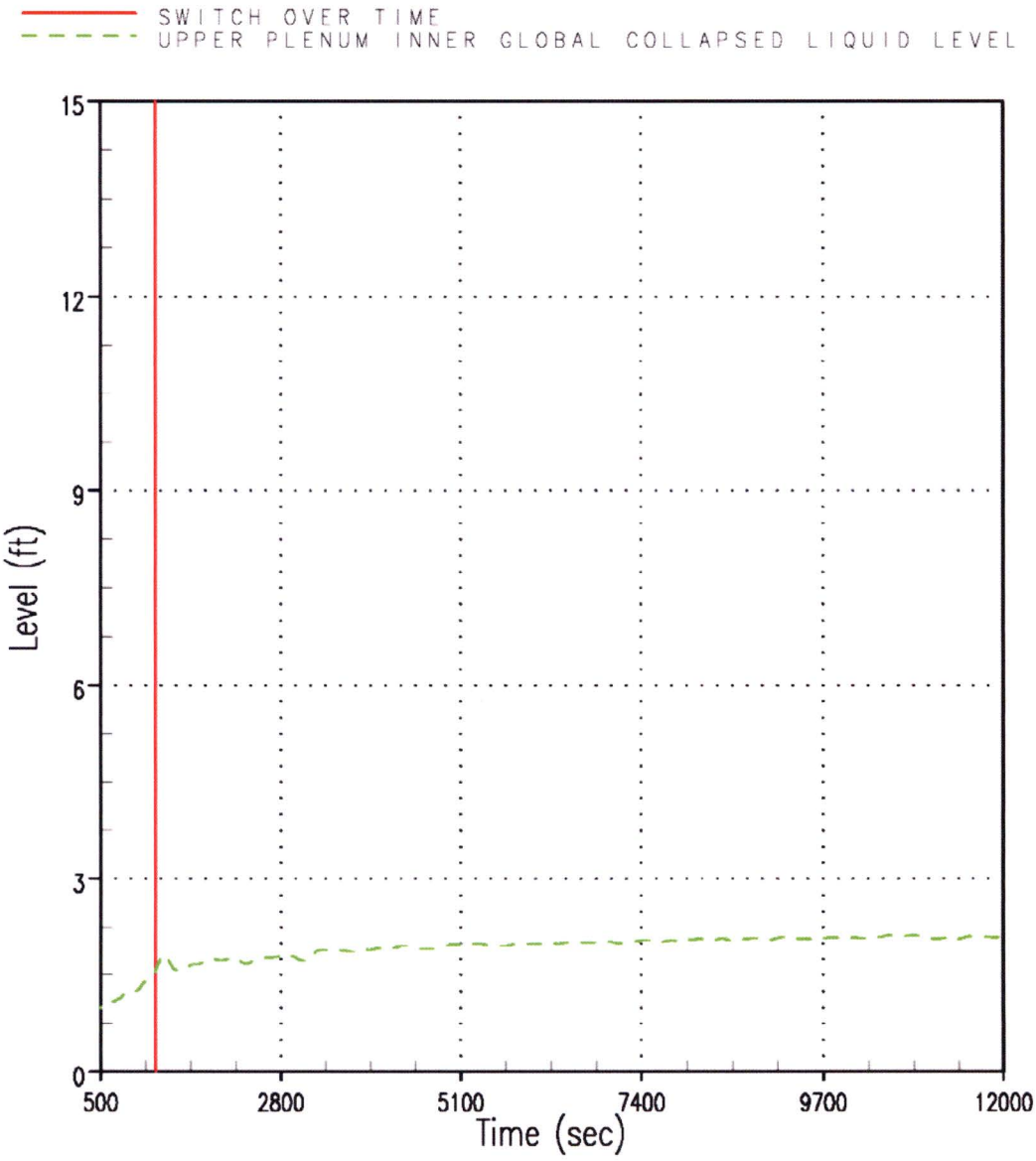

Figure RAI-4.23-38 Case 1 – UP Inner Global CLL

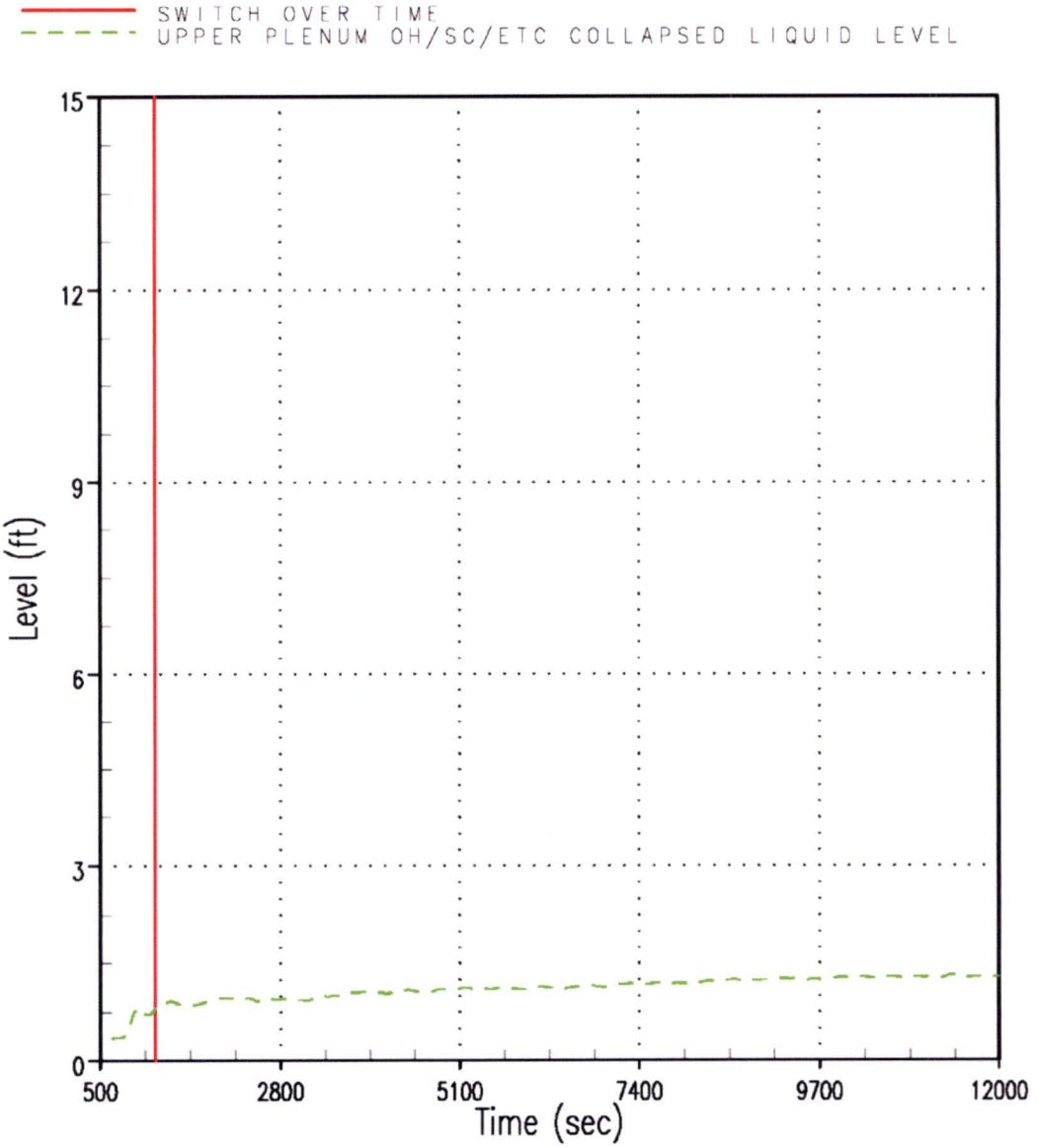

Figure RAI-4.23-39 Case 1 – UP Open Hole / Support Column / etc CLL

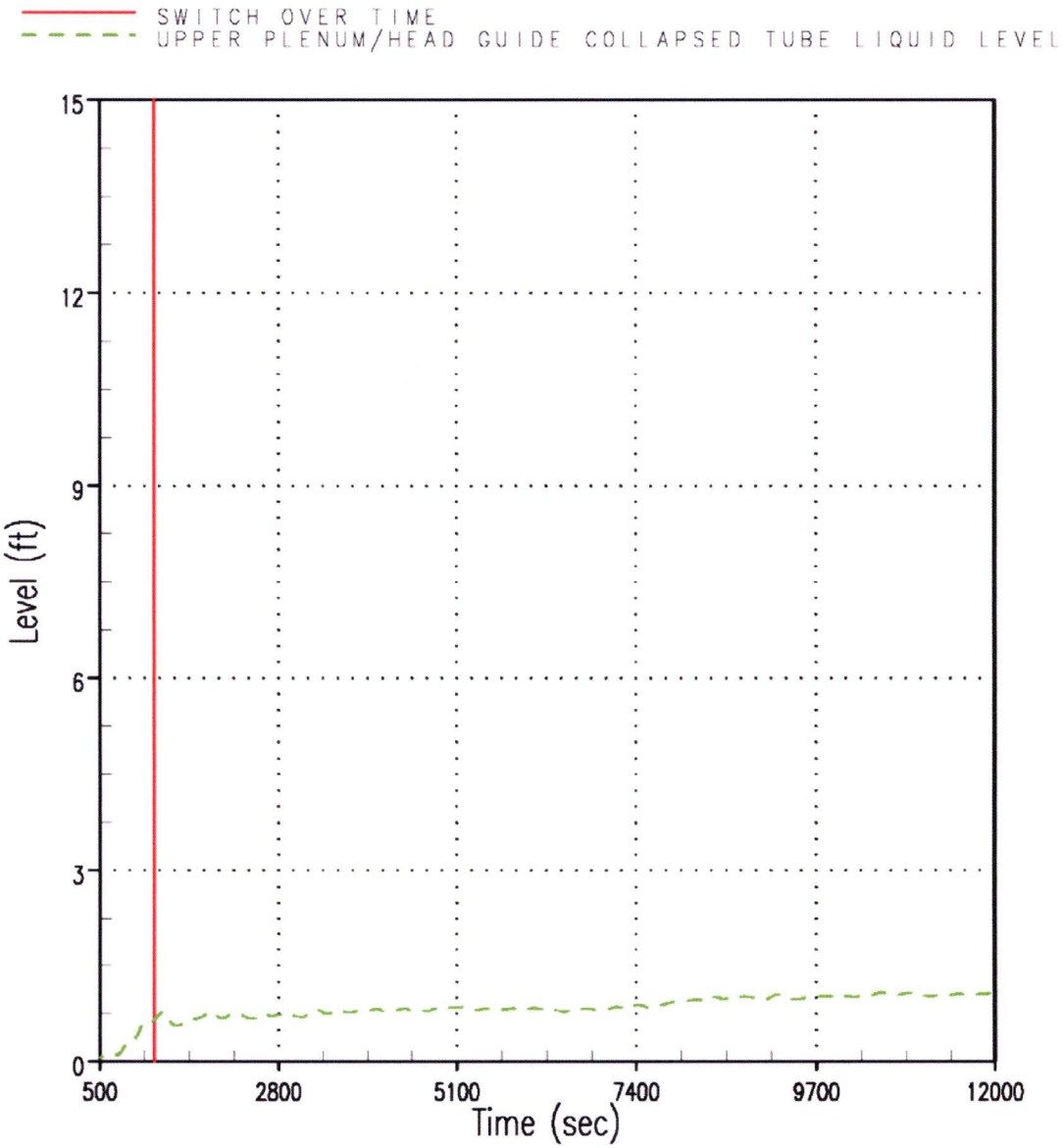

Figure RAI-4.23-40 Case 1 – UP / Upper Head Guide Tube CLL

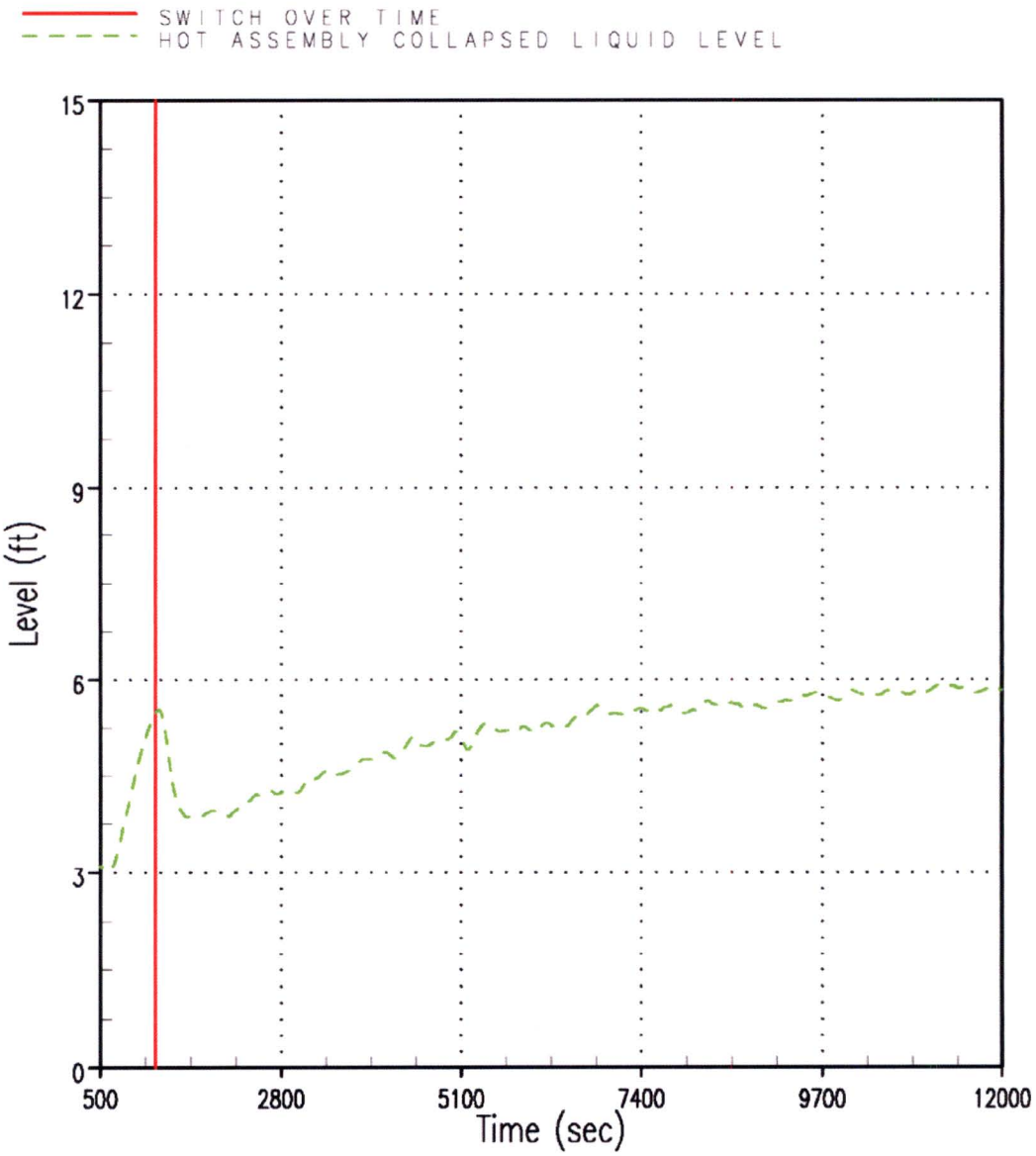

Figure RAI-4.23-41 Case 3 – Hot Assembly CLL

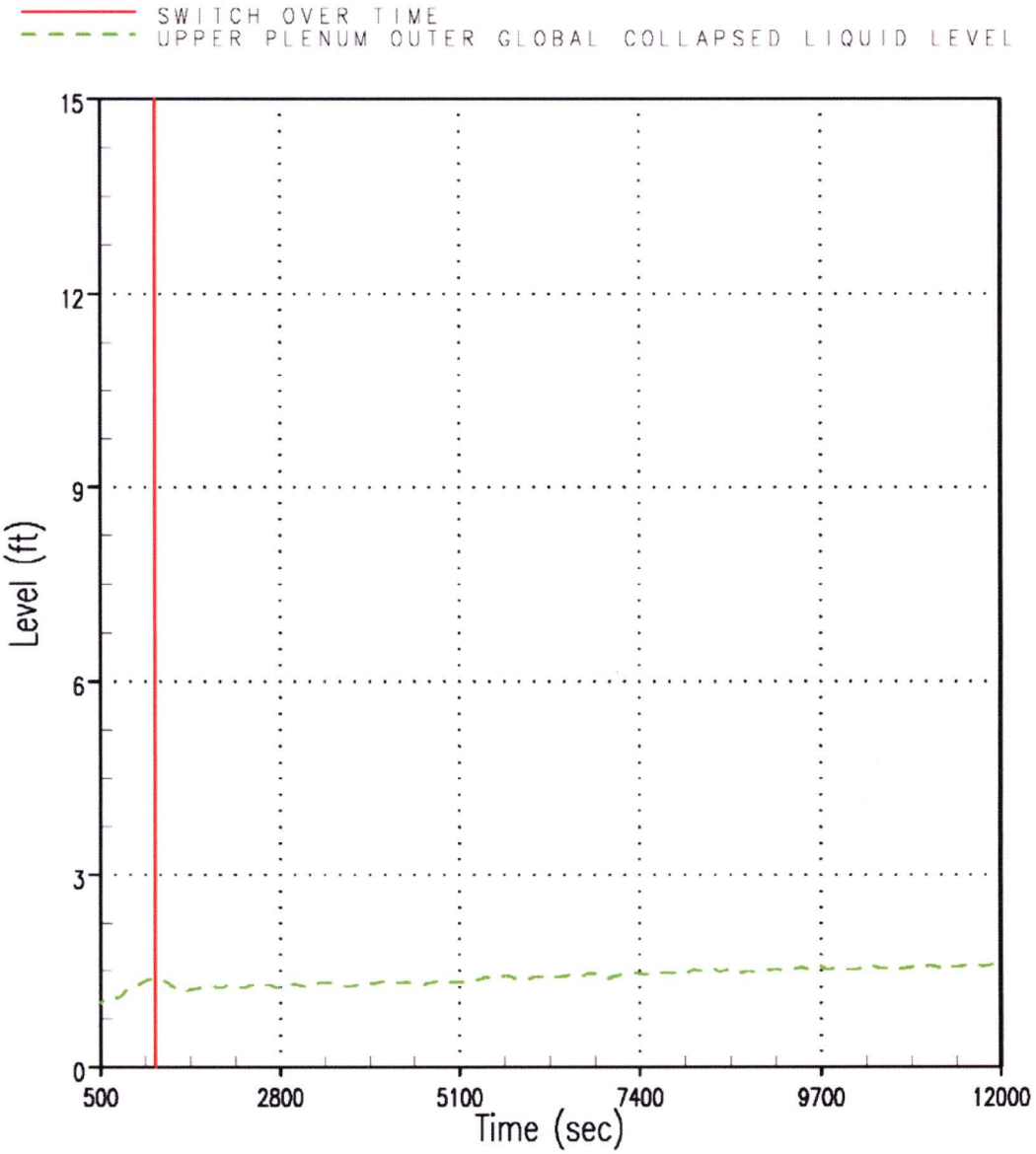

Figure RAI-4.23-42 Case 3 – UP Outer Global CLL

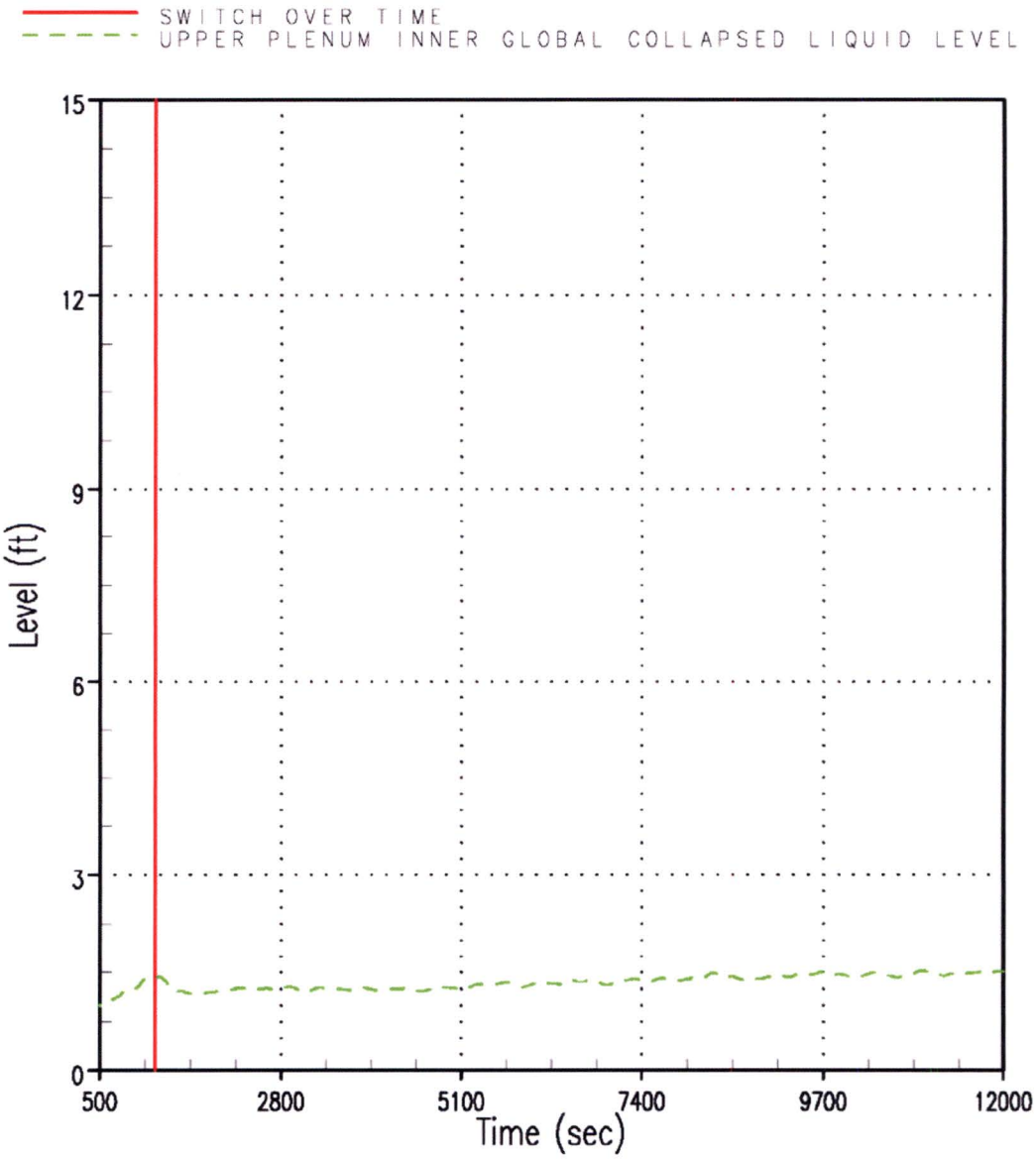

Figure RAI-4.23-43 Case 3 – UP Inner Global CLL

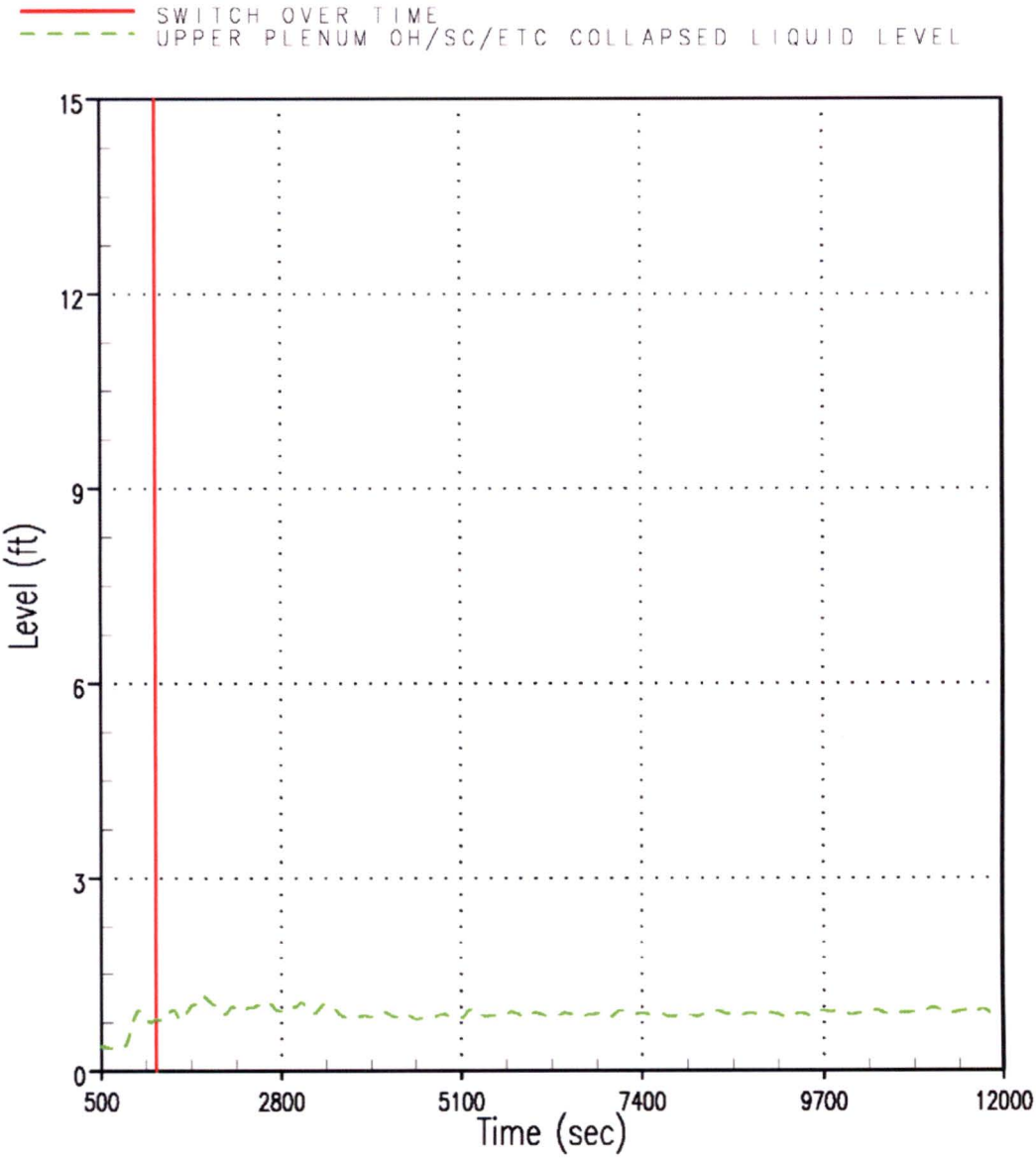

Figure RAI-4.23-44 Case 3 – UP Open Hole / Support Column / etc CLL

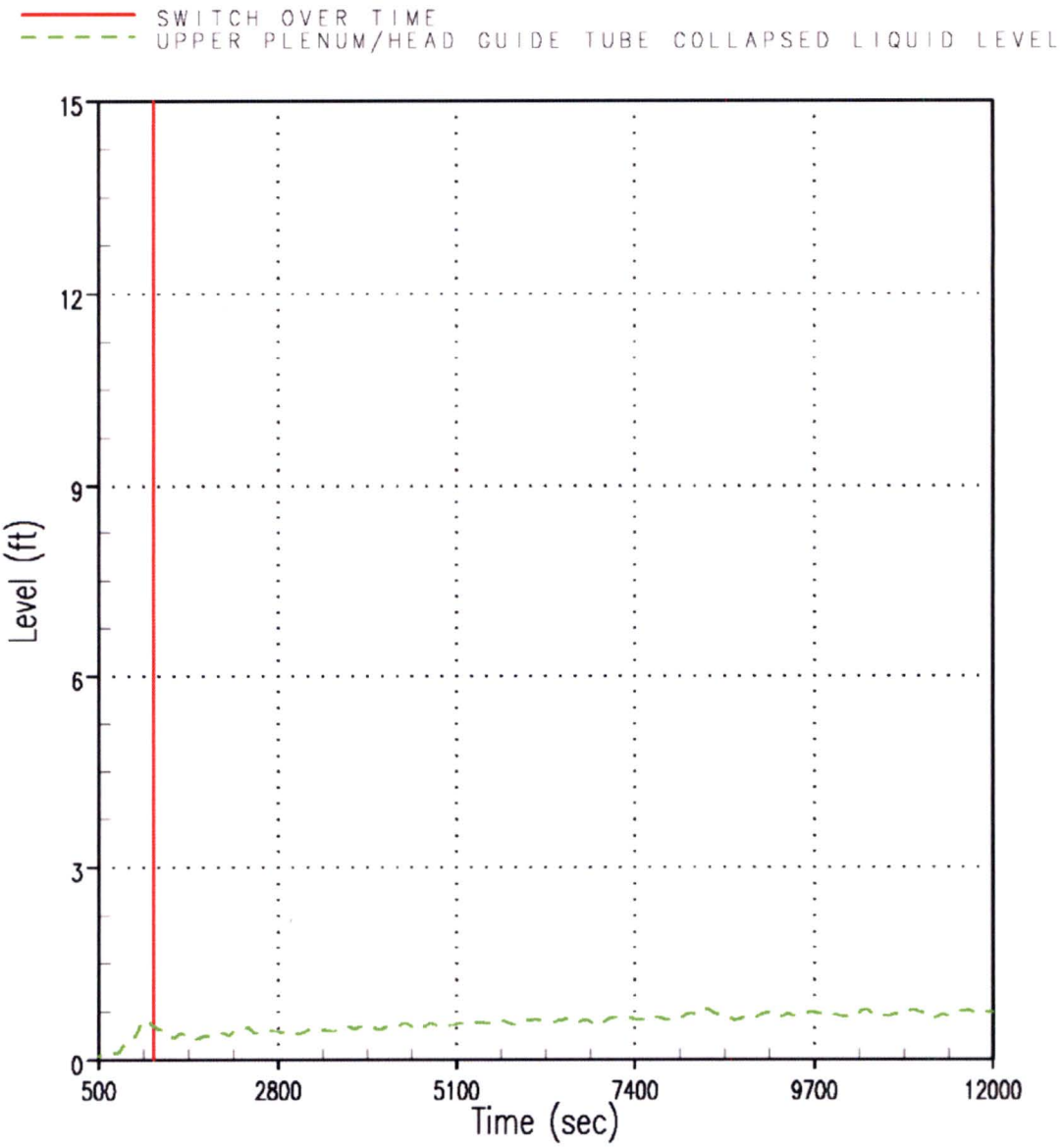

Figure RAI-4.23-45 Case 3 – UP / Upper Head Guide Tube CLL

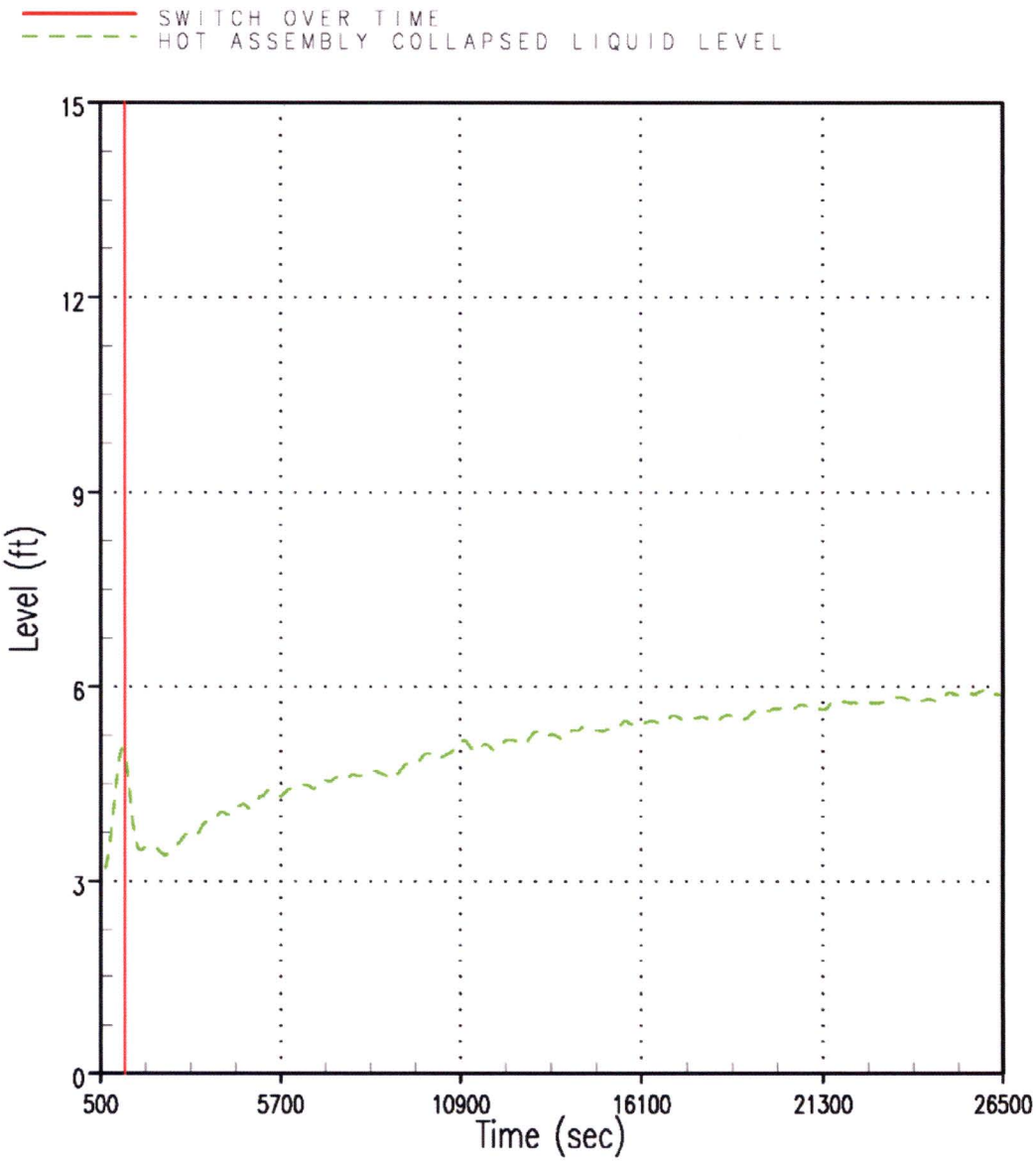

Figure RAI-4.23-46 Case 5 – Hot Assembly CLL

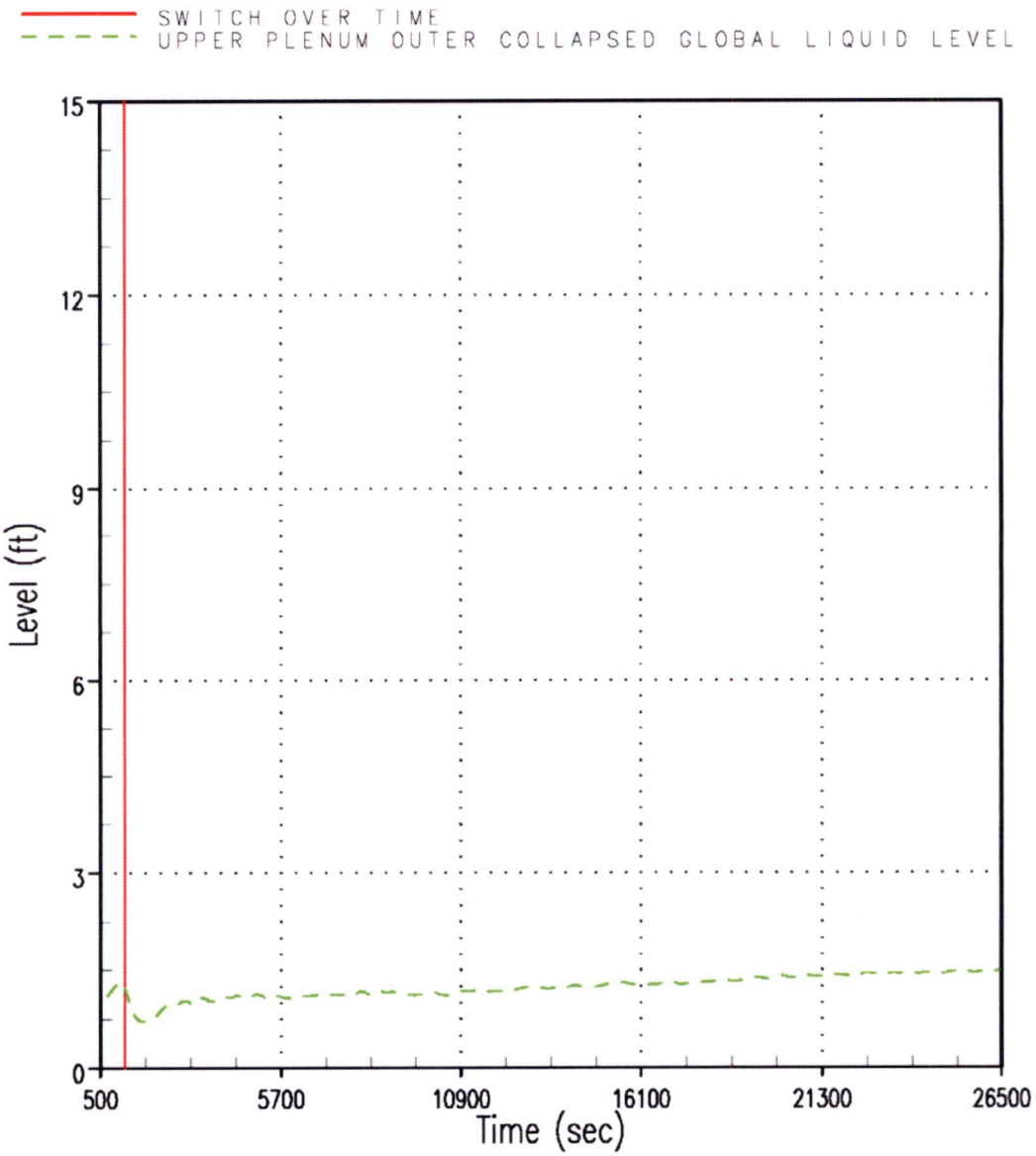

Figure RAI-4.23-47 Case 5 – UP Outer Global CLL

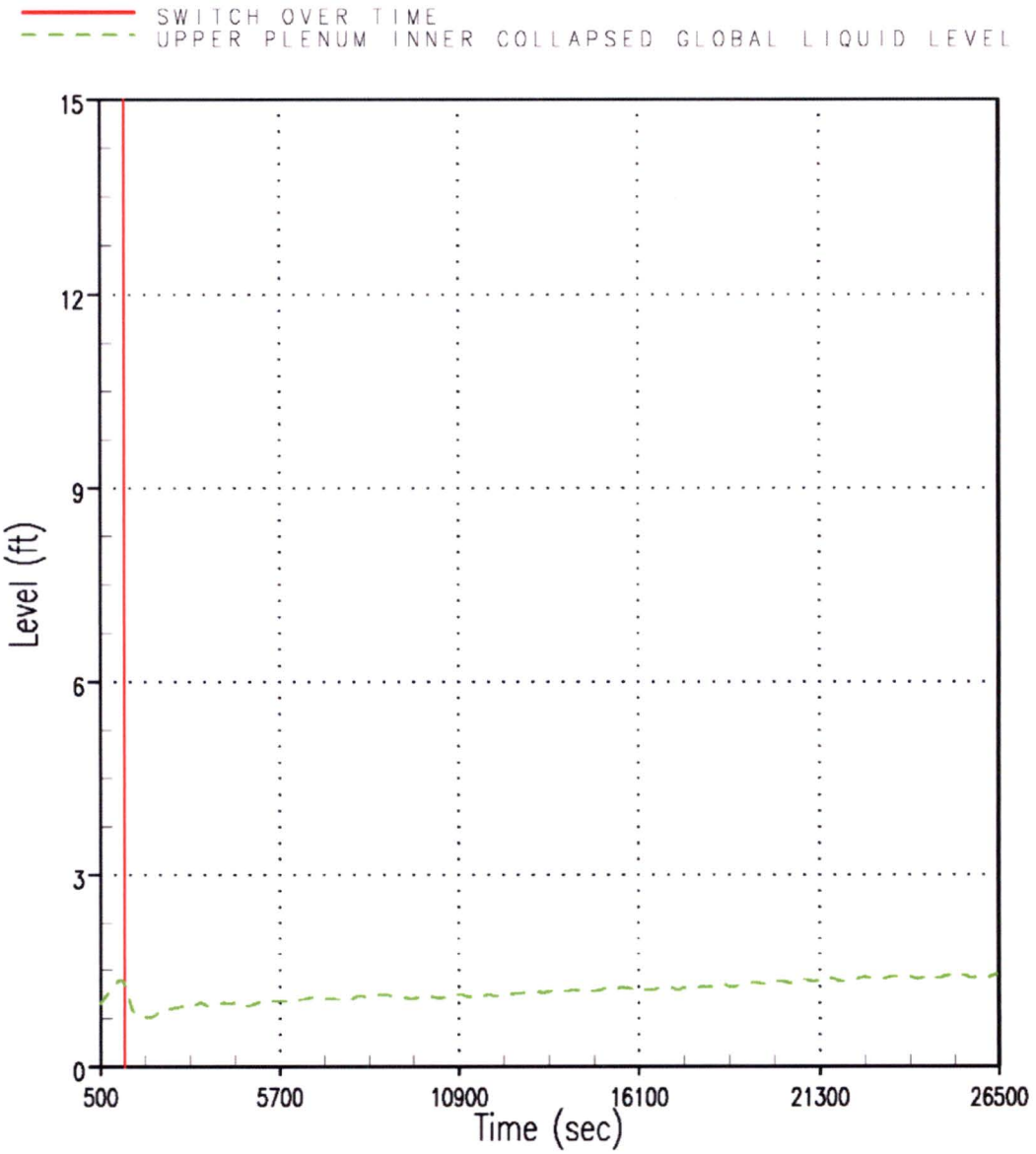

Figure RAI-4.23-48 Case 5 – UP Inner Global CLL

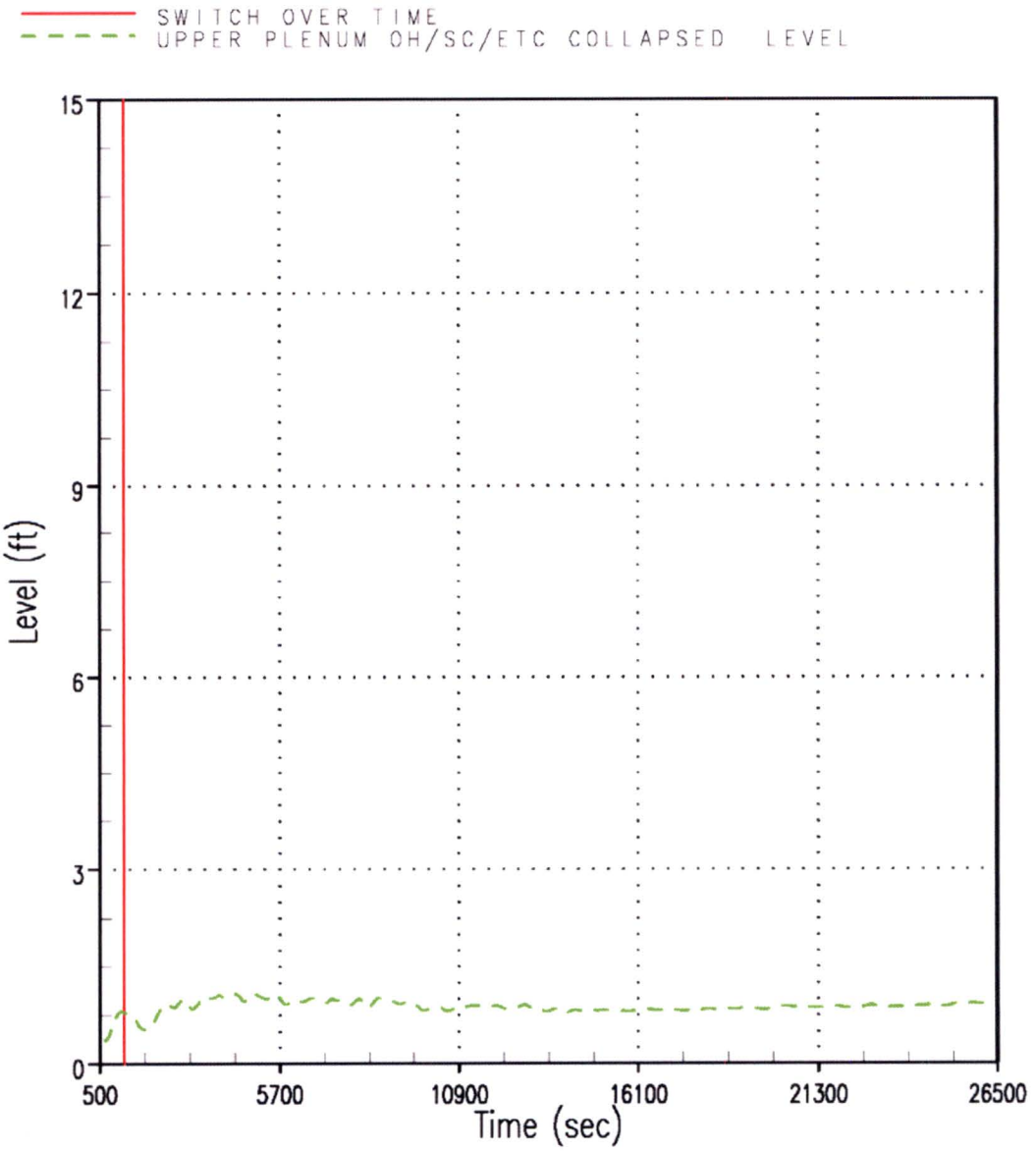

Figure RAI-4.23-49 Case 5 – UP Open Hole / Support Column / etc CLL

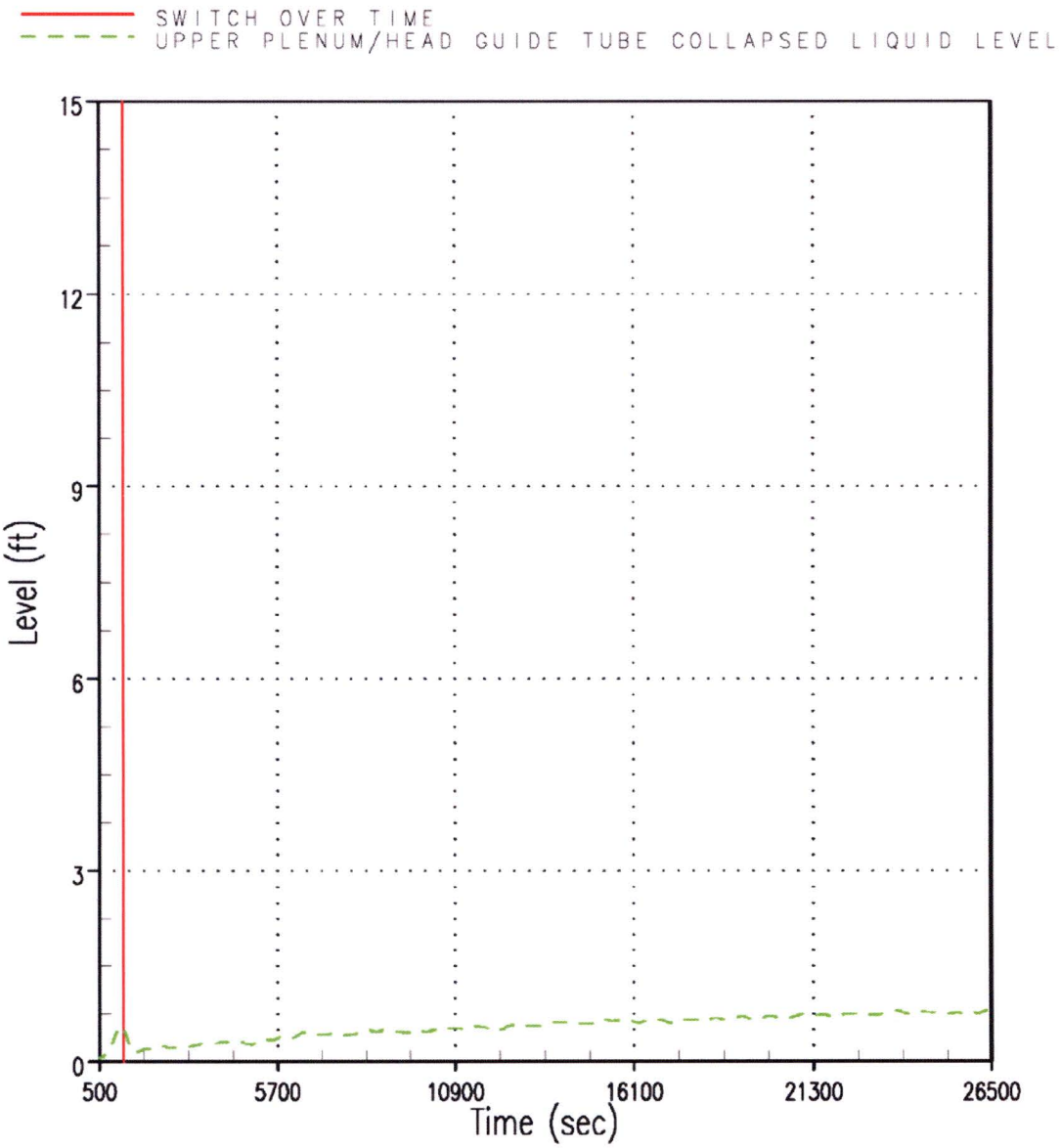

Figure RAI-4.23-50 Case 5 – UP / Upper Head Guide Tube CLL

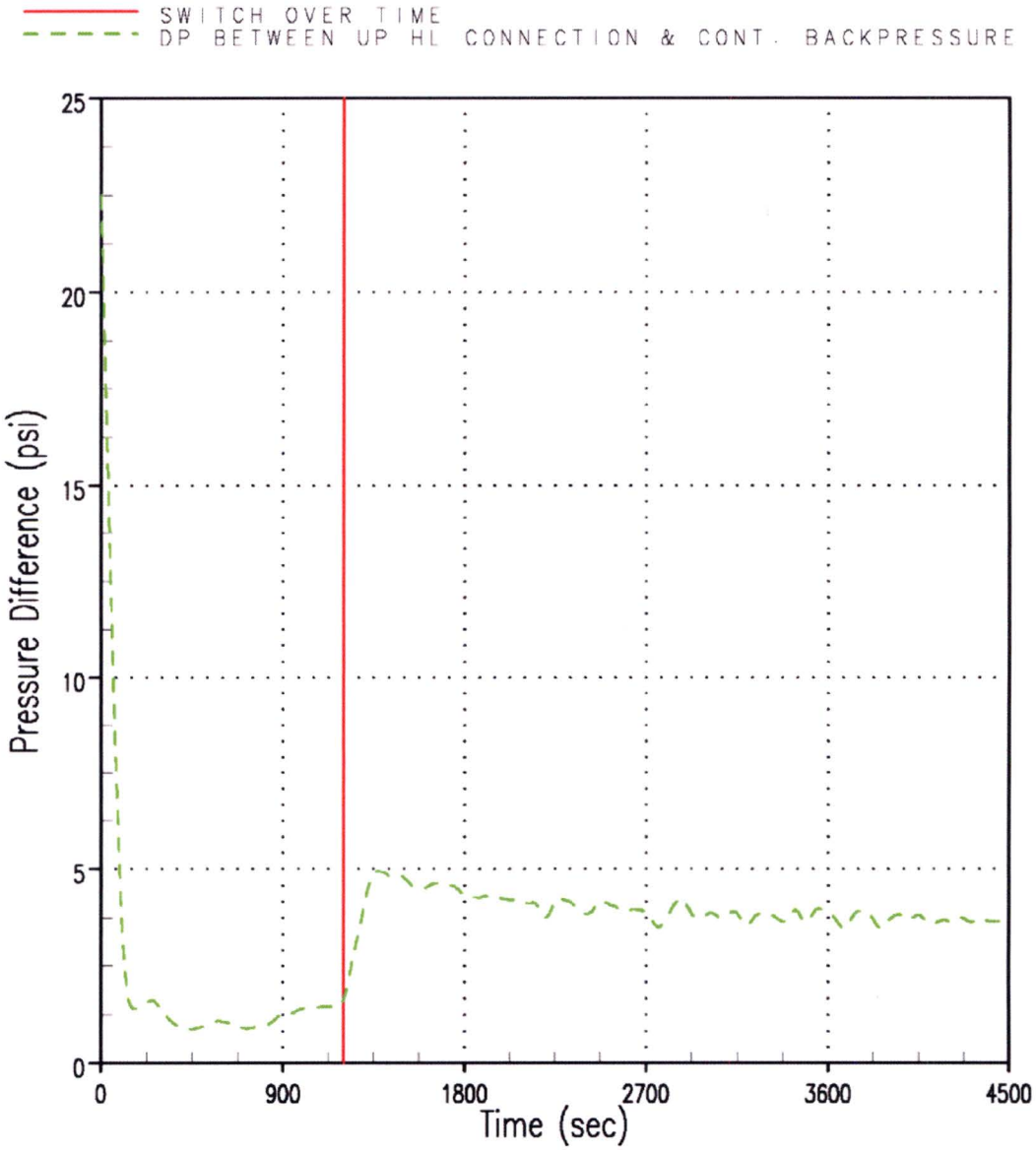

Figure RAI-4.23-51 Case 0A – Delta P between Upper Head Channel Connection to Broken HL and Containment Backpressure

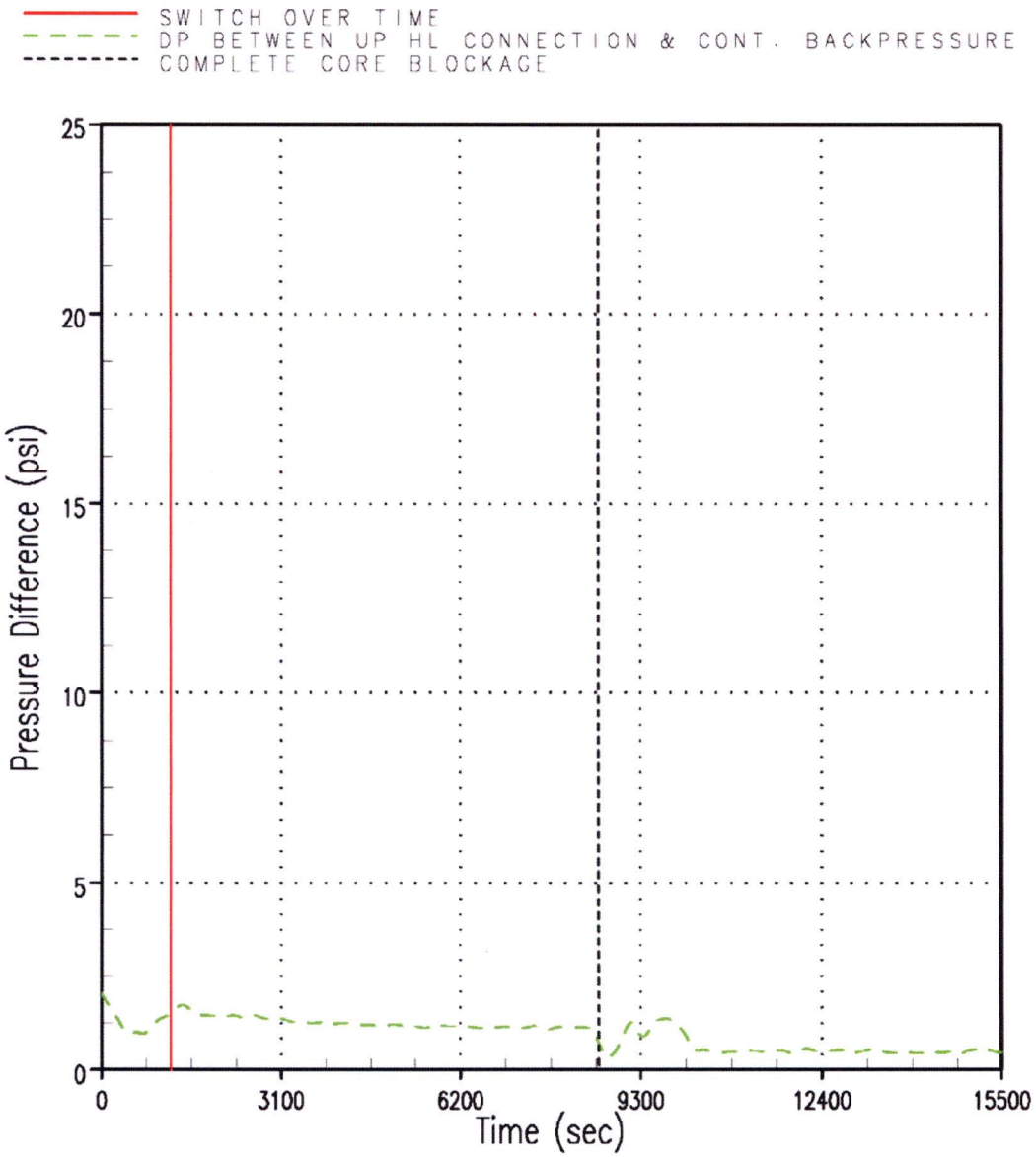

Figure RAI-4.23-52 Case 1B – Delta P between Upper Head Channel Connection to Broken HL and Containment Backpressure

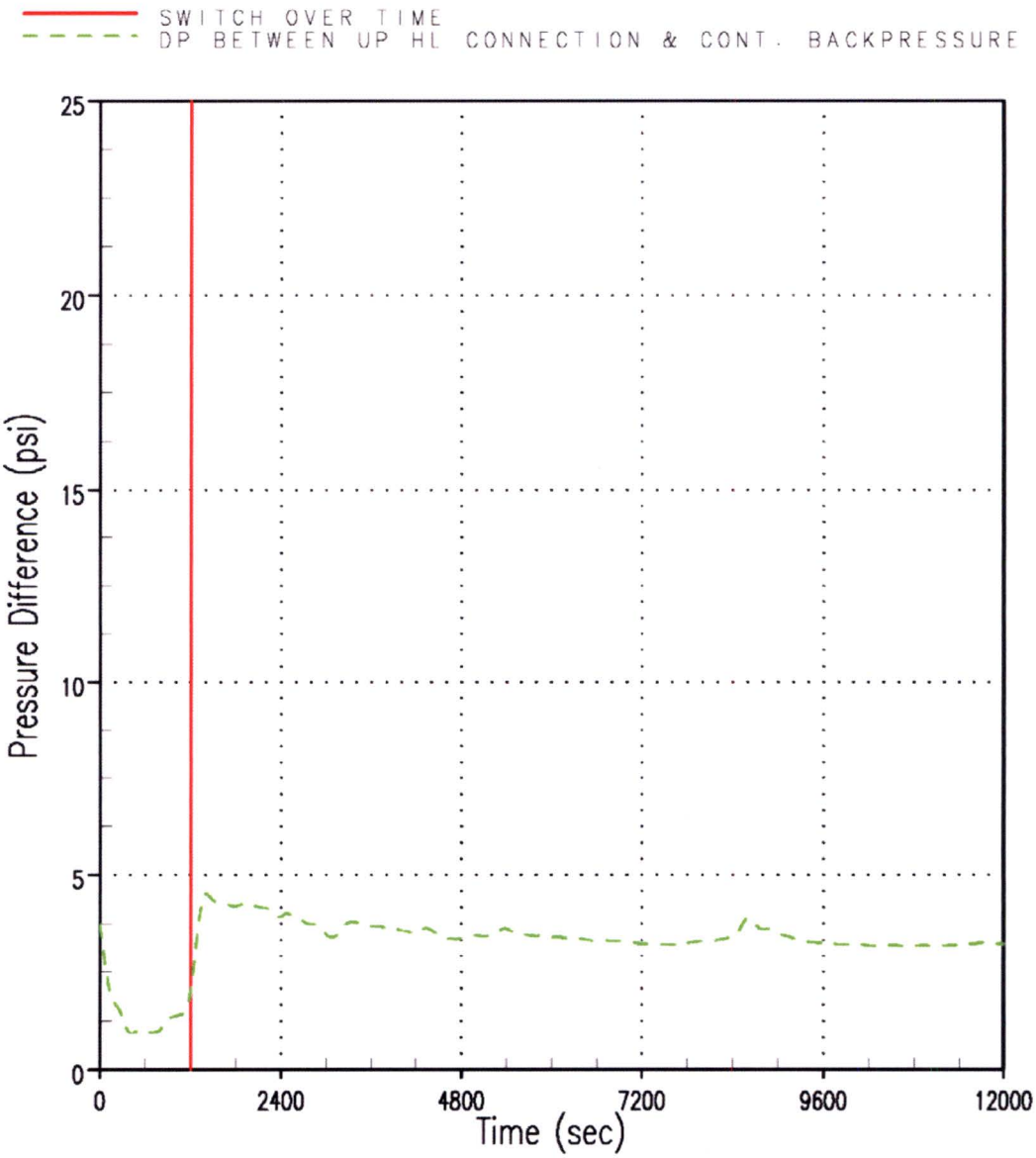

Figure RAI-4.23-53 Case 1 – Delta P between Upper Head Channel Connection to Broken HL and Containment Backpressure

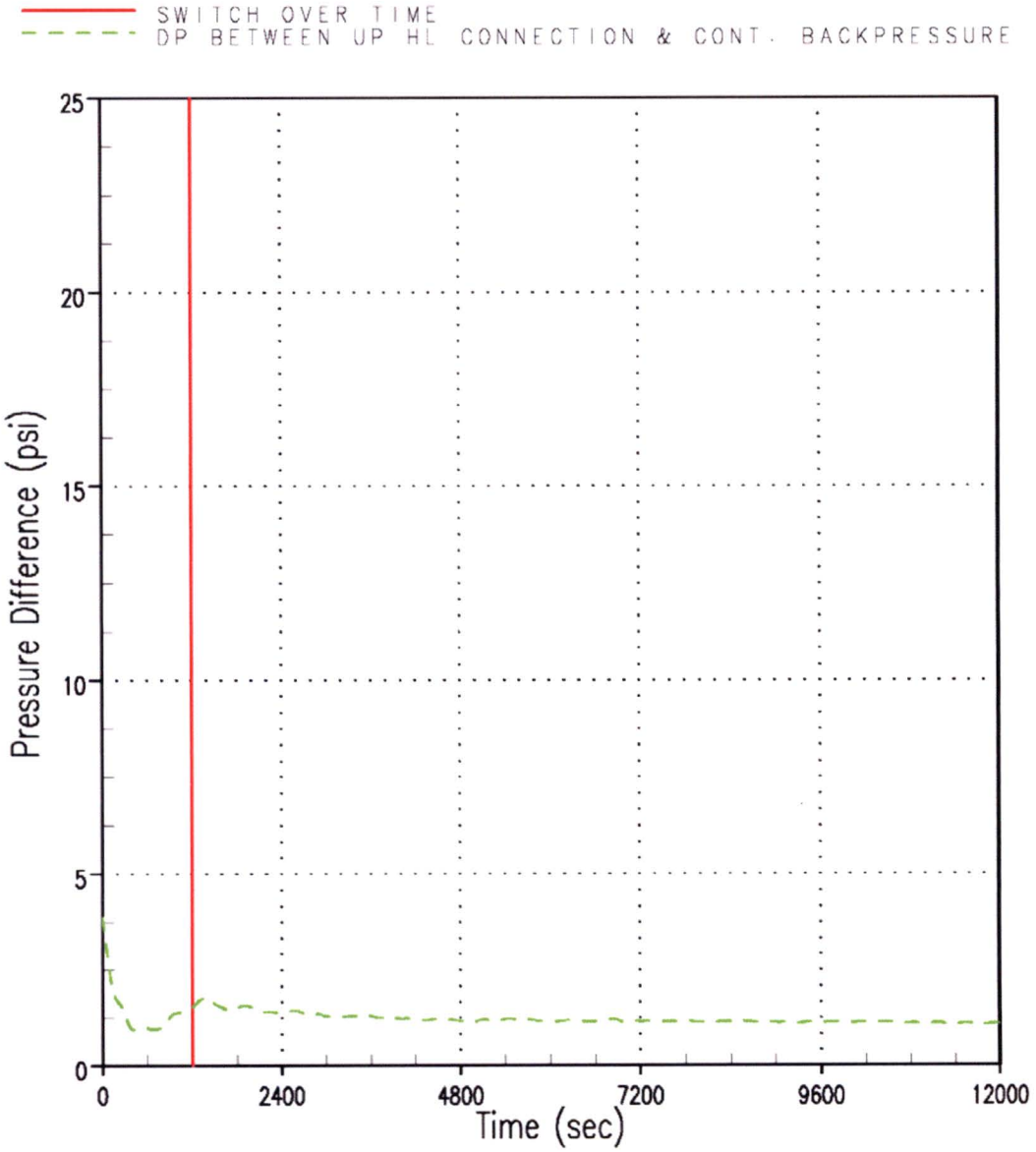

Figure RAI-4.23-54 Case 3 – Delta P between Upper Head Channel Connection to Broken HL and Containment Backpressure

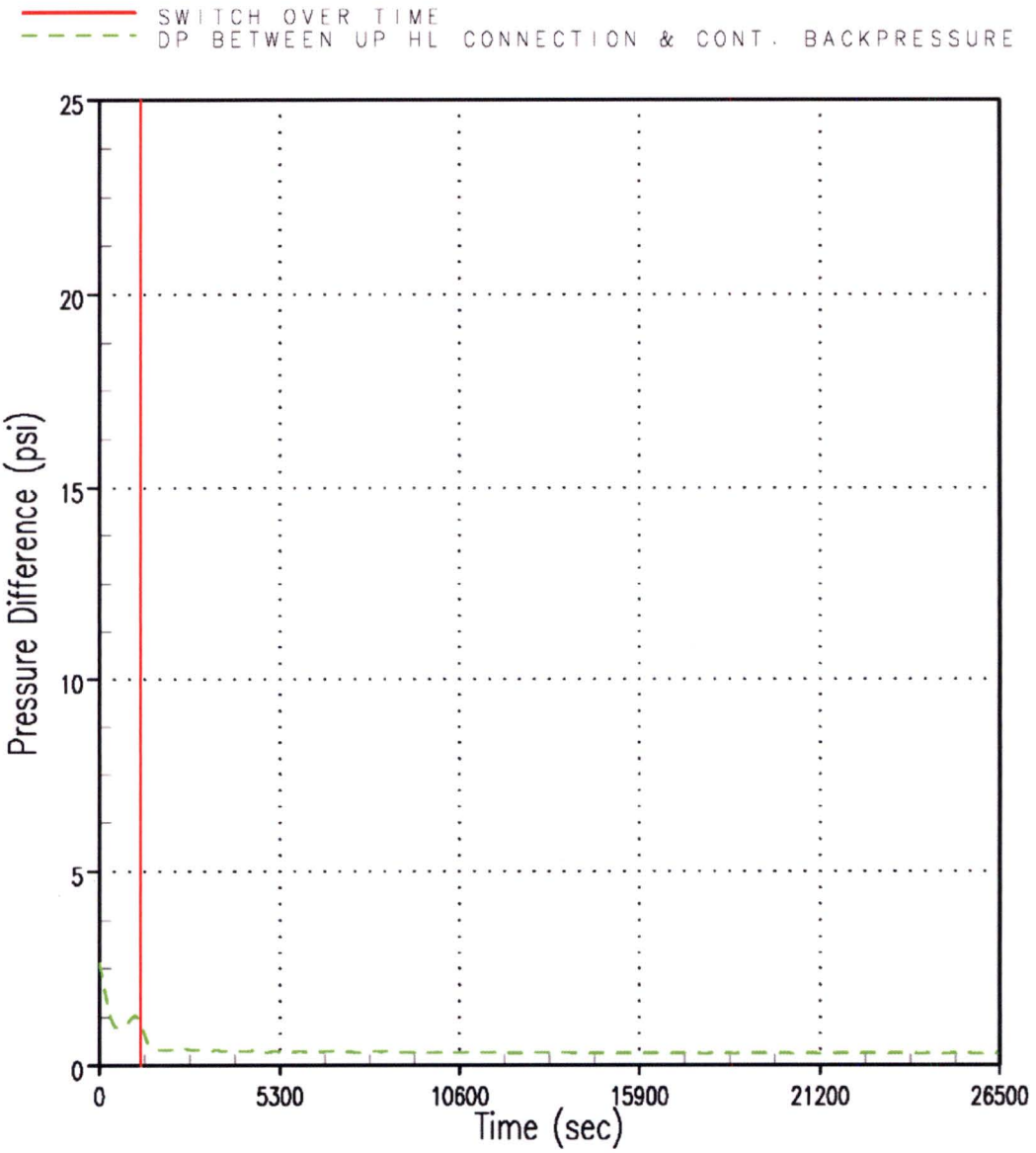

Figure RAI-4.23-55 Case 5 – Delta P between Upper Head Channel Connection to Broken HL and Containment Backpressure

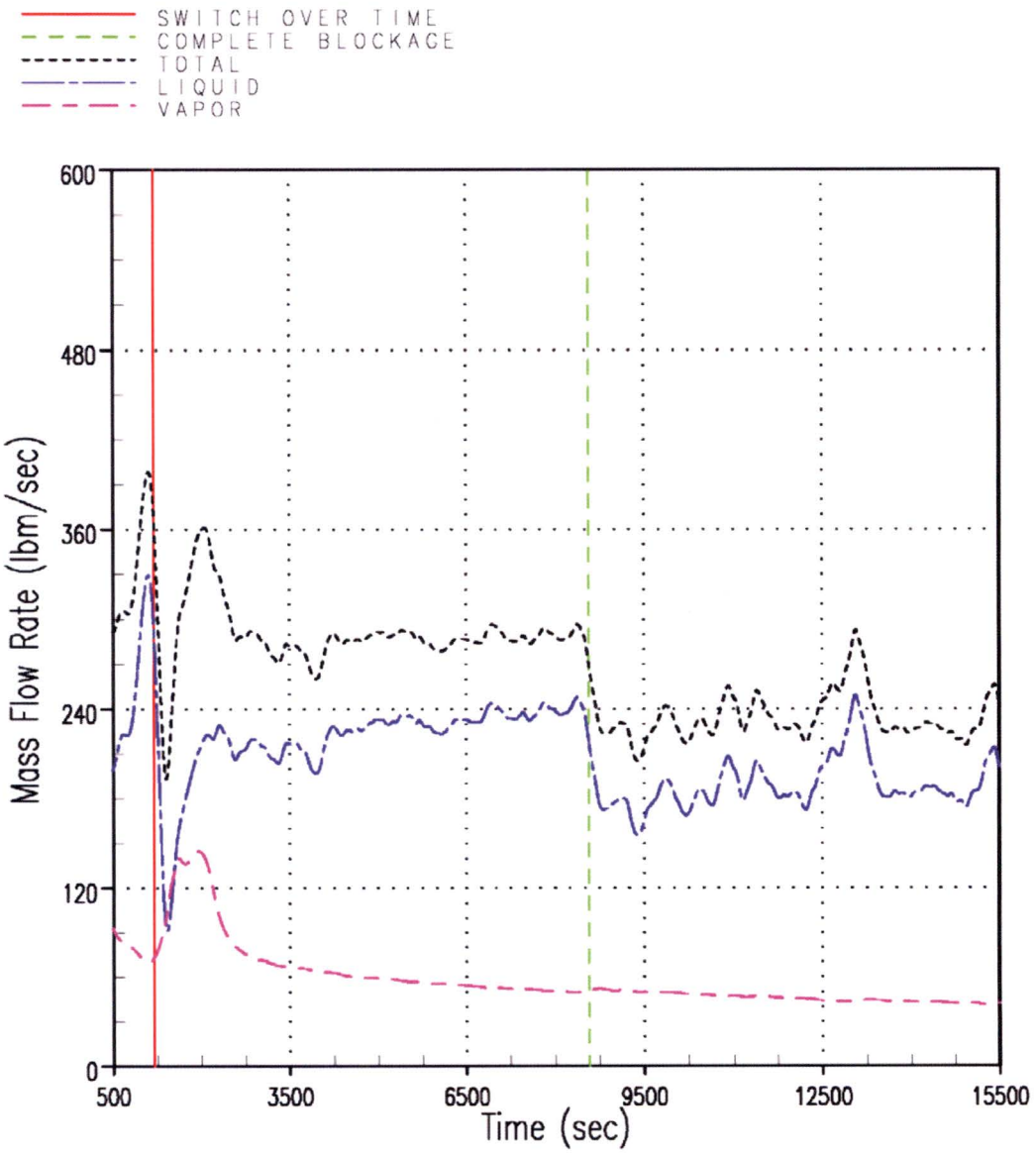

Figure RAI-4.23-56 Case 2B – Mass Flow Rates through the Vessel Side of the DEG Break

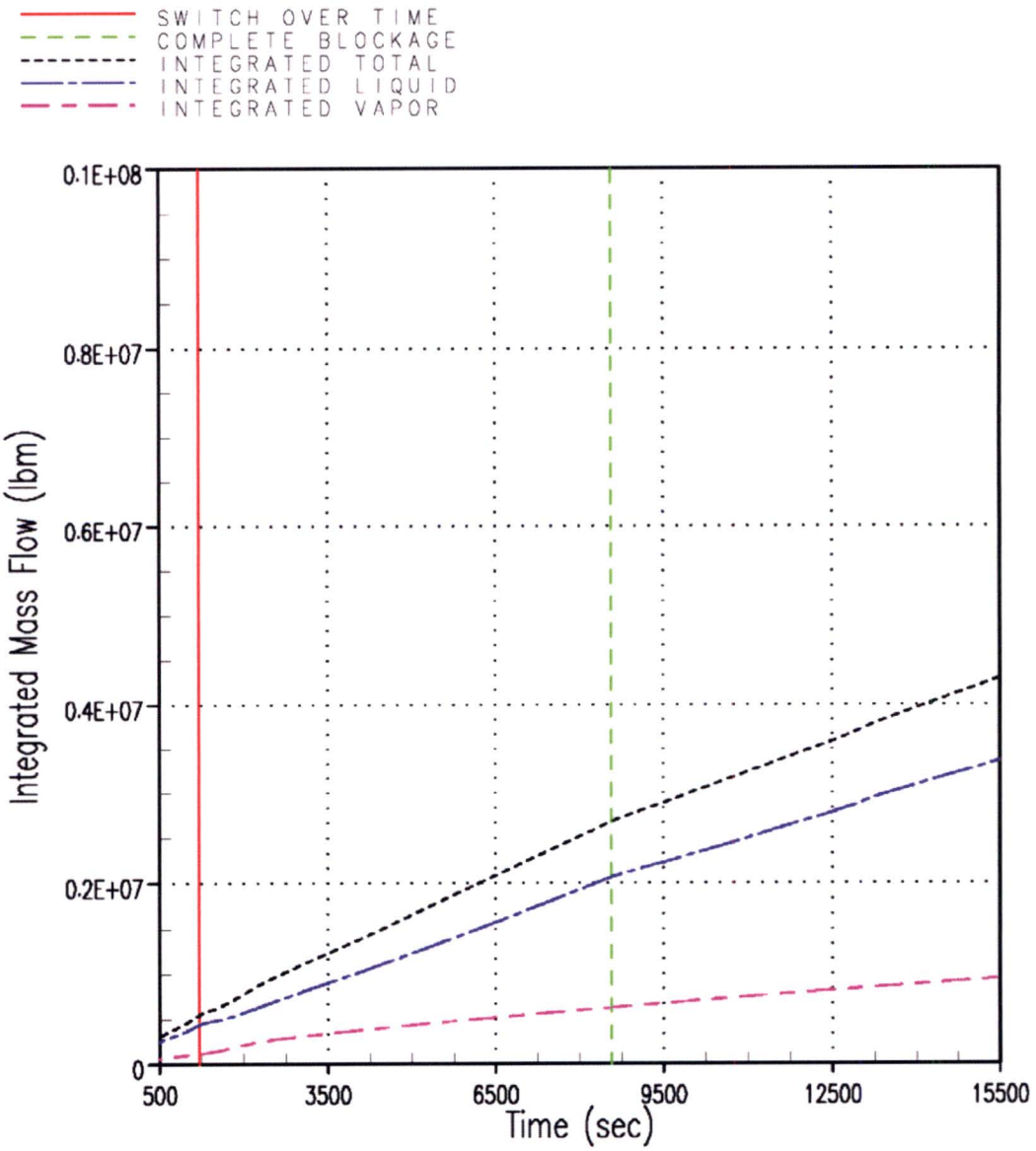

Figure RAI-4.23-57 Case 2B – Integrated Mass Flow through the Vessel Side of the DEG Break

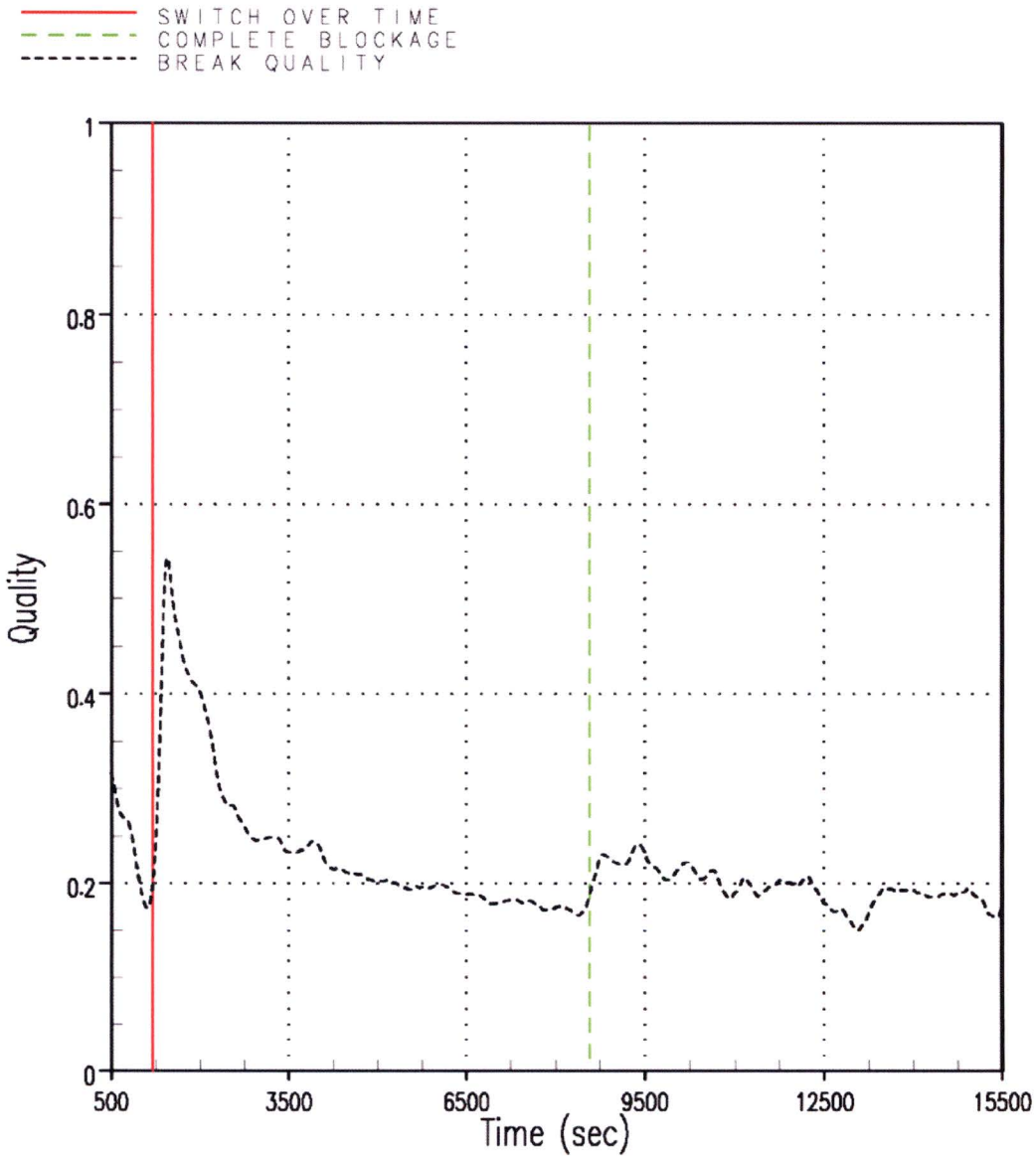

Figure RAI-4.23-58 Case 2B – Break Exit Quality – Vessel Side of DEG Break

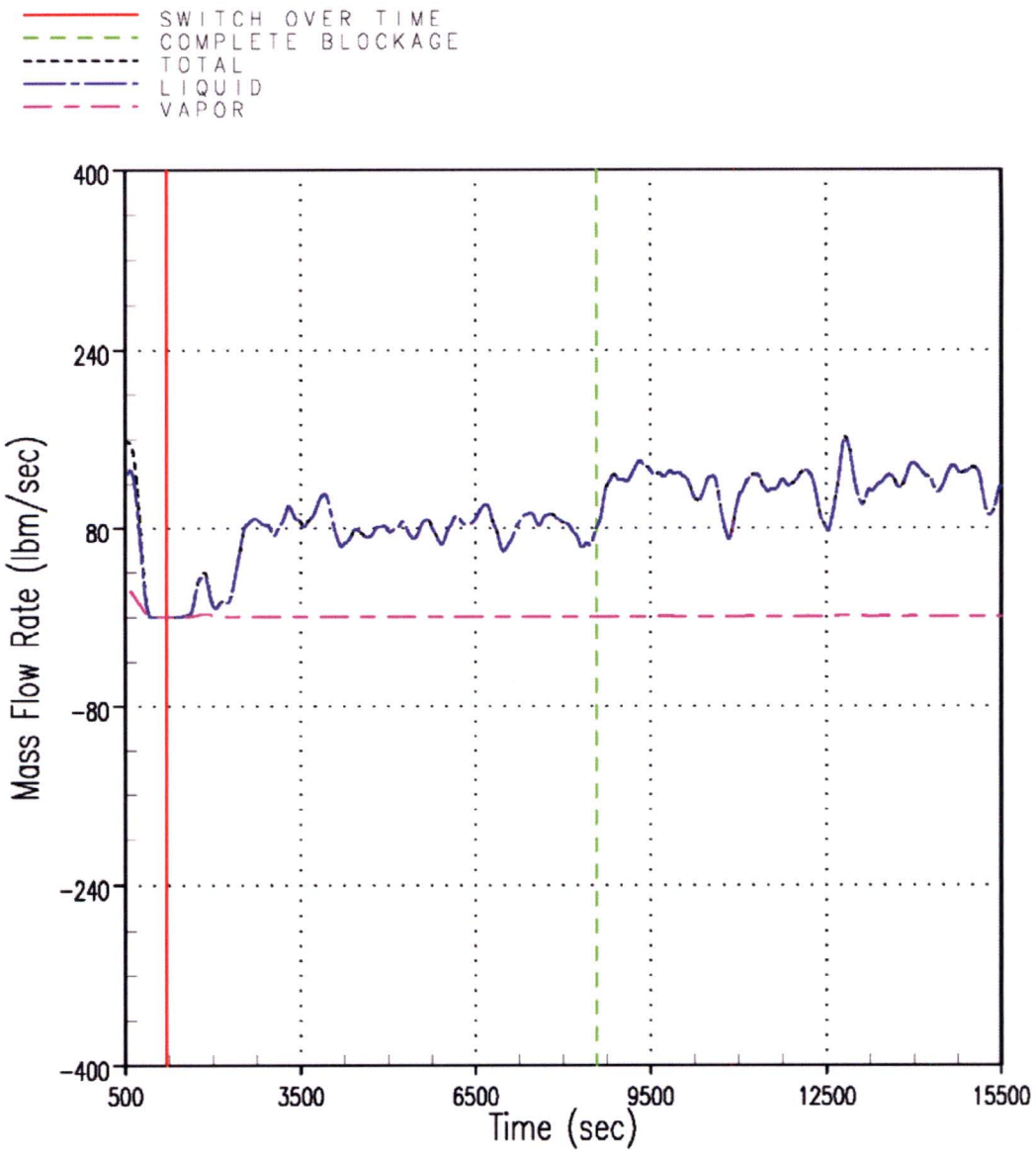

Figure RAI-4.23-59 Case 2B – Mass Flow Rates through the SG Side of the DEG Break

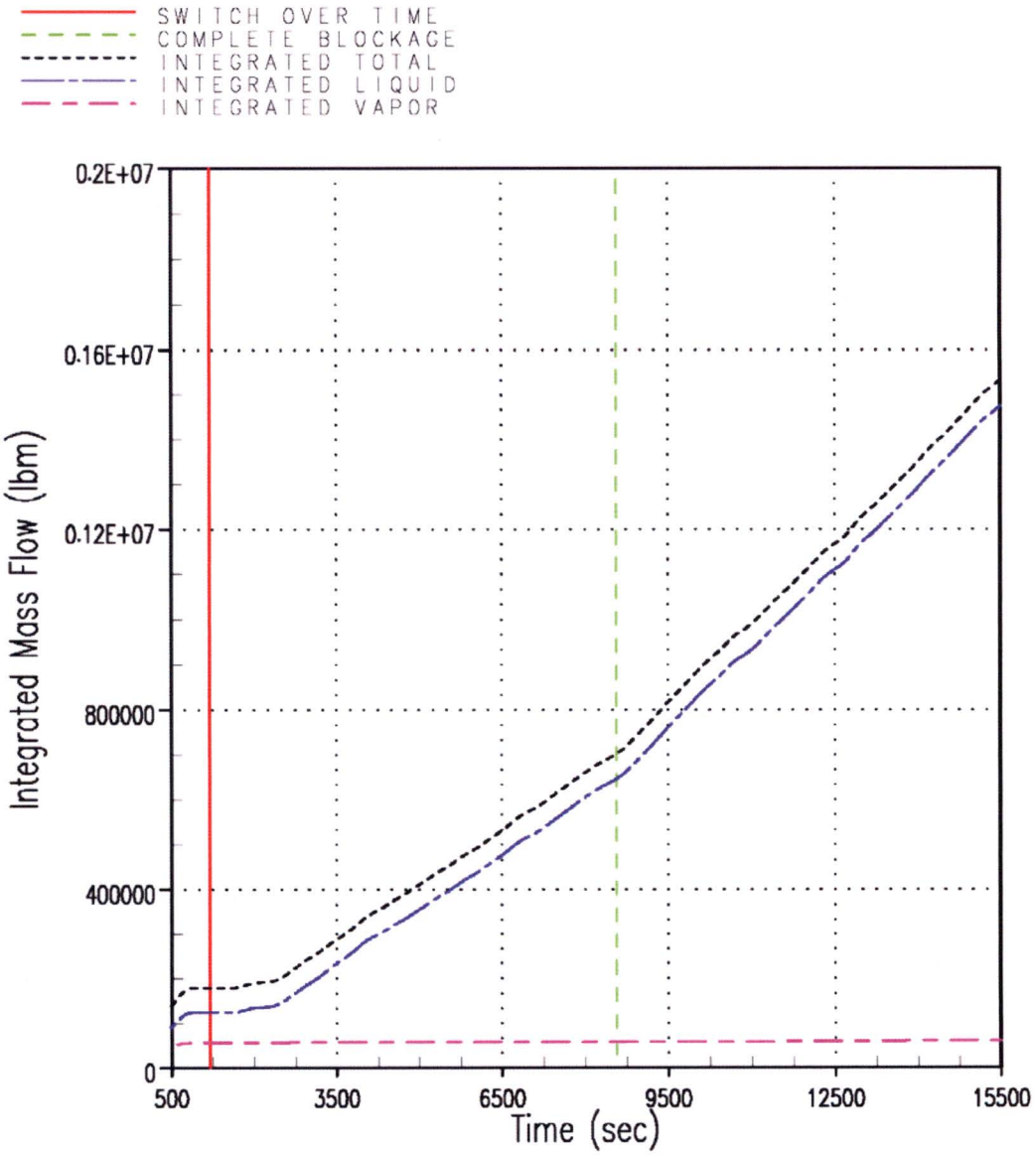

Figure RAI-4.23-60 Case 2B – Integrated Mass Flow through the SG Side of the DEG Break

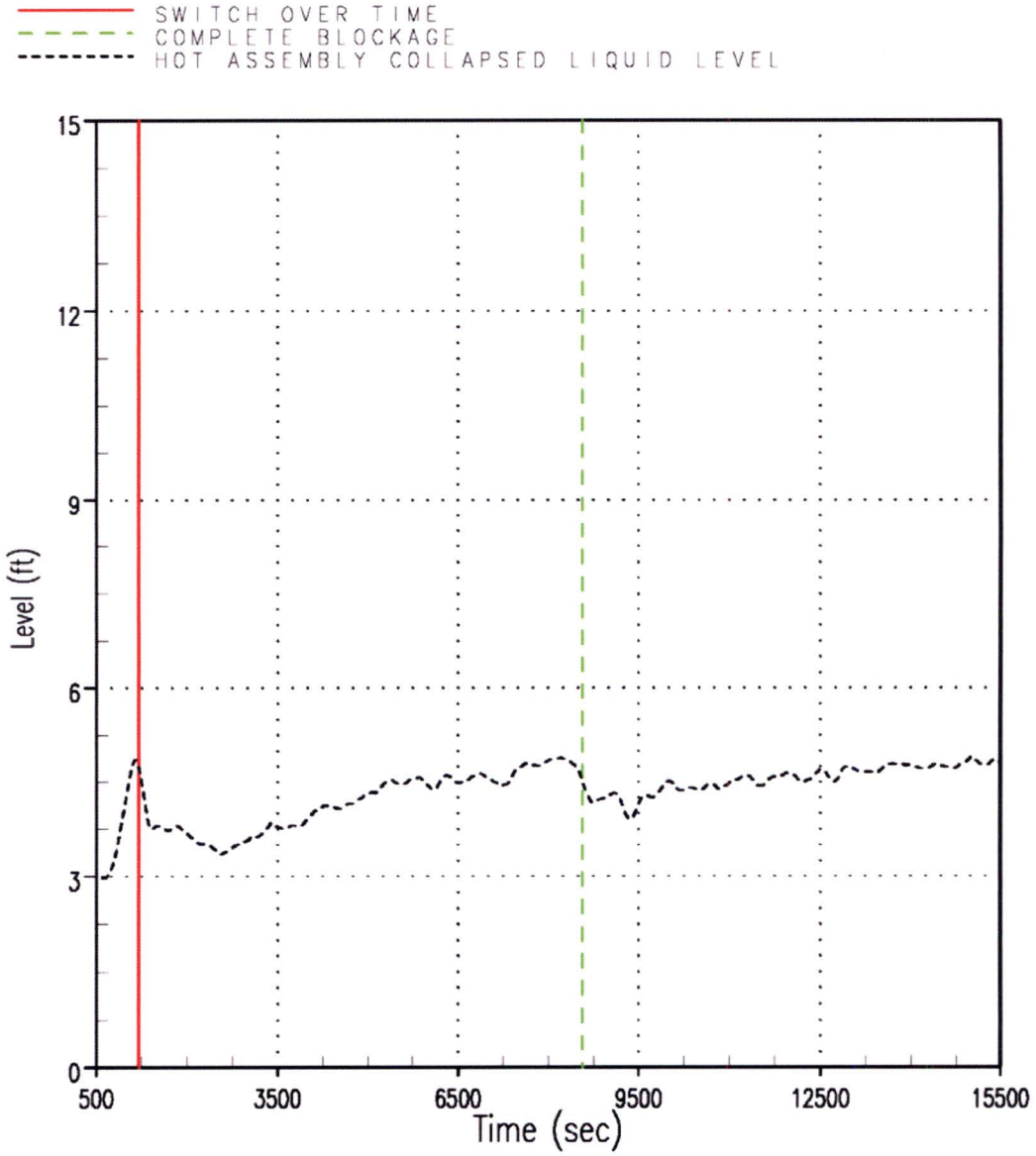

Figure RAI-4.23-61 Case 2B – Hot Assembly CLL

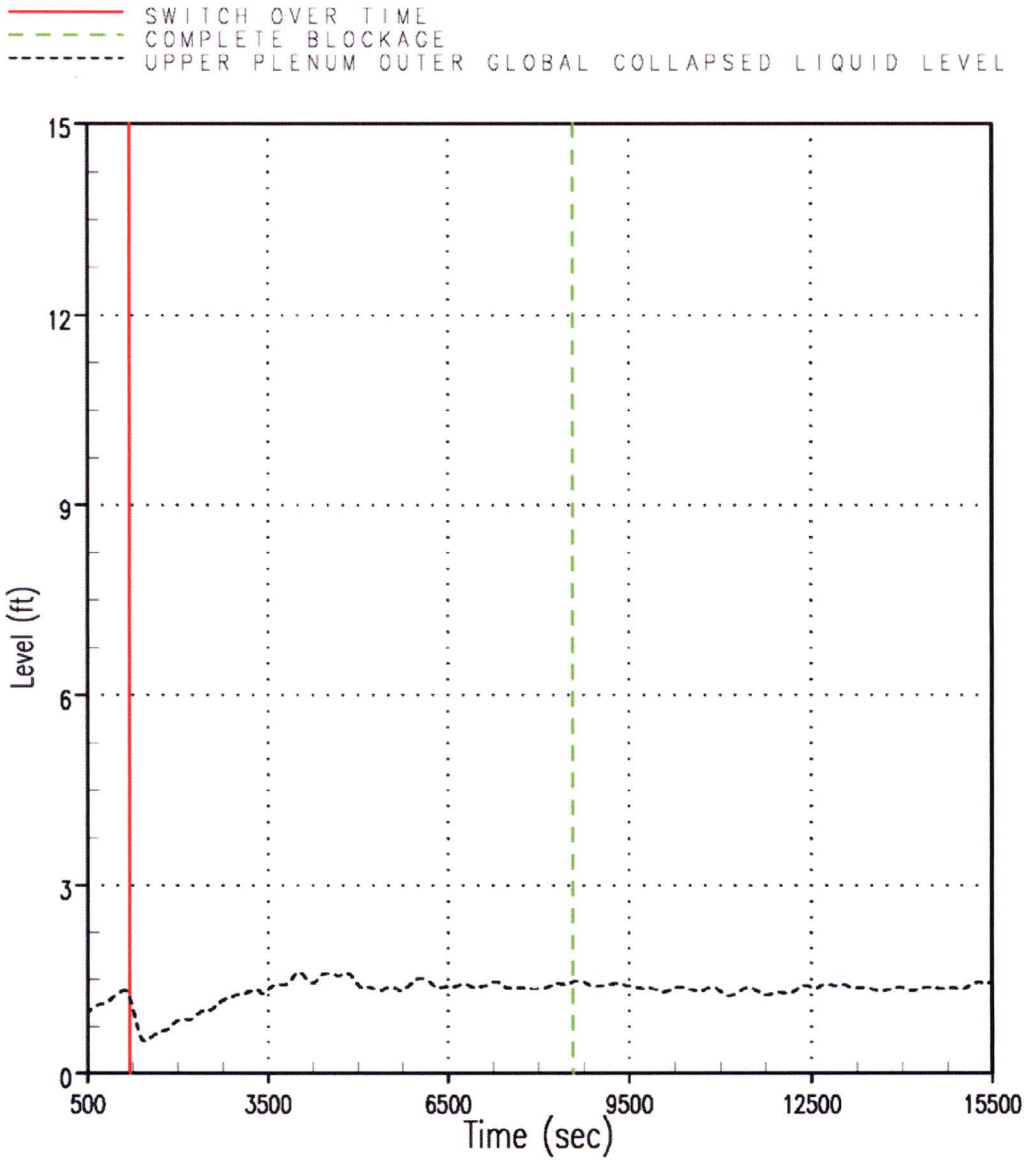

Figure RAI-4.23-62 Case 2B – UP Outer Global CLL

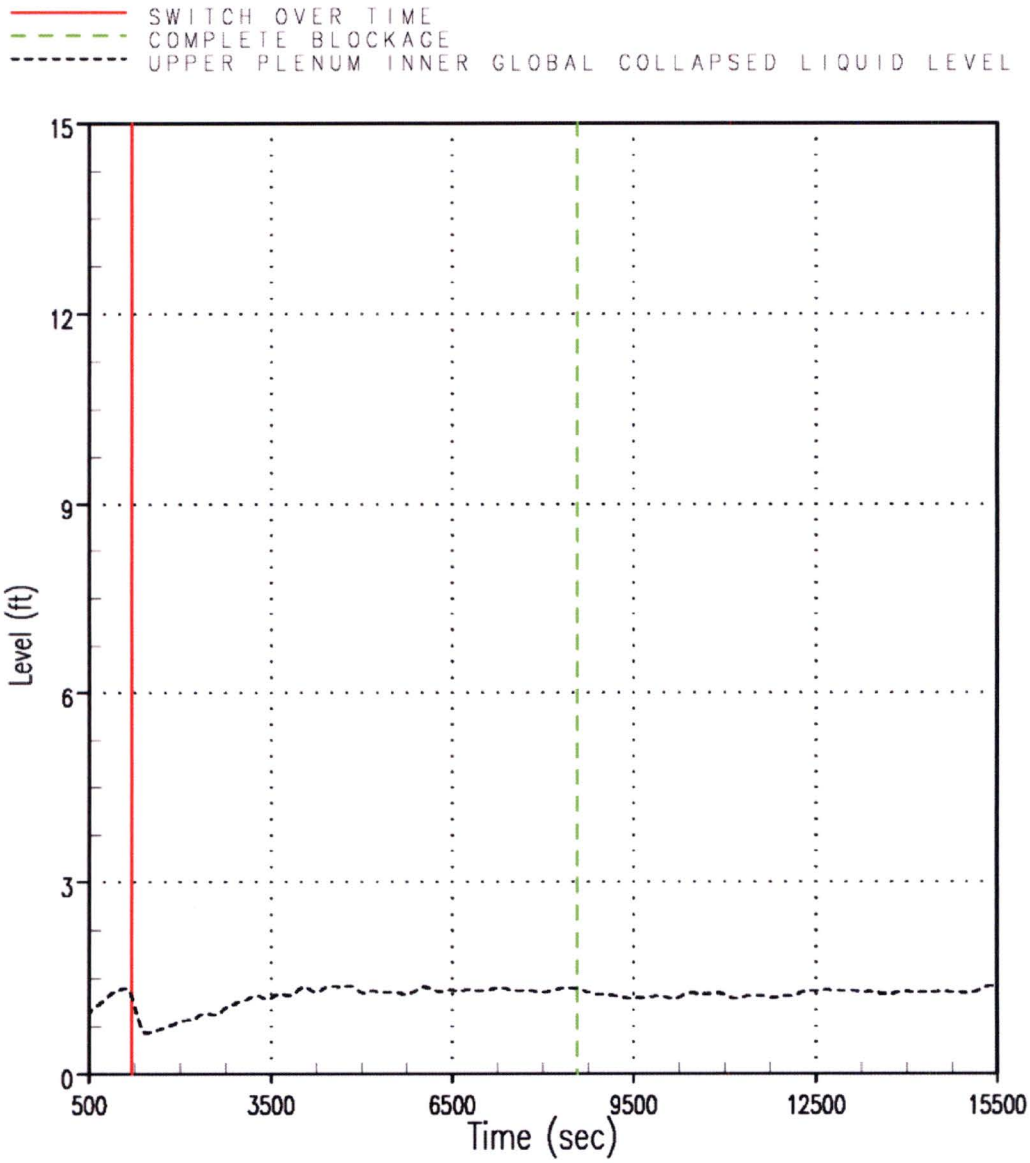

Figure RAI-4.23-63 Case 2B – UP Inner Global CLL

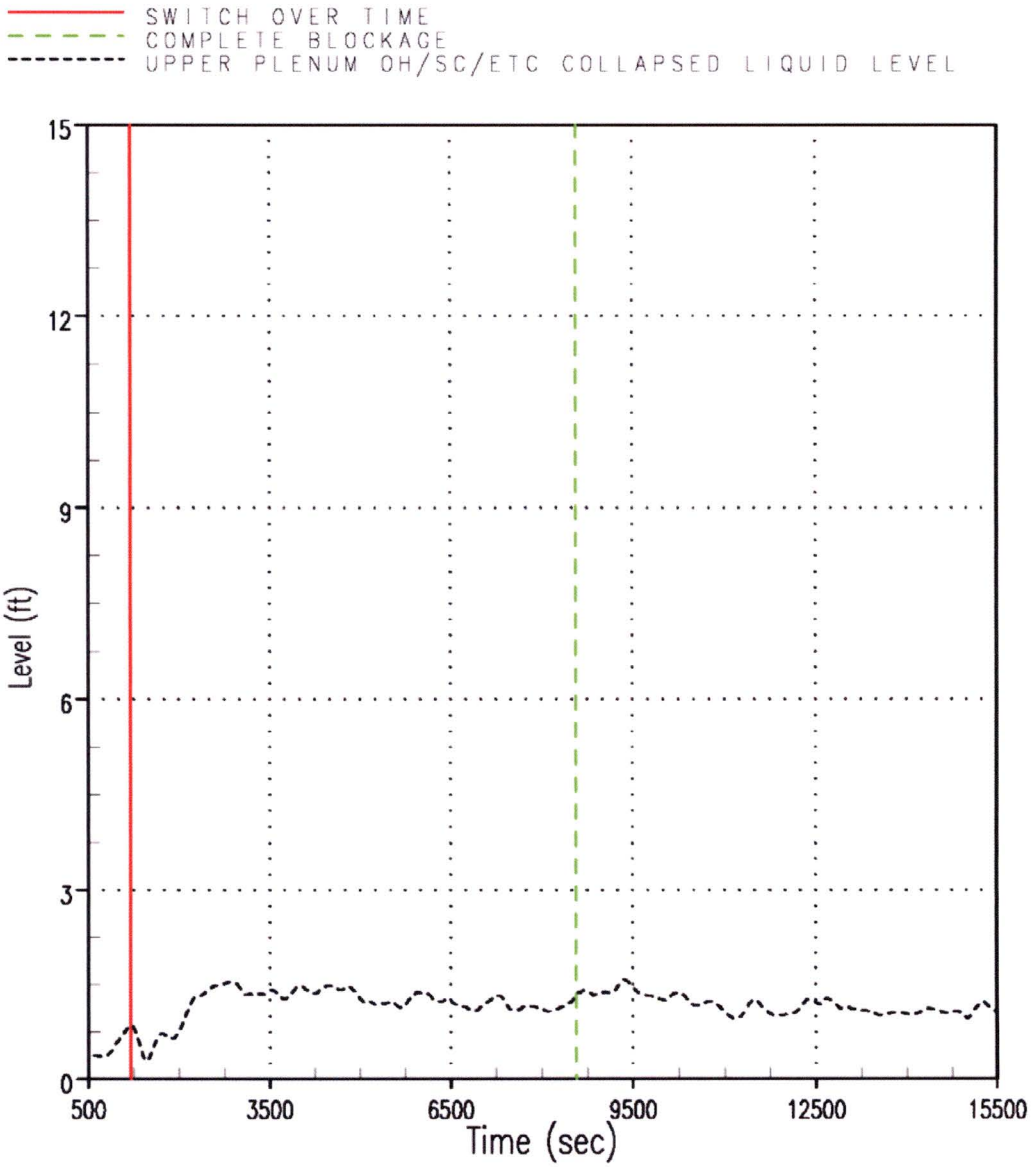

Figure RAI-4.23-64 Case 2B – UP Open Hole / Support Column / etc CLL

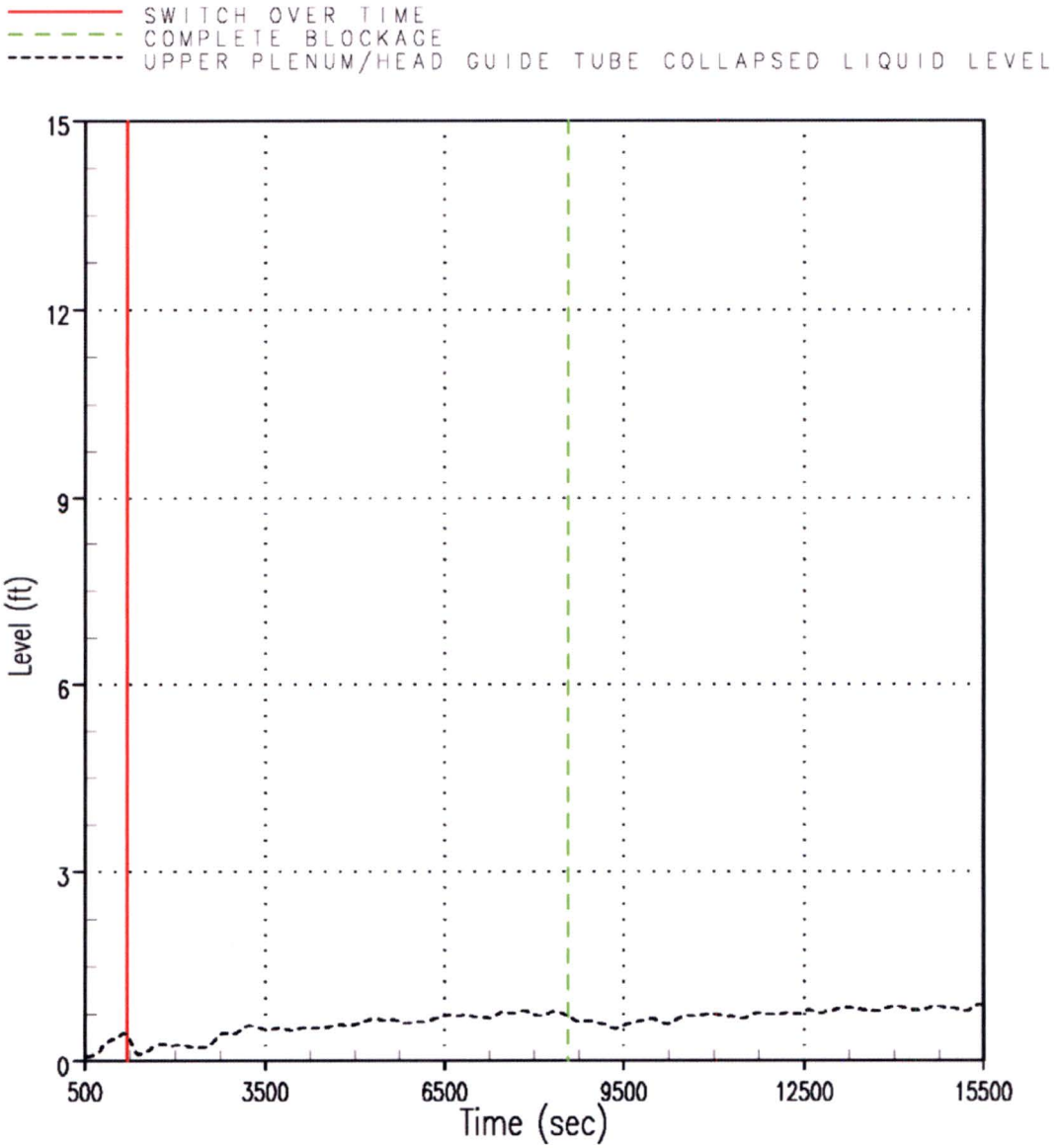

Figure RAI-4.23-65 Case 2B – UP / Upper Head Guide Tube CLL

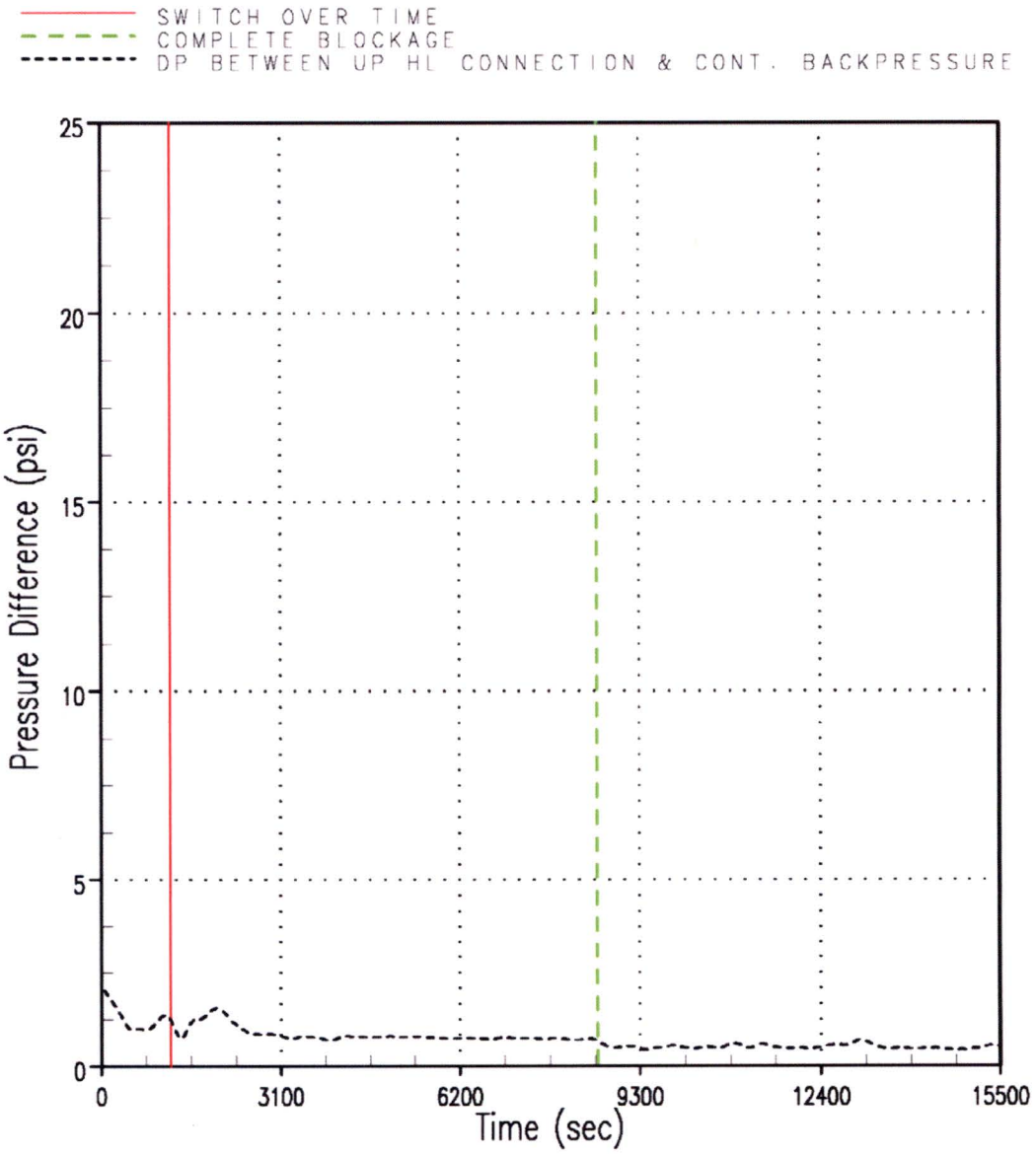

Figure RAI-4.23-66 Case 2B – Delta P between Upper Head Channel Connection to Broken HL and Containment Backpressure

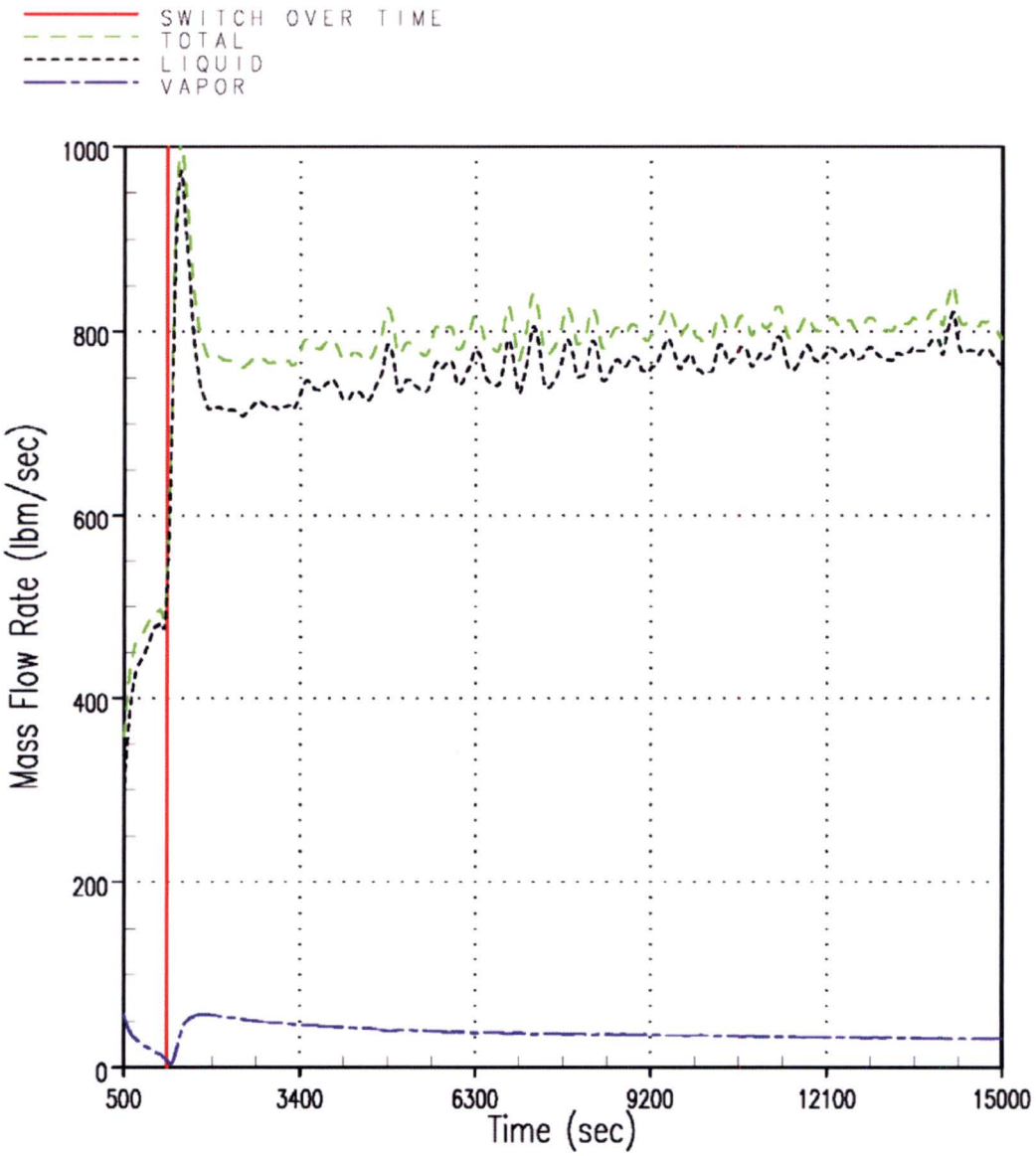

Figure RAI-4.23-67 Case 0A – Mass Flow Rates through the Vessel Side of the DEG Break

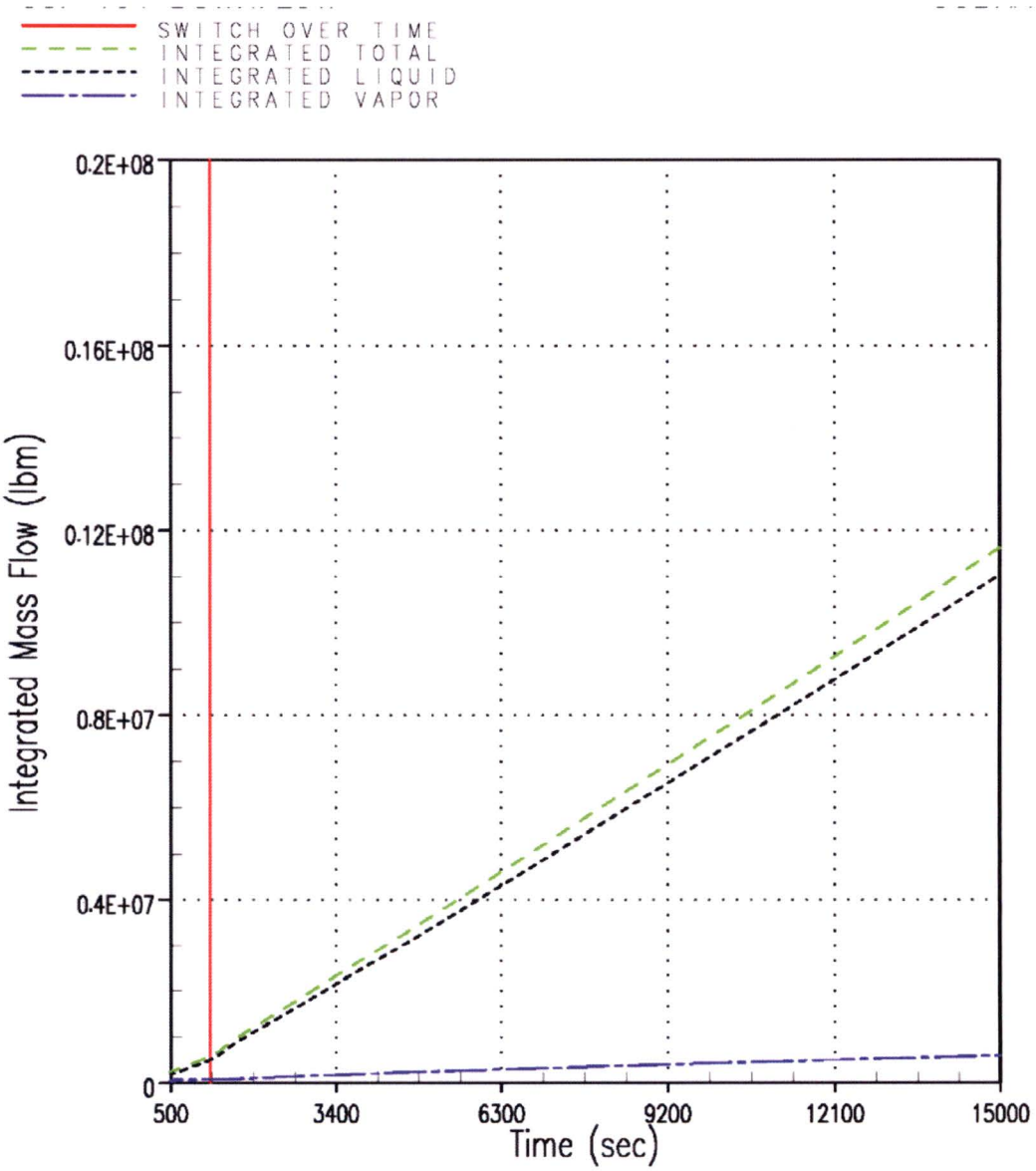

Figure RAI-4.23-68 Case 0A – Integrated Mass Flow through the Vessel Side of the DEG Break

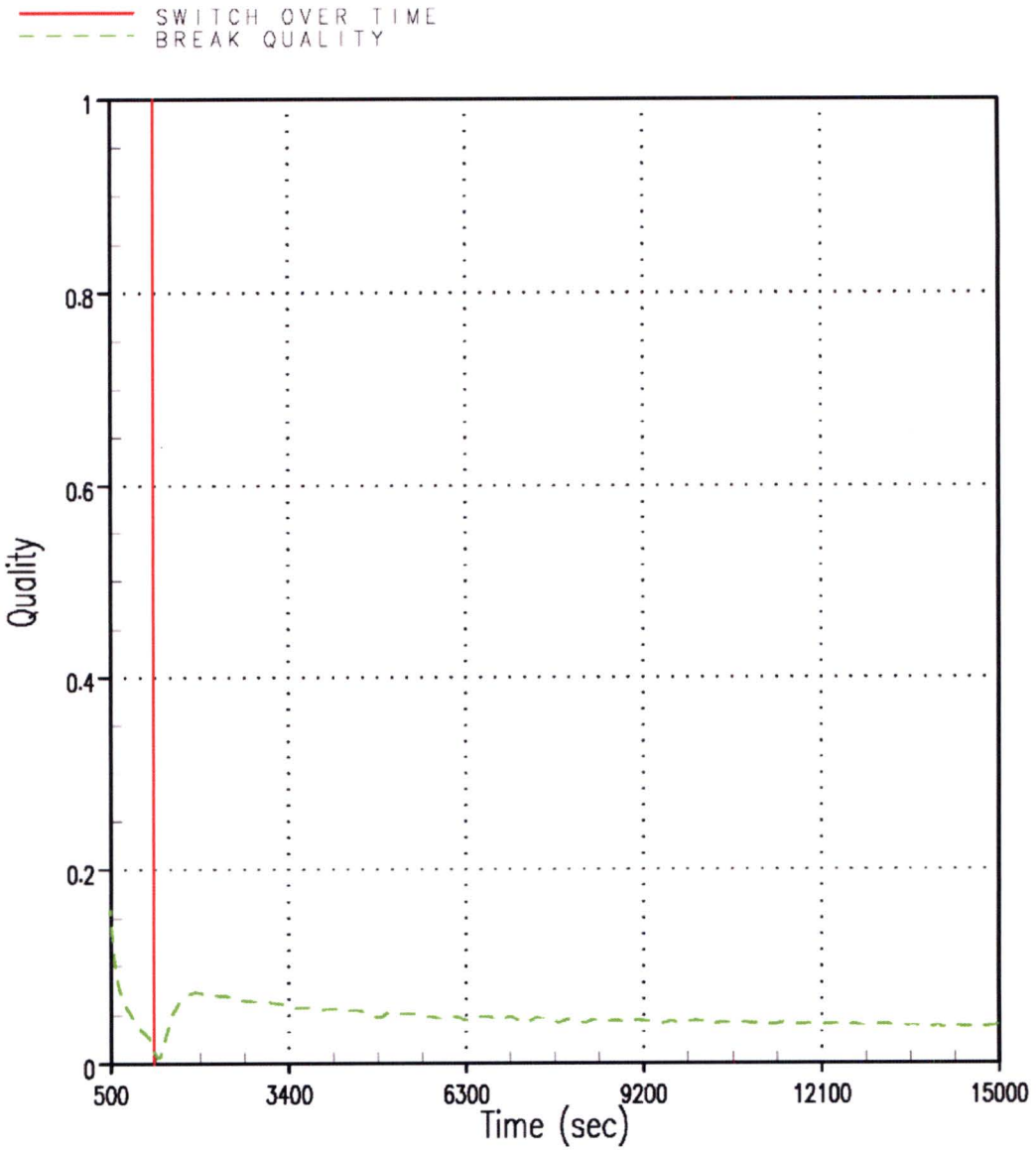

Figure RAI-4.23-69 Case 0A – Break Exit Quality – Vessel Side of DEG Break

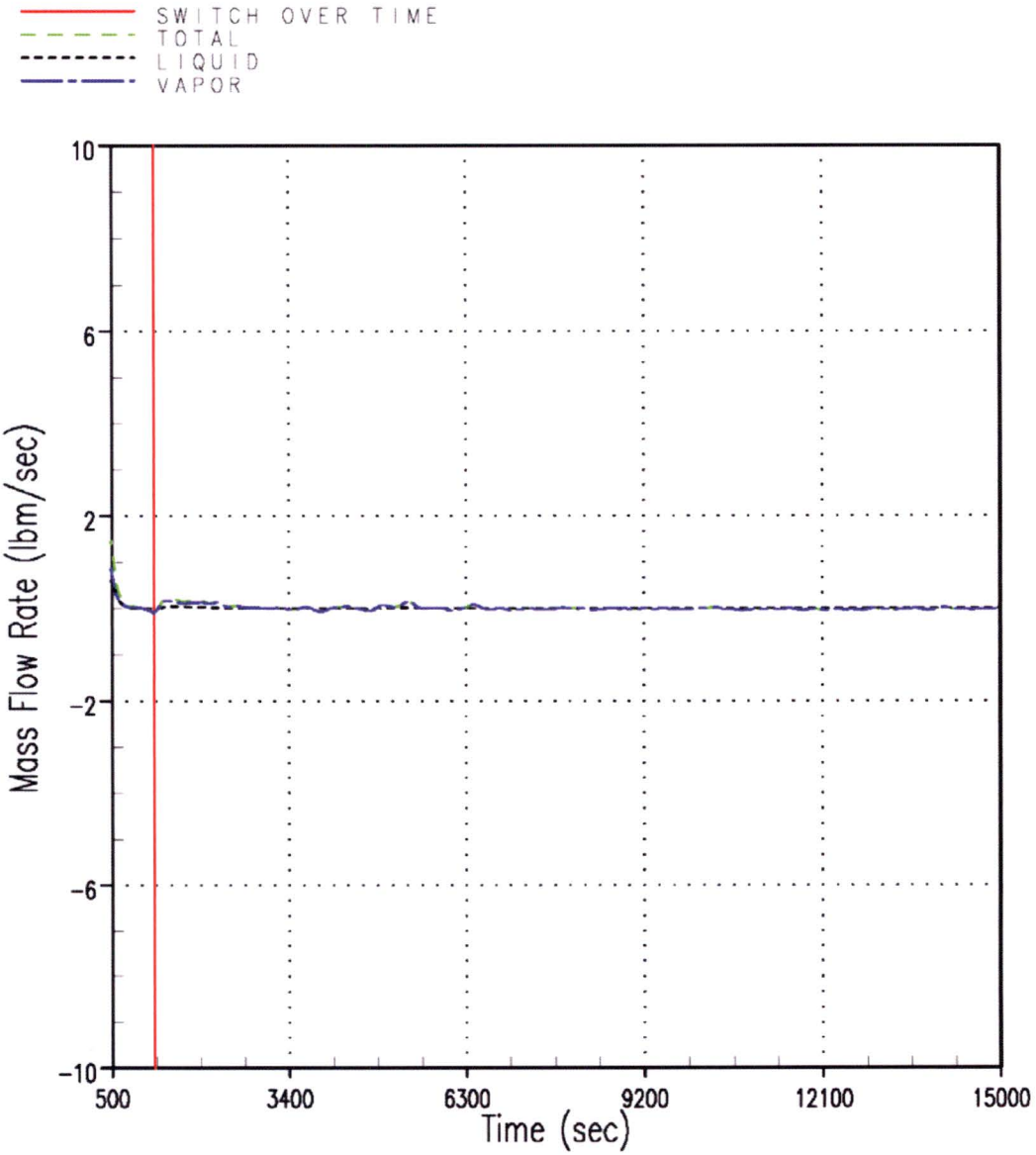

Figure RAI-4.23-70 Case 0A – Mass Flow Rates through the SG Side of the DEG Break

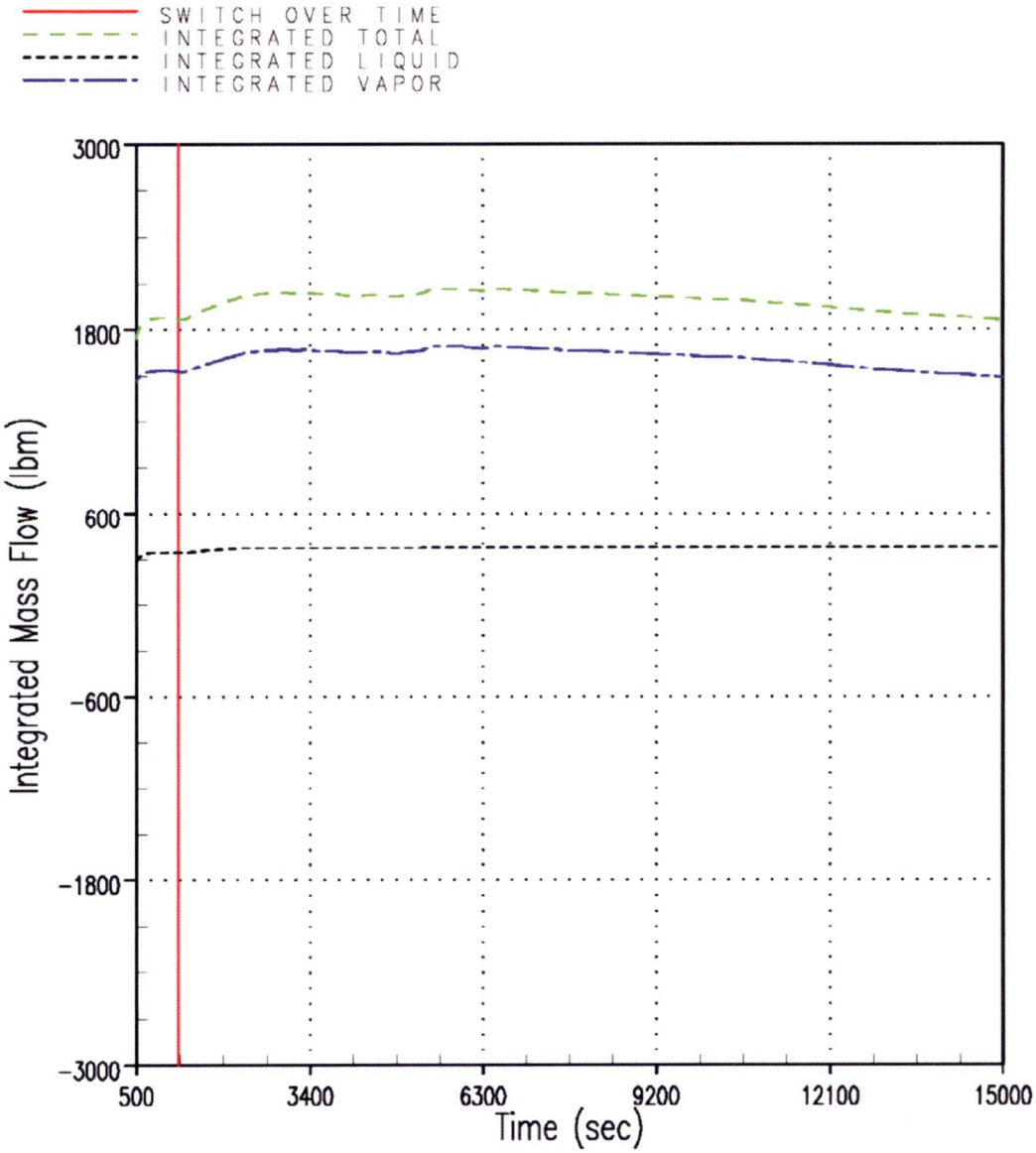

Figure RAI-4.23-71 Case 0A – Integrated Mass Flow through the SG Side of the DEG Break

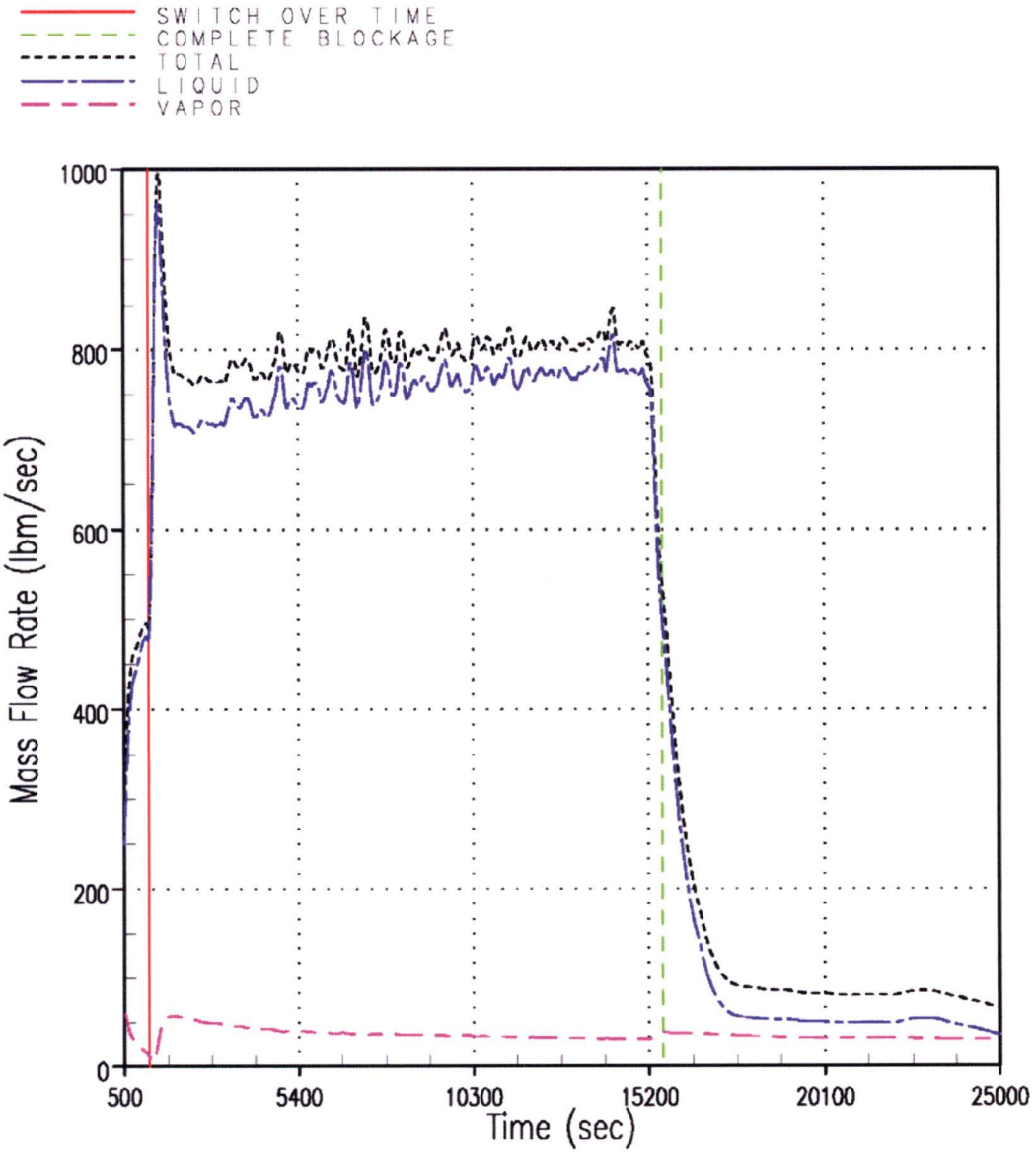

Figure RAI-4.23-72 Case 1A – Mass Flow Rates through the Vessel Side of the DEG Break

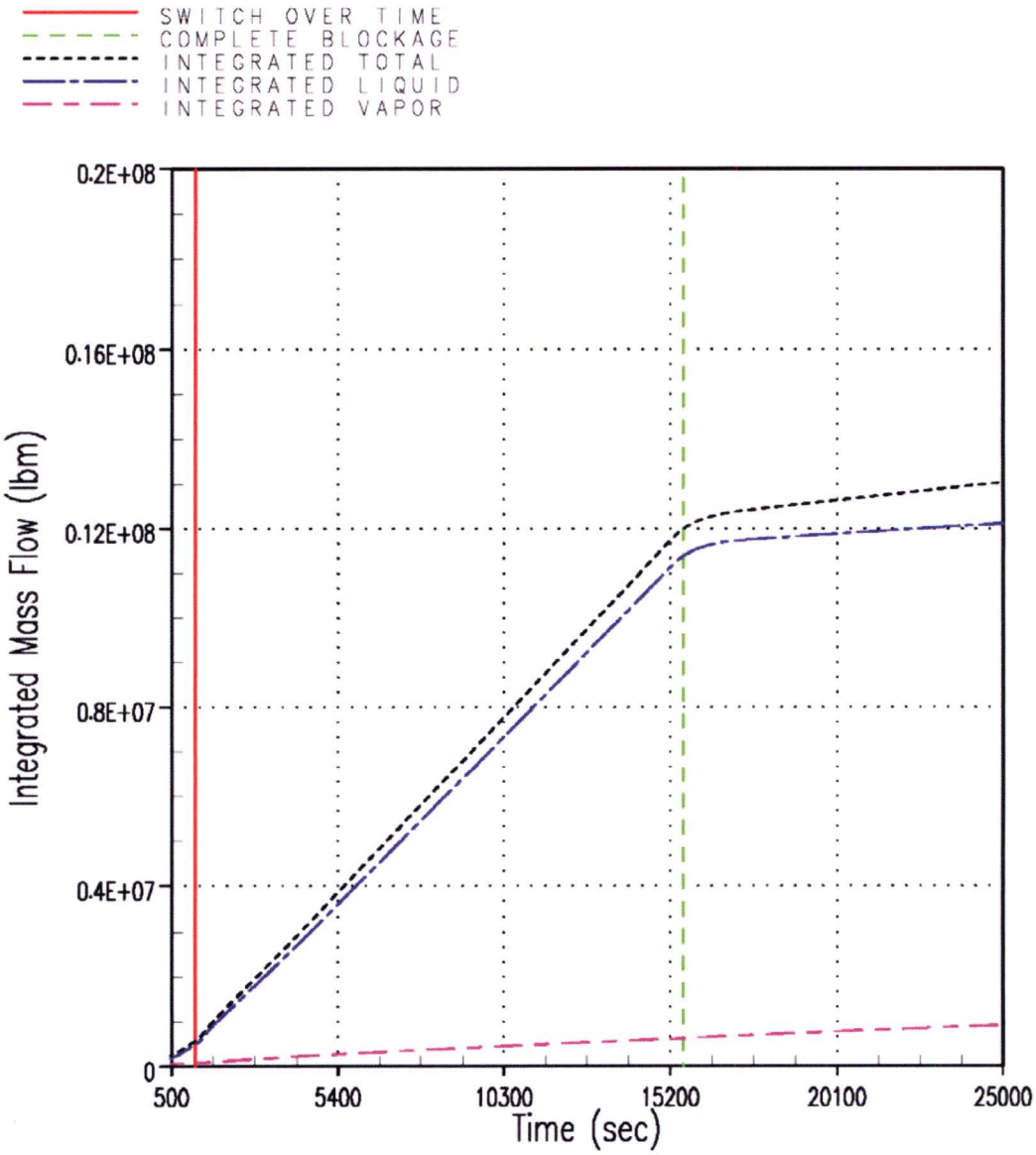

Figure RAI-4.23-73 Case 1A – Integrated Mass Flow through the Vessel Side of the DEG Break

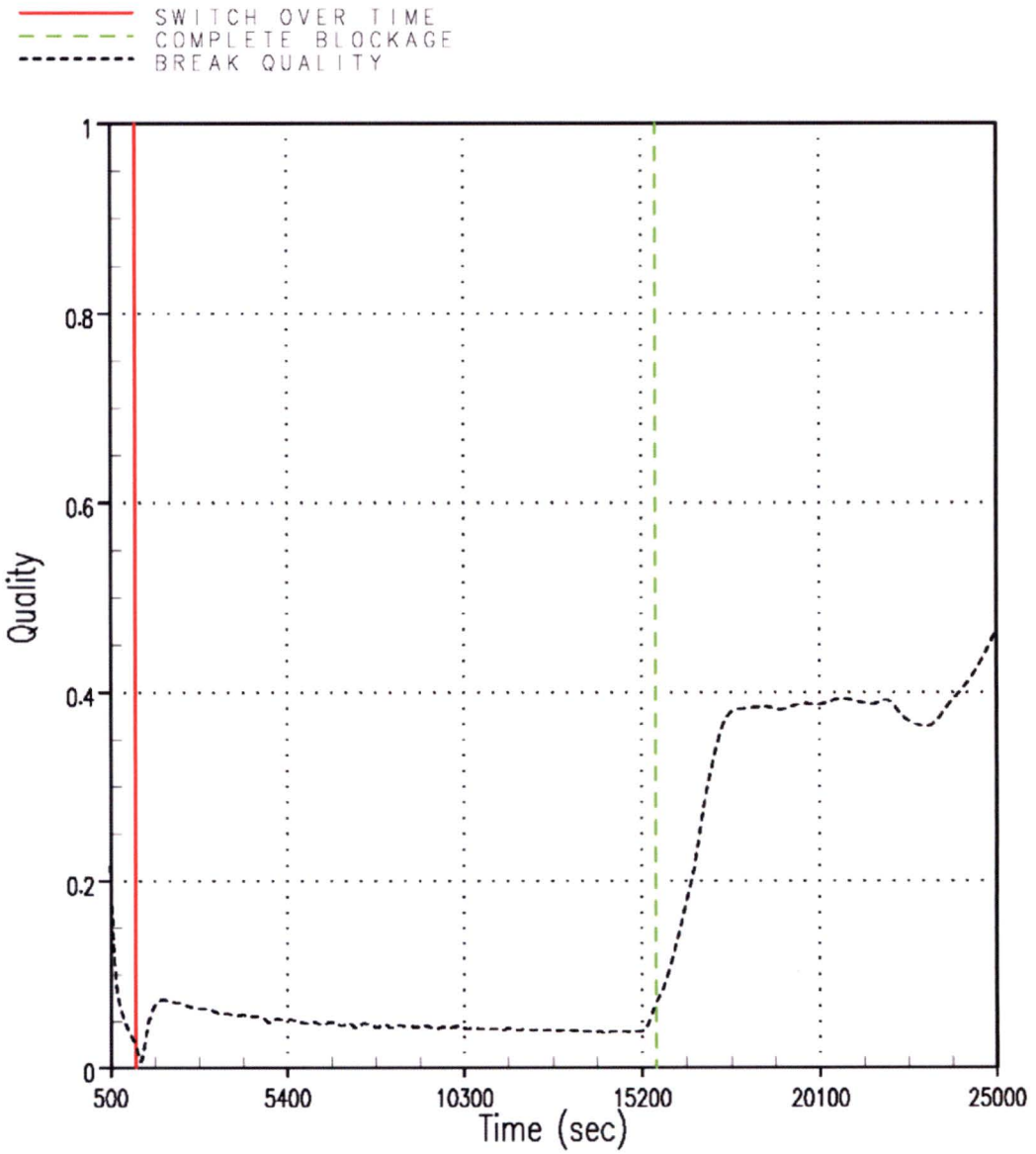

Figure RAI-4.23-74 Case 1A – Break Exit Quality – Vessel Side of DEG Break

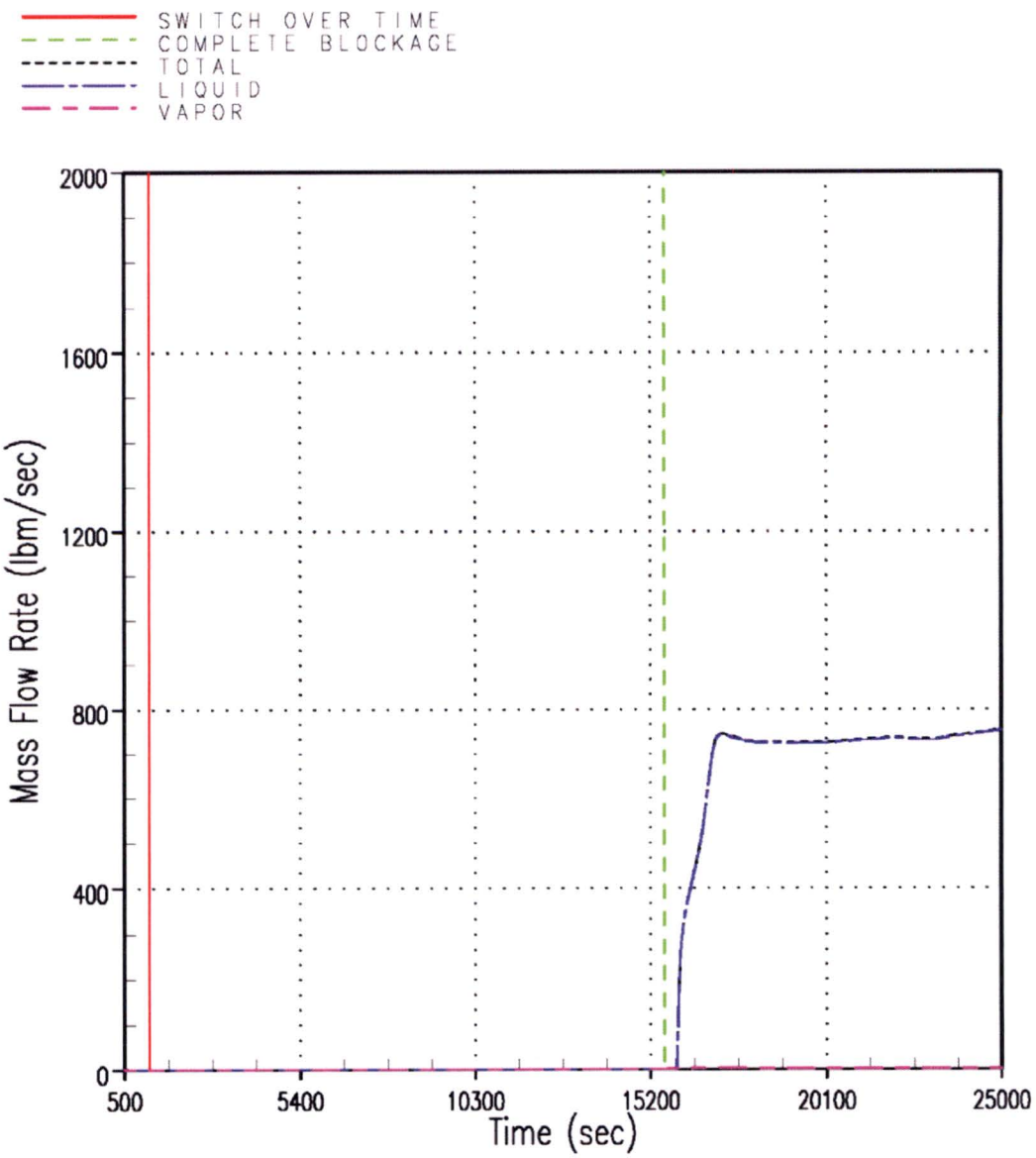

Figure RAI-4.23-75 Case 1A – Mass Flow Rates through the SG Side of the DEG Break

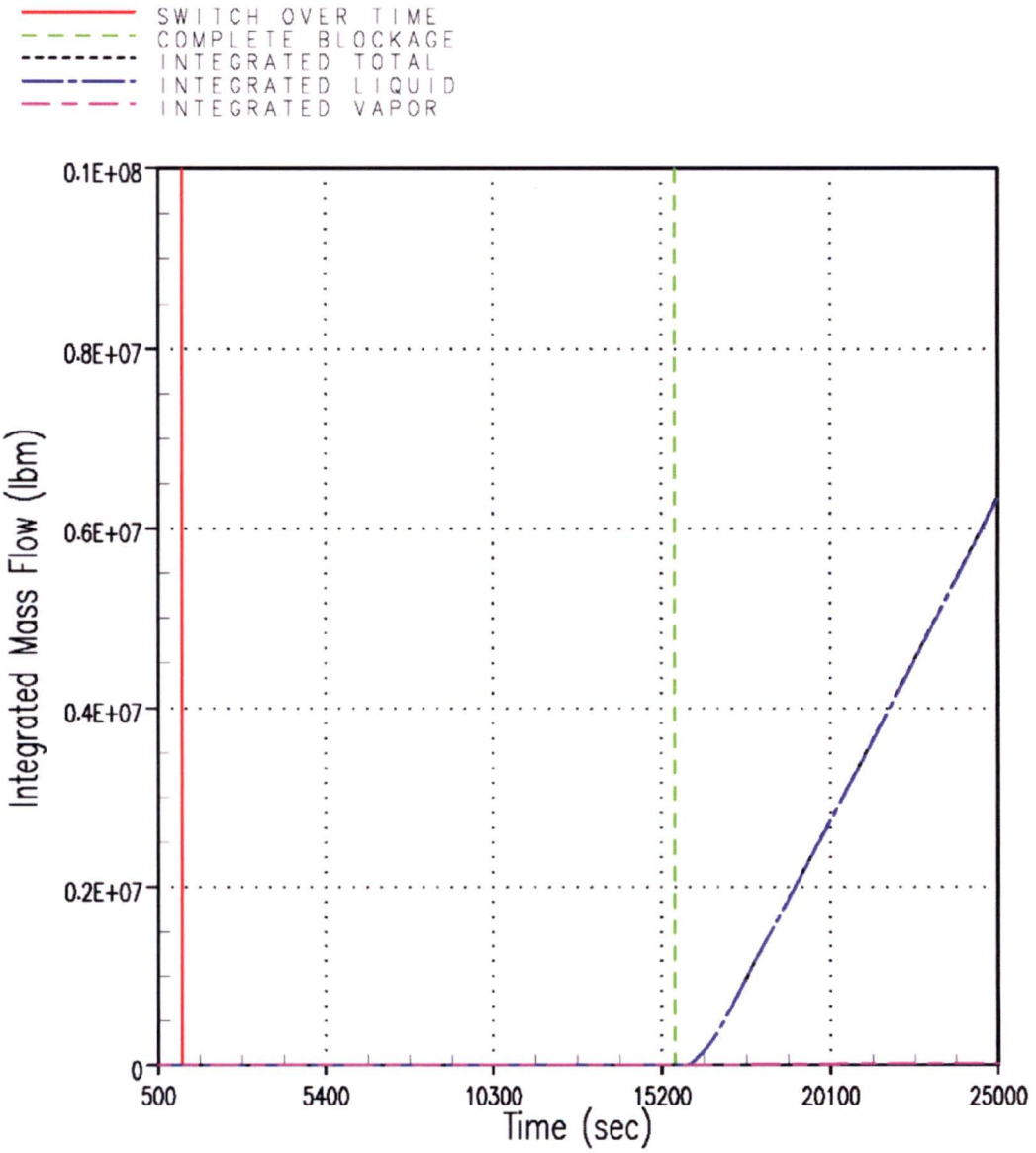

Figure RAI-4.23-76 Case 1A – Integrated Mass Flow through the SG Side of the DEG Break

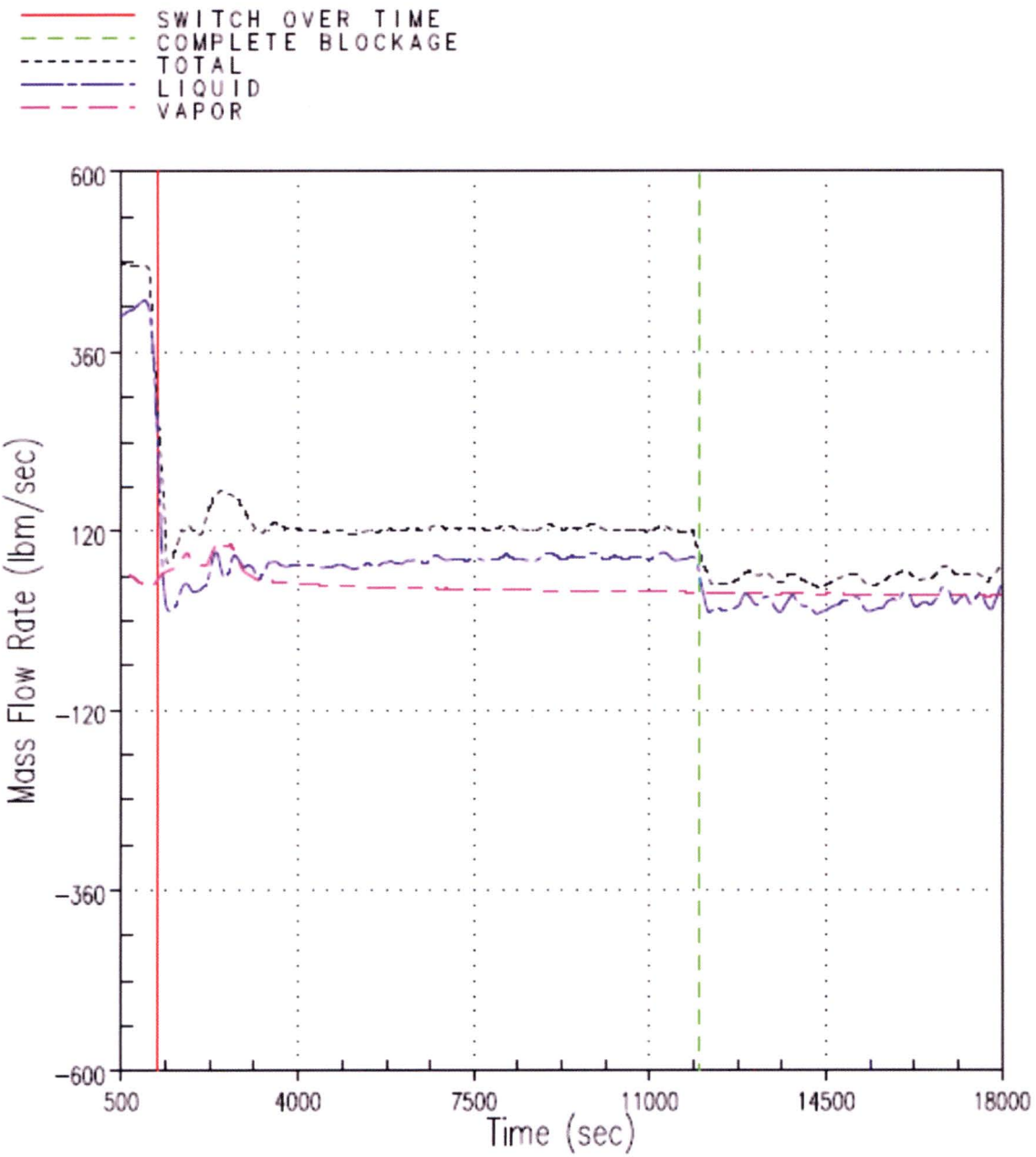

Figure RAI-4.23-77 Case 2B – Mass Flow Rates through the Vessel Side of the DEG Break

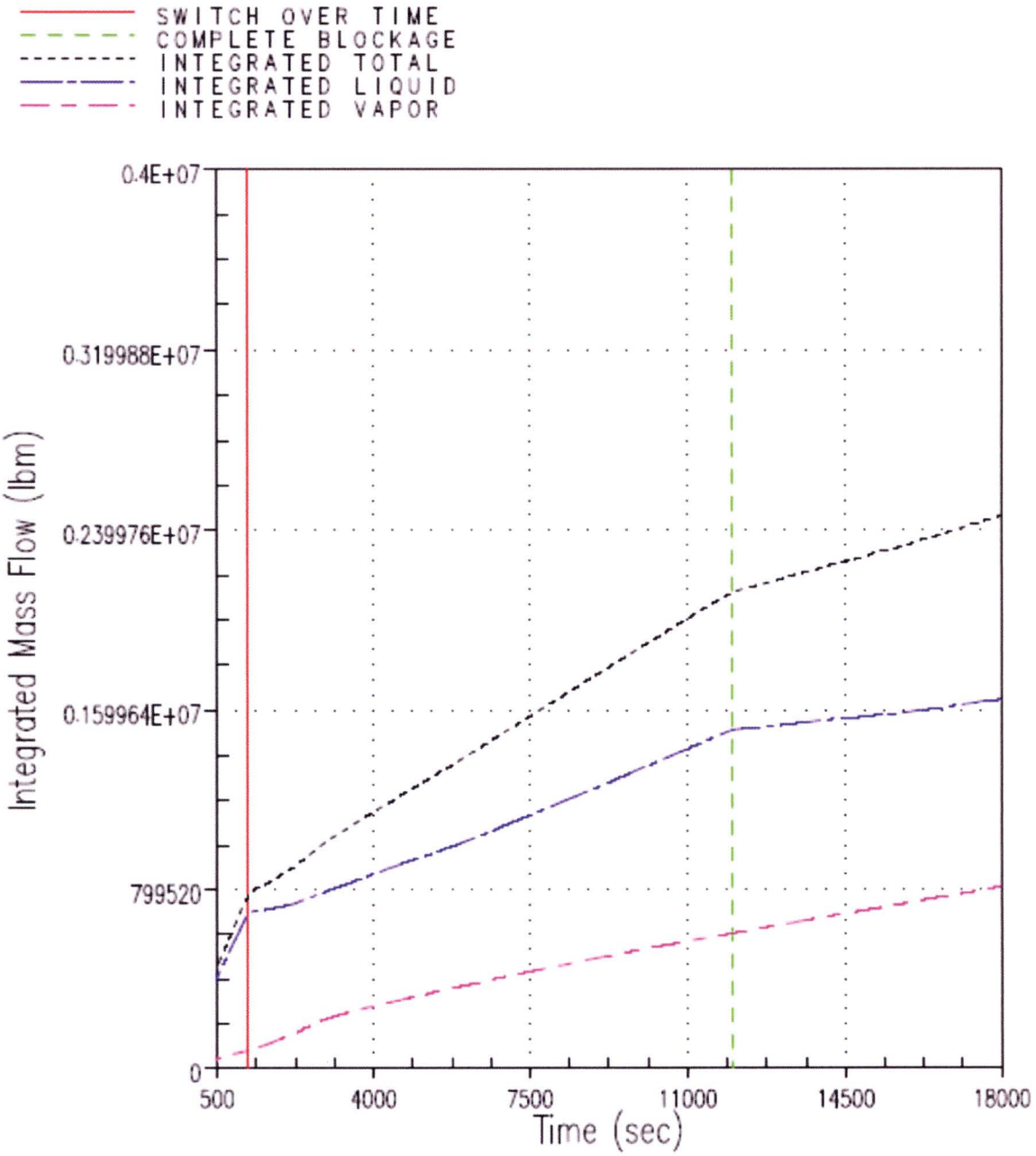

Figure RAI-4.23-78 Case 2B – Integrated Mass Flow through the Vessel Side of the DEG Break

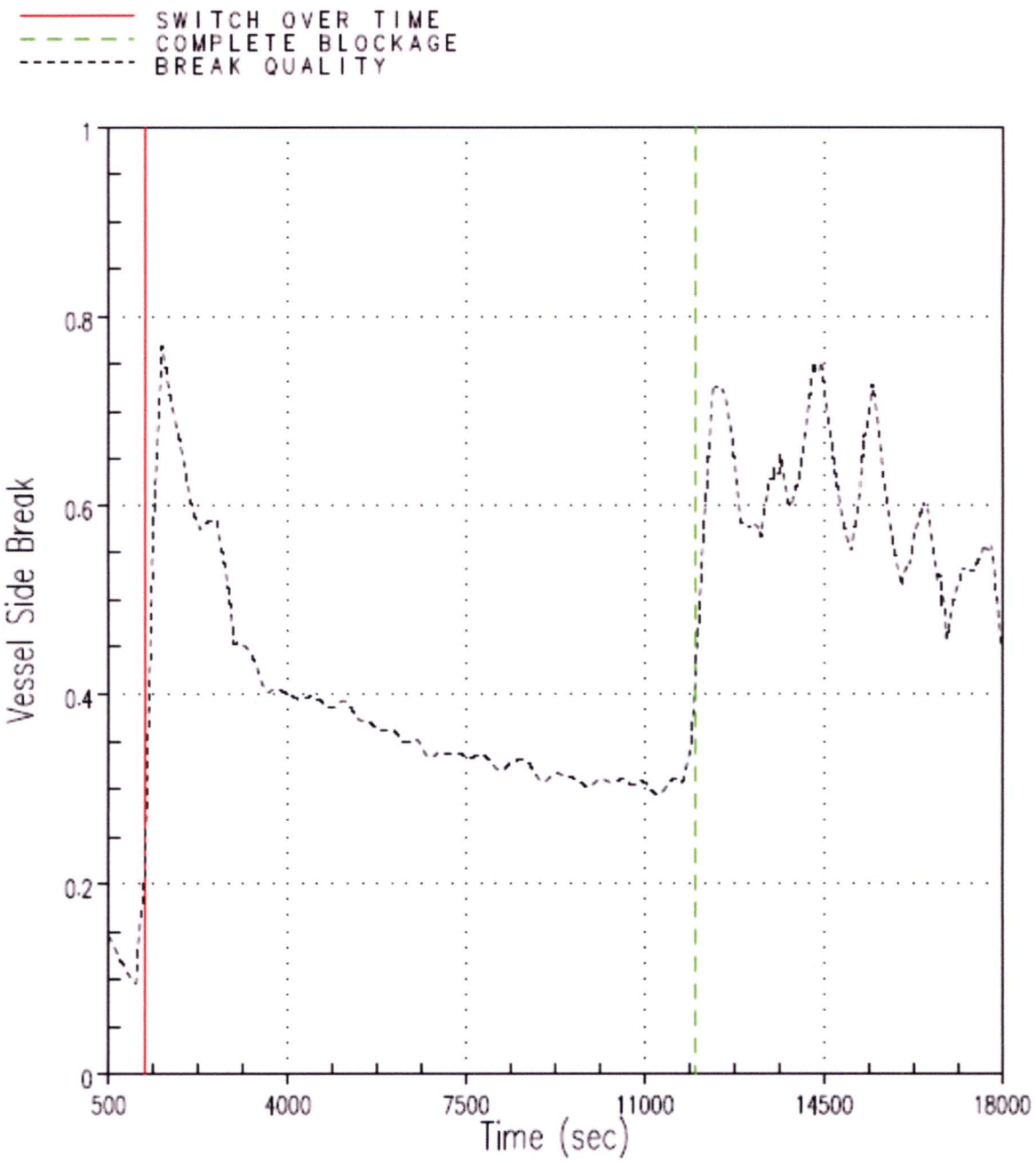

Figure RAI-4.23-79 Case 2B – Break Exit Quality – Vessel Side of DEG Break

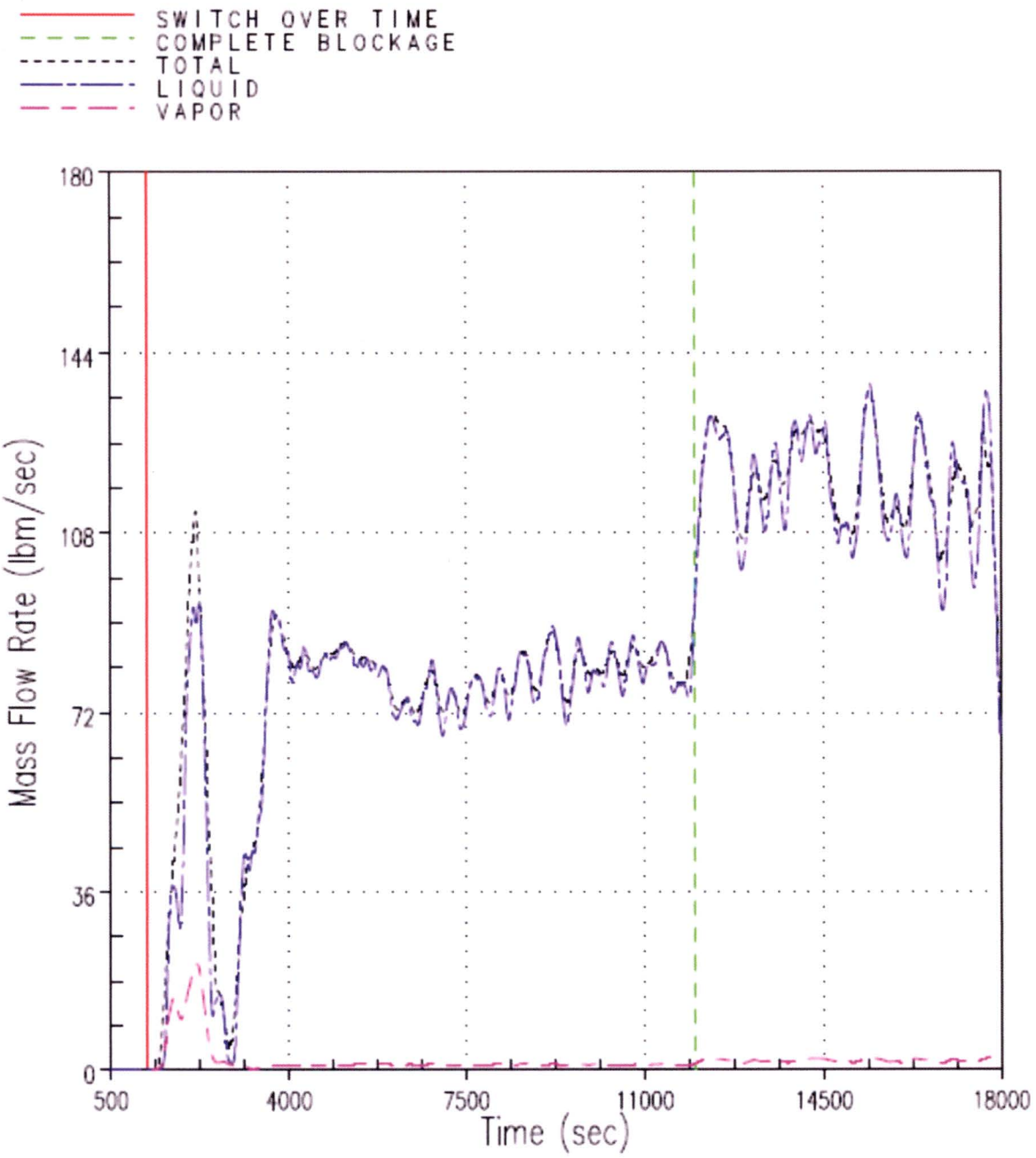

Figure RAI-4.23-80 Case 2B – Mass Flow Rates through the SG Side of the DEG Break

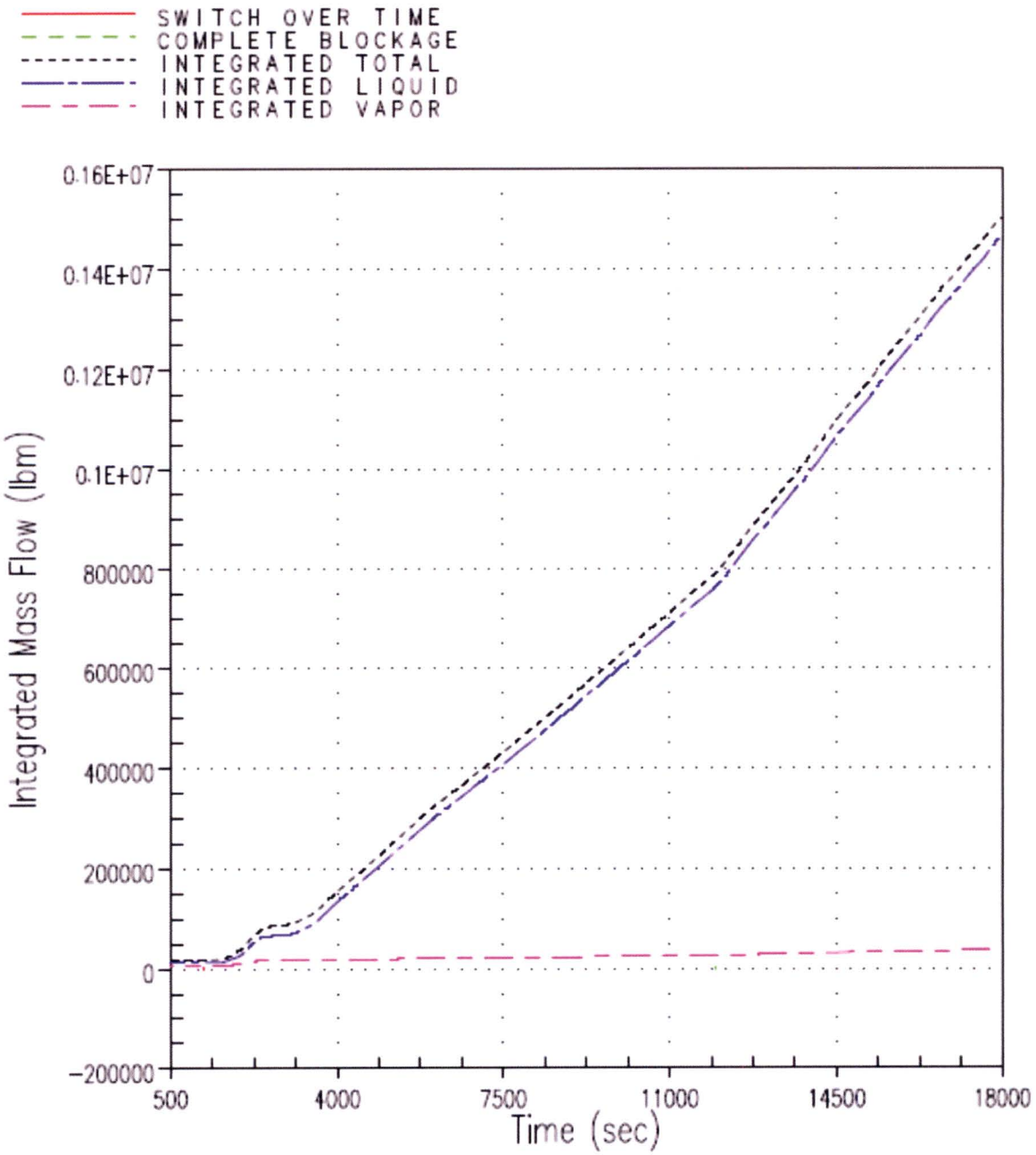

Figure RAI-4.23-81 Case 2B – Integrated Mass Flow through the SG Side of the DEG Break

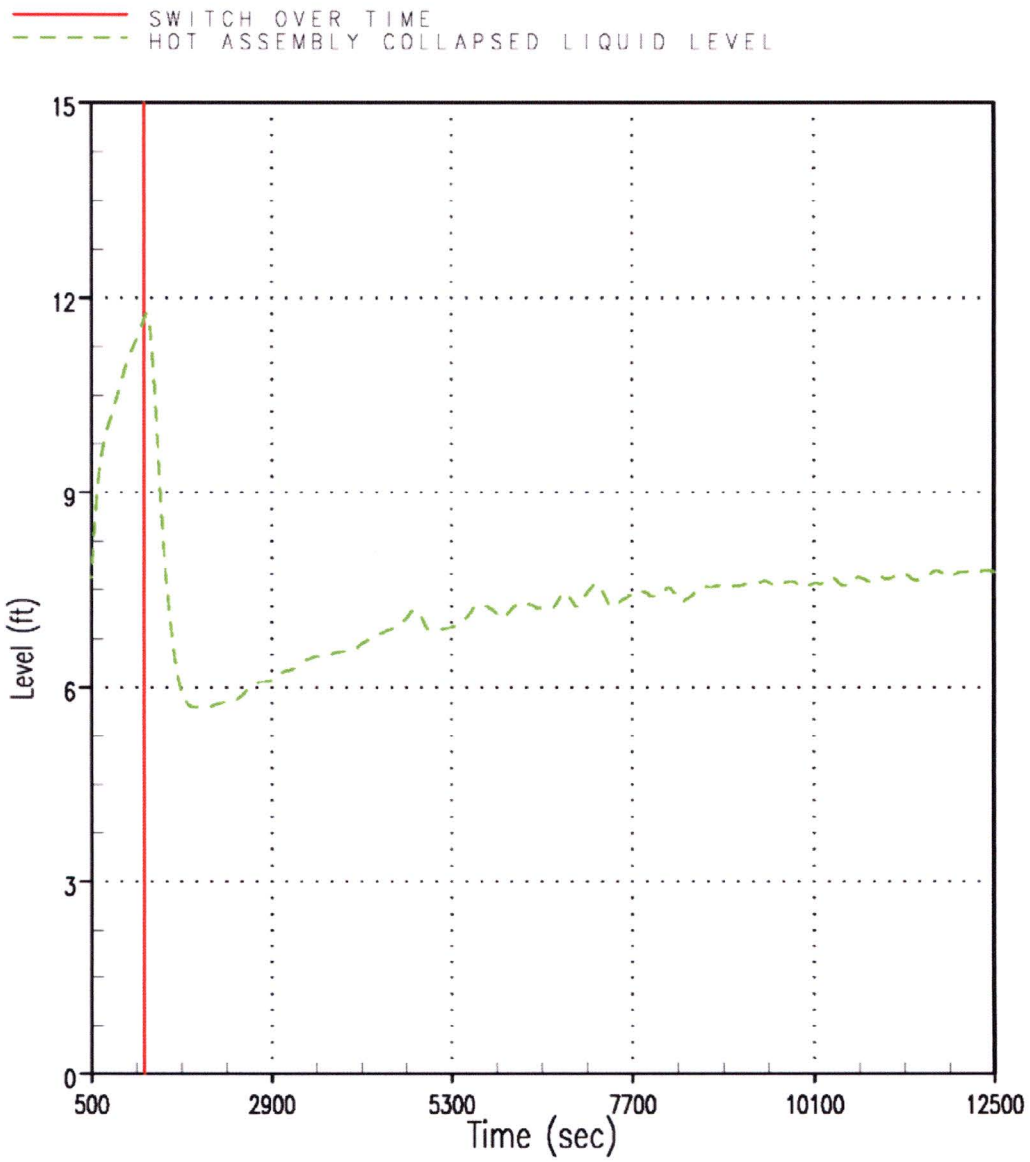

Figure RAI-4.23-82 Case 0A – Hot Assembly CLL

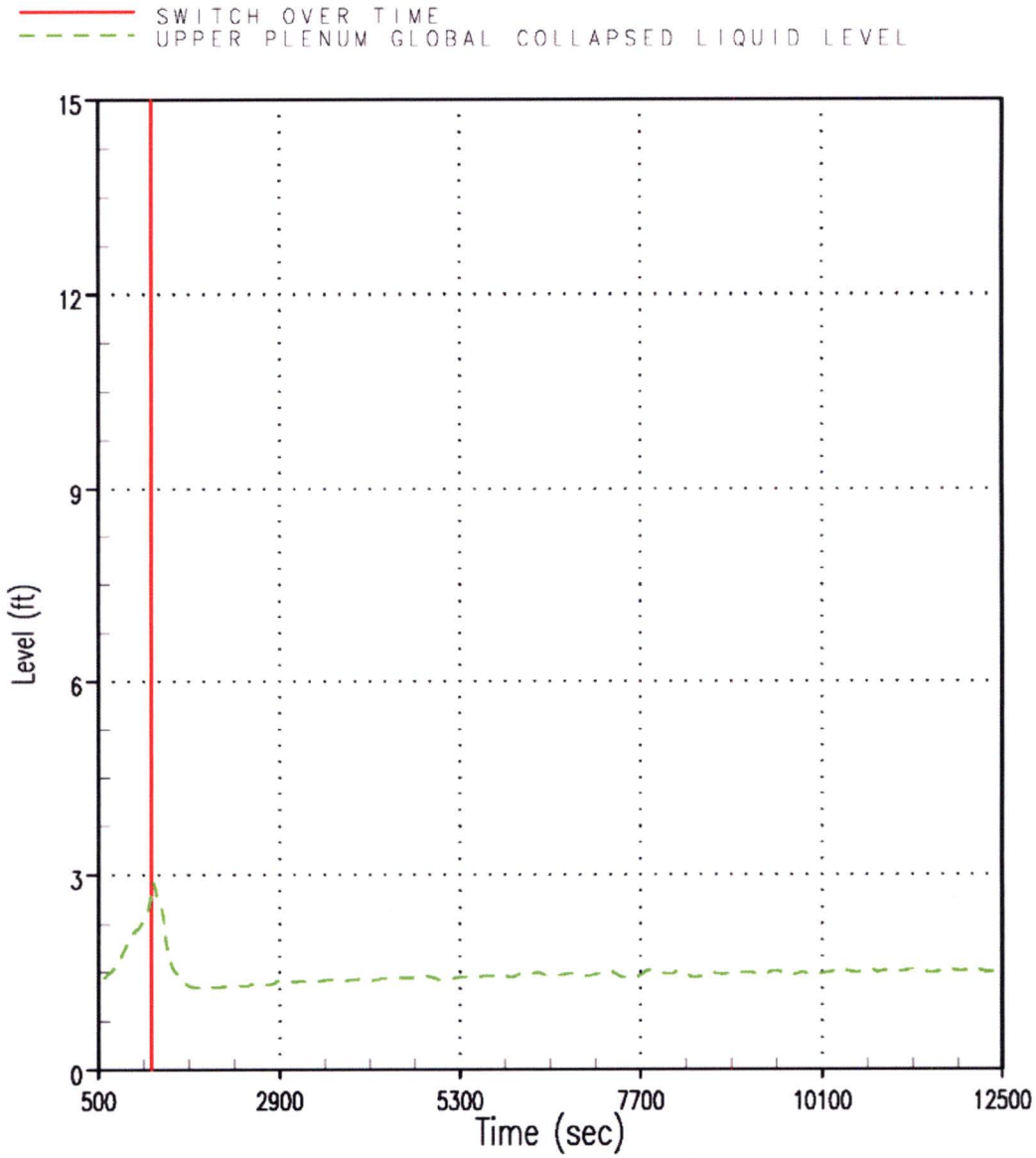

Figure RAI-4.23-83 Case 0A – UP Global CLL

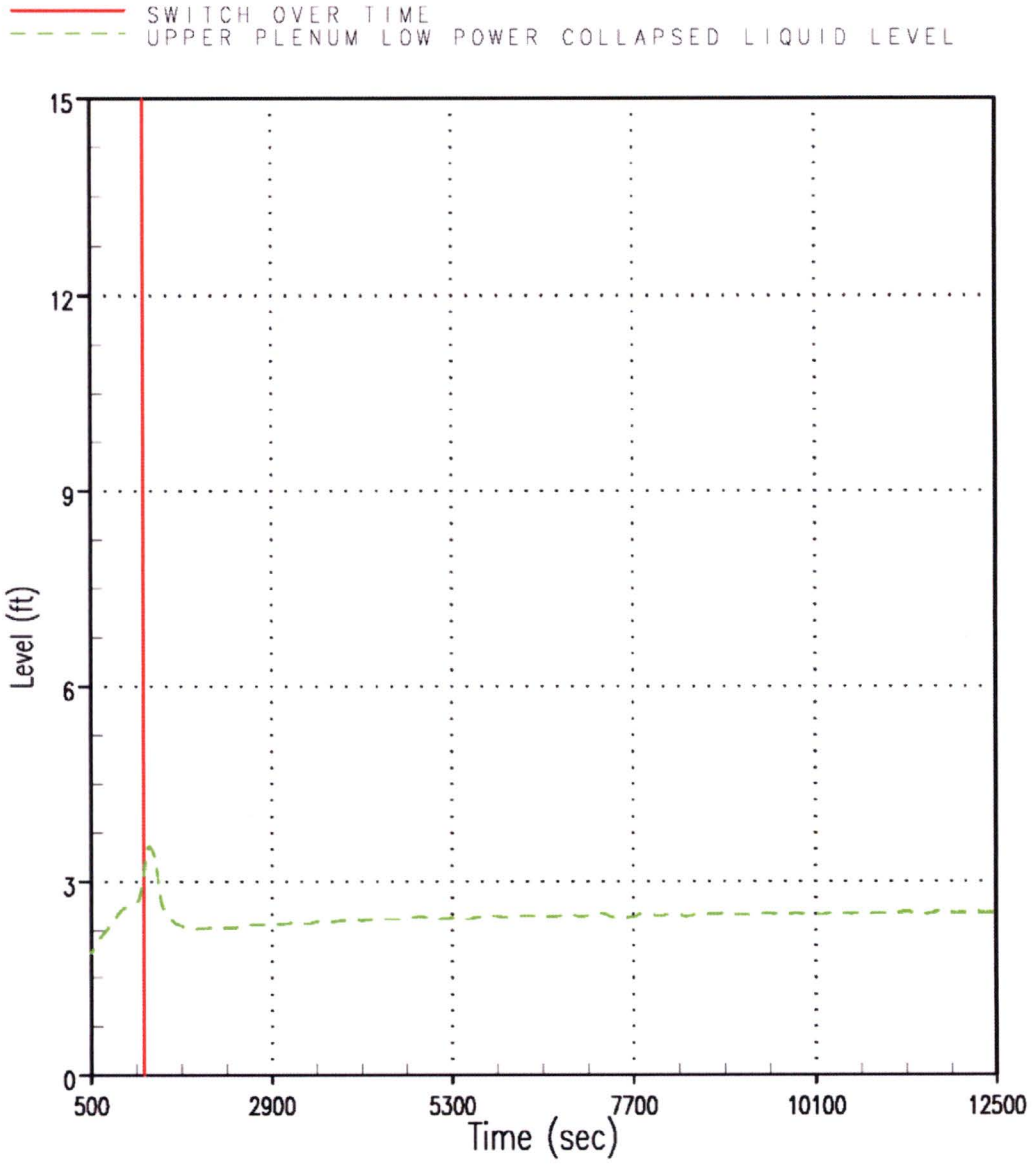

Figure RAI-4.23-84 Case 0A – UP Low Power CLL

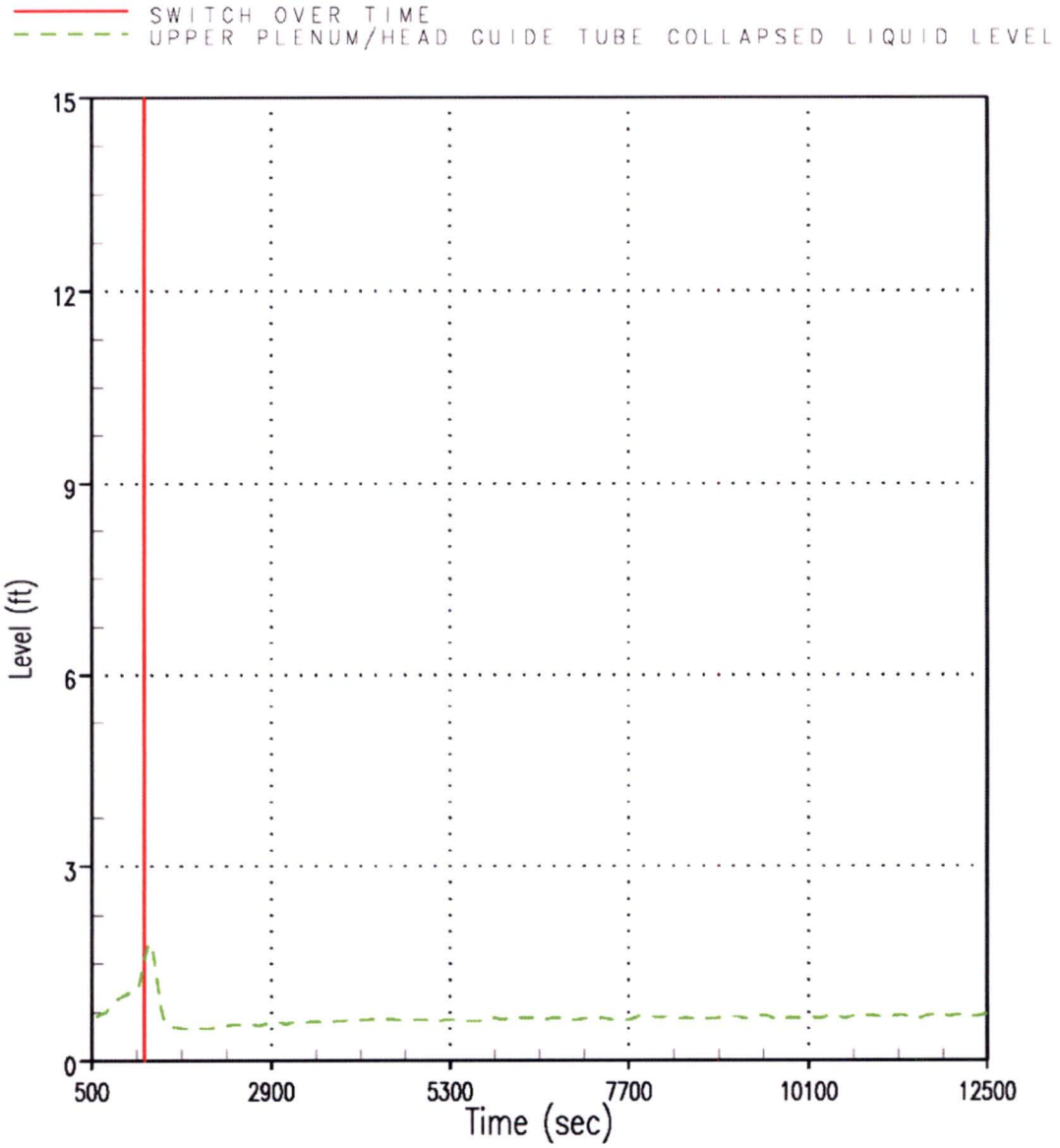

Figure RAI-4.23-85 Case 0A – UP / Upper Head Guide Tube CLL

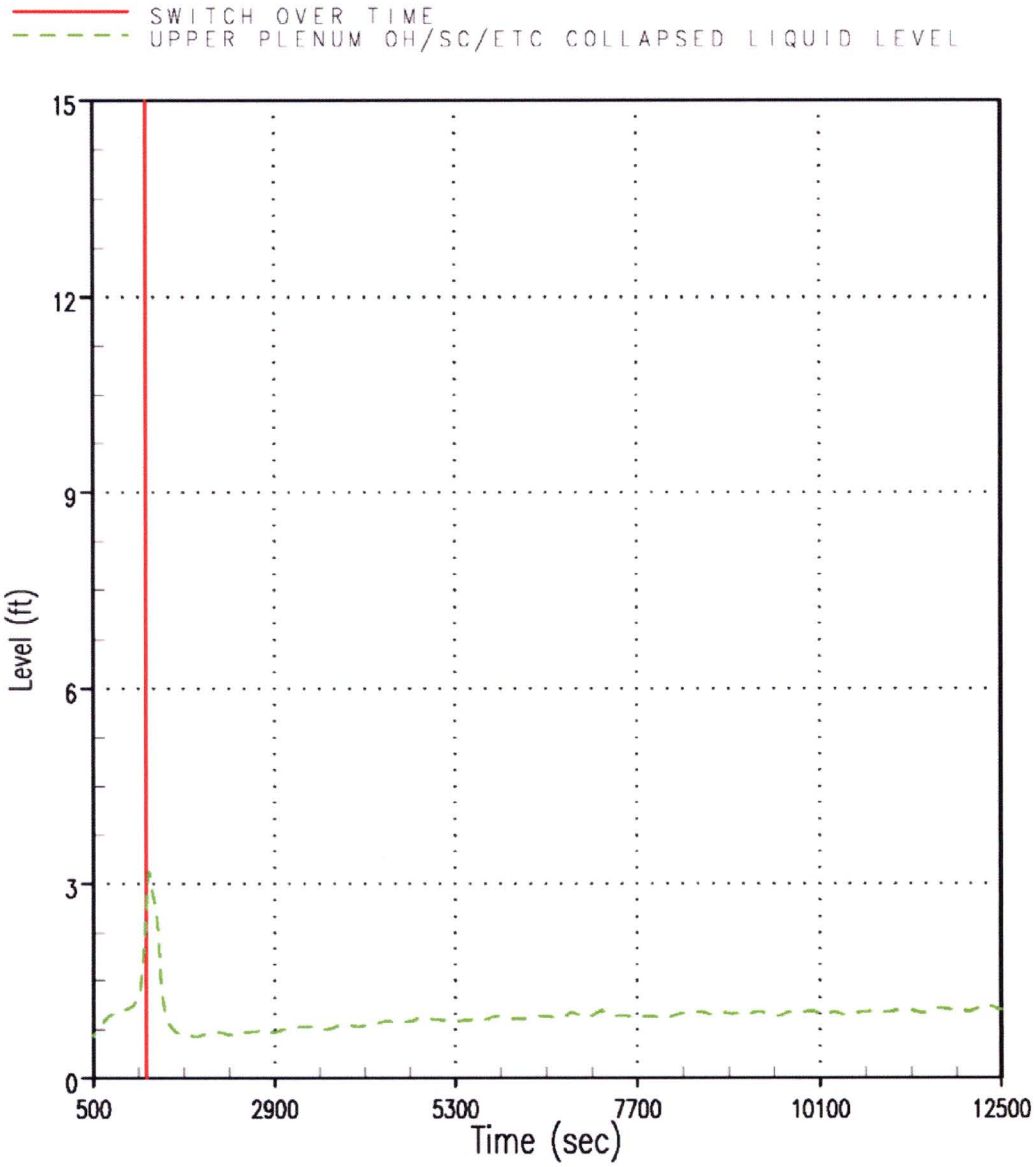

Figure RAI-4.23-86 Case 0A – UP Open Hole / Support Column / etc CLL

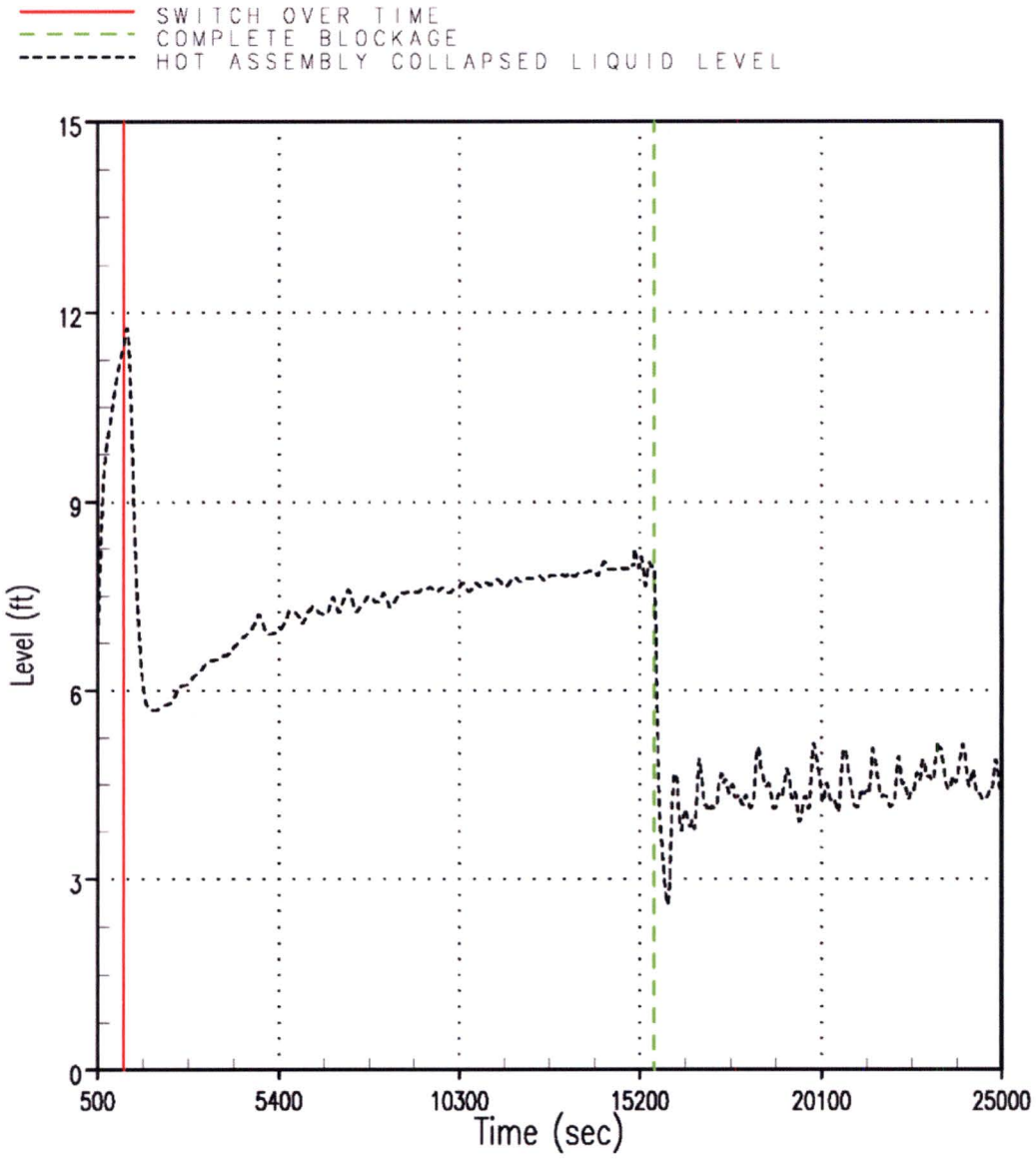

Figure RAI-4.23-87 Case 1A – Hot Assembly CLL

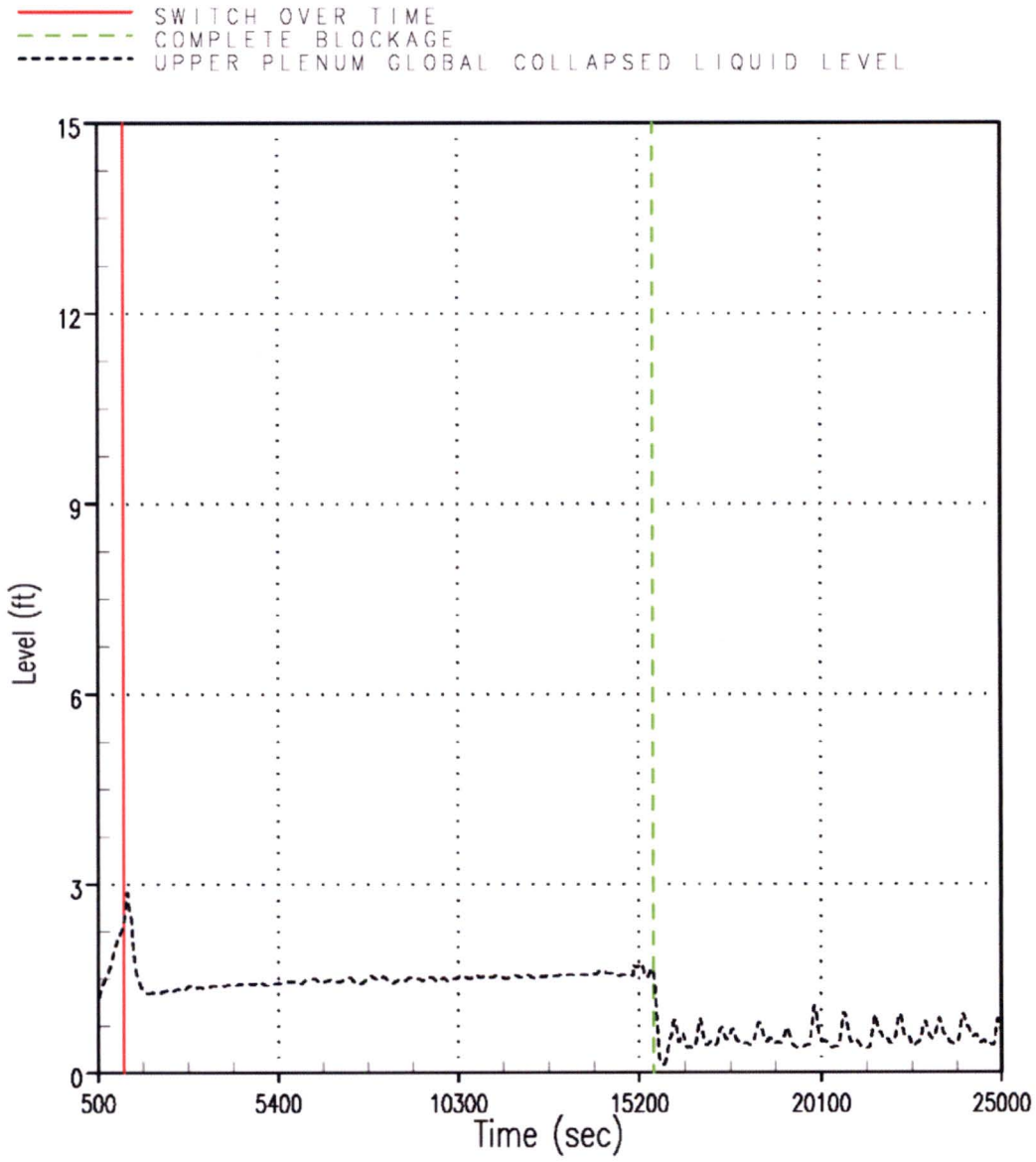

Figure RAI-4.23-88 Case 1A – UP Global CLL

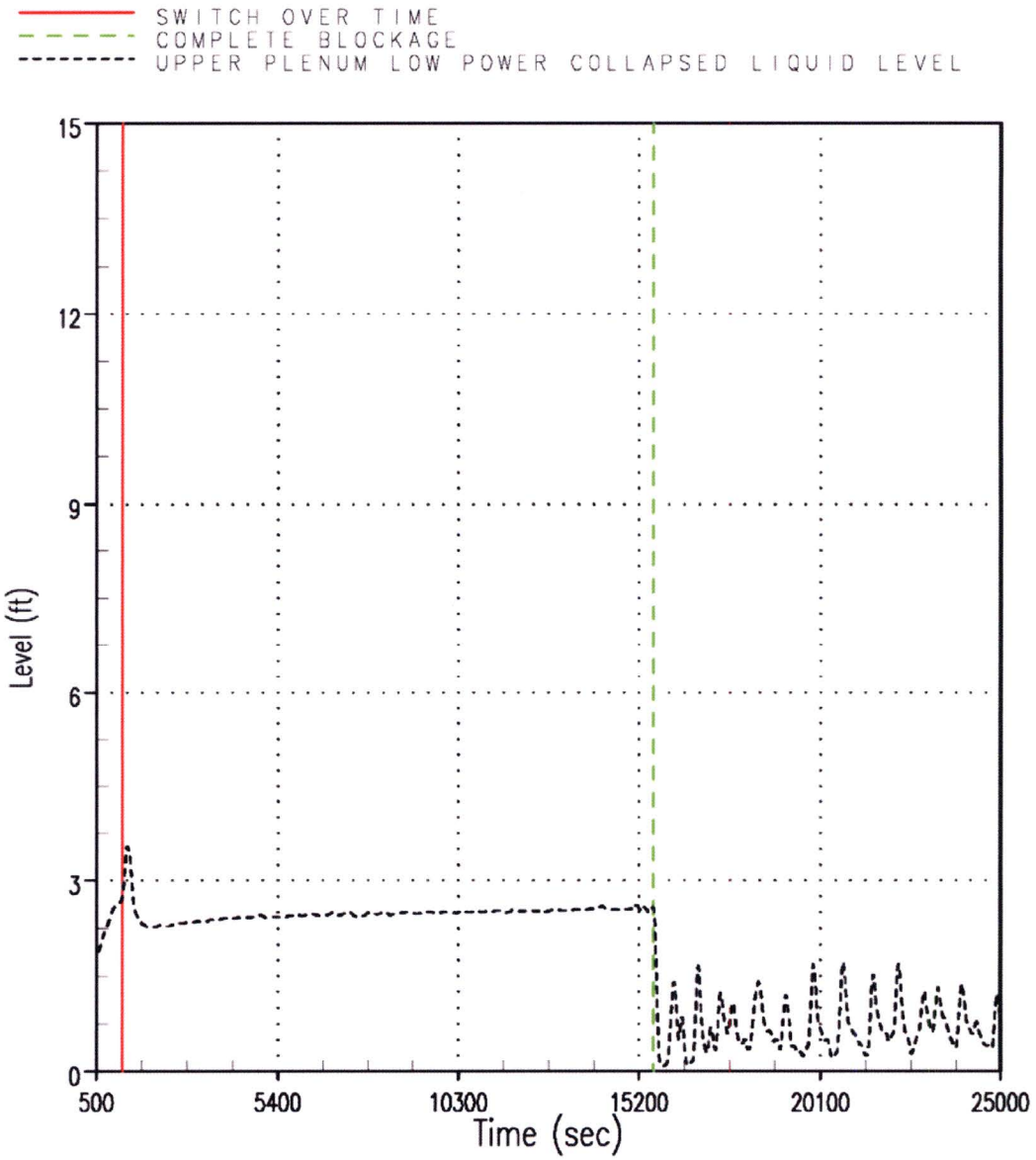

Figure RAI-4.23-89 Case 1A – UP Low Power CLL

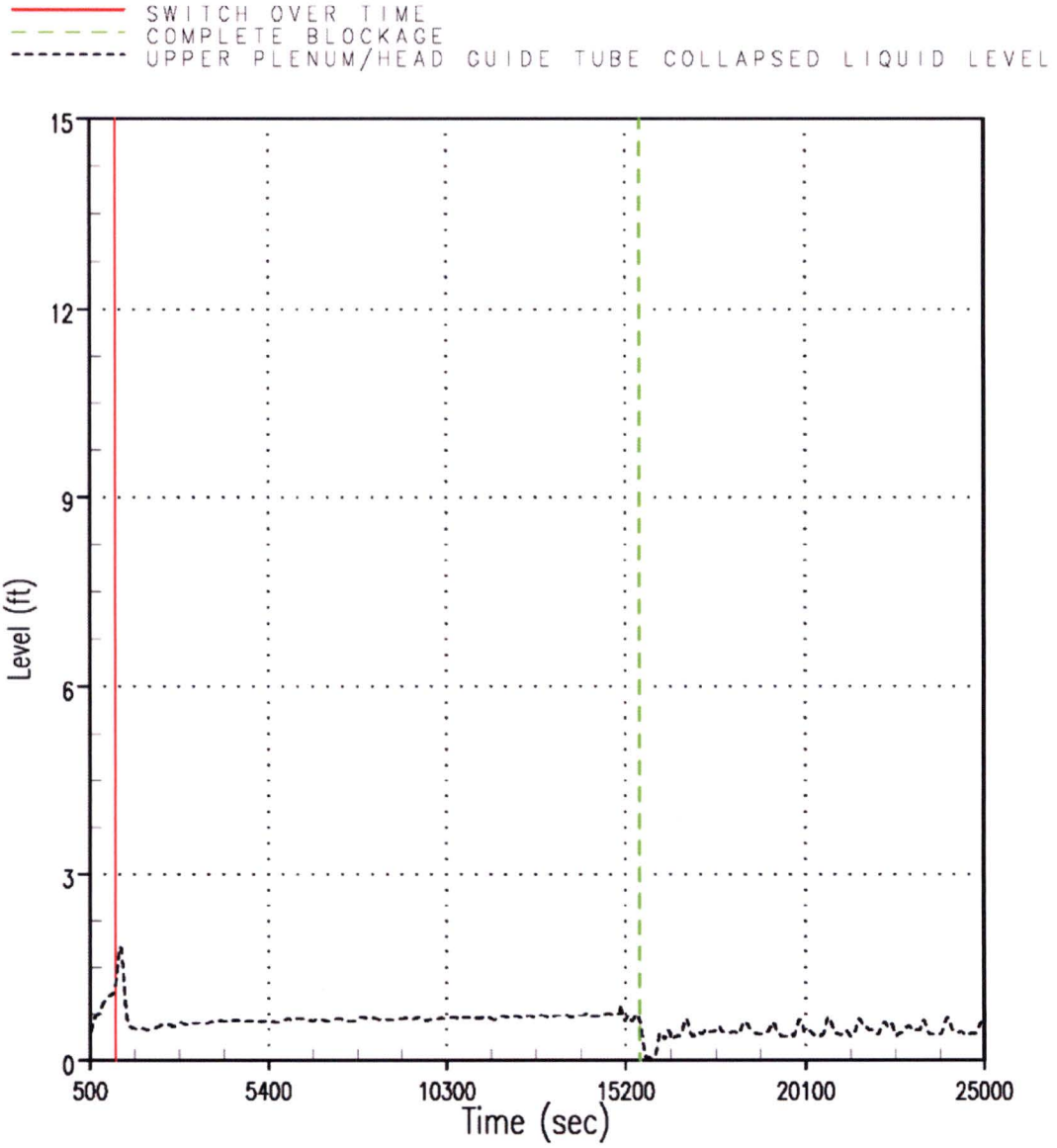

Figure RAI-4.23-90 Case 1A – UP / Upper Head Guide Tube CLL

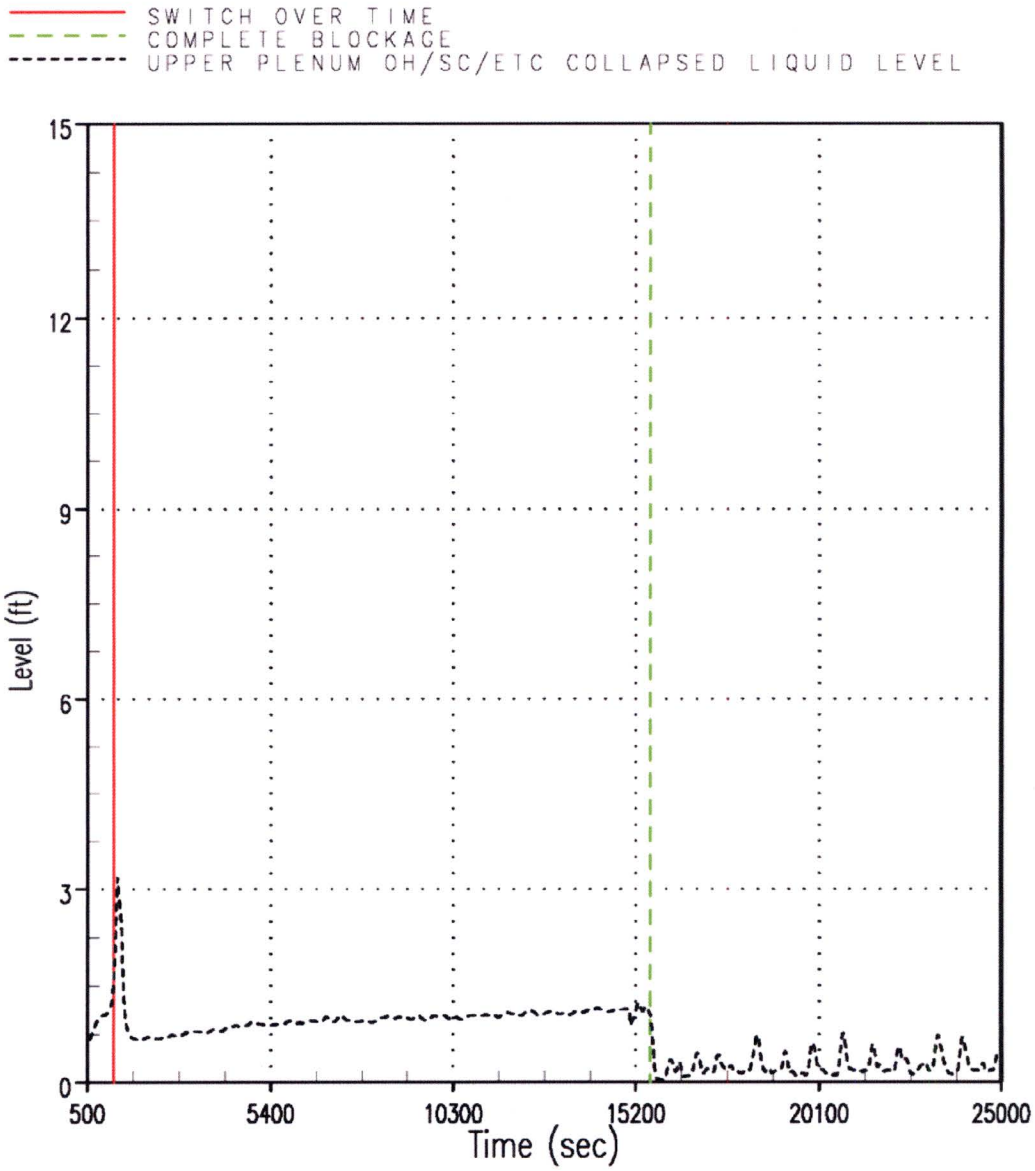

Figure RAI-4.23-91 Case 1A – UP Open Hole / Support Column / etc CLL

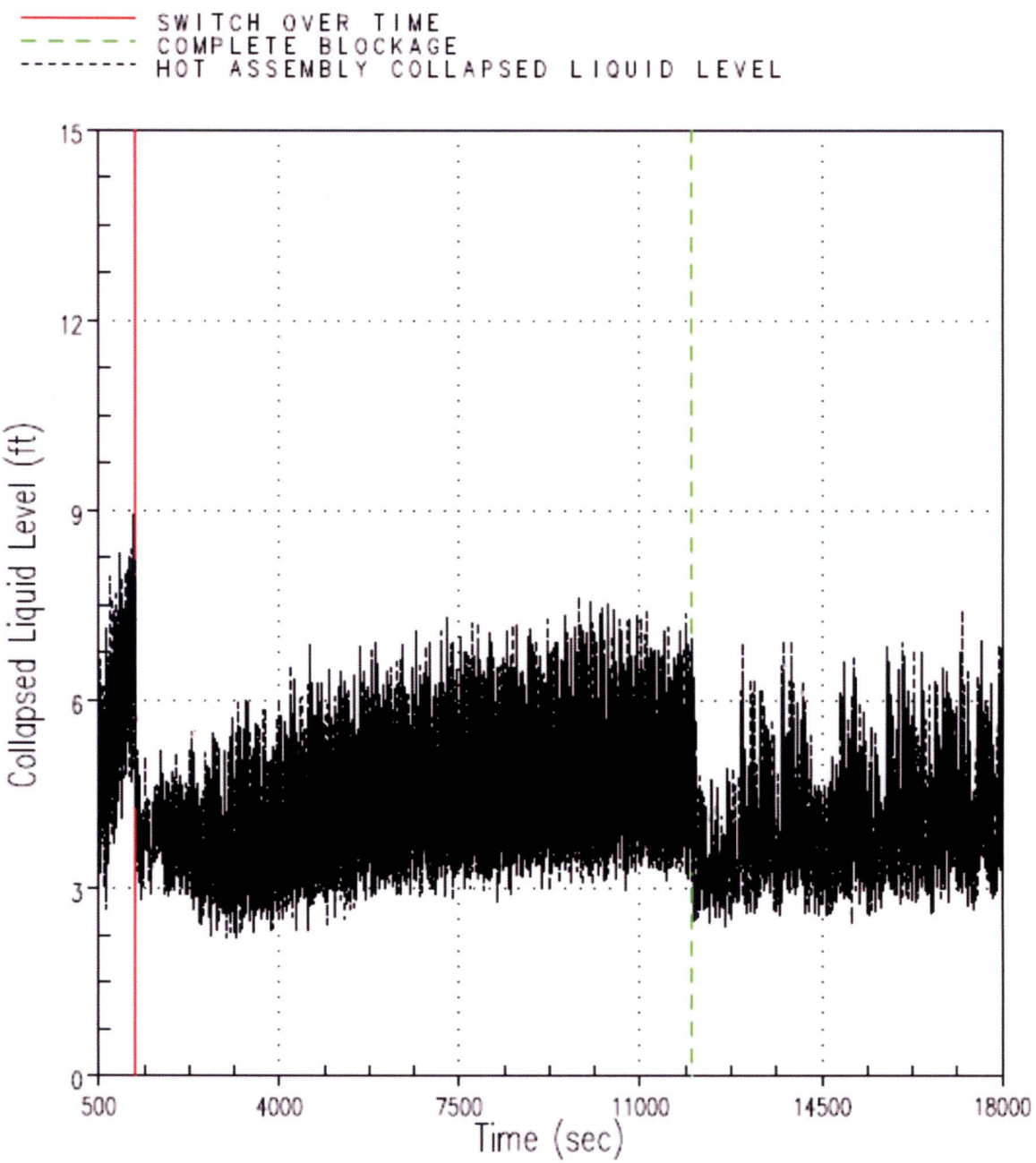

Figure RAI-4.23-92 Case 2B – Hot Assembly CLL

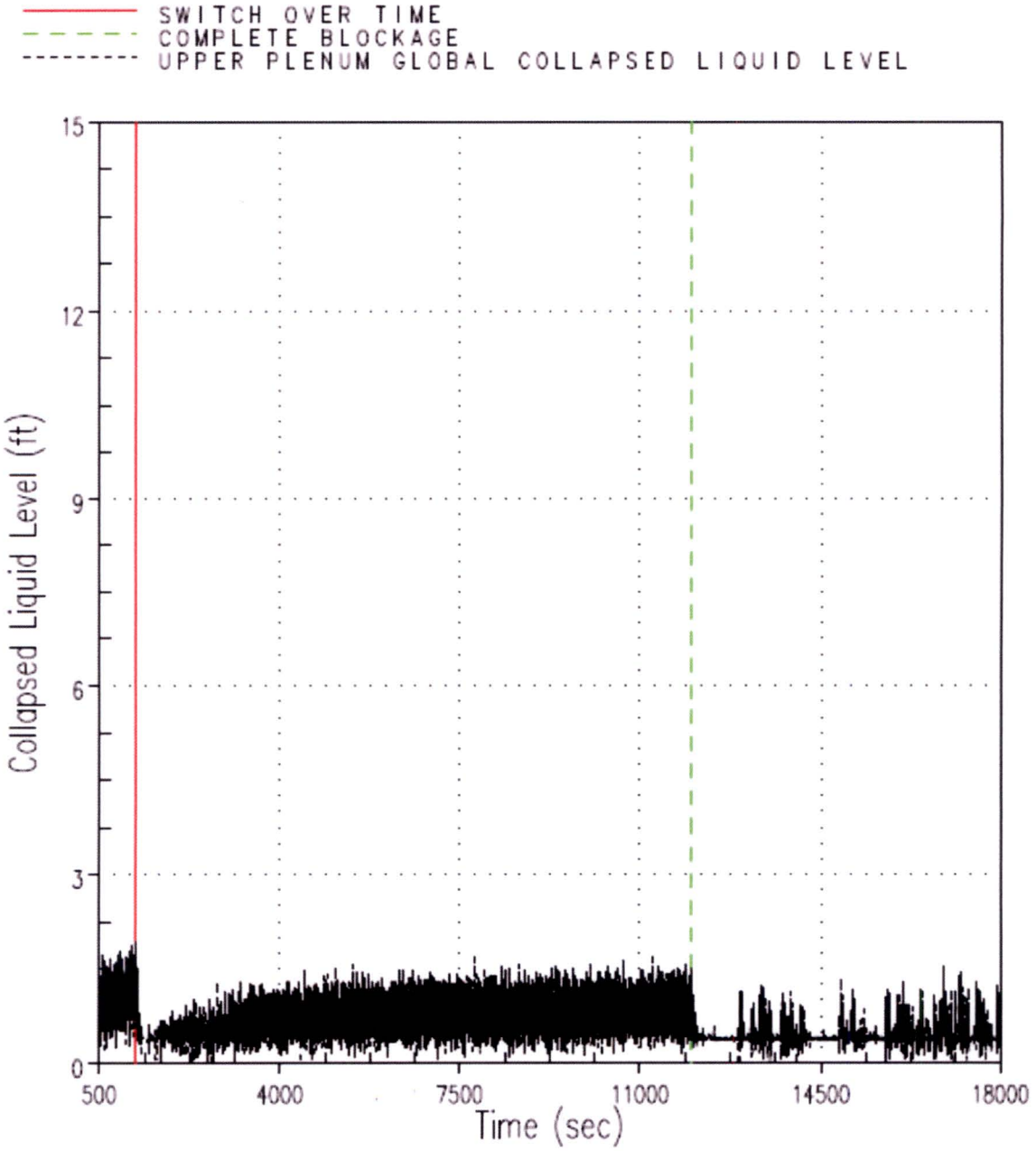

Figure RAI-4.23-93 Case 2B – UP Global CLL

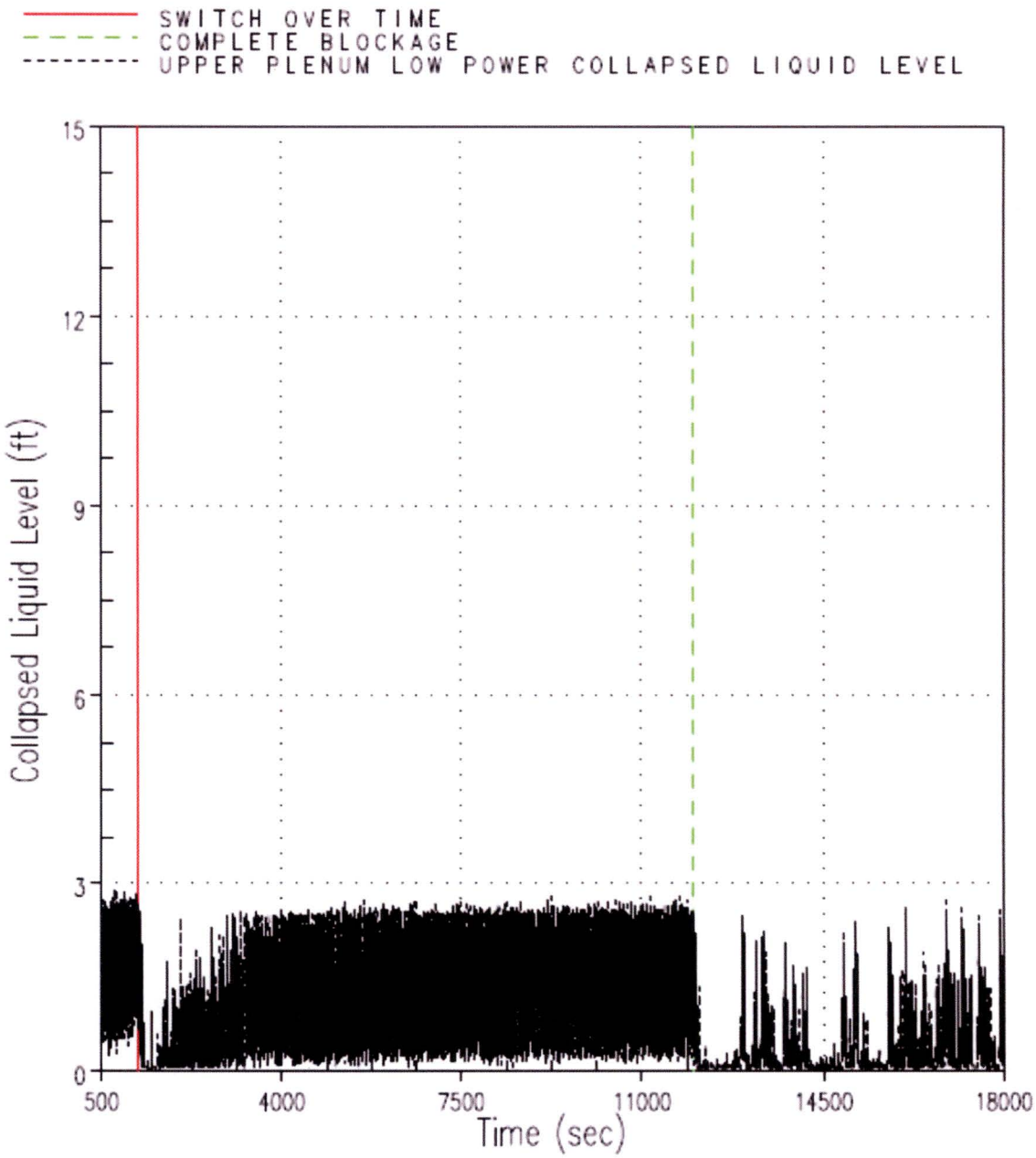

Figure RAI-4.23-94 Case 2B – UP Low Power CLL

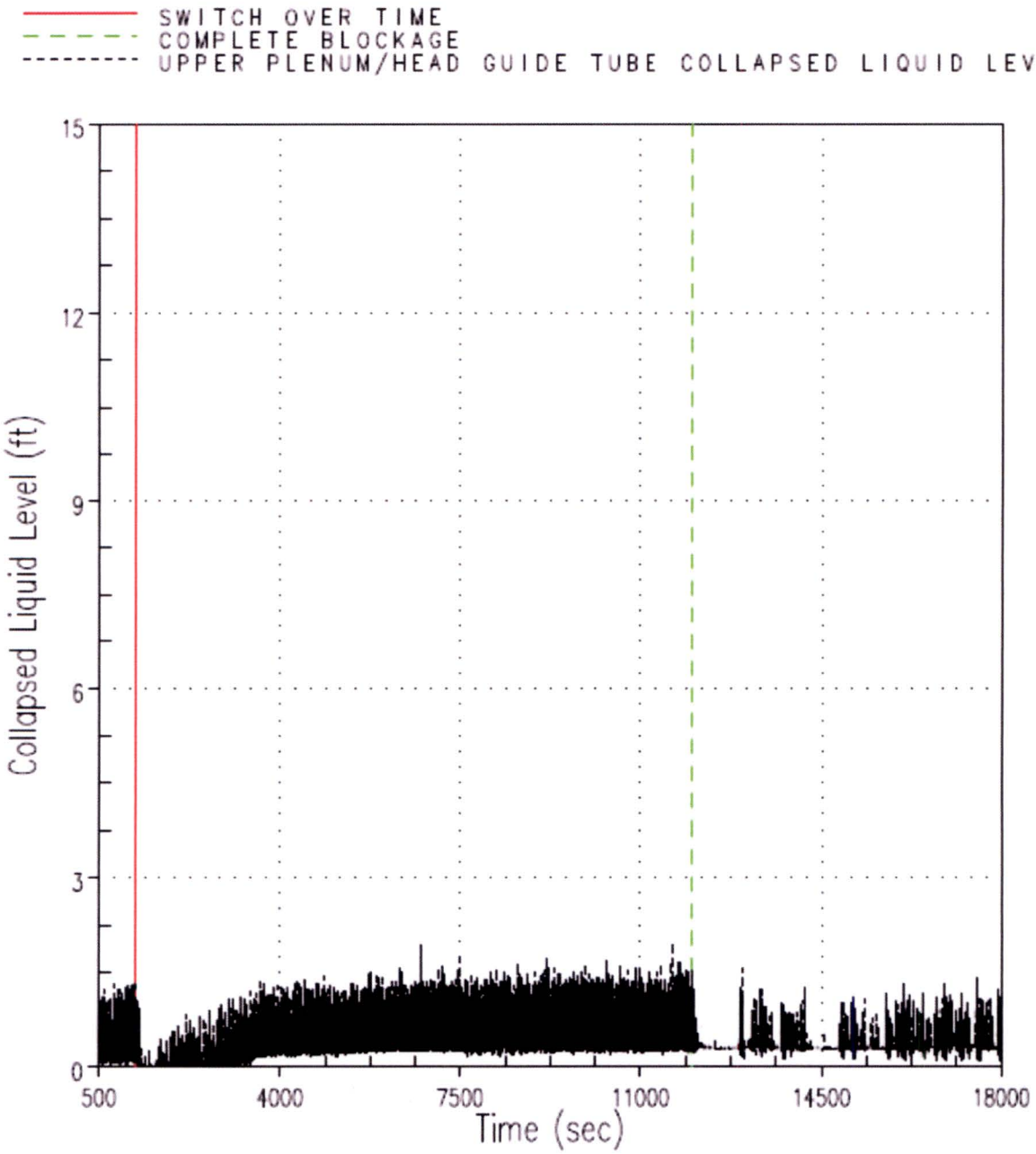

Figure RAI-4.23-95 Case 2B – UP / Upper Head Guide Tube CLL

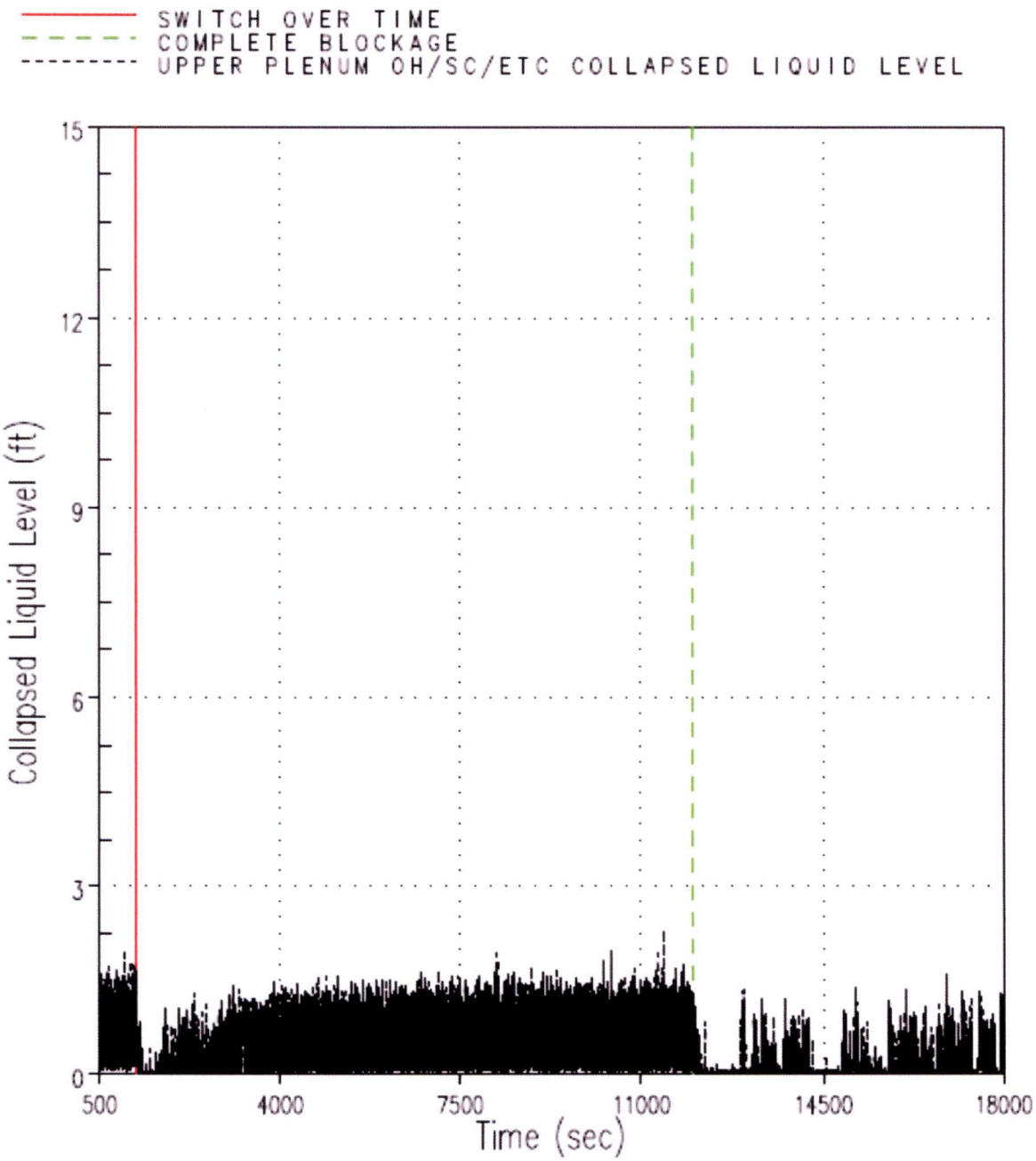

Figure RAI-4.23-96 Case 2B – UP Open Hole / Support Column / etc CLL

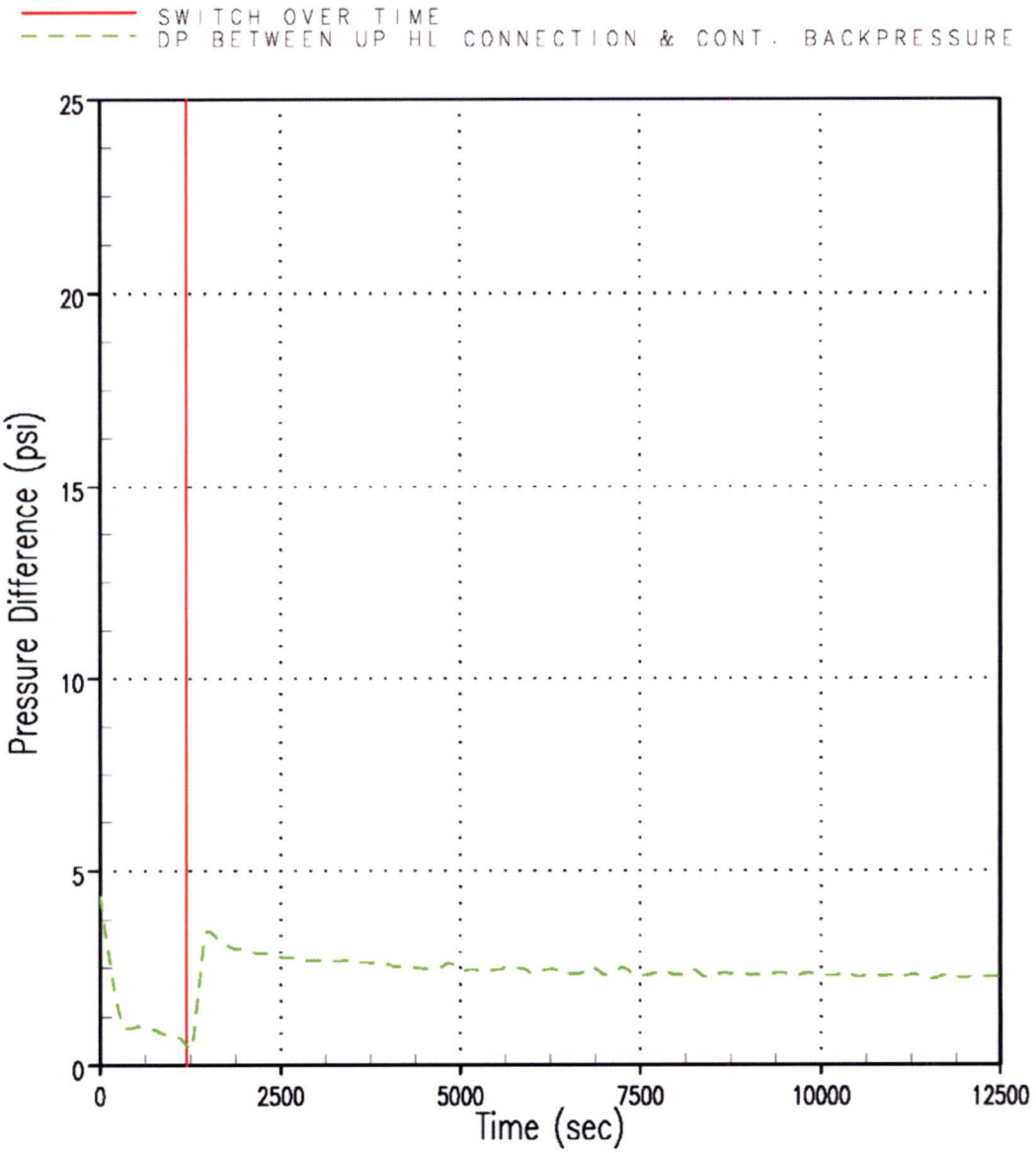

Figure RAI-4.23-97 Case 0A – Delta P between Upper Head Channel Connection to Broken HL and Containment Backpressure

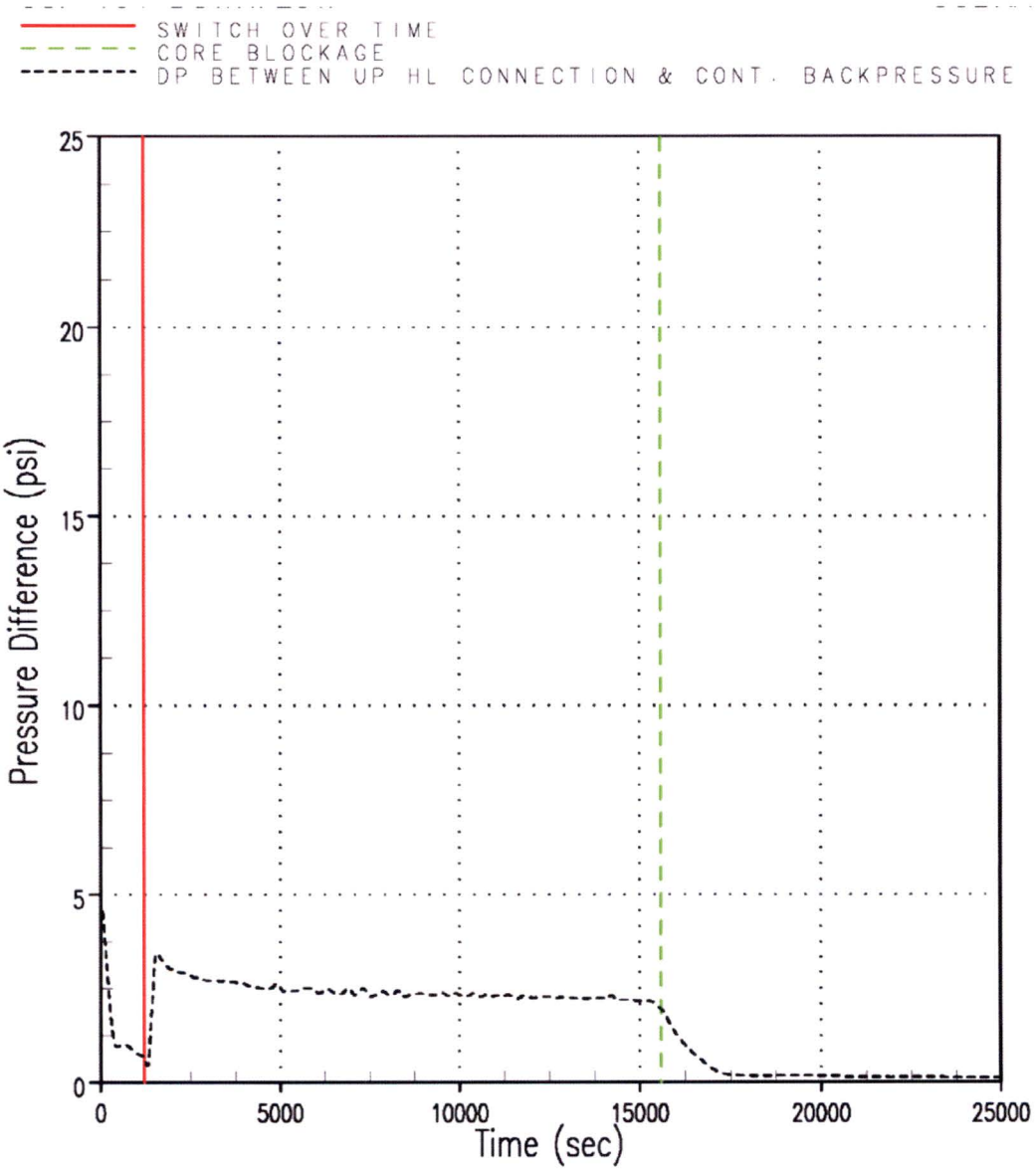

Figure RAI-4.23-98 Case 1A – Delta P between Upper Head Channel Connection to Broken HL and Containment Backpressure

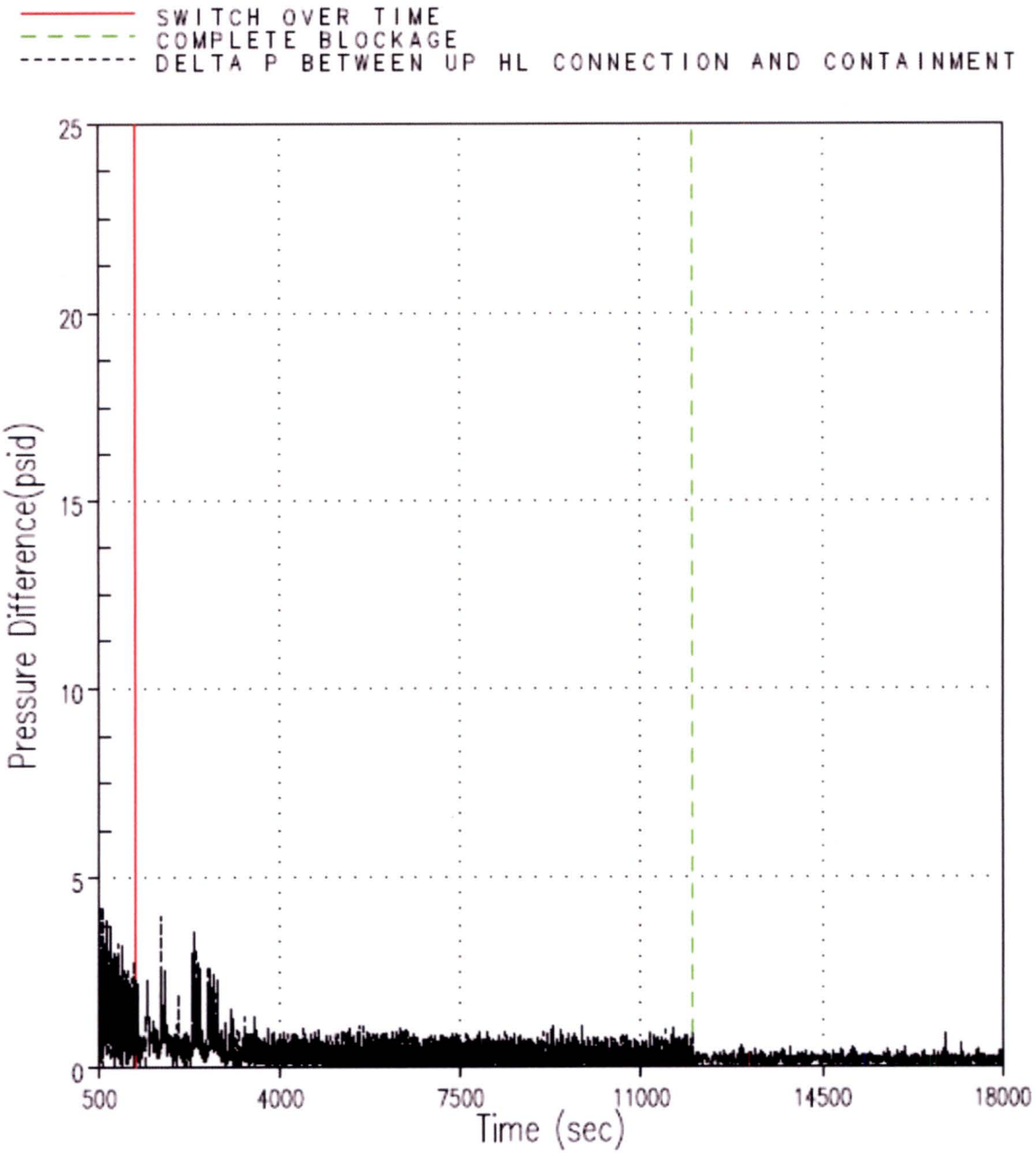

Figure RAI-4.23-99 Case 2B – Delta P between Upper Head Channel Connection to Broken HL and Containment Backpressure

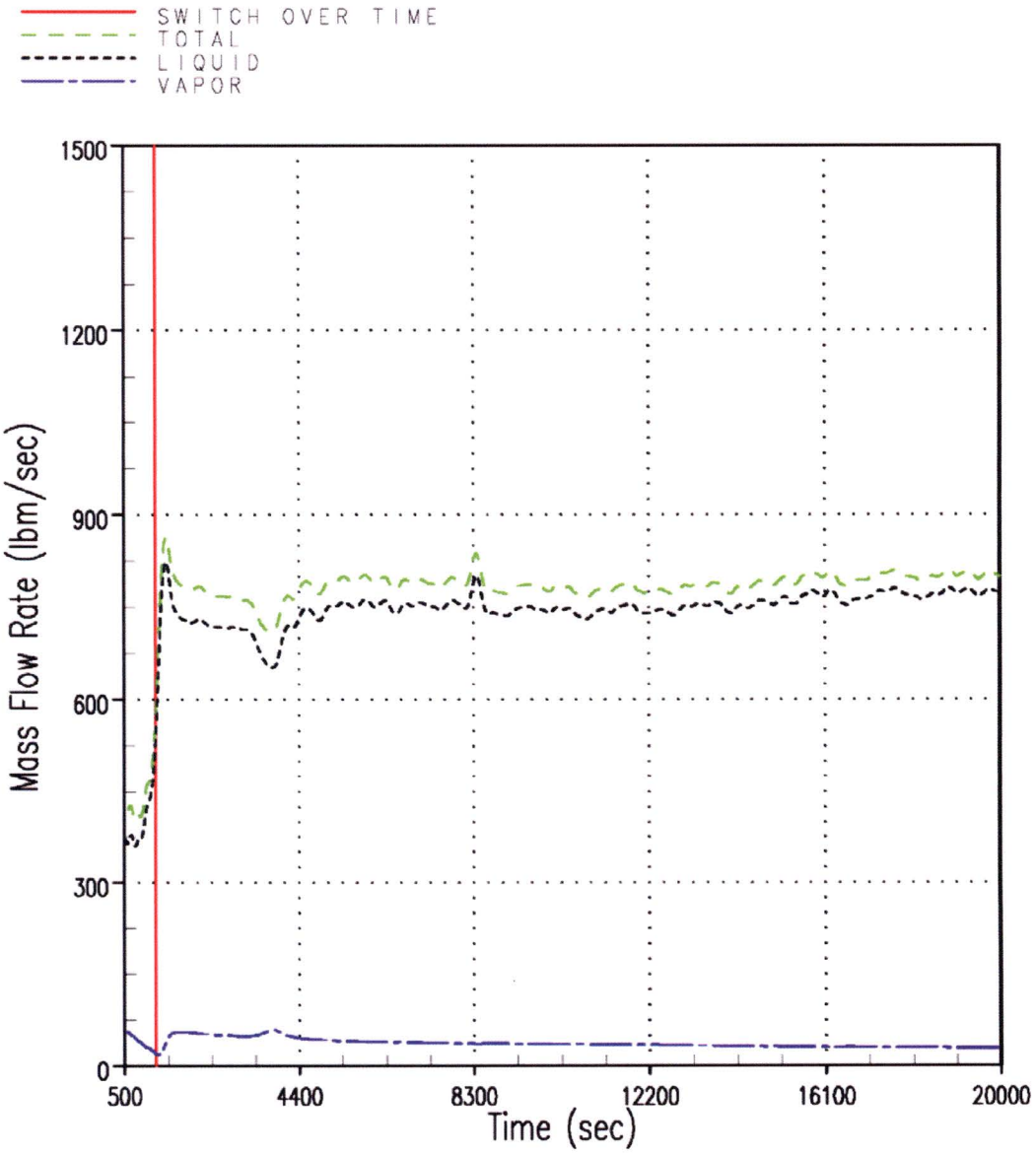

Figure RAI-4.23-100 Case 1 – Mass Flow Rates through the Vessel Side of the DEG Break

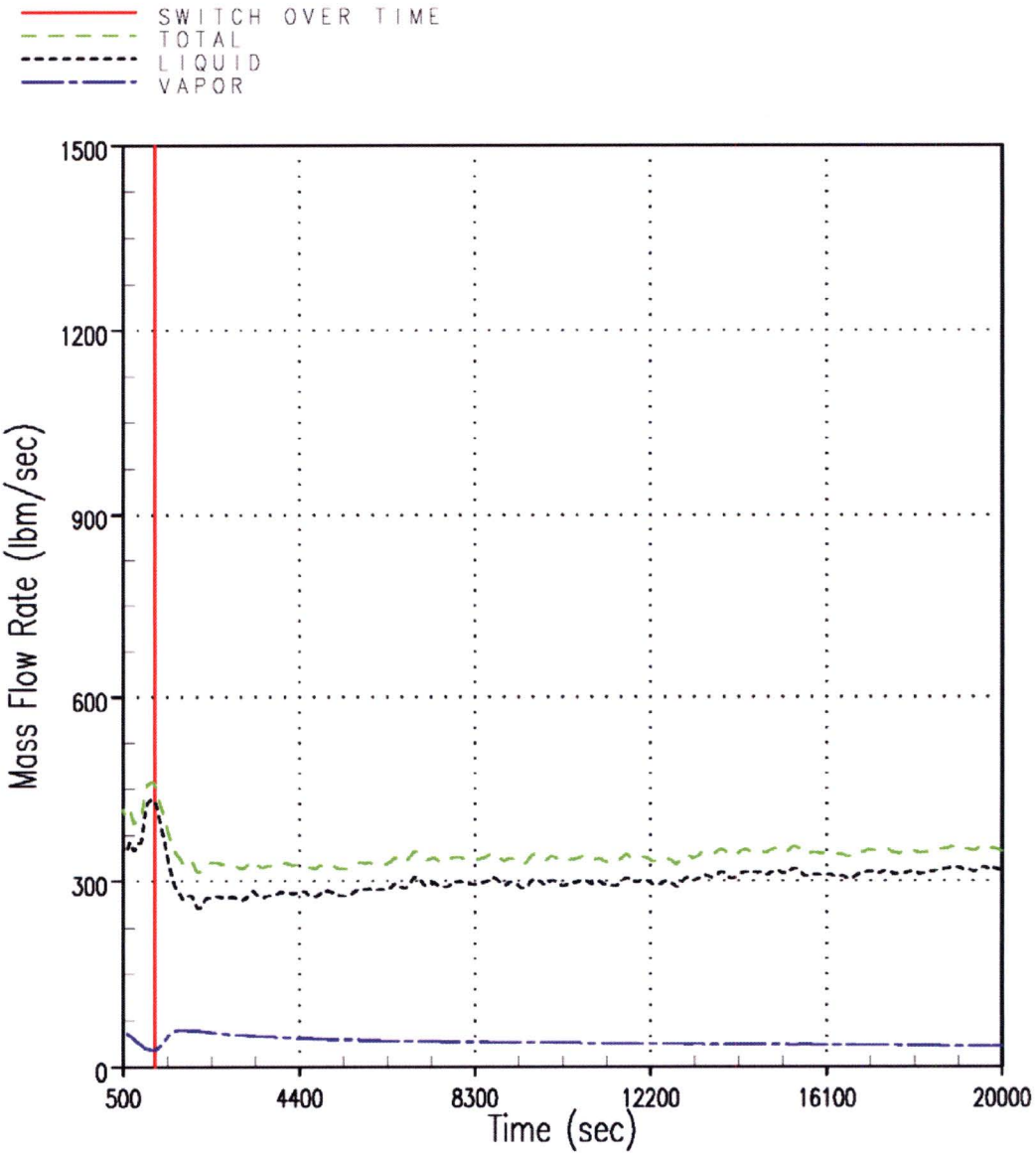

Figure RAI-4.23-101 Case 3 – Mass Flow Rates through the Vessel Side of the DEG Break

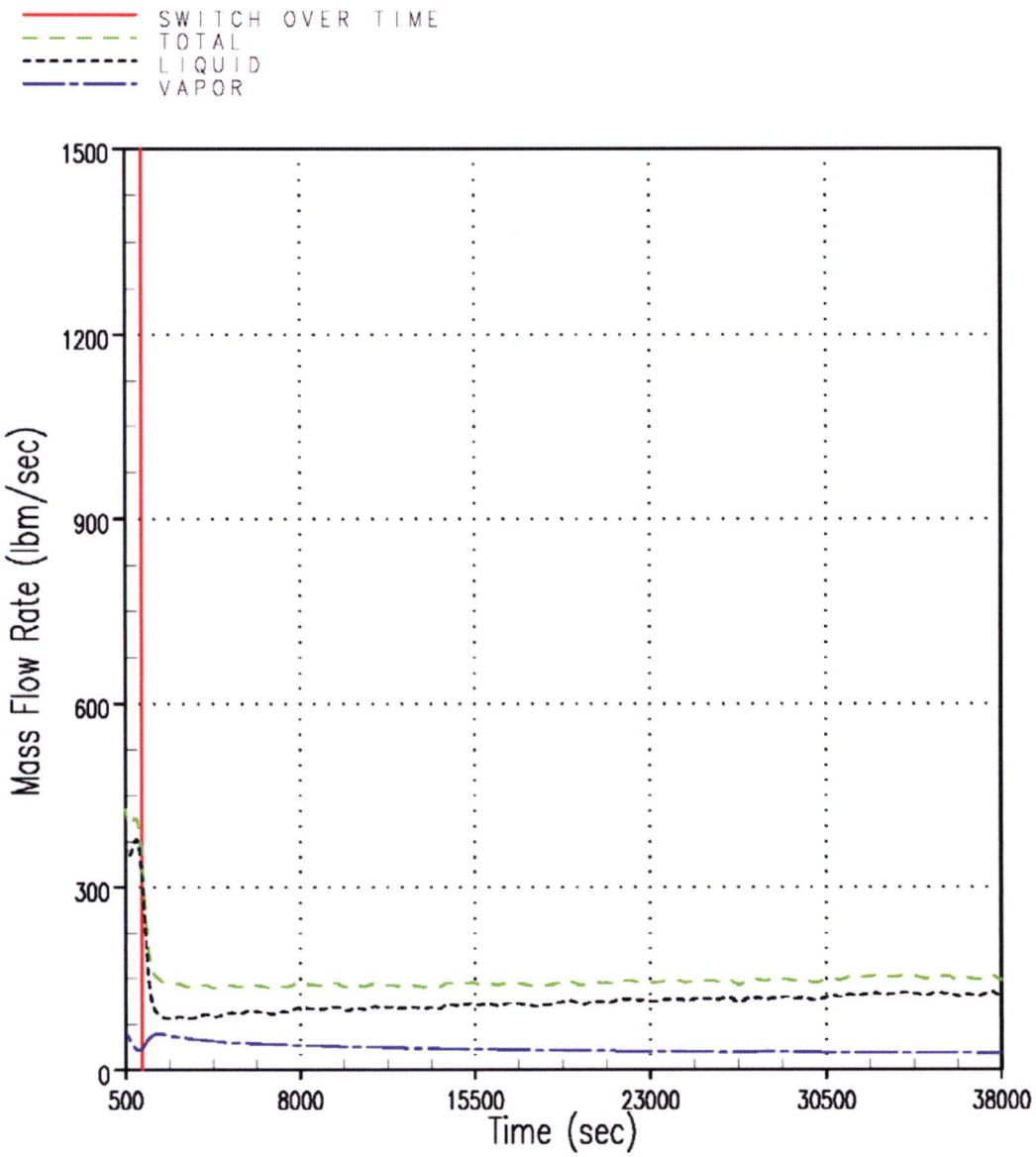

Figure RAI-4.23-102 Case 5 – Mass Flow Rates through the Vessel Side of the DEG Break

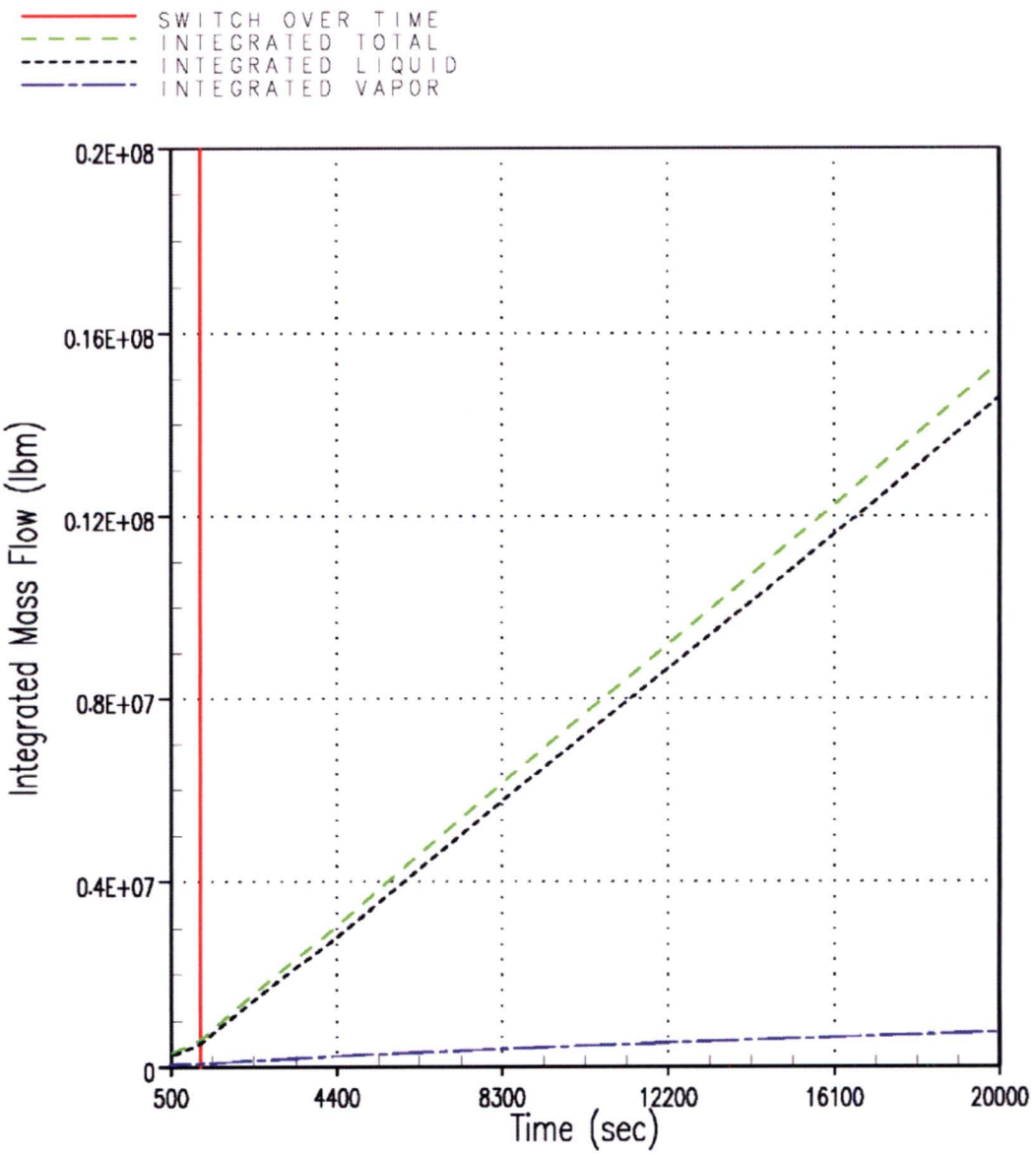

Figure RAI-4.23-103 Case 1 – Integrated Mass Flow through the Vessel Side of the DEG Break

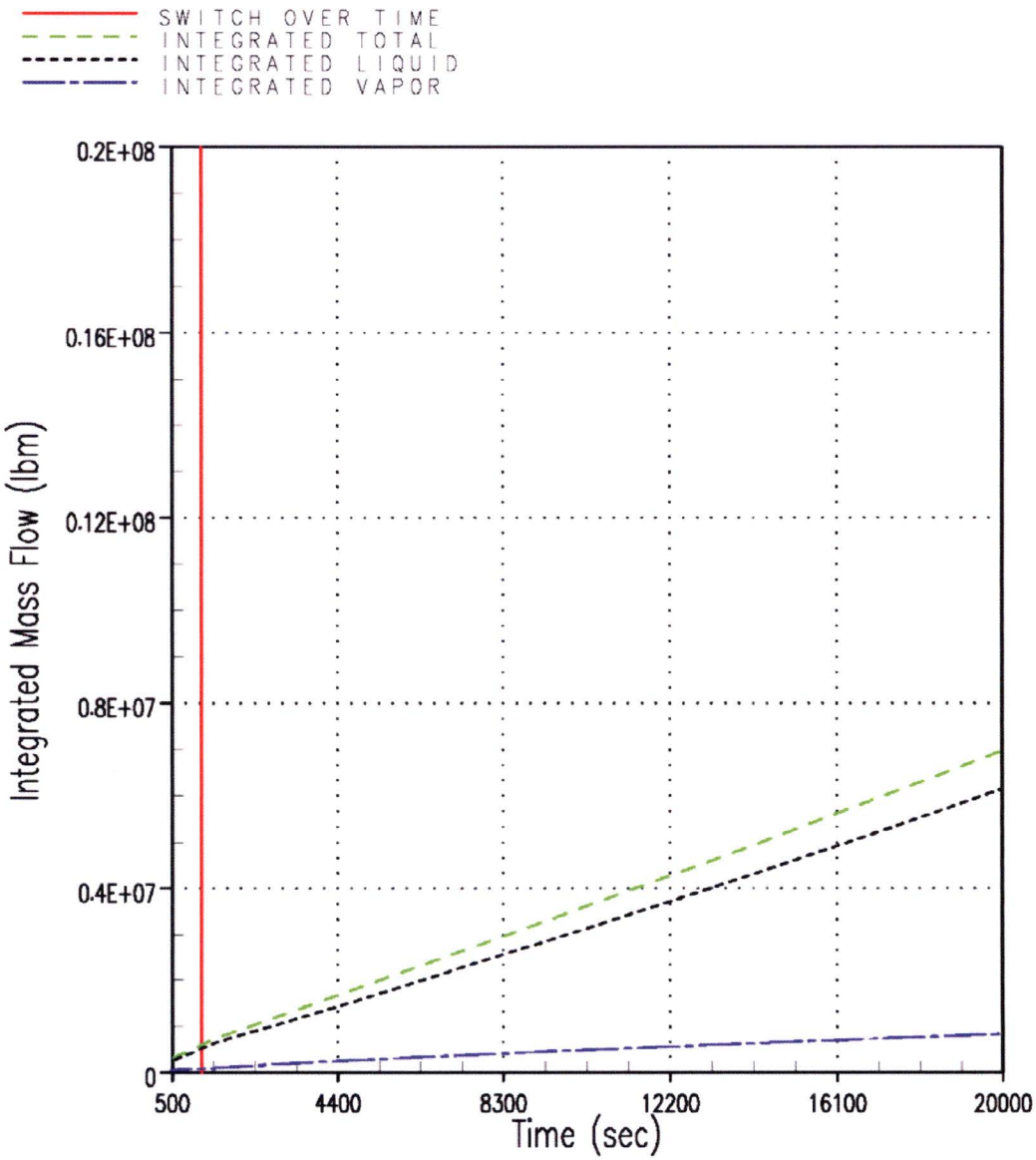

Figure RAI-4.23-104 Case 3 – Integrated Mass Flow through the Vessel Side of the DEG Break

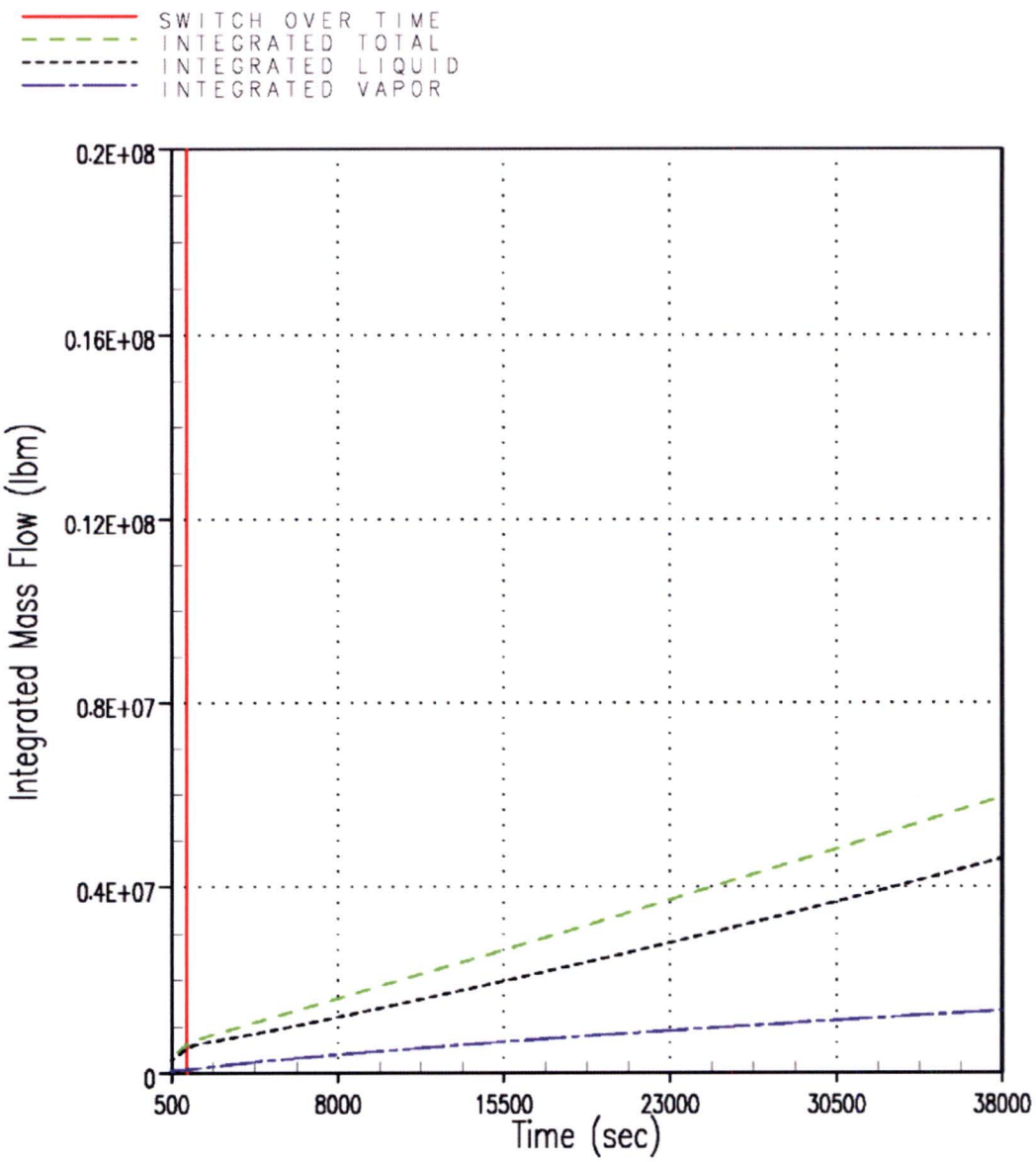

Figure RAI-4.23-105 Case 5 – Integrated Mass Flow through the Vessel Side of the DEG Break

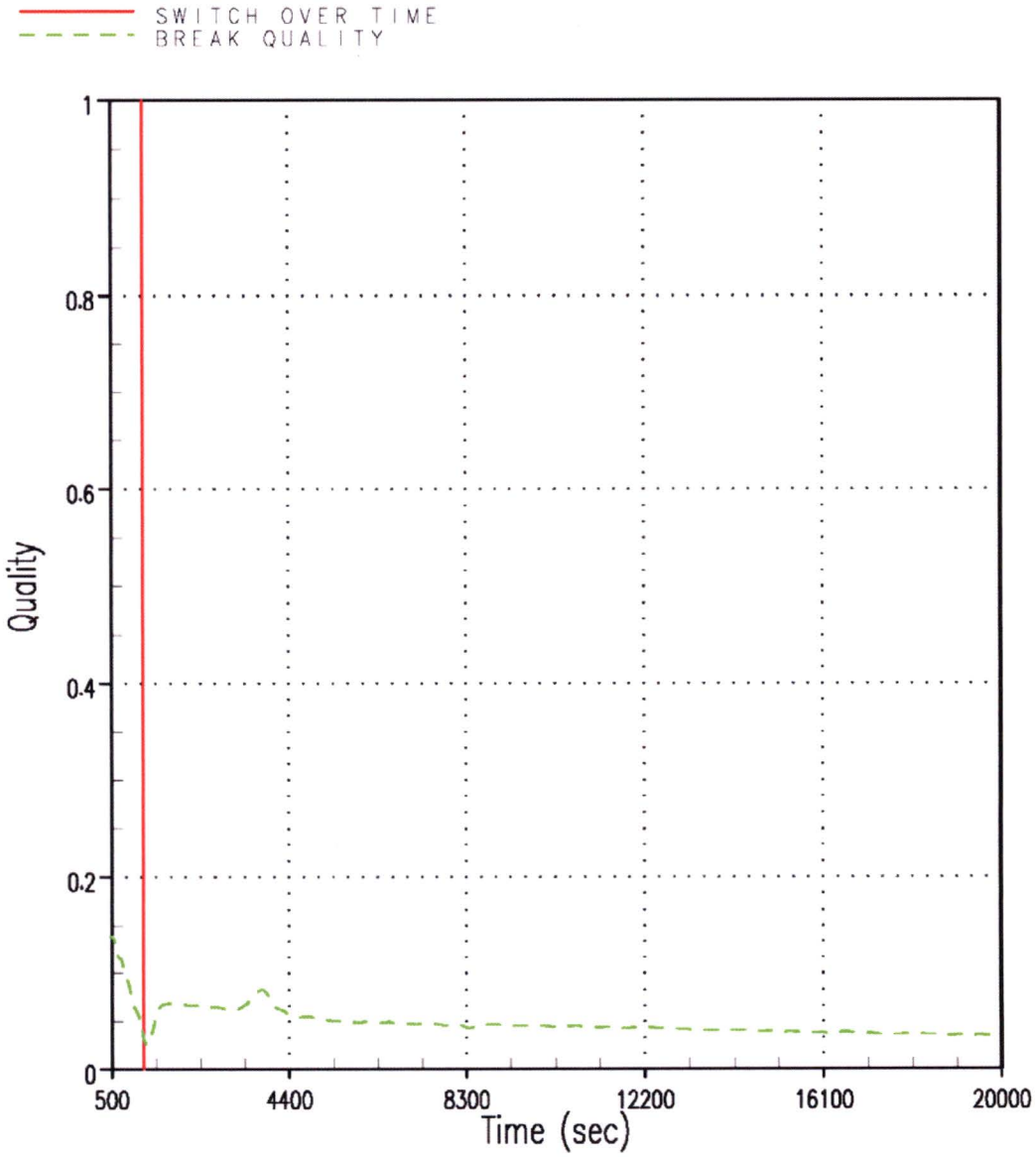

Figure RAI-4.23-106 Case 1 – Break Exit Quality – Vessel Side of DEG Break

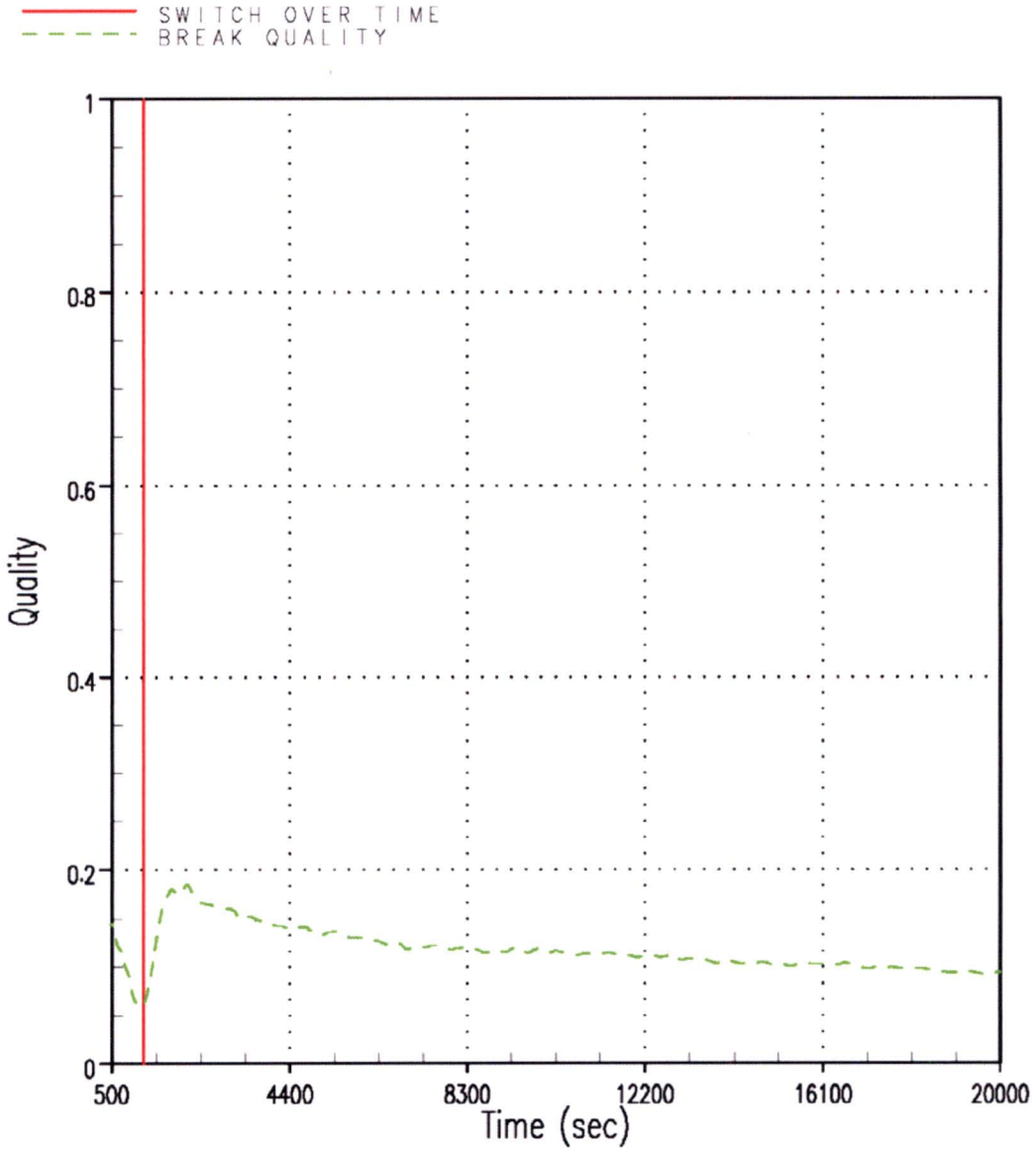

Figure RAI-4.23-107 Case 3 – Break Exit Quality – Vessel Side of DEG Break

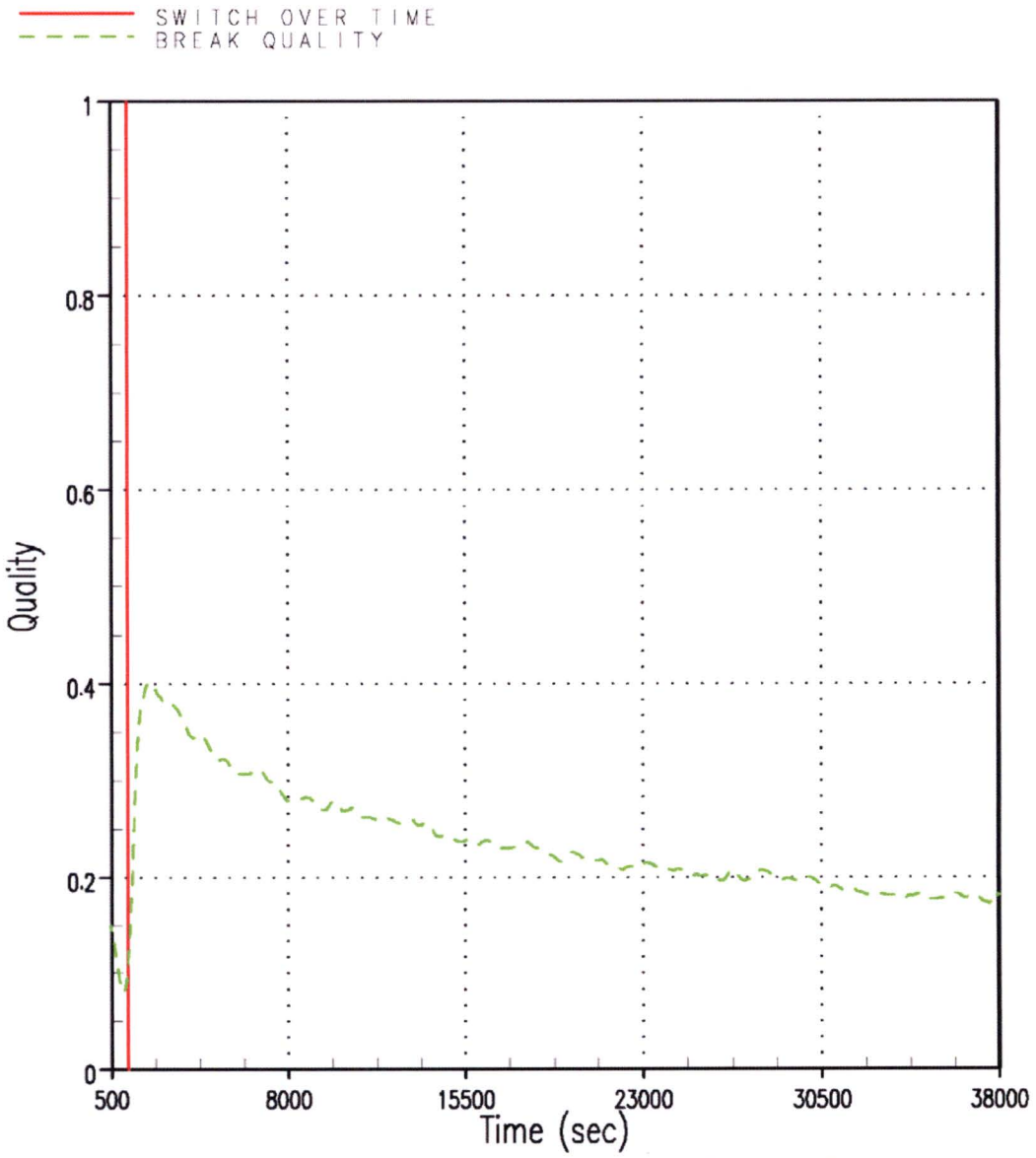

Figure RAI-4.23-108 Case 5 – Break Exit Quality – Vessel Side of DEG Break

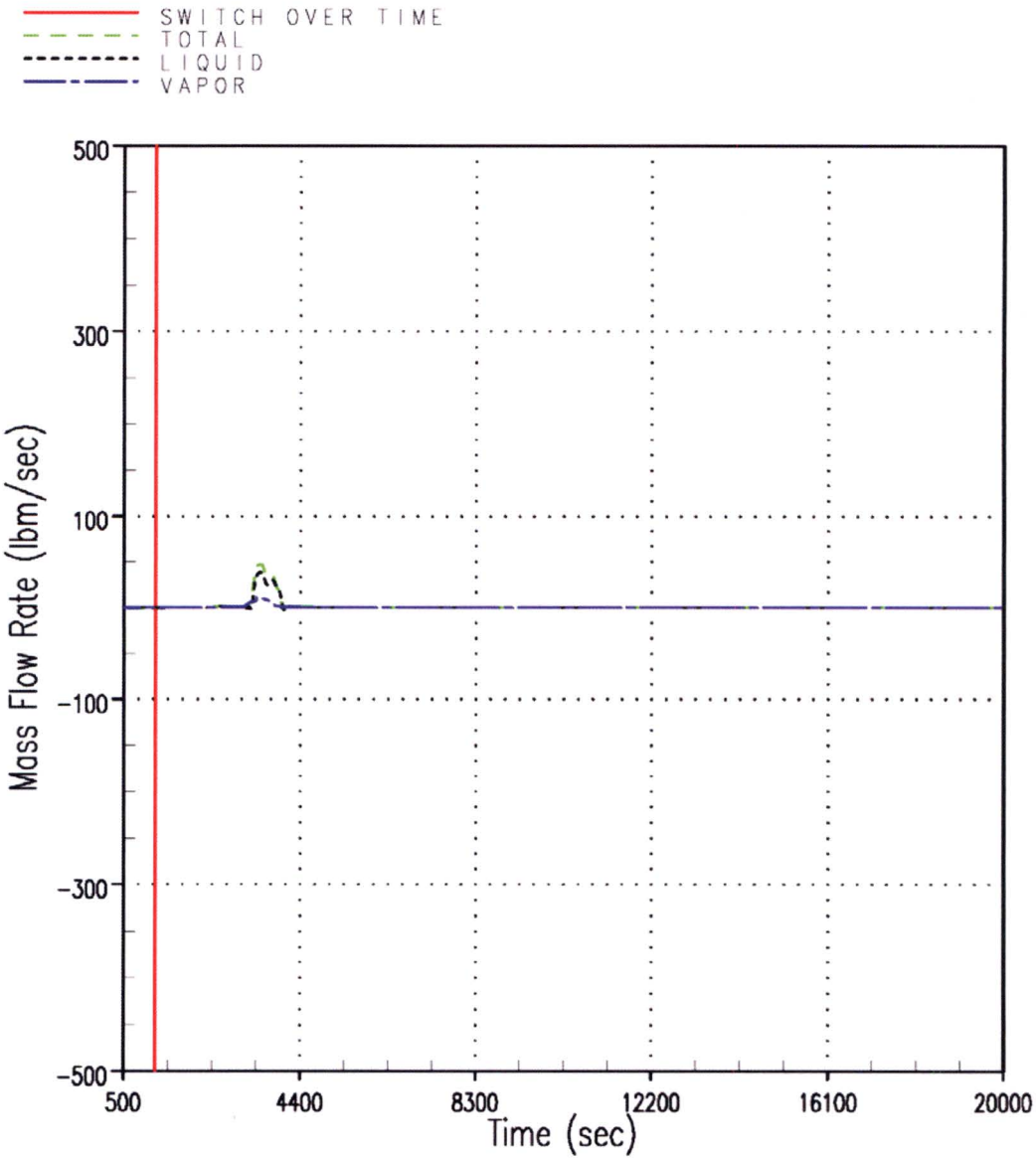

Figure RAI-4.23-109 Case 1 – Mass Flow Rates through the SG Side of the DEG Break

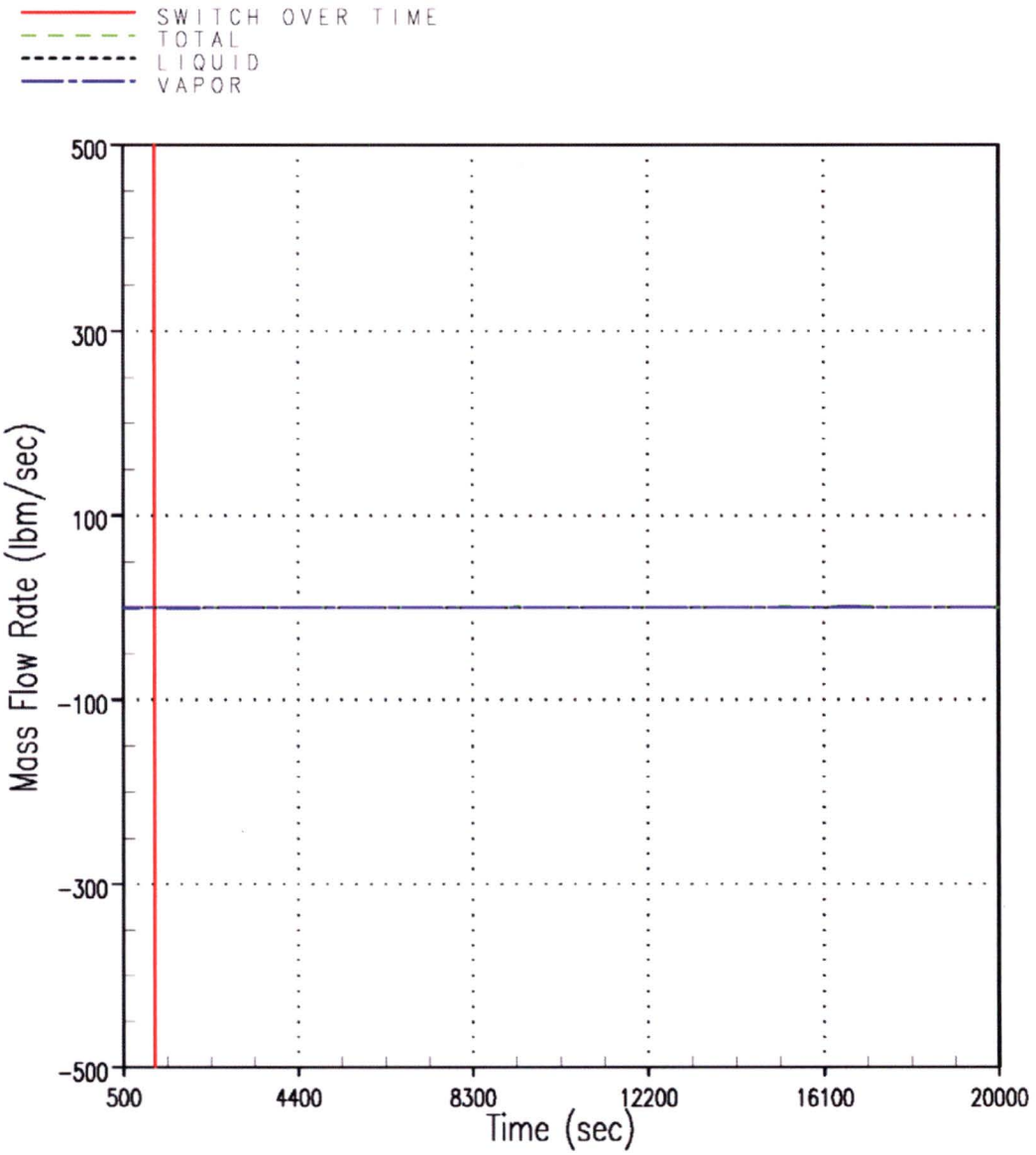

Figure RAI-4.23-110 Case 3 – Mass Flow Rates through the SG Side of the DEG Break

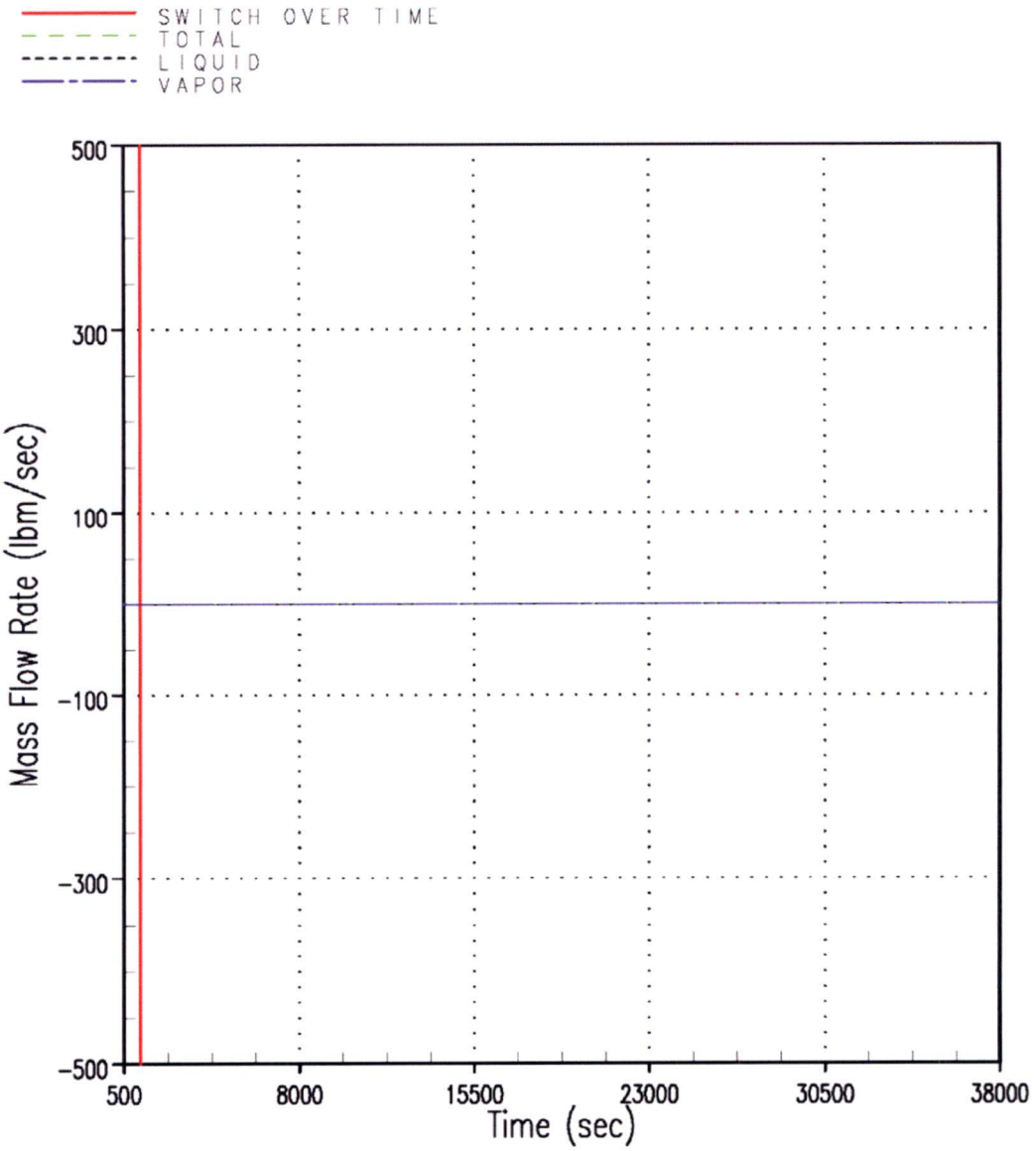

Figure RAI-4.23-111 Case 5 – Mass Flow Rates through the SG Side of the DEG Break

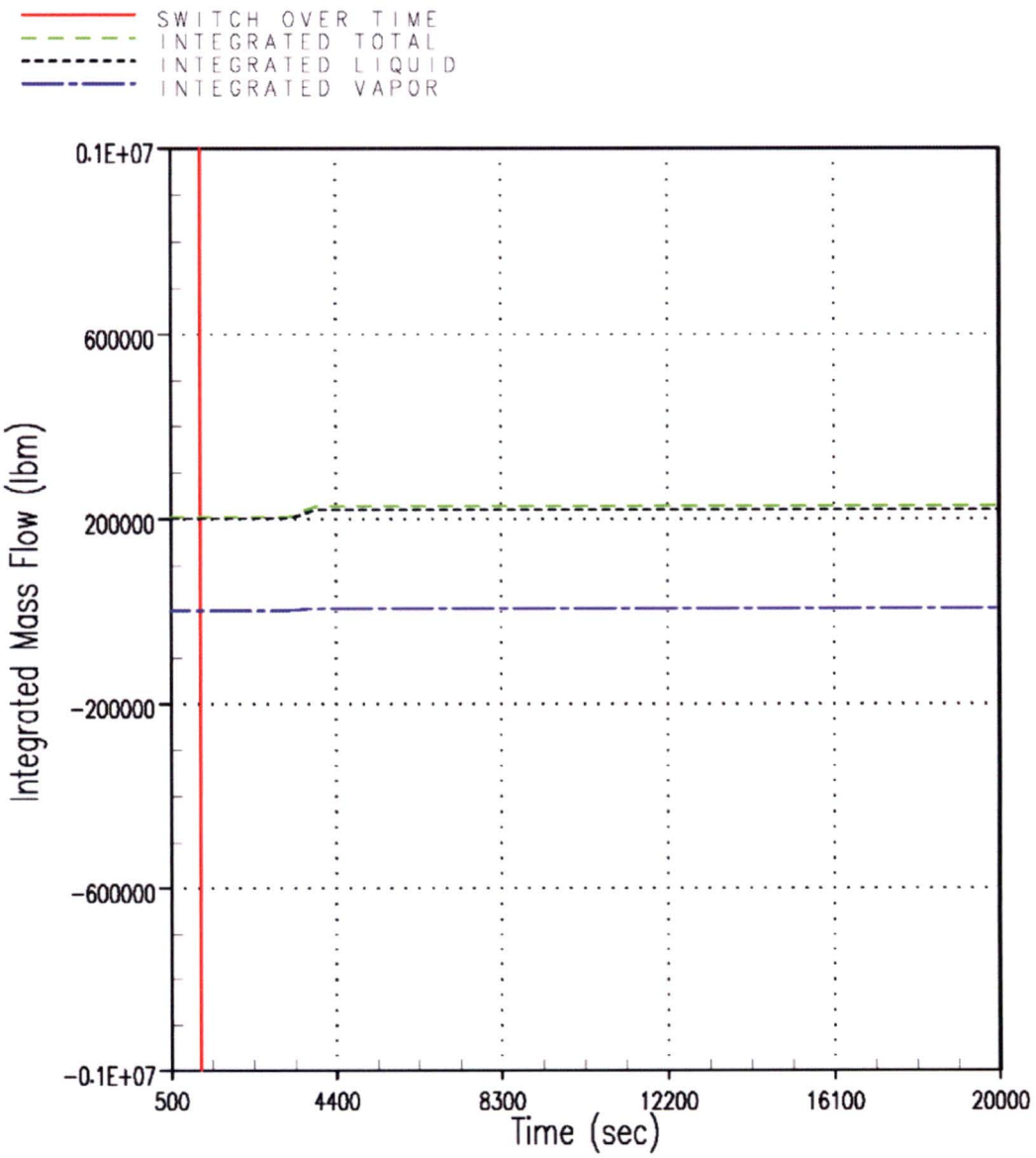

Figure RAI-4.23-112 Case 1 – Integrated Mass Flow through the SG Side of the DEG Break

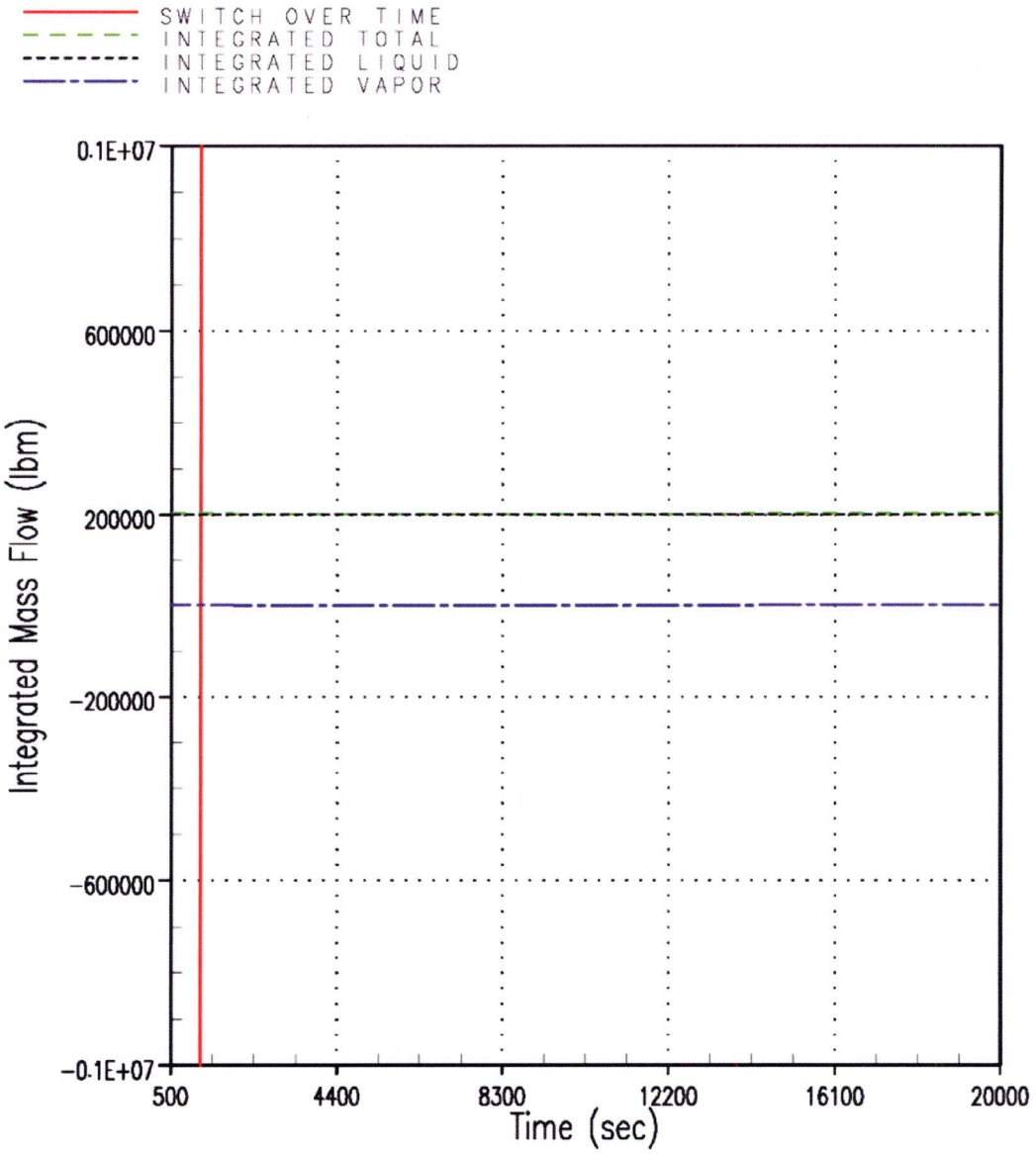

Figure RAI-4.23-113 Case 3 – Integrated Mass Flow through the SG Side of the DEG Break

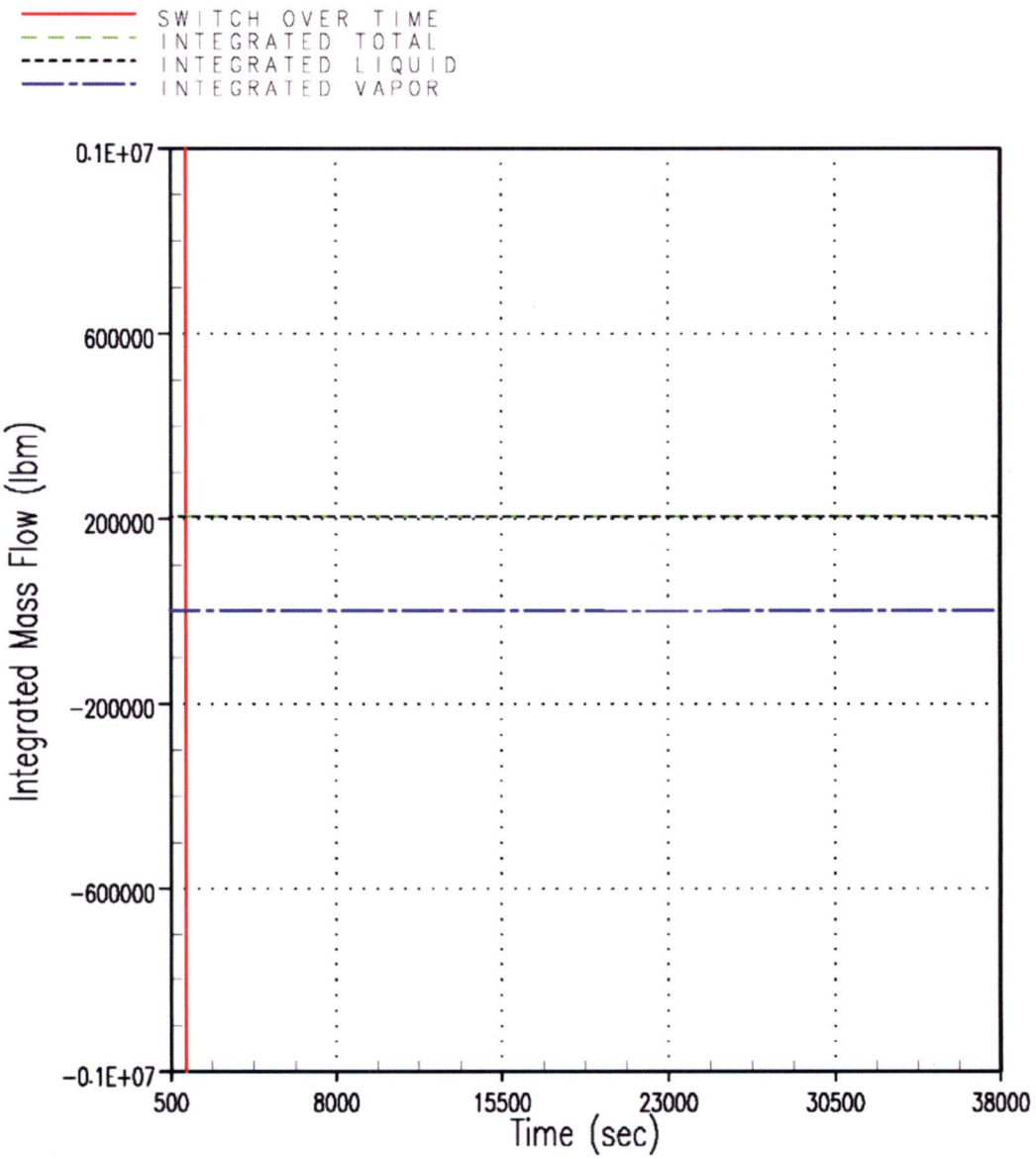

Figure RAI-4.23-114 Case 5 – Integrated Mass Flow through the SG Side of the DEG Break

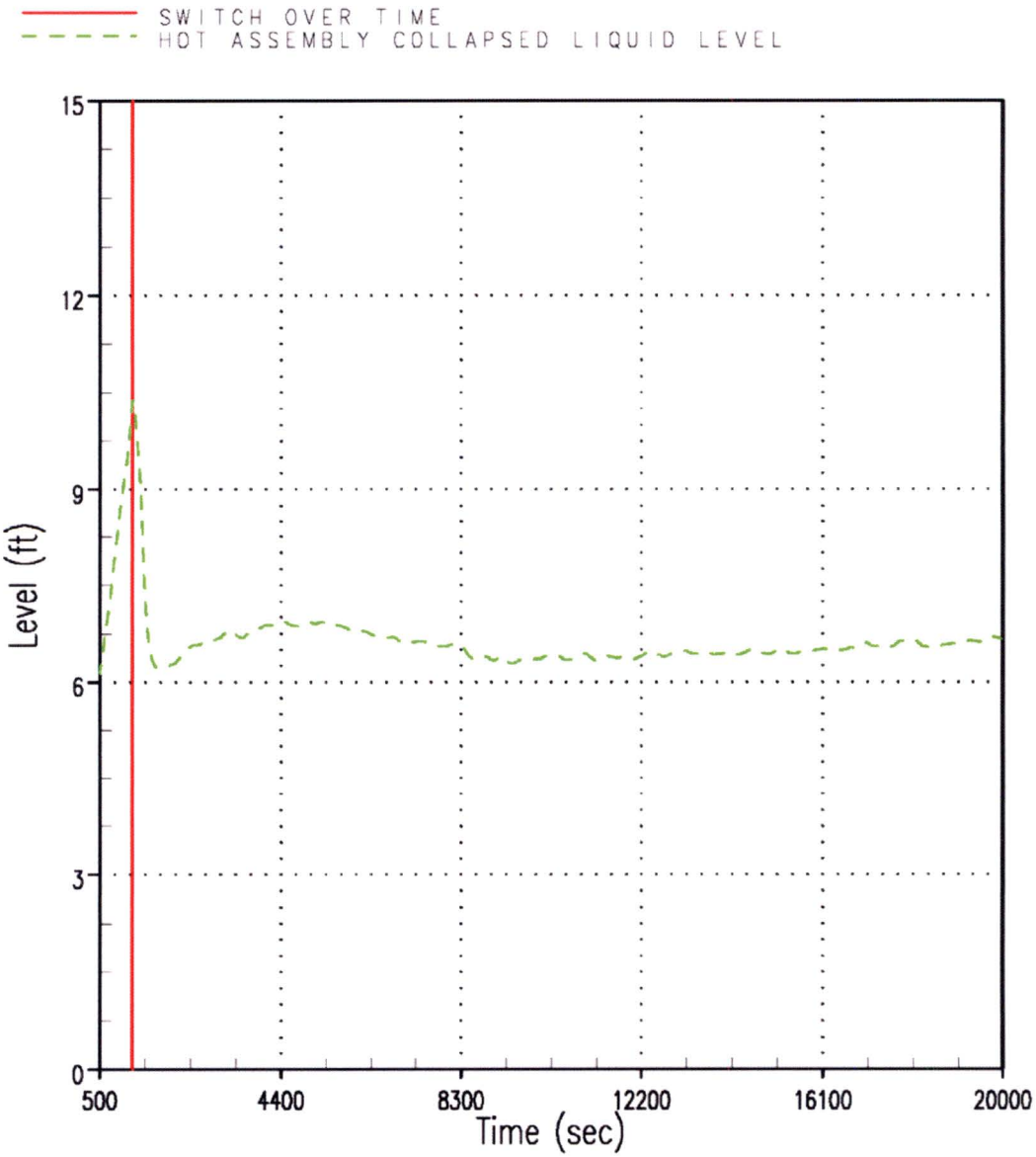

Figure RAI-4.23-115 Case 1 – Hot Assembly CLL

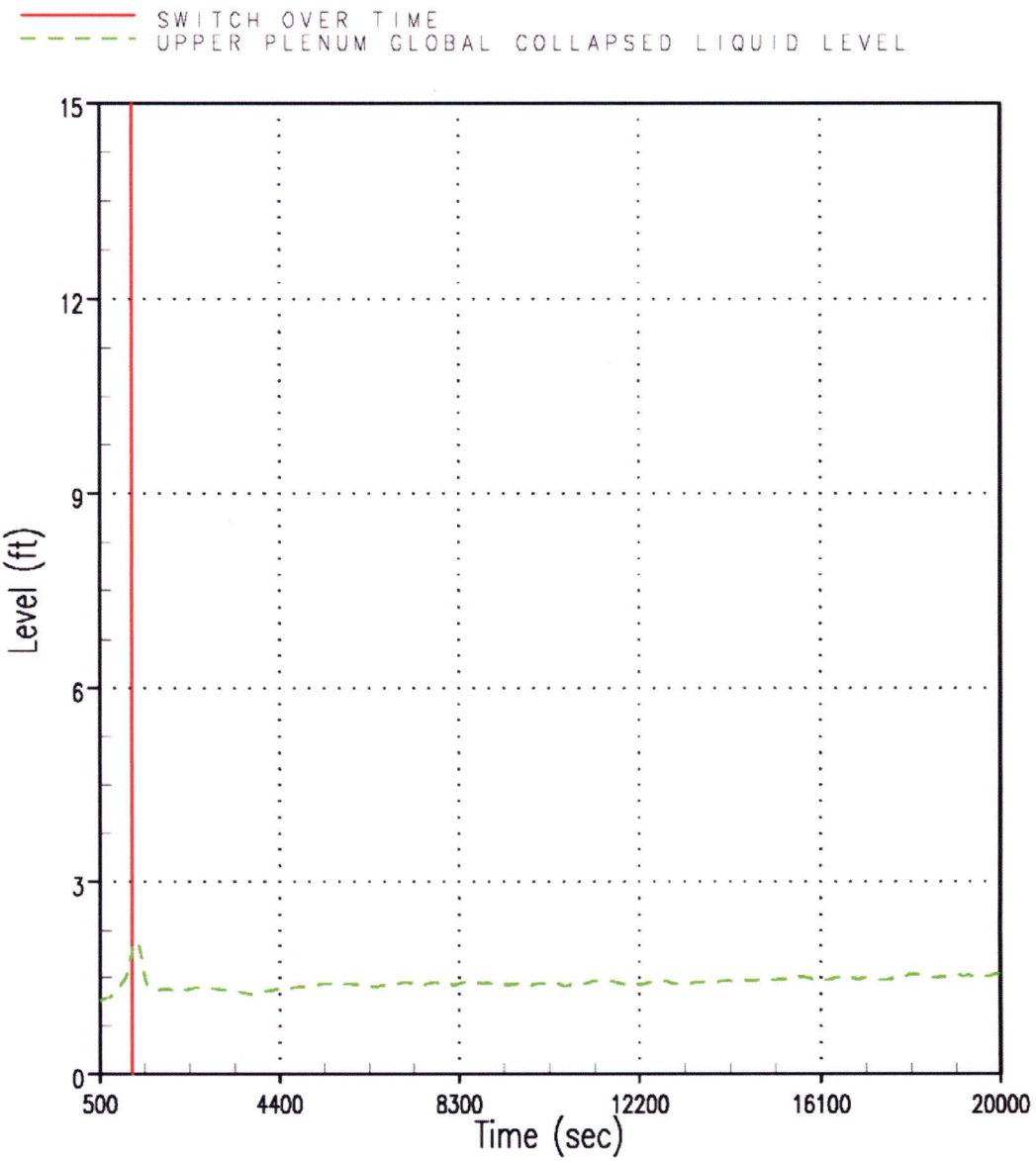

Figure RAI-4.23-116 Case 1 – UP Global CLL

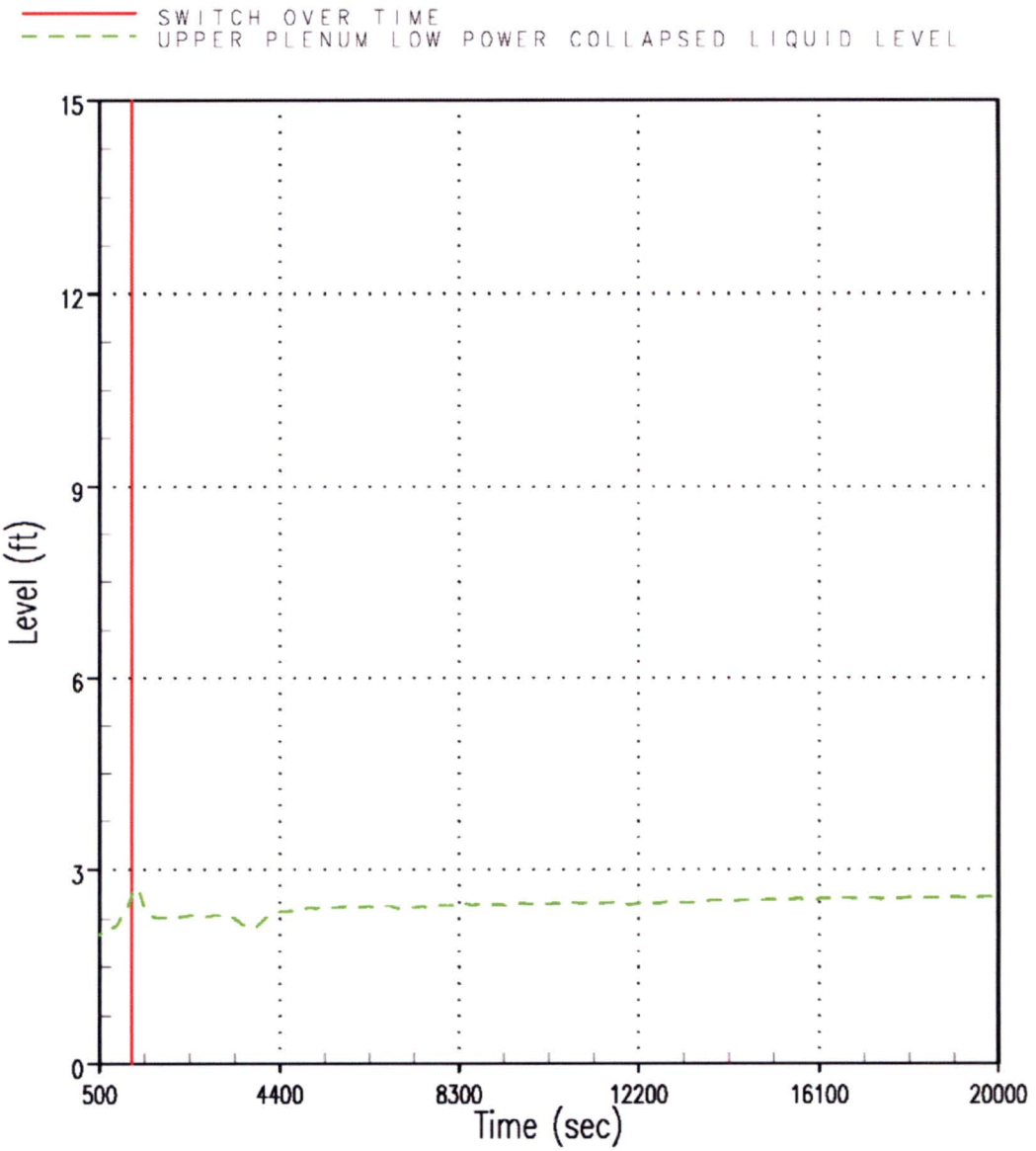

Figure RAI-4.23-117 Case 1 – UP Low Power CLL

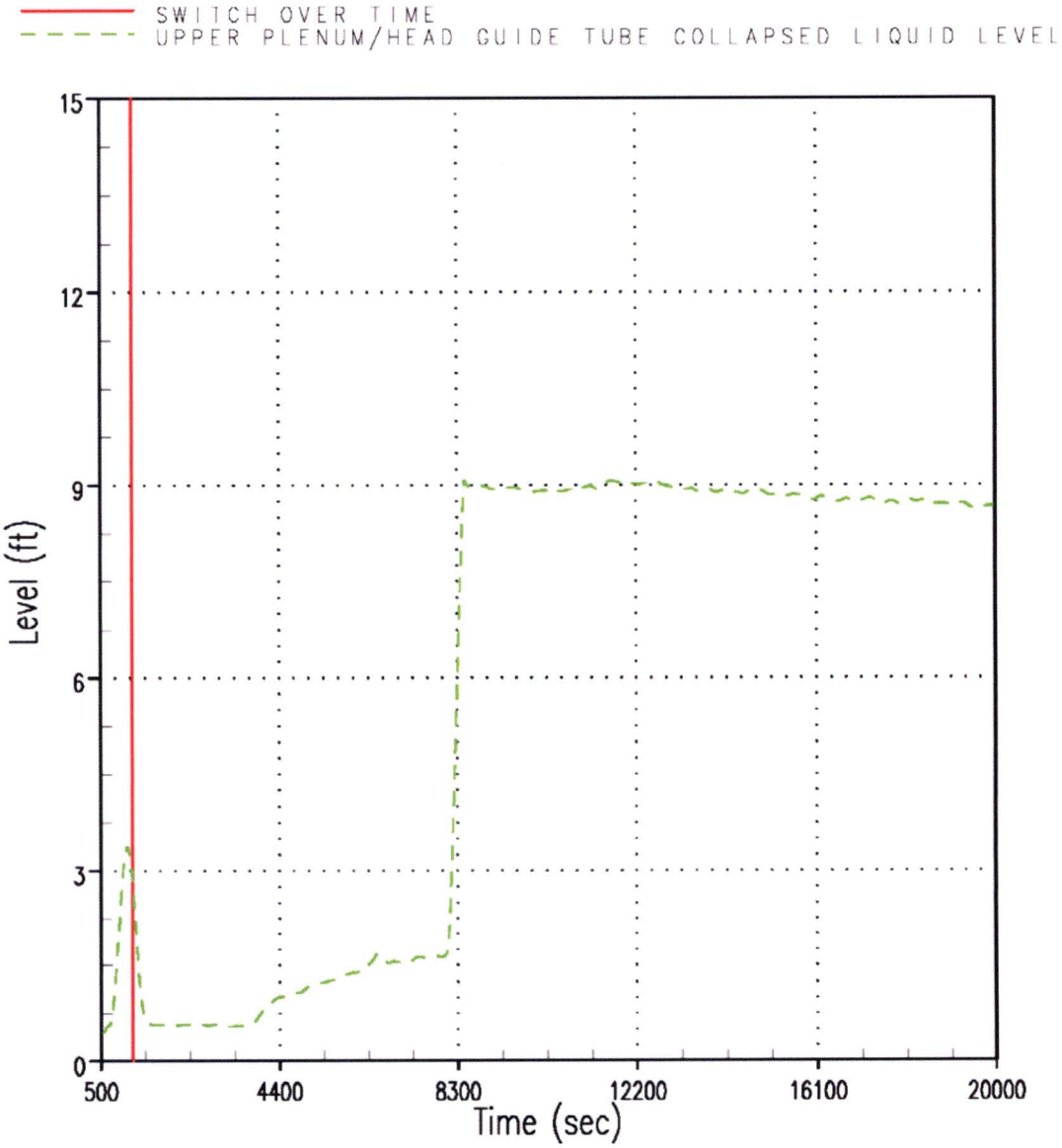

Figure RAI-4.23-118 Case 1 – UP / Upper Head Guide Tube CLL

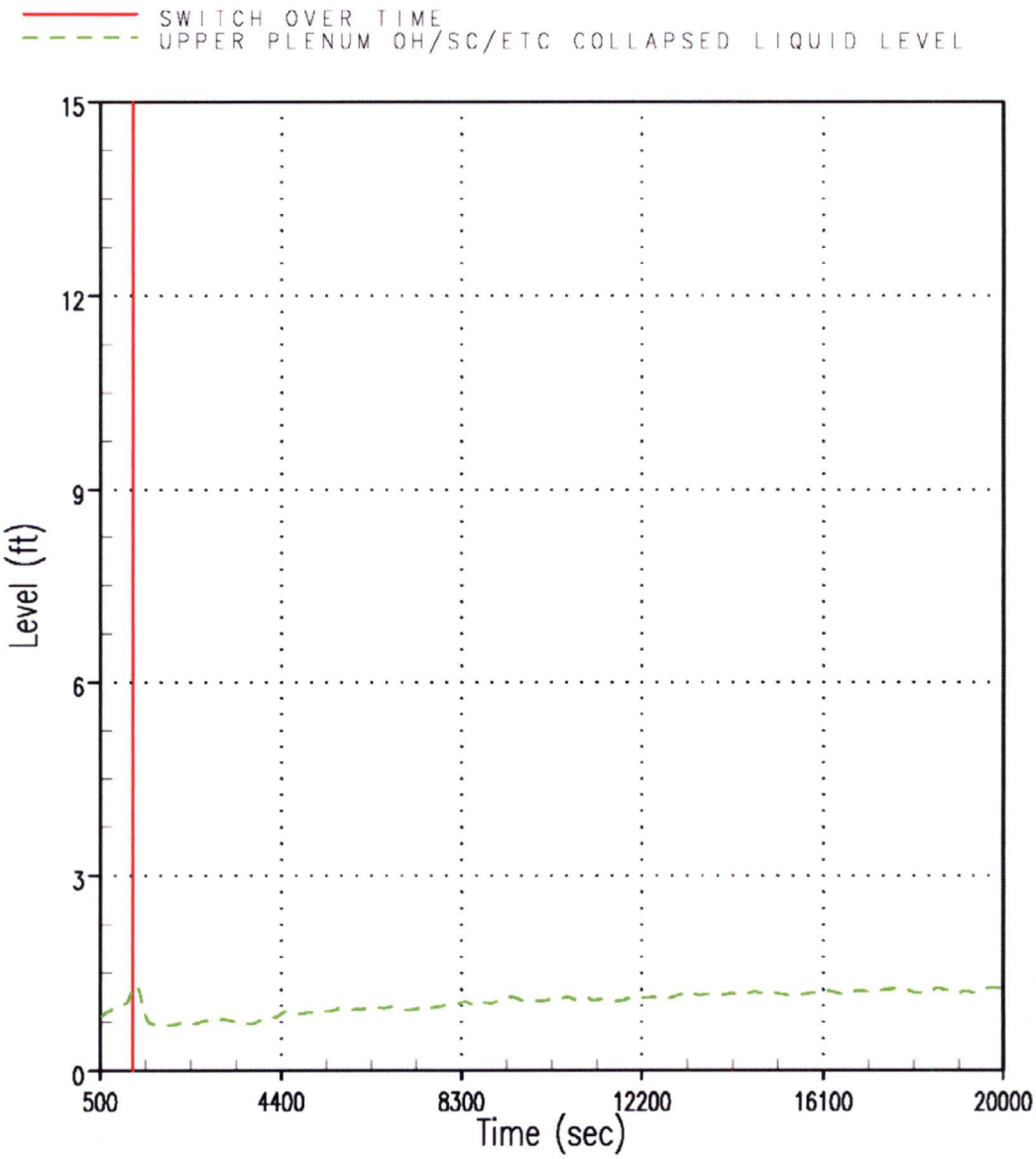

Figure RAI-4.23-119 Case 1 – UP Open Hole / Support Column / etc CLL

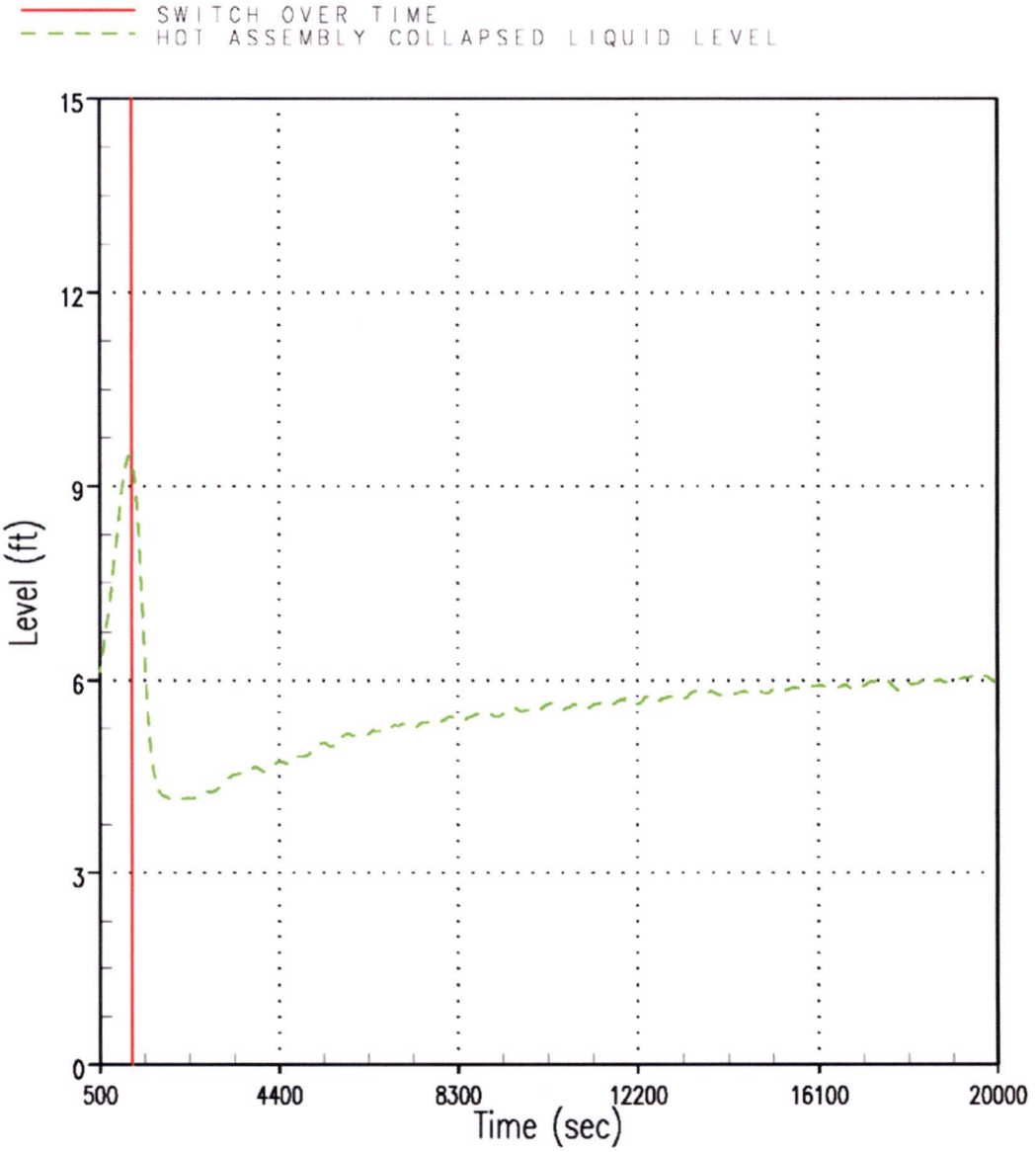

Figure RAI-4.23-120 Case 3 – Hot Assembly CLL

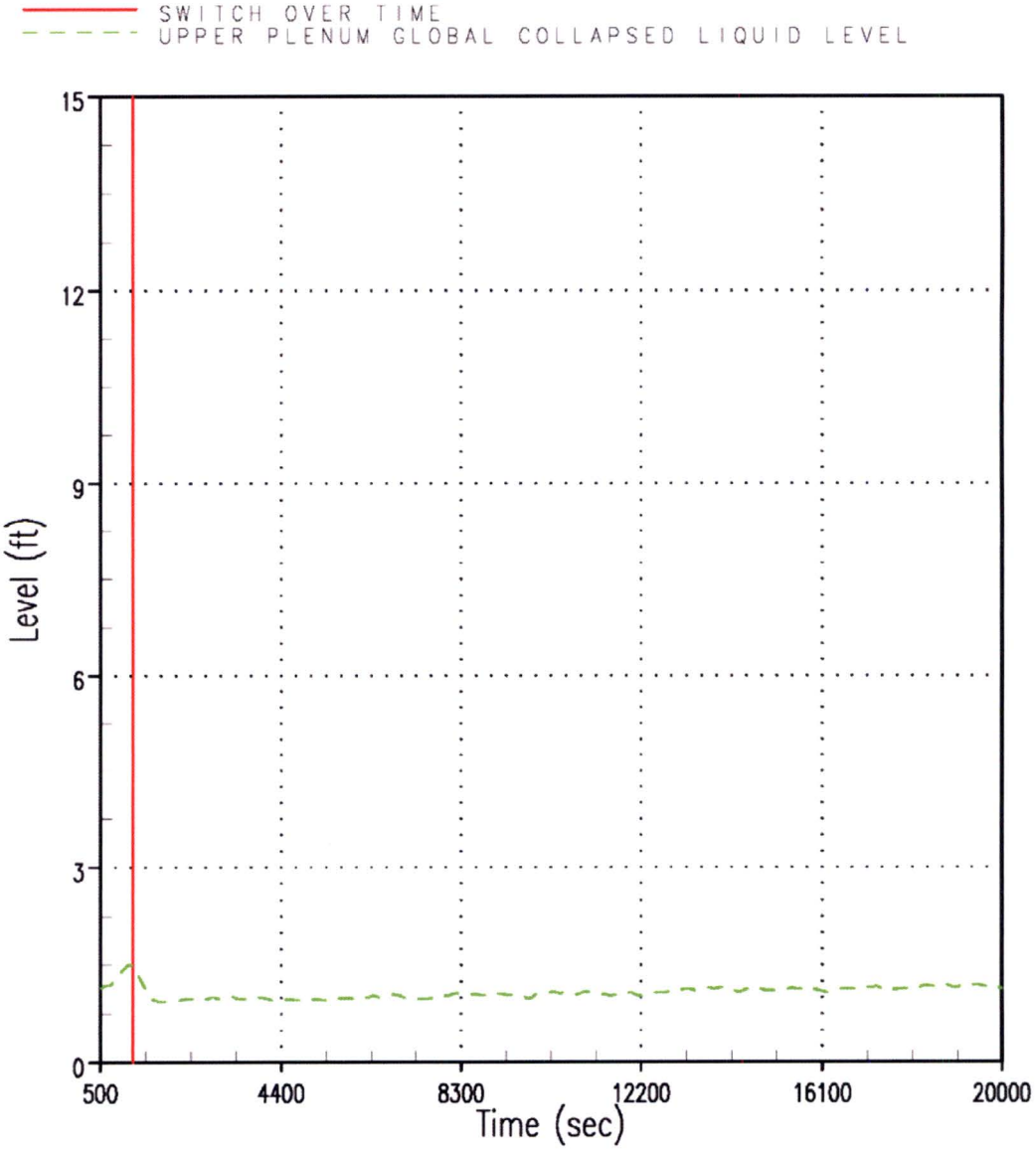

Figure RAI-4.23-121 Case 3 – UP Global CLL

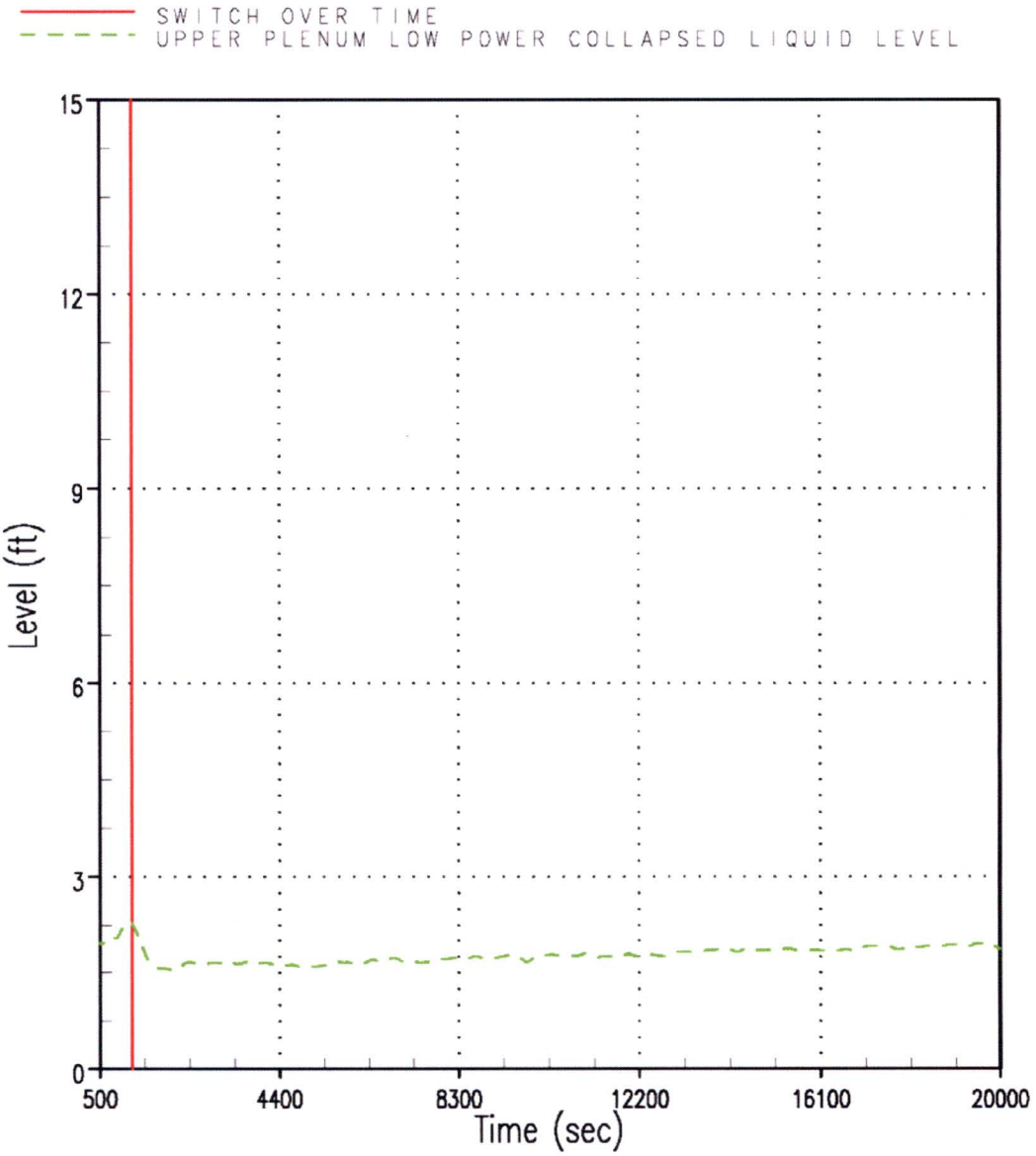

Figure RAI-4.23-122 Case 3 – UP Low Power CLL

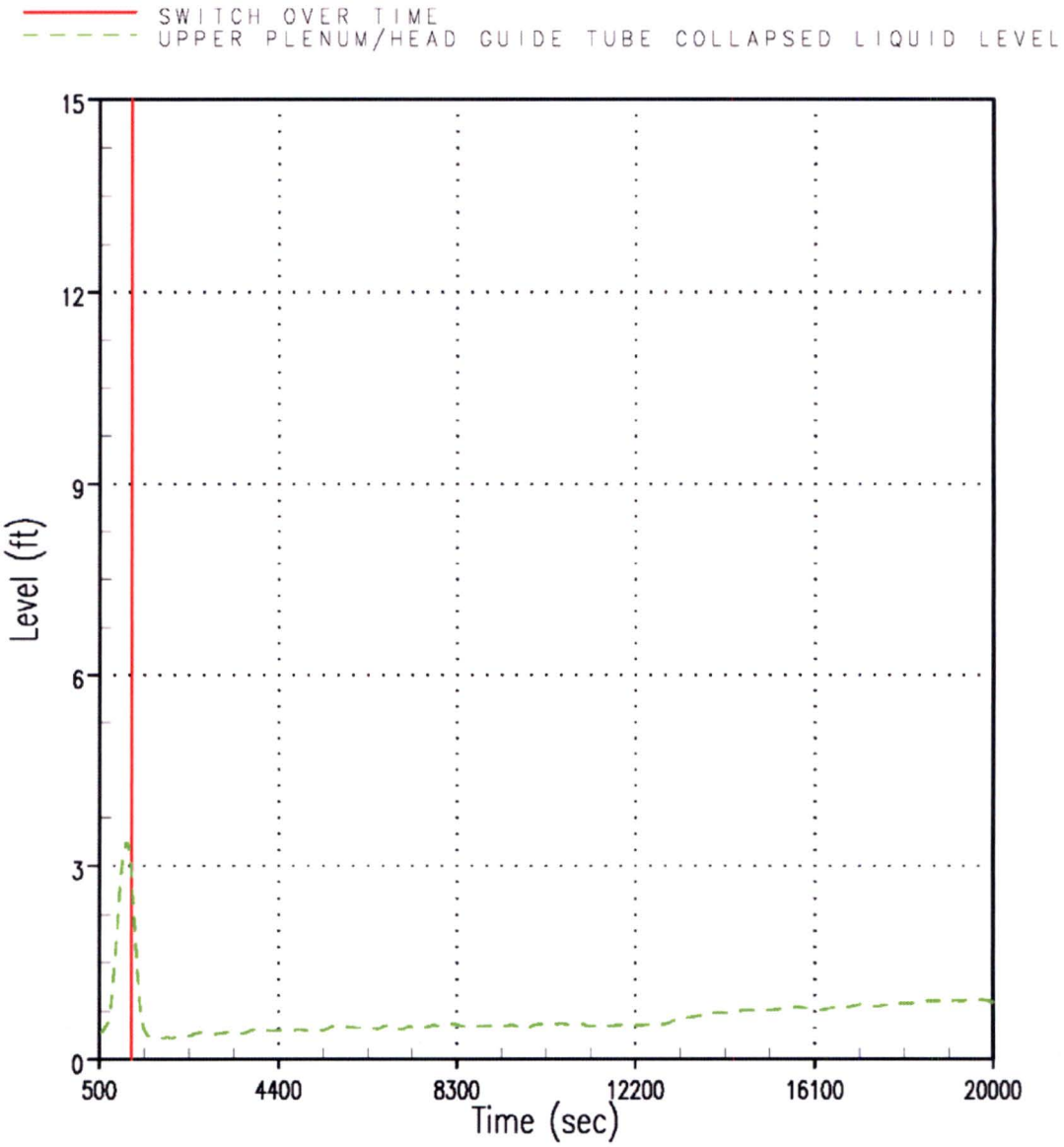

Figure RAI-4.23-123 Case 3 – UP / Upper Head Guide Tube CLL

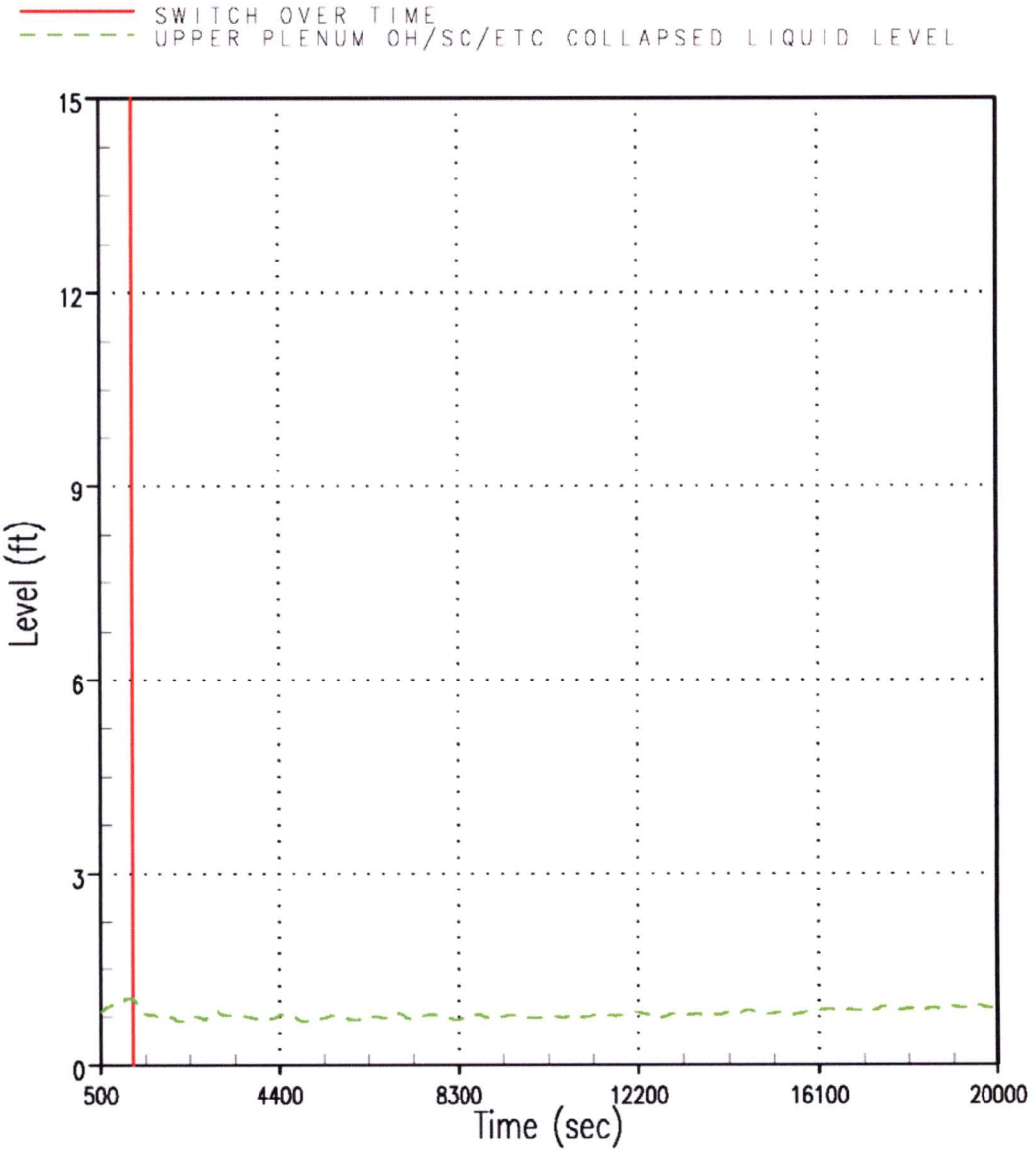

Figure RAI-4.23-124 Case 3 – UP Open Hole / Support Column / etc CLL

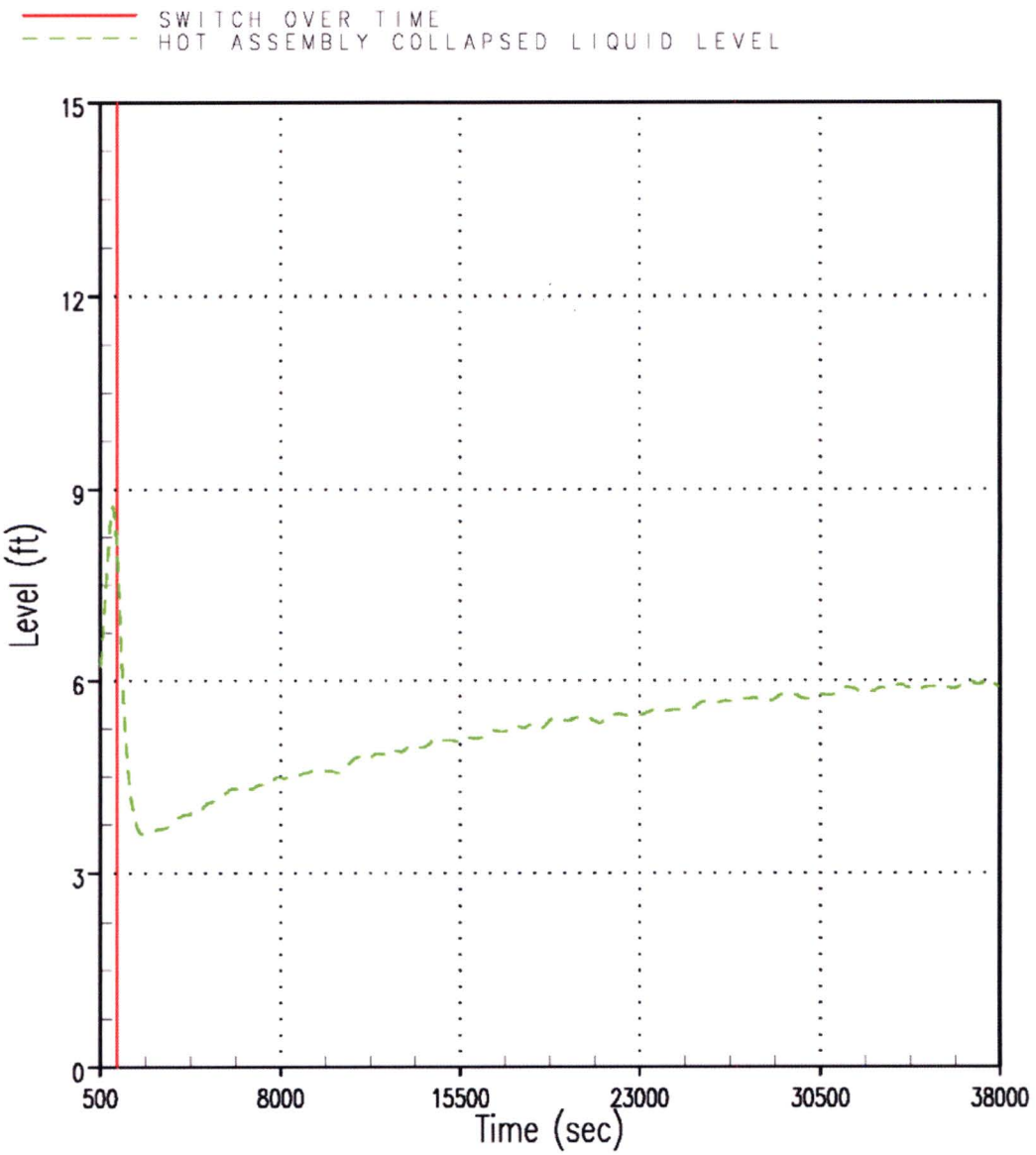

Figure RAI-4.23-125 Case 5 – Hot Assembly CLL

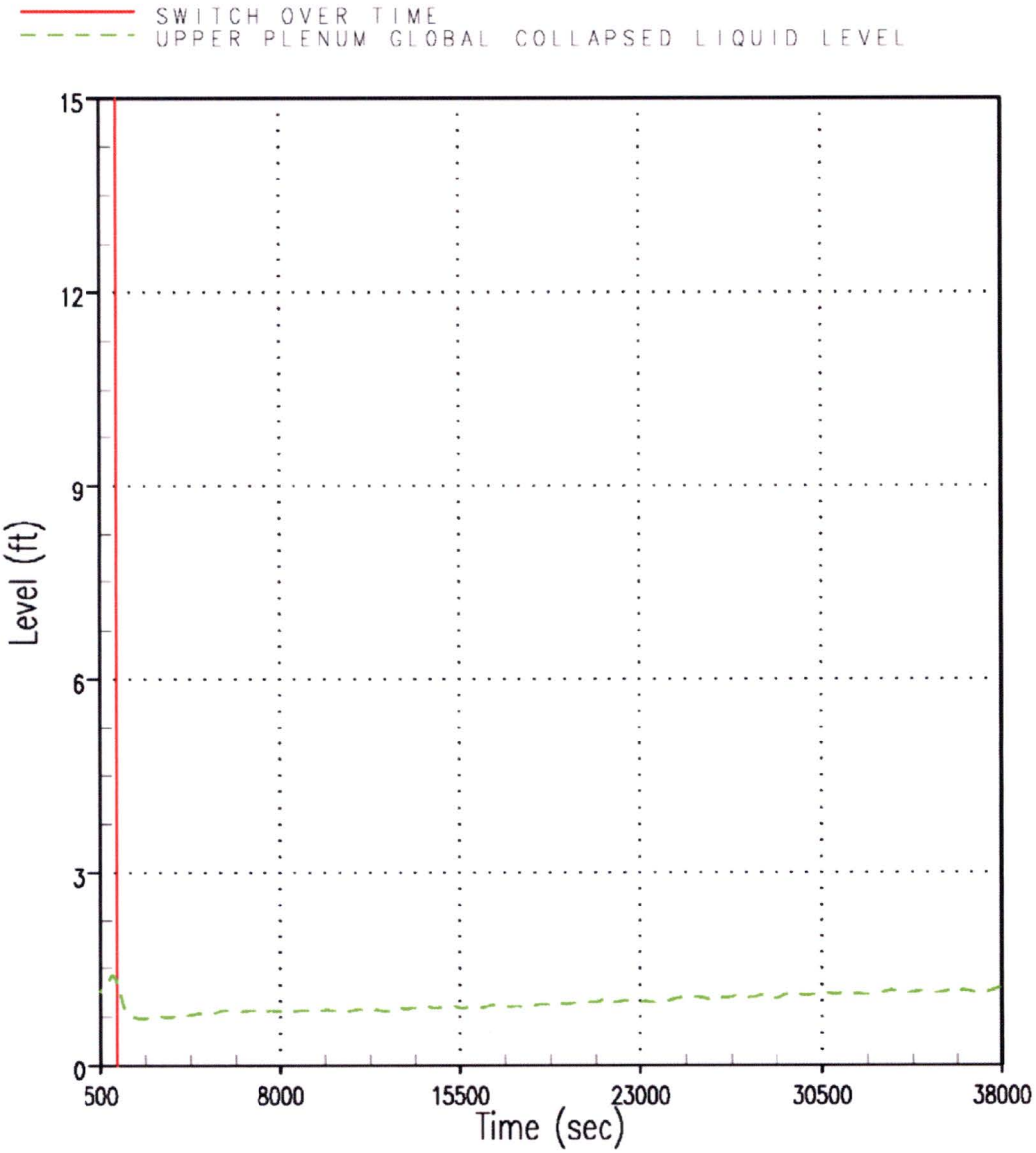

Figure RAI-4.23-126 Case 5 – UP Global CLL

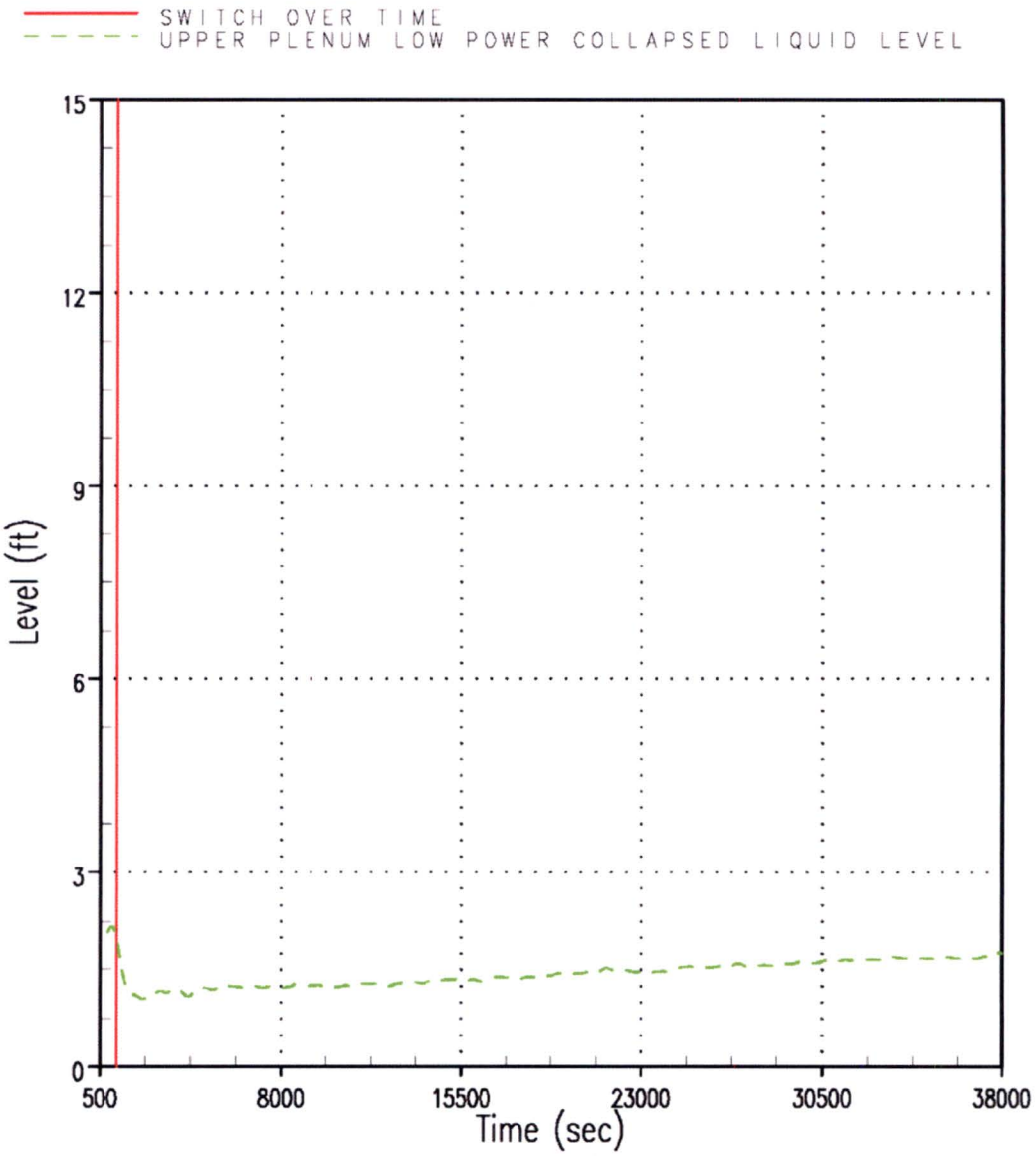

Figure RAI-4.23-127 Case 5 – UP Low Power CLL

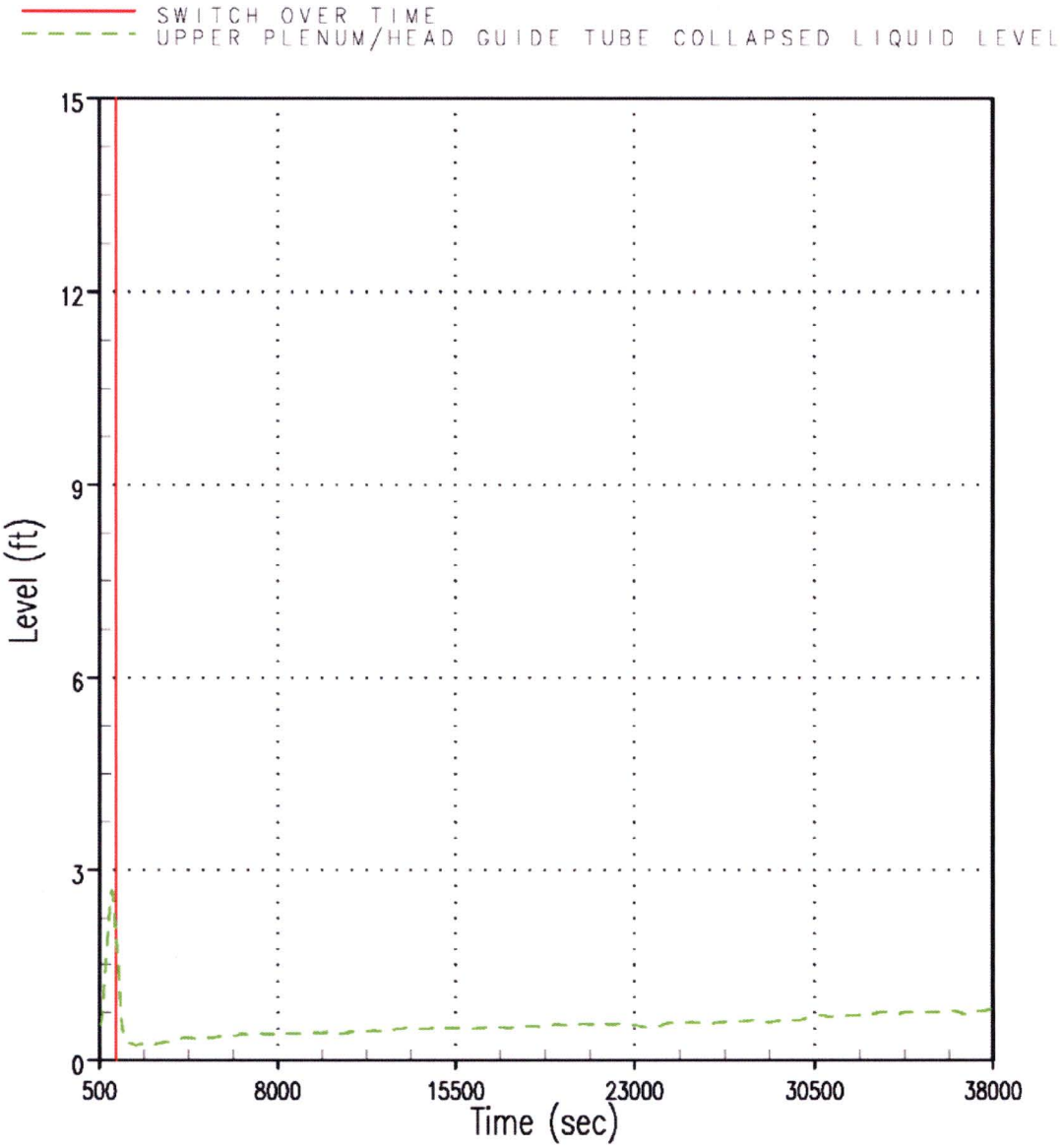

Figure RAI-4.23-128 Case 5 – UP / Upper Head Guide Tube CLL

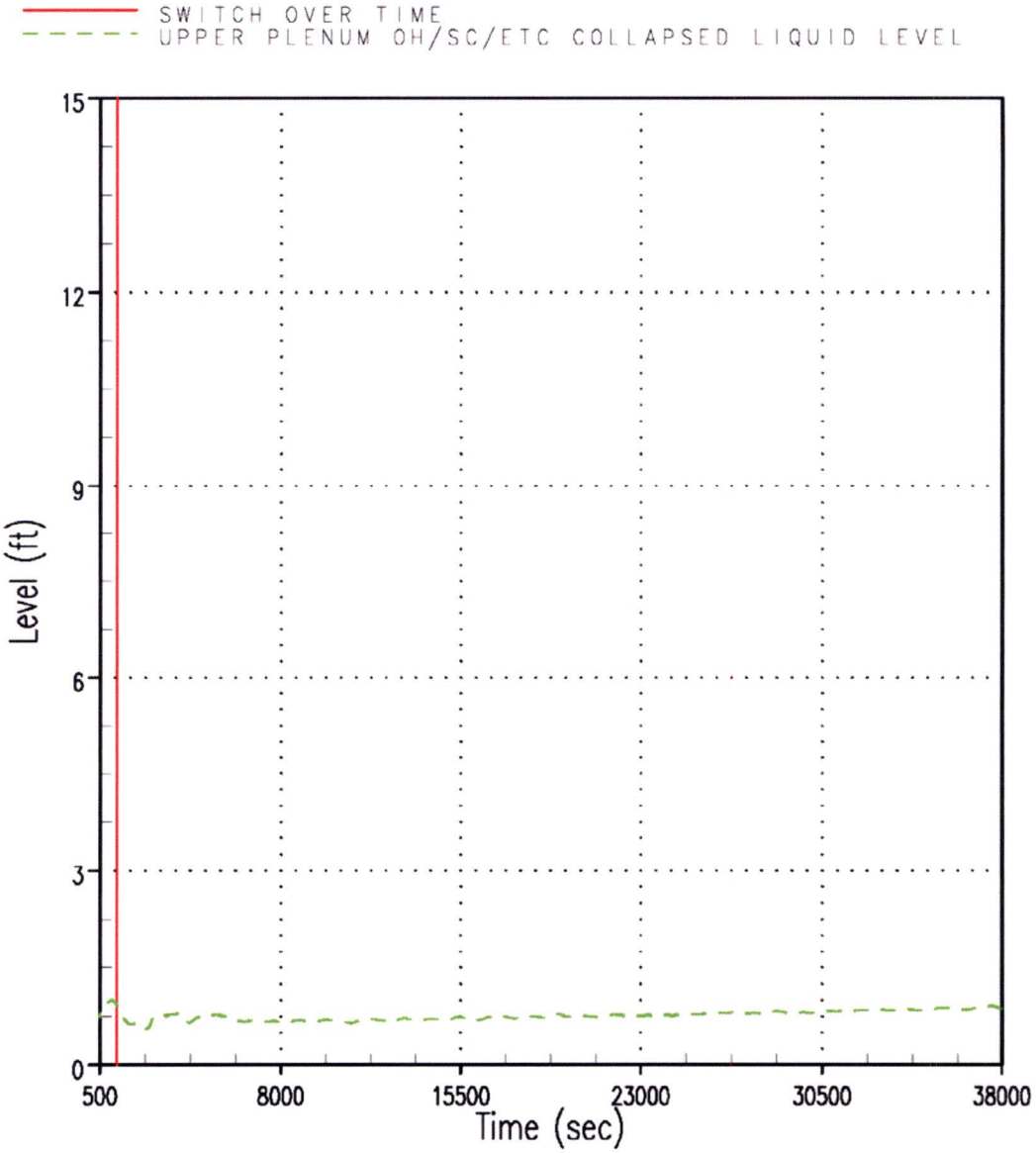

Figure RAI-4.23-129 Case 5 – UP Open Hole / Support Column / etc CLL

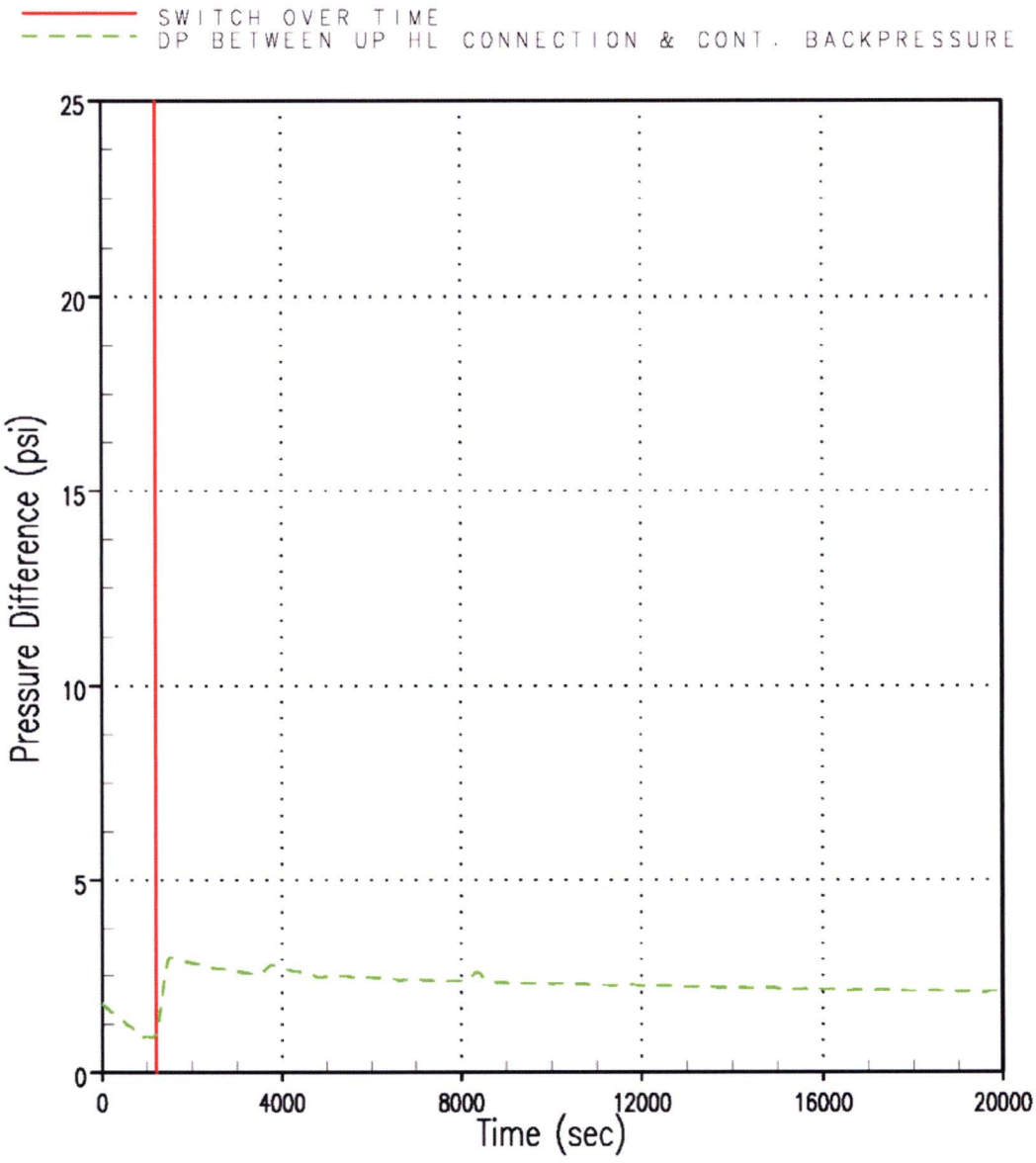

Figure RAI-4.23-130 Case 1 – Delta P between Upper Head Channel Connection to Broken HL and Containment Backpressure

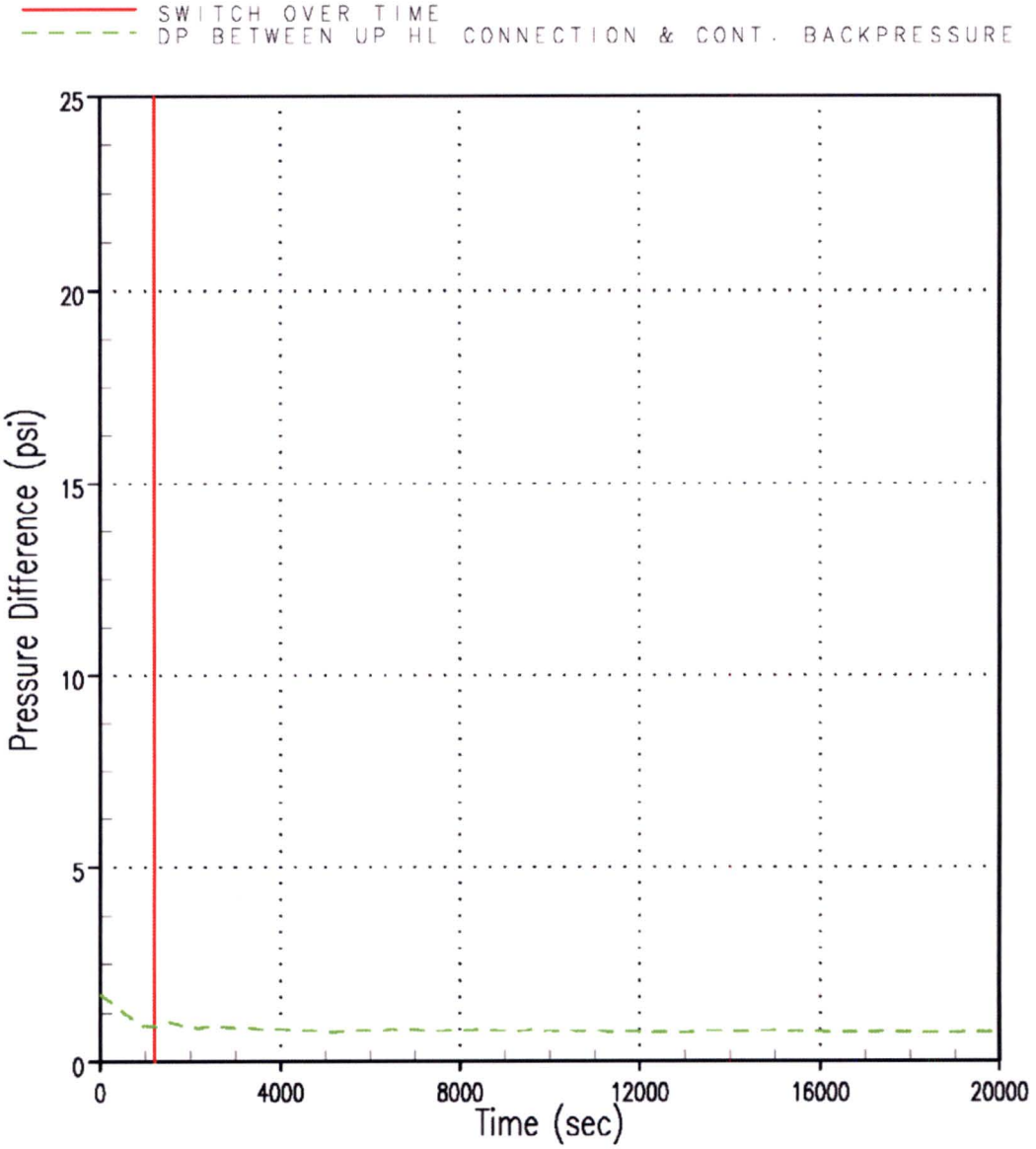

Figure RAI-4.23-131 Case 3 – Delta P between Upper Head Channel Connection to Broken HL and Containment Backpressure

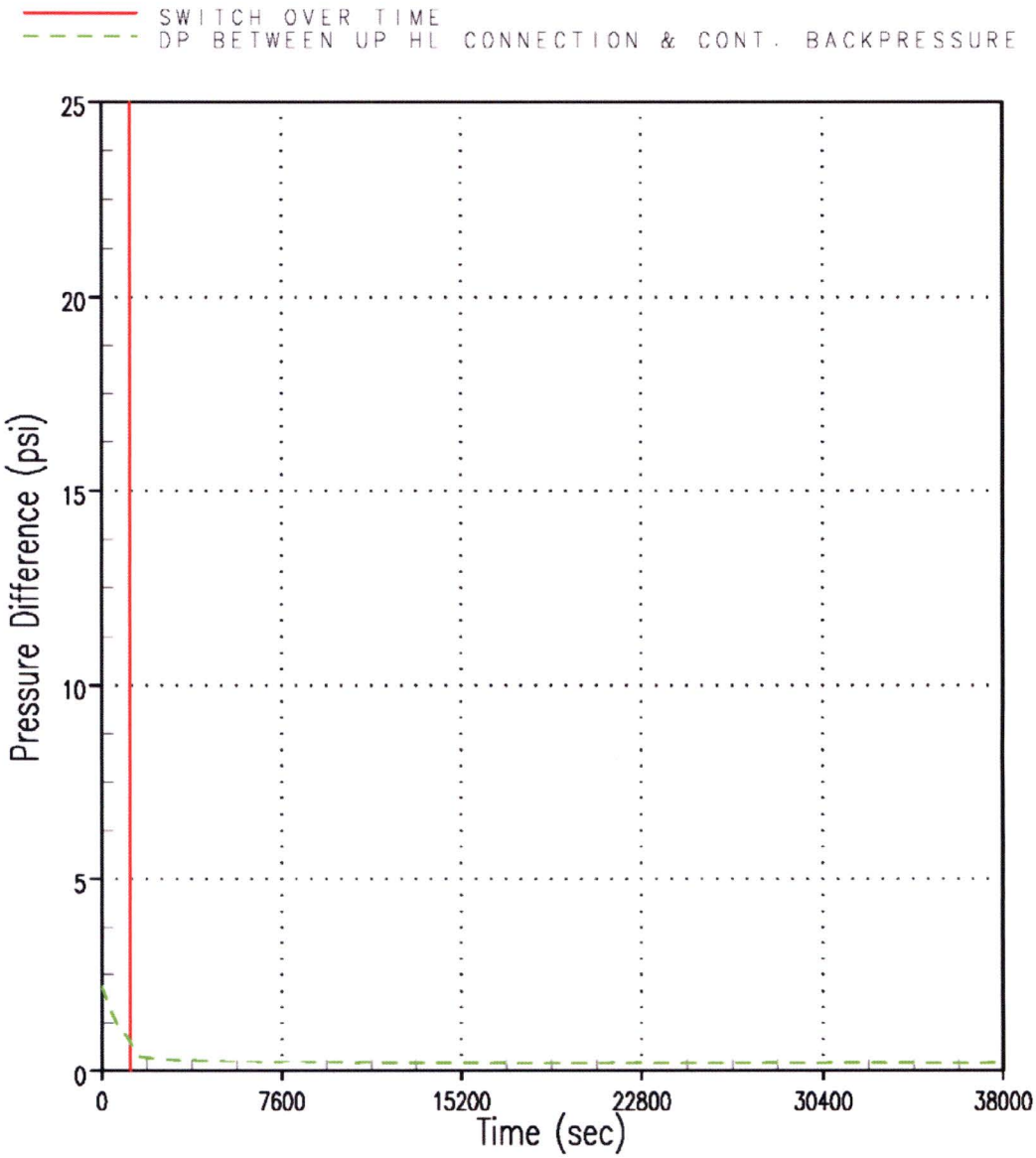

Figure RAI-4.23-132 Case 5 – Delta P between Upper Head Channel Connection to Broken HL and Containment Backpressure

f. Figure 1 below compares predicted exit qualities for the original analysis of Case 1 used to determine t_{block} for the CE plant category as documented in Section 10 and the revised analysis in Erratum, submitted with the February 12, 2016, letter OG-16-42 (t_{block} = 20,000 seconds). It is noted that the results are significantly different following the simulated blockage time in each analysis. The results also differ during some time periods prior to 15,000 seconds, which is the earlier of both simulated t_{block} times. Describe why the results prior to 15,000 seconds are not consistent between the two cases and state which case presents the correct values. Provide similar information for the time period after blockage is simulated. Please describe why the results fluctuate significantly and justify that the code performance provides a valid representation of the system.

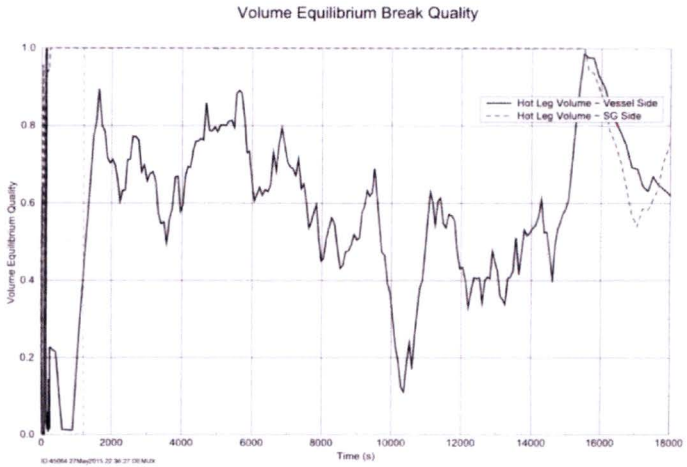

Figure 10-22 Case 1 – Break Exit Quality

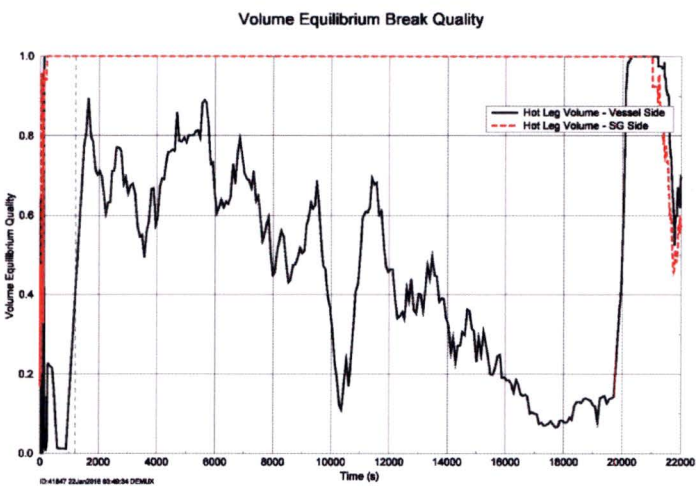

Figure 10-22 Case 1 – Break Exit Quality

Figure 1: Predicted Break Exit Qualities for Case 1 to Determine t_{block} for the CE Plant Category
(Top: original result from WCAP-17788 Rev. 0 with t_{block}=15,000 s = 250 min
Bottom: corrected result from WCAP-17788, Erratum, OG-16-42 with t_{block}=20,000 s = 333 min)

The response to these questions is provided in the CE submittal

g. During the NRC audit of the AREVA T-H analyses for the CE plant category, entrainment predictions using S-RELAP5 were presented to the NRC staff. Explain whether any code and/or plant input model changes were found necessary to address the code performance. If they were needed, identity and describe any modeling changes that were implemented along with their supporting validation bases. Justify the break liquid carry-out predictions for each of the analyses for the CE plant category in Section 10 including any revisions to these analyses. If necessary, provide updated T-H analysis results.

The response to these questions is provided in the CE submittal

h. Investigate whether the substantial scatter in the m_{split} results shown in Figure 10-5 is related to the behavior of the break liquid carry-out result. Note that if the liquid carryover is incorrect, it can render the m_{split} result unacceptable. Describe whether correction of the m_{split} results was found necessary to address the observed scatter if it was determined that effects from deficiencies in the predicted liquid entrainment were a contributing factor. Provide any updated result if applicable.

The response to these questions is provided in the CE submittal

i. Provide assessments demonstrating that t_{block}, K_{max}, K_{split}, and m_{split} results, as obtained from the analyses in Sections 8 through 11 for compliance demonstration with regard to the acceptance criteria, are accurate and not influenced unduly by deficiencies in the entrainment predictions that can be attributed to various factors such as those discussed above in Items a through h. Include consideration of the effects that the ECCS temperatures, both prior and following SSO, and modeling assumptions related to this parameter can have on the prediction results for entrainment.

Response

As described in the response to RAI-4.23.a, upper plenum two-phase mixture level is the primary factor in determining the amount of liquid discharge to the break from the reactor vessel. A number of sensitivity studies have been completed to better understand the sensitivity to break flow by varying parameters that influence the reactor vessel liquid inventory and the upper plenum two-phase mixture level. In the response to RAI-4.8, a sensitivity study is completed that varies the multiplier applied to the axial interfacial drag in the core region. Varying the multiplier tends to change the core region mixture level swell, which also impacts the upper plenum two-phase mixture level. The sensitivity study concludes that the break flow is not significantly affected by the core region interfacial drag multiplier.

Varying the ECCS subcooling is another approach to varying the upper plenum mixture level and liquid inventory since increased subcooling will reduce the steaming rate, and thus, the upper plenum void fraction. The response to RAI-4.16.d presents a sensitivity study in which the injection phase ECCS subcooling is varied, and the response to RAI-4.23.i presents a study in which the ECCS recirculation phase subcooling is varied. The results of these sensitivity studies show that ECCS subcooling does not significantly affect the liquid discharge from the break. The parameters K_{max}, t_{block}, K_{split}, and m_{split} are also not significantly impacted by ECCS subcooling.

A similar result is obtained in the decay heat sensitivity studies presented in the response to RAI-4.7. Although the liquid discharge from the break is not presented as part of the response, it can be concluded that the upper plenum liquid inventory is increased when nominal decay heat is applied, which increases the break flow. This increased upper plenum liquid inventory can be inferred from the increased reactor vessel mass and the reduced debris-induced heatup, which is partially because the increased liquid inventory in the upper plenum provides a source of coolant to the core following the application of core inlet resistance.

References

RAI-4.23-1 WCAP-12945-P-A, "Code Qualification Document for Best Estimate LOCA Analysis," March 1998.

RAI-4.23-2 WCAP-16009-P-A, "Realistic Large-Break LOCA Evaluation Methodology Using the Automated Statistical Treatment Of Uncertainty Method (ASTRUM)," January 2005.

RAI-4.24, Vol. 4

Figures 8-9 and 9-8 indicate that the total ECCS injected masses for the Westinghouse upflow and downflow design categories increase significantly at SSO even though the injection rates appear to be constant both prior to and after the observed stepwise change at SSO.

a. Provide plots of the ECCS injection rates as a function of time for Case 0A for both Westinghouse upflow and downflow plant categories.

Response

Figure RAI-4.24-1 shows the ECCS injection rate as a function of time for Case 0A from the Westinghouse upflow plant category. Figure RAI-4.24-2 shows the ECCS injection rate as a function of time for Case 0A from the Westinghouse downflow plant category.

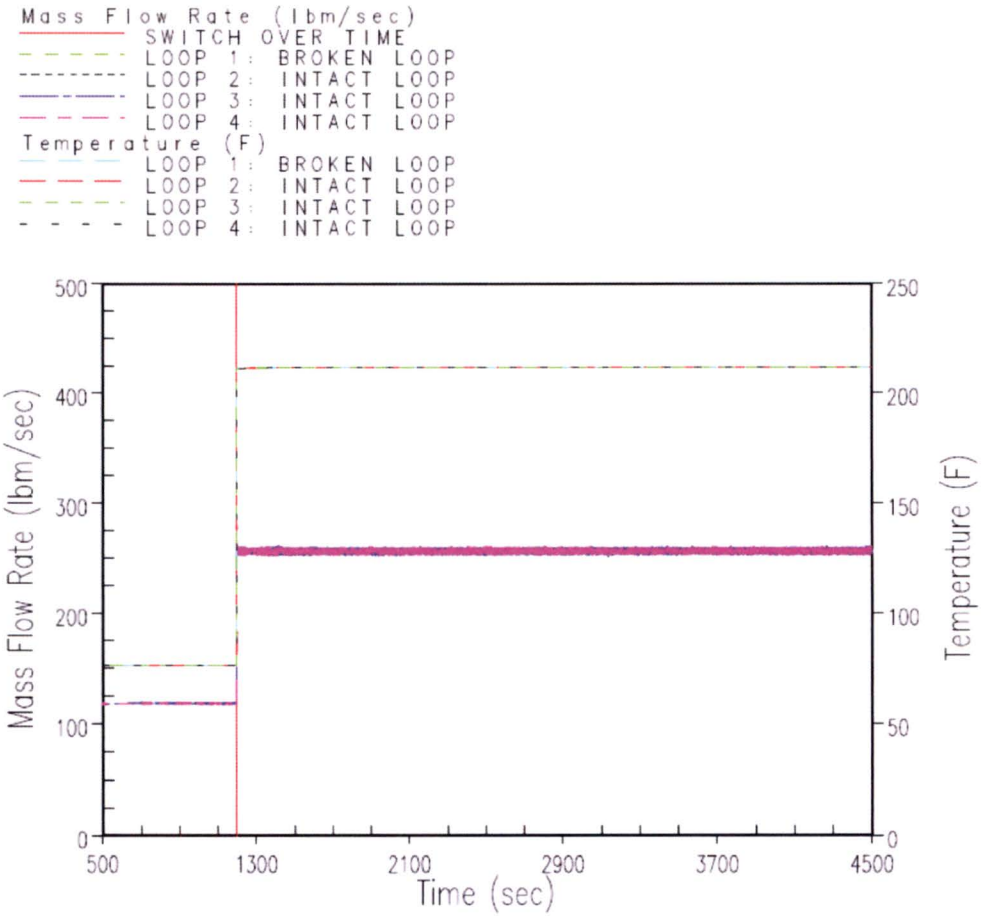

Figure RAI-4.24-1 Case 0A Injected Mass Flow Rate from the Westinghouse Upflow Plant Category

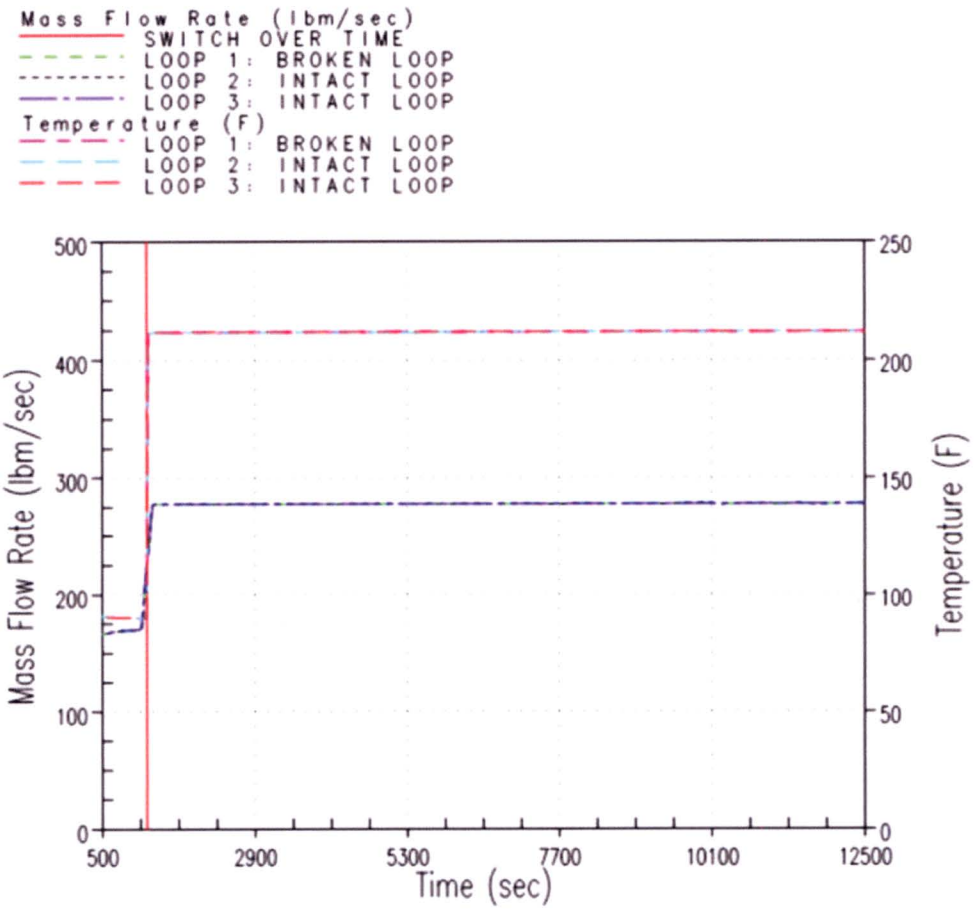

Figure RAI-4.24-2 Case 0A Injected Mass Flow Rate from the Westinghouse Downflow Plant Category

b. Explain the way in which the simulated ECCS pump injection rates prior to and following SSO were determined and identify the factors and assumptions that were considered when determining the flows. Include any temporary safety injection (SI) impediment, single failure assumptions, and pump performance characteristics among the considered factors and assumptions. In the above identified cases, the ECCS recirculation flow rate is much different from the ECCS injection rate prior to SSO.

Response

The information requested is provided in the response to RAI-4.5.

c. Clarify if varying the ECCS injection mass flow rate upon SSO had an effect on the analysis results for both plant categories.

Response

A sensitivity study was performed to determine if ECCS injection phase flow had an effect on the analysis results. The sensitivity used Westinghouse upflow plant model using Case 2B as the base case. In the sensitivity, the injection phase ECCS flow was increased to 22 gpm/FA and decreased to a value of 14 gpm/FA relative to a base case value of 18 gpm/FA. Note that, the base case flow rate of 18 gpm/FA is intended to represent the upper bound of the minimum recirculation phase flow rate since a higher flow rate increases the rate of debris transport to the core therefore resulting in an increased rate of resistance buildup at the core inlet. The case matrix is shown in Table RAI-4.24-1.

Table RAI-4.24-1 Upflow Plant Injection Phase ECCS Flow Rate Sensitivity

Case	Injection Phase Flow Rate (gpm/FA)	Recirculation Phase Flow Rate (gpm/FA)
2B (base case)	18	18
1	14	18
2	22	18

The upflow plant sensitivity results for hot assembly void fraction, core average collapsed liquid level, debris-induced PCT prediction, downcomer collapsed liquid level, barrel/baffle exit liquid flow, broken loop hot leg nozzle flow, and reactor vessel water mass are shown in Figure RAI-4.24-3 through Figure RAI-4.24-12.

Figure RAI-4.24-3, Figure RAI-4.24-4, and Figure RAI-4.24-5 show the integrated void fraction at core elevations of 103 in., 73 in., and 42 in., respectively. As shown in the figures, a higher ECCS injection flow rate tends to reduce the core void fraction in the lower core elevations prior to switchover to sump recirculation. The effect is less pronounced at higher core elevations. Following switchover to sump recirculation, and the application of core inlet resistance, the void fraction is similar across the core, as indicated by the similar slopes of the curves. This is expected since the ECCS recirculation flow is modeled the same in all the sensitivities. Although the core void

distribution is different during the injection phase, the void quickly reaches comparable distributions following switchover to sump recirculation.

Figure RAI-4.24-6 and Figure RAI-4.24-7 show the core average collapsed liquid level and the integrated core average collapsed liquid level, respectively. In Figure RAI-4.24-6, the x-axis has a range of 1000-2000 seconds to highlight the period of interest, which is when core inlet resistance is applied that leads to the core uncovery and subsequent heatup. The trends seen in the figures are expected and consistent with the void fraction. Lower ECCS injection flows tend to increase the core average collapsed liquid level prior to sump recirculation. However, after switchover to sump recirculation, the core average collapsed liquid levels are similar.

The debris-induced PCT prediction is shown in Figure RAI-4.24-8. In Figure RAI-4.24-8, the x-axis has a range of 1000-2000 seconds to highlight the period of interest, which is when core inlet resistance is applied that leads to the core uncovery and subsequent heatup. As the figure shows, the magnitude of the debris-induced PCT is affected by the ECCS injection flow rate. The 22 gpm/FA injection flow rate case resulted in a considerably lower PCT compared to the other two cases. This trend is expected since a higher injection phase flow rate tends to suppress boiling in the core and creates a condition in which more liquid inventory exists in the core. It would have been expected that the 14 gpm/FA injection flow rate case would have resulted in a higher debris-induced PCT when compared to the base case. However, Figure RAI-4.24-8 shows that the 14 gpm/FA PCT is slightly less than the 18 gpm/FA base case. This result can be attributed to the fact that the core void fraction is similar in the two cases, especially at the higher core elevations, as shown in Figure RAI-4.24-3. Any effect of ECCS injection flow rate on PCT would be the highest during the K_{max} cases since core inlet resistance is applied concurrent with switchover to sump recirculation. As the cases demonstrate, any differences due to differences in the ECCS injection flow rate quickly diminish during sump recirculation. As a result, the debris-induced PCT during the t_{block} cases would be expected to be even less sensitive to differences during the ECCS injection phase.

Figure RAI-4.24-9 shows that the injection phase downcomer collapsed liquid level is also sensitive to the ECCS injection flow rate but the sensitivity diminishes somewhat during the first 100 seconds following sump switchover. In Figure RAI-4.24-9, the x-axis has a range of 1000-2000 seconds to highlight the period of interest, which is when core inlet resistance is applied that leads to the core uncovery and subsequent heatup. This result indicates that the parameters K_{split} and m_{split} would only minimally be impacted by the ECCS injection flow rate. Since the downcomer collapsed liquid level does tend to be higher with higher injection flow rates, K_{split} would be expected to occur slightly sooner. This would also result in a slightly higher value for m_{split} during the early stages of sump recirculation. Figure RAI-4.24-10 shows the barrel/baffle channel exit integrated liquid flow. As the figure indicates, the flow through the barrel/baffle channel is slightly increased for cases with higher ECCS injection flow rates, but as the transient progresses, the differences become less significant.

Figure RAI-4.24-11 shows the broken loop hot leg nozzle integrated liquid flow rate. As expected, the liquid carryover through the broken loop hot leg nozzle increased with increased ECCS flow during the injection phase. However, during the recirculation phase, flow to the break is comparable. A similar trend is seen in the reactor vessel water mass, which is shown in Figure RAI-4.24-12. In

Figure RAI-4.24-12, the x-axis has a range of 1000-2000 seconds to highlight the period of interest, which is when core inlet resistance is applied that leads to the core uncovery and subsequent heatup. As the figure shows, increased ECCS flows during the injection phase tend to increase the reactor vessel water mass. However, as the transient progresses into the recirculation phase, the reactor vessel water masses become more comparable.

Considering results from this sensitivity study, the effect of ECCS injection flow rate is consistent with expectations. A higher ECCS injection flow rate tends to lower the debris-induced PCT predicted during the application of core inlet resistance (K_{max}) at the time of switchover to sump recirculation because the core liquid inventory is higher. Results from the sensitivity study also indicate that the sensitivity of PCT to ECCS injection flow would be diminished during later debris-induced heatups (t_{block}), provided the ECCS recirculation flow rate is the same. Any effects due to the injection phase ECCS quickly diminish during the recirculation phase. Results from this study also show that the parameter K_{split} would be expected to occur slightly sooner since increased injection flow allows creates a slightly higher downcomer collapsed liquid level upon entry into sump recirculation. The results also show that the value of m_{split} would be expected to be higher during the early stages of sump recirculation. Overall, these results demonstrate that the code behaves as expected when ECCS injection flow is varied. A similar sensitivity study is not completed for the Westinghouse downflow plant category. The phenomena that are potentially affected by the ECCS injection flow rate are not dependent on plant category. As such, the conclusions from this sensitivity study are equally applicable to the downflow plant category.

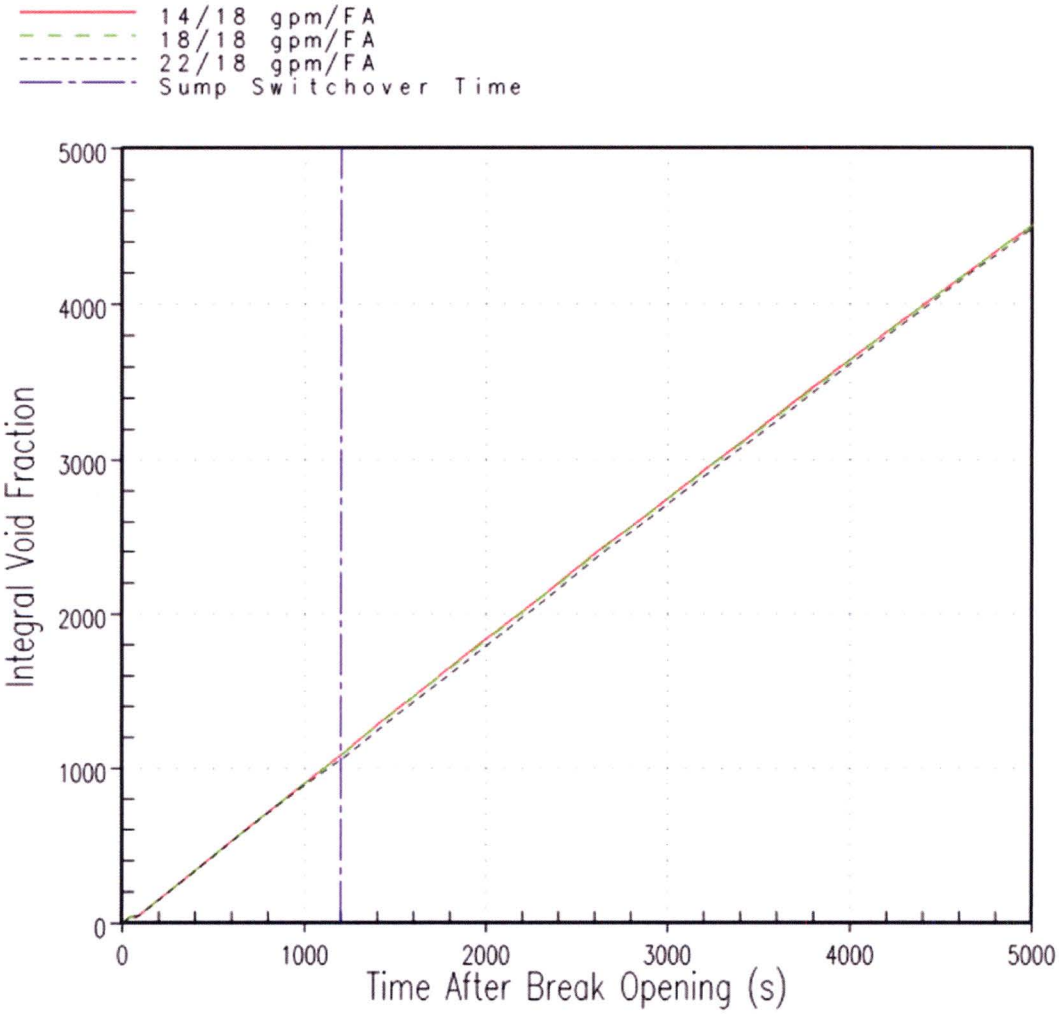

Figure RAI-4.24-3 Westinghouse Upflow Plant Injection Phase ECCS Flow Rate Sensitivity Hot Assembly Integrated Void Fraction at a Core Elevation of 103 in. Results

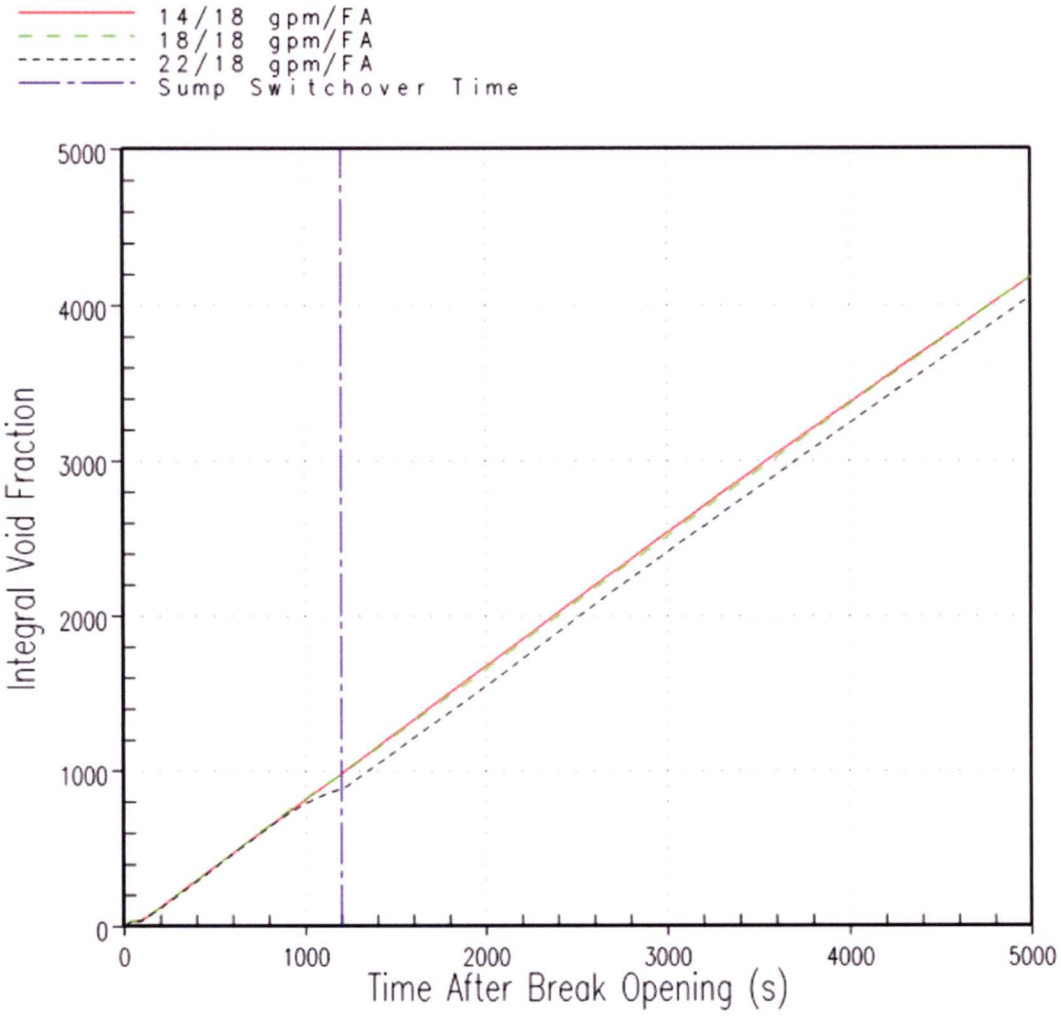

Figure RAI-4.24-4 Westinghouse Upflow Plant Injection Phase ECCS Flow Rate Sensitivity Hot Assembly Integrated Void Fraction at a Core Elevation of 73 in. Results

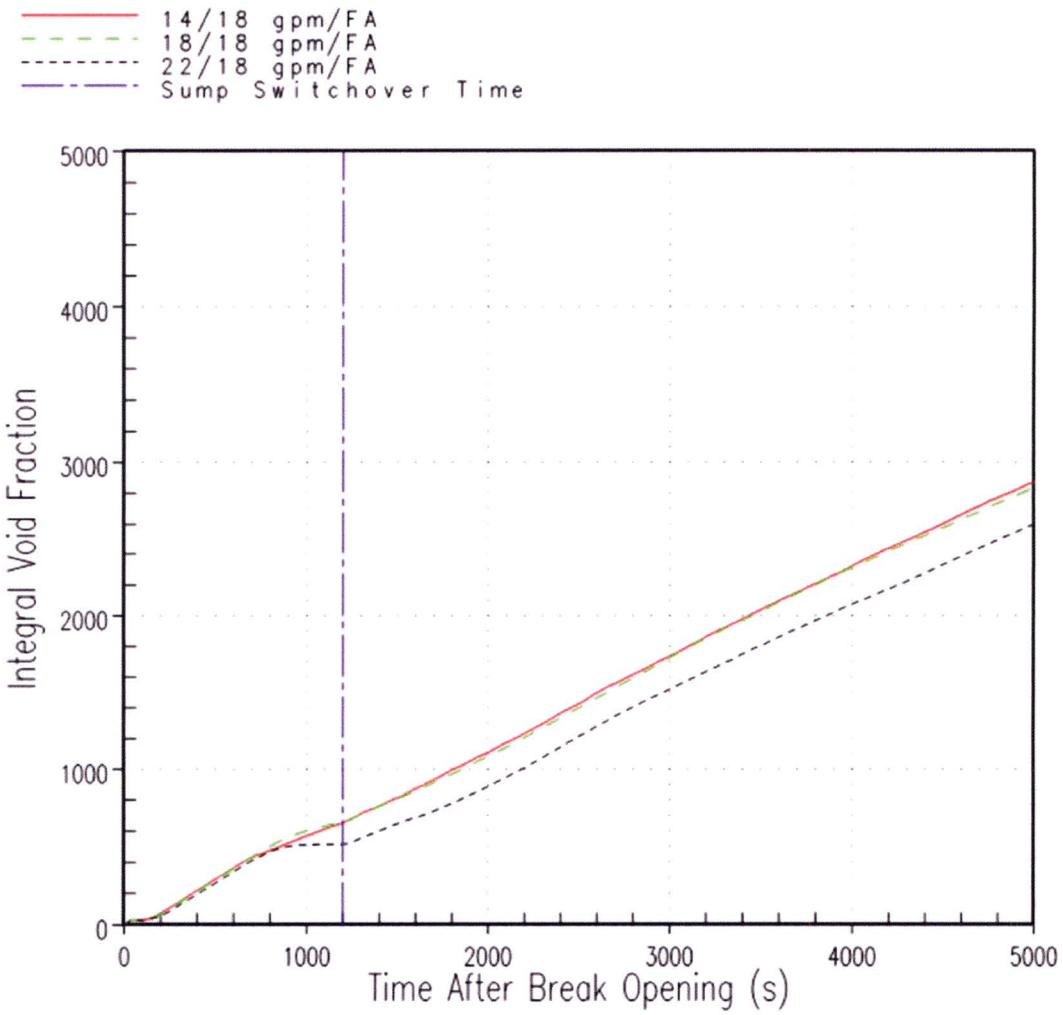

Figure RAI-4.24-5 Westinghouse Upflow Plant Injection Phase ECCS Flow Rate Sensitivity Hot Assembly Integrated Void Fraction at a Core Elevation of 42 in. Results

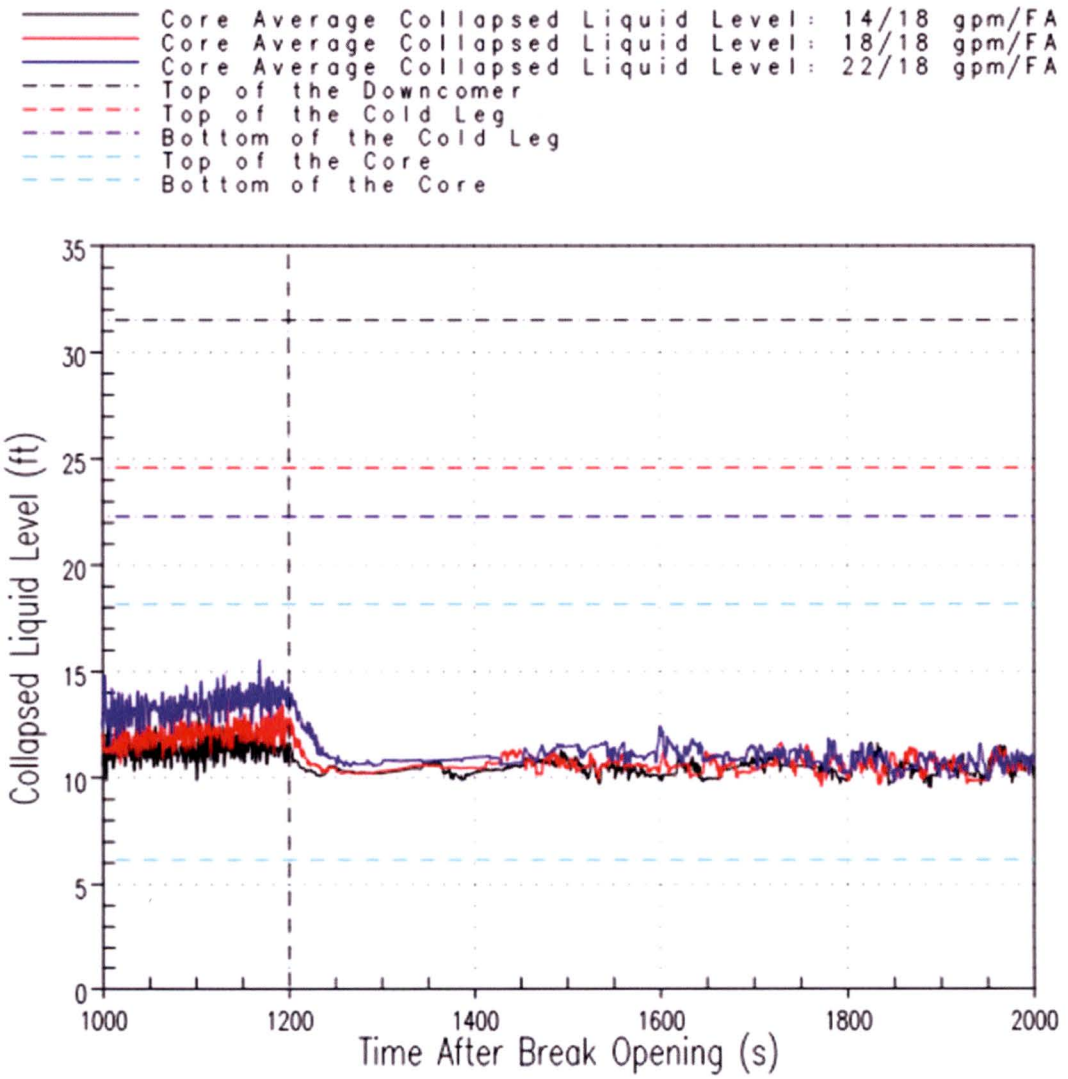

Figure RAI-4.24-6 Westinghouse Upflow Plant Injection Phase ECCS Flow Rate Sensitivity Core Average Collapsed Liquid Level Results

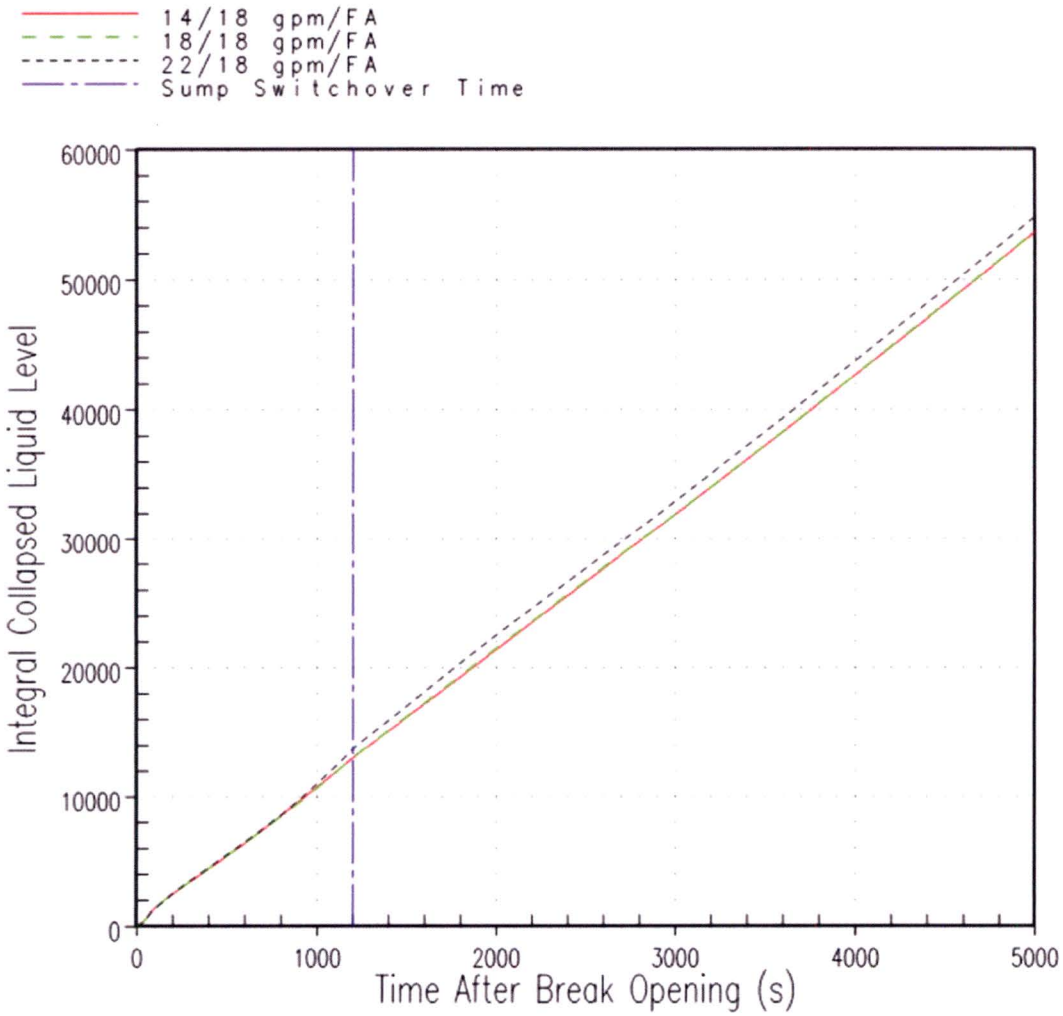

Figure RAI-4.24-7 Westinghouse Upflow Plant Injection Phase ECCS Flow Rate Sensitivity Core Average Integrated Collapsed Liquid Level Results

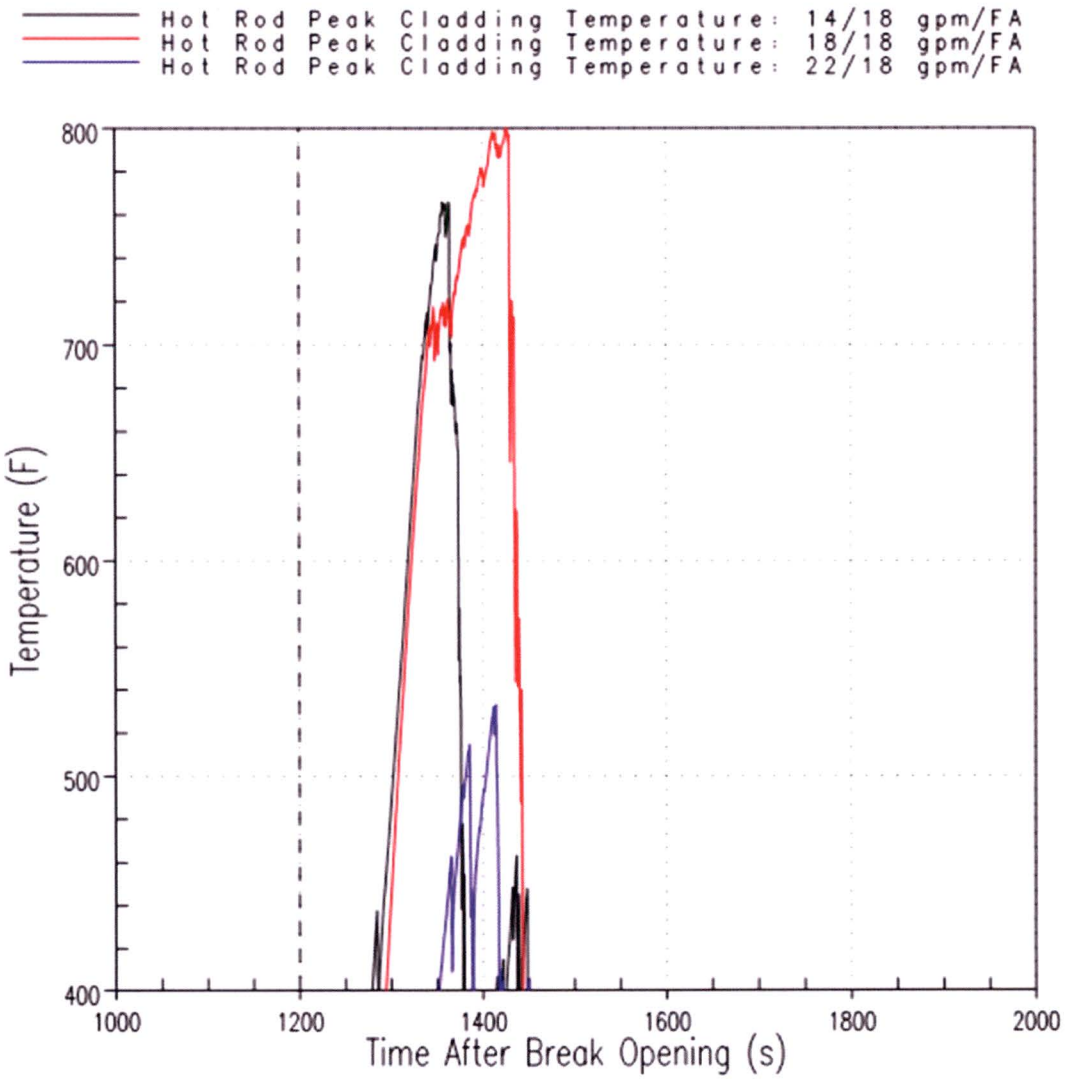

Figure RAI-4.24-8 Westinghouse Upflow Plant Injection Phase ECCS Flow Rate Sensitivity Debris-Induced PCT Results

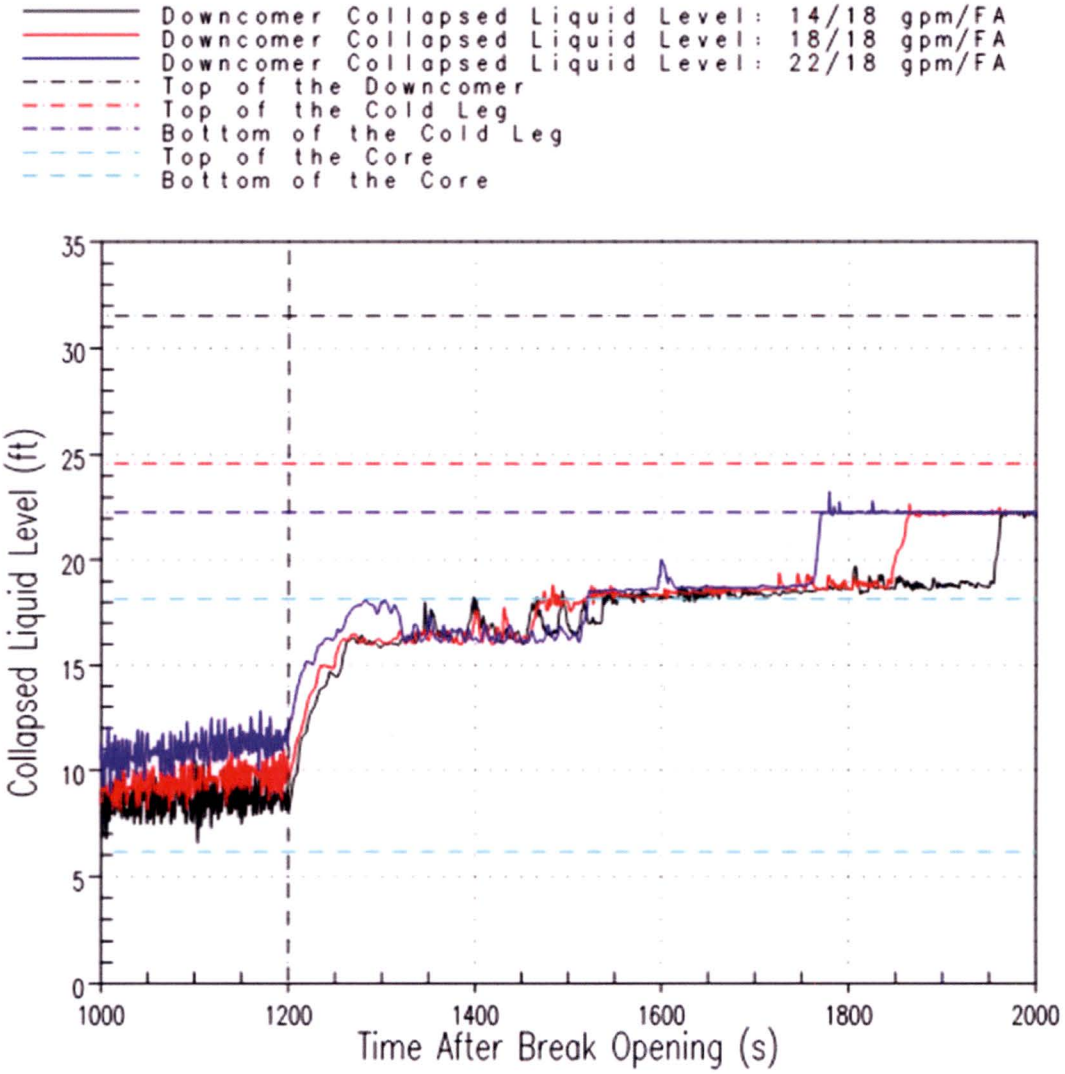

Figure RAI-4.24-9 Westinghouse Upflow Plant Injection Phase ECCS Flow Rate Sensitivity Downcomer Collapsed Liquid Level Results

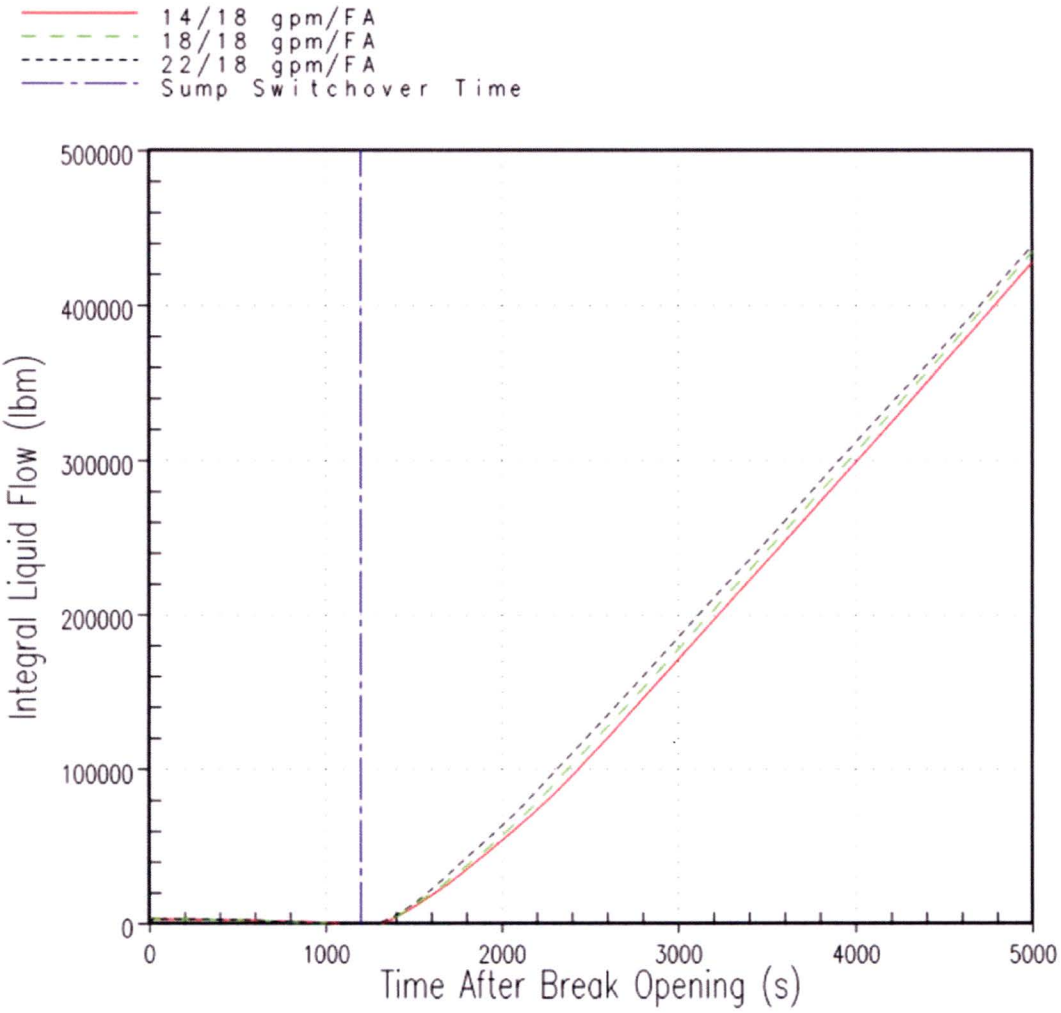

Figure RAI-4.24-10 Westinghouse Upflow Plant Injection Phase ECCS Flow Rate Sensitivity Barrel/Baffle Channel Exit Integrated Liquid Flow Results

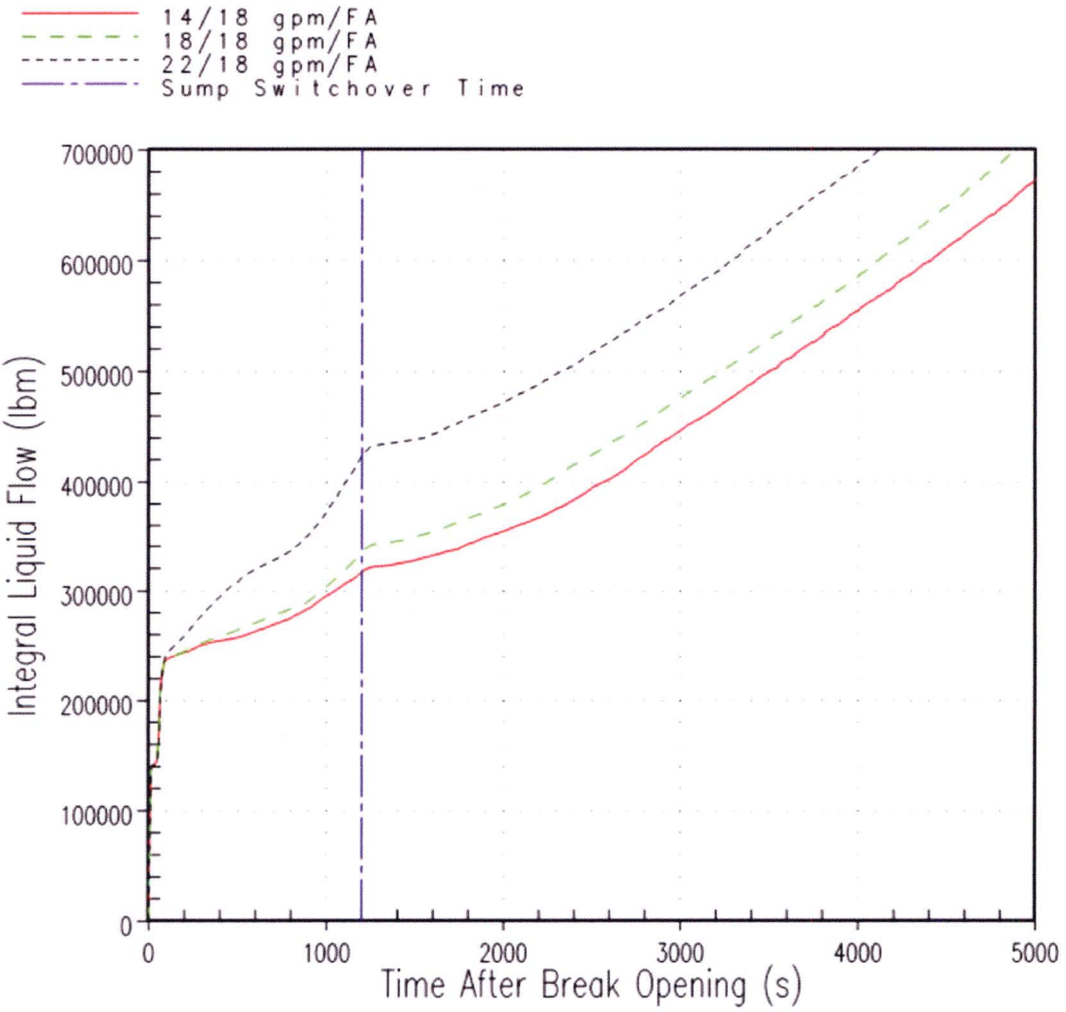

Figure RAI-4.24-11 Westinghouse Upflow Plant Injection Phase ECCS Flow Rate Sensitivity Broken Loop Hot Leg Nozzle Integrated Liquid Flow Results

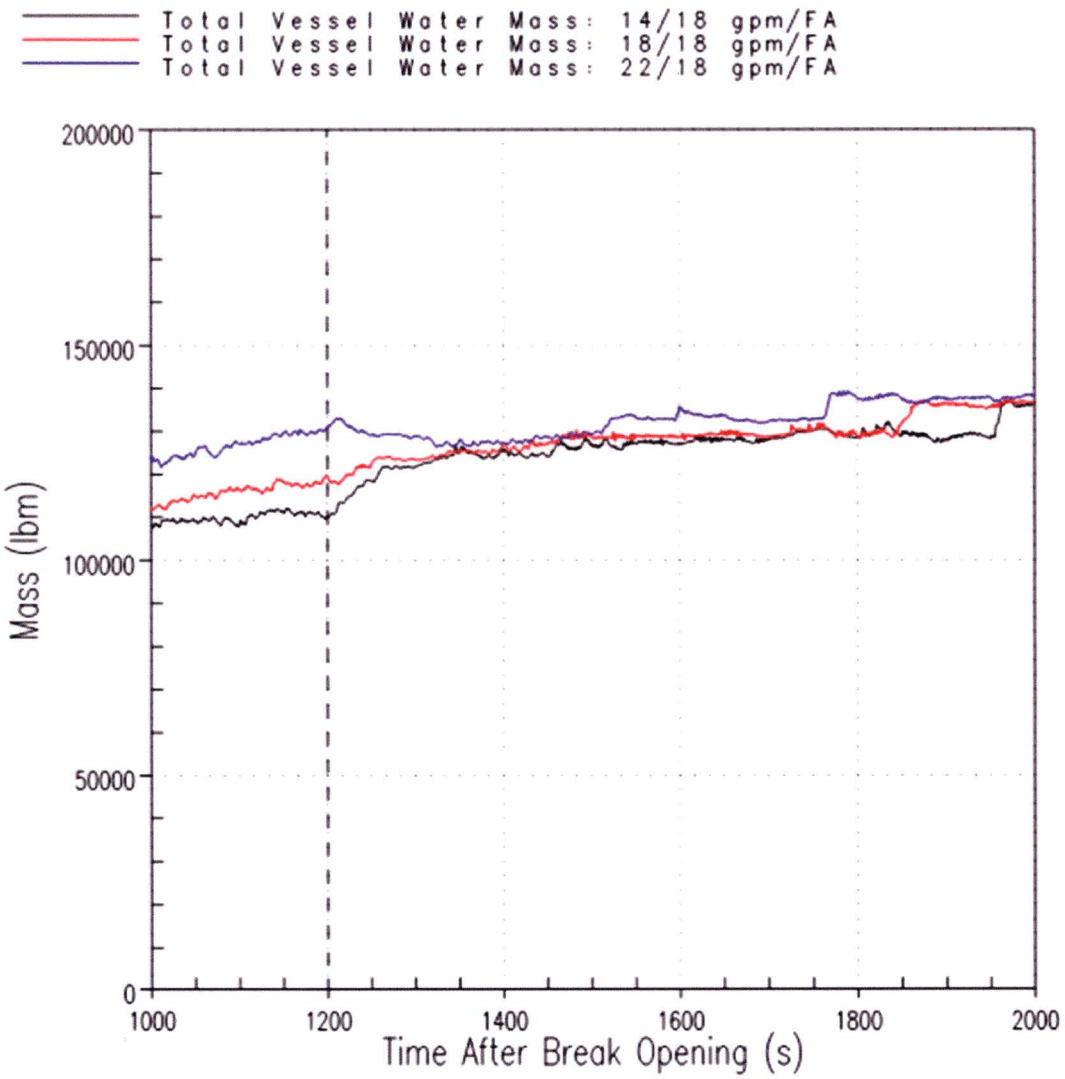

Figure RAI-4.24-12 Westinghouse Upflow Plant Injection Phase ECCS Flow Rate Sensitivity Reactor Vessel Water Mass Results

d. Table 7-1 in the revised Section 7.1.1 of Vol. 1 describes the following ECCS performance for a Westinghouse three-loop plant following a large cold leg break. From 0 to 15 min: 1 residual heat removal and 2 high head SI (HHSI) pumps are described as typical injection phase modeling with single active failure; from 15 to 45 min: 2 HHSI pumps, typical SI phase modeling for this plant; from 45 to 47 min: no flow, interruption at cold leg recirculation; from 47 min to termination: 2 HHSI pumps. This represents an ECCS performance pattern, which appears opposite to the one described above (increase vs decrease in ECCS flow rate upon SSO). Clarify if varying the ECCS injection mass flow rate upon SSO following this opposite pattern would have an effect on the analysis results for both plant categories.

Response

Simulation case and table references provided in this response are from WCAP-17788, Volume 4, Sections 8 and 9. The ECCS performance pattern described above is for the maximum ECCS recirculation flow cases (Cases 0A, 1A, 2A and 3A in Table 8-1, and Cases 0A, 1A and 2A in Table 9-1), and is opposite the ECCS performance pattern described in Table 7-1 of WCAP-17788, Volume 1. This ECCS performance pattern (i.e., a decreasing ECCS flow rate upon SSO) was also investigated in the Westinghouse thermal hydraulic analysis (Cases 0B, 1B, 2B, 3B in Table 8-1, and Cases 0B and 2B in Table 9-1). This opposite flow pattern was shown to have an effect on the analysis results. Table 8-3 and Table 9-3 summarize analysis results for t_{block} and K_{max} for the Westinghouse upflow and downflow plant categories, respectively. As shown in the tables, an ECCS flow pattern with decreasing flow rate upon SSO results in longer t_{block} times and lower K_{max} values. With regard to K_{split} and m_{split}, Tables 8-4 and 9-4 show that the ECCS flow pattern with decreasing flow rate upon SSO result in a longer time to reach K_{split}, a higher K_{split} value, and a smaller m_{split}.

e. Considering the results from Vol. 4, explain the applicable conditions and related requirements for adequately determining the values of ECCS flow. Consider injection and recirculation rates, including interruptions during switchover, on a plant-specific basis to ensure that ECCS performance is adequately represented.

Response

The information requested is provided in the response to RAI-4.5.

f. Provide the information requested in Items a through e for the CE and B&W plant categories. It is noted that Table 6-3 lists the "low pressure safety injection (LPSI) flow rate" as a key input for the CE plant category and Table 6-4 identifies "low pressure injection (LPI) flow rate" as a key input for the B&W plant category thus linking this key input to the performance of specific ECCS components.

The response to this question is provided in the CE and B&W submittals

g. Explain the reason for including Note 2 to Table 6-4 relevant to the B&W plant category stating that "the LPI flow rate followed a pump curve in the analysis. The value shown is the flow at run-out

conditions." Provide the pump curve and the flow rates used in the analysis. Justify that these parameters are applicable to all plants in this category.

The response to this question is provided in the B&W submittal

h. Provide graphs of SI flow rates as a function of time for each individual reactor coolant primary loop for the entire duration of the analysis for the cases included in the case matrices in Tables 8-1, 8-2, 9-1, 9-2, 10-1, 10-2, 11-1, and 11-2. Show the contributions from both high and low pressure SI for the cold and hot legs. Describe all applicable assumptions related to the way in which these flow rates were established and simulated in the T-H analyses.

Response

Figure RAI-4.24-1 shows the ECCS injection rate as a function of time for Case 0A from the Westinghouse upflow plant category. The same ECCS injection rate is modeled in Cases 1A, 2A, and 3A in Table 8-1 and Case 1 in Table 8-2, which corresponds to the Westinghouse upflow category.

Figure RAI-4.24-2 shows the ECCS injection rate as a function of time for Case 0A from the Westinghouse downflow plant category. The same ECCS injection rate is modeled in Cases 1A and 2A, in Table 9-1 and Case 1 in Table 9-2, which corresponds to the Westinghouse downflow category.

Figure RAI-4.24-13 shows the ECCS injection flow rates as a function of time for Cases 0B, 1B, 2B, and 3B in Table 8-1 and Case 3 in Table 8-2, which correspond to the Westinghouse upflow plant category.

Figure RAI-4.24-14 shows the ECCS injection flow rates as a function of time for Cases 0B and 2B in Table 9-1, and Case 4 in Table 9-2, which correspond to the Westinghouse downflow plant category. While responding to this RAI, an error was identified in Table 9-1. The sump recirculation flow rate for Case 0B and 2B is listed as 18 gpm/FA when the actual sump recirculation flow rate for these cases is 12 gpm/FA. Table 9-1 will be corrected in the NRC Approved version of WCAP-17788.

Figure RAI-4.24-15 through Figure RAI-4.24-17 show the ECCS injection flow rates as a function of time for Cases 3, 4, and 5 in Table 8-2, respectively. These cases correspond to the Westinghouse upflow plant category.

Figure RAI-4.24-18 through Figure RAI-4.24-20 show the ECCS injection flow rates as a function of time for Cases 2, 3, and 5 in Table 9-2, respectively. These cases correspond to the Westinghouse downflow plant category.

In all cases, ECCS flow is into the cold legs only. In the WCOBRA/TRAC plant models, there is no distinction between contributions from high and low pressure ECCS pumps. The responses to RAI-4.1 and RAI-4.5 describe all applicable assumptions related to the way in which these flow rates were established and simulated in the T-H analyses.

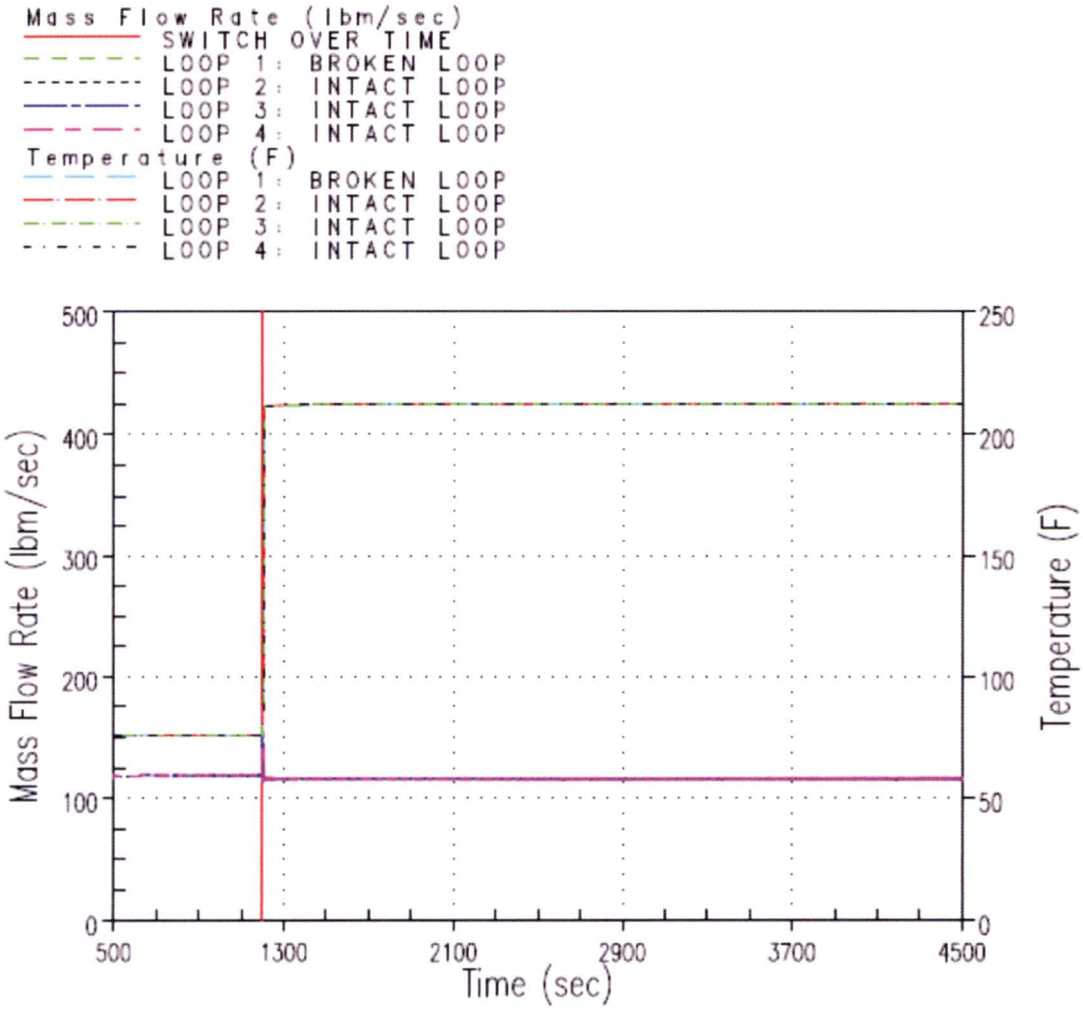

Figure RAI-4.24-13 Cases 0B, 1B, 2B, 3B, and 3 Injected Mass Flow Rate from the Westinghouse Upflow Plant Category

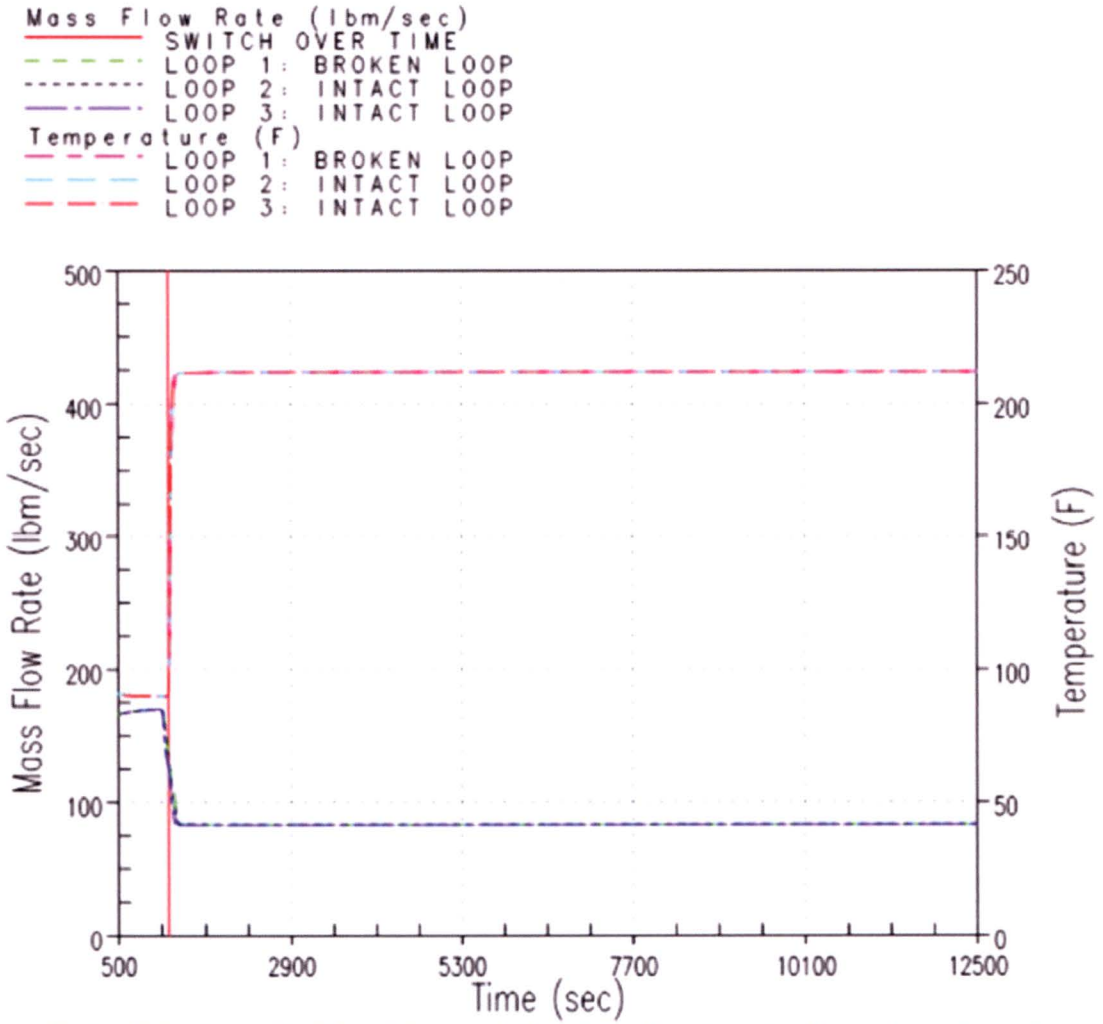

Figure RAI-4.24-14 Cases 0B, 2B, and 4 Injected Mass Flow Rate from the Westinghouse Downflow Plant Category

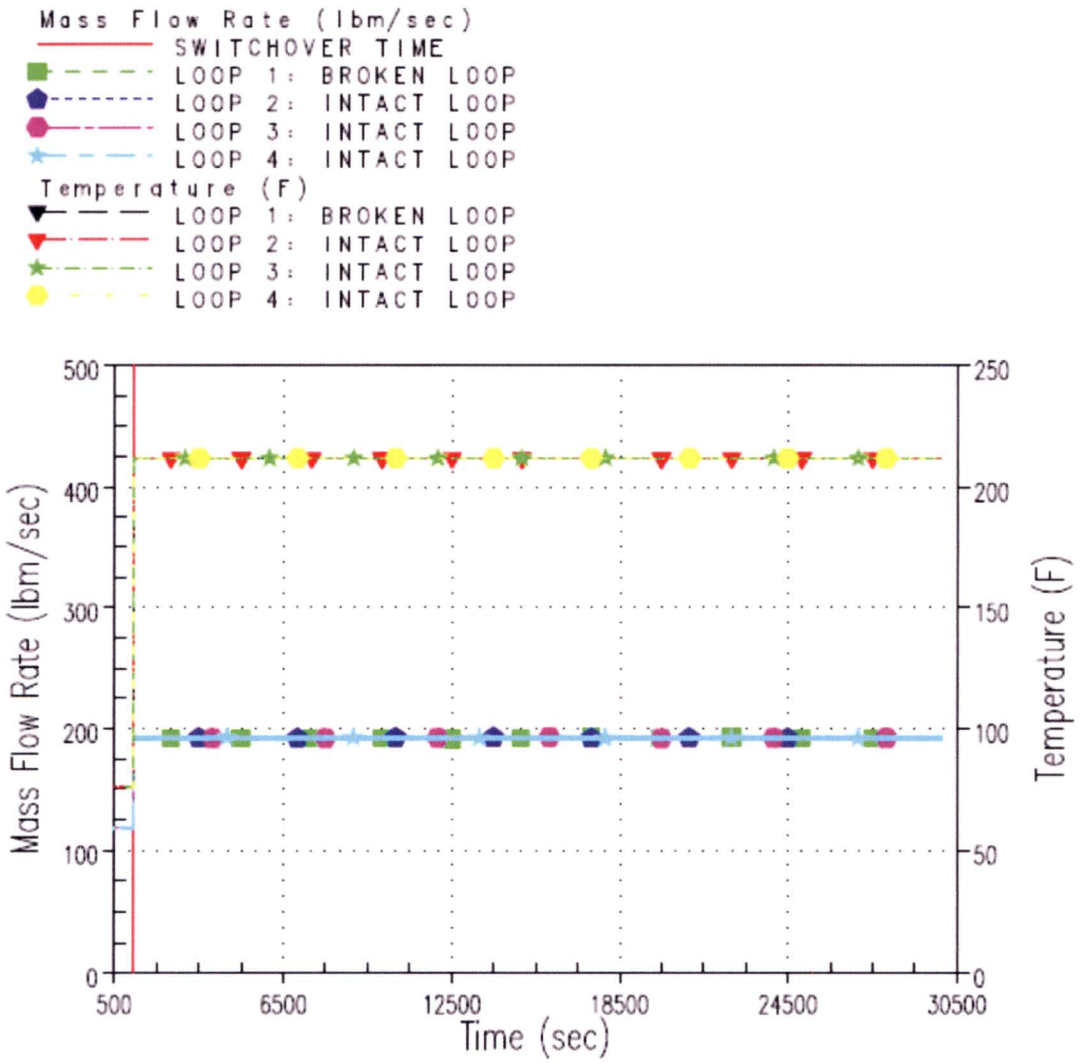

Figure RAI-4.24-15 Case 3 Injected Mass Flow Rate from the Westinghouse Upflow Plant Category

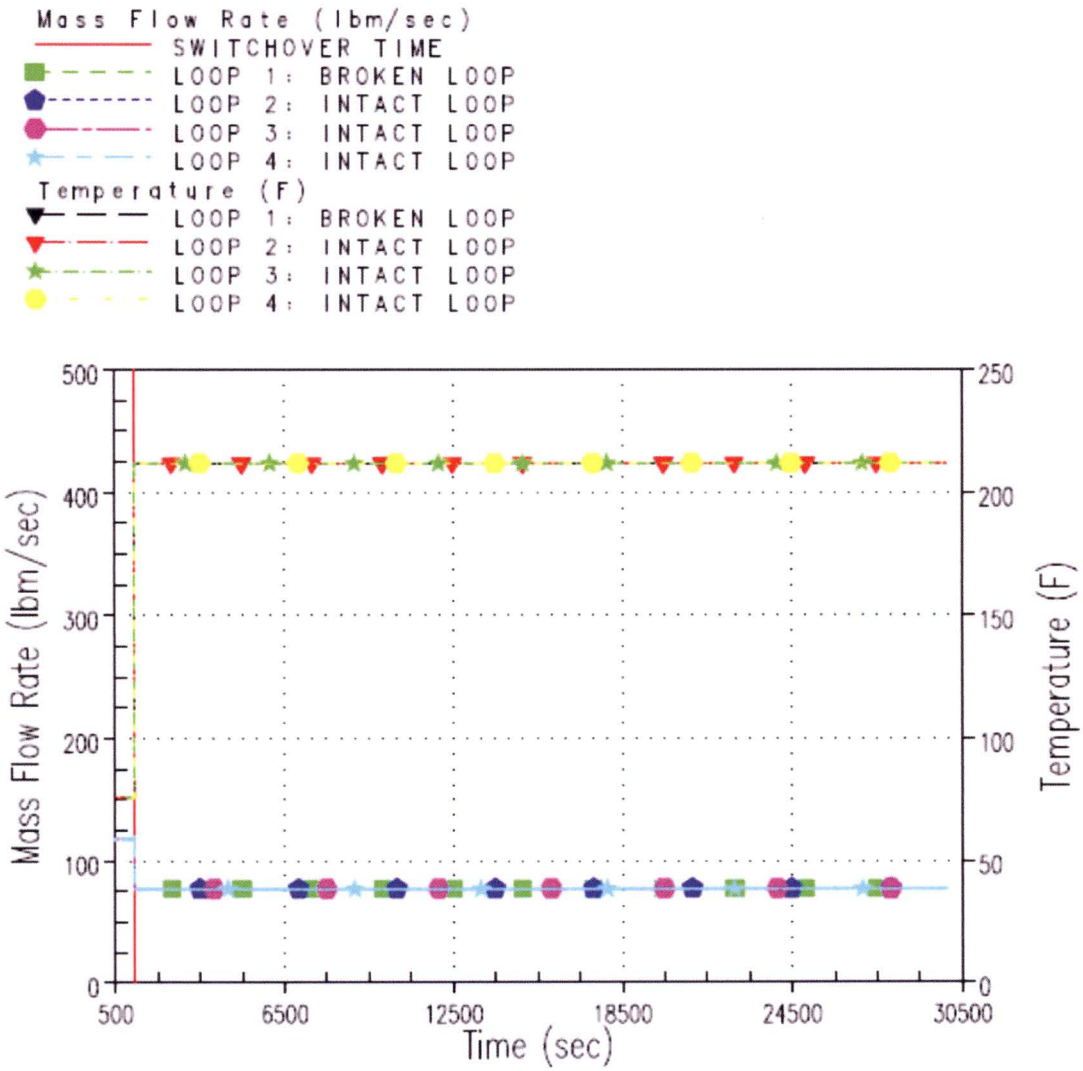

Figure RAI-4.24-16 Case 4 Injected Mass Flow Rate from the Westinghouse Upflow Plant Category

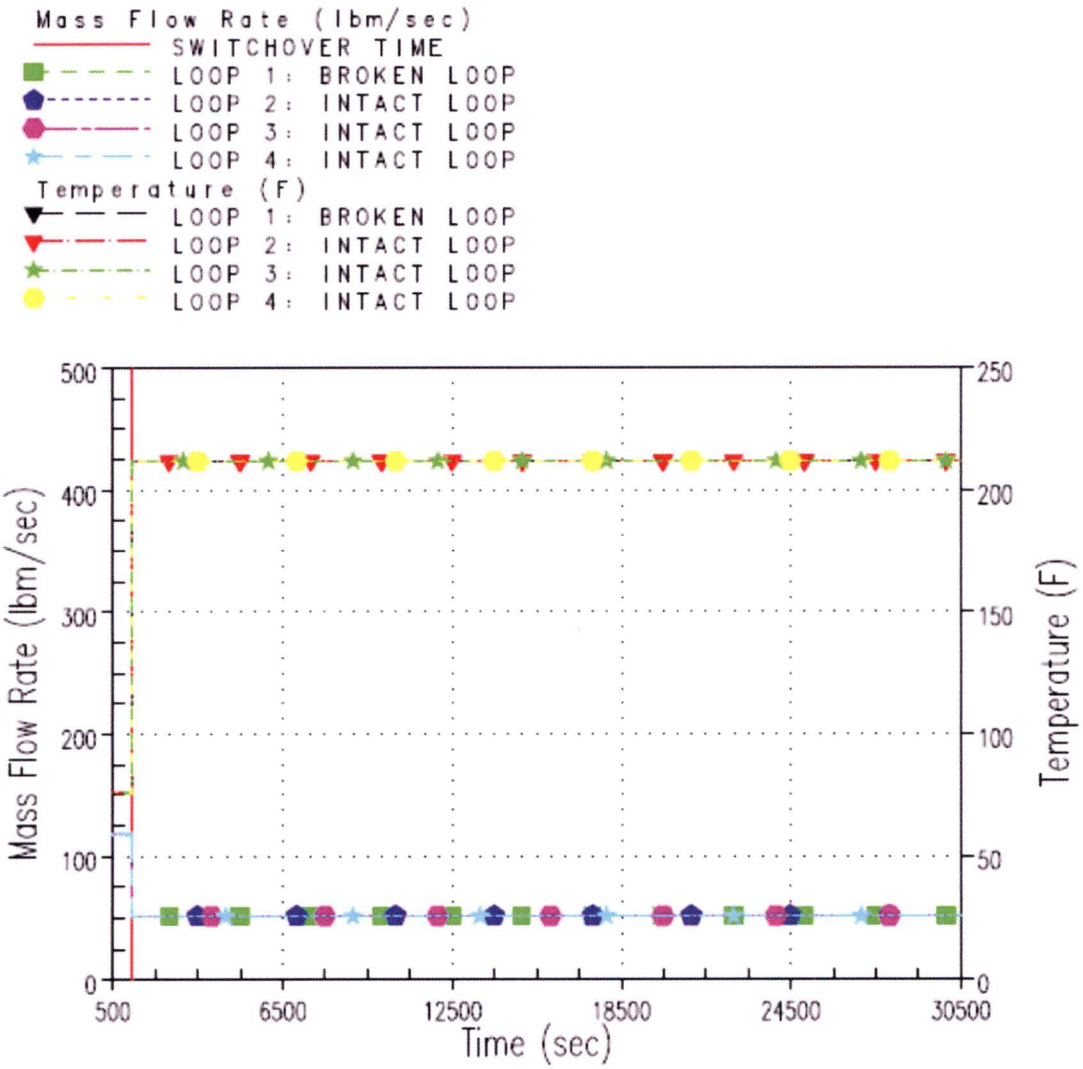

Figure RAI-4.24-17 Case 5 Injected Mass Flow Rate from the Westinghouse Upflow Plant Category

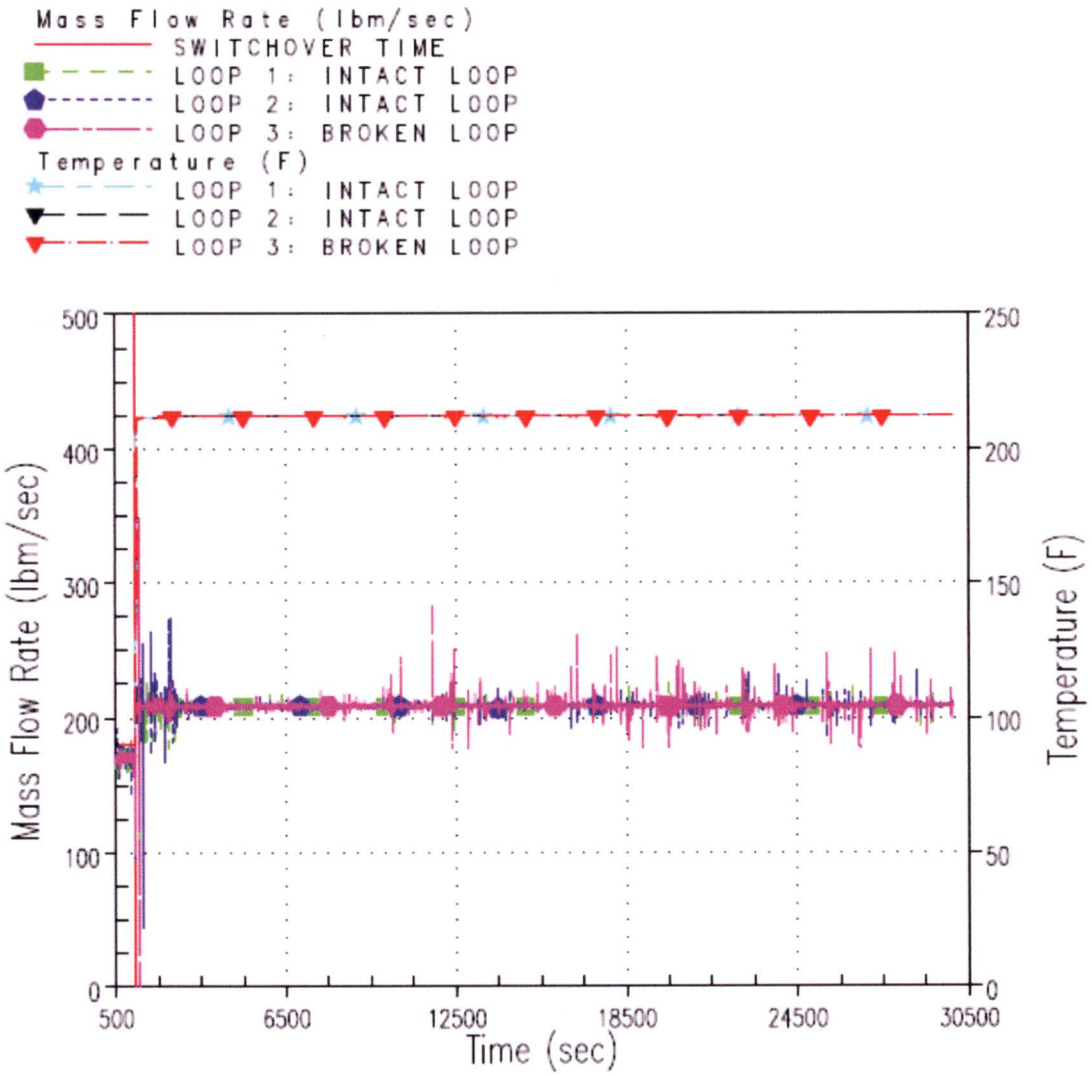

Figure RAI-4.24-18 Case 2 Injected Mass Flow Rate from the Westinghouse Downflow Plant Category

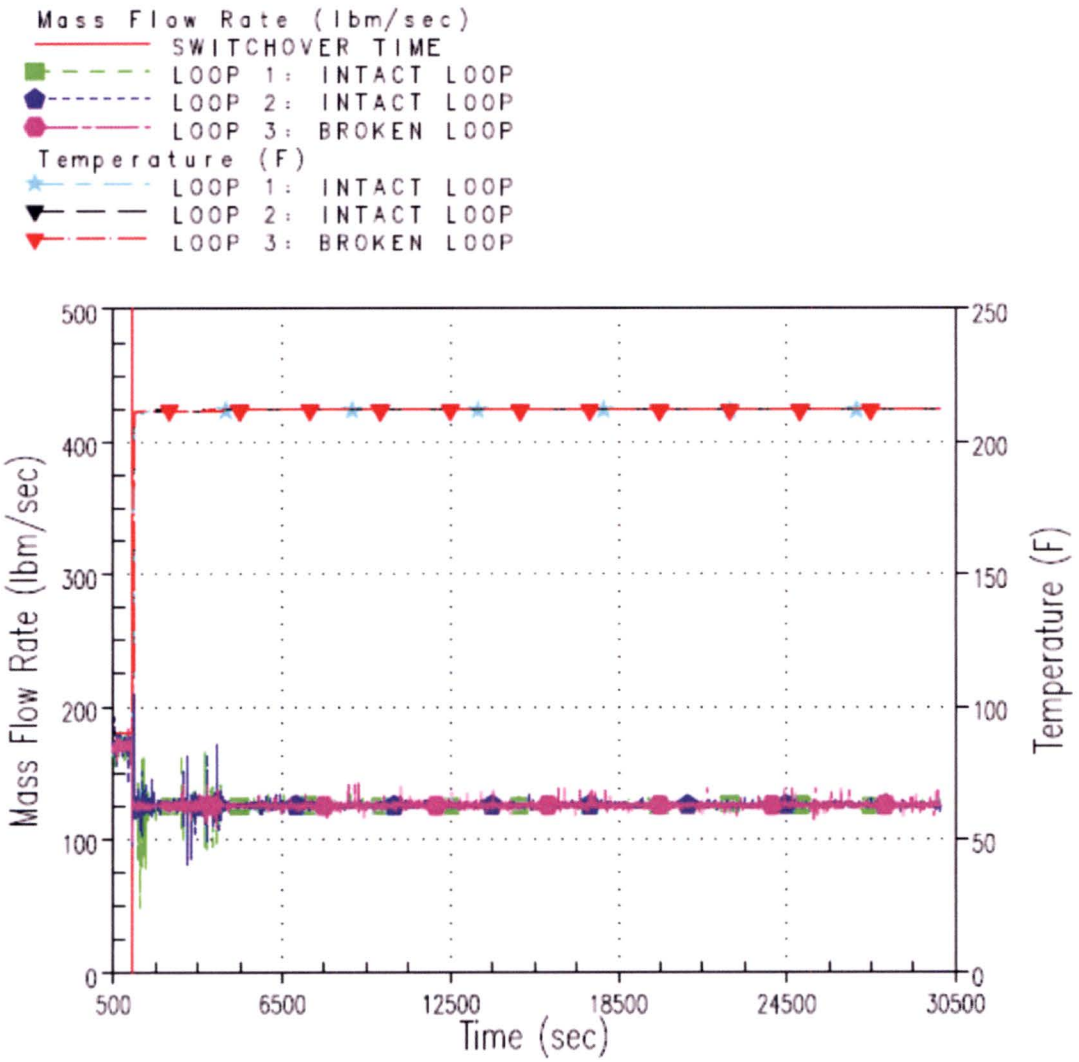

Figure RAI-4.24-19 Case 3 Injected Mass Flow Rate from the Westinghouse Downflow Plant Category

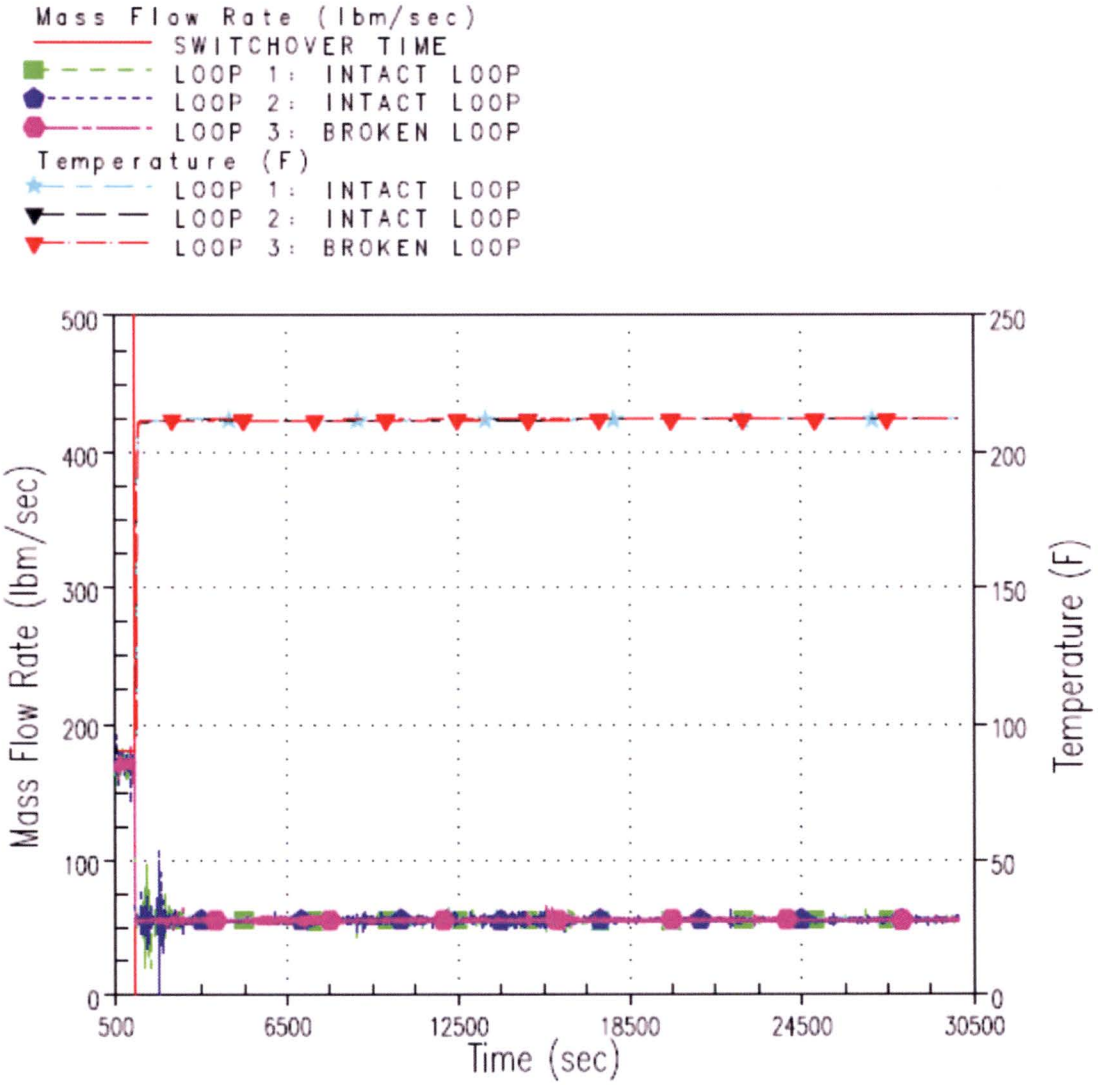

Figure RAI-4.24-20 Case 5 Injected Mass Flow Rate from the Westinghouse Downflow Plant Category

RAI-4.25, Vol. 4

In determining the t_{block} and K_{max} inputs for the Westinghouse upflow category, Section 8.1 provides a simulation matrix of cases considering only two ECCS recirculation flow rates of 18 and 40 gpm/FA. Section 8.2 states that LTCC can be maintained if the time of complete core inlet blockage, t_{block}, occurs 143 minutes, or later, after the initiation of the LOCA event. This time is taken from Case 1B simulating the minimum ECCS recirculation flow rate of 18 gpm/FA and is stated to bound "the range of recirculation flows investigated." The K_{max} input is determined from Case 2B with the same simulated ECCS recirculation flow rate of 18 gpm/FA.

a. Provide justification that the t_{block} criterion from Case 1B at 18 gpm/FA is valid for the range of flow rates from 8-40 gpm/FA as documented in Table 6-1 for this parameter.

Response

Per Table 8-1, the timing of t_{block} is valid for a range of ECCS recirculation flow rate from 18 gpm/FA to 40 gpm/FA. As demonstrated by the results of Case 1A and Case 1B, higher ECCS recirculation flow rate yields an earlier acceptable time for complete core inlet blockage. The minimum ECCS recirculation flow rate analyzed was 18 gpm/FA; therefore, the timing of t_{block} is valid for recirculation flow rates of 18 gpm/FA or higher.

b. Provide justification that the K_{max} criterion from Case 2B with a simulated ECCS recirculation flow rate of 18 gpm/FA is valid for the range of flow rates from 8-40 gpm/FA as documented in Table 6-1 for this parameter.

Response

Per Table 8-1, the magnitude of K_{max} is valid for a range of ECCS recirculation flow rate from 18 gpm/FA to 40 gpm/FA. As demonstrated by the results of Case 2A and Case 2B, higher ECCS recirculation flow rate yields a higher acceptable core inlet resistance. The minimum ECCS recirculation flow rate analyzed was 18 gpm/FA; therefore, the magnitude of K_{max} is valid for recirculation flow rates of 18 gpm/FA or higher.

c. Provide justification for using only 18 and 40 gpm/FA flow rates for determining the t_{block} and K_{max} inputs as stated in Note 1 to Table 6-1 and documented in the simulation matrix of cases provided in Section 8.1.

Response

Justification for using an ECCS recirculation flow rate range of 18 gpm/FA to 40 gpm/FA for determining t_{block} and K_{max} is provided in the responses to items a and b. As discussed in the response to RAI-4.5, a plant will need to demonstrate that it falls within the range of the ECCS flow rates considered in the thermal-hydraulic analysis.

d. Define the range of ECCS recirculation flow rates for which the t_{block}, K_{max}, K_{split}, and m_{split} results, as obtained in Section 8, are considered applicable to the Westinghouse upflow plant category and provide a justification for this range.

Response

Justification for using an ECCS recirculation flow rate range of 18 gpm/FA to 40 gpm/FA for determining t_{block} and K_{max} is provided in the responses to items a, b, and c. Per Table 8-2, K_{split} and m_{split} are valid for an of ECCS recirculation flow rate range from 8 gpm/FA to 40 gpm/FA. As discussed in the response to RAI-4.5, a plant will need to demonstrate that it falls within the range of the ECCS flow rates considered in the thermal-hydraulic analysis.

e. Provide similar responses to Items a through d for the other three plant categories to justify that the t_{block} and K_{max} inputs calculated using a single ECCS recirculation flow rate for each input are applicable to the range of flow rates defined for each plant category. For example, justify for the Westinghouse downflow category that t_{block} is determined from Case 1A simulating an ECCS recirculation flow rate of 40 gpm/FA and K_{max} is determined from Case 2B with a simulated ECCS recirculation flow rate of 18 gpm/FA.

Response

Per Table 9-1, the timing of t_{block} is valid for a range of ECCS recirculation flow rate from 12 gpm/FA to 40 gpm/FA. Case 1A performed at 40 gpm/FA is used to establish the time of t_{block} as 15,600 s (4.33 h); however, the results of Case 2B demonstrate that complete core inlet blockage could be tolerated before the established 15,600 s t_{block} time. Since the Case 2B results meet the acceptance criteria it can be concluded that an ECCS recirculation flow rate of 12 gpm/FA at 12,000 s is bounded by the results obtained for t_{block} at 15,600 s at an ECCS recirculation flow rate of 40 gpm/FA. As such, the value of t_{block} is justified for ECCS flows of 12 gpm/FA to 40 gpm/FA.

Per Table 9-1, the magnitude of K_{max} is valid for a range of ECCS recirculation flow rate from 12 gpm/FA to 40 gpm/FA. As demonstrated by the results of Case 2A and Case 2B, higher ECCS recirculation flow rate yields a higher acceptable core inlet resistance. The minimum ECCS recirculation flow rate analyzed was 12 gpm/FA; therefore, the magnitude of K_{max} is valid for recirculation flow rates of 12 gpm/FA or higher.

Justification for using an ECCS recirculation flow rate range of 12 gpm/FA to 40 gpm/FA for determining t_{block} and K_{max} is provided in the responses in the two preceding paragraphs. As discussed in the response to RAI-4.5, a plant will need to demonstrate that it falls within the range of the ECCS flow rates considered in the thermal-hydraulic analysis.

Justification for using an ECCS recirculation flow rate range of 12 gpm/FA to 40 gpm/FA for determining t_{block} and K_{max} is provided in the responses in the three preceding paragraphs. Per Table 9-2, K_{split} and m_{split} are valid for an of ECCS recirculation flow rate range from 8 gpm/FA to

40 gpm/FA. As discussed in the response to RAI-4.5, a plant will need to demonstrate that it falls within the range of the ECCS flow rates considered in the thermal-hydraulic analysis.

f. Sections 8-3 and 9-3 state that "the duration and magnitude of the heatup were heavily dependent on the timing of complete core inlet blockage and the ECCS flow rate." Considering the responses to items a through e above, demonstrate that the calculated parameters are valid for the ECCS flow rates and core inlet blockage times used in the analysis.

Response

The responses to items a through e demonstrate that the calculated output parameters t_{block}, K_{max}, K_{split}, and m_{split} are valid for the ECCS flow rates and core inlet blockage times used in the analysis.

RAI-4.26, Vol. 4

K_{max} for the CE plant category was determined by applying a gradual ramp in the simulated core inlet resistance starting from 0 at 1,800 seconds and reaching K_{max} of 6.5×10^6 at 4,200 seconds as shown in Figure 10-2. The profile represents an increase in the resistance value by applying four different constant rates of resistance increase, which change in a stepwise manner with time.

a. Justify that the K_{max} value of 6.5×10^6, using the profile from Figure 10-2, represents a robust result and is not an outcome of tuning of the core inlet resistance profile to obtain a desired result. Results from sensitivity analyses can be used to provide the justification.

b. In the case of the profile shown in Figure 10-2, the core inlet resistance was increased from 0 to 6.5×10^6 within a time window of 2,400 seconds (40 min). As the result of 6.5×10^6 for K_{max} was tied to the specific profile from Figure 10-2, justify the K_{max} input for the CE plant category by explaining how it can be assured that the K_{max} value will not be developed within a time window shorter than 40 minutes resulting in K_{max} occurring earlier than 70 minutes into the LOCA transient, which could lead to the PCT acceptance criteria being violated.

Response

The response to these questions is provided in the CE submittal

RAI-4.27, Vol. 4

T-H code predictions to demonstrate adequate core coolability under conditions associated with blocked core inlet flow passages require reasonable assurance of adequate code performance under the simulated conditions. The examination of code results during the NRC audit of the Westinghouse T-H analyses in Sections 8 and 9 on January 27-28, 2016, indicates that flow patterns involving parallel cross-connected channels to model the core following a simulated complete core inlet blockage can be complex. It was determined that obstruction of lateral flow passages between fuel assemblies due to the presence of spacer grids was not accounted for in the modeling of the lateral cross-connections between parallel core channels, including the hot channel. In addition, potential effects on the axial flows due to possible localized accumulation of debris at the locations of spacer grids in regions above the core inlet were not modeled to assess such effects.

Cross-flows between parallel channels can be a contributing factor affecting code prediction of local fuel conditions, including PCT, due to their impact on fluid velocities, void fraction, and two-phase flow patterns. Provide results from additional T-H analyses for a representative case analyzed in each plant category to assess the effects from the above identified factors related to lateral obstruction of cross-flow passages and impediment of axial flows on the PCT and t_{block} predictions. The analyses should be performed using core modeling changes that account for: (1) reduced flow area of cross-flow passages due to the spacer grids present in the active core region, (2) impact on resistances of cross-flow passages from the spacer grids present in the active core region, and (3) increase in the simulated spacer grid resistances in the axial direction at appropriately selected spacer grid locations, including impact for both axial directions, to simulate the effect from possible local fiber accumulation. Such modeling changes and modifications should be applied to the hot channel and all or some of the channels representing the entire core as found appropriate. If necessary to resolve the impact from the examined factors and processes on the PCT and t_{block} predictions, include sensitivity results related to specific factors and modeling assumptions as applicable. For each simulation, include sufficiently detailed results to explain effects on the predicted core T-H response, PCT, and t_{block} in comparison to the corresponding base cases. Include PCT, void fraction, fluid phase velocities, and two-phase flow patterns for appropriately selected hydraulic channels and cells, as well as integrated mass flows in both lateral and axial directions for selected critical flow passages. Include a description of the implemented modeling changes with a sufficient degree of detail to explain clearly how the physical processes and factors were accounted for in the model along with the introduced assumptions.

Response

A sensitivity study on the core channel lateral gap resistance, and the simulated spacer grid resistances in the axial direction was performed using the Westinghouse upflow plant category and the t_{block} base case (Case 1B). Two additional simulations were performed varying gap lengths and gap resistances between the low power/periphery channel and the average non-guide tube and guide tube channels (Gaps 13 and 14). In these cases the spacer grid axial resistance was also increased in all core channels at all spacer grid elevations. The gap lengths modeled in the cases were 3 and 5 times the fuel assembly pitch with the corresponding gap resistances for the sensitivity cases calculated using Diagram 12-29 of Idelchik

(Reference RAI-4.27-1) for flow through a bundle of circular tubes in vertical columns. The axial resistance at spacer grid locations was increased by 25 and 50% in these cases. Three grids with different resistance values are used (IFM grids, Mixing Vane Grids (MVGs), Non-Mixing Vane Grids).

Two additional simulations performed varying the gap resistance between the average non-guide tube channel and the hot assembly channel (Gap 16) and varying the axial resistance at spacer grid locations in all core channels. The sensitivity calculations model 25% and 50% more cross flow resistance. The axial resistance at spacer grid locations is increased by 25% and 50%.

Two additional sensitivities were performed that investigate the effect of axial spacer grid resistance and gap resistance individually. In the first sensitivity, the gap length and resistance is not changed and the spacer grid resistance is increased by an order of magnitude. In the second sensitivity, the axial spacer grid resistance is held constant and the average non-guide tube to hot assembly gap resistance is increased by an order of magnitude.

Table RAI-4.27-1 provides the case matrix used in the sensitivity study. These cases are effective at determining the impact on peak cladding temperature (PCT) response, void fraction and two-phase flow patterns in the core when cross-flow resistance and axial resistance at spacer grid locations is increased following the application of complete core inlet blockage.

Table RAI-4.27-1 Case matrix for varying core channel gap resistance and spacer grid axial resistances

Case	Gap Length (in)	Gap Resistance	Axial Resistance at Spacer Grids
1B (Base Case)	8.466 (All Gaps)	8.5 (All Gaps)	0.78 IFM, 1.34 MVG, 0.67 Top Grid, 0.69 Bottom Grid
2	25.4 (Gap 13 and 14)	25.5 (Gap 13 and 14)	0.98 IFM, 1.68 MVG, 0.84 Top and Bottom Grid
3	42.3 (Gap 13 and 14)	42.5 (Gap 13 and 14)	1.17 IFM, 2.01 MVG, 1.01 Top and Bottom Grid
4	8.466 (Gap 16)	10.7 (Gap 16)	0.98 IFM, 1.68 MVG, 0.84 Top and Bottom Grid
5	8.466 (Gap 16)	12.8 (Gap 16)	1.17 IFM, 2.01 MVG, 1.01 Top and Bottom Grid
6	8.466 (All Gaps)	8.5 (All Gaps)	7.8 IFM, 13.4 MVG, 6.7 Top and Bottom Grid
7	8.466 (Gap 16)	85.0 (Gap 16)	0.78 IFM, 1.34 MVG, 0.67 Top and Bottom Grid

Results from the sensitivity study are presented by comparing them to the base case results. The first comparison is made between Cases 2 and 3, which vary the gap lengths and resistance between the low power channel and the two average core channels (Gaps 13 and 14). The axial resistance at spacer grid elevations in all the core channels is also increased in these cases.

Figures RAI-4.27-1 through RAI-4.27-3 show the lateral integrated mass flow rate from the low power channel to the average non-guide tube channel (Gap 13), at the bottom, mid, and top core elevations, respectively. A positive mass flow indicates that flow is from the low power channel to the average non-guide tube channel. As expected, increasing the gap length and resistance decreases the lateral flow through each gap. Similar trends are observed in the lateral flow from the low power channel to the average guide tube channel (Gap 14), as shown in Figures RAI-4.27-4 through RAI-4.27-6.

Figures RAI-4.27-1 through RAI-4.27-6 also highlights the effect of increased gap length and resistance on the two-phase mixing patterns in the low power and average power core channels. It is seen that flow enters the average channels from the low power channel at the bottom and top of the core, while flow enters the low power channel from the average channels at the mid-core elevation. Increasing the gap length and resistance between these channels reduces the magnitude of the circulation pattern observed in the base case.

Figures RAI-4.27-7 through RAI-4.27-9 show the integrated axial mass flow rates in the low power channel and hot assembly channel at the bottom of the core, mid-core, and the top of the core, respectively. In the figures, the low power channel mass flow is normalized on a per fuel assembly basis in order to provide a direct comparison with the hot assembly channel, which represents a single fuel assembly. As the figures indicate, downflow is present in the low power channel, and upflow is present in the hot assembly channel. The figures also show that the magnitude of the axial flow increases in the sensitivity cases relative to the base case even though the axial resistance at the spacer grids is increased. This behavior indicates that the increased lateral resistance, and reduction in cross-flow, overwhelms the increased axial resistance and the core channels behave more one-dimensionally with less lateral communication.

Figure RAI-4.27-10 shows the PCT, and indicates that the base case produces the highest PCT. Increasing the low power to average channels gap lengths and resistances results in a lower PCT, and the impact is significant. Figure RAI-4.27-11 shows the vessel fluid mass, and indicates that the vessel fluid mass is not significantly impacted by varying the core channel gap lengths and resistances. This result demonstrates that varying the parameters does not significantly impact the overall reactor vessel system behavior, and the PCT sensitivity is governed by the local flow behavior in the core channels. To explain this behavior, the void fraction and fluid phase velocities in the low power channel and hot assembly channel are presented next.

Figures RAI-4.27-12 and RAI-4.27-13 show the axial void distribution in the low power channel and the hot assembly channel, respectively. The figures indicate that the increased gap length, gap resistance, and spacer grid resistance tend to reduce the void fraction above the bottom of the core. This is especially true in the mid-core region.

Figures RAI-4.27-14 and RAI-4.27-15 show the axial liquid velocity in the low power channel and the hot assembly channel, respectively. The figures indicate that the liquid velocity is increased in both channels throughout the core, which is consistent with the integrated axial mass flow rates shown in Figures RAI-4.27-7 through RAI-4.27-9.

Figures RAI-4.27-16 and RAI-4.27-17 show the axial vapor velocity in the low power channel and the hot assembly channel, respectively. The figures show some variation in the axial vapor velocity in the low power channel, but there is little variation in the hot assembly channel.

Trends observed in the figures presented above demonstrate that increasing the gap lengths and the gap resistance between the low power channel and average non-guide tube and average guide tube channels (Gaps 13 and 14), and increasing the spacer grid axial resistances in all core channels changes the flow patterns observed in the core region. In general, the lateral liquid phase flows between channels are reduced and the axial liquid phase flows are increased such that the core channels interact less and behave more one-dimensionally. This effect tends to retain more liquid in the core channels such that the PCT following the application of complete core inlet blockage is less limiting.

Reference

RAI-4.27-1 Idelchik, I. E., "Handbook of Hydraulic Resistance," 3rd Edition, CRC Press, 1994.

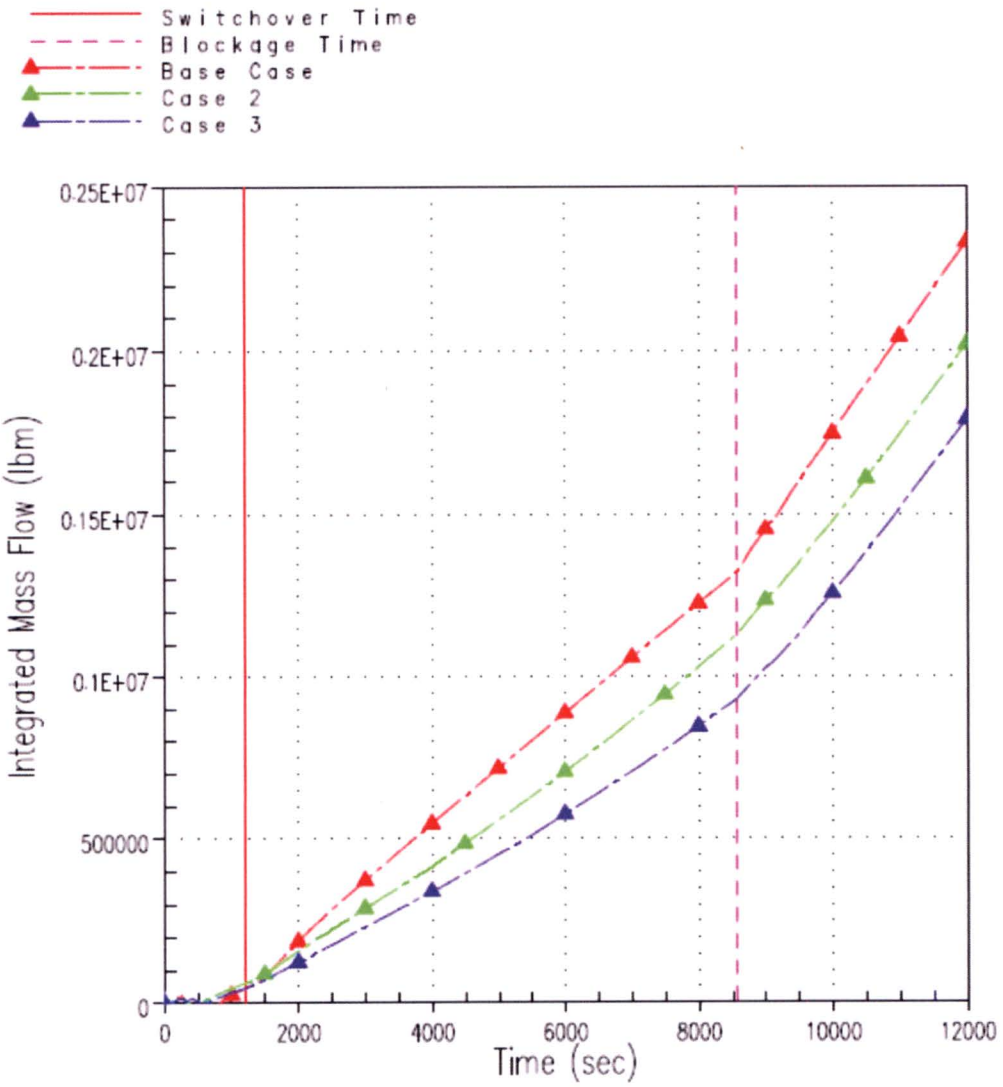

Figure RAI-4.27-1 Integrated Mass Flow Rate from the Low Power Channel to the Average Non-Guide Tube Channel at the Bottom of the Core Showing the Effect of Increased Gap Length and Resistance (Gap 13)

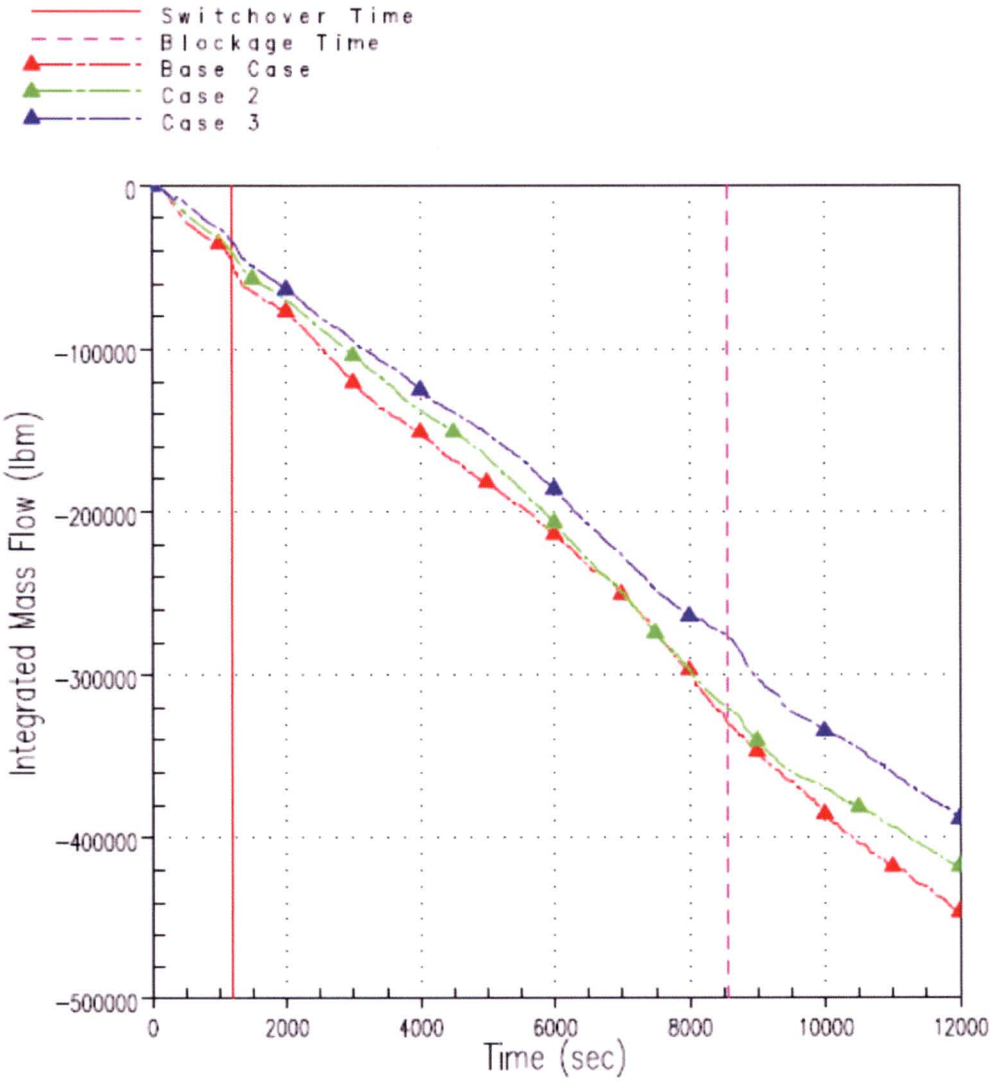

Figure RAI-4.27-2 Integrated Mass Flow Rate from the Low Power Channel to the Average Non-Guide Tube Channel Mid-Core Showing the Effect of Increased Gap Length and Resistance (Gap 13)

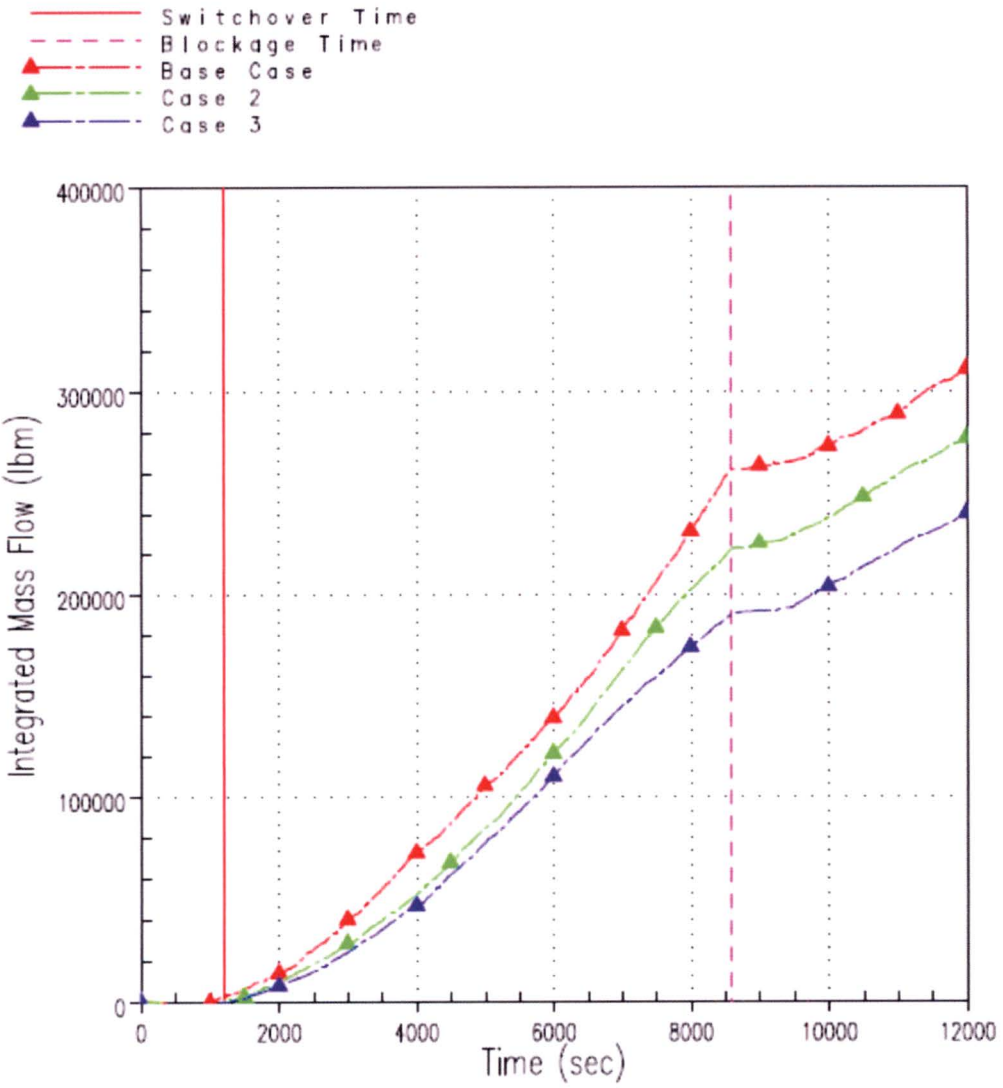

Figure RAI-4.27-3 Integrated Mass Flow Rate from the Low Power Channel to the Average Non-Guide Tube Channel at the Top of the Core Showing the Effect of Increased Gap Length and Resistance (Gap 13)

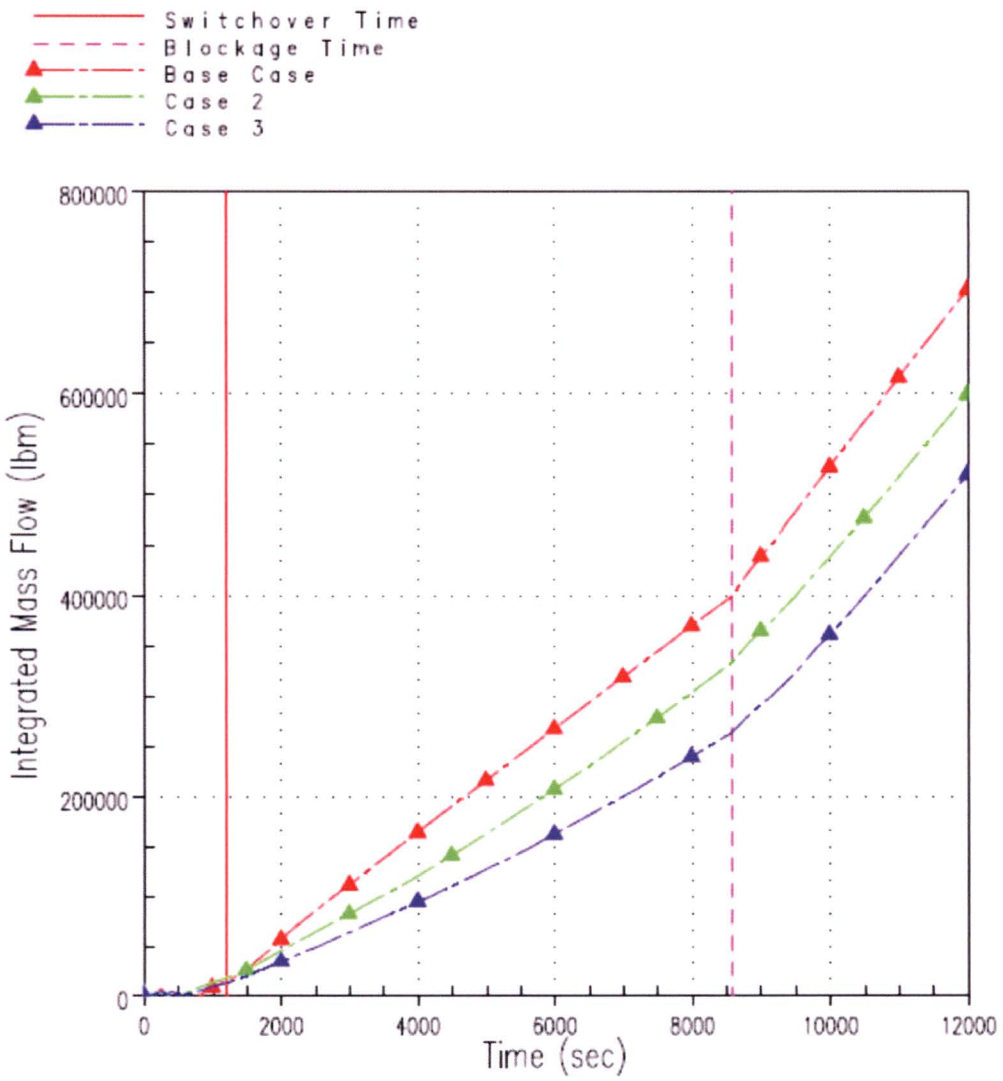

Figure RAI-4.27-4 Integrated Mass Flow Rate from the Low Power Channel to the Average Guide Tube Channel at the Bottom of the Core Showing the Effect of Increased Gap Length and Resistance (Gap 14)

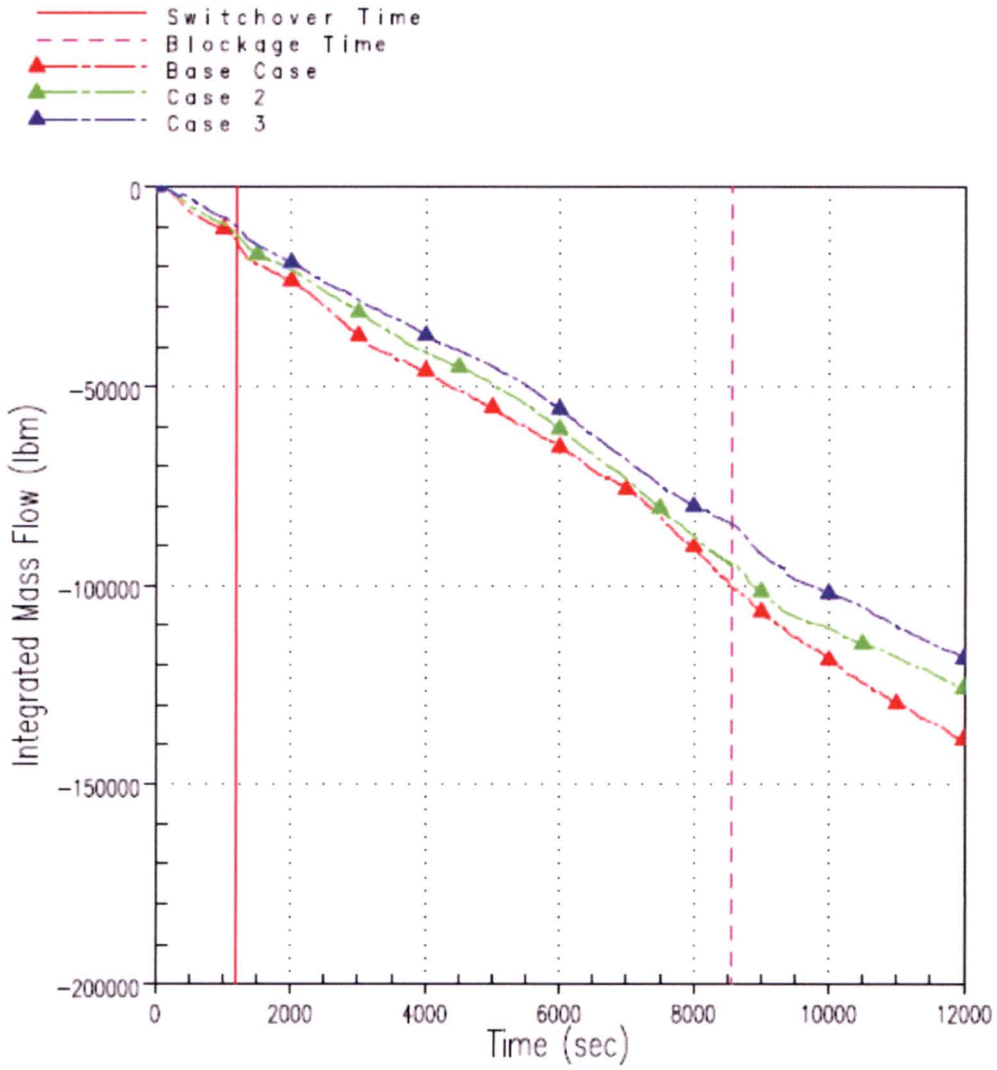

Figure RAI-4.27-5 Integrated Mass Flow Rate from the Low Power Channel to the Average Guide Tube Channel Mid-Core Showing the Effect of Increased Gap Length and Resistance (Gap 14)

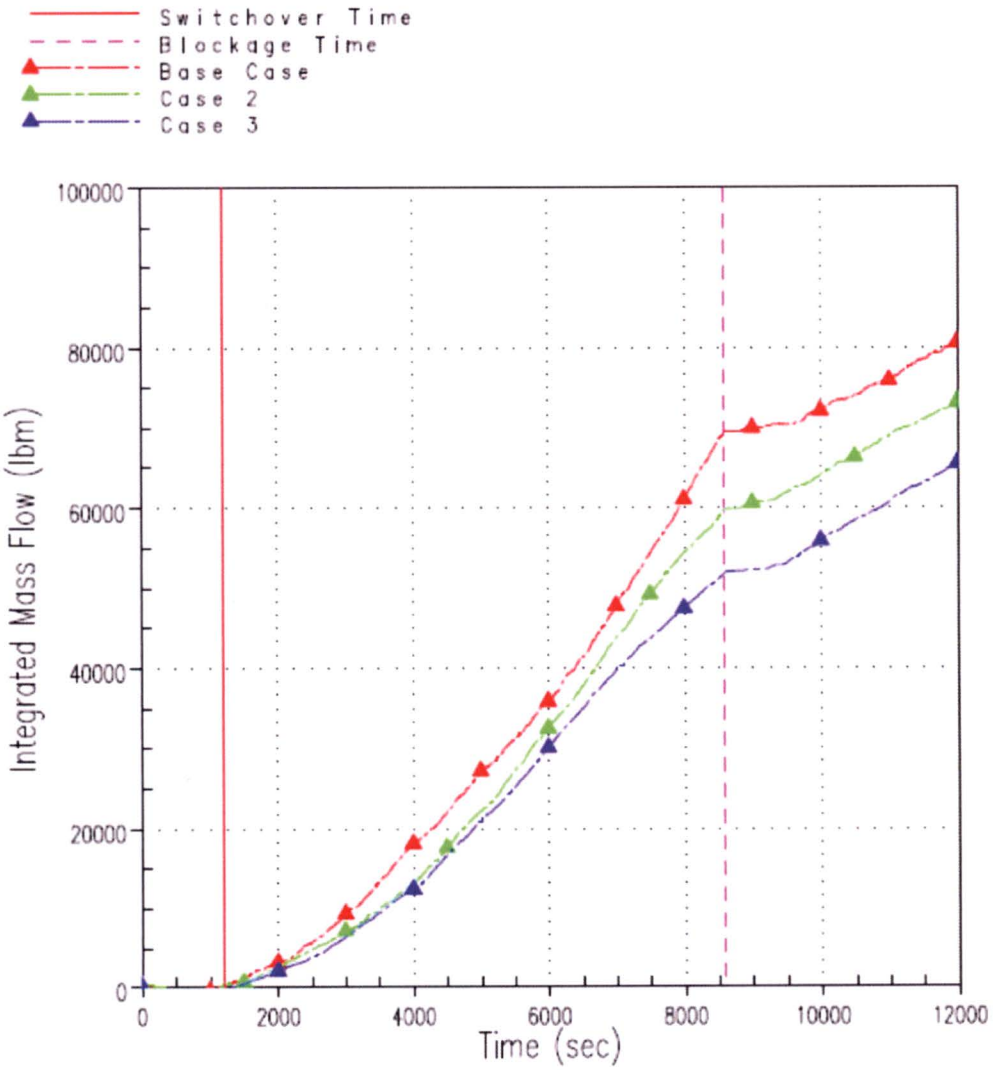

Figure RAI-4.27-6 Integrated Mass Flow Rate from the Low Power Channel to the Average Guide Tube Channel at the Top of the Core Showing the Effect of Increased Gap Length and Resistance (Gap 14)

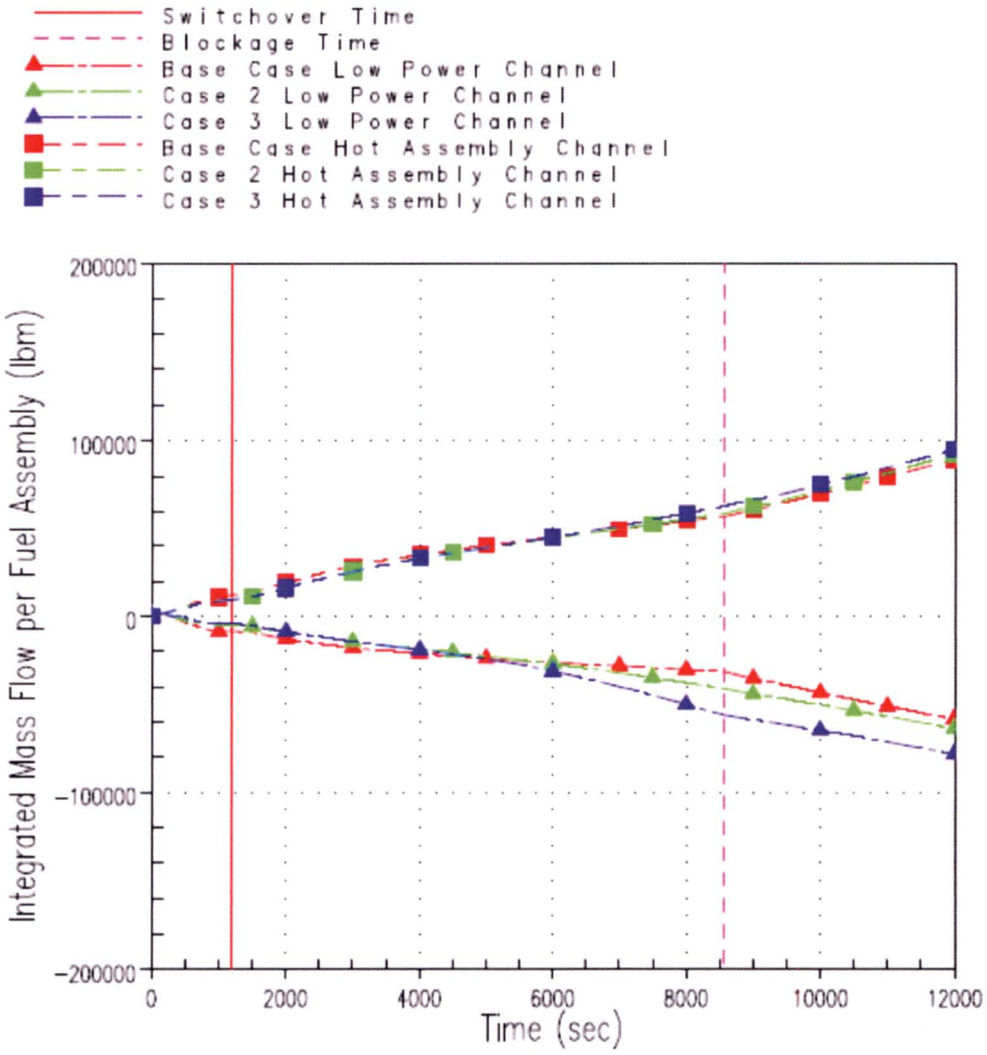

Figure RAI-4.27-7 Integrated Axial Mass Flow Rates in the Low Power Channel and the Hot Assembly Channel at the Bottom of the Core Showing Increased Axial Flow When the Low Power Channel to Average Channels Gap Lengths and Resistance is Increased

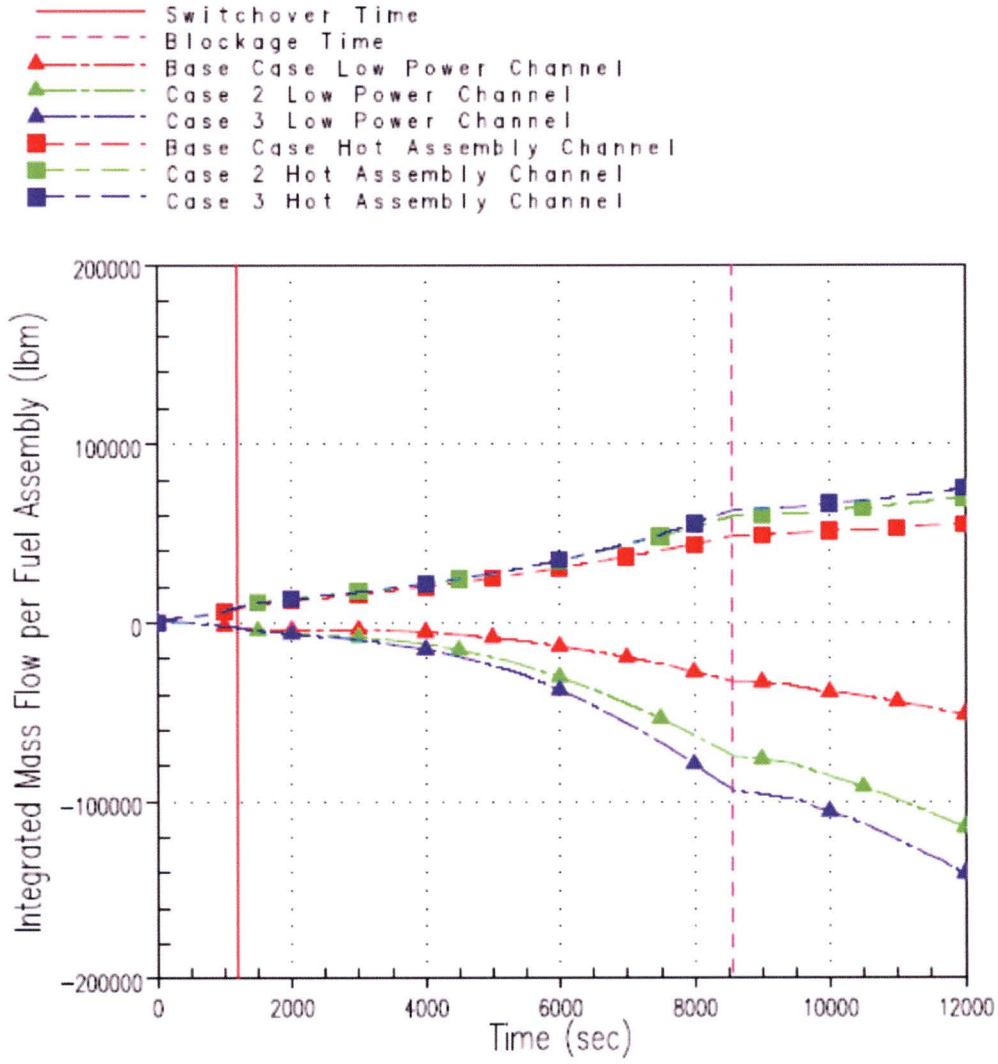

Figure RAI-4.27-8 Integrated Axial Mass Flow Rates in the Low Power Channel and the Hot Assembly Channel Mid-Core Showing Increased Axial Flow When the Low Power Channel to Average Channels Gap Lengths and Resistance is Increased

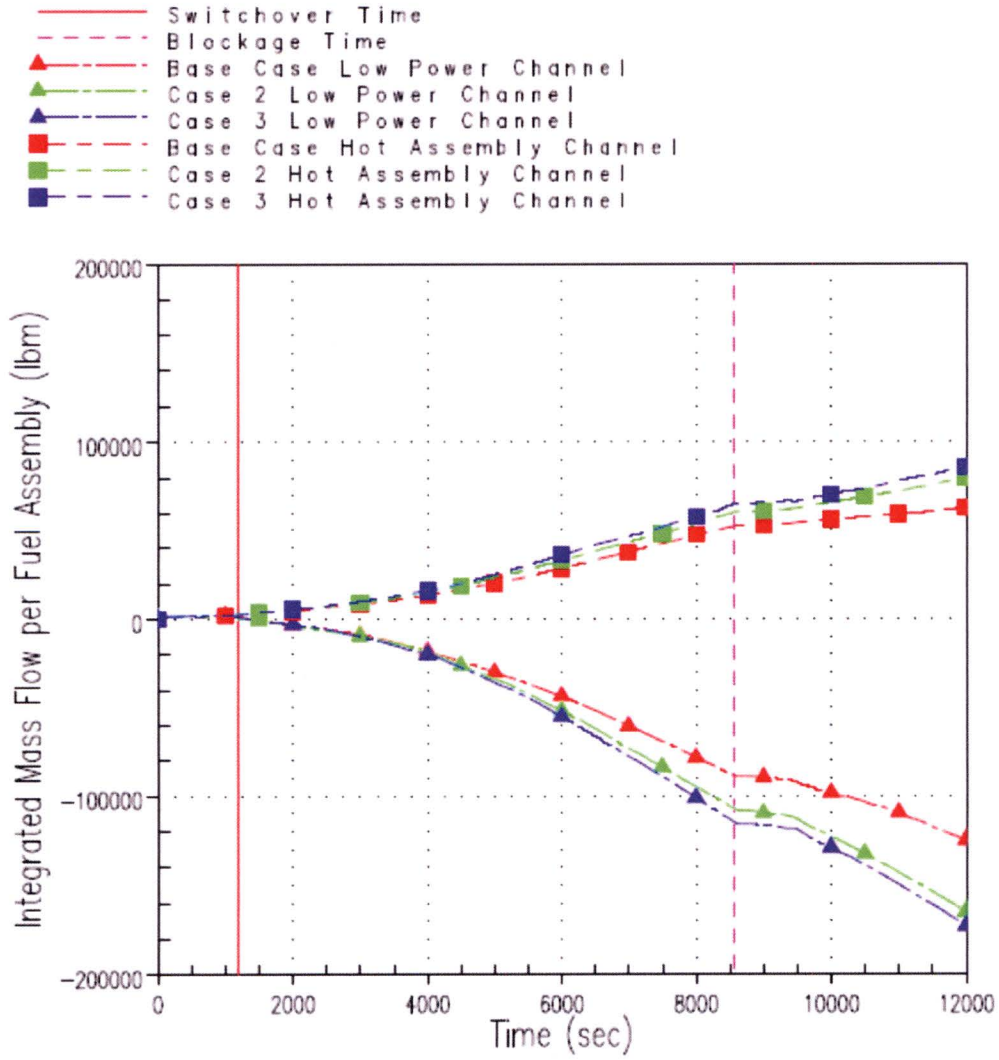

Figure RAI-4.27-9 Integrated Axial Mass Flow Rates in the Low Power Channel and the Hot Assembly Channel at the Top of the Core Showing Increased Axial Flow When the Low Power Channel to Average Channels Gap Lengths and Resistance is Increased

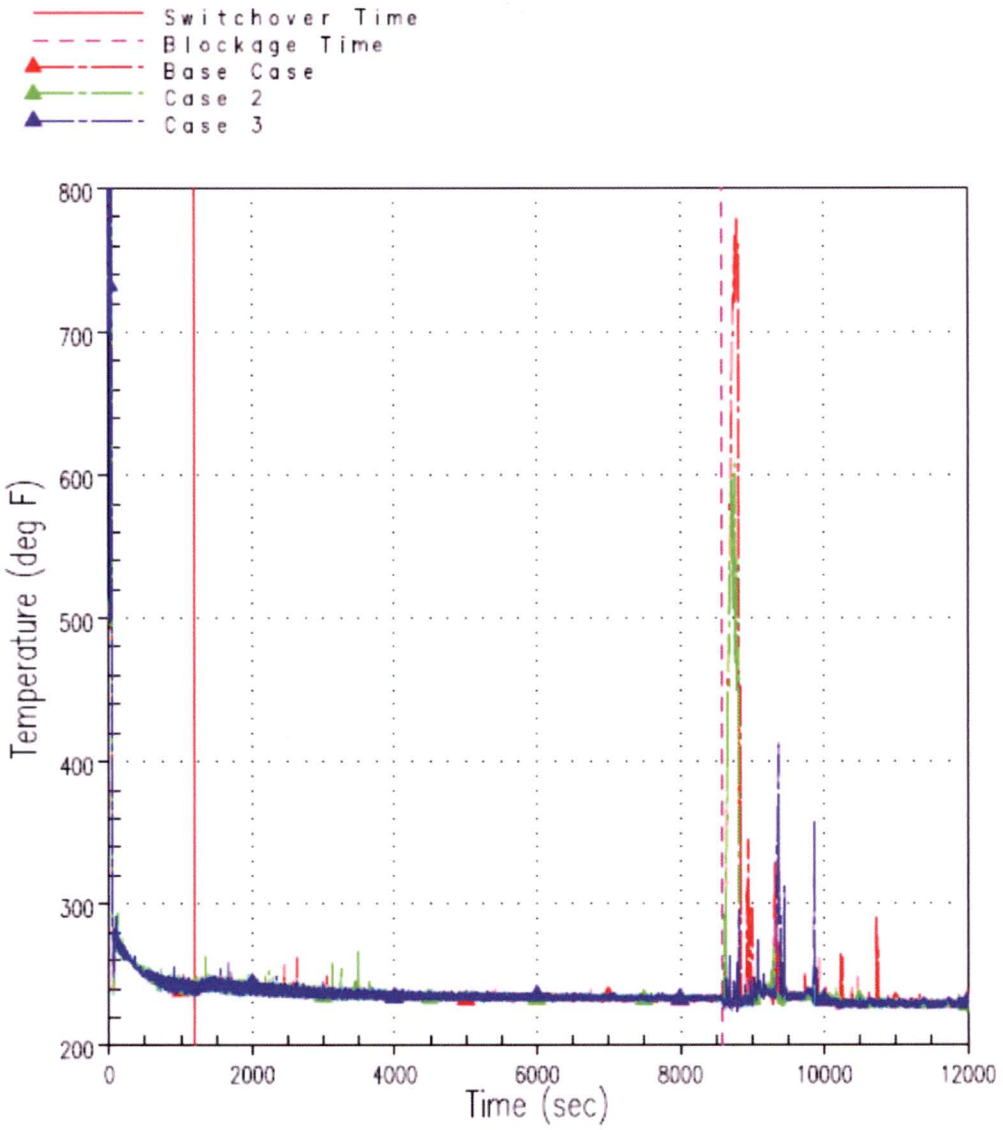

Figure RAI-4.27-10 The Effect of Increased Low Power Channel to Average Channels Gap Lengths and Resistance on Peak Cladding Temperature

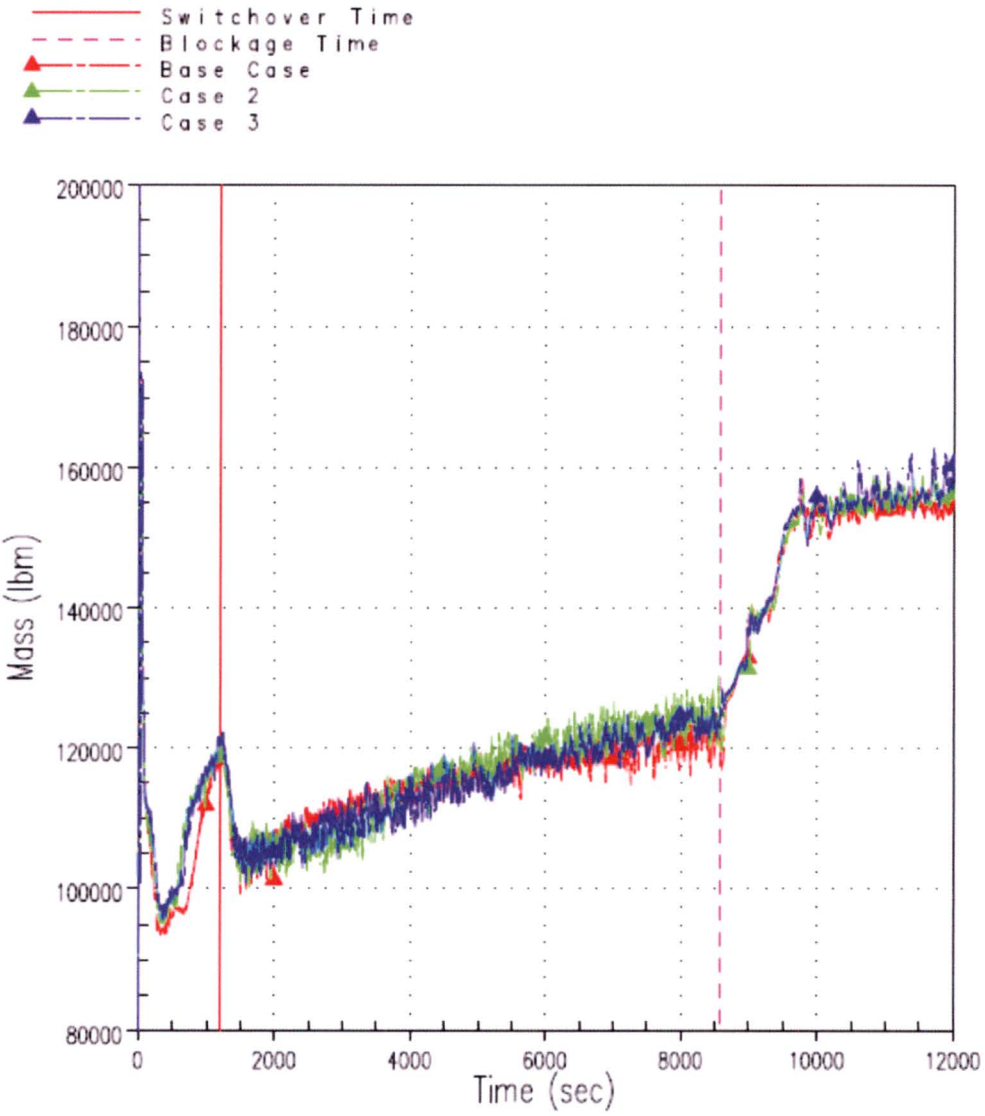

Figure RAI-4.27-11 The Effect of Increased Low Power Channel to Average Channels Gap Lengths and Resistance on Reactor Vessel Fluid Mass

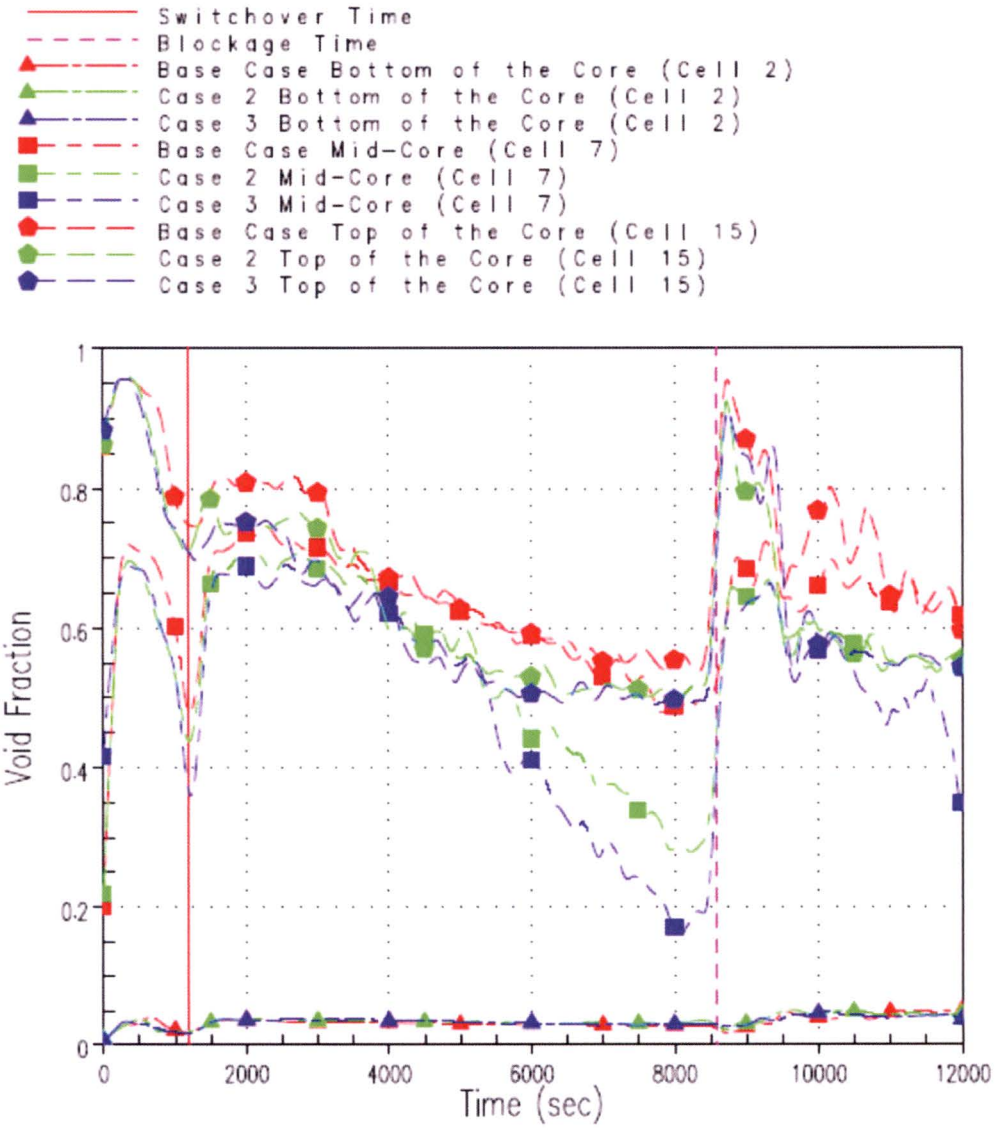

Figure RAI-4.27-12 The Effect of Increased Low Power Channel to Average Channels Gap Lengths and Resistance, and Increased Spacer Grid Resistance on the Low Power Channel Axial Void Distribution

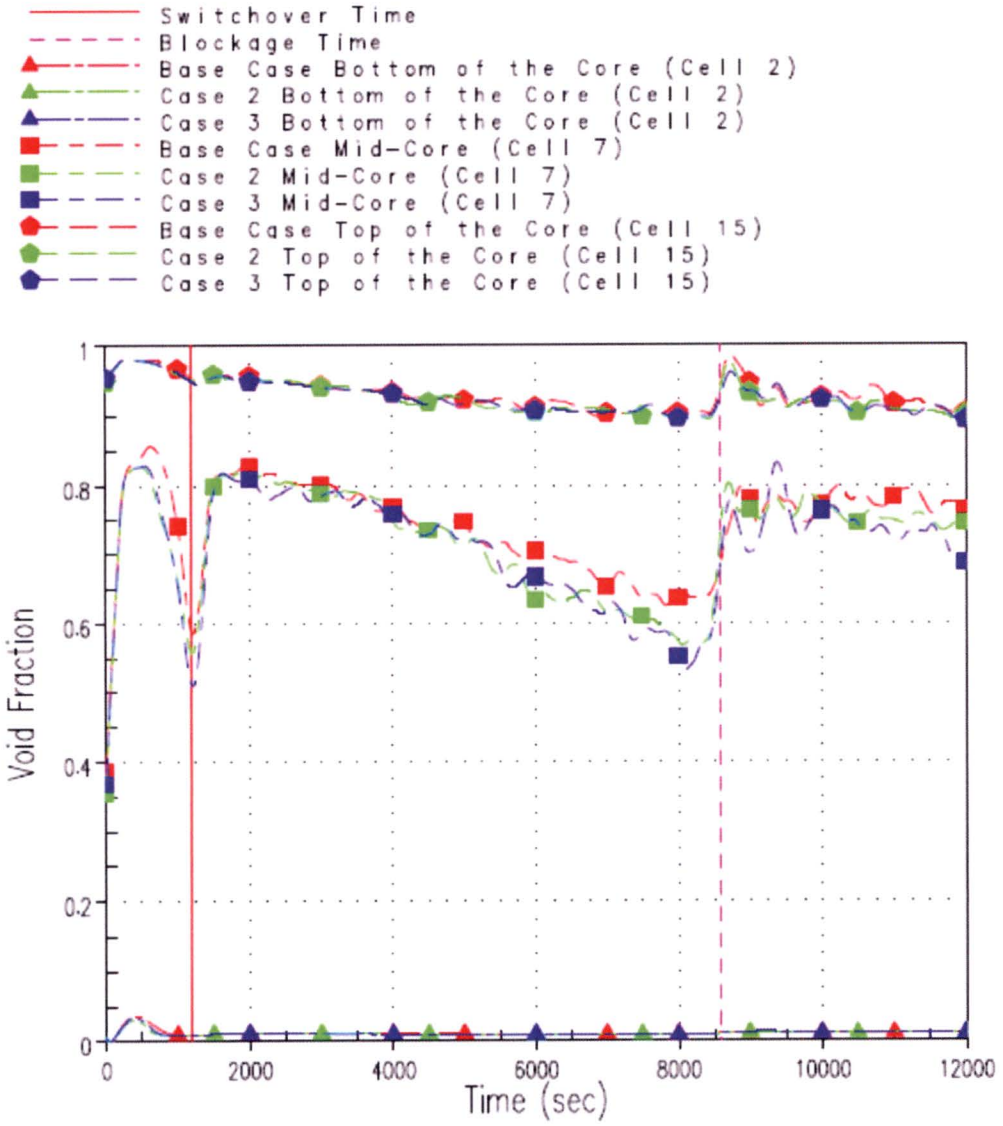

Figure RAI-4.27-13 The Effect of Increased Low Power Channel to Average Channels Gap Lengths and Resistance, and Increased Spacer Grid Resistance on the Hot Assembly Channel Axial Void Distribution

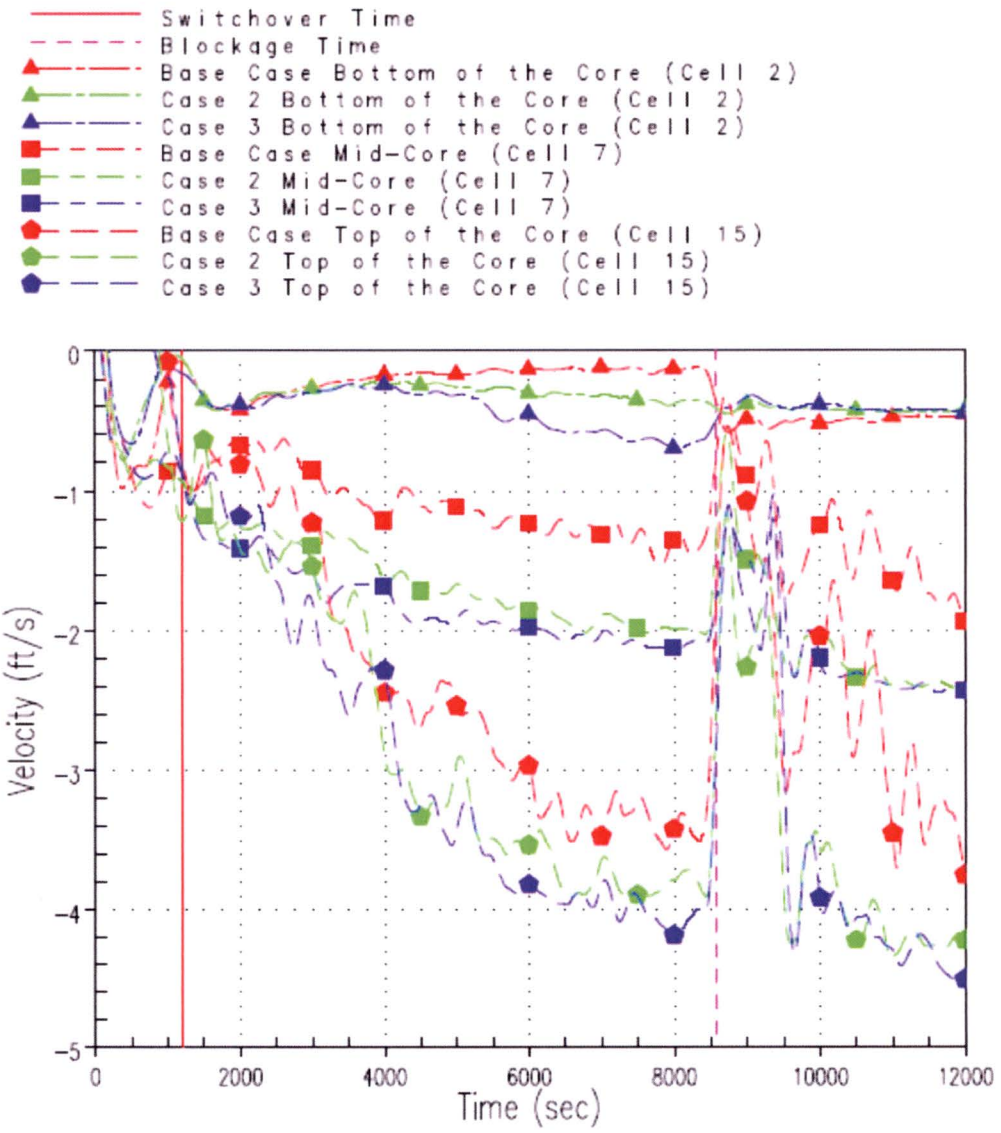

Figure RAI-4.27-14 The Effect of Increased Low Power Channel to Average Channels Gap Lengths and Resistance, and Increased Spacer Grid Resistance on the Low Power Channel Axial Liquid Phase Velocity

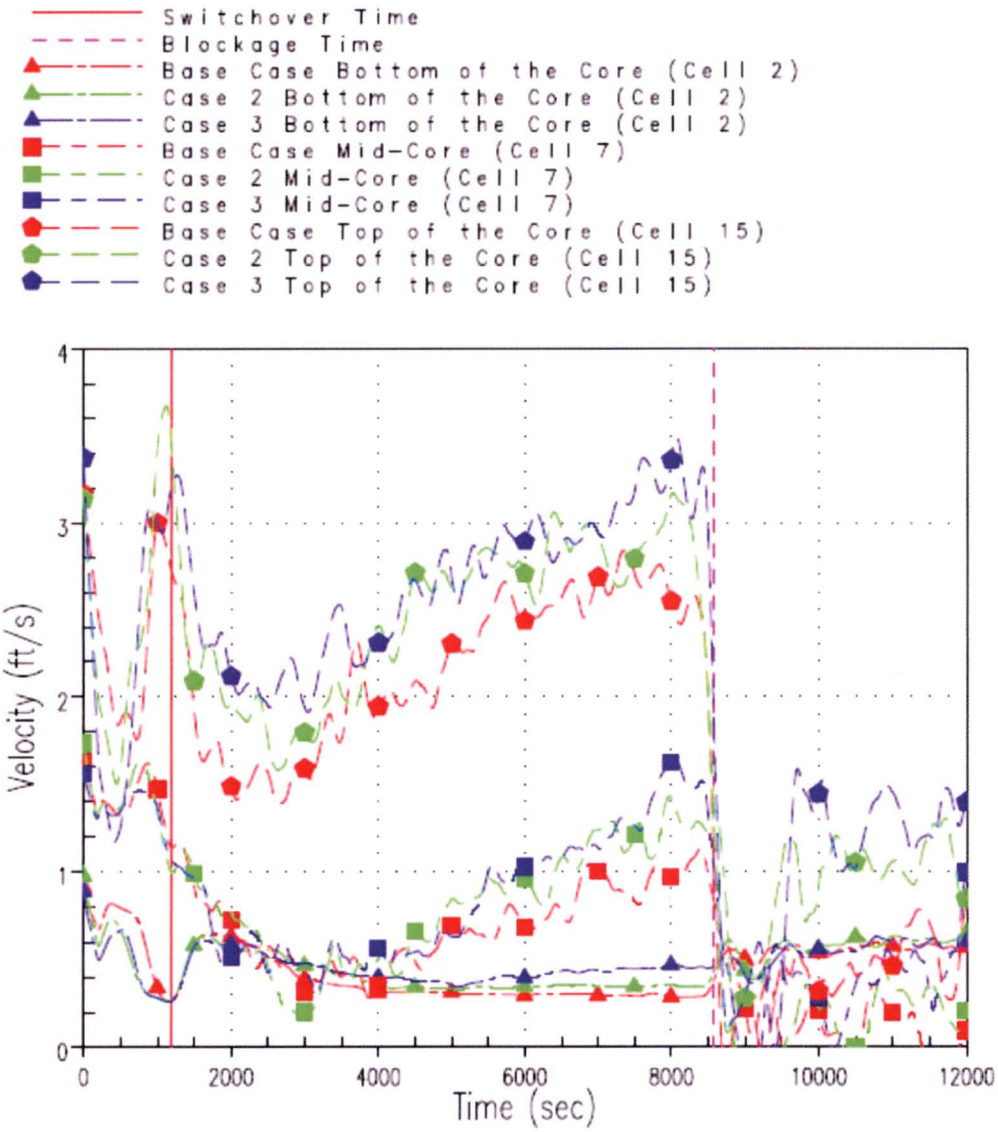

Figure RAI-4.27-15 The Effect of Increased Low Power Channel to Average Channels Gap Lengths and Resistance, and Increased Spacer Grid Resistance on the Hot Assembly Channel Axial Liquid Phase Velocity

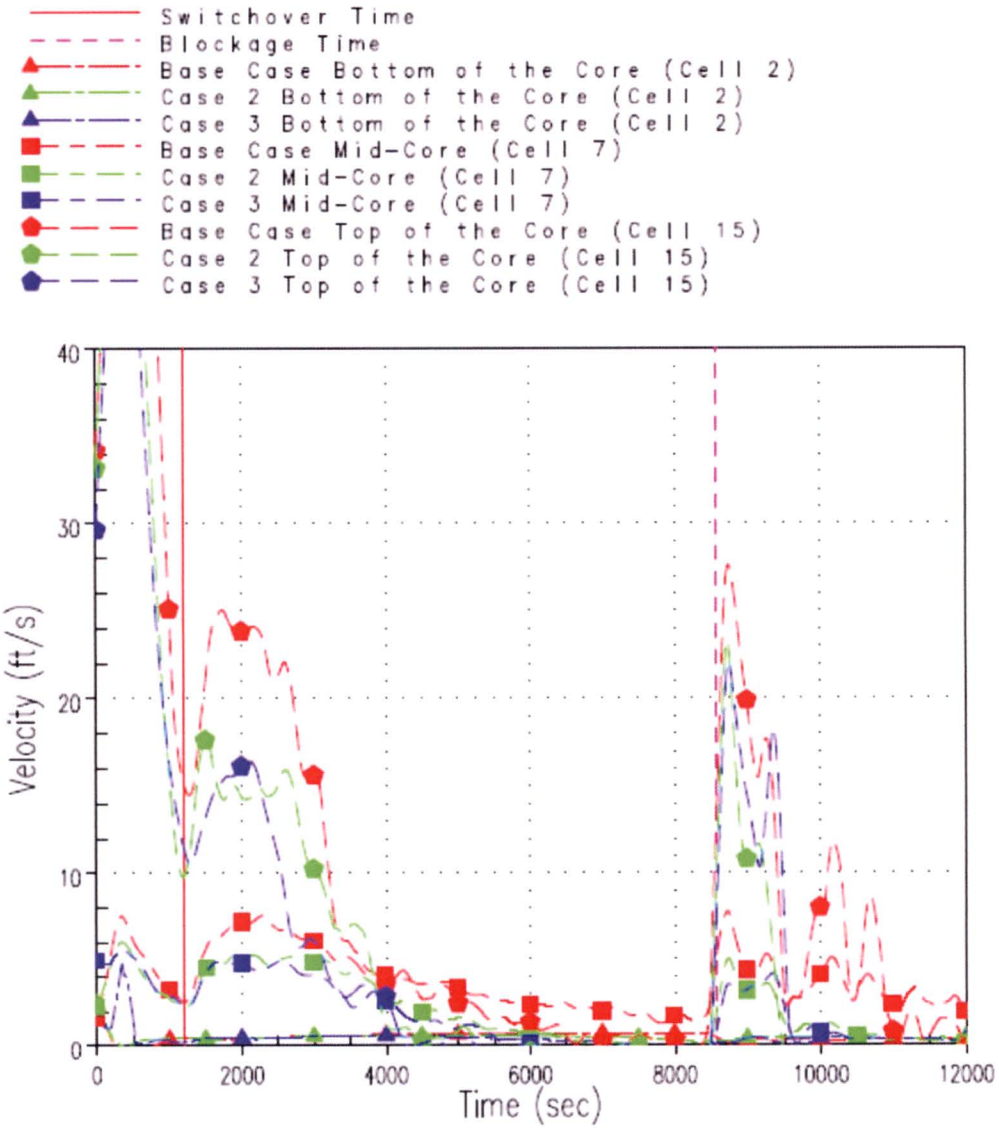

Figure RAI-4.27-16 The Effect of Increased Low Power Channel to Average Channels Gap Lengths and Resistance, and Increased Spacer Grid Resistance on the Low Power Channel Axial Vapor Phase Velocity

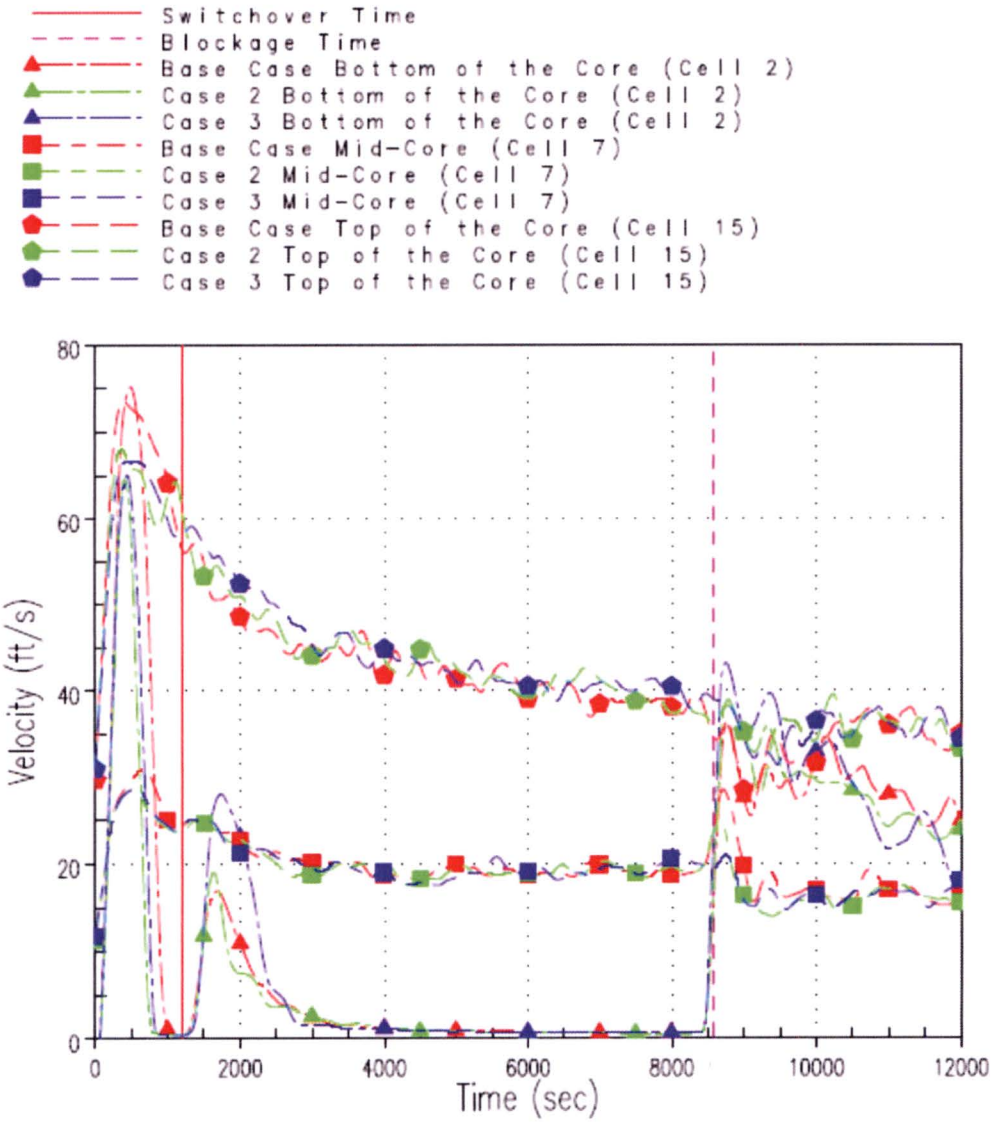

Figure RAI-4.27-17 The Effect of Increased Low Power Channel to Average Channels Gap Lengths and Resistance, and Increased Spacer Grid Resistance on the Hot Assembly Channel Axial Vapor Phase Velocity

The second comparison is made between Cases 4 and 5, which vary the resistance between the average non-guide tube channel and the hot assembly channel (Gap 16). The axial resistance at spacer grid elevations in all the core channels is also increased in these cases.

Figures RAI-4.27-18 through RAI-4.27-20 show the lateral integrated mass flow rate from the average non-guide tube channel to the hot assembly channel (Gap 16), at the bottom, mid, and top core elevations, respectively. A positive mass flow indicates that flow is from the average non-guide tube channel to the hot assembly channel. As expected, increasing the gap resistance decreases the lateral flow through each gap.

Figures RAI-4.27-18 through RAI-4.27-20 also highlights the effect of increased gap resistance on the two-phase mixing patterns in the average non-guide tube and hot assembly core channels. It is seen that flow enters the hot assembly channel from the non-guide tube channel at the bottom and top of the core, while flow enters the average non-guide tube channel from the hot assembly channel at the mid-core elevation. Increasing the gap length and resistance between these channels reduces the magnitude of the circulation pattern observed in the base case.

Figures RAI-4.27-21 through RAI-4.27-23 show the integrated axial mass flow rates in the average non-guide tube channel and the hot assembly channel at the bottom of the core, mid-core, and the top of the core, respectively. In the figures, the average non-guide tube channel mass flow is normalized on a per fuel assembly basis in order to provide a direct comparison with the hot assembly channel, which represents a single fuel assembly. As the figures indicate, upflow is present in both channels. In these sensitivity cases, the magnitude of the axial flows is shown to decrease with increased axial resistance at the spacer grid locations.

Figure RAI-4.27-24 shows the PCT, and indicates that the PCT prediction is less sensitive in this comparison, compared to the previous one. The case that increases the average non-guide tube to hot assembly channel gap resistance by 50% and the axial resistance at spacer grid elevations in all core channels results in a PCT that is slightly higher than the base case. Figure RAI-4.27-25 shows the vessel fluid mass, and indicates that the vessel fluid mass is not significantly impacted by varying the core channel gap and spacer grid resistances. There is some deviation early in the sump recirculation phase of the transient, but the vessel mass prior to and after the application of complete core inlet blockage is similar in all cases. This result demonstrates that varying these parameters does not significantly impact the overall reactor vessel system behavior, and the PCT sensitivity is governed by the local flow behavior in the core channels.

Figures RAI-4.27-26 and RAI-4.27-27 show the axial void distribution in the average non-guide tube channel and the hot assembly channel, respectively. The figures indicate that the increased gap resistance and spacer grid resistance applied in these sensitivities do not have as significant an impact to the void fraction as the previous sensitivities did. This indicates that the PCT sensitivity is consistent with the void fraction sensitivity. If the void fraction varies significantly, it is expected that the PCT will vary significantly.

Figures RAI-4.27-28 and RAI-4.27-29 show the axial liquid velocity in the average non-guide tube channel and the hot assembly channel, respectively. Similar to void fraction, the velocity in these cases does not vary as much as in the previous cases.

Figures RAI-4.27-30 and RAI-4.27-31 show the axial vapor velocity in the average non-guide tube channel and the hot assembly channel, respectively. The figures show little variation in the axial vapor phase velocities.

Trends observed in the figures presented above demonstrate that increasing the gap resistance between the average non-guide tube and the hot assembly channel (Gap 16), and increasing the spacer grid axial resistances in all core channels changes the flow patterns observed in the core region. However, the change is not as significant as that observed when the gap lengths and the gap resistances between the low power channel and the average core channels was increased. Although the PCT in the case completed with the highest gap resistance produced a slightly higher PCT compared to the base case, the sensitivity to PCT was not as significant in these cases.

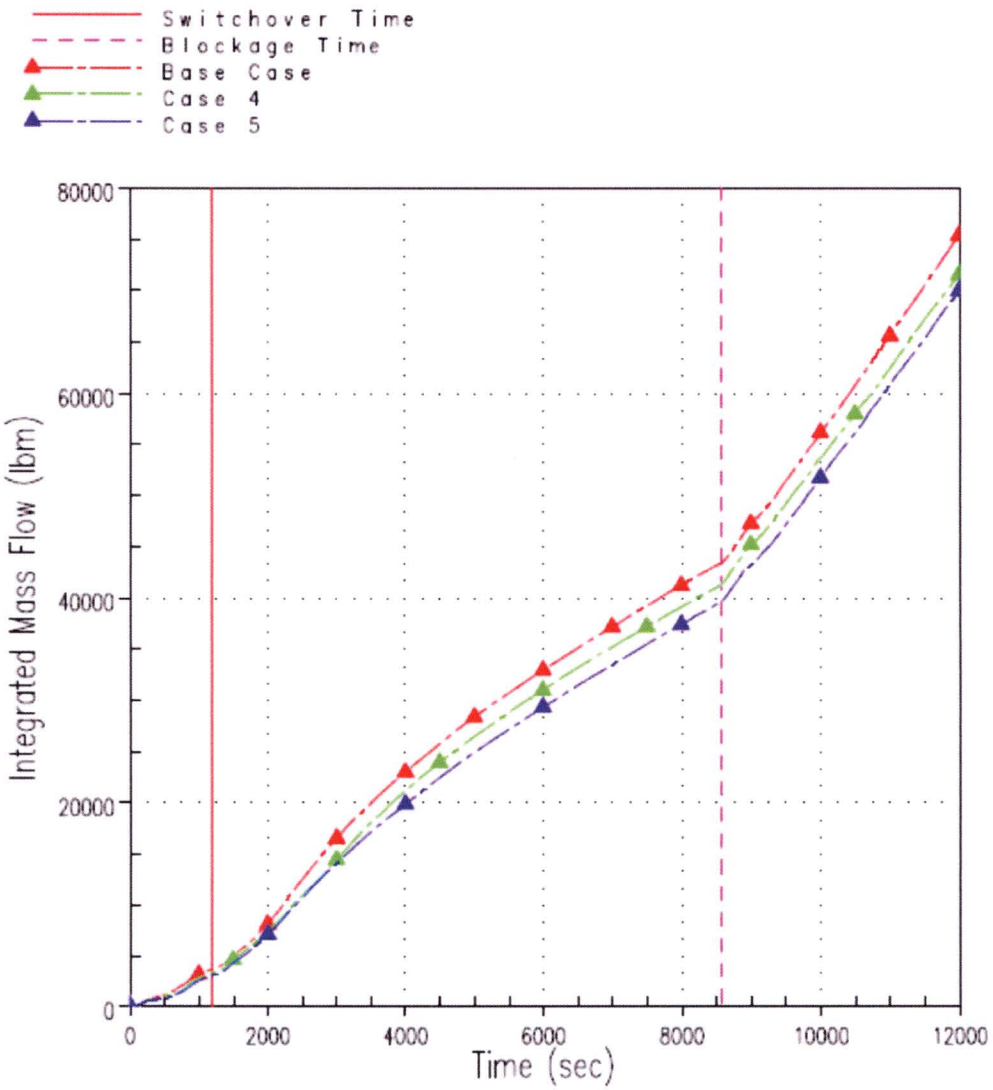

Figure RAI-4.27-18 Integrated Mass Flow Rate from the Average Non-Guide Tube Channel to the Hot Assembly Channel at the Bottom of the Core Showing the Effect of Increased Gap Resistance (Gap 16)

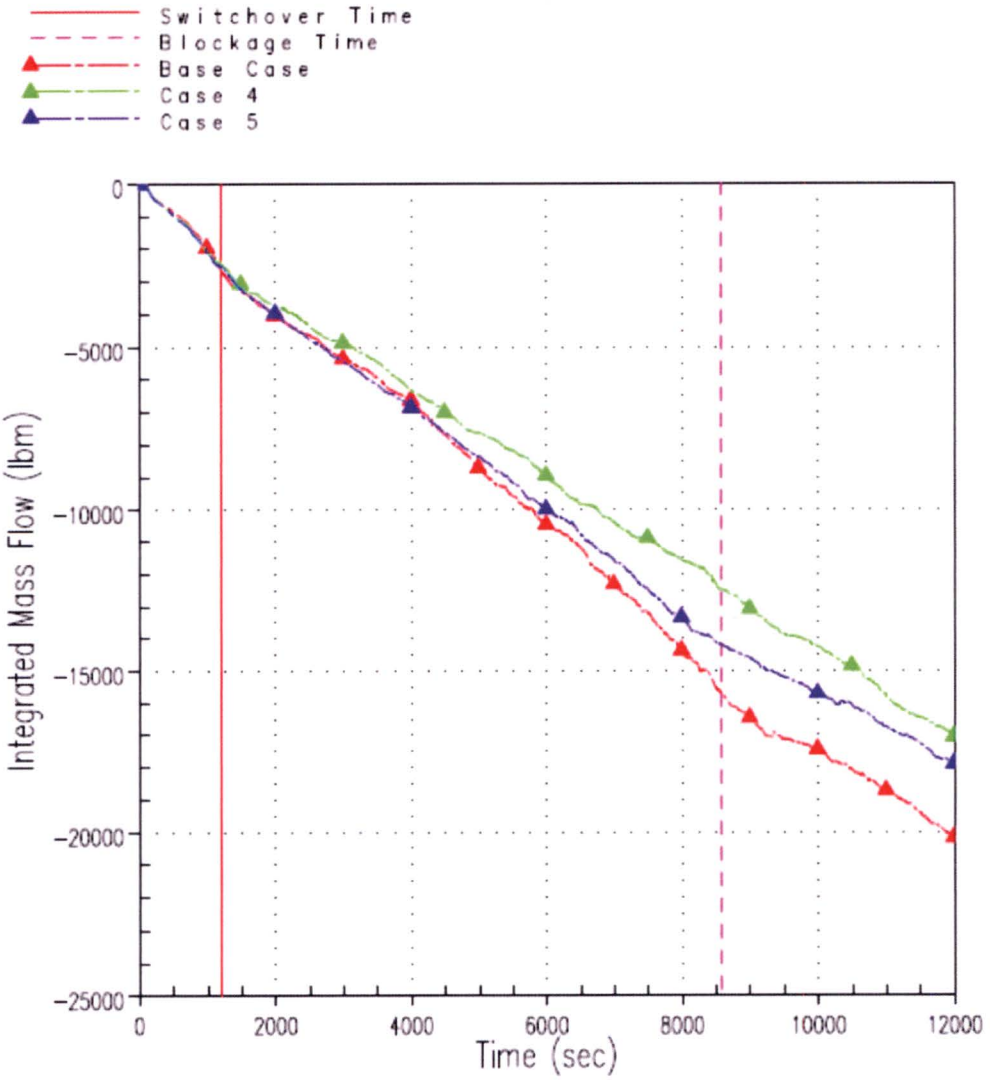

Figure RAI-4.27-19 Integrated Mass Flow Rate from the Average Non-Guide Tube Channel to the Hot Assembly Channel Mid-Core Showing the Effect of Increased Gap Resistance (Gap 16)

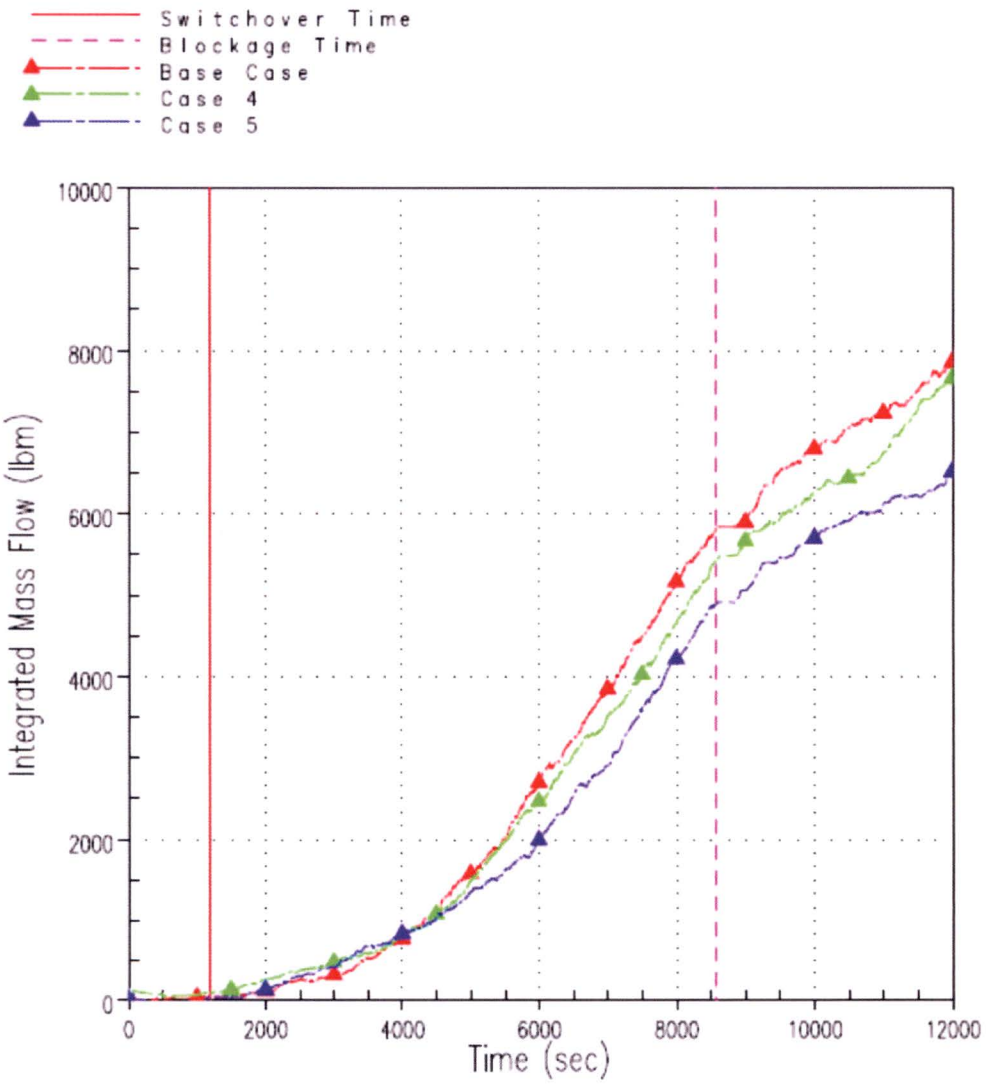

Figure RAI-4.27-20 Integrated Mass Flow Rate from the Average Non-Guide Tube Channel to the Hot Assembly Channel at the Top of the Core Showing the Effect of Increased Gap Resistance (Gap 16)

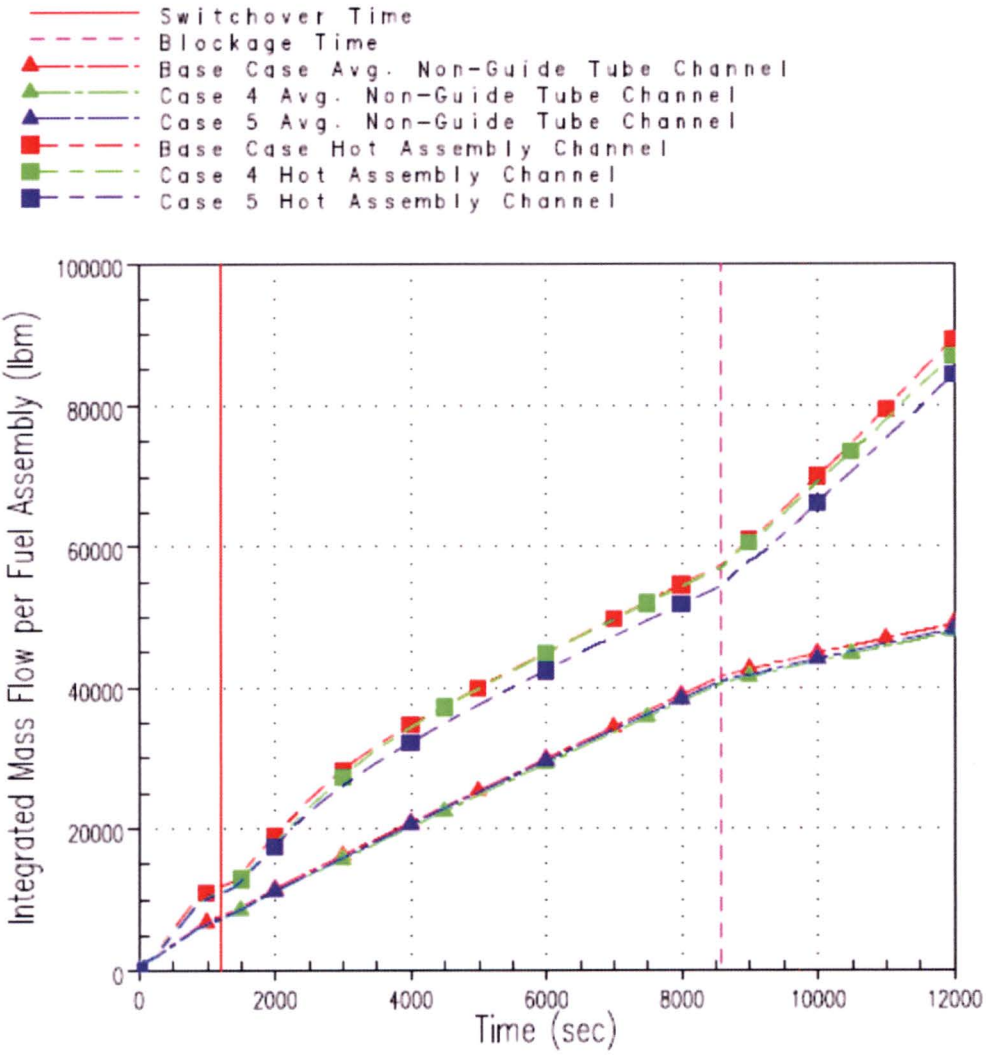

Figure RAI-4.27-21 Integrated Axial Mass Flow Rates in the Average Non-Guide Tube Channel and the Hot Assembly Channel at the Bottom of the Core Showing the Effect of Increased Gap Resistance Between the Average Non-Guide Tube Channel and the Hot Assembly Channel (Gap 16)

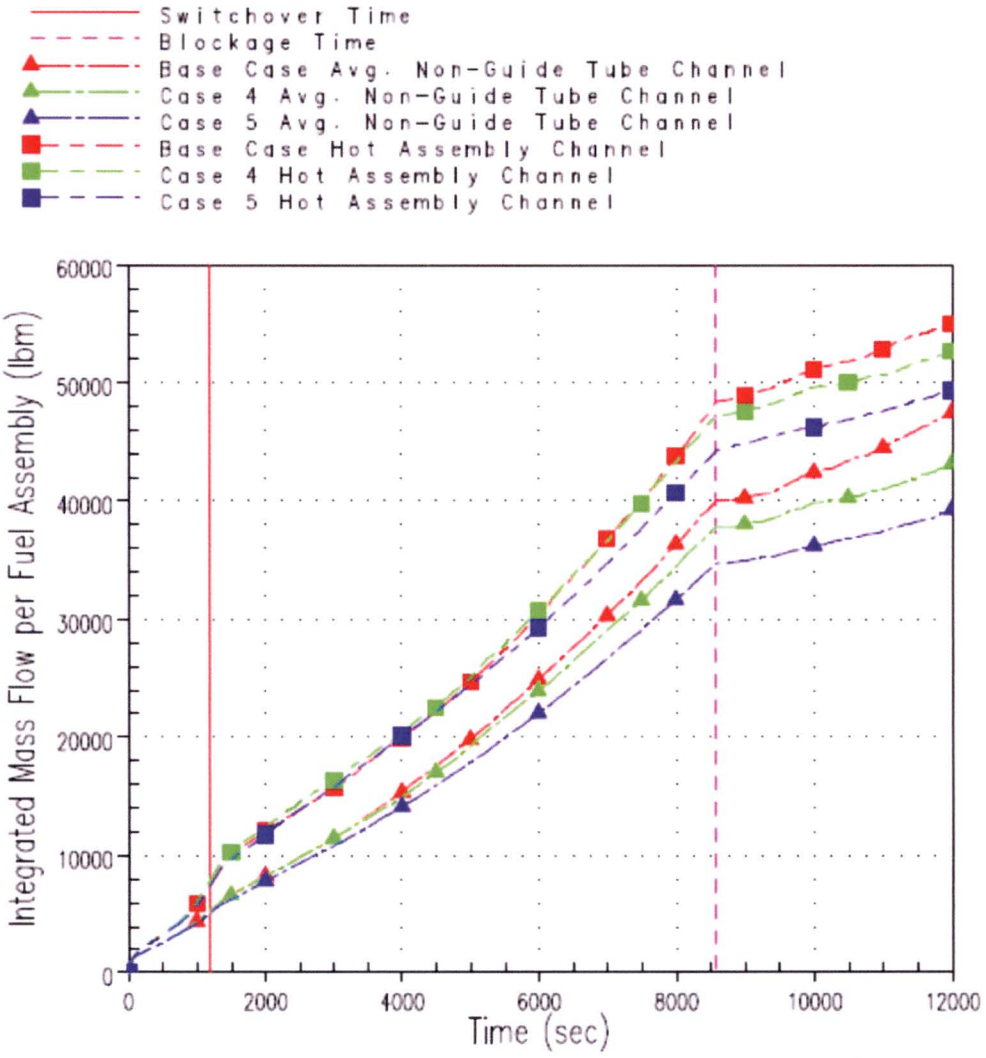

Figure RAI-4.27-22 Integrated Axial Mass Flow Rates in the Average Non-Guide Tube Channel and the Hot Assembly Channel Mid-Core Showing the Effect of Increased Gap Resistance Between the Average Non-Guide Tube Channel and the Hot Assembly Channel (Gap 16)

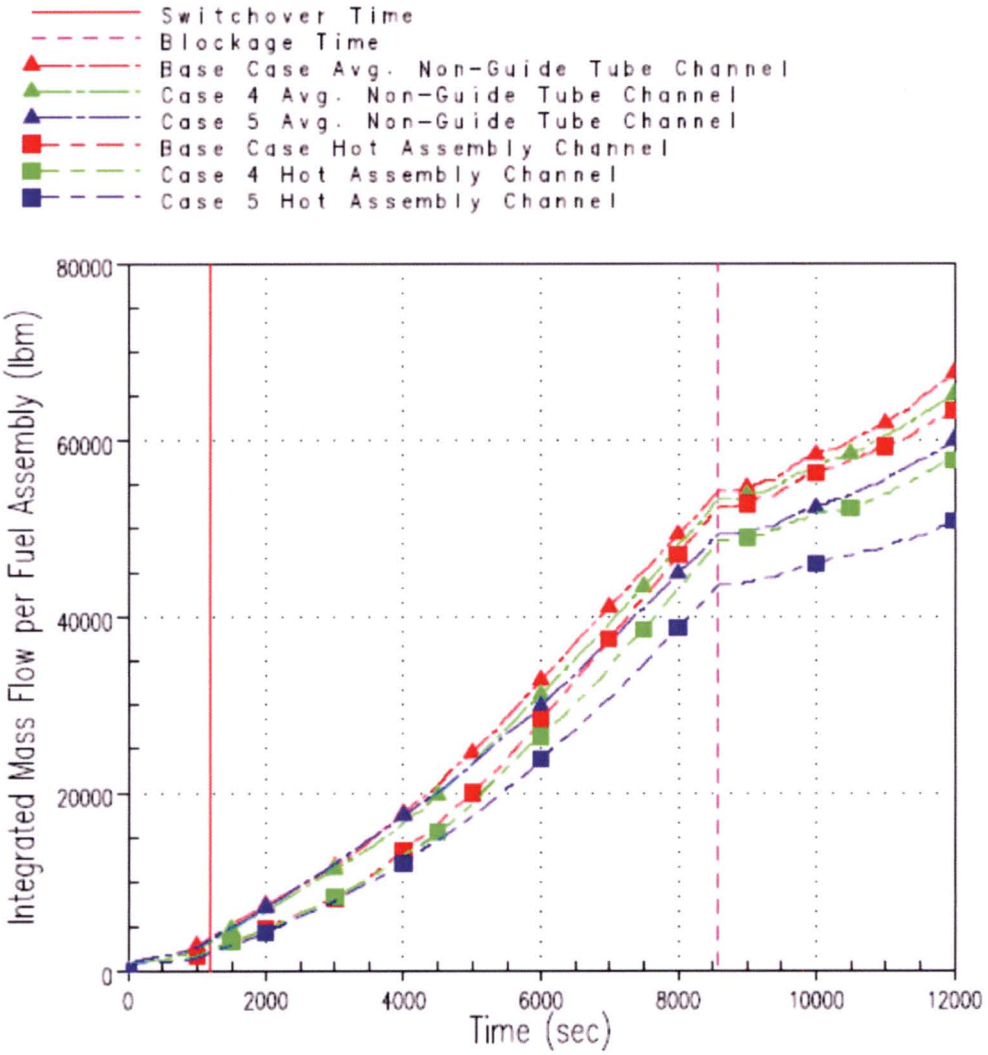

Figure RAI-4.27-23 Integrated Axial Mass Flow Rates in the Average Non-Guide Tube Channel and the Hot Assembly Channel at the Top of the Core Showing the Effect of Increased Gap Resistance Between the Average Non-Guide Tube Channel and the Hot Assembly Channel (Gap 16)

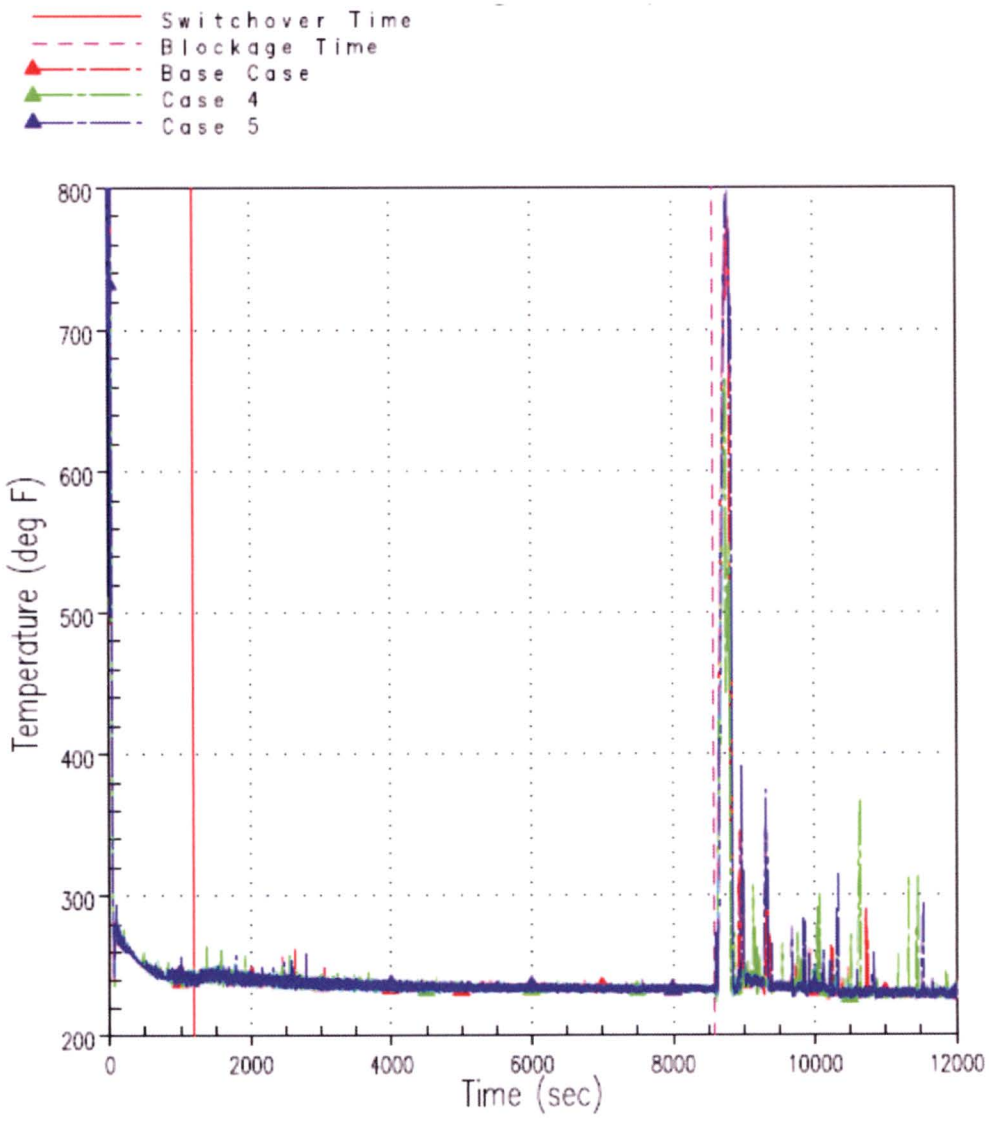

Figure RAI-4.27-24 The Effect of Increased Average Non-Guide Tube Channel to Hot Assembly Channel Gap Resistance on Peak Cladding Temperature

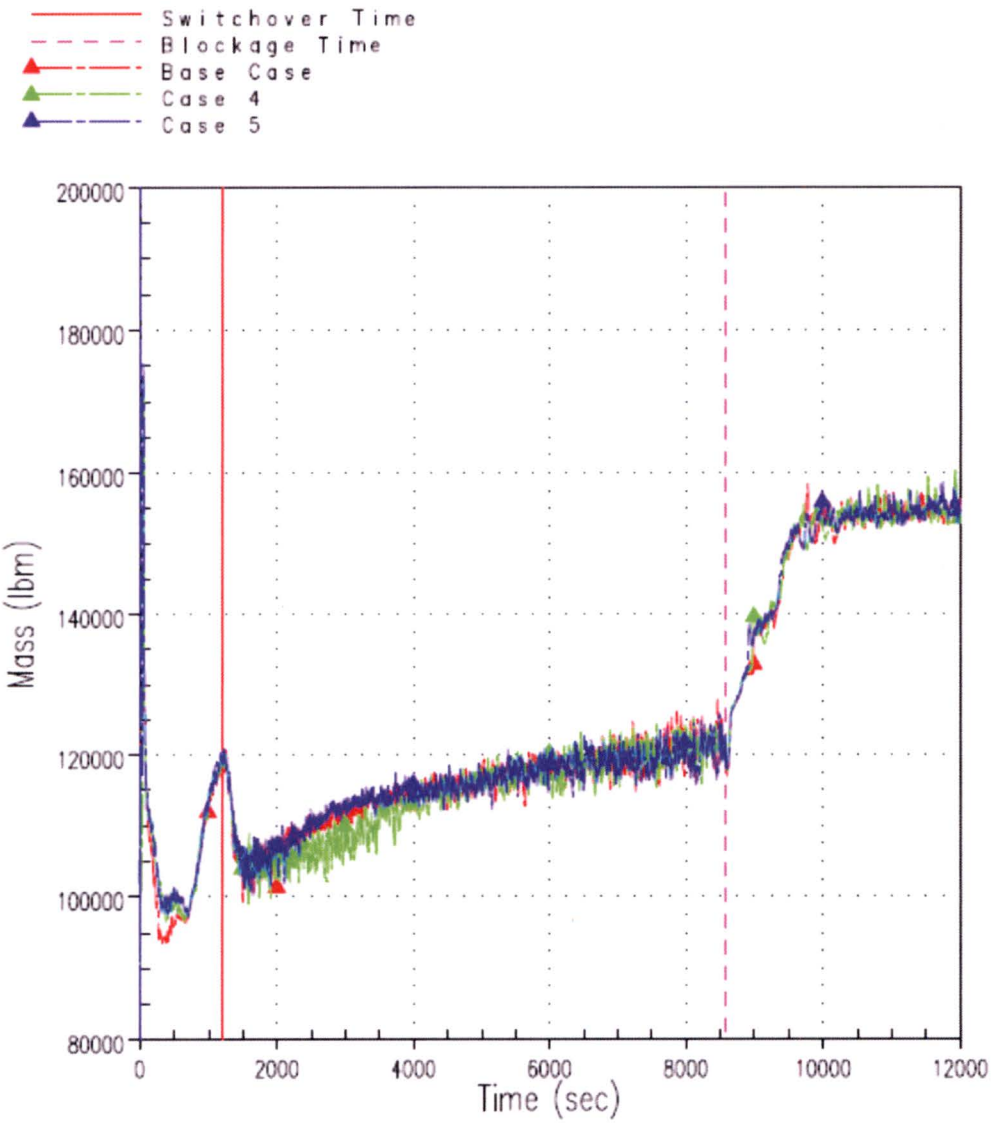

Figure RAI-4.27-25 The Effect of Increased Average Non-Guide Tube Channel to Hot Assembly Channel Gap Resistance on Reactor Vessel Fluid Mass

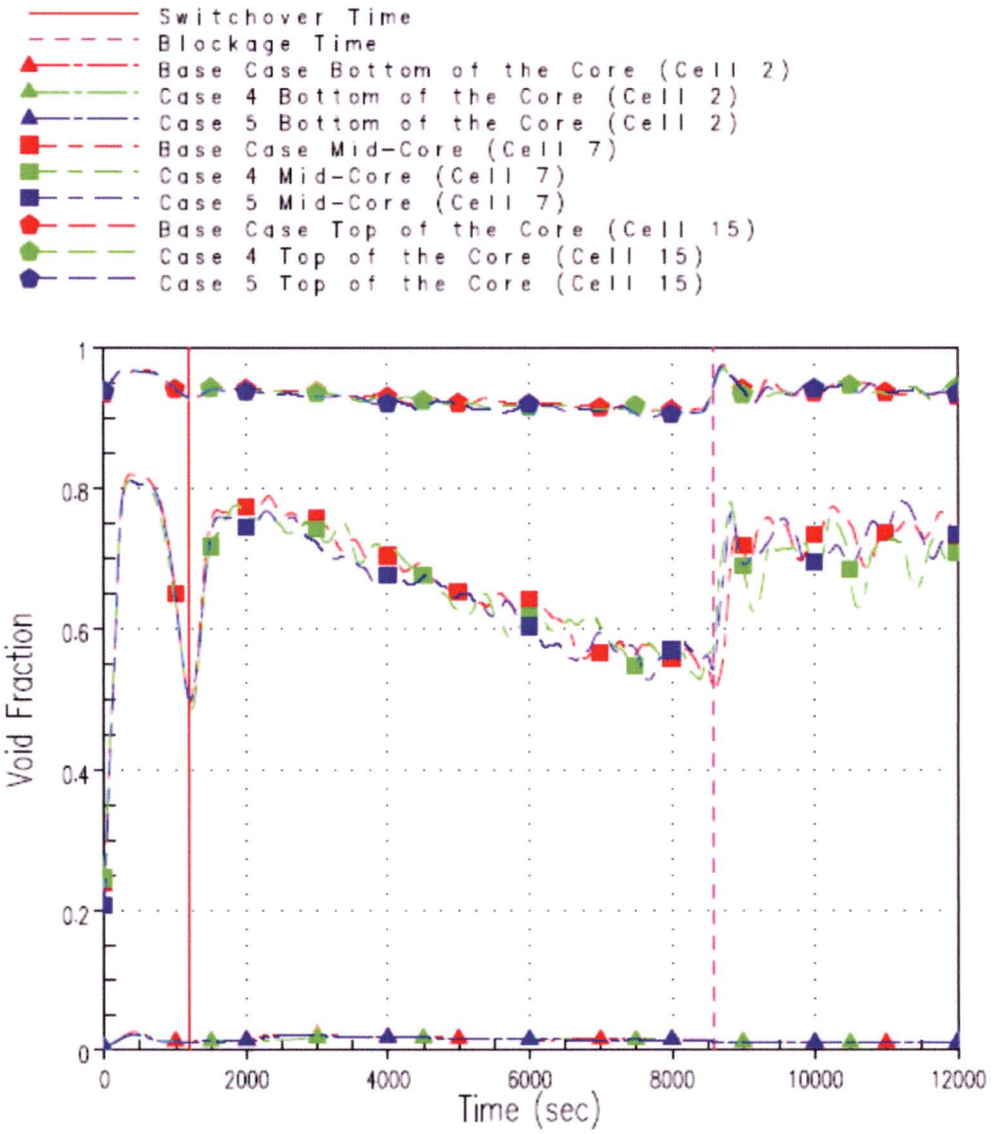

Figure RAI-4.27-26 The Effect of Increased Average Non-Guide Tube Channel to Hot Assembly Channel Gap Resistance, and Increased Spacer Grid Resistance on the Average Non-Guide Tube Channel Axial Void Distribution

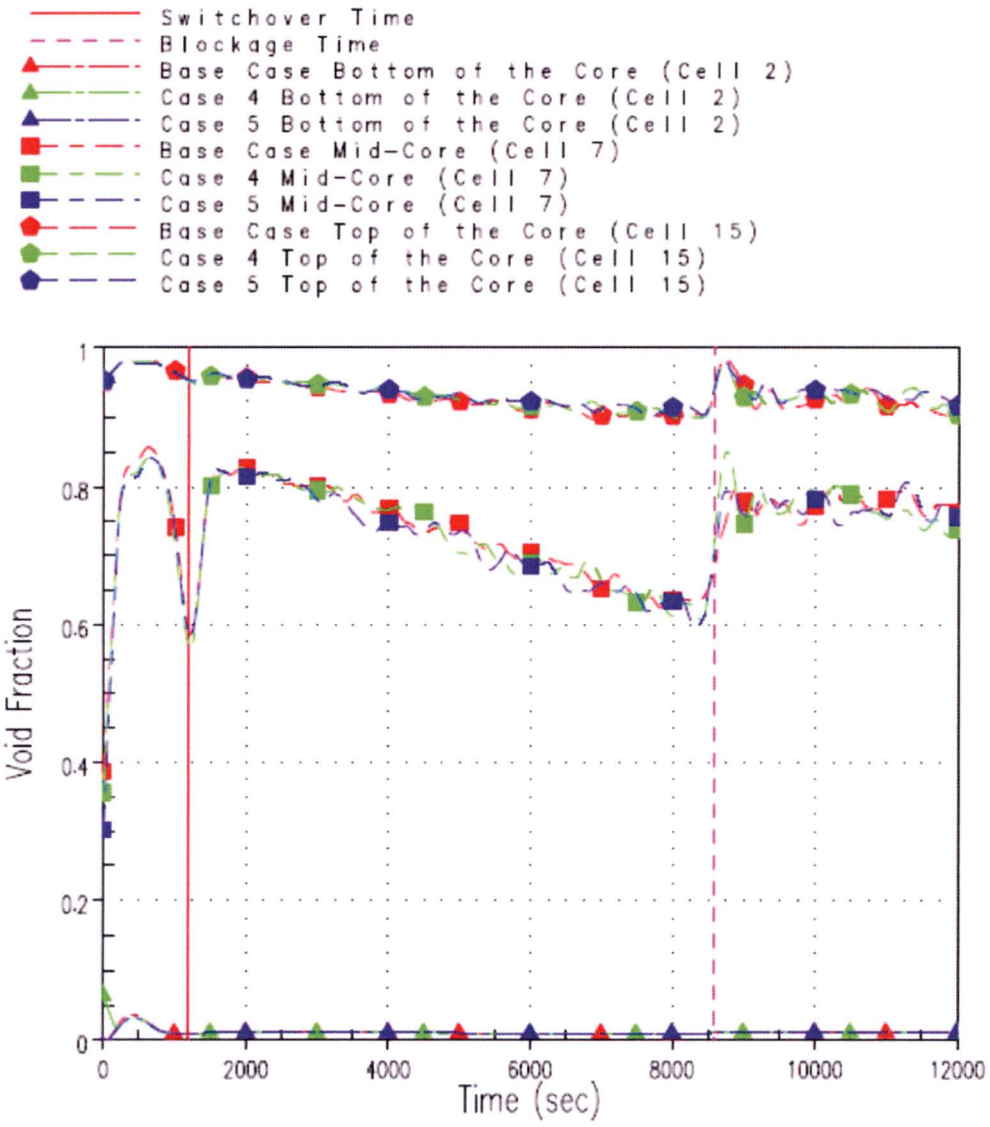

Figure RAI-4.27-27 The Effect of Increased Average Non-Guide Tube Channel to Hot Assembly Channel Gap Resistance, and Increased Spacer Grid Resistance on the Hot Assembly Channel Axial Void Distribution

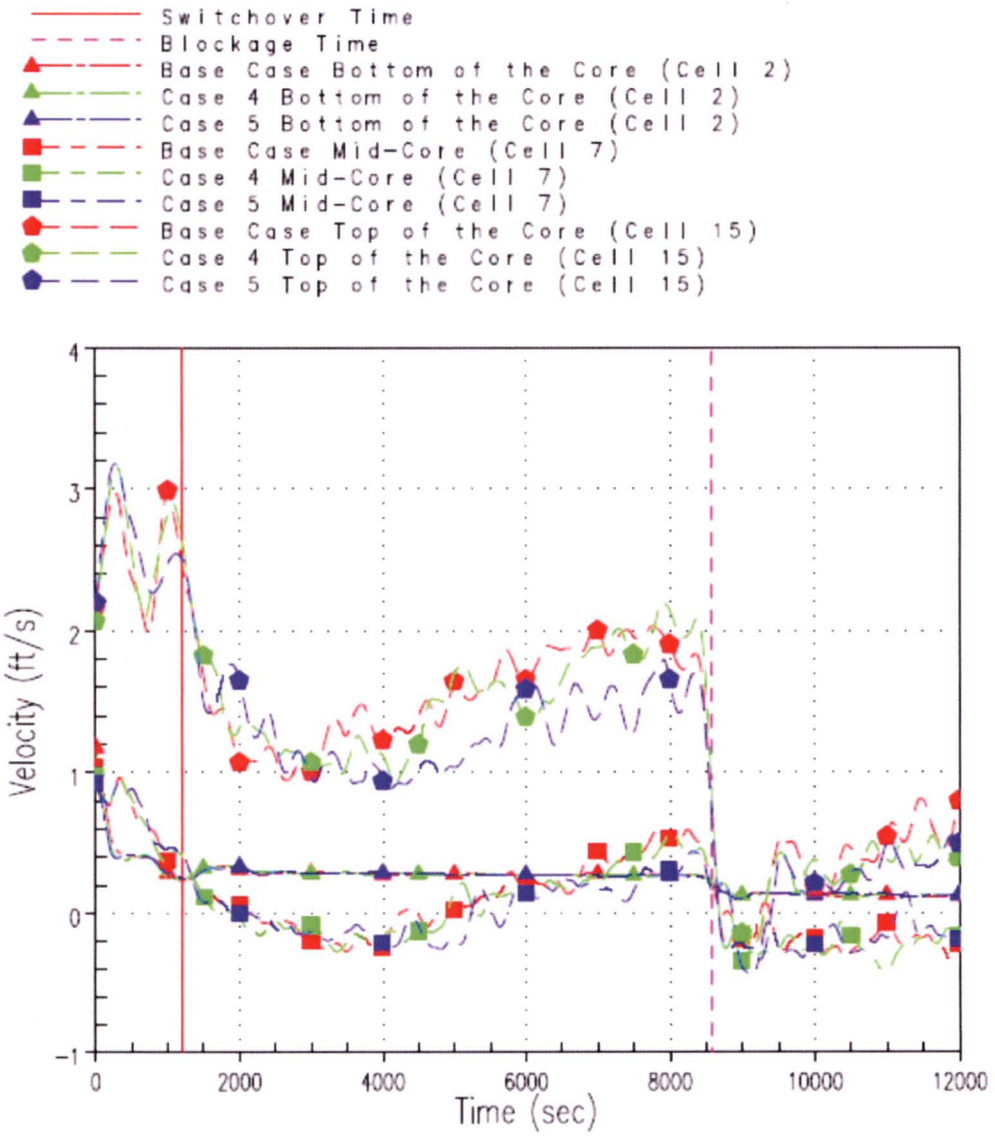

Figure RAI-4.27-28 The Effect of Increased Average Non-Guide Tube Channel to Hot Assembly Channel Gap Resistance, and Increased Spacer Grid Resistance on the Average Non-Guide Tube Channel Axial Liquid Phase Velocity

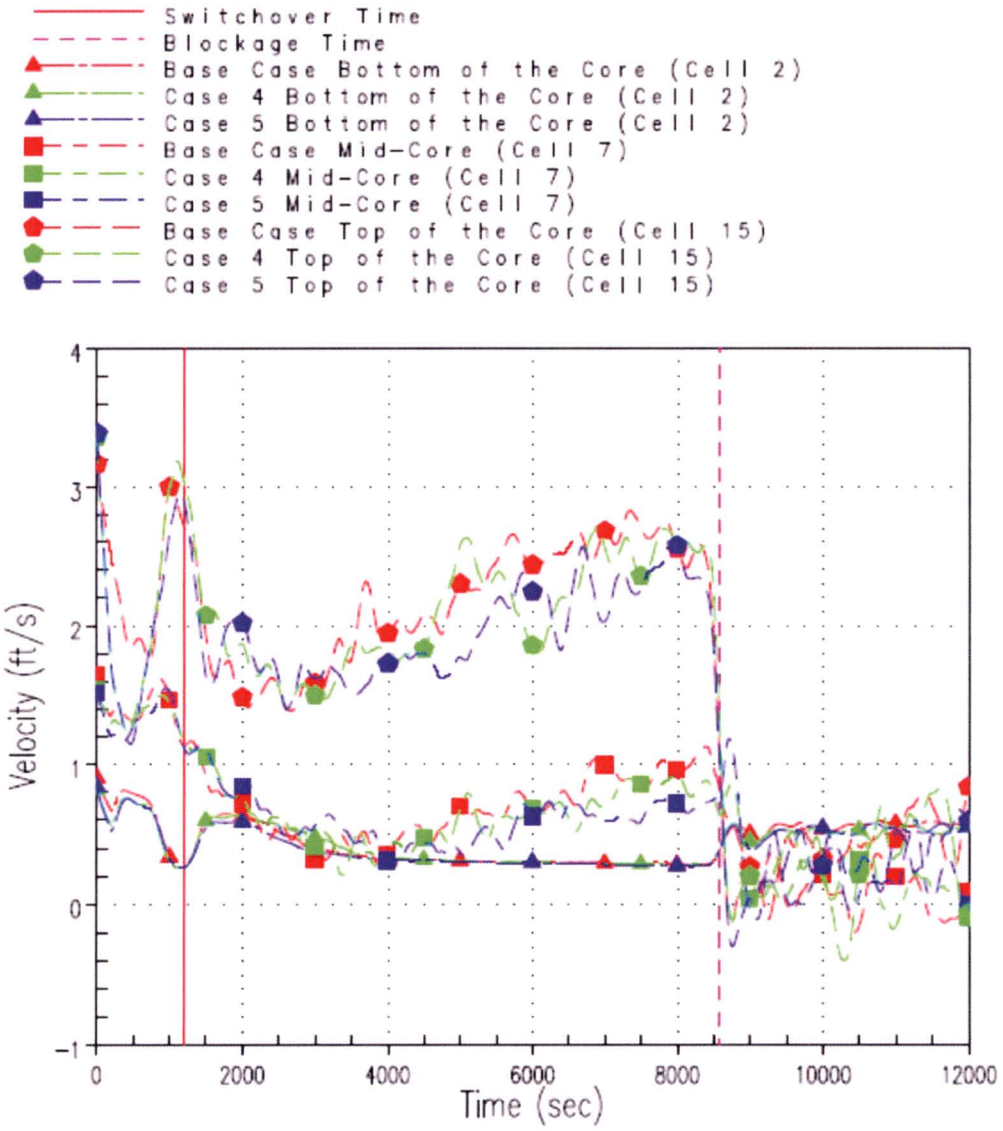

Figure RAI-4.27-29 The Effect of Increased Average Non-Guide Tube Channel to Hot Assembly Channel Gap Resistance, and Increased Spacer Grid Resistance on the Hot Assembly Channel Axial Liquid Phase Velocity

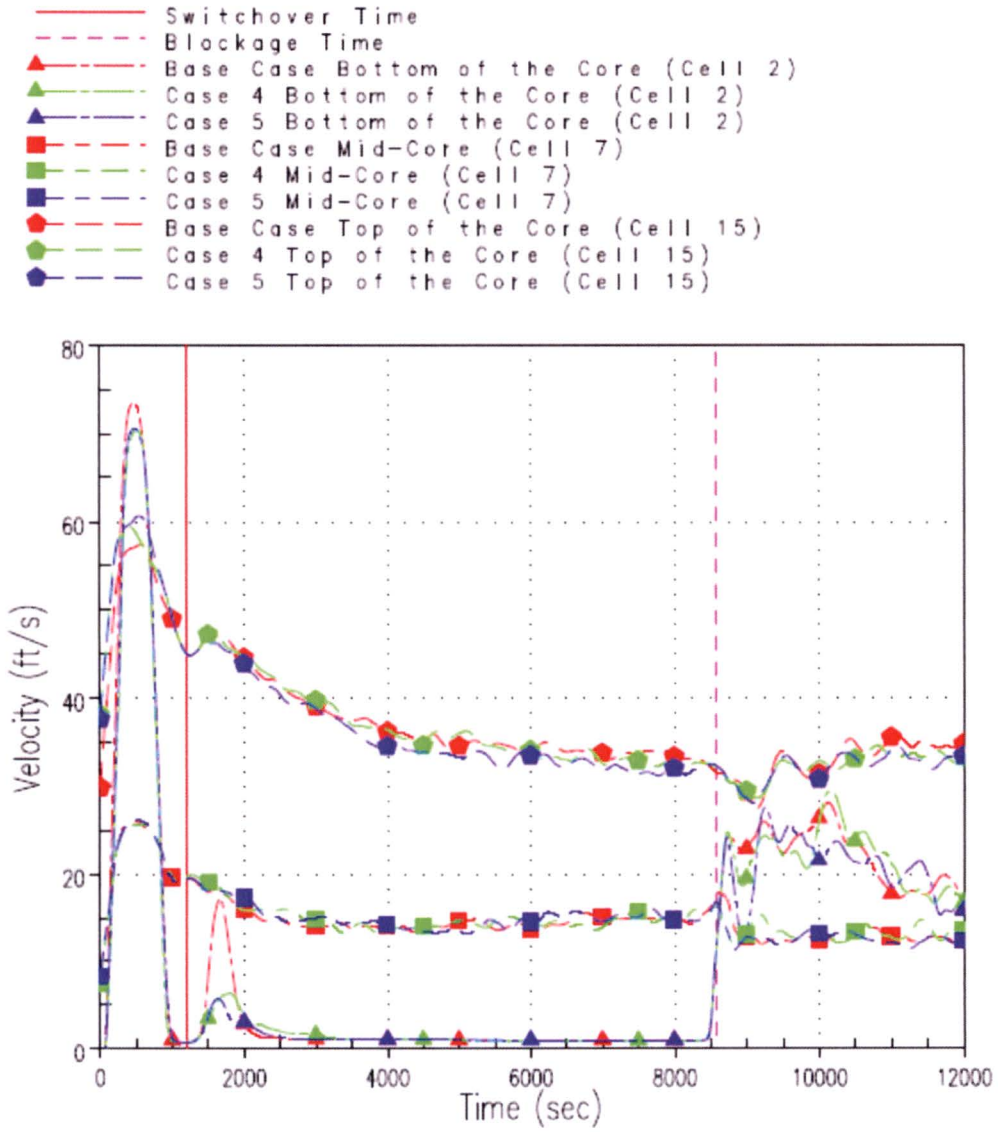

Figure RAI-4.27-30 The Effect of Increased Average Non-Guide Tube Channel to Hot Assembly Channel Gap Resistance, and Increased Spacer Grid Resistance on the Average Non-Guide Tube Channel Axial Vapor Phase Velocity

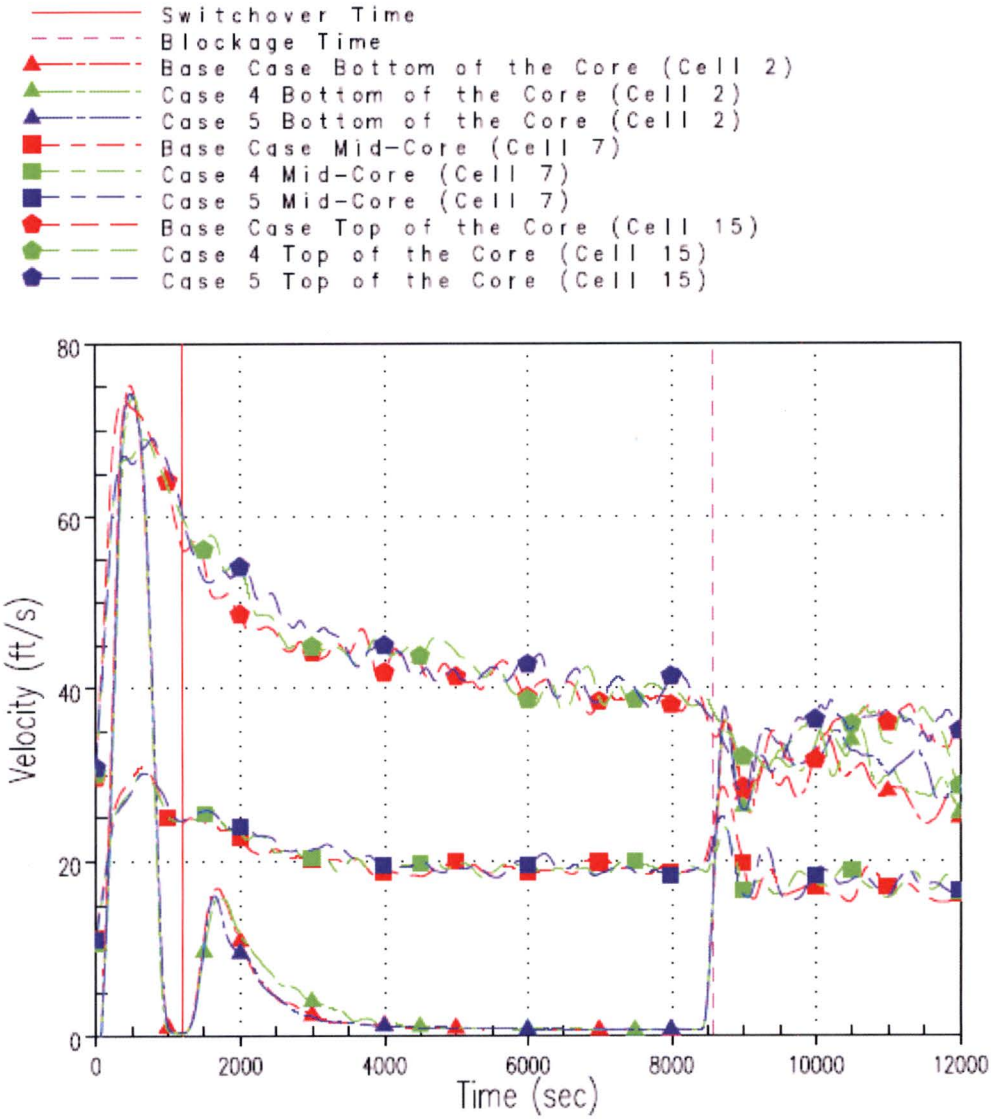

Figure RAI-4.27-31 The Effect of Increased Average Non-Guide Tube Channel to Hot Assembly Channel Gap Resistance, and Increased Spacer Grid Resistance on the Hot Assembly Channel Axial Vapor Phase Velocity